

Aerodynamics and Wind-Field Models for Wind Turbine Control

María Lourdes Gala Santos

A thesis presented in fulfilment of the requirements for the
degree of doctor of Philosophy

CDT in Wind Energy Systems
Department of Electronic and Electrical Engineering
University of Strathclyde
Glasgow G1 1XW
Scotland, UK

March 2018

This thesis is the result of the author's original research. It has been composed by the author and has not previously been submitted for examination which has led to the award of a degree.

The copyright of this thesis belongs to the author under the terms of the United Kingdom Copyrights Act as qualified by University of Strathclyde regulation 3.50. Due acknowledgements must always be made of the use of any material contained in, or derived from, this thesis.

Dedicated to my Parents Lourdes Santos Martín and José María Gala Rodríguez

“With ordinary talent and extraordinary perseverance, all things are attainable.” –
Sir Thomas Fowell Buxton

Acknowledgements:

Firstly, I would like to thank EPSRC for giving the opportunity of pursuing this PhD through their grant EP/G037728/1.

I would like to thank everyone that has supported me and believed in me during this long road that has been writing my thesis: there have been many whose encouragement and goodwill have helped me along the way. Before I start, I can but apologise that I have not been able to name each and every one of them, yet rest assured,

I am deeply grateful for all the support given.

Thank you to Professor Leithead for the patience and dedication over the years, ‘I stand on the shoulder of giants’ is the only way that I can describe the incredible privilege that has been being a PhD student of yours. Thank you to Peter Jamieson, not just for his input in this research, but also for his perpetual smile and tango dances, and to my second supervisor Hong Yue for always having a word of encouragement. To Sheila Campbell and Drew Smith for keeping the CDT and everyone’s schedule running smoothly: against all the odds you arranged an impossible amount of meetings to help keep me on track. To David Robb for believing in my research and potential and offering me a job position to continue my research at SgurrControl and above all, for being an excellent person all around. To my work colleagues at SgurrControl, Carlos González, Charlie Plumley and Adam Stock for providing me with technical skills, good advice and for suffering my occasional rants! To my fellow CDTs and Strathclyde University colleagues and the lecturers who have made the years spent in the University a joy, particularly: Simon Gill, Robert Young, Maria Carla di Vincenzo, Kamila Nieradzinska, David Thompson, Albert Caubet Domingo and Julian Feuchtwang, many of whom have become close friends.

On a more personal note, special thanks must go to my family, without whose support I would have been unable to complete this PhD. I would also like to thank my cycling team GGCC for keeping me sane over the years with special mention to my GGCC-ladettes (mon the Prosecco!). To my friends Graham Chilles, David Foo,

Michael Gaddis, Steven Allan, Yvonne Allan and Tony Smith for the good times, taking care of me and unconditionally cheering me up all the way, I cannot thank you enough. Thank you also to my friends back home in Spain and Italy for having been there through it all, even if physically we were far apart.

Last but not least, I have always been known for being a little unconventional, and as such, I will depart convention one more time by ultimately saying thank you to myself, for not giving up.

Abstract

The aerodynamics of a wind turbine (WT) exhibit a particular property which is important for the design of control systems for WTs. It is referred to here as Separability. In this thesis, the Separability property of the wind turbine's aerodynamics is explored in much greater detail than before. Based on Separability, a novel effective wind-field model with potential for broad application in advanced wind turbine control is developed and validated against Bladed.

The Separability property is thoroughly investigated for constant speed WTs and variable speed WTs. The procedure to obtain the best possible representation of the aerodynamics in terms of its separated form, is developed. This process entails two aspects, firstly to determine the functional nature of the most appropriate representation and secondly to optimise the parameters of the fits.

It has been demonstrated that Separability exists in both constant and variable speed WTs and that it holds for a very large neighbourhood with a very good accuracy. In fact, on average, it comfortably covers more than double the rated torque of all the WTs explored.

The Separability property is exploited to develop effective wind-field models in the form of lump parameter ordinary differential equation models that are used in the modelling of WTs. These have been thoroughly validated against Bladed.

3.3. From Local Additivity to Global Separability Behaviour	45
3.4. Separability in the Context of Wind Turbines.....	46
3.4.1. Constant Speed Wind Turbines.....	46
3.5. Determination of the Separated form of Torque.....	48
3.5.1. Procedure for Determining $g_{\omega_0}(V)$ and $h_{\omega_0}(\beta)$	48
3.5.2. Procedure for determining $\tau_{\omega_0}(\cdot)$	53
3.6. Results.....	55
3.7. Conclusions.....	61
Chapter 4: Separability for Variable Speed Wind Turbines.....	62
4.1. Direct Extension of Separability to Variable Speed Wind Turbines.....	64
4.2. Wind Speed Based Separability.....	73
4.3. Tip Speed Ratio Based Separability.....	76
4.3.1. Comparison of Aerodynamic Relationships.....	79
4.4. Modified Tip Speed Ratio Based Separability.....	86
4.4.1. Characterisation of the Additivity Equations $h(\beta)$ and $g(\lambda)$	87
4.4.2. Modified Tip Speed Ratio Separability, from Local to Global Behaviour.....	91
4.4.3. Results for Modified Tip Speed Ratio Based Separability.....	94
4.5. Comparison of Wind Speed Based Separability and Tip Speed Ratio Based Separability.....	97
4.6. Conclusions.....	100
Chapter 5: Effective Wind-Field Model.....	102
5.1. Structure of Effective Wind-Field and Wind Turbine Models.....	102
5.2. Stochastic Component of the Effective Wind-Field Model.....	109
5.2.1. Stochastic Model.....	113
5.2.1.1. Spectral Factorisation.....	122
5.2.2. Results for the Stochastic Component of the Effective Wind-Field Model....	145
5.3. Deterministic Component of the Effective Wind-Field Model.....	155
5.3.1. Wind Shear Results.....	155
5.3.2. Tower Shadow Results.....	167
5.3.3. Combined Wind Shear and Tower Shadow Results.....	182
5.4. Complete Effective Wind-Field Model.....	191
5.5. Comparison to Bladed with Stiff Structural Dynamics.....	202

5.6. Comparison to Bladed with Structural Dynamics.....	208
5.7. Discussion on Wind-Field Modelling and Separability.....	213
Chapter 6: Conclusions.....	215
6.1. Future Work.....	217
Chapter 7: References.....	215
Appendix A: Wind Turbines Models.....	219
Appendix B: Wind-Field Model Transfer Functions Design.....	226
Appendix C: Wind-Field Stochastic Component Results.....	242
Appendix D: Wind Traces of Wind-Field Deterministic Component	252
Appendix E: Wind-Field Deterministic Component Results.....	265
Appendix F: Wind Traces Complete Wind-Field.....	287
Appendix G: Complete Wind-Field Results.....	297
Appendix H: Bladed Comparison. Stiff Structural Dynamics.....	307
Appendix I: Bladed Comparison. Active Structural Dynamics	313
Appendix J: Single Blade Element Separability.....	325
Appendix K: Commentary on Reference [42].....	329
Appendix L: Matlab Scripts and Instructions.....	330

Nomenclature

SI units have been used throughout unless otherwise stated.

A	rotor area or blade area (specified in contextual use)
A_r	area of the rotor disc
$A_n(t), A_m(t)$	Fourier coefficients
C_p	power coefficient
C_{pmax}	maximum value of power coefficient
C_q	torque coefficient
$C(\omega, D)$	coherence function
$E[\cdot]$	Expectation
$G(\lambda)$	Separability equation related to wind speed for tip speed ratio based Separability
$G_{0,\dots,3}(\omega)$	transfer functions
$H(\beta)$	Separability equation related to pitch angle for tip speed ratio based Separability
$H_t(\omega)$	frequency response function for von Karman spectrum
I_t	turbulence intensity
K_F, T_F	shaping filter parameters dependent on low frequency wind speed
	$v_m(t)$
L	turbulence length scale or blade length (specified in contextual use)
$L_{k\Omega_o}(t)$	rotationally sampled wind speed at $k\Omega_o$
M_e	edgewise RBM moment of a blade
M_f	flapwise RBM moment of a blade
P	power
R	rotor radius
R_T	wind turbine tower diameter
$R_{\Delta T}(t)$	torque transient covariance
$R_{nm}(t)$	cross-covariance

$R_T(t)$	torque covariance function
$R_{T_O T_I}(t)$	cross-covariance between the torque of the outer and inner area of a ring shaped area
$R_{v(r_1)v(r_2)}(t)$	time domain cross-covariance wind speed
$R(\tau, D)$	covariance between two point wind speeds
$R^r(\tau, D)$	covariance of wind speed at rotating points
$\tilde{R}_{n,m}(\tau, r_1, r_2)$	covariance between Fourier coefficients
RBM	Root Bending Moment
$S(\omega)$	spectral density function of the effective wind speed
$S_D(\omega)$	Dryden spectrum
$S_{II}(\omega)$	spectral density function of the inner part of a ring shaped area
$S_K(\omega)$	Kaimal spectrum
$S_{k\Omega_o}(t)$	spectral density function of $L_{k\Omega_o}(t)$
$S_{nm}(\omega)$	cross-spectral density function
$S_{vv}(\omega_i)$	spectral density function at frequency ω_i
$S_{\Delta T}(\omega)$	spectral density function of the torque disturbances
$S_{v(r_1)v(r_2)}(\omega)$	cross-spectral density function of the wind turbulent fluctuations
$S_v(\omega)$	spectral density function of wind speed fluctuations at a fixed point
$S_{VK}(\omega)$	Von Karman spectrum
$S^e(\omega)$	spectral density matrix
$S^e(\omega, \Delta\psi)$	spectral density function of the effective wind speed associated with the rotation
$S^r(\tau, D)$	spectral density function of rotating points
$\tilde{S}_{nn}^e(\omega)$	harmonic spectrum of the blade effective wind speed
T	aerodynamic torque
TI	turbulence intensity
TS	tower shadow
T_0	rated torque
T_s	sampling interval
\bar{T}	mean torque
$T_A(t)$	axial hub torque due to a blade
$T_{\omega_0}(\cdot)$	torque at constant rotor speed equal to rated rotor speed

$T_{\omega_o}(\cdot)$	torque at constant rotor speed on the locus of operating points
$T(\underline{\beta}, \underline{V})$	torque derived by the total contribution of blade elements
$TS a_{nP}, TS b_{nP}$	Tower shadow Fourier coefficients contribution to each <i>layer P</i> of the wind-field
U_{∞}	wind speed far upstream
V	wind speed
$V_e(\cdot)$	effective wind speed
V_{eff}	effective wind speed
V_m	mean wind speed
V_{WB}	base wind velocity
V_{WG}	gust wind component
V_{WR}	ramp wind component
V_{WN}	noise wind component
\bar{V}	mean wind speed
\bar{v}	mean hourly wind speed
\bar{V}_a	annual mean wind speed value
\hat{V}	quasi-static mean, mean wind speed encountered over several revolutions of the rotor
$V(\mathbf{r}, t)$	field of wind speed over the rotor disc
$V_{sep}(\cdot)$	Effective wind speed derived from Separability
$V(\theta, t)$	weighted average of wind speed
WS	wind shear
WT	wind turbine
$W(r)$	weighting function that depends solely on the geometry of the blades
$W(\mathbf{r}, V(\mathbf{r}, t))$	weighting function dependent on both position and wind speed
$WS a_{nP}, WS b_{nP}$	Wind shear Fourier coefficients contribution to each <i>layer P</i> of the wind-field
X	overhang of the wind turbine
a	axial flow induction factor or site specific parameter of $v_m(t)$ (specified in contextual use)
a_D, b_D	Best fit parameters for Dryden spectrum

$a_{k\Omega_o}, b_{k\Omega_o}$	frequency response function parameters (page 25)
c	scale parameter of Weibull distribution function
$e_x(\omega)$	frequency representation of Gaussian white noise
$f_1, f_2, f_3, f_4, f_{31}, f_{32}$	filters
$g(\cdot)$	Separability equation related to wind speed
$g_{\omega_o}(\cdot)$	Separability equation related to wind speed for constant rotor speed equal to rated rotor speed
$g_{\omega_o}(\cdot)$	Separability equation related to wind speed for constant rotor speed
$g_{r,\underline{v}}(\cdot)$	blade element Separability equation related to wind speed
$g_{\underline{v}}(\cdot)$	blade Separability equation related to wind speed
g_1, g_2	white Gaussian noise
h	hub height
$h(\cdot)$	separability equation related to pitch angle
$h_{r,\underline{\beta}}(\cdot)$	blade element Separability equation related to pitch angle
$h_{\omega_o}(\cdot)$	separability equation related to pitch angle for constant rotor speed equal to rated rotor speed
$h_{\omega_o}(\cdot)$	separability equation related to pitch angle for constant rotor speed
$h_{\underline{\beta}}(\cdot)$	blade Separability equation related to pitch angle
j, i	imaginary number $\sqrt{-1}$
k	shape parameter of Weibull distribution function
k_{σ, v_m}	slope on regression line
$k_{\underline{v}}$	gradient of $g_{\underline{v}}(\cdot)$
$k_{r,\underline{v}}$	gradient of $g_{r,\underline{v}}(\cdot)$
ℓ	locus of equilibrium points
l	distance between 2 points
\mathbf{r}	position on the rotor disc
r	position on a blade
r_o	distance between hub centre and the base of the blade
suffix 0	generally refers to rated
suffix o	generally refers to operating point
suffix xx	generally denotes uniform weighting

suffix yy	generally denotes linear weighting
suffix xy	generally denotes weighting of the cross terms
t	time
v	perturbations in wind speed about \bar{V}
v_s	current value of the 10min mean
v_T	tower shadow wind speed
v_H	wind speed at hub height
v_{sh}	wind shear wind speed
v_D	wind speed at the rotor disc
v^e	wind speed on one rotor blade
$v(r)$	wind distribution assumed orthogonal to the plane of rotation
$v_m(t)$	low frequency wind speed component
$v_t(t)$	high frequency wind speed component
$\bar{v}_m(t)$	averaged low frequency component wind speed
$v(\mathbf{r}, t)$	perturbations relative to the wind-field about the quasi-static mean
$\tilde{v}_n(t, r)$	time varying Fourier coefficients
wc	weighting coefficient
$X(r)$	weighting function that describes the influence of the wind along the blade
z	height from the ground
z_o	roughness length
β	pitch angle
β^*	equivalent pitch angle
γ	turbulent wind speed decay factor
γ_k	Fourier coefficients page 24
δ	angular offset
$\Delta T(t)$	torque transient
$\Delta T(\beta_o, V_{ro})$	contribution to the torque generated by the blade element at position \mathbf{r} keeping the value of the torque from the blade element constant
$\Delta T_r(\underline{\beta}, \underline{V})$	contribution to the torque by a blade element at station position \mathbf{r} keeping the total torque from the blade constant
$\varepsilon(\cdot)$	Function $h(\cdot) - g(\cdot)$

$\varepsilon_{\omega_0}(\cdot)$	Function $\varepsilon(\cdot)$ at rated rotor speed
$\varepsilon_{\omega_o}(\cdot)$	Function $\varepsilon(\cdot)$ at a particular point on the locus of operating points
$\varepsilon_1(t) , \varepsilon_2(t)$	independent coloured noise outputs
θ	azimuthal angle of rotation
λ	tip speed ratio
$\mu(\cdot)$	function that describes the weak non-linear dependence of T of the modified tip speed ratio separability
ξ	weighting function
ρ	air density
σ_V	standard deviation
$\hat{\sigma}_v$	estimated value of the standard deviation
$\tau(\cdot)$	function that describes the weak non-linear dependence of T on the $\varepsilon(\cdot)$ function
$\tau_{\omega_0}(\cdot)$	Function $\tau(\cdot)$ at rated rotor speed
$\tau_{\omega_o}(\cdot)$	Function $\tau(\cdot)$ at some point on the locus of operating points
φ_i	random generated phase between $[-\pi , \pi]$
ϕ	angular displacement
$\chi(\cdot)$	coherence function
ψ	azimuth angle
$\dot{\psi}$	angular velocity
ω	rotor speed or frequency (specified in contextual use)
$\omega_1, \omega_2, \omega_3, \omega_4, \omega_5, \omega_6$	independent point wind speeds
$\omega_1(t) , \omega_2(t)$	white Gaussian noise (page 25)
$\omega_c(t)$	coloured noise
$\omega(t)$	white noise
ω_i	discrete angular frequency page 15
$\Omega(\omega)$	frequency representation of white noise
Ω_o , ω_0	rated rotor speed
ω	frequency
$\mathcal{T}(\cdot)$	complete gamma function
$\mathcal{F}[\cdot]$	Fourier transform

A conscious effort has been made in respecting the nomenclature proposed by other authors when quoting their work. This has led to some duplicated nomenclature. Every effort has been made in the associated text to explain the notation involved.

Due to the complexity and length of this thesis, in some instances nomenclature has had to be recycled for specific purposes. When this is the case, it has been made clear in the text. For clarity, only the most common use of every nomenclature entry is reported on the table above.

Chapter 1

Introduction

Often thought as a right or granted commodity in the developed world, energy is the veiled source of freedom core to humankind - who controls the energy sources holds the power to control society.

The 21st century has inherited both the benefits of the intense industrialisation over the 19th and 20th centuries and the man-made environmental emergency related to having developed our technologies around fossil fuels. Furthermore the finite nature of the former and its non-homogeneous geographical distribution, has led to a current state of energy crisis and countries being energy dependent on foreign states that do not necessarily share the same views, priorities or ethics. Energy is a matter of national security.

Whereas the solution to the energy and environmental challenges that we are faced with is an interdisciplinary one, that has to include re-education of the global population about energy consumption, construction of more efficient buildings that require less energy and institutionalisation of recycling, there is no alternative but to migrate from the out-dated, limited and polluting fossil fuels to renewable energy sources, which are free, unlimited and green.

This leads us to wind. Wind is one of the most ancient forms of renewable energy harvested by humankind, used traditionally for sailing, grinding grains and extracting water. Its potential for electricity production went unnoticed during the second industrial revolution even if electric engines were already commonplace - perhaps due to a narrow approach taken around battery costs at the time. It was the invention of the incandescent light bulb and its subsequent commercialisation in the second half of the 19th century - which marked the arrival of electricity to the every day's life of the general population, with street and domestic lighting - that opened the door for wind energy to be utilised in what it is in present days its most familiar form. It all began in July 1887 when Scottish Professor James Blyth of Anderson's College, now University of Strathclyde, as culmination of his pioneering studies on wind power as a source of electricity, installed a vertical axis 'windmill' in his holiday home in Marykirk, Aberdeenshire. And it is so, that the first wind turbine for electricity production as we know it today was born 131 years ago, in Scotland. The following two centuries will see the technology flourish from its humble beginnings as a low rating kW machine on a backyard garden, to the modern horizontal axis wind turbines for off-shore use with ratings exceeding 10 MW that are

part of a thriving global multi-billion industry.

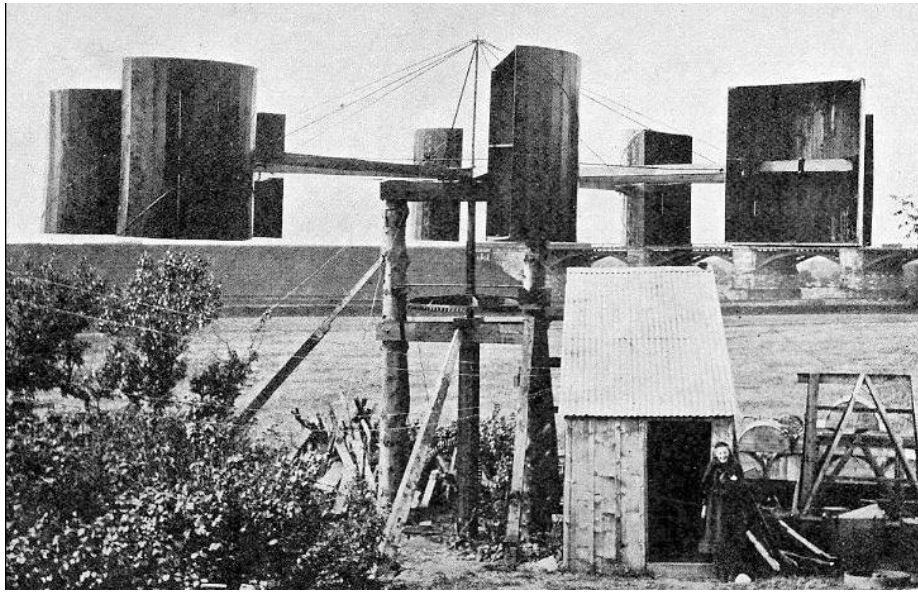


Figure 1-1. Professor James Blyth's wind turbine at his cottage in Marykirk 1891 circa [1]

The global deployment and exponential growth of the wind turbine's size has not been without its technical challenges. Bigger machines pose structural and material complexities on their own right, if those machines are also to be rotating in challenging environments under the full force of the wind, keeping them safe and operable takes a different edge. To maximise the power production and maintain an economical life span for wind turbines of this calibre, further improvements must be made and major gains will come from improving control strategies.

Wind turbine control has grown from being simple strategies applied to wind turbines subsequent to their design, to being an integrating part of the design of wind turbines. This is due to bigger machines having operational requirements that cannot otherwise be met; for example, managing the large and complex loads that can severely diminish wind turbines useful lifespan.

The control design task becomes increasingly demanding as turbine size increases since structural frequencies reduce and the interactions between the different aspects of the dynamics becomes stronger. Accordingly, improving the controllers requires better models of the rotor/wind-field interaction.

The aerodynamic torque, T , of a wind turbine is defined by complex non-linear equations that characterise the interaction between its three main variables: wind speed, V , blade pitch angle, β , and rotor speed, ω ; under the form,

$$T = \frac{1}{2}\rho ARV^2 C_q(\lambda, \beta) \quad (1.1)$$

$$\lambda = \frac{R\omega}{V} \quad (1.2)$$

where ρ is the density of air, A is the rotor area, R the rotor radius, C_q is the torque coefficient and λ the tip speed ratio. The non-linear nature of (1.1) can be seen in Figure 1-2. When the dynamics of the system are strongly non-linear, as they are here, the control design methodologies in general place restrictions on the nature of the non-linearities and/or result in conservative designs, making it hard to meet performance requirements.

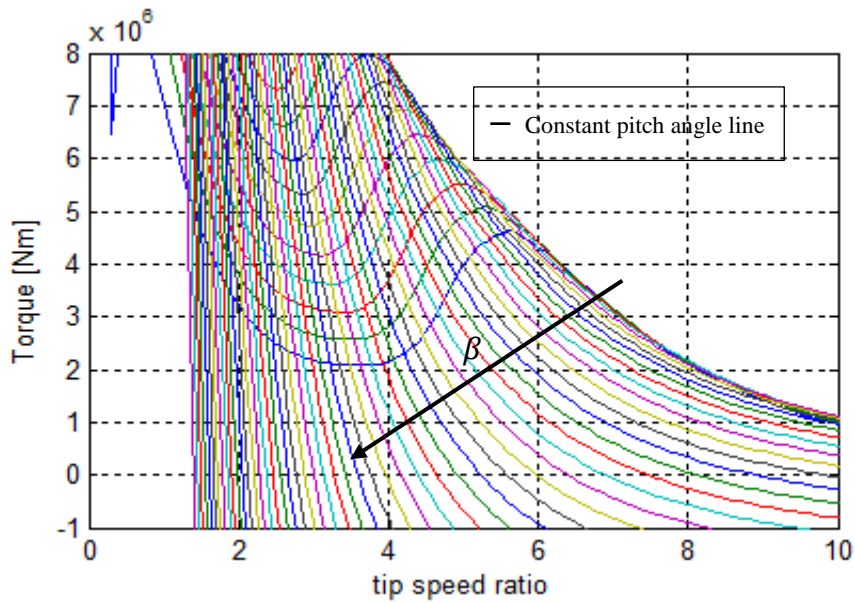


Figure 1-2. Graphical representation of the non-linear nature of the aerodynamic torque with respect of tip speed ratio and blade pitch

Greater insight into the non-linear nature of (1.1), that can be exploited in the control context, is provided by a reformulation which separates out the dependencies on variables: the Aerodynamics Separability - or as it will be more generally referred throughout this thesis, 'Separability'. Separability enables the aerodynamic torque to be reformulated in terms of independent additive functions, effectively separating wind speed, V , the only variable that cannot be actively controlled, from the rotor speed, ω , and pitch angle of the blades, β which can be. Specifically,

$$T = T_0 + h(\beta, \omega) - g(V) \quad (1.3)$$

where the Separability holds for a very large set of values of the variables. The significance of (1.3) for wind turbine control, is that the rotor speed feedback control loop becomes independent from the wind speed, which can now be considered an additive disturbance.

Typically, Separability holds for all turbines over a very large domain that encompasses all normal operating conditions, see literature review in Chapter 3 and Chapter 4. For illustrative purposes, Figure 1-3, shows the torque obtained through Separability against the torque derived from the characteristic C_q table for a particular WT. In this case, rated torque, T_0 , is 1.586×10^6 Nm. The equivalence of (1.3) to (1.1) is obvious, particularly, for values from 0 to $2 T_0$, highlighted with a red box in Figure 1-3.

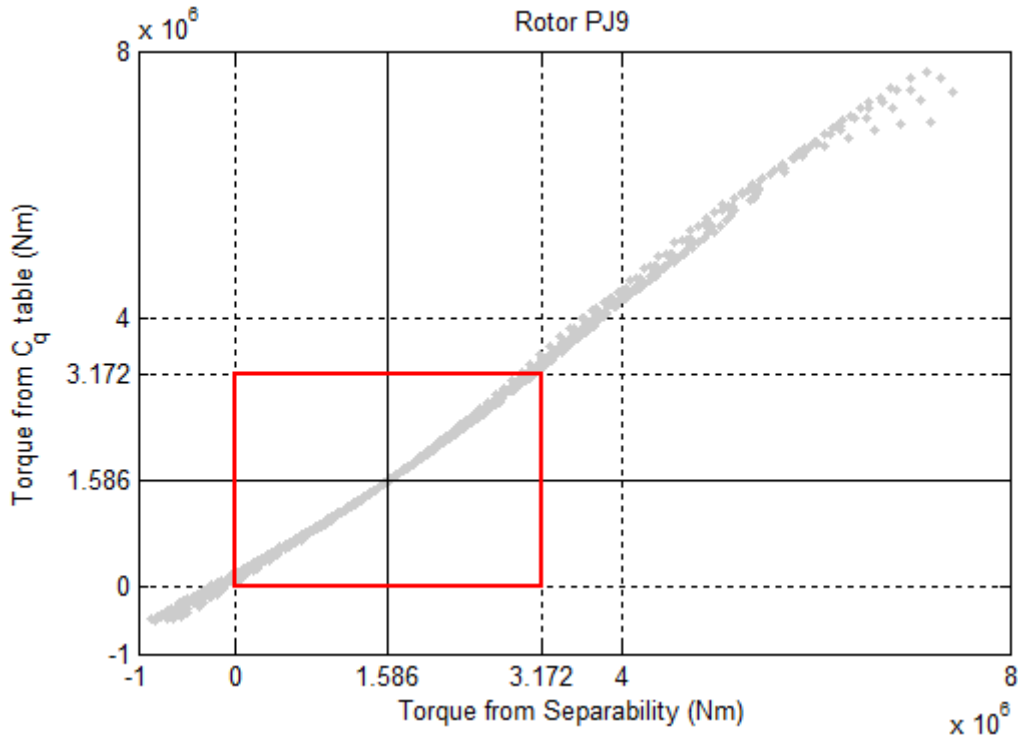


Figure 1-3. Comparison between torque derived by Separability and torque dictated by the WT C_q table

A typical constant speed wind turbine has no control below rated wind speed, whereas above rated wind speed the power or torque are controlled through pitch.

A typical torque control strategy for a variable speed wind turbine can be divided into 4 regions as illustrated in Figure 1-4. Region 1 is known as the 1st constant speed region and starts at the cut-in wind speed of the WT and sees the torque increasing until the $C_{p \max}$ curve is reached. When the torque reaches $C_{p \max}$, it marks the beginning of region 2, called $C_{p \max}$ tracking region. As the name suggests, in this region the WT operation tracks the $C_{p \max}$ curve by letting the rotor speed and torque to vary until rated rotor speed, ω_0 is reached. After the WT has reached ω_0 , the operating Region 3, named second constant speed region, starts. In this region, the rotor speed is kept at ω_0 and the WT torque increases with wind speed until T_0 is reached, which also coincides with rated wind speed. In regions 1, 2 and 3, the rotor speed is controlled using the generator reaction torque. After T_0 is achieved, if the wind speed is above rated wind speed, rotor speed and torque are maintained at rated

by varying pitch angle and the generator reaction torque respectively, this is Region 4. Separability specifically applies to Regions 4 and in part to 3.

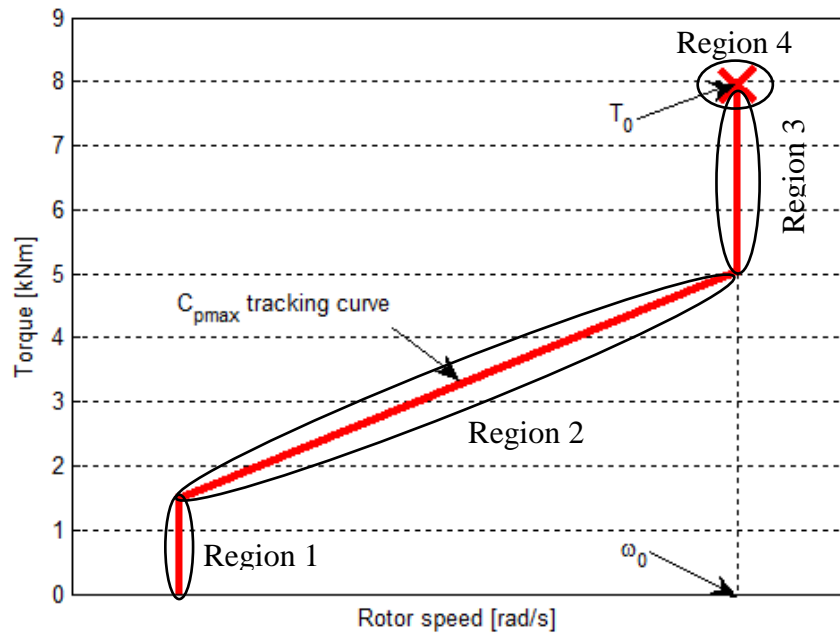


Figure 1-4. Typical torque control strategy for a variable speed WT

Separability, which in its own right is exploited in control solutions, is also key for building effective wind-field models that are statistically accurate when representing the rotor/wind-field interaction, a very useful property in the context of advanced controller design.

To date, there is no model of the rotor/wind-field interaction of a wind turbine, suitable for control purposes that reproduces, at least, the correct torque on each blade and the thrust on the tower with the correct correlations over the frequency range up to $6P$. Therefore, the overall research question poised is “How do we model, suitably for control purposes, the rotor/wind-field interaction to reproduce, at least, the correct torque on each blade and the thrust on the tower with the correct correlations over the frequency range up to $6P$?”. Central to answering that question is Separability.

1.1. Overview of the Thesis

In Chapter 1, a brief introduction for this thesis is provided.

In Chapter 2, a thorough background on wind modelling for control purposes of wind turbines is provided.

In Chapter 3, Separability is applied to constant speed wind turbines is discussed. A review of previous work regarding the Separability property is given. A formal mathematical analysis of the issue of separating a two variable function into two additive components is introduced, and the initial conditions and the range for which the property applies is identified. The best structure for the

representation for these functions has been explored and optimised. Discussion of results and conclusions are also provided.

In Chapter 4, Separability is extended to variable speed wind turbines. Three possible ways of formulating Separability are investigated and the best way of approaching these is determined. The first formulation is based on the mathematical development of the theory in Chapter 3, the second is driven by applicability and the third is based on the physics of the aerodynamic torque. The range of validity and applicability is established. Discussion of results and conclusions for the Separability property as a whole are provided.

In Chapter 5, a novel effective wind-field model based on the Separability property is developed. The proposed lump parameter model representation, which uses a finite number of ordinary differential equations, is tested and validated against Bladed. The chapter closes with a discussion of results.

In Chapter 6, a summary of the results of the research presented in this thesis and final conclusions can be found together with future work.

In Chapter 7, references list is provided and it is followed by appendixes.

1.2. Contributions to Knowledge

The contributions to knowledge of this thesis are:

- 1) A mathematical analysis of the Separability property has been undertaken and an existence theorem for the separated form established.
- 2) It has been demonstrated that Separability exists in both constant and variable speed wind turbines and that it holds for a very large neighbourhood with a very good accuracy. In fact, on average, it comfortably covers more than double the rated torque of all the wind turbines explored.
- 3) The best functional structure for the separated form has been determined and using it, procedures to optimise its representation have also been determined.
- 4) Two different version of Separability are investigated for variable speed wind turbines.
- 5) A novel effective wind-field model that exploits the Separability property is developed. This effective wind-field model is developed with the capacity, within the region of validity of Separability, to induce the correct in-plane moments such as the rotor torque and the in-plane root bending moment (RBM) of a blade. By extension of the close relationship between the in-plane and out-of-plane moments and forces the wind-field model the thrust and out-of-plane moments are also satisfactorily induced.

- 6) The novel effective wind-field model is sufficiently validated to establish its suitability for control analysis and design purposes.

1.3. Publications

Jamieson, P., Leithead, W.E., Gala Santos, M.L., *'The Aerodynamic Basis of a Torque Separability Property'*. Proceedings of EWEA 2011, Brussels, 2011.

Gala Santos M.L., Leithead W.E., Jamieson P., *'Aerodynamic Separability in Tip Speed Ratio and Separability in Wind - a Comparison'*, Torque, Oldenburg, 2012.

Chapter 2

Wind Resource and Wind Modelling

This chapter describes the nature and dynamics of the wind resource. Most common techniques used to model wind for wind turbine control design and analysis purposes are also discussed. The first topic is covered in Section 2.1 which is intended as an introduction to the phenomena involved in the formation of wind and through Section 2.2 the mathematical modelling of the wind is reviewed.

2.1. The Wind

Wind is the result of changing atmospheric pressure, the engine of Earth's complex weather system. These differences in atmospheric pressure are caused by the uneven heating of the surface of the Earth by the Sun, due to the different angles of incidence and the differential heating of land and water bodies. [2][3][4]

Thus, the main instigator of global wind circulation is the pressure gradient created by the difference in temperature between the equator and the poles. The air in the equator as it gets hotter expands, reducing its density and rising vertically to higher altitudes and cooling down to leave a low pressure area behind. At the poles the process is inverted. Colder air sinks onto the surface as its density is increased creating an area of high pressure. The result is that the air will flow from the high pressure areas of the planet to the low pressure ones, that is, from the polar regions toward the Equator. [2][3][4]

This trajectory is not completed smoothly and in one phase. In fact, each hemisphere has three cells, namely, Hadley, Ferrel and Polar, in which the air flow circulates through the whole depth of the troposphere. The direction of the flow in each one of the cells alternates, making them work together as a gear. In the process some of the air that was travelling to the poles will be deflected back to the equator, this returning flow is known as trade winds. [2][3][4]

The global circulation is also importantly affected by the rotation of the Earth, by what it is known as the Coriolis effect. Essentially the Coriolis effect makes the flow of air from high to low pressure zones deviate from a straight line. In the northern hemisphere this deflection will be to the right (if standing on the North Pole as a point of reference) and winds will rotate anticlockwise around low

pressure areas and clockwise around high pressure zones. Again, this trend is inverted in the Southern hemisphere. [2][3][4]

There are also important local patterns that affect the way wind behaves in a particular region. These local pressure changes are related to the topography of the site considered, the most common being mountain and valley winds and sea breeze. Mountain and valley winds are easily explained through the concepts already underlined. During the day the air around the slopes of the mountains becomes hotter than the air at the same latitude but farther away from the slope, where colder air applies pressure on the warmer valley air to force it up the slope of the mountain. At night through radiation from the soil, air on the slope of the mountain gets colder and denser and sinks into the valley. [2][3][4]

The sea breeze is a little different since it is caused by the differential heating of water and land bodies, with the ground heating faster than water but also cooling faster than water. The result is that during the day warm air rises from the ground and is substituted by cold air flowing inland from the sea and by night the reverse occurs since water takes longer to cool down. [2][3][4]

Both of these local phenomena have a daily pattern and the strength of their effect is subjected to seasonality (overall changes in temperature, thus pressure) and can be easily overcome by bigger weather systems.

If the long and short term variations of the wind at a certain location were to be shown in a wind speed spectral density function together with the turbulent component of the wind such as the Van der Hoven spectrum (see Figure 2-1), there would be 3 distinct peaks, namely, the synoptic peak of passing weather systems with a period of 4 days, daily variations with 24h period with sometimes a peak at 12h indicating the reversal of the winds in locations where phenomena like sea breeze are important and a final peak around 1min which accounts for the higher frequency turbulence component of the wind.

The flat region between the diurnal and turbulent peaks of the wind, indicate that there is not much energy available in the region between 10min and 2h ($\sim 0.5\text{mHz}$). This is known as spectral gap and suggests that the turbulence component of the wind can be modelled as a zero mean random process.[5][6]

Hence, as long as the spectral gap is present and well defined, it is possible to visualise the wind as a dual component system, with a baseline value correspondent to the mean wind speed that is determined by the seasonal, synoptic and diurnal effects (thus varying in a time scale starting at the

hour mark) and superimposed higher frequency turbulent fluctuations with mean value of zero when averaged over 10min. [5]

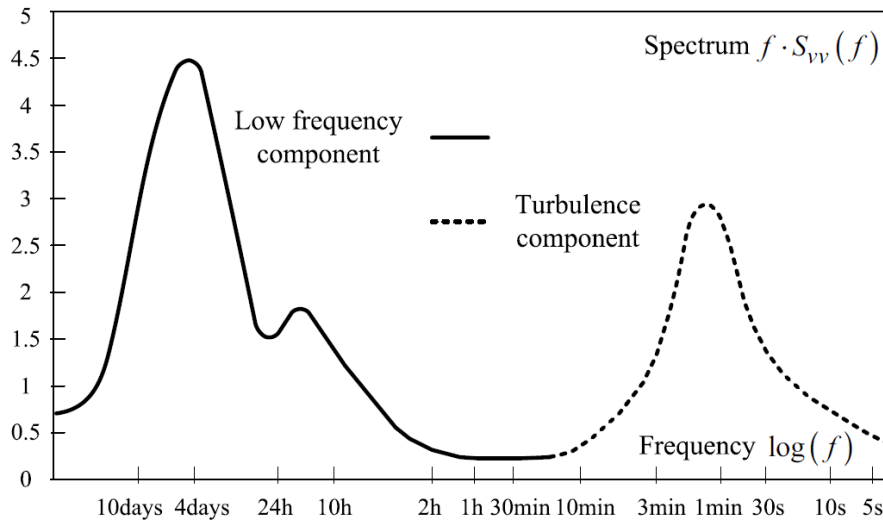


Figure 2-1. Van der Hoven spectra of wind speed [6]

The most common way to determine the 'quality' of the wind resource at a site is through the Weibull distribution at that site, that will indicate how much in a given year the mean hourly wind speed, \bar{V} , in that location tends to deviate from the annual mean wind speed value¹, \bar{V}_a . [5] The probability density function of the Weibull distribution can be defined as a two-parameter function that takes the form:

$$f(\bar{V}) = \frac{k}{c} \left(\frac{\bar{V}}{c}\right)^{k-1} \exp\left(-\left(\frac{\bar{V}}{c}\right)^k\right) \quad (2.1)$$

where c and k are the scale and shape parameters respectively and are related to the annual mean wind speed by the relationship:

$$\bar{V}_a = c\Gamma(1 + 1/k) \quad (2.2)$$

where $\Gamma(\cdot)$ is the complete gamma function.

The influence of the k parameter on the probability density function is presented in Figure 2-2, with the scale factor c , kept constant and equal to 6 [6]. Variations of \bar{V} from \bar{V}_a get smaller as the value of parameter k gets bigger². When $k = 2$, the Weibull distribution becomes the Rayleigh distribution.

¹ If the site under study shows distinctly different wind climates in summer and winter the use of a double peaked Weibull distribution, with different scale and shape factors for the two seasons, should be implemented for accurate results [5]

² k values of 2.5 and above are considered to be very good. [6]

The scale factor c is an indicator of how high the annual mean wind speed is, and its influence on the probability density function is presented in Figure 2-3, with the shape factor k kept constant and equal to 2. [6]

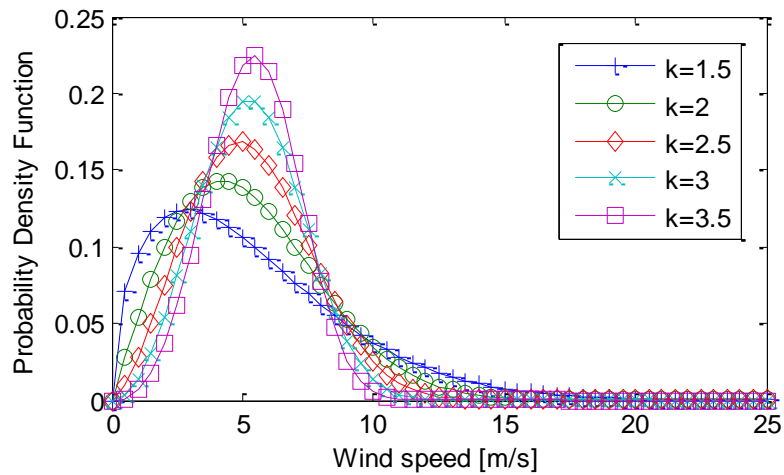


Figure 2-2. Weibull distribution as a function of k (constant $c = 6$)

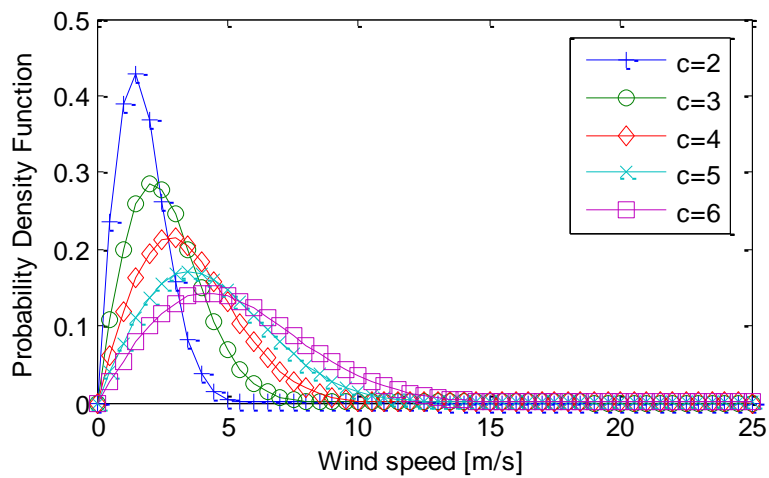


Figure 2-3. Weibull distribution as a function of c (constant $k = 2$)

2.1.1. Power in the Wind

Given a defined area, the power available in the wind at a certain moment in time is

$$P = \frac{1}{2} \rho A V^3 \quad (2.3)$$

where ρ is the density of the air equal to 1.225 kg/m^3 , A the area being considered and V the wind speed.

With A the swept area for the rotor, (2.3) indicates the hypothetical maximum power that a wind

turbine with 100% efficiency could generate. In other words, if a wind turbine was able to stop the wind. However, to have a realistic output, a factor of extraction needs to be included in this formula, this factor is called the power coefficient, C_p , of the wind turbine. Actuator Disc theory demonstrates that the power coefficient's maximum value is in fact 0.593, also known as the Betz's Limit. The maximum power coefficient, C_{pmax} , of a well designed wind turbine is typically of about 0.45.

From (2.3) it can also be appreciated that the power that a wind turbine can extract from the wind is proportional to the swept area and the cube of the wind speed that that rotor sees. This relationship implies that doubling the area of the rotor would double the energy output, but placing the turbine in an area with double the wind speed will provide eight times more power, thus, making appropriate site identification vital.

When upscaling a wind turbine, it is also important to keep in mind that the 'square-cube law' of wind turbines applies. The 'square-cube law' estimates that for every increase of the diameter of a wind turbine the power extracted will increase by the square of this value, but the cost of that turbine will increase with the cube of the diameter. [5][7]

2.2. Modelling the Wind for Wind Turbines

Correctly modelling the wind that a wind turbine sees and the interaction between them is critical for maximisation of power output, reduction of loads and overall control of the wind turbine. For this reason any wind-field model that is meant to be interfaced with the wind turbine control system needs to at least accurately describe the core stochastic and deterministic components of that interaction, that is, atmospheric turbulence (stochastic), wind shear (deterministic) and tower shadow (deterministic), as well as rotational sampling effects.

In order to assist the control design process, the wind models involved need to be not only reasonably accurate but also suitable for fast simulations sufficiently simple that can be included in control. Due to this, more complex models of the wind, such as those based on CFD wind-field, are avoided in favour of simple non-distributed models of the wind that can be used as input to BEM theory. In this context, the wind speed models are simple in that they ultimately reduce a 3D phenomenon to a one dimensional time varying filter and that their mathematical description consists of simple ordinary differential equations. Since the filters are derived from the spectral density functions, it is necessary that they spectrally factorise into frequency response functions with integers power of frequency. To date, this need has led to effective wind speed models combined with spectral peak models (rotational sampling) as the preferred approach. [8][9]

2.2.1. Atmospheric Turbulence Spectra

As already mentioned in Section 2.1, the wind can be defined in terms of a mean wind speed and turbulence. The turbulence is essentially fluctuations of wind speed relative to its mean. Their frequency content is described by their spectral density function. Being a short term phenomena, turbulence corresponds to the frequency spectral peak of the Van der Hoven spectrum centred on 1 min in Figure 2-1. [5]

The most commonly used models to describe turbulence have Kaimal, Von Karman or Dryden spectra [6]. The three of them are given below in [rad/s] and double sided spectrum form,

$$\text{Kaimal spectrum:} \quad S_K(\omega) = 2\sigma_V^2 \frac{(L/\hat{V})}{(1+(6\omega L/\hat{V}))^{5/3}} \quad (2.4)$$

$$\text{Von Karman spectrum:} \quad S_{VK}(\omega) = 2\sigma_V^2 \frac{(L/\hat{V})}{(1+(1.339\omega L/\hat{V})^2)^{5/6}} \quad (2.5)$$

$$\text{Dryden spectrum:} \quad S_D(\omega) = \frac{1}{2\pi} \frac{b_D^2}{(\omega^2 + a_D^2)} \quad (2.6)$$

with σ_V the standard deviation, L the turbulence length scale³ dependent on surface roughness of the site, \hat{V} the mean wind speed over the 5-10min of wind speed turbulence in question and ω the frequency. Parameters b_D and a_D of the Dryden spectrum are chosen to be the best fit that approximates the Von Karman spectrum. They are as suggested in [6][8][9] to be

$$a_D = 1.14 \left(\hat{V}/L \right); \quad b_D = \sigma_V \sqrt{2a} \quad (2.7)$$

$$\sigma_V = I_t \times v_s \quad (2.8)$$

where v_s is the current value of the 10min mean and I_t the turbulence intensity. [6]

From (2.4) to (2.6) it can be easily seen that in fact all spectra have decidedly similar mathematical definitions. The Kaimal spectrum gives a better fit to empirical observations of atmospheric turbulence whereas Von Karman gives a good description for turbulence in wind tunnels. Thus, Von Karman spectrum tends to be more broadly used for consistency with analytical expressions. However Von Karman spectrum only describes satisfactorily atmospheric turbulence above 150m having deficiencies at lower altitudes. This has led to the development of modified versions found in

³ L , represents the turbulence dynamic properties, in other words the function's bandwidth

most of the more complex software packages as Bladed. [5]

The Dryden spectrum on the other hand, matches quite reasonably the von Karman spectrum except at high frequencies (see Figure 2-4) but offers the advantage of being a rational expression in frequency squared. Since simulations for wind turbine control purposes rarely go over 10min, the Dryden spectrum is adequate for representing the turbulent component of the wind. Hence, it is possible to take advantage of this simplification in the calculations. For any given 10min time series, it is not possible to discern whether the time series is totally incompatible with either spectrum.

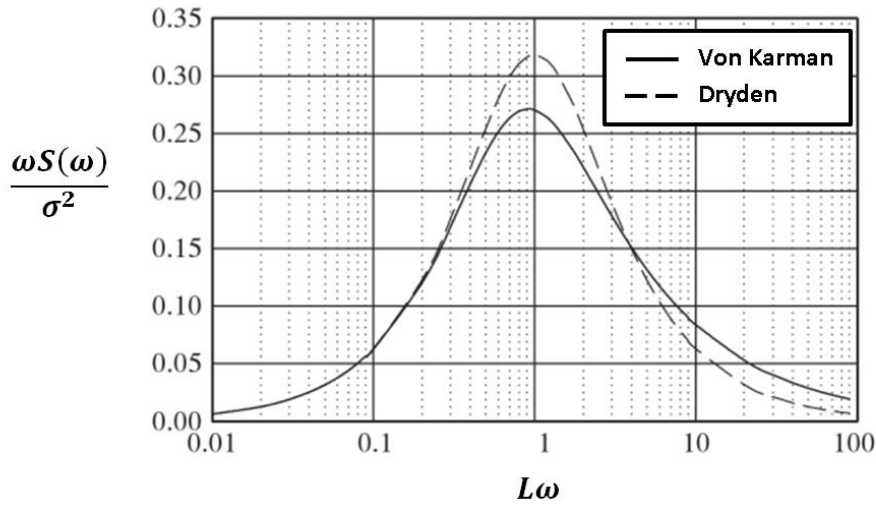


Figure 2-4. Comparison between Von Karman and Dryden Spectrums [10]

2.2.2. Wind Shear

Due to the friction between the Earth's surface and the air, the speed of the wind decreases as it approaches the ground with a logarithmic profile. This is known as wind shear and causes a periodic variation of the wind speed seen by a blade as it rotates with a period of rotation of the rotor $2\pi/1P$ [11]. The wind that the rotor sees at different heights due to wind shear, v_{sh} , can be described as:

$$v_{sh} = v_D \frac{\ln\left(\frac{z}{z_0}\right)}{\ln\left(\frac{h}{z_0}\right)} = v_D \frac{\ln\left(\frac{h + L\cos(\theta)}{z_0}\right)}{\ln\left(\frac{h}{z_0}\right)} \quad (2.9)$$

$$v_D = U_\infty(1 - a) \quad (2.10)$$

where v_D is the wind speed at the rotor disc, z the height from the ground where the wind speed is computed, h the hub height used as a reference height, L the length of the blade, θ the azimuthal angle of rotation, z_0 the roughness length, U_∞ the wind speed far upstream and a the axial flow induction factor. [5][6]

The surface roughness, z_o , depends on the characteristics of the terrain and the higher its value the bigger the decrease in the wind that the turbine effectively sees. It varies from around unitary value in cities to 0.0001 over open water. A comprehensive set of values for z_o can be found in [5][6][12]

Wind shear is a deterministic phenomenon and as such, its spectral density function is in the form of a series of sharp peaks. The typical shape of a deterministic peak in a power spectral density function can be seen in Figure 2-5.

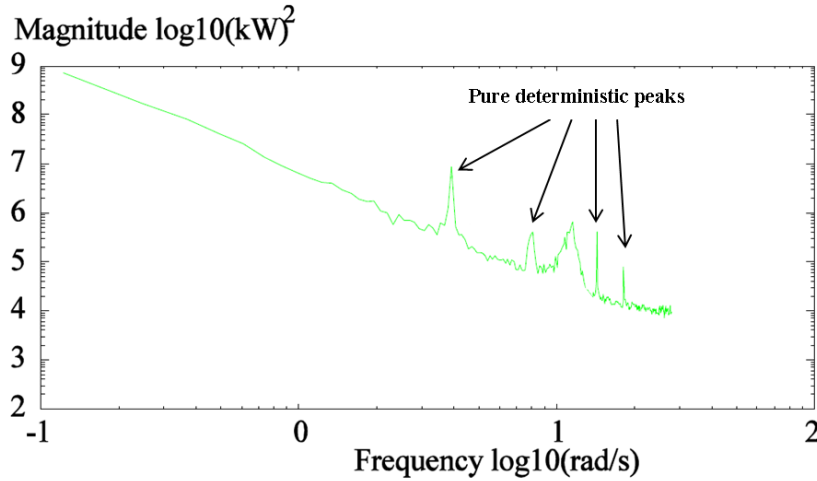


Figure 2-5. Measured power spectral density function of a 3-bladed wind turbine with blade imbalance. [13]

2.2.3. Tower Shadow

The presence of the turbine's tower creates a natural blockage to the wind flow, known as tower shadow. It results in a periodic decrease of the torque that the wind turbine produces every time a blade passes in front of the tower. The tower shadow effect can be described as,

$$v_T(t) = v_H R_T^2 \frac{x^2(t) - y^2(t)}{[x^2(t) + y^2(t)]^2} \quad (2.11)$$

where v_H is the wind speed at hub height before tower shadow effect is included, R_T the radius of the tower, x the lateral component of the point being assessed with regards to the centre of the tower and y the longitudinal component of the same. Usually y is specified as the overhang, X , of the machine and the x component as a combination of the radial position on the blade, r , and the azimuthal angle of rotation, θ , becoming

$$v_T(t) = v_H R_T^2 \frac{r^2 \sin^2(\theta) - X^2}{[r^2 \sin^2(\theta) + X^2]^2} \quad (2.12)$$

the tower shadow effect is only of importance between 90 and 270 degrees. [5][6]

Like wind shear, tower shadow is also a deterministic phenomenon and it too induces characteristic sharp peaks in the spectral density function, as seen in Figure 2-5.

2.2.4. Evolution of Wind Modelling for Wind Turbine Technology

After briefly having introduced the major phenomena and concepts, the main wind models used in wind turbine modelling are explored in the following.

2.2.4.1. Point Wind Speed

Early wind speed models used for wind turbines did not account for the wind field-rotor interaction. Under the assumption that the wind turbine would have a yaw system, it was also assumed that changes of wind direction would be sufficiently slow to allow the yaw system to maintain the wind turbine pointed into the wind. Therefore only the longitudinal component of the wind would be needed [6][14]. These models were commonly used in the early 80s and consisted of a simple wind speed acting uniformly over the rotor disc combining additively several wind speed components. The most basic ones, such as the Krause and Man model [15], would account only for some of the deterministic characteristics of the wind whereas the Anderson and Bose model [16] started also to incorporate the stochastic components [9]. In the case of the former, the wind speed, V_W , had the form,

$$V_W = V_{WB} + V_{WG} + V_{WR} + V_{WN} \quad (2.13)$$

where

V_{WB} = base wind velocity [min/h], represents the mean wind speed and is treated as a constant

V_{WG} = gust wind component [min/h], accounts for fast wind gusts (1-cosine gust)

V_{WR} = ramp wind component [min/h], accounts for slow variations of wind (step ramp)

V_{WN} = noise wind component [min/h], represents the turbulent component of the with the wind spectral density function defined by [17]

Based on the van der Hoven spectrum, see Figure 2-1, the point wind speed is described as the sum of two components: a low frequency component, $v_m(t)$, which describes long term and slow variations, and a high frequency component, $v_t(t)$, which describes fast variations (turbulence). The wind speed, $v(t)$, is now defined as [6],

$$v(t) = v_m(t) + v_t(t) \quad (2.14)$$

with $v_m(t)$ considered constant (equal to the average wind speed) on the time-scale of the turbulence. The averaging for $v_m(t)$ is usually performed over a 10 minute time window [6]. The low frequency component can be used for site assessment and, as already mentioned in Section 2.1, can be described by a Weibull distribution, or alternatively by a Rayleigh's distribution [6][18] which is nevertheless a special case of the Weibull distribution when $k = 2$, thus,

$$v_m(t) = a \cdot v_s \cdot e^{\frac{-1}{2}a\bar{v}^2} \quad (2.15)$$

where parameter a , which is site specific, depends on the wind speed's very long term average (varies over years) and \bar{v} is the mean hourly wind speed. Whereas the Weibull and Rayleigh distributions are commonly used, other general methods such as sampling the Van der Hoven spectrum itself can be used to generate the time series for the low frequency component. [6] If this method is chosen, then $v_m(t)$ is defined as,

$$v_m(t) = V_0 + \sum_{i=1}^N A_i \cos(\omega_i t + \varphi_i) \quad (2.16)$$

$$A_i = \frac{2}{\pi} \sqrt{\frac{1}{2}(S_{vv}(\omega_i) + S_{vv}(\omega_{i+1}))(\omega_{i+1} - \omega_i)} \quad (2.17)$$

with V_0 the mean wind speed calculated over a period considerably longer than the largest period of the van der Hoven spectrum, A_i the amplitude, ω_i the discrete angular frequency that varies between $i = 1 \dots N$, φ_i the random generated phase between $[-\pi, \pi]$, and $S_{vv}(\omega_i)$ the power spectral density at frequency ω_i . [6][14]. The reason why the above procedure should not be extended to model the high frequency component of the wind is that it would implicitly imply that the magnitude of the turbulence is the same regardless of the mean wind speed variations at low frequency. That is, the turbulence properties are independent of the low frequency domain, which is not correct. [19]

The turbulent component, $v_t(t)$, describes the fast wind speed variations located on the high frequencies of the Van der Hoven spectrum (within 10 min) and it is typically modelled by one of the spectra introduced in Section 2.2.1 which all depend on \hat{V} , the mean wind speed over the 5-10 min of wind speed turbulence in question. [20]

In [20] the modelling of $v_t(t)$ is approached as illustrated in the dashed rectangle of Figure 2-6. White noise, $\omega(t)$, is passed through a filter which is based on the von Karman's spectrum and has a frequency response function equal to,

$$H_t(\omega) = \frac{K_F}{(1 + j\omega T_F)^{5/6}} \quad (2.18)$$

with,

$$T_F = L_t / \bar{v}_m \quad (2.19)$$

where K_F and T_F depend on the mean of the low-frequency wind speed, $v_m(t)$ [6]. The parameter K_F can be defined in relation to T_F , as

$$K_F \approx \sqrt{\frac{2\pi}{\beta(1/2, 1/3)} \cdot \frac{T_F}{T_s}} \quad (2.20)$$

where β is the beta function and T_s the sampling time of the turbulent component (typically 1s).

The output signal from the filter $H_t(j\omega)$, referred to as coloured noise $\omega_c(t)$, is then multiplied by the estimated value on the standard deviation, $\hat{\sigma}_v$, defined in [20] as

$$\hat{\sigma}_v = k_{\sigma, \bar{v}_m} \bar{v}_m(t) \quad (2.21)$$

where k_{σ, \bar{v}_m} is the slope of the regression line that describes the dependency between the standard deviation and $\bar{v}_m(t)$, and $\bar{v}_m(t)$ is the mean value of the low frequency component of the wind speed.

The wind speed model is then completed by simple addition of $v_m(t)$ to $v_t(t)$, see Figure 2-6. It is important to note that the sampling time, T_s , of the two components of the wind is different, usually 10 min for $v_m(t)$ and 1s for $v_t(t)$ [6]. By having different time scales the system is effectively made non-stationary. [6][19]

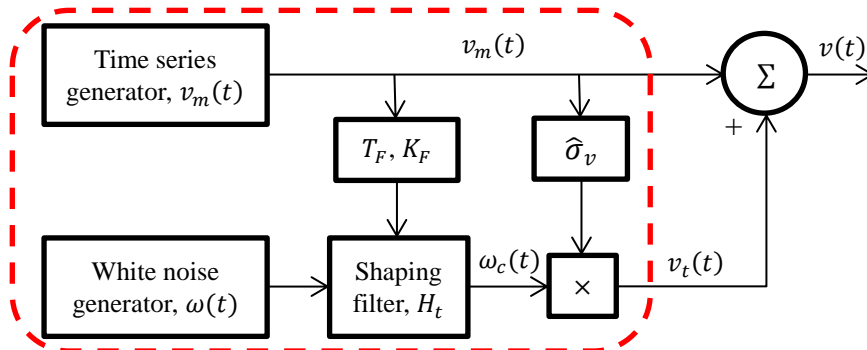


Figure 2-6. Non-stationary wind speed model [6]

Whereas these methods are effective in representing the mean wind speed variations at a fixed point for time scales ranging from seconds to years [14], it fails to account for essential variations in the

wind-field introduced by the wind field-turbine interaction, which would be misleading. In addition it does not represent the 3D nature of the wind field.

2.2.4.2. Effective Wind Speed

The concept of an effective wind speed, V_{eff} , was introduced in 1984, [21]. An effective wind speed is some averaging of the spatially and temporarily varying wind speed over the rotor disc to obtain a scalar time varying representative wind speed. It is required that this scalar effective wind speed has the same statistical properties as the wind speed over the rotor. It is the statistical properties that are preserved rather than the time series properties. The properties that are inherited by the effective wind speed from the wind speeds over the rotor disc are frequency domain ones rather than time domain ones.

With regards to the averaging of the wind speed, two different philosophies have evolved while developing effective wind speed models. In the first philosophy, the averaging is done prior to the interaction with the rotor, focusing on the statistical properties of the input to the WT, that is, determining a single uniform wind speed that replicates the spectrum of the *average wind speed* over the rotor disc. Philosophy 1 is adopted in [21]. In the second philosophy, the focus is on the outputs of the WT (i.e. forces and moments), the averaging is applied after the wind has interacted with the non-linear aerodynamics of the WT, by determining a single uniform wind speed that induces the same spectral properties in the rotor torque or some other scalar force or moment as the *wind speeds* over the rotor disc. Philosophy 2 is adopted in [13].

When the second philosophy was introduced in 1992, [13], it was identified that in order to link the statistical properties of the torque (the scalar object of interest in [13]) to the statistical properties of the wind speed, their relationship needed to be simplified. The aerodynamics needed to be linearised. To this end, two conditions are requested:

- 1) Quasi-static variation of the mean wind speed over the rotor: the rotation of the rotor is sufficiently fast that there is not much change in the wind-field over the period of one revolution of the blades.
- 2) Small perturbations in wind speed relative to the average wind speed over the rotor: the average wind speed is that over the rotor disc at some time, as opposite to the more usual average wind speed over 10min.

Unlike the first philosophy, it is clear from this development in the second philosophy that the

effective wind speed models have some restrictions on their validity: first, they are only valid for low frequencies below 1P and second, the turbulence intensity, TI, cannot be too high.

In other words, an effective wind speed model on its own can only appropriately represent the low frequency components of the wind⁴ up to 1P. This is because it only holds if the time-scale of change in the wind-field is comparable to or longer than the period of 1 revolution (or a small number of revolutions) of the rotor. Also, the turbulent fluctuations in the wind-field are considered as perturbations over a uniform quasi-static mean wind speed over the rotor disc.

The first effective wind speed model reported in 1984, [21], adopted the first philosophy with no discussion regarding the frequency range of validity, whereas the effective wind model reported in 1992, [13], was the first one to adopt the second philosophy. Both approaches model the interaction between the WT rotor and the wind-field by simple ordinary differential equations as required for control system analysis and design.

The wind speed models in [13], in which the emphasis is on the derivation of the axial hub torque from a single effective wind speed, have been used successfully in many control studies [9][22][24][25]. To provide more insight into effective wind speed models within the context of the second philosophy, the derivation from [13] is given below.

The axial hub torque, $T_A(t)$, induced by the wind on a blade is defined as

$$T_A(t) = \int_A W(\mathbf{r}, V(\mathbf{r}, t)) dA \quad (2.22)$$

where $V(\mathbf{r}, t)$ is the field of wind speed over the rotor disc, $W(\mathbf{r}, V(\mathbf{r}, t))$ ⁵ is a weight function dependent on both position, \mathbf{r} , and wind speed, $V(\mathbf{r}, t)$, and A is the area of a blade.

In [13], it is observed that the aerodynamic torque does not vary much over the outer 2/3 of the blade which is responsible for most of the torque generated; see Figure 2-7. Furthermore, in [13] it is pointed out that since at low frequencies the change in the wind-field is slower than a period of revolution of the rotor, the low frequency components of the torque are related to the wind-field over the complete rotor disc (condition 1). These two observations are exploited to simplify the axial hub torque from (2.22) to

⁴ Effective wind speed models are not intended to represent the deterministic components of the wind-field as tower shadow and wind shear, nor the high frequency spectral peaks (both deterministic and stochastic) due to rotational sampling. [13]

⁵ $W(\mathbf{r}, V(\mathbf{r}, t))$ can be interpreted as the contribution to the total torque of an element of a blade.

$$T_A(t) \simeq \int_{A_r} \xi(V(\mathbf{r}, t)) dA \quad (2.23)$$

where ξ is some weighting function that depends only on the wind speed, and A_r the area swept by the rotor.

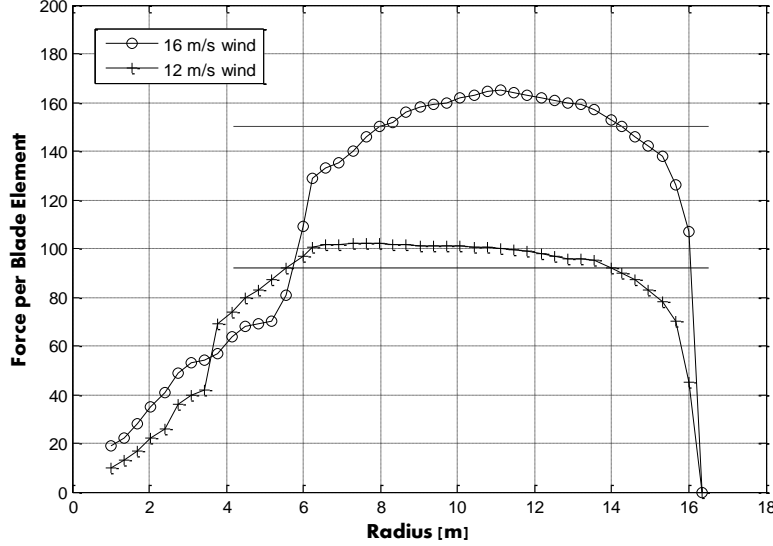


Figure 2-7. Force per unit Blade element [9]

The $V(\mathbf{r}, t)$ can be described as the sum of a quasi-static mean wind speed, \hat{V} , which is the mean wind speed encountered over several revolutions of the rotor (of the order of 20 seconds)⁶, and the perturbations relative to the wind-field about the quasi-static mean, $v(\mathbf{r}, t)$, which are relatively small compared to \hat{V} (condition 2). As a result (2.23) becomes,

$$T_A(t) = \int_{A_r} \xi(\hat{V} + v(\mathbf{r}, t)) dA \quad (2.24)$$

The $\xi(\hat{V} + v(\mathbf{r}, t))$ can be linearised through Taylor's expansion

$$\xi(\hat{V} + v(\mathbf{r}, t)) \approx \xi(\hat{V}) + \frac{\partial \xi}{\partial \hat{V}}(v(\mathbf{r}, t)) + \text{higher order terms} \quad (2.25)$$

where the higher order terms can be neglected. In this way, only the perturbations, $v(\mathbf{r}, t)$, about the quasi-static mean, \hat{V} , and hence their resulting torque fluctuations, need to be considered. It follows that (2.24) can be simplified to the torque transients, $\Delta T(t)$, as

$$\Delta T(t) \simeq k \int_{A_r} v(\mathbf{r}, t) dA \quad (2.26)$$

where $v(\mathbf{r}, t)$ continues to be a field of turbulent perturbations in the wind speed about the quasi-static mean perpendicular to the rotor disc and k is some normalising constant.[12]

⁶ To be stressed that this is not the 10min mean.

Therefore the covariance for the torque transient can be defined as

$$\begin{aligned}
R_{\Delta T}(t) &= E[T(t+s)T(s)] \\
&\approx k^2 \int_{A_r} \int_{A_r} E[v(\mathbf{r}_1, t+s)v(\mathbf{r}_2, s)] dA_1 dA_2 \\
&\approx k^2 \int_{A_r} \int_{A_r} R_{v(\mathbf{r}_1)v(\mathbf{r}_2)}(t) dA_1 dA_2
\end{aligned} \tag{2.27}$$

where $R_{v(\mathbf{r}_1)v(\mathbf{r}_2)}(t)$ is the time domain cross-covariance between the wind at position \mathbf{r}_1 and position \mathbf{r}_2 .

By taking the Fourier transform on both sides of (2.27) the relation between the spectral density function of the torque disturbances, $S_{\Delta T}(\omega)$, and the cross-spectral density function of the wind turbulent fluctuations, $S_{v(\mathbf{r}_1)v(\mathbf{r}_2)}(\omega)$, is established

$$S_{\Delta T}(\omega) = k^2 \int_{A_r} \int_{A_r} S_{v(\mathbf{r}_1)v(\mathbf{r}_2)}(\omega) dA_1 dA_2 \tag{2.28}$$

By then assuming that the power of wind speed fluctuations at a fixed point is independent from the position of the rotor disc, (2.28) becomes

$$S_{\Delta T}(\omega) = k^2 S_v(\omega) \int_{A_r} \int_{A_r} \chi(\mathbf{r}_1, \mathbf{r}_2, \omega) dA_1 dA_2 \tag{2.29}$$

where $S_v(\omega)$ is the spectral density function of wind speed fluctuations at a fixed point and χ the coherence function of the wind speed at the two points, \mathbf{r}_1 and \mathbf{r}_2 . The coherence function depends mainly on the separation, l , between the points \mathbf{r}_1 and \mathbf{r}_2 , and is specified in [13] to be chosen to be that from Davenport [23],

$$\chi(\mathbf{r}_1, \mathbf{r}_2, \omega) \simeq \exp\left(\frac{-\gamma l \omega}{\bar{V}}\right) \tag{2.30}$$

$$l = \sqrt{\mathbf{r}_1^2 + \mathbf{r}_2^2 - 2\mathbf{r}_1 \cdot \mathbf{r}_2} \tag{2.31}$$

where γ is the turbulent wind speed decay factor and \bar{V} is the mean wind speed⁷. An explicit form for the spectral density function of the aerodynamic torque transients for a blade is determined in [13] to be of the form,

⁷ \bar{V} is assumed here to be the same as \hat{V} . Any difference between them can be accounted for by adjusting γ

$$S_{\Delta T}(\omega) \simeq k^2 S_v(\omega) \int_{A_r} \int_{A_r} \exp\left(\frac{-\gamma l \omega}{\bar{V}}\right) dA_1 dA_2 \quad (2.32)$$

$$\simeq k^2 S_v(\omega) \phi(x)$$

where

$$x = \left(\frac{\gamma R}{\bar{V}}\right) \omega = \sigma \omega \quad (2.33)$$

$$a = 0.55 \quad (2.34)$$

and $\phi(x)$ is approximately [13],

$$\phi(x) \approx \pi^2 R^4 \frac{(2 + x^2)}{(2 + ax^2)(1 + x^2/a)} \quad (2.35)$$

that is

$$S_{\Delta T}(\omega) \approx k^2 \pi^2 R^4 S_v(\omega) \frac{(2 + x^2)}{(2 + ax^2)(1 + x^2/a)} \quad (2.36)$$

The relationship of x to frequency is clarified by the following re-arrangement,

$$x = \left(\frac{\gamma R}{\bar{V}}\right) \omega = \gamma \left(\frac{\omega_R R}{V_o}\right) \frac{V_o}{\bar{V}} \frac{\omega}{\omega_R} \quad (2.37)$$

where $V_o = R\omega_R/\lambda_{max}$

At 1P, $\omega/\omega_R = 1$ and it follows that,

$$x = \gamma(\lambda_{max}) \frac{V_o}{\bar{V}} \cong 10 \frac{V_o}{\bar{V}} \quad (2.38)$$

With V_o having a typical value of 9-10 m/s and \bar{V} from 4-25 m/s, a representative range of values of x is 4-25.

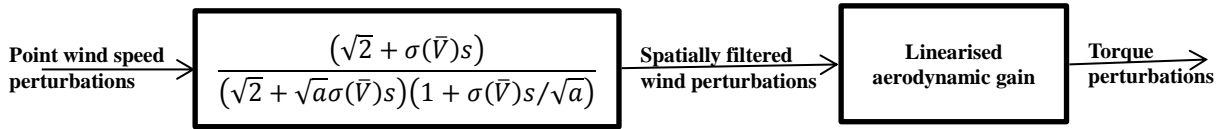
As established in (2.26) the perturbations in the torque can be interpreted as being due to the perturbations on $\xi(V(\mathbf{r}, t))$, which is in other words an effective wind speed, $V_{eff}(t)$, uniform over the rotor disc. It follows that the spectral density function of the effective wind speed, $S(\omega)$, is

$$S(\omega) = \frac{(2 + x^2)}{(2 + ax^2)(1 + x^2/a)} S_v(\omega) \quad (2.39)$$

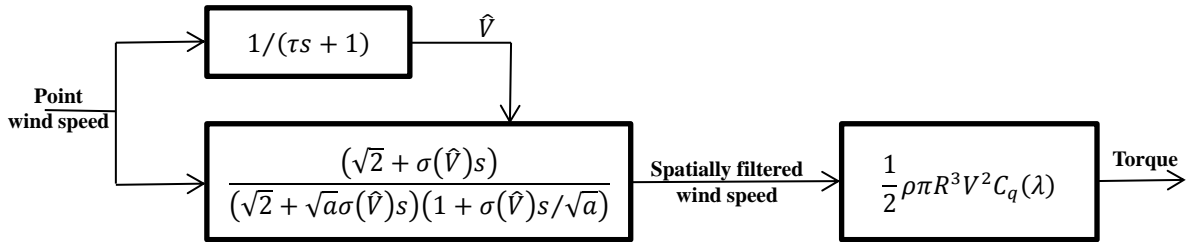
The linear model relating perturbations in torque to perturbations in point wind speed, as depicted in Figure 2-8a, is derived directly from the spectral factorisation of (2.39). With the spatial averaging of the wind speed modelled by the filter, $f(s)$, [13]

$$f(s) = \frac{(\sqrt{2} + \sigma s)}{(\sqrt{2} + \sqrt{a}\sigma s)(1 + \sigma s/\sqrt{a})} \quad (2.40)$$

If instead the input to the spatial filter is the total point wind speed including the quasi-static mean, the output of the filter can be used in conjunction with the non-linear torque coefficient, $C_q(\lambda)$, to estimate the axial hub torque generated by the blade, see Figure 2-8b. [9]



a. Linear model of torque perturbations



b. Non-linear model of torque

Figure 2-8. Models of axial hub torque [9]

The quasi-static mean wind speed, \hat{V} , is estimated by subjecting the point wind speed to the filter $1/(\tau s + 1)$, which is equivalent to averaging the wind speed over τ seconds. An appropriate choice for τ is equivalent to a small number of rotations by the rotor. The same procedure can be used to estimate the axial hub torque due to the complete rotor. [9]

2.2.4.2.1. Rotational Sampling – Corrections to Effective Wind Speed Models

Wind turbines are non-static structures, their blades continuously cut through the wind-field as they rotate, altering the time varying wind speed that the blade experiences. Any wind model that is intended to represent the interaction between the wind and the wind turbine needs to take this rotational sampling of wind-field into consideration as it introduces significant components to the spectral density function of the moments and forces of interest [6][18][26]. The rotational sampling or spectral peak model, as it is also known, has both stochastic and deterministic (tower shadow, wind shear) due to turbulence.

Since the effective wind speed models on their own only apply for frequencies up to 1P and do not cater for the deterministic components, rotational sampling corrections for both the stochastic and deterministic components are needed for higher frequencies and WS and TS. These corrections are applied a posteriori to the moments and forces of interest.

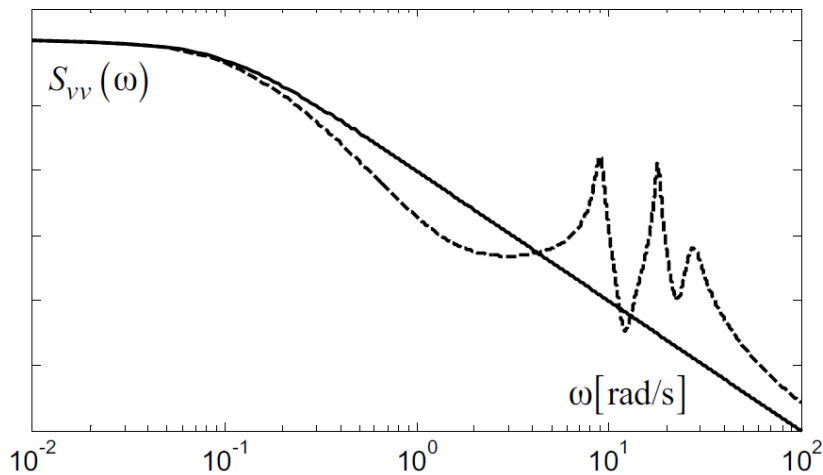


Figure 2-9. Wind power spectral density: fixed-point (solid line) vs. rotationally-sampled (dashed line) [6]

2.2.4.2.1.1. Rotational Sampling: Deterministic

Deterministic peaks in the spectrum due to rotational sampling are perceived by each blade as a periodic disturbance in the wind speed. This is because effects like gravity, wind shear and tower shadow change little over 5-10min (if not at all) which is a time scale significantly bigger than the time required for one revolution of the rotor.

Because these deterministic disturbances are periodic, their covariance, $R(t + \phi)$, is also periodic and the contribution to spectra is a series of delta functions at $k\Omega_o$ weighted by the Fourier

coefficients⁸, that is,

$$R(t + \phi) = \sum_k \gamma_k \cos(k\Omega_o t + \phi) \quad (2.39)$$

where γ_k , are the Fourier coefficients. Note that there are no sin terms due to the symmetry of WS and TS about the vertical axis.

Furthermore, because the covariance is continuous the magnitude of the weights, γ_k , tends to decrease as $1/k^2$. In reality, the peaks are not delta functions but very sharp peaks. [27]

Extending the covariance from 1 blade to the whole rotor of a typical three-bladed wind turbine, blade 2 and blade 3 are delayed behind blade 1 by T/n and $2T/n$ respectively, where T is the period of rotation and n the number of blades. The total contribution to the hub torque is proportional to

$$\begin{aligned} & \cos(k\Omega_o t + \phi) + \cos(k\Omega_o(t - T/n) + \phi) + \cos(k\Omega_o(t - 2T/n) + \phi) \\ & = \cos(k\Omega_o t + \phi) + \cos(k\Omega_o(t - 2\pi/n) + \phi) + \cos(k\Omega_o(t - 4\pi/n) + \phi) \end{aligned} \quad (2.42)$$

In other words, at the hub, there should only be deterministic peaks at integer multiples of the peaks at $n\Omega_o$. This is because, when k is not equal to a multiple of n , the loads at the hub cancel due to the symmetry of the rotor. The loads will still be present at single blade level and contribute to fatigue damage. However, should there be blade imbalance due to differences in the inertias or aerodynamic characteristics of the blades, peaks will be present at each integer multiple of Ω_o . Figure 2-5 shows this scenario with deterministic peaks in the power spectrum of a 3-bladed wind turbine at 1,2,4 and 5P with a further deterministic peak at 3P which is not visible due to the stochastic component at that frequency. As expected, the stochastic component carries more energy than the deterministic component and thus it is not unusual for the deterministic peak to ‘disappear’ under the stochastic one. [27]

2.2.4.2.1.2. Rotational Sampling: Stochastic

As seen in Figure 2-5, there are other peaks present in the spectral density function that are higher in energy content than the deterministic ones and have a distinctive triangular shape with a broad base. These are stochastic components caused by the wind speed turbulence varying over the rotor disc. As in the deterministic case, the stochastic variation over the rotor disc is rotationally sampled by the rotating blade and concentrated at integer multiples of Ω_o , thereby inducing spectral peaks at $k\Omega_o =$

⁸ Because the wind shear and tower shadow are both symmetric about the vertical axis, there are no sine terms in the Fourier coefficients, only cosine terms.

1,2, ..., in the spectra of forces and moments related to the single blade (like blade torque spectra) and on nP frequencies on the drive train variables. Figure 2-10 shows a clear example of the spectral density function for a rotationally sampled peak of stochastic nature. [27]

A representation of the wind speed variations, underlying these stochastic rotationally sampled peaks in the blade spectra is

$$L_{k\Omega_o}(t) = \varepsilon_1(t) \cos(k\Omega_o t) + \varepsilon_2(t) \sin(k\Omega_o t) \quad (2.43)$$

with, $L_{k\Omega_o}(t)$ being a sinusoid with randomly varying amplitude and phase, and $\varepsilon_1(t)$ and $\varepsilon_2(t)$ independent coloured noise outputs of

$$\dot{\varepsilon}_1 = -a_{k\Omega_o} \varepsilon_1 + b_{k\Omega_o} g_1 \quad (2.44)$$

$$\dot{\varepsilon}_2 = -a_{k\Omega_o} \varepsilon_2 + b_{k\Omega_o} g_2 \quad (2.45)$$

where g_1 and g_2 are white Gaussian noise. The stochastic terms, $\varepsilon_1(t)$ and $\varepsilon_2(t)$, can be interpreted to be the outputs of LTI systems with inputs $\omega_1(t)$ and $\omega_2(t)$, respectively, and frequency response function, $K(\omega)$, defined as

$$K(\omega) = \frac{b_{k\Omega_o}}{(j\omega + a_{k\Omega_o})} \quad (2.46)$$

where $\omega_1(t)$ and $\omega_2(t)$ are independent white Gaussian noise. The spectral density function, $S_{k\Omega_o}(\omega)$, corresponding to $L_{k\Omega_o}(t)$, is

$$S_{k\Omega_o}(\omega) = \frac{1}{2\pi} \frac{b_{k\Omega_o}^2 [\omega^2 + (a_{k\Omega_o}^2 + (k\Omega_o)^2)]}{[\omega^2 - (a_{k\Omega_o}^2 + (k\Omega_o)^2)]^2 + 4a_{k\Omega_o}^2 \omega^2} \quad (2.47)$$

which has the required peak centred at $k\Omega_o$. Therefore, the frequency response function is of the form

$$K(\omega) = \frac{b_{k\Omega_o} \left[j\omega + \sqrt{(a_{k\Omega_o}^2 + (k\Omega_o)^2)} \right]}{-\omega^2 + (a_{k\Omega_o}^2 + (k\Omega_o)^2) + 2a_{k\Omega_o} j\omega} \quad (2.48)$$

where the equivalent representation for the stochastic rotationally sampled wind speed as the output from the LTI system can be found by imputing white noise to (2.46) after it has been transformed to time domain. The height and width of the resulting peak can be adjusted by varying $b_{k\Omega_o}$ and $a_{k\Omega_o}$, respectively. [27]

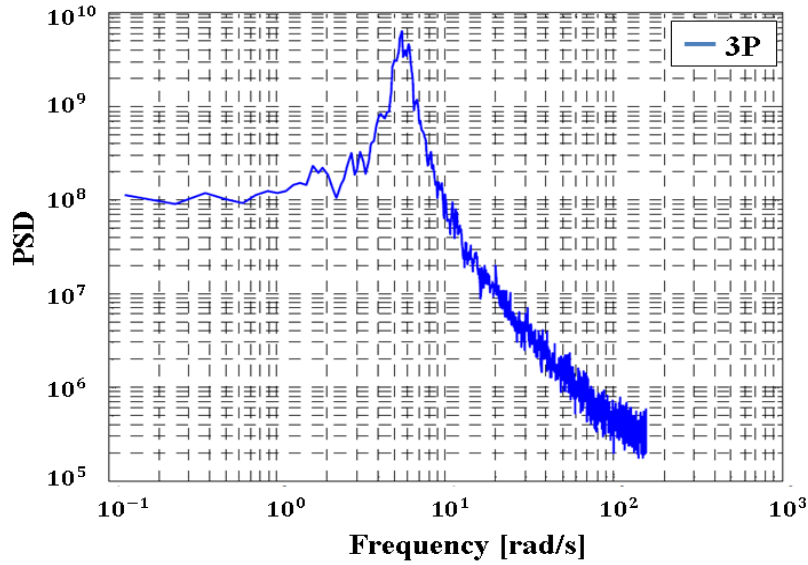


Figure 2-10. Example of stochastic 3P peak in the torque spectral density function of a 3-bladed wind turbine [27]

2.2.4.2.2. Two Correlated Effective Wind Speeds Model

The concept of effective wind speed was extended to 2 correlated wind speeds in [13] in the context of using fledge and sledge devices on the blades and with broader scope in [9] where the correlation of the inner and outer parts of the rotor was explored in detail. This development is subject to the same kind of conditions that restrict the validity of the second philosophy 2.

The correlated wind speed model, as its name suggests, provides simultaneous models to enable two forces or moments to be generated with the correct correlation. In essence, if the auto-covariance and cross-covariance and, thus, the spectral density functions and cross-spectral density functions, of the two forces or moments under consideration remain unchanged, then it does not matter if they were obtained by two different effective wind speeds uniform over their respective swept areas or by interaction with a full wind-field.

To recreate the correlated axial hub torque, with areas A_I and A_O defined as per Figure 2-11, following Section 2.2.4.2, the spectral density function for the inner part of the rotor would take the form:

$$S_{II}(\omega) = S_v(\omega)\phi_{II}(x); \phi_{II}(x) = \bar{\phi}_{II}(x)/\bar{\phi}_{II}(0) \quad (2.49)$$

where

$$\bar{\phi}_{II}(x) = \frac{2\pi^2 R_1^4}{x^2} \left\{ 1 + \frac{4}{\pi} \int_0^{\pi/2} (1 - 3 \sin^2 \theta) e^{-2x \cos \theta} d\theta \right\} \quad (2.50)$$

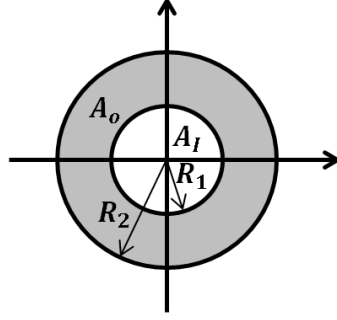


Figure 2-11. Inner and outer sections of rotor disc

The cross-covariance, $R_{T_O T_I}(t)$, between the torque of the outer-area, T_O , and the torque of the internal area, T_I , is

$$R_{T_O T_I}(t) = k^2 \int_{A_O} \int_{A_I} R_{v(r_1)v(r_2)}(t) dA_1 dA_2 \quad (2.51)$$

with $R_{v(r_1)v(r_2)}(t)$ the cross-covariance between the wind at \mathbf{r}_1 and the wind at \mathbf{r}_2 . It follows that the cross-spectral density function for (2.51) becomes

$$S_{T_O T_I}(\omega) = k^2 S_v(\omega) \int_{A_O} \int_{A_I} \chi(\mathbf{r}_1, \mathbf{r}_2, \omega) dA_1 dA_2 = k^2 S_v(\omega) \bar{\Phi}_{IO}(x) \quad (2.52)$$

where,

$$\bar{\Phi}_{IO}(x) = 4\pi R_1^4 \int_0^\delta dz (1+z) \int_0^{\sin^{-1}\left(\frac{1}{1+z}\right)} d\theta \int_{(z+1)\cos\theta - \sqrt{1-(z+1)^2 \sin^2\theta}}^{(z+1)\cos\theta + \sqrt{1-(z+1)^2 \sin^2\theta}} d\bar{l} \bar{l} e^{-x\bar{l}} \quad (2.53)$$

$$\delta = \frac{R_2 - R_1}{R_1}; x = \left(\frac{\gamma R_1}{\bar{V}}\right) \omega = \sigma_1 \omega \quad (2.54)$$

Hence the cross-spectral density function between the effective wind speeds of the inner and outer area is

$$S_{IO}(\omega) = S_v(\omega) \phi_{IO}(x); \phi_{IO}(x) = \bar{\Phi}_{IO}(x) / \bar{\Phi}_{IO}(0) \quad (2.55)$$

with the spectral density function for the effective wind speed of the outer area

$$S_{OO}(\omega) = S_v(\omega) \phi_{OO}(x); \phi_{OO}(x) = \bar{\Phi}_{OO}(x) / \bar{\Phi}_{OO}(0) \quad (2.56)$$

where

$$\bar{\phi}_{OO}(x) = \bar{\phi}_{(I+O)(I+O)}(x) - \bar{\phi}_{II}(x) - 2\bar{\phi}_{IO}(x) \quad (2.57)$$

and

$$\bar{\phi}_{(I+O)(I+O)}(x) = \frac{2\pi^2 R_2^4}{x^2} \left\{ 1 + \frac{4}{\pi} \int_0^{\frac{\pi}{2}} (1 - 3 \sin^2 \theta) e^{-2x \cos \theta} d\theta \right\} \quad (2.58)$$

From (2.55) and (2.56),

$$\begin{bmatrix} S_{II}(\omega) & S_{IO}(\omega) \\ S_{IO}(\omega) & S_{OO}(\omega) \end{bmatrix} = \begin{bmatrix} \phi_{II}(x)S_v(\omega) & \phi_{IO}(x)S_v(\omega) \\ \phi_{IO}(x)S_v(\omega) & \phi_{OO}(x)S_v(\omega) \end{bmatrix} \quad (2.59)$$

After spectral factorisation of ϕ_{II} , ϕ_{IO} and ϕ_{IO} , such

$$|f_1(j\omega)|^2 = \phi_{II}(x) - \frac{\phi_{IO}(x)}{\psi(x)} \quad (2.60)$$

$$|f_2(j\omega)|^2 = \phi_{OO}(x) - \phi_{IO}(x) \psi(x) \quad (2.61)$$

$$|f_3(j\omega)|^2 = \phi_{IO}(x) \quad (2.62)$$

$$|f_4(j\omega)|^2 = \psi(x) \quad (2.63)$$

where the spectrum $\psi(x)$ is chosen so $\psi(0) = 1$ and f_1 , f_2 , f_3 and f_4 can be chosen to be causal and stable.

Finally the models for inner and outer effective wind speeds, V_I and V_O , as derived in [9], are of the form

$$V_I = f_1(s)\omega_1 + \frac{f_3(s)}{f_4(s)}\omega_3 \quad (2.64)$$

$$V_O = f_2(s)\omega_2 + f_3(s)f_4(s)\omega_3 \quad (2.65)$$

where ω_1 , ω_2 and ω_3 are independent point wind speeds and $f_1(s)$, $f_2(s)$, $f_3(s)$ and $f_4(s)$ suitable filters.

The model described in this section is only capable of accurately representing the loads at intermediate frequencies.

2.2.4.2.3. Three Correlated Effective Wind Speeds Model

An attempt to develop 3 correlated effective wind speeds for the rotor, one for each blade was presented in 2009, [28]. In this work the first philosophy is adopted.

The particular focus of [28] is on the correlation between 3 effective wind speeds placed on each one of the rotor blades, v^e , defined as,

$$v^e = \frac{\int_{r_o}^R X(r)v(r)dr}{\int_{r_o}^R X(r)dr} \quad (2.66)$$

with r the position along the blade span, r_o the distance between the hub centre and the base of the blade, R the radius of the rotor, $v(r)$ the wind distribution assumed orthogonal to the plane of rotation and $X(r)$ a weighting function that describes the influence of the wind along the blade. The latter has been chosen to be linear for all the blade forces considered, $X(r) = r$

For the derivation of the wind model, [28], 2 point wind speeds are considered at azimuth angles ψ_1 , ψ_2 and radii r_1 , r_2 , denoted as $v(t, r_1, \psi_1)$ and $v(t, r_2, \psi_2)$. These wind speeds are periodic in azimuth angle at any given time, t . Therefore, the Fourier expansion in azimuth angle, ψ , for a fixed time, t , at a radial position, r , is defined as

$$v(t, r, \psi) = \sum_{n=-\infty}^{\infty} \tilde{v}_n(t, r) e^{in\psi} \quad (2.67)$$

with $\tilde{v}_n(t, r)$ the time-varying Fourier coefficients.

Assuming that the covariance between the two point wind speeds only depends on the Euclidean distance between them,

$$D = \sqrt{r_1^2 + r_2^2 - 2r_1r_2\cos(\Delta\psi)} \quad (2.68)$$

where $\Delta\psi = \psi_2 - \psi_1$, the covariance, $R(\tau, D)$, becomes,

$$\begin{aligned} R(\tau, D) &= \mathbb{E}[\overline{v(t, r_1, \psi_1)v(t + \tau, r_2, \psi_2)}] \\ &= \sum_{n, m=-\infty}^{\infty} \mathbb{E}[\overline{\tilde{v}_n(t, r_1)\tilde{v}_m(t + \tau, r_2)}] e^{i(m\psi_2 - n\psi_1)} \\ &= \sum_{n, m=-\infty}^{\infty} \tilde{R}_{n, m}(\tau, r_1, r_2) e^{i(m\psi_2 - n\psi_1)} = \sum_{n=-\infty}^{\infty} \tilde{R}_{n, n}(\tau, r_1, r_2) e^{in\Delta\psi} \end{aligned} \quad (2.69)$$

where $\tilde{R}_{n, m}(\tau, r_1, r_2)$, is the covariance between the Fourier coefficients

$$\begin{aligned}
\tilde{R}_{n,m}(\tau, r_1, r_2) &= \frac{1}{(2\pi)^2} \int_0^{2\pi} \int_0^{2\pi} E[v(t, r_1, \psi_1)v(t, r_2, \psi_2)] e^{-i(m\psi_2 - n\psi_1)} d\psi_1 d\psi_2 \\
&= \begin{cases} \frac{1}{2\pi} \int_0^{2\pi} R(\tau, D) e^{-im\Delta\psi} d\Delta\psi & , m = n \\ 0 & \text{otherwise} \end{cases} \quad (2.70)
\end{aligned}$$

In [28] it is assumed that the blades rotate at a constant angular velocity $\dot{\psi} = \omega_r$, leading to a constant time evolution of the azimuth angles

$$\psi_1(t) = \omega_r t + \psi_1 \quad ; \quad \psi_2(t) = \omega_r t + \psi_2 \quad (2.71)$$

The covariance of the wind speeds at the rotating points becomes,

$$\begin{aligned}
R^r(\tau, D) &= E[\overline{v(t, r_1, \psi_1(t))v(t + \tau, r_2, \psi_2(t))}] \\
&= \sum_{n,m=-\infty}^{\infty} E[\overline{\tilde{v}_n(t, r_1)\tilde{v}_m(t + \tau, r_2)}] e^{im\omega_r\tau} e^{i(m\psi_2 - n\psi_1)} e^{i\omega_r(m-n)t} \\
&= \sum_{n=-\infty}^{\infty} \tilde{R}_{n,n}(\tau, r_1, r_2) e^{in\omega_r\tau} e^{in\Delta\psi} \quad (2.72)
\end{aligned}$$

and the spectral density function of the rotating points,

$$S^r(\omega, D) = \mathcal{F}\{R^r(\tau, D)\} = \sum_{n=-\infty}^{\infty} \tilde{S}_{nn}(\omega - n\omega_r, r_1, r_2) e^{in\Delta\psi} \quad (2.73)$$

To remove the dependency on the radial coordinates, (2.66) is used, leading to the harmonic spectrum of the blade effective wind speed being defined as,

$$\tilde{S}_{nn}^e(\omega) = \frac{\int_{r_0}^R X(r_2) \int_{r_0}^R X(r_1) F_n(\omega, r_1, r_2) dr_1 dr_2}{\int_{r_0}^R \int_{r_0}^R X(r_2) X(r_1) dr_1 dr_2} S(\omega) = F_n^e(\omega) S(\omega) \quad (2.74)$$

where

$$F_n(\omega, r_1, r_2) = \frac{1}{2\pi} \int_0^{2\pi} C(\omega, D) e^{-in\Delta\psi} d\Delta\psi \quad (2.75)$$

with $C(\omega, D)$ the coherence function.

It follows that the cross spectral density function of the effective wind speeds associated with the rotation (2.71) becomes

$$S^e(\omega, \Delta\psi) = \sum_{n=-\infty}^{\infty} \tilde{S}_{nn}^e(\omega - n\omega_r) e^{in\Delta\psi} \quad (2.76)$$

Assuming that the spacing between the three blades is $\Delta\psi = \frac{2\pi}{3}$, the effective wind speed vector for all three blades is,

$$v^e = [v_1^e(t) \quad v_2^e(t) \quad v_3^e(t)]^T = \left[v_1^e(t, 0) \quad v_2^e\left(t, \frac{2\pi}{3}\right) \quad v_3^e\left(t, \frac{4\pi}{3}\right) \right]^T \quad (2.77)$$

The corresponding spectral density matrix becomes

$$S^e(\omega) = \sum_{n=-\infty}^{\infty} \tilde{S}_{nn}^e \mathbf{E} \quad (2.78)$$

where

$$\mathbf{E} = \begin{bmatrix} 1 & e^{in\frac{2\pi}{3}} & e^{in\frac{4\pi}{3}} \\ e^{in\frac{-2\pi}{3}} & 1 & e^{in\frac{2\pi}{3}} \\ e^{in\frac{-4\pi}{3}} & e^{in\frac{-2\pi}{3}} & 1 \end{bmatrix} \quad (2.79)$$

To progress the spectral factorisation, [28], the wind model is simplified with only the diagonal elements of (2.78) being retained. The proposed wind model for a blade, j , then has the following structure in the frequency domain:

$$v_j^e(\omega) = G_0(\omega)e_0(\omega) + G_1(\omega)e_{j,1}(\omega) + G_2(\omega)e_{j,2}(\omega) + G_3(\omega)e_{j,3}(\omega) \quad , \quad j = 1,2,3 \quad (2.80)$$

where the $e_x(\omega)$ are the frequency representation of Gaussian white noise and $G_{0,\dots,3}(\omega)$ the transfer functions, corresponding to the frequency response functions. The transfer functions are obtained in [28] by minimising a frequency domain cost functions and are listed below, in Table 2-1, with their Bode plots in Figure 2-12.

n	G_n
0	$\frac{0.017004(s + 68.99)}{(s + 2.873)(s + 0.03357)}$
1	$\frac{-0.2807(s + 2.617)(s + 0.2683)}{(s + 0.4707)(s^2 + 0.1992s + 4.399)}$
2	$\frac{-1.4387(s^2 + 0.006123s + 0.1993)}{(s + 1.148)(s + 0.5589)(s^2 + 0.3449s + 17.61)}$
3	$\frac{-1.6613(s^2 + 1.059s + 1.241)}{(s^2 + 3.143s + 2.939)(s^2 + 0.4393s + 39.58)}$

Table 2-1. Transfer functions for wind model by [28]

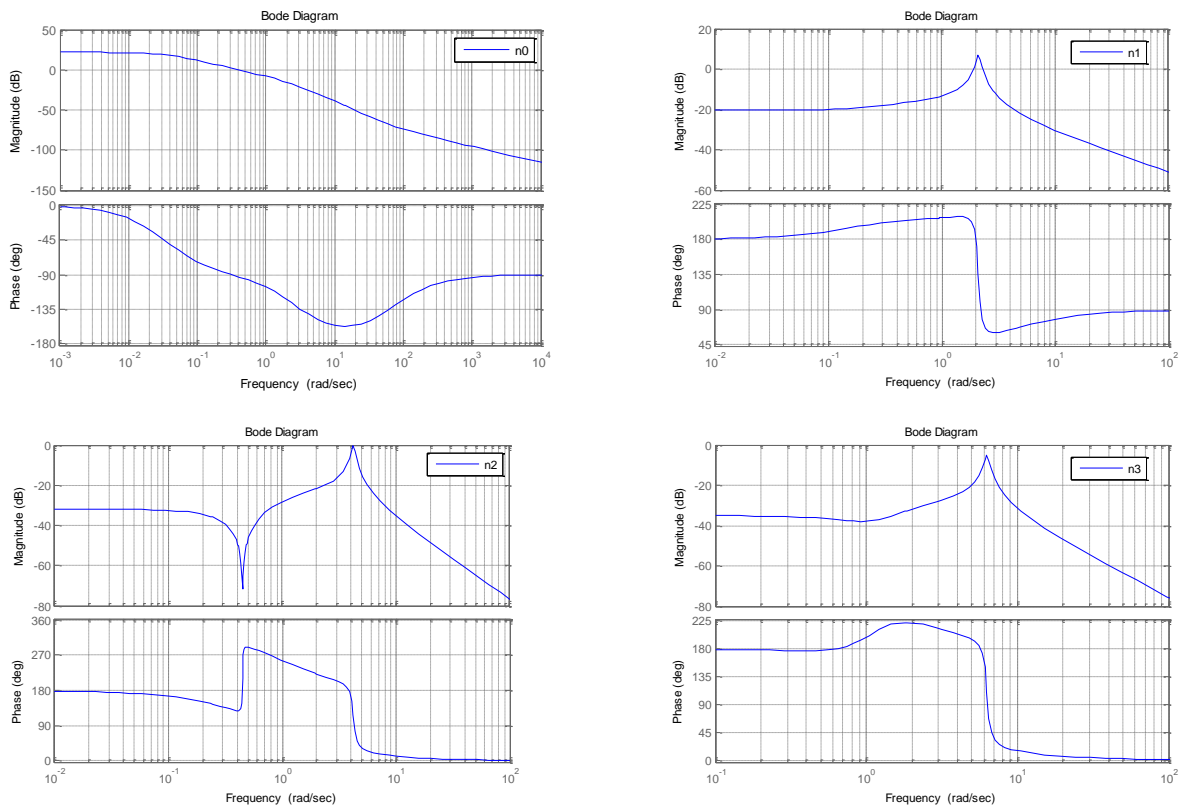


Figure 2-12. Transfer functions bode plots for [28]. Top left $n = 0$, top right $n = 1$, bottom left $n = 2$, bottom right $n = 3$

2.3. Conclusions

This chapter provides a short literature review of the nature and dynamics of the wind resource and most common techniques used to model wind for wind turbine control design and analysis purposes. The general characteristics of wind speed, in particular, the stochastic (atmospheric turbulence) and deterministic (wind shear and tower shadow) components, together with previously developed wind models suitable for control purposes are discussed.

Initially, simple models were used, which represented the wind as a uniform point wind speed over the whole rotor disc through simple addition of several deterministic wind components [15], then more sophisticated point wind speed models, which accounted for the stochastic and turbulent components of the wind [16][20]. In none of these models was the wind-field/rotor interaction considered. Subsequently, the notion of effective wind speed modelling was introduced to aggregate the wind speeds acting over the whole rotor. A stochastic effective wind speed model of the turbulence component, which merely averages the wind over the rotor, was proposed in [21]. In [13], it was refined so that the statistical properties of rotor torque would be reproduced. It was indicated that over the frequency range up to $1P$, torque is reproduced with reasonable accuracy. This aspect of the model was not addressed in [21]. In [9], the approach adopted in [13] was extended to obtain 2 correlated effective wind speed models to reproduce 2 different rotor moments including the correlation between them. In [9], an attempt was made to extend the approach in [21] to obtain 3 correlated wind speed models, one for each blade. However, although models for 3 wind speeds were constructed, they were uncorrelated.

From this literature review it is clear that an effective wind-field model suitable for control purposes that reproduces the torque on each blade and the thrust on the tower with the correct correlations over a frequency range up to $6P$ has not been previously developed.

Chapter 3

Separability for Constant Speed Wind Turbines

The rotor/wind-field interaction model is dependent on the relationship between the statistical characteristics of the wind speeds acting on the rotor and the statistical characteristics of the subsequent torques and forces induced on the rotor, this relationship is highly non-linear. However, that relationship would essentially be linear provided Separability is a sufficiently accurate representation of the aerodynamics over a sufficiently large domain. Separability is, thus, a key facilitator in developing an effective wind-field model for the rotor/wind-field interaction. In Chapter 3, the accuracy of Separability and the extent of its domain are explored for constant speed wind turbines.

Consider an aerodynamic force or moment dependent on 2 or more variables that can be expressed over some neighbourhood of a locus of points as the combination of two additive components dependent on independent variables, e.g. $f(\beta, V) = h(\beta) - g(V)$, where β is the pitch angle of the blades and V the wind speed for constant speed wind turbines or $f(\beta, V, \omega) = h(\beta, \omega) - g(V)$, for variable speed wind turbines, where ω is the rotor speed. When such behaviour is exhibited by a wind turbine aerodynamic relationship and the neighbourhood is large, this property is referred to as Separability.

Separability has been exploited for over 20 years in the context of feedback control for wind turbines. It was first observed in the aerodynamic pitching moment of the blades of a 330kW constant speed wind turbine [29]. However, only Separability local to the locus, was required in [29] and no attempt was made to determine the extent of the neighbourhood. Nevertheless, it was the first demonstration and exploitation of Separability for control design purposes to simplify complex non-linear aerodynamics of wind turbines. In [30], the Separability of aerodynamic torque of a 300kW constant speed wind turbine was explored. A comparison between torque, T , values derived from the standard BEM based non-linear relationship and the values for torque derived from the Separability based representation is depicted in Figure

3-1. The scope of the work in [30] was to establish the extent of the neighbourhood for which this Separability property holds, it can be appreciated that, although the domain range of data is big, the density of data is low and furthermore the data set includes values in the stall region for which Separability does not seem to apply. The values in the stall region are highlighted in Figure 3-1. The results confirm that the property holds for torque values ranging from 0 to 2.5 times rated torque, T_0 . The increasingly dispersed values above 1.6×10^5 Nm are well outside the normal operational range of pitch regulated wind turbines. The accuracy of approximation and the range over which it holds is sufficient for feedback control purposes. In [31], Separability of classic BEM models for a 300kW variable speed WT with T_0 equal to 71.75 kNm was investigated. Figure 3-2 highlights that for this variable speed WT, when looking into values restricted to the normal operating envelop, Separability does occur for a range of $\pm 23\%$ around rated torque (area boxed between 55 and 90 kNm). The approximation can be considered sufficiently good for the representation of the aerodynamic torque for the purposes of feedback control design. No attempt to derive the best possible Separability functions or maximise their domain was made, some of the spread in the results may be due to this. In contrast to the previous example, the data density is high in this instance but the neighbourhood is limited to the vicinity of the normal operating range of the WT.

It is clear from this early work that Separability existed when derived from aerodynamic torques related to BEM modelling, and that it had a range and domain suitable for control. But an essential question remained, was Separability the outcome of the simplification of the rotor aerodynamics that BEM introduces or was it a real property of the aerodynamics of wind turbines? In [32] the aerodynamic model of a 1MW commercial wind turbine was identified from field data and Separability established. The normalisedⁱ result of the comparison between the aerodynamic torque derived from experimental field data and Separability relationship derived from the same data set can be seen on Figure 3-3. The data in Figure 3-3 has been normalised to the interval, (0,1), with the rated torque 0.5. Regardless of the restricted nature of the range of aerodynamic torques that were used, close to T_0 , due to the data being obtained during normal operation of the WT (big excursions from optimal operation would not occur) the results are remarkable. The correlation between Separability results for a real operating strategy of a variable speed WT and field data demonstrates that Separability is exhibited by

ⁱ The data has been normalised to protect commercial interests.

experimental data (WT aerodynamics derived directly from field measurements) and thus it cannot be an artefact related to BEM simplifications. [29][30][31][32]

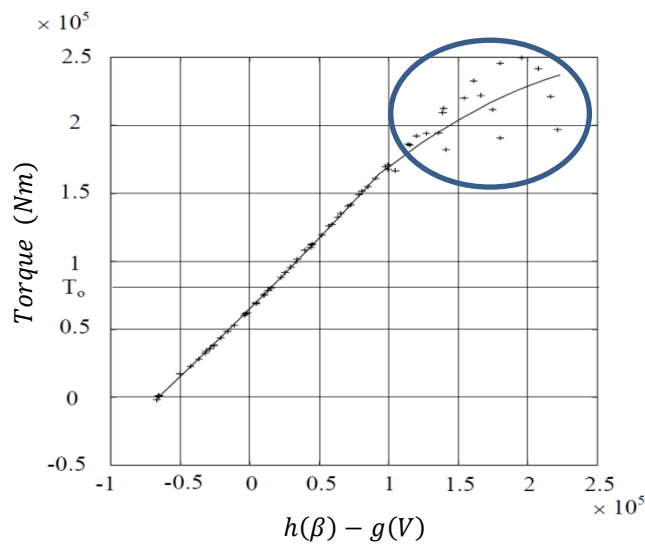


Figure 3-1. Separability in a constant speed 300kW wind turbine [30]

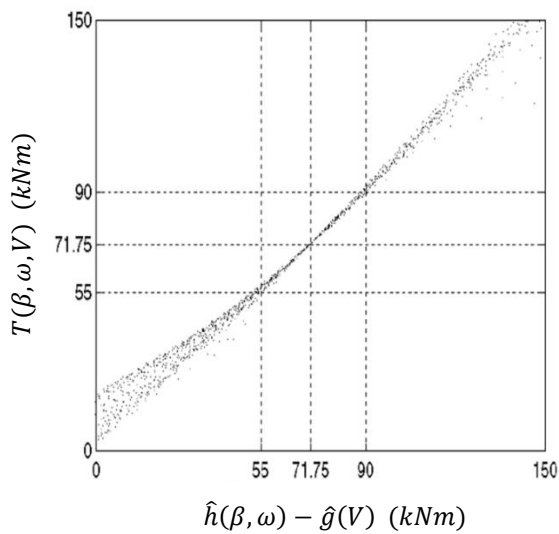


Figure 3-2. Separability for a 300kW variable-speed wind turbine [31]

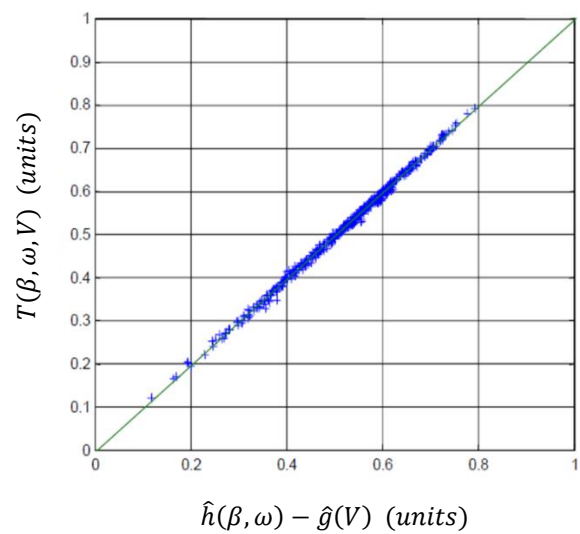


Figure 3-3. Separability (normalised) for a 1MW variable speed wind turbine [32]

The significance of the above, particularly in the context of wind turbine control, is that the speed feedback control loop is independent from the wind speed. The wind turbine can be modelled as a non-linear dynamic system dependent on the nonlinearity $h_{\omega_o}(\beta)$ and an additive external disturbance, $g_{\omega_o}(V)$, dependent only on wind speedⁱⁱ [31]. Figure 3-4 shows a control block diagram incorporating the aerodynamic Separability relationship and the speed

ⁱⁱ Functions $h_{\omega_o}(\beta)$ and $g_{\omega_o}(V)$ are unique for each ω_o and rotor

feedback control loop. The speed feedback loop is independent of wind speed and its dynamics are only non-linear in pitch angle.

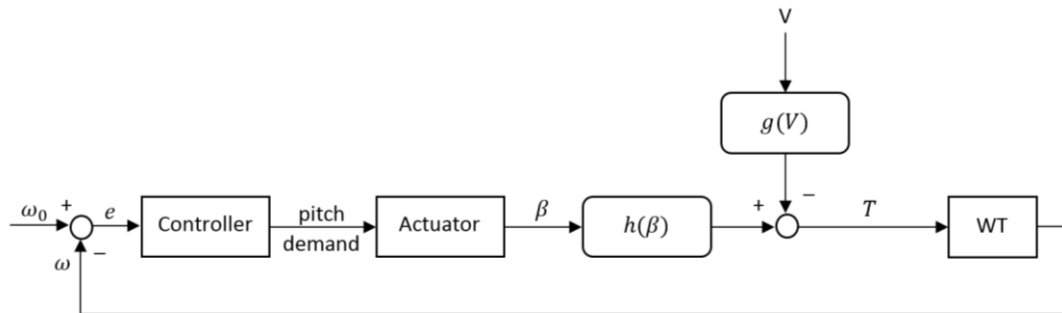


Figure 3-4. Block diagram decomposition of aerodynamic non-linearity and speed feedback control loop

During these early studies the main objective was to ascertain that Separability held sufficiently well for feedback control purposes. There was no concerted effort to determine how good an approximation it could provide. However, this initial research did not only provide answers to the initial questions posed, but it also brought new ones. Since Separability had been proven to apply to both BEM aerodynamics and field derived aerodynamics (derived from direct measurements on a real WT), there was a strong suggestion that Separability was indeed a property of the aerodynamics of WTs. The strength of the property mainly depends on how good a representation of the aerodynamic torque it could provide. If Separability is proven to be highly accurate over large neighbourhoods, then more questions arise: such as, what exactly does Separability tell about the aerodynamics of a WT? What are the implications? Is it related to optimum design of the rotor? What is the best functional representation of Separability?

Furthermore, the control of WTs has evolved and become more complex with controllers including feed forward terms and sophisticated effective wind speed models, e.g. PAC for wind turbine control [33]. The higher complexity of modern WT control is one of the main reason for looking into the Separability property in detail, here. The second is that Separability enables an effective wind-field model to be developed in Chapter 5. To this end the study of Separability is divided between Chapter 3, which focuses on constant speed WTs, and Chapter 4, which covers variable speed WTs.

In this Chapter, Separability of the aerodynamic torque for a constant speed wind turbine, i.e. the additive property, $T(\beta, V) = h(\beta) - g(V)$, is investigated in detail. In Section 3.1, basic additive approximation methods are discussed. In Section 3.2, an Additivity Property theorem

core to the Separability property is introduced. In Section 3.3, global Separability behaviour is discussed. In Section 3.4, the application of Separability to the aerodynamic torque of a wind turbine is considered. Section 3.5, derivation of the functions involved in the separated representation is investigated. In Section 3.6, the results for Separability for constant speed WTs are discussed and, in Section 3.7, the conclusions for the Separability property for constant speed WT are summarised.

3.1. Simple Additive Approximations

Consider a function $F(x, y)$ for which $F(x_s, y_s) = F_0$ for all points, (x_s, y_s) , on some locus, ℓ . There are several approaches to obtaining an approximation of $F(x, y)$ as an additive combination of a function of x and a function of y such that $F(x, y) = h(x) - g(y)$. Some standard approaches are discussed in this chapter. To support the Separability property, the minimal requirement is that the approximation has the correct values and derivatives for $F(x, y)$ on ℓ .

3.1.1. Taylor's Expansion

At a point, (x_s, y_s) on the locus, ℓ , by Taylor's series linearisation

$$F(x, y) \approx F_0 + (x - x_s) \left. \frac{\partial F(x, y)}{\partial x} \right|_{(x_s, y_s)} + (y - y_s) \left. \frac{\partial F(x, y)}{\partial y} \right|_{(x_s, y_s)} \quad (3.1)$$

Clearly, this approximation is additive with

$$h(x) = F_0 + (x - x_s) \left. \frac{\partial F(x, y)}{\partial x} \right|_{(x_s, y_s)} \quad \text{and} \quad g(y) = -(y - y_s) \left. \frac{\partial F(x, y)}{\partial y} \right|_{(x_s, y_s)} \quad (3.2)$$

Provided (x, y) remain within a sufficiently small neighbourhood of (x_s, y_s) , then $F(x, y) = h(x) - g(y)$ to arbitrary accuracy with both the value and derivatives correct at (x_s, y_s) .

When this additive property is applied to a given function, the main characteristics exhibited are:

- At a specific point, (x_s, y_s) , the value of the function is correct, i.e. $F(x_s, y_s) = F_0$.
- The derivatives at (x_s, y_s) are correct.
- A measure of nearness to (x_s, y_s) is simply the Euclidean distance.
- The approximation is specific to the point, (x_s, y_s) only and does not extend over all points for which $F(x_s, y_s) = F_0$.

3.1.2. Direct Approach

Since the Taylor's expansion linearization only applies to a specific point, it is unsatisfactory and a better approach, that applies over the whole locus, ℓ , is required. For any function, $g(y)$, define the function $h(x)$ by

$$h(x)|_{x=x_o} = g(y)|_{y=y_o} + F(x_o, y_o) \quad (3.3)$$

for all points, (x_o, y_o) , on ℓ then

$$F(x, y) = h(x) - g(y) \quad (3.4)$$

that is, the dependence of F on x and y can always be expressed additively on the locus. At the points on the locus, (3.4) gives the correct value of $F(x, y)$ but, depending on the choice of $g(y)$, the difference between $F(x, y)$ and $h(x) - g(y)$ can increase rapidly as the distance from the locus increases. Furthermore, the gradients of the derivatives on the locus need not be correct.

When this additive property is applied to a given function, the main characteristics exhibited are:

- At the points on the locus, the correct value of the function is obtained.
- Information about the correctness of the derivatives on the points on the locus cannot be inferred.
- In general $h(x) - g(y)$ need not be a good approximation to $F(x, y)$ outside the locus.

3.2. Additivity Property Theorem

The approaches to obtaining an additive approximation to $F(x, y)$ discussed in Section 3.1 are clearly insufficient to provide insight into the Separability property. The following Theorem, [34], provides that insight.

Theorem 3.2: Consider a function $F(x, y)$ with domain $D_F \subset \mathbb{R}_2$. Suppose $F(x, y)$ is continuously differentiable on $\ell \subset \mathbb{R}_2$, a continuous locus closed in \mathbb{R}_2 , on which

$$F(x_o, y_o) = F_0 \quad (3.5)$$

with F_0 constant. Provided that, for all $(x_o, y_o) \in \ell$,

$$\frac{\partial F(x_o, y_o)}{\partial y} \neq 0 \quad (3.6)$$

and, for almost all $(x_o, y_o) \in \ell$,

$$\frac{\partial F(x_o, y_o)}{\partial x} > 0 \text{ or } \frac{\partial F(x_o, y_o)}{\partial x} < 0 \quad (3.7)$$

then there exist continuously differentiable functions, $h(x)$ and $g(y)$, such that

- i) for all $(x_o, y_o) \in \ell$, $g(y_o) = h(x_o)$
- ii) for all $(x_o, y_o) \in \ell$, $\frac{\partial F(x_o, y_o)}{\partial x} = h'(x_o)$ and $\frac{\partial F(x_o, y_o)}{\partial y} = -g'(y_o)$
- iii) for all $(x_o, y_o) \in \ell$, $F_o + h(x) - g(y)$ is tangential to $F(x, y)$
- iv) for any $\mu > 0$, there exists a $\delta > 0$ such that $|F(x, y) - (F_o + \varepsilon(x, y))| < \mu$ for all $(x, y) \in \{(x, y) : |\varepsilon(x, y)| < \delta\}$, where $\varepsilon(x, y) = h(x) - g(y)$
- v) for any $\mu > 0$, there exists a $\delta_1, \delta_2 > 0$ such that $|\frac{\partial F(x, y)}{\partial x} - h'(x)| < \mu$, for all $(x, y) \in \{(x, y) : |\varepsilon(x, y)| < \delta_1\}$, and $|\frac{\partial F(x, y)}{\partial y} - g'(y)| < \mu$, for all $(x, y) \in \{(x, y) : |\varepsilon(x, y)| < \delta_2\}$

Proof: By the implicit function theorem, for any $(x_o, y_o) \in \ell$, there exists an open set $U \subset \mathbb{R}$ containing x_o and a unique continuously differentiable function $f(\cdot)$ such that, for all $x \in U$, $(x, f(x)) \in \ell$ and

$$\frac{\partial F(x, f(x))}{\partial x} = -\frac{df(x)}{dx} \frac{\partial F(x, f(x))}{\partial y} \quad (3.8)$$

Hence, since ℓ is continuous, there exists a unique continuously differentiable function, $F(\cdot)$, such that, for all $(x_o, y_o) \in \ell$, $y_o = f(x_o)$ and

$$\frac{\partial F(x_o, y_o)}{\partial x} = -\frac{df(x_o)}{dx} \frac{\partial F(x_o, y_o)}{\partial y} \quad (3.9)$$

Clearly, for almost all $x \in \{x_o : (x_o, f(x_o)) \in \ell\}$, $f'(x) > 0$ or $f'(x) < 0$. Let $h(\cdot)$ and $g(\cdot)$ be continuously differentiable functions with domains, $D_h = \{x | (x, y) \in \ell \text{ for some } y\}$ and $D_g = \{y | (x, y) \in \ell \text{ for some } x\}$, respectively, and ranges R_h and R_g , respectively. Furthermore, let $h^{-1}(\cdot)$ exist with domain R_h and $g'(y_o) \neq 0$, for all $y_o \in D_g$. The derivative of $h^{-1}(\cdot)$ exists and is continuous almost everywhere in R_h and $g^{-1}(\cdot)$ exists with domain R_g and its derivative exists with domain R_g . Consider the transformation, $(x, y) \rightarrow (u, v)$ for all

$(x_o, y_o) \in \ell$, such that

$$u = h(x) + g(y) \quad (3.10)$$

$$v = h(x) - g(y) \quad (3.11)$$

then, for all $(u_o, v_o) \in \hat{\ell} = \{(u, v) | u = h(x) + g(y), v = h(x) - g(y), \text{ for all } (x, y) \in \ell\}$, the inverse transformation, $(u, v) \rightarrow (x, y)$, also exists such that

$$x = h^{-1}\left(\frac{1}{2}(u+v)\right) \quad (3.12)$$

$$y = g^{-1}\left(\frac{1}{2}(u-v)\right) \quad (3.13)$$

Hence, there exists a function, $G(u, v)$, such that

$$F(x_o, y_o) = G(u_o, v_o) \quad (3.14)$$

for all $(u_o, v_o) \in \hat{\ell}$. Furthermore, other than at those points $(x_o, y_o) \in \ell$ for which the derivative of $h^{-1}(\cdot)$ does not exist, $G(u, v)$ is continuously differentiable with

$$\begin{bmatrix} \frac{\partial F(x_o, y_o)}{\partial x} \\ \frac{\partial F(x_o, y_o)}{\partial y} \end{bmatrix} = \begin{bmatrix} h'(x_o) & h'(x_o) \\ g'(y_o) & -g'(y_o) \end{bmatrix} \begin{bmatrix} \frac{\partial G(u_o, v_o)}{\partial u} \\ \frac{\partial G(u_o, v_o)}{\partial v} \end{bmatrix} \quad (3.15)$$

Without loss of generality, it is possible to choose $h(\cdot)$ such that, for all $(x_o, y_o) \in \ell$,

$$h(x_o) = g(f(x_o)) = g(y_o) \quad (3.16)$$

thereby meeting (i). It follows that

$$h'(x_o) = f'(x_o)g'(f(x_o)) = f'(x_o)g'(y_o) \quad (3.17)$$

and, for almost all $x \in \{x_o : (x_o, f(x_o)) \in \ell\}$, $h'(x) > 0$ or $h'(x) < 0$ as required by existence of $h^{-1}(\cdot)$. Hence, for almost all $(x_o, y_o) \in \ell$,

$$\begin{aligned} 0 &= \frac{\partial F(x_o, y_o)}{\partial x} + \frac{df(x_o)}{dx} \frac{\partial F(x_o, y_o)}{\partial y} \\ &= (h'(x_o) + \frac{df(x_o)}{dx} g'(y_o)) \frac{\partial G(u_o, v_o)}{\partial u} + (h'(x_o) - \frac{df(x_o)}{dx} g'(y_o)) \frac{\partial G(u_o, v_o)}{\partial v} \\ &= 2 \frac{df(x_o)}{dx} g'(y_o) \frac{\partial G(u_o, v_o)}{\partial u} = 2h'(x_o) \frac{\partial G(u_o, v_o)}{\partial u} \end{aligned} \quad (3.18)$$

And, for almost all $(u_o, v_o) \in \hat{\ell}$,

$$\frac{\partial G(u_o, v_o)}{\partial u} = 0 \quad (3.19)$$

Furthermore, since, for all $(x_o, y_o) \in \ell$, $\frac{\partial F(x_o, y_o)}{\partial y} \neq 0$ and $g'(y_o) \neq 0$, it is possible without loss of generality to choose $g(\cdot)$ such that

$$g'(y_o) = -\frac{\partial F(x_o, y_o)}{\partial y} \quad (3.20)$$

for all $(x_o, y_o) \in \ell$. Consequently, since $\frac{\partial F(x_o, y_o)}{\partial y} = -g'(y_o) \frac{\partial G(u_o, v_o)}{\partial v}$ for almost all $(u_o, v_o) \in \hat{\ell}$,

$$\frac{\partial G(u_o, v_o)}{\partial v} = 1 \quad (3.21)$$

for almost all $(u_o, v_o) \in \hat{\ell}$. In addition, since $h(\cdot)$ and $F(x, y)$ are continuously differentiable for all $(x_o, y_o) \in \ell$ and $\frac{\partial F(x_o, y_o)}{\partial x} = h'(x_o) \frac{\partial G(u_o, v_o)}{\partial v}$ for almost all $(x_o, y_o) \in \ell$,

$$h'(x_o) = \frac{\partial F(x_o, y_o)}{\partial x} \quad (3.22)$$

for all $(x_o, y_o) \in \ell$, thereby meeting (ii).

Part (iii) follows directly from (i) and (ii) and near any $(x_o, y_o) \in \ell$,

$$F(x, y) \approx F_0 + (h(x) - g(y)) \quad (3.23)$$

To be more precise, since $F(x, y)$, $h(x)$ and $g(y)$ are continuous, for any $(x_o, y_o) \in \ell$ and $\mu > 0$, there exists a $\delta > 0$ such that $|F(x, y) - (F_0 + h(x) - g(y))| < \mu$ and, since $h(x)$ and $g(y)$ are continuously differentiable on D_h and D_g , respectively, $\varepsilon(x, y) \in (\varepsilon_{\min}, \varepsilon_{\max})$ for all $(x, y) \in \{(x, y) : \|(x, y) - (x_o, y_o)\|_2 < \delta\}$. Moreover, since ℓ is closed in \mathbb{R}_2 , it is compact in \mathbb{R}_2 , and, therefore, for any $\mu > 0$, there exists $\delta > 0$ and associated $\varepsilon_{\min} < 0$ and $\varepsilon_{\max} > 0$ such that $(x, y) \in \{(x, y) : \varepsilon(x, y) \in (\varepsilon_{\min}, \varepsilon_{\max})\}$ implies $\{(x, y) : \|(x, y) - (x_o, y_o)\|_2 < \delta, \text{ for some } (x_o, y_o) \in \ell\}$ and so $|F(x, y) - (F_0 + \varepsilon(x, y))| < \mu$. Hence, for any $\mu > 0$, there exists a $\delta > 0$ such that $|F(x, y) - (F_0 + \varepsilon(x, y))| < \mu$ for all $(x, y) \in \{(x, y) : |\varepsilon(x, y)| < \delta\}$ as required by (iv).

Part (v) is established in a similar manner to (iv).

In short, what Theorem 3.2 implies is that provided (x, y) remain within a sufficiently small neighbourhood of the locus, ℓ , as measured by ε , then, the function $F(x, y)$ is to arbitrary

accuracy uniformly equal to the additive combination of functions of x and y , i.e.

$$F(x, y) = F_0 + \varepsilon \quad ; \quad \varepsilon = h(x) - g(y) \quad (3.24)$$

Similarly, the derivatives are uniformly equal to arbitrary accuracy as measured by ε .

From Theorem 3.2 and its proof, several useful properties of the functions involved in the Separability property are observed:

- 1) Functions $h(\cdot)$ and $g(\cdot)$ are continuously differentiable functions with domains, $D_h = \{x | (x, y) \in \ell \text{ for some } y\}$ and $D_g = \{y | (x, y) \in \ell \text{ for some } x\}$, respectively.
- 2) The gradients, $\frac{\partial F(x_o, y_o)}{\partial x}$ and $\frac{\partial F(x_o, y_o)}{\partial y}$, must not change sign on the locus, ℓ .
- 3) For all $(x_o, y_o) \in \ell$, $\frac{\partial F(x_o, y_o)}{\partial x} = h'(x_o)$ and $\frac{\partial F(x_o, y_o)}{\partial y} = -g'(y_o)$
- 4) For all $(x_o, y_o) \in \ell$, $h(x_o) = g(y_o)$, where $y_o = f(x_o)$.
- 5) Hence, with respect to accuracy, ε acts as the measure of displacement from the locus, ℓ .

The maximum possible domain for $F(x, y)$, over which the Separability property is valid, is restricted by the above observations. By 1), the region of validity is $D_h \times D_g \subset D_F$. In other words, it is the points, $(x, y) \in D_F$, for which there exists a y_o such that $(x, y_o) \in \ell$ and a x_o such that $(x_o, y) \in \ell$. By 2), if either $\frac{\partial F(x_o, y_o)}{\partial x}$ or $\frac{\partial F(x_o, y_o)}{\partial y}$ changes sign within $D_h \times D_g$, then additional boundaries arise from the loci of points on which either derivative is zero. For example, since the derivative of aerodynamic torque with respect to rotor speed changes sign on entering stall, the data points in the stall region in Figure 3-1 should be discounted.

3.3. From Local Additivity to Global Separability Behaviour

When the neighbourhood of applicability of the additivity property defined in Section 3.2 is big, that is, when the property becomes global rather than local, then Separability as defined at the beginning of this chapter applies. When considering this global relationship, a generalisation of the non-linear dependence on ε is possible. The additivity property in Section 3.2, is modified such that,

$$F(x, y) = \tau(F_0 + \varepsilon) = \tau(F_0 + h(x) - g(y)) \quad (3.25)$$

where function τ is a non-linear function. By choosing $\tau(F_0) = F_0$, where F_0 is a constant, (3.25) is consistent with (3.5) of Theorem 3.2. Also, by choosing $\tau'(F_0 + \varepsilon_0) = \tau'(F_0) = 1$,

where $\varepsilon_0 = h(x_0) - g(y_0) = 0$, it is ensured that the gradients of the derivatives are correct by construction. In a sufficiently small neighbourhood of the locus, (3.25) can be simplified to:

$$F(x, y) = F_0 + h(x) - g(y) \quad (3.26)$$

which is, in fact, (3.23).

3.4. Separability in the Context of Wind Turbines

In Section 3.2 a local Additivity property is introduced and, in Section 3.3 its extension to Separability is considered. In the current section the Separability property is investigated in the context of the aerodynamic torque, T , for constant speed WTs, which is non-linearly dependent on the pitch angle, β , and wind speed, V .

In applying the theory from Section 3.3 to WTs, (β, V) supplant the generic variables (x, y) . Similarly, $h_{\omega_0}(\cdot)$ and $g_{\omega_0}(\cdot)$ supplant the generic functions $h(\cdot)$ and $g(\cdot)$, $\varepsilon_{\omega_0}(\cdot)$ supplants $\varepsilon(\cdot)$ and $\tau_{\omega_0}(\cdot)$ supplants $\tau(\cdot)$.

3.4.1. Constant Speed Wind Turbines

For a constant speed wind turbine, with a constant rotor speed, ω_0 and rated torque, T_0 , in above rated conditions, there is a pitch angle at which T_0 is attained for each wind speed; that is, there is a locus of equilibrium operating points on which the torque is T_0 . Provided that as per (3.9), $f_{\omega_0}(V)$ is monotonic, where $f_{\omega_0}(V)$ is the relationship of β to V along this locus of equilibrium points, and $h_{\omega_0}(\beta)$ and $g_{\omega_0}(V)$ are chosen following (3.16), then, by part ii), the Additivity Theorem in Section 3.2, it follows that,

$$h'_{\omega_0}(\beta) = \frac{\partial T(\beta, f_{\omega_0}^{-1}(\beta))}{\partial \beta} \quad (3.28)$$

$$g'_{\omega_0}(V) = -\frac{\partial T(f_{\omega_0}(V), V)}{\partial V} \quad (3.29)$$

(3.23) becomes,

$$T(\beta, V) = T(\beta, V, \omega)|_{\omega_0} = T_0 + \varepsilon_{\omega_0}(\beta, V) = T_0 + (h_{\omega_0}(\beta) - g_{\omega_0}(V)) \quad (3.30)$$

with $(h_{\omega_0}(\beta) - g_{\omega_0}(V)) = 0$ on the locus. The partial derivatives by construction are, also, correct on the locus as required.

Locally to the locus of equilibrium operating points, $T_0 + \varepsilon_{\omega_0}(\beta, V)$ is a good representation of $T(\beta, V)$; that is, within a sufficiently small neighbourhood of the locus the difference can be made arbitrarily small. More generally, bringing in the discussion in Section 3.3, near the locus,

$$T_{\omega_0}(\beta, V) \approx \tau_{\omega_0}(T_0 + \varepsilon_{\omega_0}) = \tau_{\omega_0}\left(T_0 + \left(h_{\omega_0}(\beta) - g_{\omega_0}(V)\right)\right) \quad (3.31)$$

for some function τ_{ω_0} such that,

$$\tau_{\omega_0}(T_0 + \varepsilon_{\omega_0})\Big|_{\varepsilon_{\omega_0}=0} = T_0 \quad (3.32)$$

$$\tau_{\omega_0}'(T_0 + \varepsilon_{\omega_0})\Big|_{\varepsilon_{\omega_0}=0} = 1 \quad (3.33)$$

By judicious choice of $\tau_{\omega_0}(\cdot)$, the size of the neighbourhood can be maximised. In effect, in a region that includes the whole set of equilibrium operating points, the dependence of aerodynamic torque on pitch angle is through $h_{\omega_0}(\beta)$ and on wind speed through $g_{\omega_0}(V)$ whilst the dependence on displacement of the operating point from the locus is through τ_{ω_0} , see observation 5) in Section 3.2.

As is known from previous work [29][30][31][32], somewhat surprisingly, $T_{\omega_0}(\beta, V) = \tau_{\omega_0}\left(T_0 + \left(h_{\omega_0}(\beta) - g_{\omega_0}(V)\right)\right)$ applies for a very large neighbourhood for a very wide range of rotors, in fact, for all investigated to date. Furthermore, $\tau_{\omega_0}(\cdot)$, is generally a weak nonlinear function. Typically, the neighbourhood includes values of aerodynamic torque between 0 and $2T_0$.

The Additivity Property Theorem, Section 3.2, provides insight into the domain of β and V for which Separability may apply, since a necessary condition for Separability is that the Additivity Property must hold locally to the locus of equilibrium operating points. The valid domain for β and V is restricted to those points such that there exists a pitch angle of the blade for that wind speed for which the torque is T_0 and that there exists a wind speed for that pitch angle for which the torque is T_0 . Other restrictions are that values of β and V for which the torque is negative and those for which there is a change of sign in the derivatives compared to the locus should not be considered. Nevertheless for illustrative purposes, some of them have been included in the analysis. [29][30][31][32]

3.5. Determination of the Separated form of Torque

There are two main approaches when it comes to determining the separated equations for torque, direct integration of the partial derivatives, for example as used in [31], see Figure 3-2. The second approach avoids the need for derivatives and can achieve higher accuracy when the derivatives would be noisy [29]. The second approach is adopted here. The data used are C_q tables from aerodynamic simulations in Bladed, which can be coarse, see Figure 3-5, where the constant pitch angle lines are not especially smooth. These tables would need to be numerically differentiated to get the derivatives, which would be noisy leading to the separated form having inaccuracy near T_0 , which is unfortunate.

3.5.1. Procedure for Determining $g_{\omega_0}(V)$ and $h_{\omega_0}(\beta)$

An empirical/graphical explanation of the method used to determine the equations in Separability to high accuracy. This method was initially introduced in [29] but its full potential is only explored here. The method is explained step by step in the following and the Matlab code used can be found in Appendix L. A 3MW WT with a well-designed rotor, PJ9, is used to illustrate the procedure.

The starting point of the process is the C_q table of the WT of interest. The C_q table used is obtained from Bladed for a pitch range of -3 to 50 degrees in 1 degree increments and a tip speed ratio range of 0.1 to 21.9 with 0.1 increments. The values of C_q are plotted in Figure 3-5, where each line represents a constant pitch angle and the arrow indicates increasingly positive values of pitch angle. Since the rotor speed is constant, this table is re-tabulated in terms of pitch and wind speed instead of pitch angle and tip speed ratio.

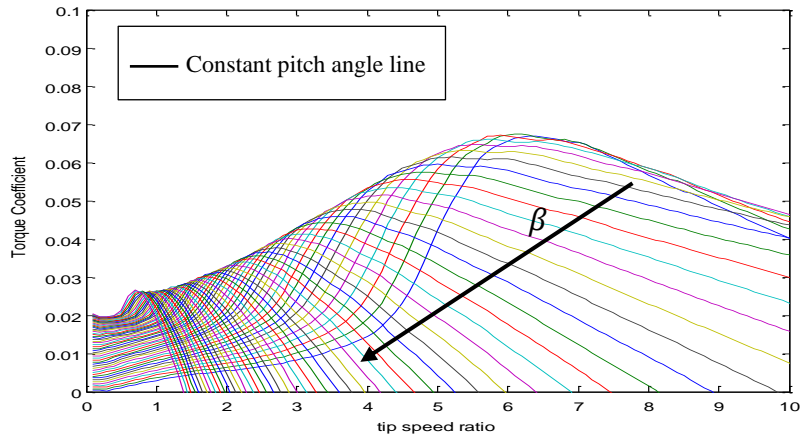


Figure 3-5. C_q table for rotor PJ9

Having re-tabulated the C_q table, the following steps ensue:

- 1) Calculate the equilibrium wind speed at each pitch angle, for which C_q is tabulated, to obtain $f_{\omega_0}(V)$, that is, the pitch scheduling, see Figure 3-6. This function is monotonic as required by Theorem 3.2.
- 2) Transform the wind speed values of the C_q table into pitch angles using the pitch scheduling, these pitch angles are referred to as equivalent pitch angle, $\beta^* = f_{\omega_0}(V)$. This process is illustrated with red arrows in Figure 3-6, where a wind speed of 15m/s is transformed into an equivalent pitch angle of 10 degrees.

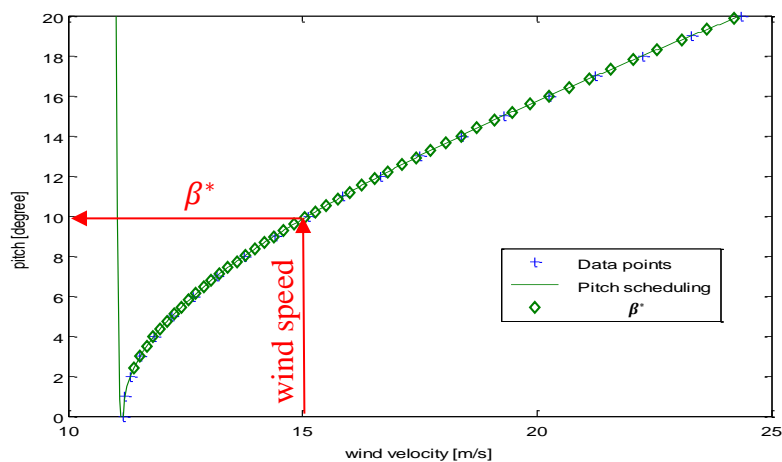


Figure 3-6. Pitch scheduling for rotor PJ9

- 3) Calculate the aerodynamic torque at each combination of pitch angle and wind speed, for which C_q is tabulated. In Figure 3-7. , these values are plotted for constant pitch angle against the equivalent pitch angle, β^* . Unsuitable data are neglected, specifically negative

torque values, stall region torque values and generally any value that cannot physically allow the WT to regain equilibrium.

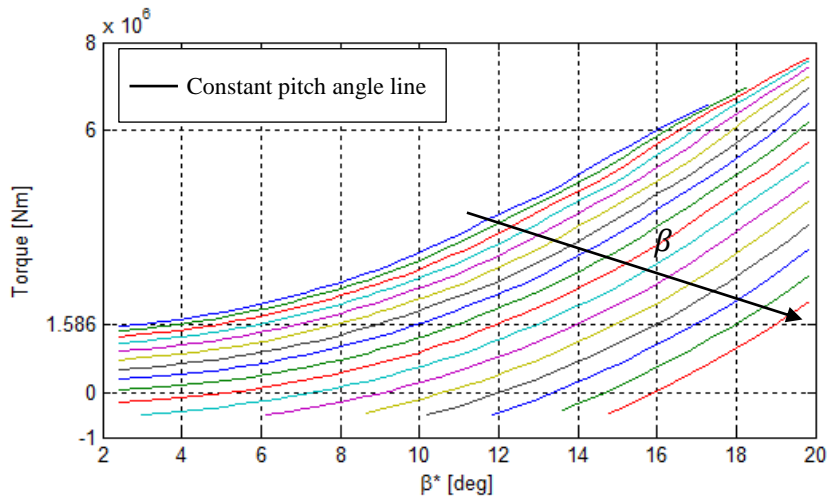


Figure 3-7. Torque table with modified axes for rotor PJ9

- 4) From the set of torque values calculated in 2), those closest to rated torque are indicated on each plot of constant pitch angle in Figure 3-8.

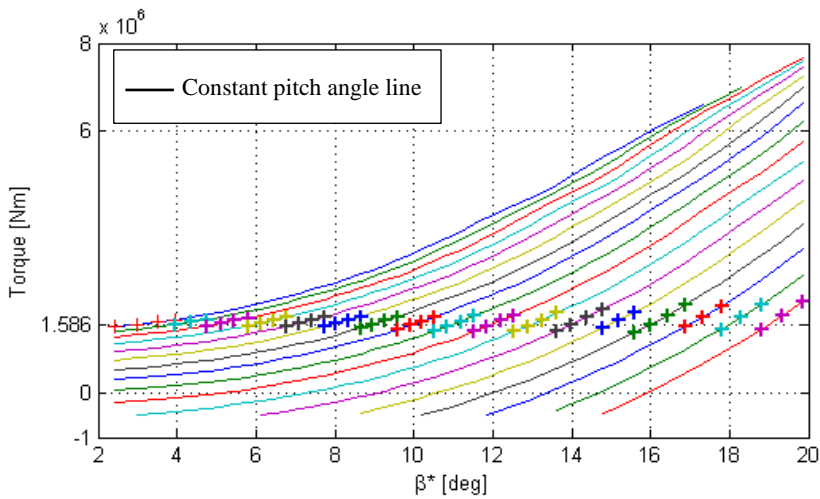


Figure 3-8. Torque table with modified axes and T_{rated} surrounding values for rotor PJ9

From observation 4) in Section 3.2, when the local sections in Figure 3-8 are displaced vertically to form a continuous plot, see Figure 3-9. , the relationship obtained between torque and β^* is the function, $-h_{\omega_0}(\cdot)$.

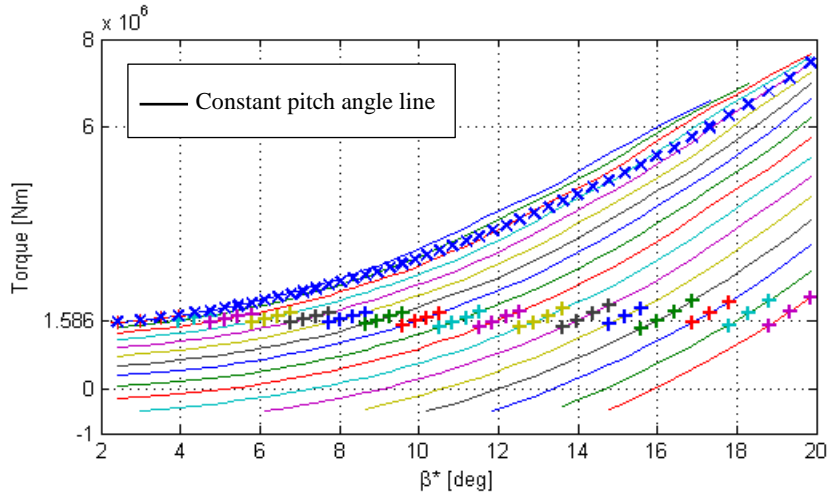


Figure 3-9. Torque table with modified axes, rated torque surrounding values and $g(\beta^*)$ function for rotor PJ9

- 5) With each pitch angle, for which C_q is tabulated, represented by a single data point, the mirror image of the relationship shown in Figure 3-9. is constructed, see Figure 3-10, and then the least squares quadratic fit

$$h_{\omega_0}(\beta) = (-1.46 \times 10^4)\beta^2 + (-1.21 \times 10^4)\beta + 1.75 \times 10^6$$

for $h_{\omega_0}(\cdot)$ is determined. It represents this relationship well, see Figure 3-11.

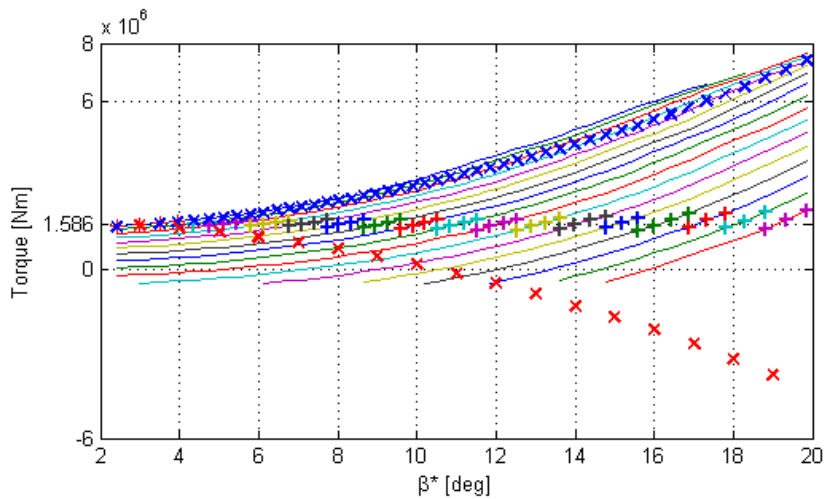


Figure 3-10. Torque table with modified axes, rated torque surrounding values, $g_{\omega_0}(\beta^*)$ and $h_{\omega_0}(\beta)$ functions for rotor PJ9

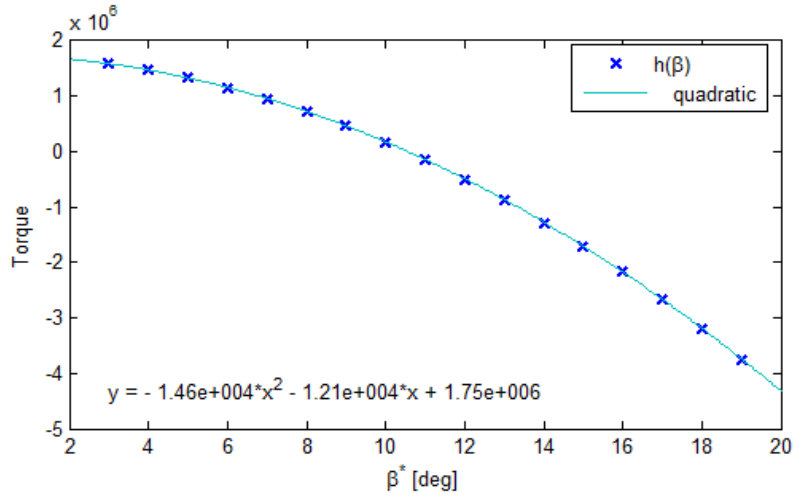


Figure 3-11. Function $h(\beta)$ for rotor PJ9

- 6) The function $g_{\omega_0}(V)$ is constructed by combining the relationships between torque and β^* and between pitch angle and wind speed, Figure 3-11 and Figure 3-6, respectively, and then the quadratic fit

$$g_{\omega_0}(V) = -(7.40 \times 10^2)V^2 - (1.95 \times 10^5)V + 1.65 \times 10^6$$

is determined, see Figure 3-12.

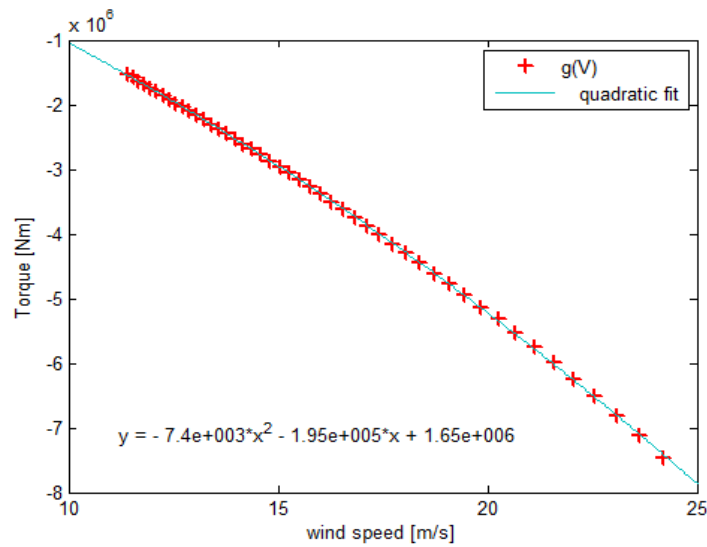


Figure 3-12. Function $g_{\omega_0}(V)$ for rotor PJ9

The above procedure ensures that $T_0 + (h_{\omega_0}(\beta) - g_{\omega_0}(V)) = T_0$ with the correct derivative values along the locus of equilibrium points; that is, the local behaviour from the Theorem 3.2 is preserved. It, also, avoids the need to invert functions. For each combination of wind speed and pitch angle, for which C_q is tabulated, the torque values calculated using the functions, $g_{\omega_0}(V)$ and $h_{\omega_0}(\beta)$, obtained from following the above procedure are compared in Figure 3-

13 to those using the C_q table directly. Inevitably, some of the data in Figure 3-13 is close to the boundary of admissible points, e.g. those points close to the stall boundary, when deviation from Separability can be expected.

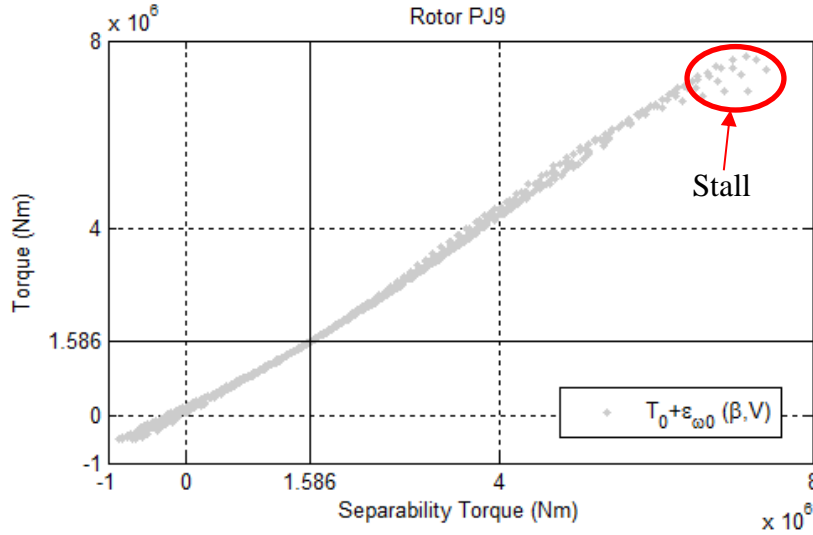


Figure 3-13. Comparison between the torque values predicted by Bladed and the torque values calculated through the Separability theory equations for rotor PJ9

3.5.2. Procedure for determining $\tau_{\omega_0}(\cdot)$

The $\tau_{\omega_0}(\cdot)$ function describes the weak non-linear dependence of T on the $\epsilon_{\omega_0}(\cdot)$ function. The application of general purpose fitting methods to all the data points in Figure 3-13 would be influenced by those points which are close to the boundary of admissible point and so not really valid. Instead, a few key values far from the boundary are selected, see Figure 3-14.

When determining the appropriate fit to those representative points, it has been taken into account that the region for which there should be most accuracy, lies around the value of T_0 . Roughly between 0 Nm and $2 \times T_0 \text{ Nm}$. Specifically, to comply with Theorem 3.2 at T_0 , $\tau_{\omega_0}(T_0) = T_0$ and $\tau_{\omega_0}'(T_0) = 1$. When analysing cubic and quartic fittings in this region, it was found that a quartic fitting would provide a better fit with the gradient value closer to 1, whilst still avoiding overfitting, see Figure 3-15.

Therefore a quartic polynomial fit is then applied, see Figure 3-16, which for rotor PJ9 is

$$\begin{aligned} \tau_{\omega_0}(T_0 + \epsilon_{\omega_0}) = & -(2.24 \times 10^{-21})(T_0 + \epsilon_{\omega_0})^4 + (1.86 \times 10^{-14})(T_0 + \epsilon_{\omega_0})^3 \\ & + (7.6710^{-9})(T_0 + \epsilon_{\omega_0})^2 + 0.849(T_0 + \epsilon_{\omega_0}) + (1.57 \times 10^5) \end{aligned}$$

which when normalised by T_0 becomes,

$$\begin{aligned} \tau_{\omega_0}(T_0 + \varepsilon_{\omega_0}) = & -(1.4173 \times 10^4) \left(\frac{T_0 + \varepsilon_{\omega_0}}{1.586 \times 10^6} \right)^4 + (7.4203 \times 10^4) \left(\frac{T_0 + \varepsilon_{\omega_0}}{1.586 \times 10^6} \right)^3 \\ & + (1.9296 \times 10^4) \left(\frac{T_0 + \varepsilon_{\omega_0}}{1.586 \times 10^6} \right)^2 + (1.3465 \times 10^6) \left(\frac{T_0 + \varepsilon_{\omega_0}}{1.586 \times 10^6} \right) \\ & + 1.57 \times 10^5 \end{aligned}$$

The comparison of the fit with and without $\tau_{\omega_0}(\cdot)$ is depicted in Figure 3-17.

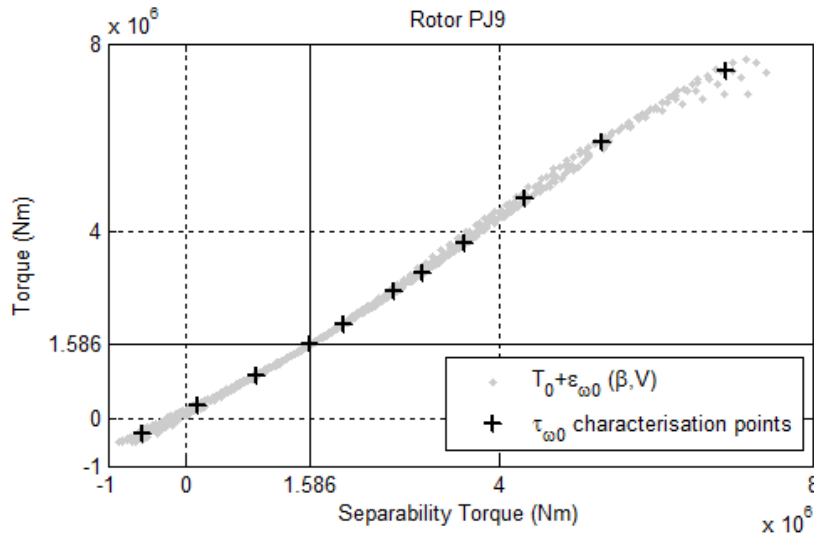


Figure 3-14. Manually selected points for characterisation of $\tau_{\omega_0}(\cdot)$, rotor PJ9

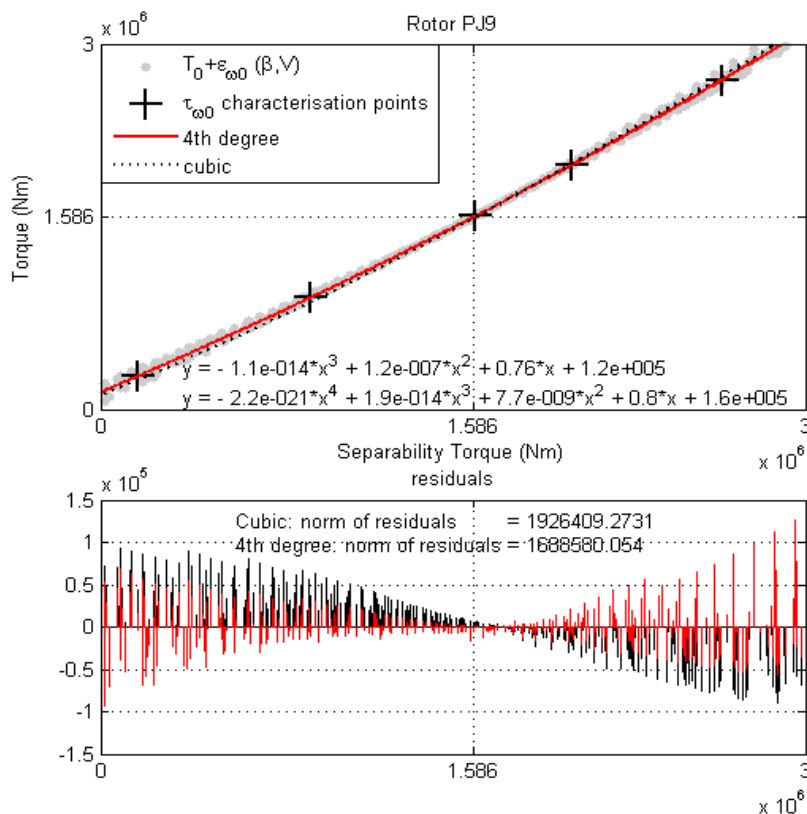


Figure 3-15. Comparison of cubic and quartic fit for $\tau_{\omega_0}(\cdot)$, rotor PJ9

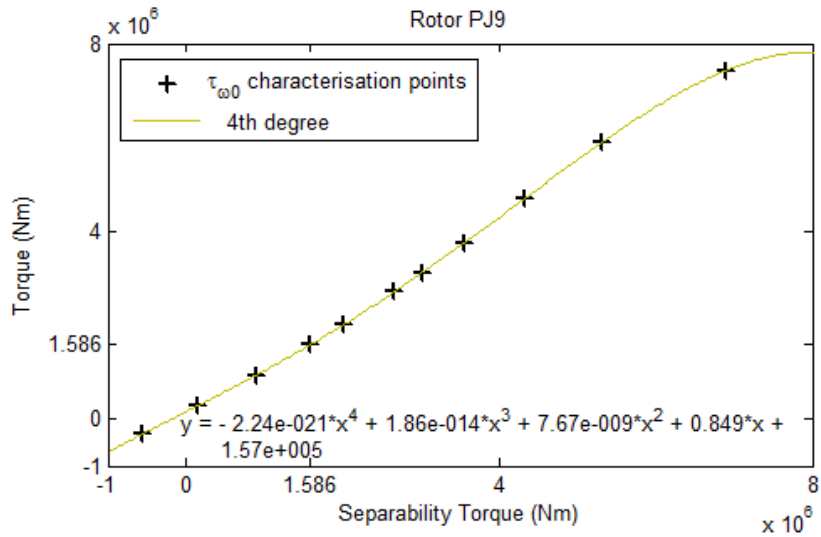


Figure 3-16. Polynomial fit for $\tau_{\omega_0}(\cdot)$, rotor PJ9

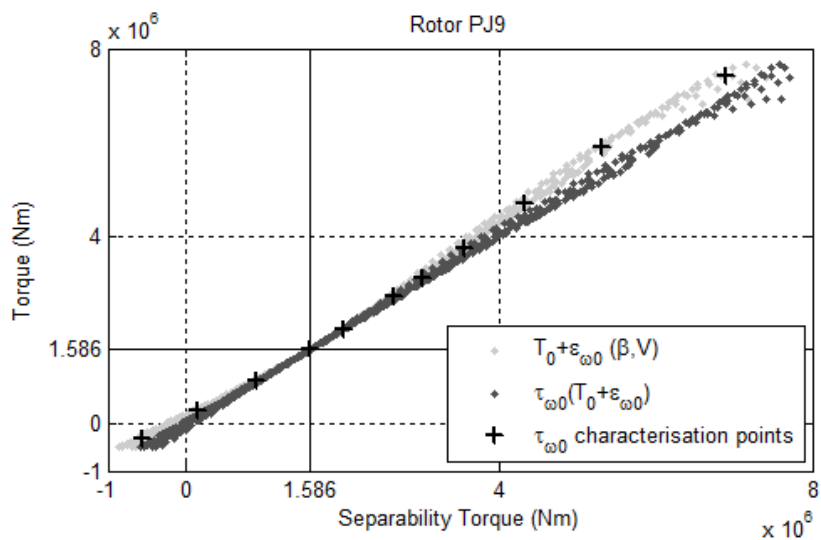


Figure 3-17. Comparison of $T_0 + \varepsilon_{\omega_0}(\beta, V)$ and $\tau_{\omega_0}(\cdot)$, with $\tau_{\omega_0}(\cdot)$ characterisation points, rotor PJ9

3.6. Results

Over many years, the Separability property has been observed for many different rotors and has been exploited in many control applications. What remained to be investigated is how good an approximation the Separability property provides and whether it is related to a specific aerodynamic property of the blades of the WT. In the following this is investigated in detail by exploring the results for 3 different rotors. Two of these rotors are aerodynamically efficient, the already introduced 3MW rotor PJ9 and the 2MW Demo rotor which is available on Bladed itself. The third is an aerodynamically inefficient 2MW rotor denoted as Demo-modified. This

rotor, as the name suggests, is based on the Demo rotor but its blade profile is modified to be a simple rectangle with no twist.

For the aerodynamically efficient rotors, PJ9 and Demo, it can be appreciated from Figure 3-13. and Figure 3-18, that, over data points ranging from $0T_0$ to $2.5T_0$, except for a weak non-linearity there is a close match between the directly calculated torque values using the C_q table and those using $\varepsilon_{\omega_0}(\beta, V)$. As expected, the accuracy is especially good near T_0 . In other words, there is full coverage over the common operating points range and beyond. Values that lie close to stall region together with negative torque values, are included in order to provide insight into the behaviour of the theory at the extremes of its range of applicability; this should not be interpreted as the property breaking down.

For the non-aerodynamically efficient rotor Demo-modified, Figure 3-19, there is still a reasonable match between for $T_0 + \varepsilon_{\omega_0}(\beta, V)$ and the correct values. The results are more scattered than for the aerodynamically efficient rotors.

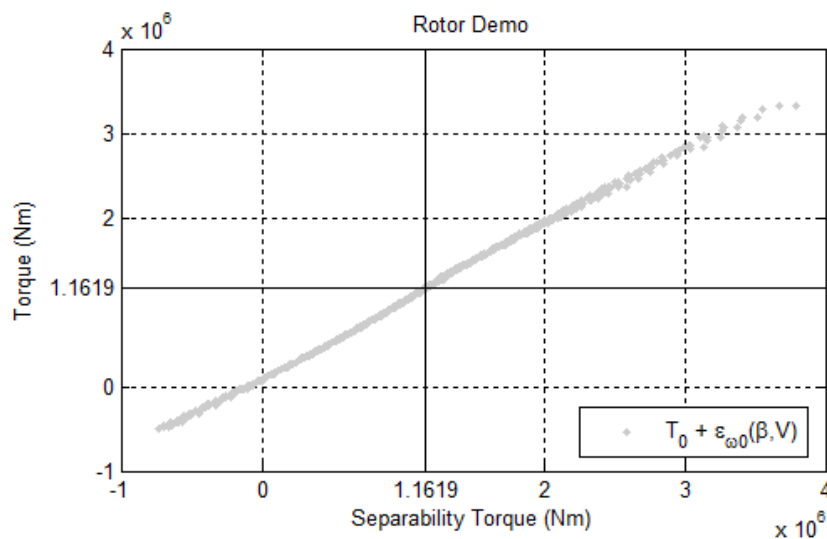


Figure 3-18. Function $T_0 + \varepsilon_{\omega_0}(\beta, V)$, rotor Demo

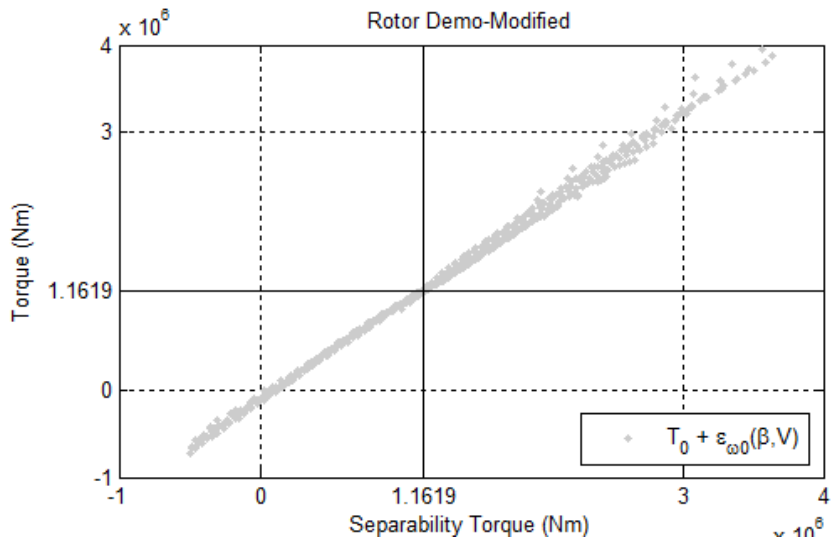


Figure 3-19. Function $T_0 + \epsilon_{\omega_0}(\beta, V)$, rotor Demo-modified

In Figure 3-20, Figure 3-21 and Figure 3-22, a direct comparison between $T_0 + \epsilon_{\omega_0}(\beta, V)$ and $\tau_{\omega_0}(T_0 + \epsilon_{\omega_0}(\beta, V))$ for the rotors PJ9, Demo and Demo-modified, respectively, are provided. For all three cases, the $\tau_{\omega_0}(\cdot)$ function is reasonably effective.

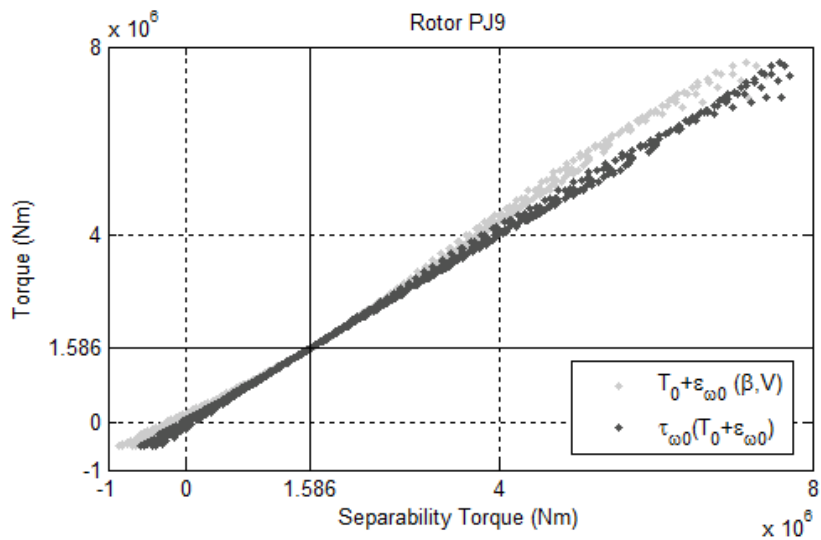


Figure 3-20. Comparison of $T_0 + \epsilon_{\omega_0}(\beta, V)$ and $\tau_{\omega_0}(\cdot)$, rotor PJ9

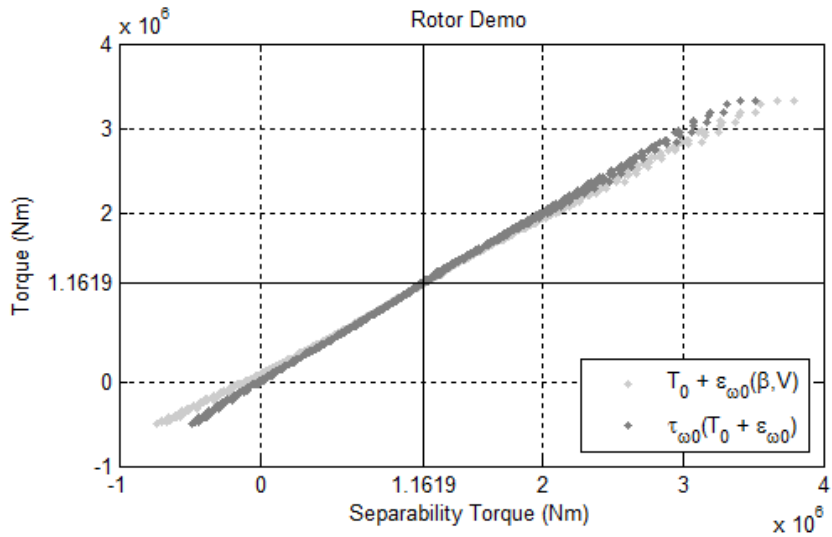


Figure 3-21. Comparison of $T_0 + \varepsilon_{\omega_0}(\beta, V)$ and $\tau_{\omega_0}(\cdot)$, rotor Demo

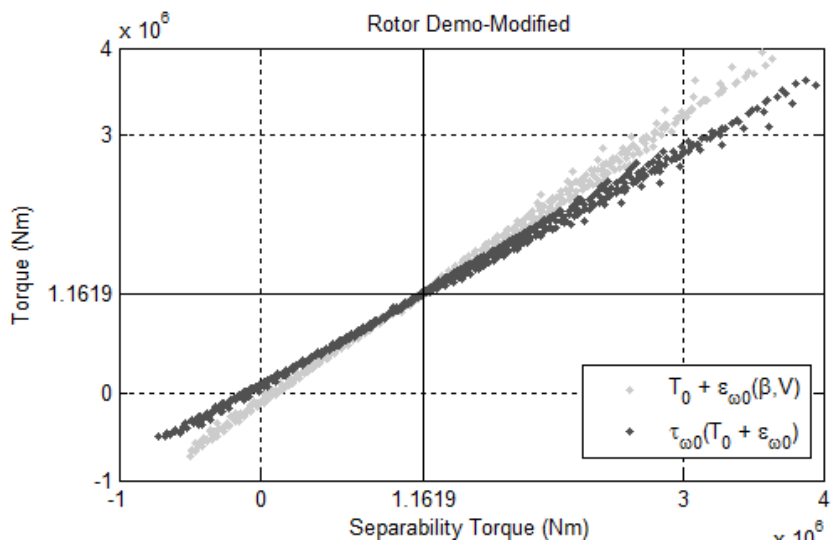


Figure 3-22. Comparison of $T_0 + \varepsilon_{\omega_0}(\beta, V)$ and $\tau_{\omega_0}(\cdot)$, rotor Demo-modified

For rotor PJ9, the contours of constant error for $T_0 + \varepsilon_{\omega_0}(\beta, V)$ and $\tau_{\omega_0}(T_0 + \varepsilon_{\omega_0}(\beta, V))$ are presented in Figure 3-23 and Figure 3-24, respectively. The improvement in the error achieved by the introduction of $\tau_{\omega_0}(\cdot)$ is evident. In a similar manner, Figure 3-25 and Figure 3-26 show the error contours for rotor Demo. Note that the errors for rotor Demo are considerably smaller than for rotor PJ9.

Clearly from comparison of the results for the three rotors, the extent to which Separability holds is dependent of the design of the rotors. In particular, it is stronger for aerodynamically efficient rotors than for less aerodynamically efficient rotors.

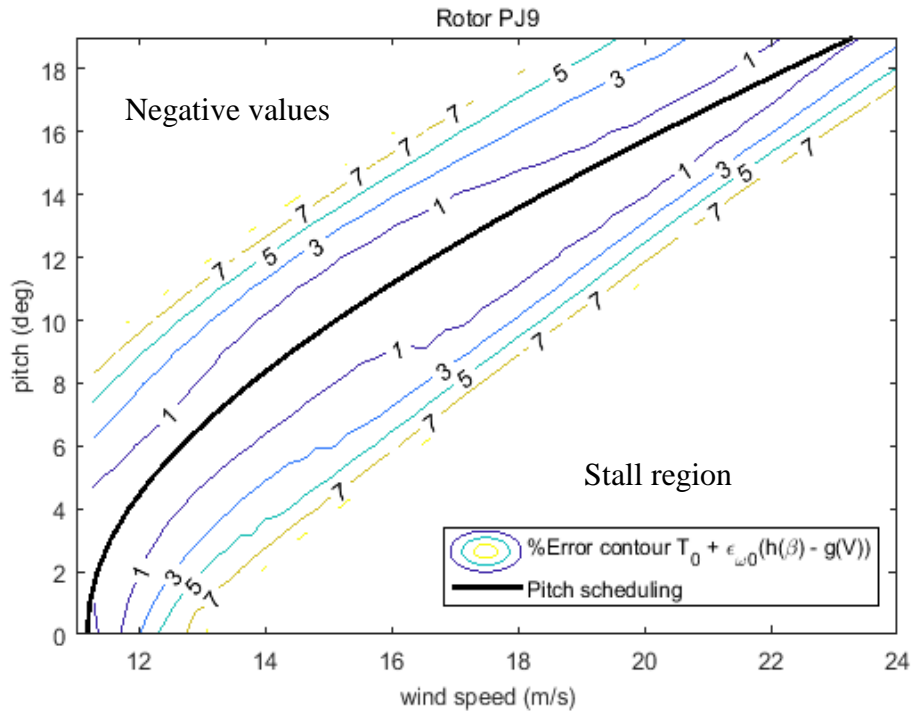


Figure 3-23. Error contour plot for $T_0 + \epsilon_{\omega_0}(\beta, V)$, rotor PJ9

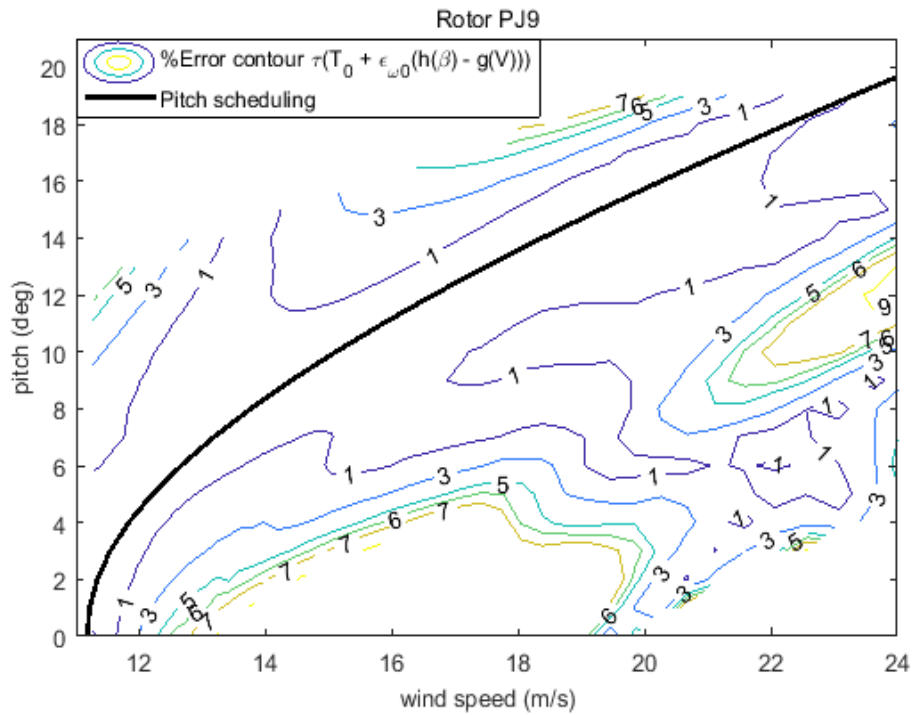


Figure 3-24. Error contour plot for $\tau_{\omega_0}(T_0 + \epsilon_{\omega_0}(\beta, V))$, rotor PJ9

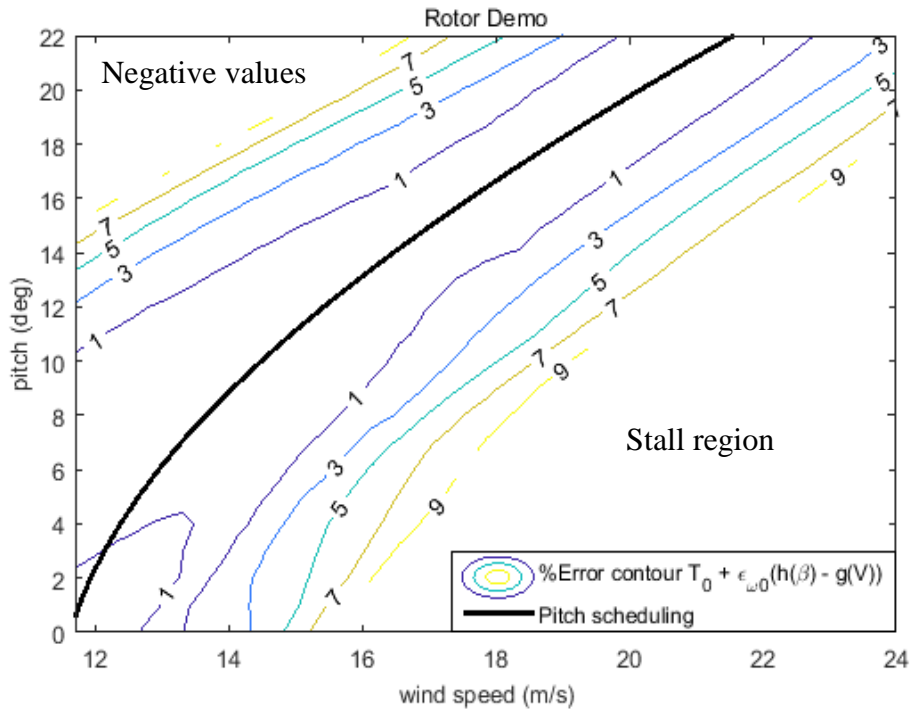


Figure 3-25. Error contour plot for $T_0 + \epsilon_{\omega_0}(\beta, V)$, rotor Demo

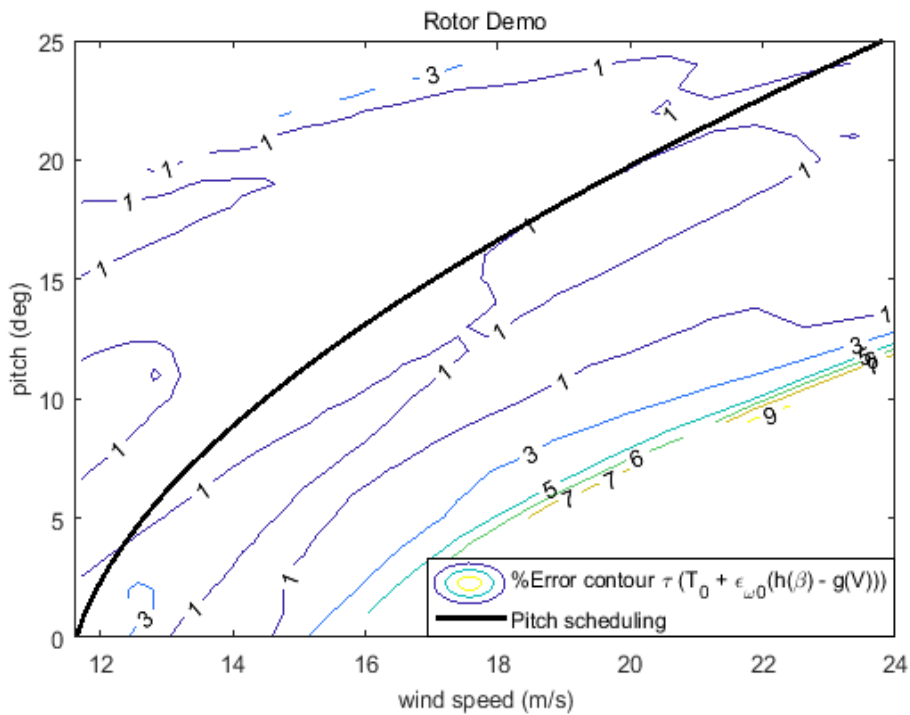


Figure 3-26. Error contour plot for $\tau_{\omega_0}(T_0 + \epsilon_{\omega_0}(\beta, V))$, rotor Demo

3.7. Conclusions

The main conclusions regarding Separability property in the context of constant speed WTs are,

- Separability has been observed over the past 25 year for a substantial range of different WTs. In fact, to date, there has been not a single example of lack of Separability in the WTs that have been studied. The detailed examination of rotors PJ9, Demo and Demo-modified, provides a clear demonstration of the strength of the Separability property and a better understanding of the degree of accuracy of Separability.
- The range of data points, for which Separability is valid has been clarified. It provides a good approximation to aerodynamic torque within the region for which data points are valid according to Theorem 3.2, including all the normal operating points of the wind turbine.
- The strength to which Separability holds is related to the efficiency of the rotor design.
- Both functions $g_{\omega_0}(\cdot)$ and $\tau_{\omega_0}(\cdot)$ are weakly non-linear.
- The general fit for the Separability property equations for constant speed WT is quadratic for functions, $h_{\omega_0}(\beta)$ and $g_{\omega_0}(V)$, and polynomial for the function, $\tau_{\omega_0}(\cdot)$.

Therefore, it is demonstrated in Chapter 3 that representing the aerodynamics in separated form is highly accurate over a very large domain, certainly sufficiently so to support the development of the rotor/wind-field interaction model for constant speed wind turbines.

Chapter 4

Separability for Variable Speed Wind Turbines

Modern WTs are, in their majority, variable pitch and variable speed machines. Therefore, for the purpose of designing the rotor/wind-field interaction model, it is important, as per the constant speed case, to explore the accuracy and domain of Separability, and to determine the best structure of the separated form for control purposes for this particular case.

Consequently, in the current Chapter, the Separability property is explored for an aerodynamic moment or force in the context of variable speed WTs. As discussed in the introduction to Chapter 3, Separability of the form of $f(\beta, V, \omega) = T_0 + h(\beta, \omega) - g(V)$, where f is non-linearly dependent on rotor velocity, ω , pitch angle, β , and wind speed, V , has been observed to apply to variable speed WTs. The (β, ω) pair are controllable variables, whereas V is non-controllable.

The magnitude of the wind speed over the blades in the outer third of the rotor is typically dominated by the component induced by the rotation of the rotor. Thus, aerodynamic characteristics of the rotor are, indeed, sensitive to the rotor speed. The first indication that Separability may apply and be of a range broad enough to be useful, is that contour lines relating torque to rotor speed with constant wind speed at constant pitch angle of 0 degrees, are relatively parallel within the normal operating envelope when away from stall, see Figure 4-1.

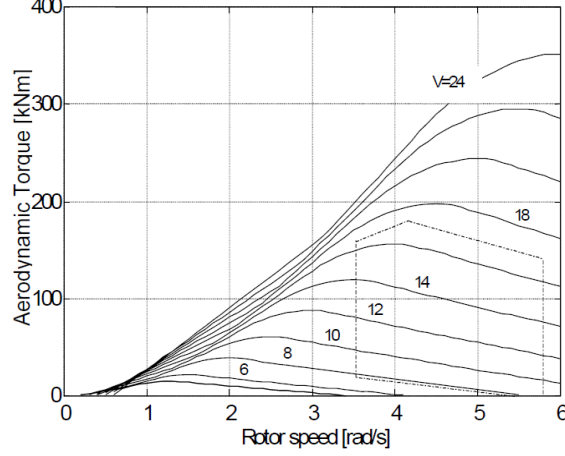


Figure 4-1. Aerodynamic torque versus rotor speed for 300 kW variable speed wind turbine with operating envelope [35]

For variable speed wind turbines, the Additivity property functions, see Section 3.1, $h_{\omega_o}(\beta)$, $g_{\omega_o}(V)$, and the Separability equation $\tau_{\omega_o}(\cdot)$, see Section 3.3, can be determined for different values of rotor speeds, ω_o . Hence, for all operating points, (β, V, ω) , for which $T(\beta, V, \omega)$ is T_0 ,

$$T(\beta, V, \omega) = T_0 + (h(\beta, \omega) - g(V, \omega)) \quad (4.1)$$

where $h(\beta, \omega)$ and $g(V, \omega)$ are defined by

$$h(\beta, \omega)|_{\omega=\omega_o} = h_{\omega_o}(\beta) \quad (4.2)$$

$$g(V, \omega)|_{\omega=\omega_o} = g_{\omega_o}(V) \quad (4.3)$$

Note, ω_o has a range of possible values, that includes rated rotor speed, ω_r , and that the locus of operating points for which $T(\beta, \omega, V) = T_0$, is now a 2-dimensional surface in a 4-dimensional space. In the neighbourhood of the locus of equilibrium operating points,

$$T(\beta, V, \omega) \simeq \tau(\omega, T_0 + \varepsilon(\beta, V, \omega)) = \tau(\omega, T_0 + (h(\beta, \omega) - g(V, \omega))) \quad (4.4)$$

where $\tau(\omega, \cdot)|_{\omega=\omega_o} = \tau_{\omega_o}(\cdot)$. Consider the set of points, (β, ω, V) , on the locus, for which the aerodynamic torque has constant value, T_0 . These points can be continuously parameterised by α such that

$$T(\alpha) = T(\beta(\alpha), \omega(\alpha), V(\alpha)) = T_0 \quad (4.5)$$

and since

$$\frac{\partial T}{\partial \beta} \frac{d\beta(\alpha)}{d\alpha} + \frac{\partial T}{\partial \omega} \frac{d\omega(\alpha)}{d\alpha} + \frac{\partial T}{\partial V} \frac{dV(\alpha)}{d\alpha} = \frac{dT(\alpha)}{d\alpha} = 0 \quad (4.6)$$

the partial derivative with respect to ω is simply related to the other two partial derivatives. Since the partial derivatives with respect to β and V of the separated form, $(T_0 + h(\beta, \omega) - g(V, \omega))$, on the locus of equilibrium points are correct by construction, the partial derivative with respect to ω is also correct. [36]

There is more than one way of formulating Separability for a 3-dimensional function, it can be purely mathematically motivated, (4.4), driven by applicability i.e. suitable for control engineering purposes, or related to the physics of the aerodynamic torque. In Chapter 4, the choice of that formulation, together with the characteristics and nature of the functions themselves, is explored. The extent of the Separability functions' domains are also explored. Separability in wind speed, in its most generic form with functions $h(\beta, \omega)$ and $g(V, \omega)$, it is explored in Section 4.1. Subsequently, a simplified form of the Separability functions of the form $h(\beta, \omega)$ and $g(V)$, is investigated in Section 4.2. Separability in tip speed ratio, is discussed in Section 4.3 and Section 4.4. Section 4.5, provides a direct comparison of the Separability results for the simplified wind speed version and tip speed version. Section 4.6 summarises findings and conclusions.

4.1. Direct Extension of Separability to Variable Speed Wind Turbines

The natural extension of Separability to the variable speed case, (4.4), as discussed in the introduction, is investigated here for the same rotors as in Chapter 3.

For rotor PJ9, an extended range of variations covering $\pm 20\%$ variations from rated rotor speed, ω_0 , with increments of 10%, have been applied. Results for function $g(V, \omega)$ can be seen in Figure 4-2 and for function $h(\beta, \omega)$ in Figure 4-3. The comparison of $T_0 + (h(\beta, \omega) - g(V, \omega))$ for the different values of ω can be found in Figure 4-4 and Figure 4-5. As per Chapter 3 some points outside the range of applicability of the Separability property have been kept for illustration i.e. negative values, stall regions values, non-physical values; this is also true for rotor Demo and Demo-modified. The main exploration of the nature of the

Separability fits is done using rotor PJ9, and therefore, more extensive tests than for the other rotors, which are used for further illustration, have been performed.

For rotor Demo, only $\pm 10\%$ ω_0 are determined. Results for function $g(V, \omega)$ can be seen in Figure 4-6 and for function $h(\beta, \omega)$ in Figure 4-7. These equations are derived using the same methodology described in Section 3.5. The comparison of $T_0 + (h(\beta, \omega) - g(V, \omega))$ for the different values of ω can be found in Figure 4-8.

For rotor Demo-modified, as for rotor Demo, only $\pm 10\%$ ω_0 are determined. Results for function $g(V, \omega)$ can be seen in Figure 4-9 and for function $h(\beta, \omega)$ in Figure 4-10. The comparison of $T_0 + (h(\beta, \omega) - g(V, \omega))$ for the different values of ω can be found in Figure 4-11.

A remarkable result is that for the aerodynamically efficient rotors PJ9 and Demo, when looking at function $g(V, \omega)$ in Figure 4-2 (rotor PJ9) and Figure 4-6 (rotor Demo), there is a strong suggestion that function $g(V, \omega)$ can be considered independent from ω . However, for the non-aerodynamically efficient rotor Demo-modified, see Figure 4-9, this observation does not hold. On the other hand, results for function $h(\beta, \omega)$ for all three rotors, in Figure 4-3, Figure 4-7 and Figure 4-10, confirm that the pitch dependent function is strongly dependent on ω , as expected. Furthermore, results in Figure 4-4, Figure 4-5 and Figure 4-8 would suggest that the $\tau(\omega, \cdot)$ of each aerodynamically efficient rotor does not change with variations of ω .

Overall, for both aerodynamically efficient rotors, results in Figure 4-4, Figure 4-5 and Figure 4-8 show a strong presence of Separability. This is true not just for the envelope of operating points related to rated conditions but Separability also holds reasonably well when variations occur between 10-20% of ω_0 . For the rotor Demo-modified in Figure 4-11, the Separability property as an approximation becomes poorer than the one exhibited by the aerodynamically efficient rotor counterparts. Nevertheless, results would suggest that Separability would still find application for control purposes on an ill-designed rotor, still, particular caution should be taken in that case.

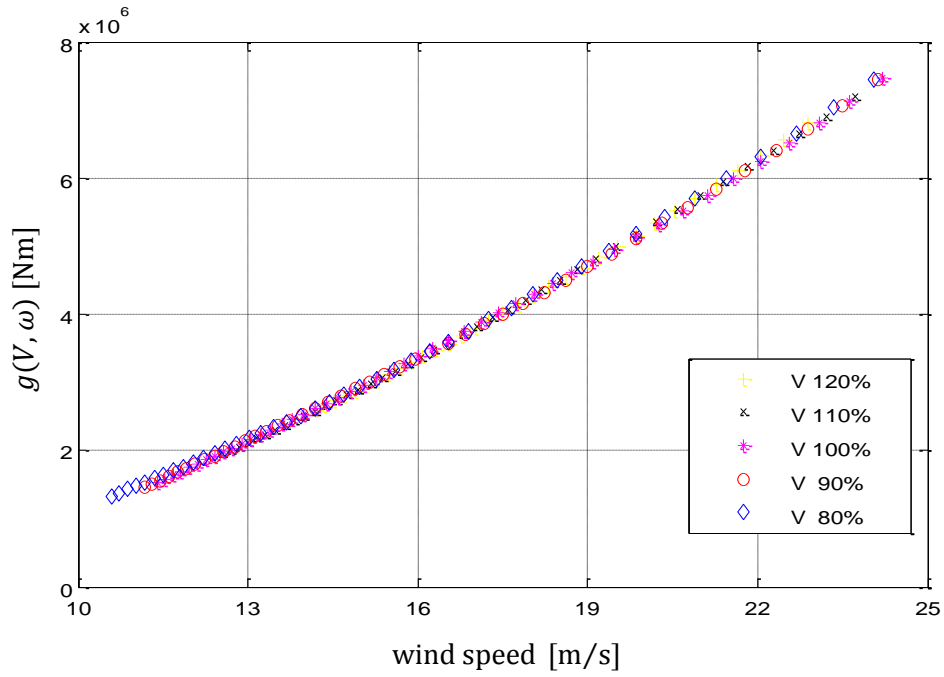


Figure 4-2. Function $g(V, \omega)$ for rotor PJ9 with different rated rotor velocities

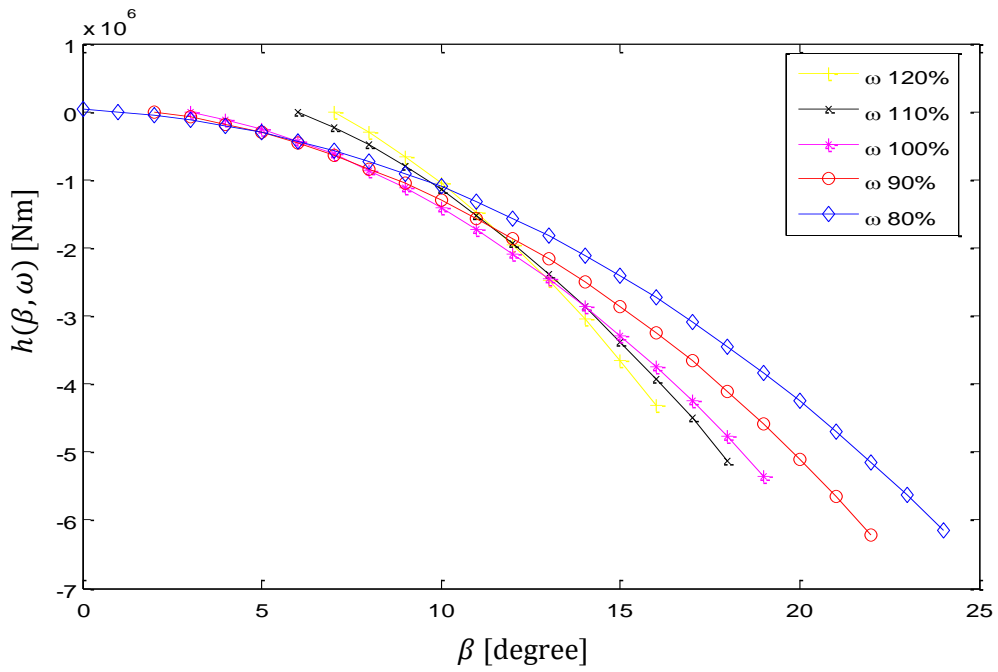


Figure 4-3. Function $h(\beta, \omega)$ for rotor PJ9 with different rated rotor velocities

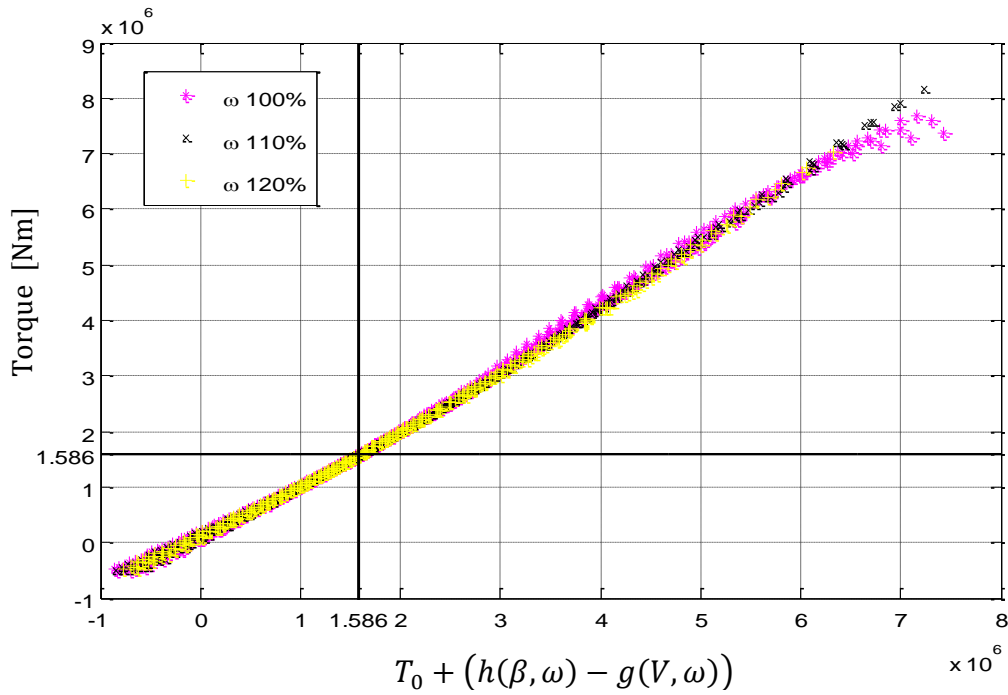


Figure 4-4. Comparison between the torque values predicted by BLADED and the torque values calculated through the Separability theory equations for rotor PJ9 for ω 100%, 110% and 120%

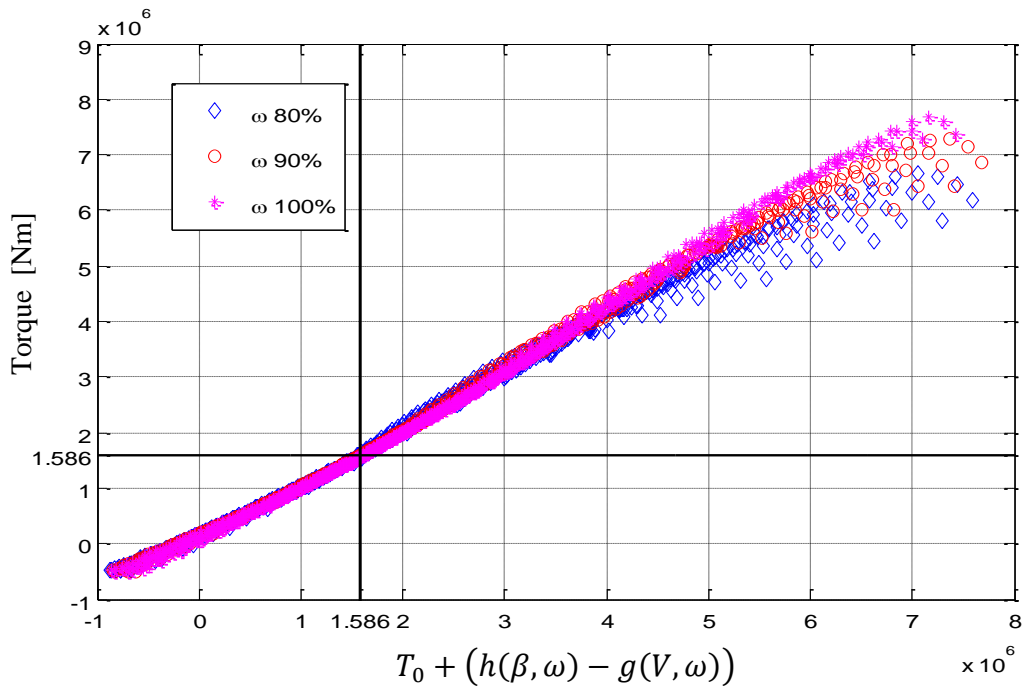


Figure 4-5. Comparison between the torque values predicted by BLADED and the torque values calculated through the Separability theory equations for rotor PJ9 for ω 100%, 90% and 80%

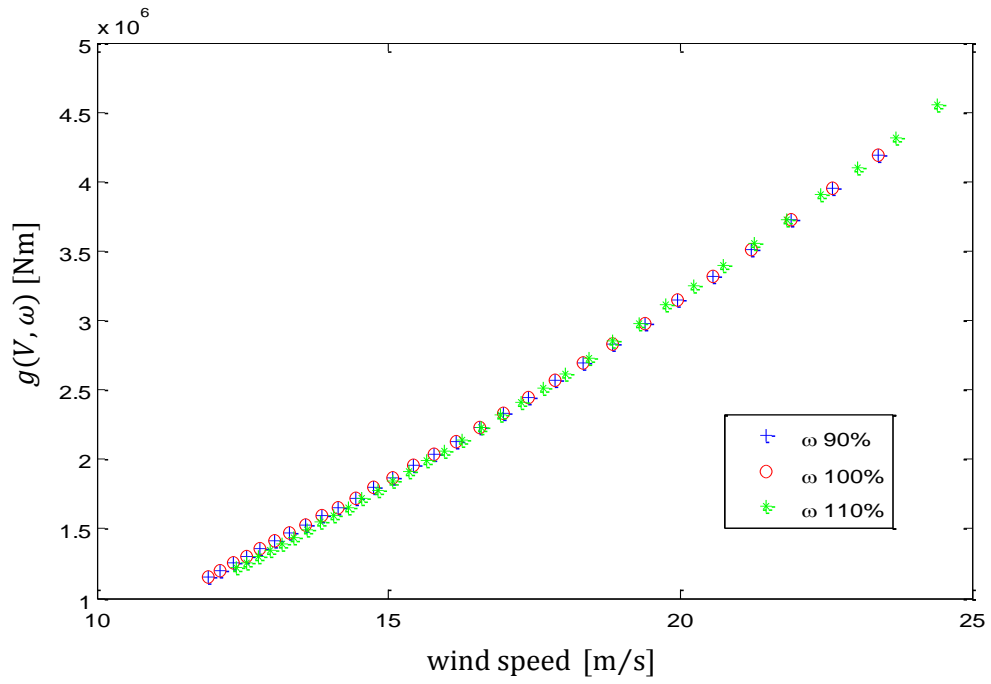


Figure 4-6. Function $g(V, \omega)$ for Demo rotor for different rated rotor velocities

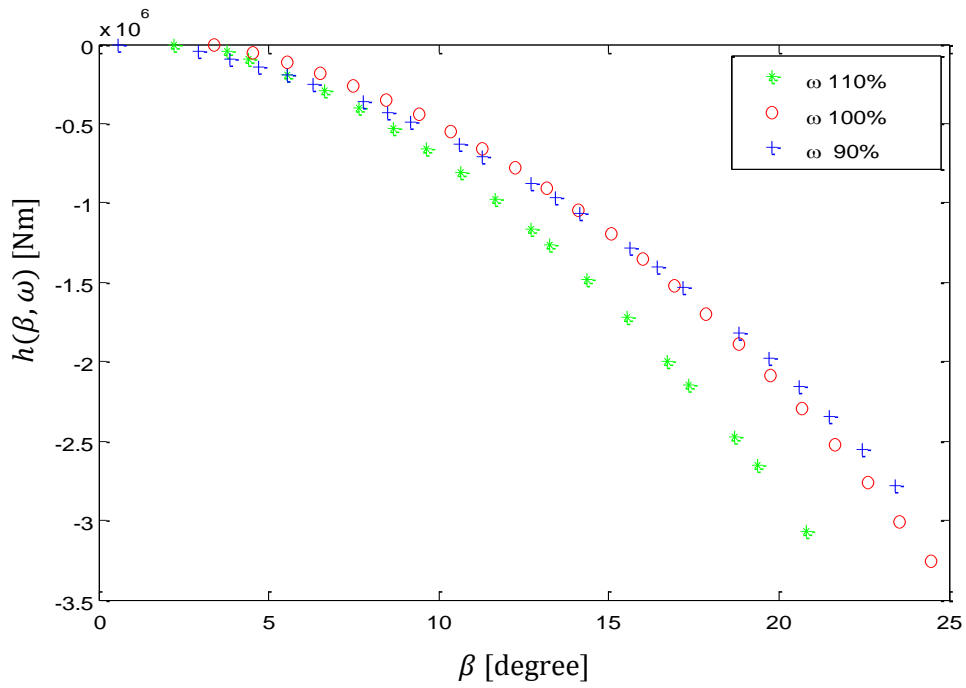


Figure 4-7. Function $h(\beta, \omega)$ for Demo rotor for different rated rotor velocities

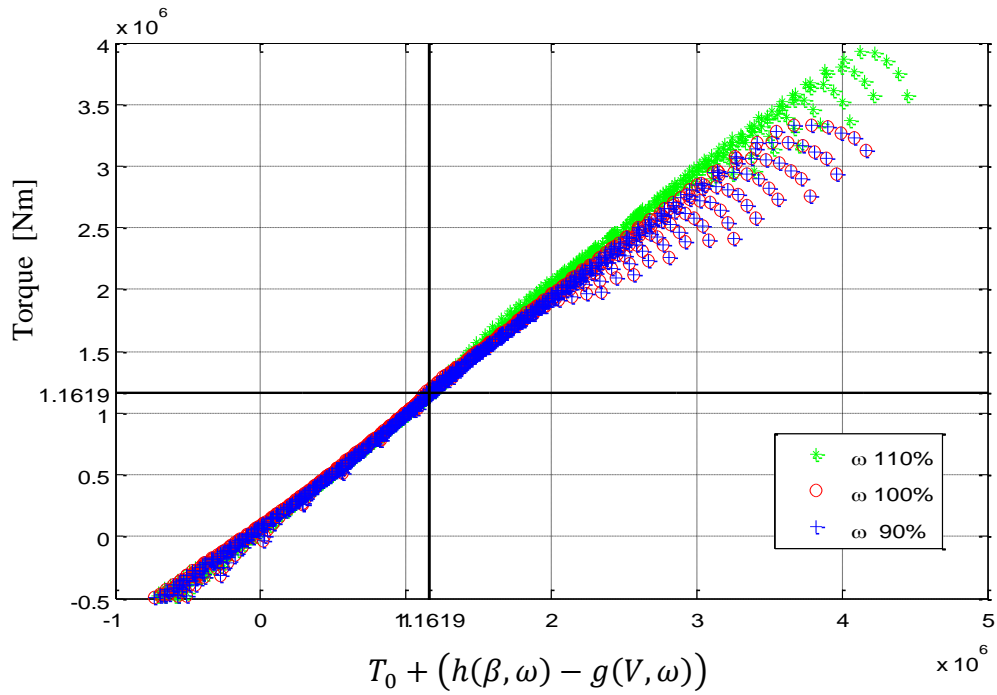


Figure 4-8. Comparison between the torque values predicted by BLADED and the torque values calculated through the Separability theory equations for Demo rotor for different rated rotor velocities

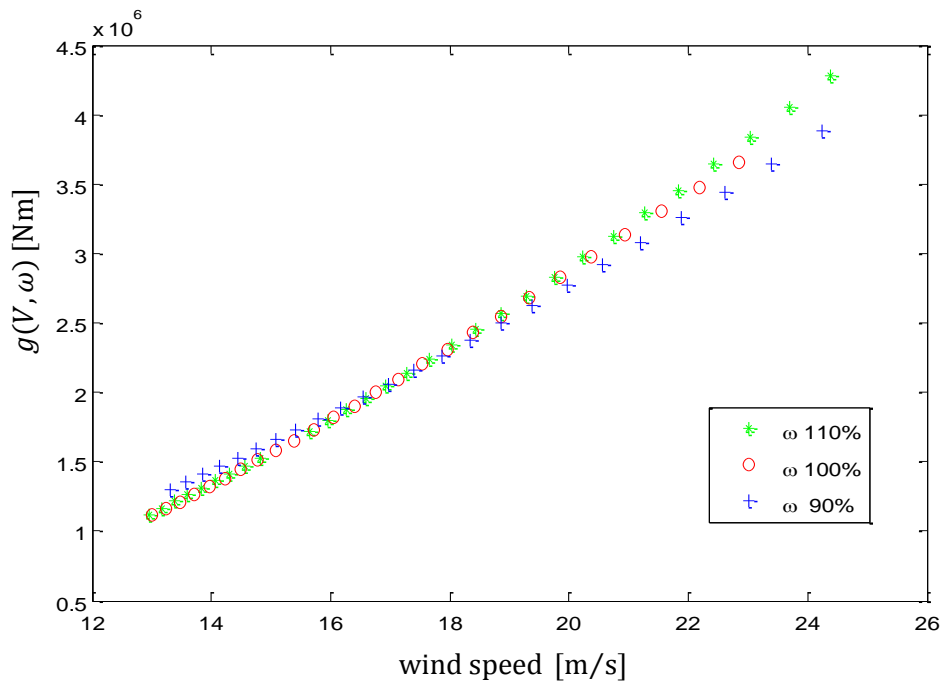


Figure 4-9. Function $g(V, \omega)$ for Demo-modified rotor for different rated rotor velocities

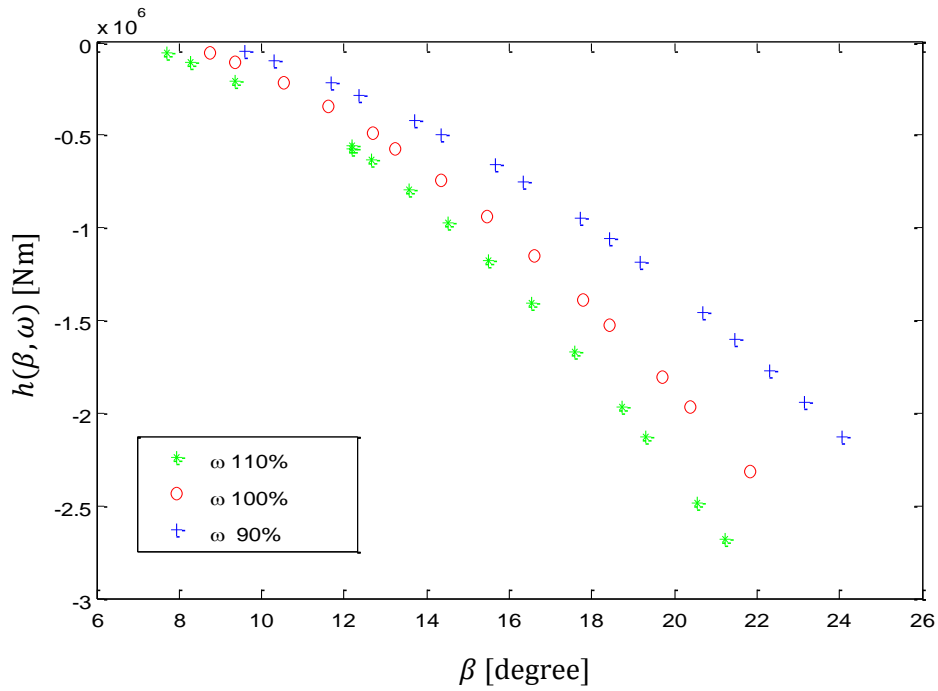


Figure 4-10. Function $h(\beta, \omega)$ for Demo-modified rotor for different rated rotor velocities

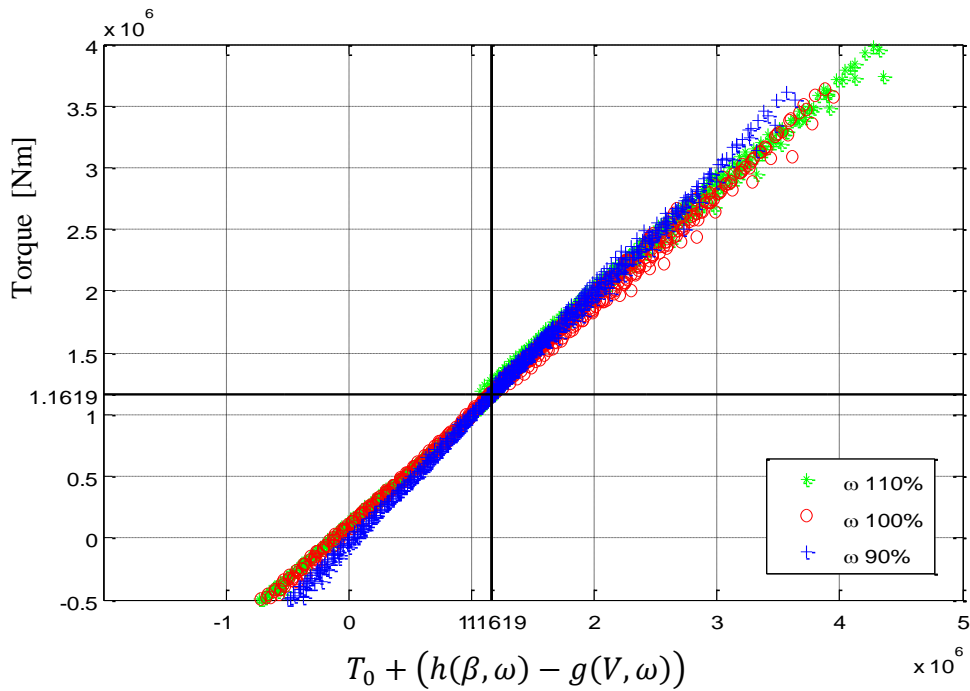


Figure 4-11. Comparison between the torque values predicted by BLADED and the torque values calculated through the Separability theory equations for Demo-modified rotor for different rated rotor velocities

For the rotor PJ9, further tests are conducted. The behaviour of the aerodynamics when at the same time as ω is modified, the rated torque of the WT is also modified by the same percentual measure, is explored. The results can be seen in Figure 4-12 for function $g(V, \omega)$, Figure 4-13 for function $h(\beta, \omega)$ and Figure 4-14 for $T_0 + (h(\beta, \omega) - g(V, \omega))$.

In contrast to results seen in Figure 4-2, Figure 4-6 and to an extent Figure 4-9, the $g(V, \omega)$ functions cannot be superimposed as they maintain their dependence on ω ; as it would be initially expected from the theory. The variation of $g(V, \omega)$ with ω is due to rated torque changing and thus, the Separability functions also changing.

The individual fits in Figure 4-14 are successful regarding Separability but they do not work together in the same measure that it was seen in Figure 4-4, Figure 4-5 and Figure 4-8. This strongly suggests that also, function $\tau(\omega, \cdot)$ maintains its dependency on ω . When looking at the individual behaviour of the Separability fits, $T_0 + (h(\beta, \omega) - g(V, \omega))$ starts to deteriorate when encountering points outside the region of applicability of Separability, as expected. This is especially evident when approaching the stall region which is more prominent on the +20% and +10% case studies, highlighted with a circle in Figure 4-14.

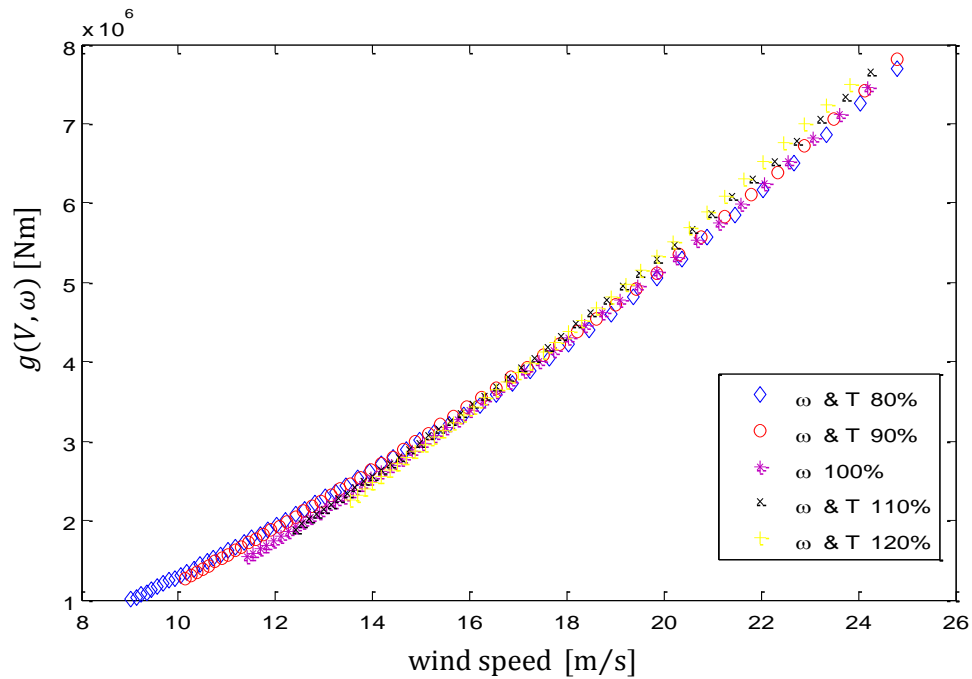


Figure 4-12. Function $g(V, \omega)$ for rotor PJ9 for different rated torque and rated rotor velocities

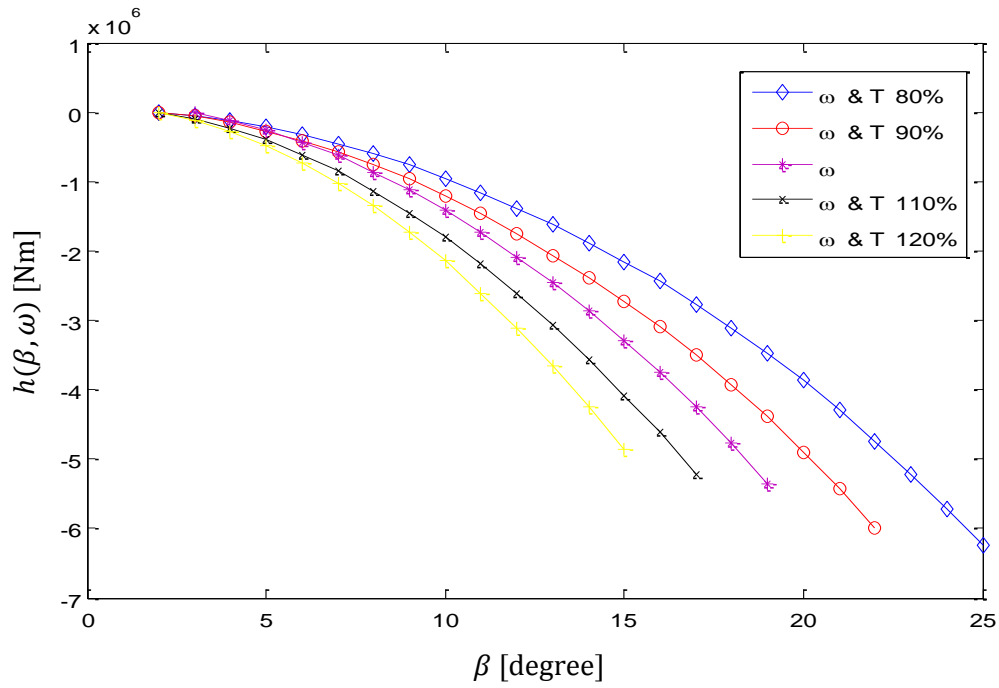


Figure 4-13. Function $h(\beta, \omega)$ for rotor PJ9 for different rated torque and rated rotor velocities

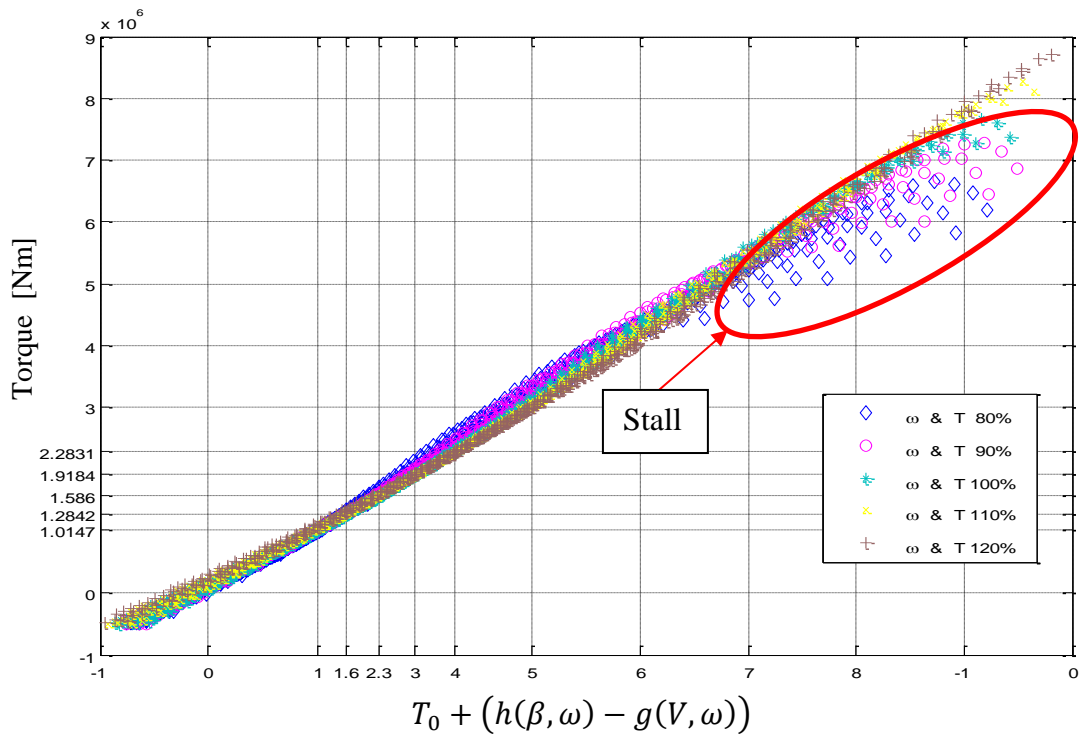


Figure 4-14. Comparison between torque values predicted by BLADED and torque values calculated through Separability theory equations for rotor PJ9 for different rated torque and rated rotor velocities

4.2. Wind Speed Based Separability

The observation made in Section 4.1, that the plots of function $g(V, \omega)$ in Figure 4-2 and Figure 4-6 are very similar, strongly suggests that the Separability property could have a simplified form with $g(V, \omega)$ only dependent on V and $\tau(\omega, T_0 + \varepsilon(\cdot))$ only dependent on $(T_0 + \varepsilon(\cdot))$, that is, on the locus of equilibrium operating points,

$$T(\beta, V, \omega) = \tau(T_0 + \varepsilon(\beta, \omega, V)) = \tau(T_0 + (h(\beta, \omega) - g(V))) \quad (4.7)$$

For any choice of constant rotor speed, ω_o , on the locus of equilibrium operating points,

$$\begin{aligned} \varepsilon_{\omega_o}(\beta, V) &= h_{\omega_o}(\beta) - g_{\omega_o}(V) \\ &= h_{\omega_o}(\beta) + g_{\omega_o}(V) - g_{\omega_o}(V) - g_{\omega_o}(V) \\ &= h_{\omega_o}(\beta) + g_{\omega_o}(f_{\omega_o}^{-1}(\beta)) - g_{\omega_o}(f_{\omega_o}^{-1}(\beta)) - g_{\omega_o}(V) \\ &= g_{\omega_o}(f_{\omega_o}^{-1}(\beta)) - g_{\omega_o}(V) = \bar{\varepsilon}_{\omega_o}(\beta, V) \end{aligned} \quad (4.8)$$

where ω_o is rated rotor speed. Along the locus of equilibrium operating points, there is a relationship between the V and the β and between the $h(\cdot)$ and the $g(\cdot)$ through $f(\cdot)$. This relationship is encapsulated by Observation 4) in Section 3.2, whereby on the locus, $g_{\omega_o}(V) = g_{\omega_o}(f_{\omega_o}^{-1}(\beta))$ and also $h_{\omega_o}(\beta) = g_{\omega_o}(f_{\omega_o}^{-1}(\beta))$, from which (4.8) results.

Let $\bar{\varepsilon}_{\omega_o} = (g_{\omega_o}(f_{\omega_o}^{-1}(\beta)) - g_{\omega_o}(V))$. On the locus $\bar{\varepsilon}_{\omega_o} = 0$ as required, but the partial derivatives are no longer correct since

$$\frac{\partial \bar{\varepsilon}_{\omega_o}}{\partial V} = -g'_{\omega_o}(V) \neq -g'_{\omega_o}(V) = \frac{\partial \varepsilon_{\omega_o}}{\partial V} \quad (4.9)$$

$$\frac{\partial \bar{\varepsilon}_{\omega_o}}{\partial \beta} = g'_{\omega_o}(f_{\omega_o}^{-1}(\beta)) f'_{\omega_o}{}^{-1}(\beta) \neq g'_{\omega_o}(f_{\omega_o}^{-1}(\beta)) f'_{\omega_o}{}^{-1}(\beta) = \frac{\partial \varepsilon_{\omega_o}}{\partial \beta} \quad (4.10)$$

It follows that $T_0 + (g_{\omega_o}(f_{\omega_o}^{-1}(\beta)) - g_{\omega_o}(V)) = T_0 + \bar{\varepsilon}_{\omega_o}$ is not related to $T(\beta, V, \omega)$ by the Additivity property as per Section 3.2 but by the Additivity property as per Section

3.1.2 Nevertheless, when $g_{\omega_o}(V) \approx g_{\omega_o}(V)$, as observed in Figure 4-16, and, therefore, $\tau_{\omega_o}(T_0 + \bar{\varepsilon}_{\omega_o}) \approx \tau_{\omega_o}(T_0 + \varepsilon_{\omega_o}) = T_0$ at $\bar{\varepsilon}_{\omega_o} = \varepsilon_{\omega_o} = 0$,

$$\bar{\varepsilon}_{\omega_o} = \left(g_{\omega_o} \left(f_{\omega_o}^{-1}(\beta) \right) - g_{\omega_o}(V) \right) \approx \left(g_{\omega_o} \left(f_{\omega_o}^{-1}(\beta) \right) - g_{\omega_o}(V) \right) = \varepsilon_{\omega_o}$$

$$\frac{\partial \tau_{\omega_o}(T_0 + \bar{\varepsilon}_{\omega_o})}{\partial V} \approx \frac{\partial \tau_{\omega_o}(T_0 + \varepsilon_{\omega_o})}{\partial V} \quad (4.11)$$

$$\frac{\partial \tau_{\omega_o}(T_0 + \bar{\varepsilon}_{\omega_o})}{\partial \beta} \approx \frac{\partial \tau_{\omega_o}(T_0 + \varepsilon_{\omega_o})}{\partial \beta}$$

Hence, choosing $g(V)$ to be $g_{\omega_o}(V)$, an appropriate choice for $h(\beta, \omega)$ is

$$h(\beta, \omega)|_{\omega=\omega_o} = g_{\omega_o} \left(f_{\omega_o}^{-1}(\beta) \right) \quad (4.12)$$

In Figure 4-15, $h_{\omega_o}(\beta)$ and $g_{\omega_o} \left(f_{\omega_o}^{-1}(\beta) \right)$ are compared with ω_o values of 80%, 100% and 120% of rated rotor speed, ω_o , for rotor PJ9. The pairs of functions match closely.

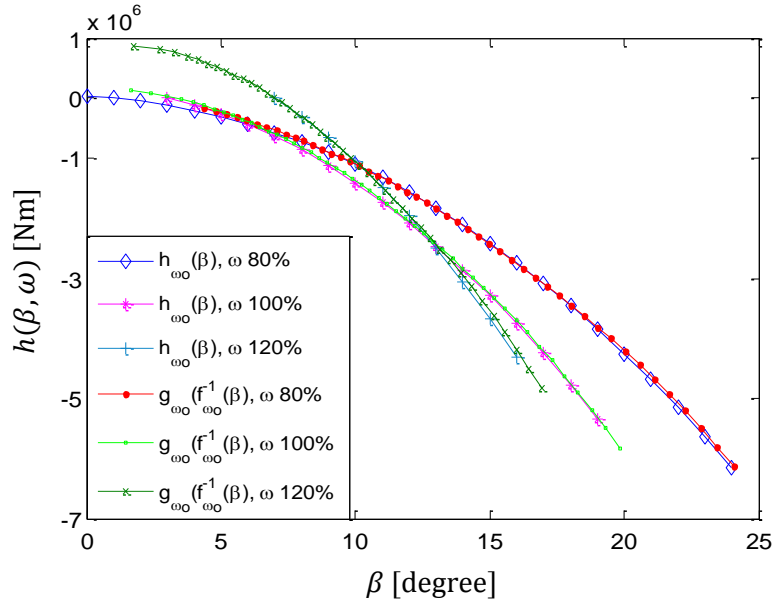


Figure 4-15. Validation of simplified wind speed Separability for rotor PJ9

By using the least square method on the data for all the ranges 80% to 140% ω_o , the function $g(V)$ has been optimised. The result of the optimised $g(V)$ function, together with the associated $h_{\omega_o}(\beta)$ functions to cater for the specified range, is shown in Figure 4-16. The

optimised fit is quadratic with coefficients shown in Table 4-1. The coefficients for function $\tau(\cdot)$ for rotor PJ9, which is independent from the rotor speed can be found in Table 4-2 with a 4th order polynomial fit.

Separation in wind speed is based on an empiric observation that $g(V)$ does not depend on ω . However, it might be that basing the derivation of the separated functions, h and g , on the Additivity property in Section 3.1.2 rather than the Additivity property in Section 3.2, compromises the degree of accuracy of the separated form. To test whether this is the case, a more principled version of Separability for variable speed WTs is better. Separability based on tip speed ratio is such an approach, and is discussed in detail in Section 4.3 and Section 4.4.

Results and discussion for the simplified Separability in wind speed can be found in Section 4.5 alongside the comparison with Separability in tip speed ratio.

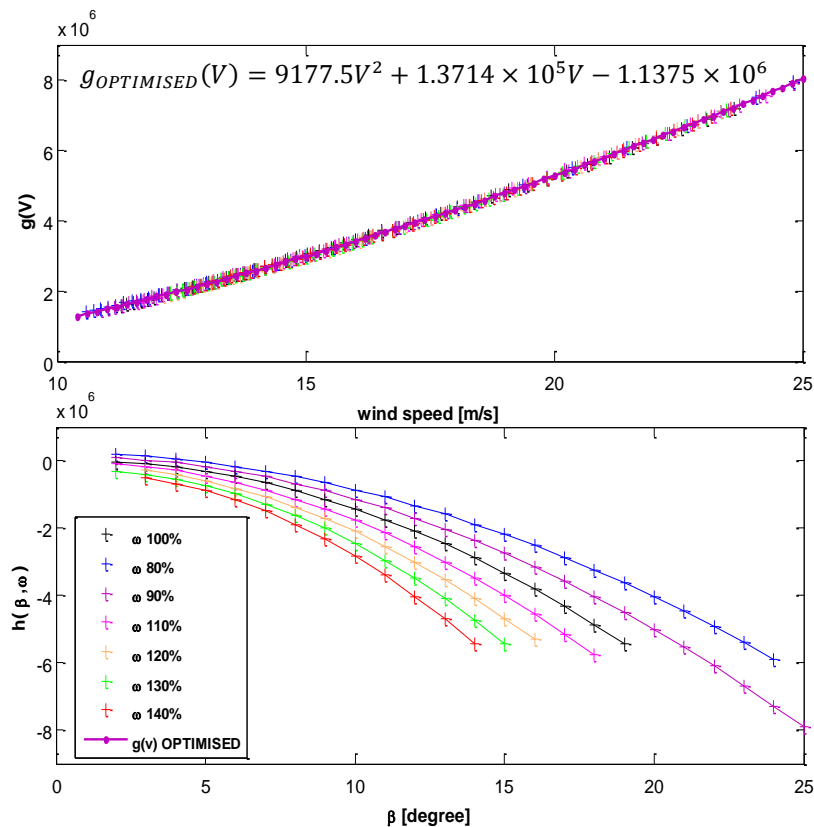


Figure 4-16. Wind speed based Separability for rotor PJ9

		Function Coefficients: $aV^2 + bV + c$			
		Rotor Speed	a	b	c
$g(V)$	Any		9177.51	137136.99	-1137466.98
$h_{\omega_0}(\beta)$	40% ω_0		-28920.16	43995.09	-392548.12
	30% ω_0		-25304.80	37291.54	-305735.25
	20% ω_0		-21315.35	17972.22	-156346.38
	10% ω_0		-18022.19	5270.26	-31787.00
	ω_0		-16124.76	20225.35	-23332.39
	-10% ω_0		-12993.33	2752.10	131741.14
	-20% ω_0		-10357.91	-6598.68	235101.73

Table 4-1 Coefficients for function $g(V)$ optimised and associated $h_{\omega_0}(\beta)$ for rotor PJ9

		Function Coefficients: $a(\cdot)^4 + b(\cdot)^3 + c(\cdot)^2 + d(\cdot) + e$					
		Rotor Speed	a	b	c	d	e
$\tau(\cdot)$	Any		-2.2372×10^{-21}	1.8647×10^{-14}	7.6695×10^{-9}	0.84856	1.5665×10^5

Table 4-2 Coefficients for function $\tau(\cdot)$ for rotor PJ9

4.3. Tip Speed Ratio Based Separability

The Additivity property can also be derived from the physics of the torque, with aerodynamic torque defined as:

$$T(\omega, \beta, V) = \frac{1}{2} \rho A R V^2 C_q(\beta, \lambda) = k V^2 C_q(\beta, \lambda) \quad (4.13)$$

$$k = \frac{1}{2} \rho A R \quad (4.14)$$

where ρ is air density, A area swept by the rotor, R radius of the rotor and k is a constant. The torque coefficient, C_q , is dependent on the variables β and λ , thus it would be convenient to have all related dependencies on V replaced by λ :

$$\lambda = \frac{\omega R}{V} \longrightarrow V^2 = \frac{\omega^2 R^2}{\lambda^2} \quad (4.15)$$

$$T(\omega, \beta, V) = kV^2 C_q(\beta, \lambda) = k \frac{\omega^2 R^2}{\lambda^2} C_q(\beta, \lambda) = K \omega^2 \frac{C_q(\beta, \lambda)}{\lambda^2} \quad (4.16)$$

where K is a constant.

Applying the additivity property to $C(\beta, \lambda) = \frac{C_q(\beta, \lambda)}{\lambda^2}$ along the locus of operating points on which $C(\beta, \lambda) = C(\beta_0, \lambda_0) = C_0$ with $\lambda_0 = R\omega_0/V_0$,

$$C(\beta, \lambda) = C_0 + (H(\beta) - G(\lambda)) \quad (4.17)$$

on the locus. In Figure 4-17 and Figure 4-18, for this form of Additivity, function $G(\lambda)$ with a quadratic fit, and function $H(\beta)$ with a cubic fit, are shown for rotor PJ9. The functions have been found using the same method as in Section 3.5, with $C_0 = 6.6694 \times 10^{-4}$ for rated torque, see Table 4-3 for function $G(\lambda)$ and Table 4-4 for function $H(\beta)$.

Once the Additivity equations are established, the existence and range of Separability is investigated. The data used includes wind speeds from 11m/s to 25m/s (catering for rated wind speed up to cut-off wind speed), rotor speed varying from 80% to 120% of ω_0 and pitch angle values from 0 to 23 degrees. It can be seen from Figure 4-19 that the separated form, $C_0 + (H(\beta) - G(\lambda))$, is a good representation for $C(\beta, \lambda)$ for a very large neighbourhood enclosing the locus of equilibrium points with values of $C(\beta, \lambda)$ that vary from 0 to $2C_0$. As per previous Separability results, the data present in Figure 4-19 does include values outside the range of applicability of Separability i.e. negative values and stall region values.

The main drawn back from applying the Additivity property to the tip speed ratio is that the locus of points for which the Additivity properties, like correctness of partial derivatives, are warranted, does not correspond with the operating points of the WT.

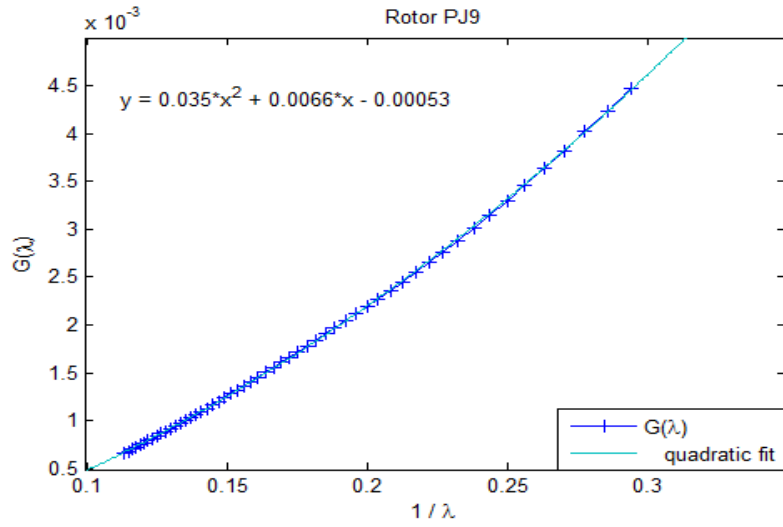


Figure 4-17. Function $G(\lambda)$ for rotor PJ9

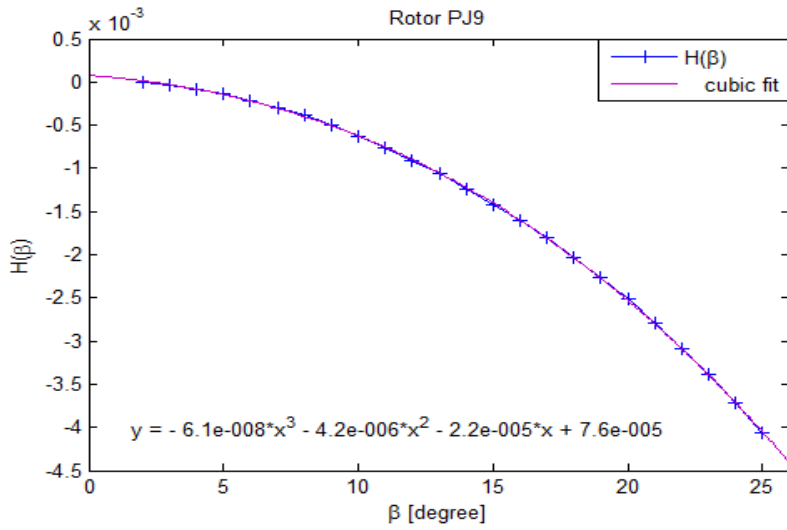


Figure 4-18. Function $H(\beta)$ for rotor PJ9

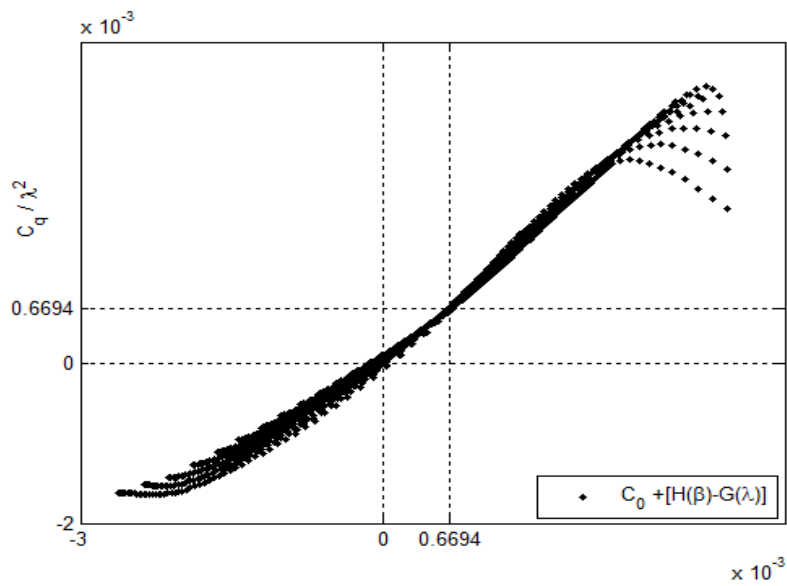


Figure 4-19. Separability for constant C_0 for variations of 80%, 90%, 100%, 110%, and 120%, of ω

Function Coefficients: $a\lambda^2 + b\lambda + c$			
	a	b	c
$G(\lambda)$	0.035117	0.0066006	-0.00053145

Table 4-3. Function $G(\lambda)$ coefficients

Function Coefficients: $a\beta^3 + b\beta^2 + c\beta + d$				
	a	b	c	d
$H(\beta)$	-6.1224×10^{-8}	-4.1873×10^{-6}	-2.206×10^{-5}	7.5734×10^{-5}

Table 4-4. Function $H(\beta)$ coefficients

4.3.1. Comparison of Aerodynamic Relationships

One main requirement of the Separability property is that the gradients of the derivatives of points on the locus of operating points are correct by construction and as required, see Observation 3) in Section 3.2.

Separability in tip speed ratio is applied to rotor PJ9, rotor Demo and rotor Demo-modified at their rated rotor speed and $\pm 10\%$ variations of it, no $\tau(\omega, \cdot)$ function has been applied. By looking at C_q/λ^2 vs λ , a visual representation of how good the surfaces, including the fact that they are tangential to each other at the locus of equilibrium points and the existence of a substantial range, can be achieved. For the separated form, the domain of λ is restricted to that for which Additivity applies. The results can be seen in Figure 4-20 to Figure 4-22 for rotor PJ9, Figure 4-23 to Figure 4-25 for rotor Demo and Figure 4-26 to Figure 4-28 for rotor Demo-modified.

It is, of course, also useful to be able to visualise the same on C_q vs λ plots. Results can be seen in Figure 4-29 to Figure 4-31 for rotor PJ9, Figure 4-32 to Figure 4-34 for rotor Demo and Figure 4-35 to Figure 4-37 for rotor Demo-modified.

From Figure 4-20 to Figure 4-37, the continuous lines indicate Bladed results for both C_q/λ^2 vs λ and C_q vs λ , the dashed lines are for the separated representation and the plus signs (+)

represent the locus of operating points. Each line of data corresponds to a constant pitch value. More data points than the strictly applicable ones for Separability theory have been included to study the behaviour beyond ideal conditions, this is particularly obvious where there is a change of sign of the gradient in the Separability results (dashed lines) in the plots.

The results from all three rotors display that Separability is a good approximation. It clearly breaks down in the stall region which limits the domain.

The results are clear in confirming that the derivatives of the functions involved in Separability are correct along the locus of equilibrium points as posited in Section 3.2 and that there exists a substantial range of reasonable accuracy. To be noted that the results are good even in absence of the $\tau(\omega, \cdot)$ function, the inclusion of which would had provided better results over a bigger domain.

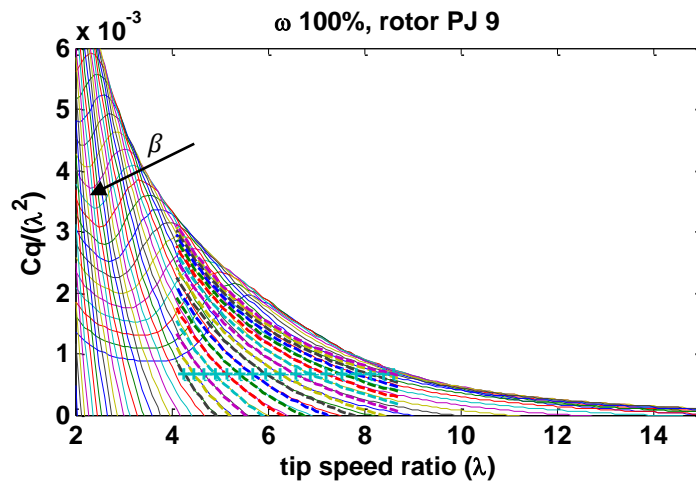


Figure 4-20. C_q/λ^2 vs λ (continuous lines) for rotor PJ9, predicted values from equations (dashed lines) and equilibrium points (plus signs)

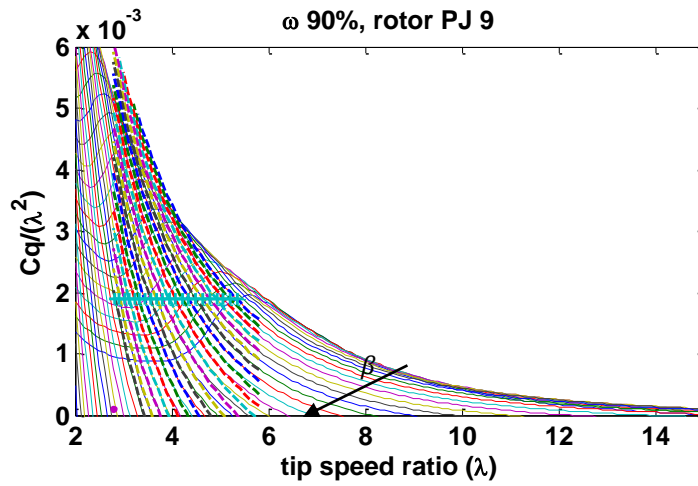


Figure 4-21. C_q/λ^2 vs λ (continuous lines) for rotor PJ9 with rotor speed diminished by -10%, predicted values from equations (dashed lines) and equilibrium points (plus signs).

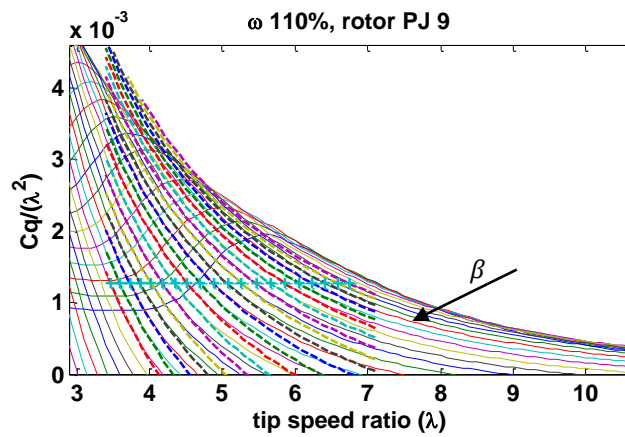


Figure 4-22. C_q/λ^2 vs λ (continuous lines) for rotor PJ9 with rotor speed increased by +10%, predicted values from equations (dashed lines) and equilibrium points (plus signs)

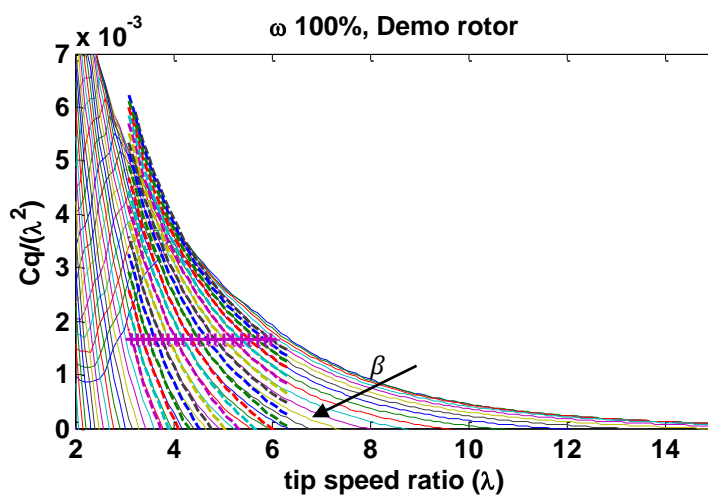


Figure 4-23. C_q/λ^2 vs λ (continuous lines) for Demo rotor, predicted values from equations (dashed lines) and equilibrium points (plus signs)

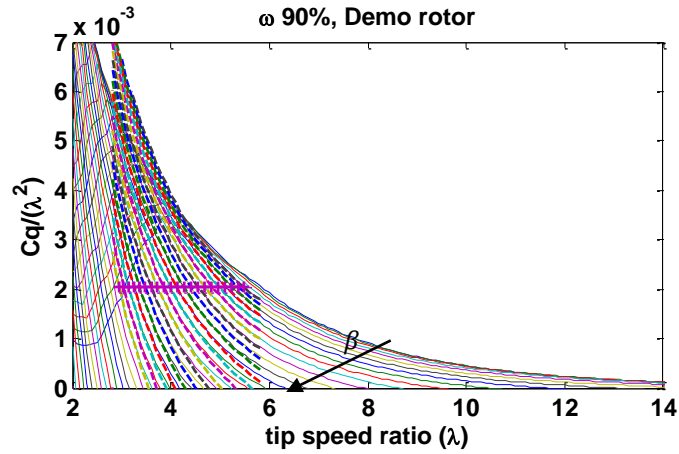


Figure 4-24. C_q/λ^2 vs λ (continuous lines) for Demo rotor with rotor speed diminished by -10%, predicted values from equations (dashed lines) and equilibrium points (plus signs)

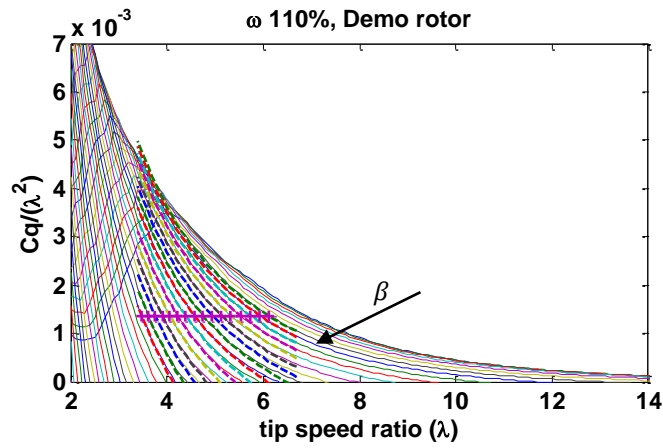


Figure 4-25. C_q/λ^2 vs λ (continuous lines) for Demo rotor with rotor speed increased by +10%, predicted values from equations (dashed lines) and equilibrium points (plus signs)

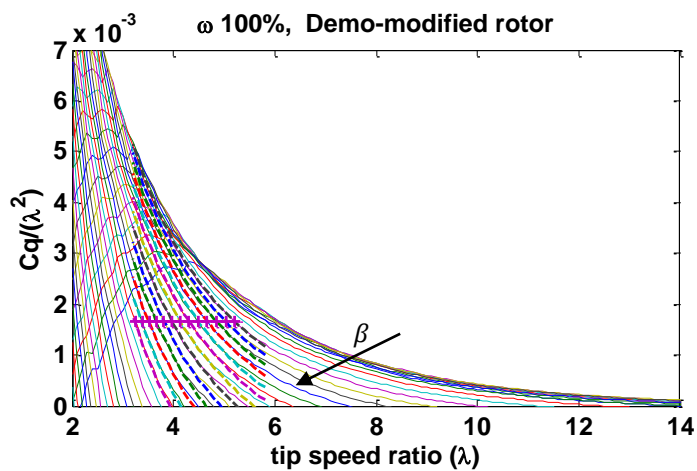


Figure 4-26. C_q/λ^2 vs λ (continuous lines) for Demo-modified rotor, predicted values from equations (dashed lines) and equilibrium points (plus signs)

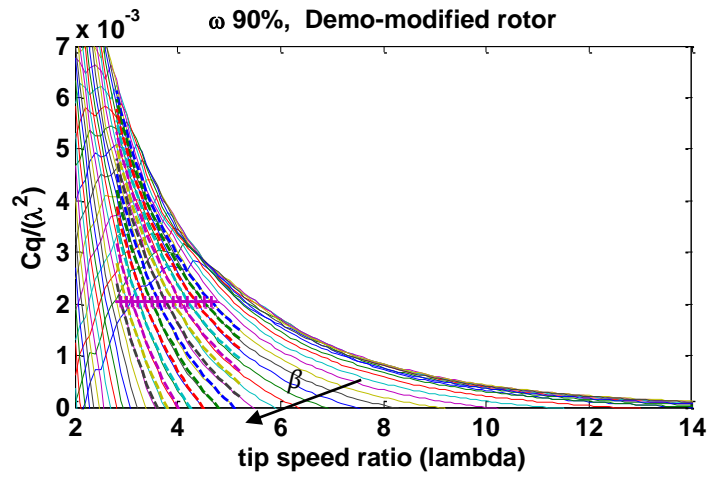


Figure 4-27. C_q/λ^2 vs λ (continuous lines) for Demo-modified rotor with rotor speed diminished by -10%, predicted values from equations (dashed lines) and equilibrium points (plus signs)

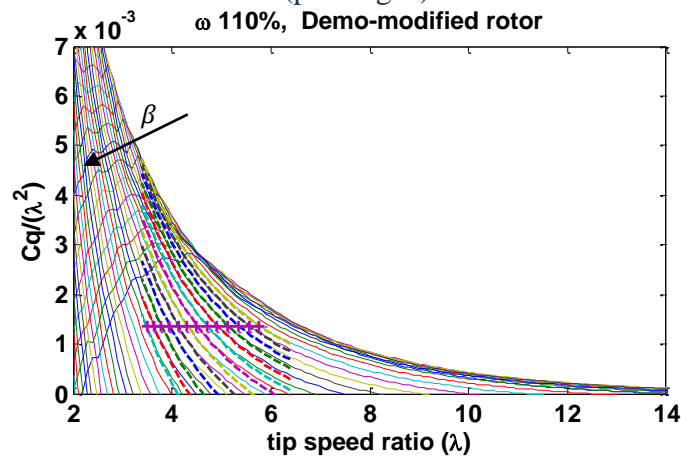


Figure 4-28. C_q/λ^2 vs λ (continuous lines) for Demo-modified rotor with rotor speed increased by +10%, predicted values from equations (dashed lines) and equilibrium points (plus signs)

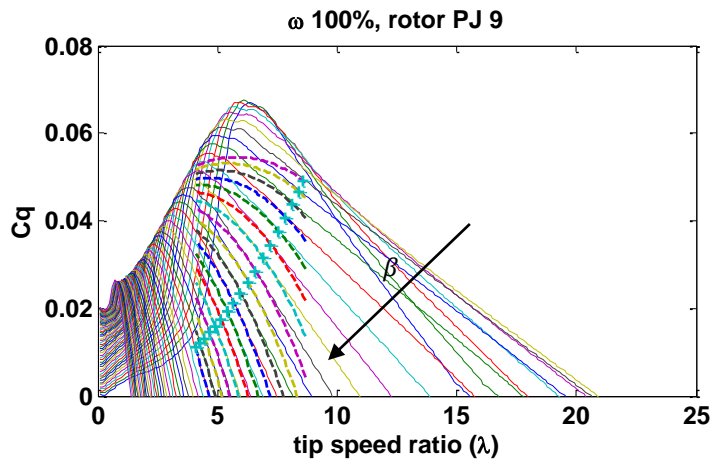


Figure 4-29. C_q vs λ (continuous lines) for rotor PJ9, predicted values from equations (dashed lines) and equilibrium points (plus signs)

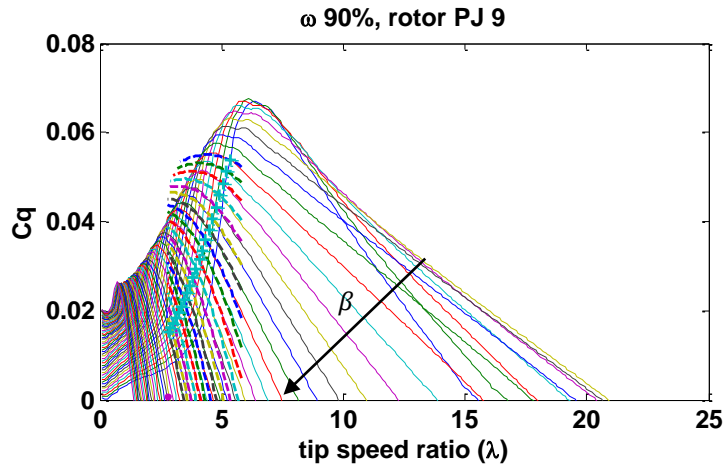


Figure 4-30. C_q vs λ (continuous lines) for rotor PJ9 with rotor speed diminished by -10%, predicted values from equations (dashed lines) and equilibrium points (plus signs)

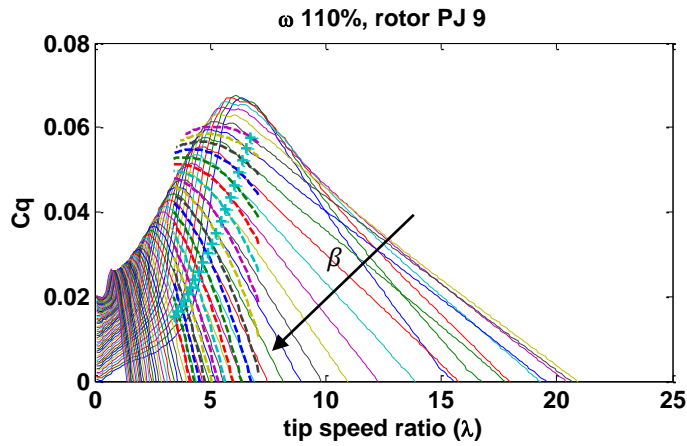


Figure 4-31. C_q vs λ (continuous lines) for rotor PJ9 with rotor speed increased by +10%, predicted values from equations (dashed lines) and equilibrium points (plus signs)

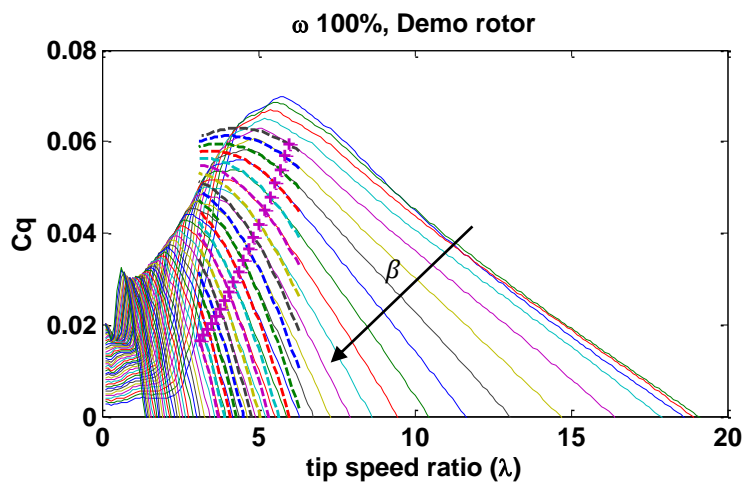


Figure 4-32. C_q vs λ (continuous lines) for Demo rotor, predicted values from equations (dashed lines) and equilibrium points (plus signs)

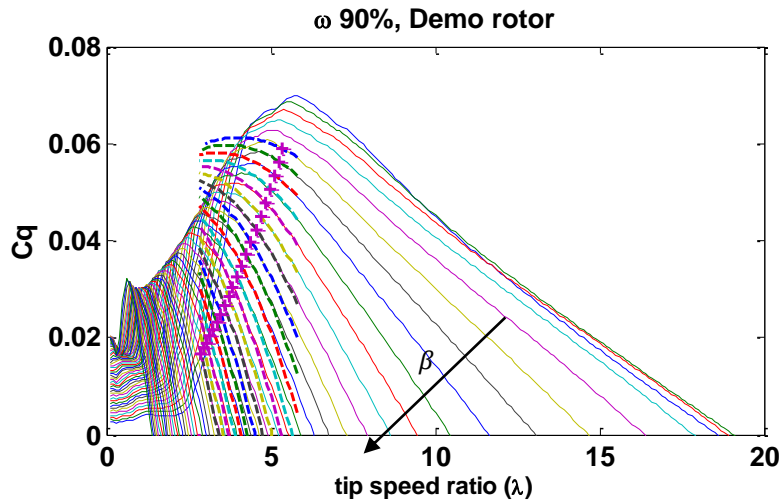


Figure 4-33. C_q vs λ (continuous lines) for Demo rotor with rotor speed diminished by -10%, predicted values from equations (dashed lines) and equilibrium points (plus signs)

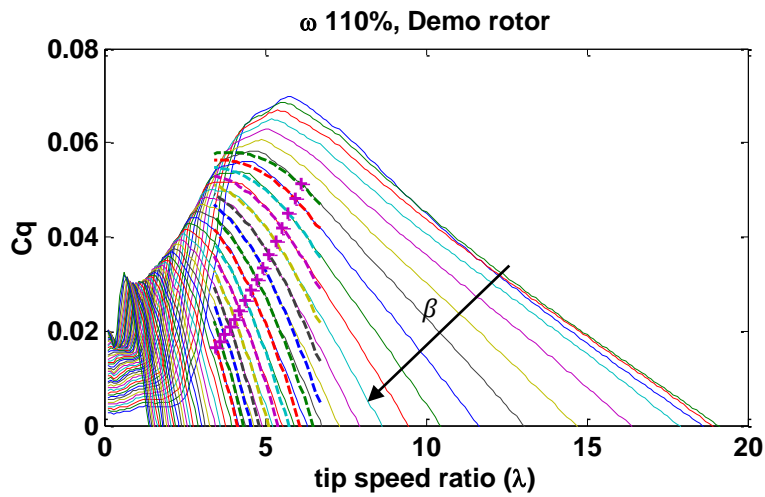


Figure 4-34. C_q vs λ (continuous lines) for Demo rotor with rotor speed increased by +10%, predicted values from equations (dashed lines) and equilibrium points (plus signs)

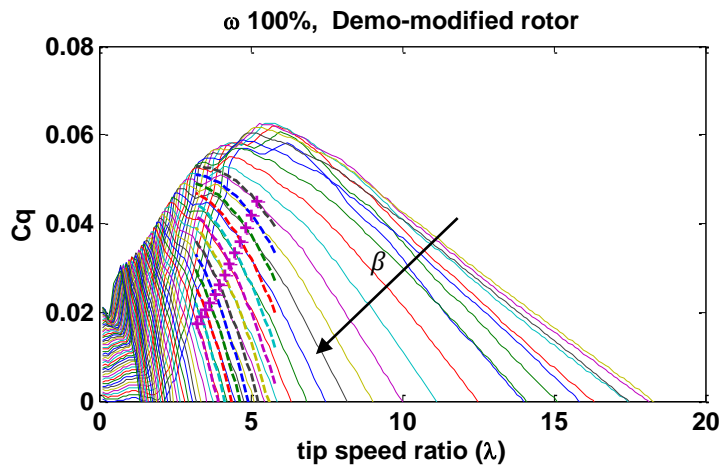


Figure 4-35. C_q vs λ (continuous lines) for Demo-modified rotor, predicted values from equations (dashed lines) and equilibrium points (plus signs)

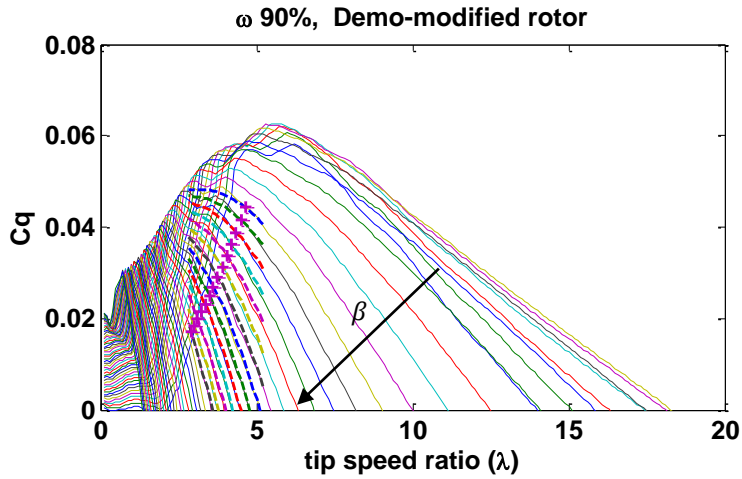


Figure 4-36. C_q vs λ (continuous lines) for Demo-modified rotor with rotor speed diminished by -10%, predicted values from equations (dashed lines) and equilibrium points (plus signs)

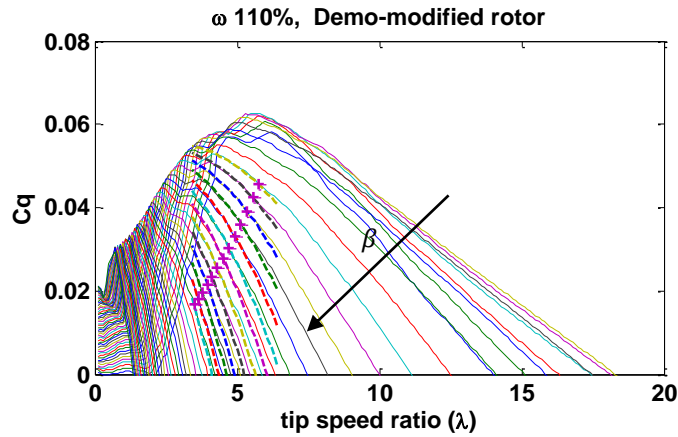


Figure 4-37. C_q vs λ (continuous lines) for Demo-modified rotor with rotor speed increased by +10%, predicted values from equations (dashed lines) and equilibrium points (plus signs)

4.4. Modified Tip Speed Ratio Based Separability

Because the tangential nature of the separated form to the plots of C_q/λ^2 can be seen to hold pretty well within a broad region about the locus of equilibrium points in Figure 4-20 to Figure 4-28, it is justifiable to apply additivity in λ and β along the locus for which T is constant rather than C ; that is the Additivity in the more desirable form

$$T(\beta, \lambda, \omega) = \omega^2(T_0/\omega_0^2 + (h(\beta) - g(\lambda))) \quad (4.18)$$

on the locus of equilibrium points with $T(\beta, \lambda, \omega) = T_0$. However, the Additivity property in Section 3.2 no longer applies. Instead, only the Basic Additivity of the form described in

Section 3.1.2 applies. More generally, preserving the correct values at the equilibrium points, Separability is formulated as,

$$T(\beta, \lambda, \omega) \approx \omega^2 \mu(T_0/\omega_0^2 + (h(\beta) - g(\lambda))) \quad (4.19)$$

for some $\mu(\cdot)$ such that $\mu(T_0/\omega_0^2) = T_0/\omega_0^2$. Where the $\mu(\cdot)$ function could be thought to be to the tip speed ratio Separability as the $\tau(\cdot)$ function is for the wind speed Separability.

4.4.1. Characterisation of the Additivity Equations $h(\beta)$ and $g(\lambda)$

The initial observation on the basis of results in Section 4.3 that (4.19) may apply, although with Basic Separability, suggests that a fitting procedure similar to Section 3.5, could be appropriate. Unfortunately, when applied, results are not satisfactory. Better results are obtained by fitting the gradients as functions of $1/\lambda$, then integrating the resulting polynomials.

The reason for using functions of $1/\lambda$ can be seen from Figure 4-38. The asymptotic behaviour implies that a fit as a polynomial in λ is likely to be inappropriate. However, Figure 4-39 strongly suggests that a fit in $1/\lambda$ would be better. The functions, $h'(\beta)$ and $g'(\lambda)$, are determined for the separated form of $T(\beta, \lambda, \omega)/\omega^2$ using data sets for which $T(\beta, \lambda, \omega)$ is close to T_0 , with rotor speeds of 80%, 90%, 100%, 110%, 120% and 140% ω_0 . To find $g'(\lambda)$ the fits to $\frac{\partial(T/\omega^2)}{\partial\lambda}$ are determined as functions of $1/\lambda$. A satisfactory fit is cubic, as can be seen from Figure 4-40. Hence:

$$g'(\lambda) = a \left(\frac{1}{\lambda}\right)^3 + b \left(\frac{1}{\lambda}\right)^2 + c \left(\frac{1}{\lambda}\right) + d \quad (4.20)$$

$$g(\lambda) = \int g'(\lambda) d\lambda = A \left(\frac{1}{\lambda}\right)^2 + B \left(\frac{1}{\lambda}\right) + C \ln(\lambda) + D\lambda + E \quad (4.21)$$

with $A = \frac{1}{3}a$, $B = b$, $C = c$ and $D = d$. Note, the presence of the $\ln(\lambda)$ term in (4.21). It is the reason why fitting the $g'(\lambda)$ as a polynomial in $1/\lambda$ rather than $g(\lambda)$ is a better approach.

Following the same methodology for $h'(\beta)$, the initial $\frac{\partial(T/\omega^2)}{\partial\beta}$ vs β data can be seen in Figure 4-41. The best fitting for $h'(\beta)$ is also cubic, as can be seen in Figure 4-42. Hence:

$$h'(\beta) = k\beta^3 + l\beta^2 + m\beta + n \quad (4.22)$$

$$h(\beta) = \int h'(\beta) d\beta = K\beta^4 + L\beta^3 + M\beta^2 + N\beta + P \quad (4.23)$$

with $K = \frac{1}{3}k$, $L = l$, $M = m$ and $N = n$.

Having determined the form of the fits (4.21) and (4.23), the coefficients for $g(\lambda)$ and $h(\beta)$ are optimised directly, using the least squares method. The $g(\lambda)$ and $h(\beta)$ equations are shown on Figure 4-43 and the coefficients are as in Table 4-5.

Optimised coefficients for functions $g(\lambda)$ and $h(\beta)$	
K	-4.36
L	188.47
M	-6543.44
N	14058.73
P	-20181.90
A	-54699405.81
B	28264102.03
C	4940730.35
D	-240218.21
E	-11552999.06

Table 4-5. Optimised coefficients for functions $g(\lambda)$ and $h(\beta)$

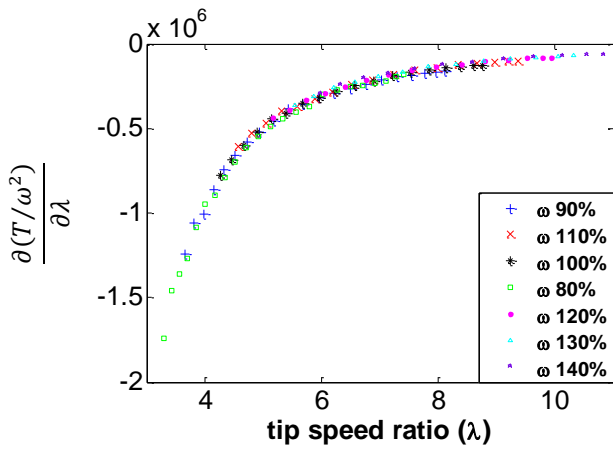


Figure 4-38. $\frac{\partial(T/\omega^2)}{\partial\lambda}$ vs λ

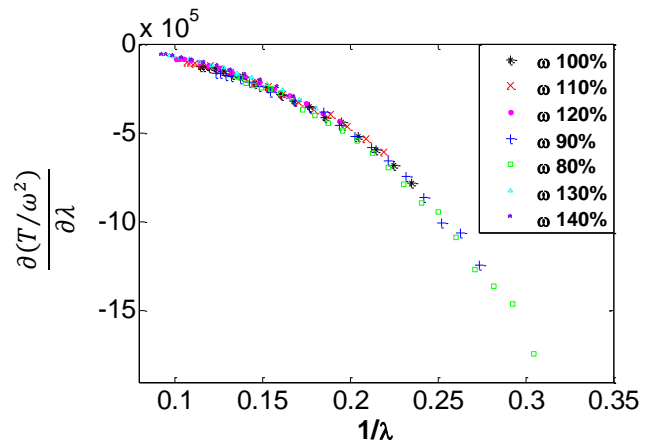


Figure 4-39. $\frac{\partial(T/\omega^2)}{\partial\lambda}$ vs $1/\lambda$

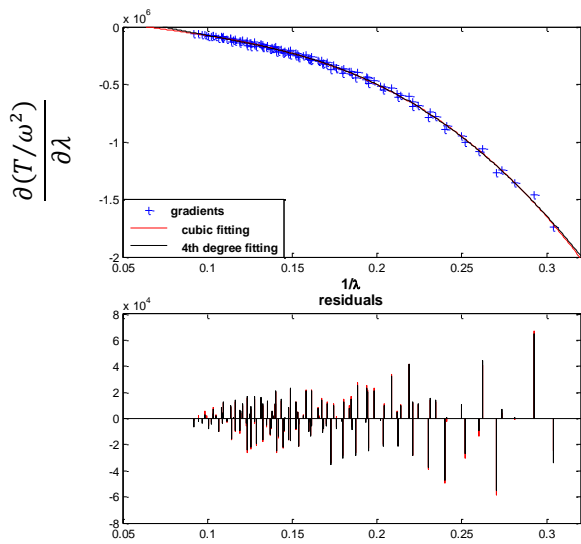


Figure 4-40. Equation fitting for $g'(\lambda)$

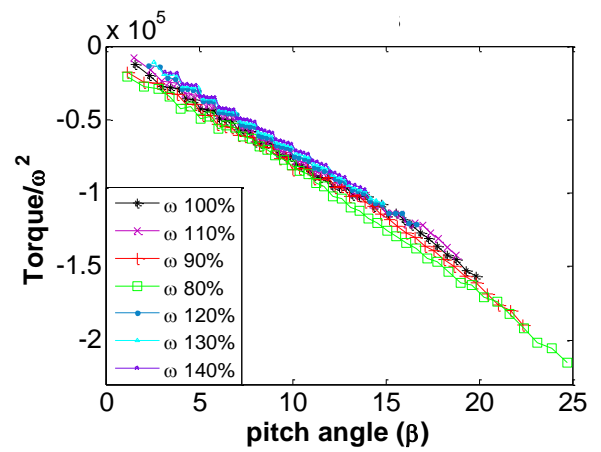


Figure 4-41. $\frac{\partial(T/\omega^2)}{\partial\beta}$ vs pitch angle

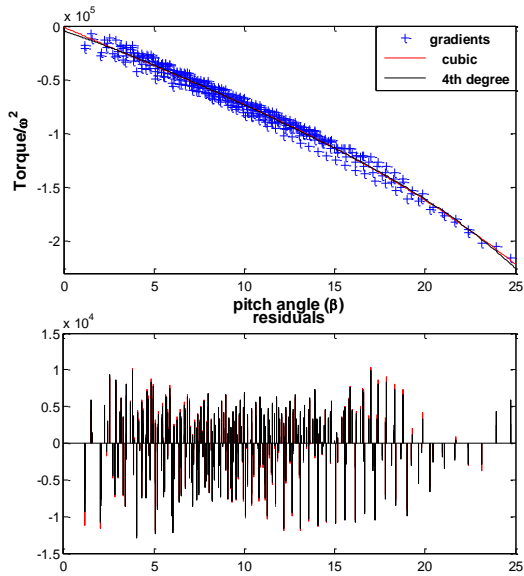


Figure 4-42 Equation fitting for $h'(\beta)$

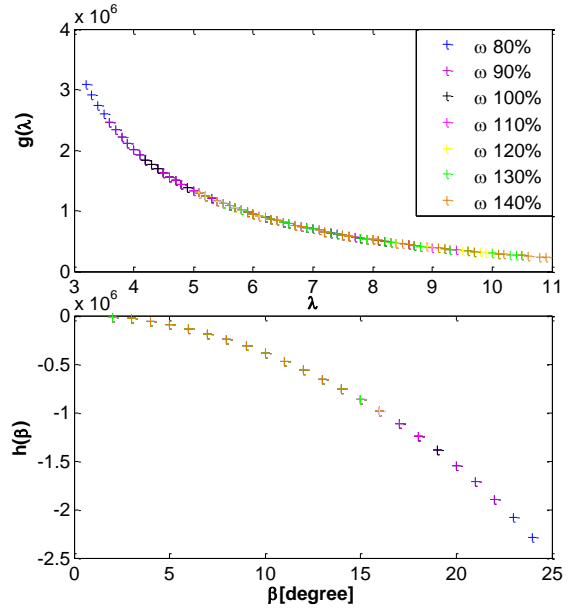


Figure 4-43. Equations $g(\lambda)$ and $h(\beta)$ with optimised coefficients

The values of $T(\beta, \lambda, \omega)/\omega^2$ at the operating points along the locus of constant T_0 are compared to the above fit in Figure 4-44. It can be seen that basing the fit on Observation 3) Section 3.2, is successful even though only the Basic Additivity as described in Section 3.1.2 really applies.

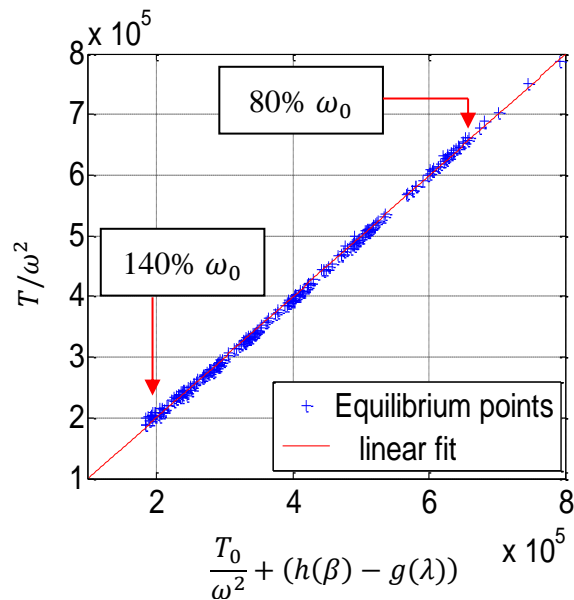


Figure 4-44. Equilibrium points after separation

4.4.2. Modified Tip Speed Ratio Separability, from Local to Global Behaviour

The $\mu(\cdot)$ function is determined separately for the different rotor speeds between 80% and 140% ω_0 as depicted in Figure 4-45, with the $\mu(\cdot)$ functions scaled by ω^2 , as per (4.19).

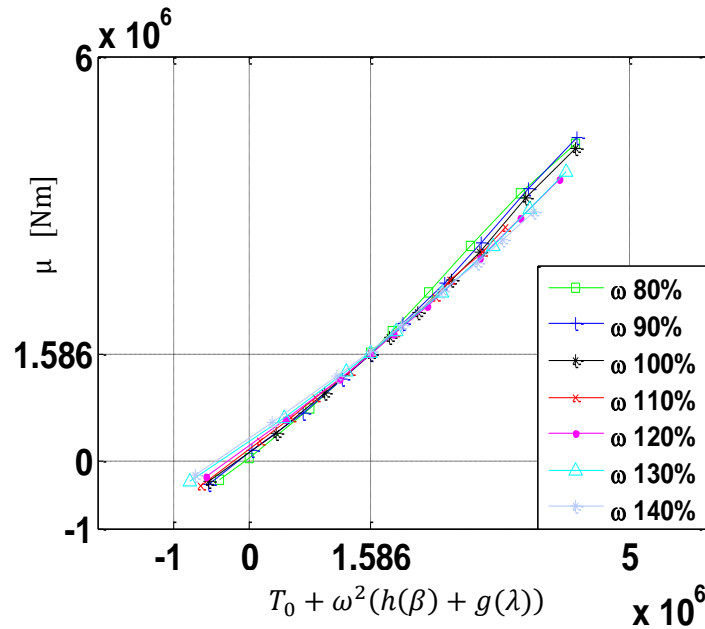


Figure 4-45. Function $\mu(\cdot)$ scaled by ω^2 for Rotor PJ9

It can be appreciated from Figure 4-45, that there is a noticeable difference between the $\mu(\cdot)$ functions for the different rotor speeds, in particular $\mu'(T_0/\omega_0) \neq 1$, but all fits are clearly weakly non-linear. This is a clear consequence from the Additivity property in Section 3.2 not applying anymore. Instead, the Basic Additivity in Section 3.1.2 applies, but the fitting of the equations has continued to be based on Observation 3). The function $\mu(\cdot)$ coefficients for rotor speeds varying from 80% to 140% ω_0 can be seen in Table 4-6.

		Function Coefficients: $a(\cdot)^3 + b(\cdot)^2 + c(\cdot) + d$				
		Rotor Speed	a	b	c	d
$\mu(\cdot)$	80% ω_0		-1.49×10^{-14}	1.2101×10^{-7}	0.84237	41478
	90% ω_0		-1.54×10^{-14}	1.4431×10^{-7}	0.75763	96090
	ω_0		-1.2306×10^{-14}	1.3031×10^{-7}	0.75355	1.0591×10^{-5}
	110% ω_0		-7.2452×10^{-15}	9.6426×10^{-8}	0.76346	1.5002×10^{-5}
	120% ω_0		-2.5267×10^{-15}	6.2676×10^{-8}	0.76755	2.2174×10^{-5}
	130% ω_0		-2.414×10^{-15}	6.6202×10^{-8}	0.71419	3.2405×10^{-5}
	140% ω_0		-1.9659×10^{-15}	2.2092×10^{-8}	0.78475	3.4826×10^{-5}

Table 4-6. Function $\mu(\cdot)$ coefficients for rotor PJ9

To ascertain the extent of the deviation of μ' from 1 at the equilibrium points, the equilibrium points have been analysed for 80%-140% ω_0 . The results can be seen from Figure 4-46 to Figure 4-52. The gradients vary for the different ω but remain reasonably close to 1 for a broad range of ω .

Because the $\mu(\cdot)$ functions differ for each choice of ω , comparisons in Section 4.4.3 of $T(\beta, \lambda, \omega)$ to the separated fit, do not include the $\mu(\cdot)$ functions nor $\tau(\cdot)$.

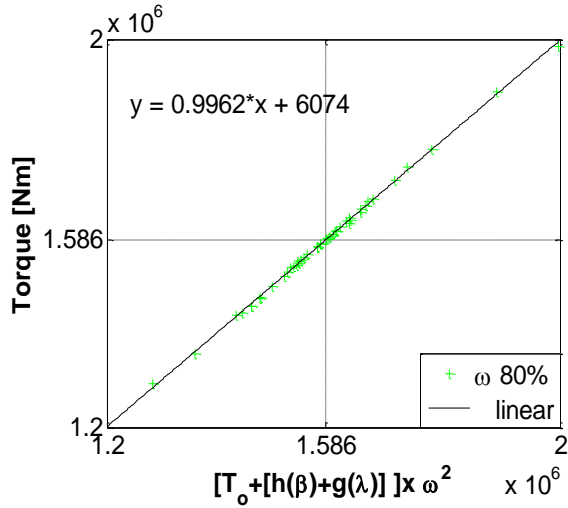


Figure 4-46. Equilibrium points ω 80%

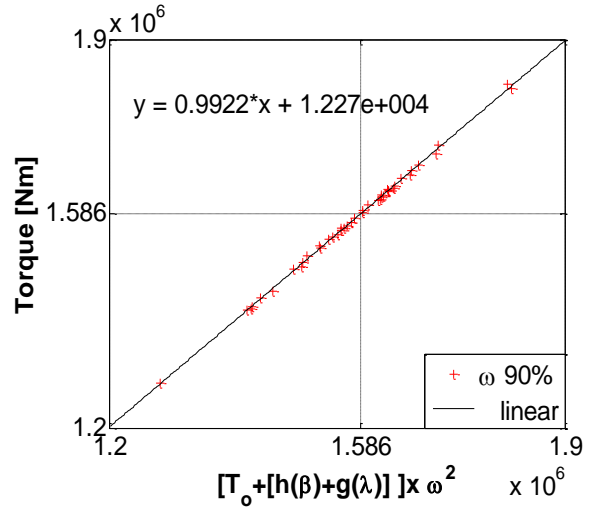


Figure 4-47. Equilibrium points ω 90%

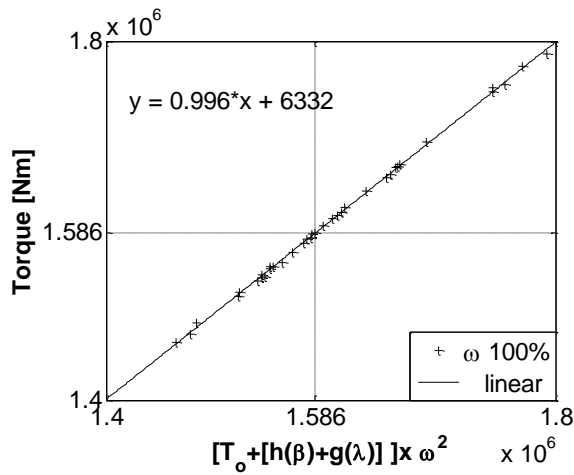


Figure 4-48. Equilibrium points ω 100%

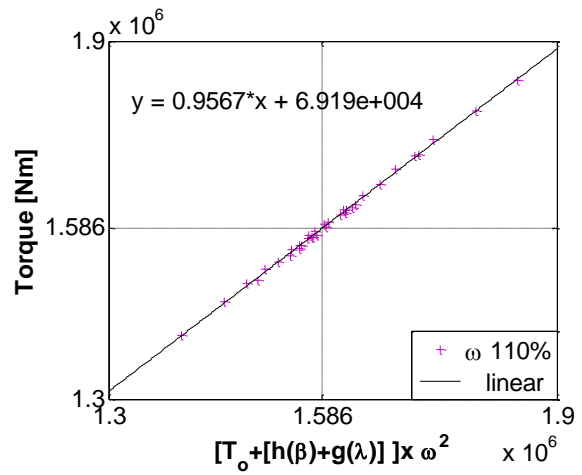


Figure 4-49. Equilibrium points ω 110%

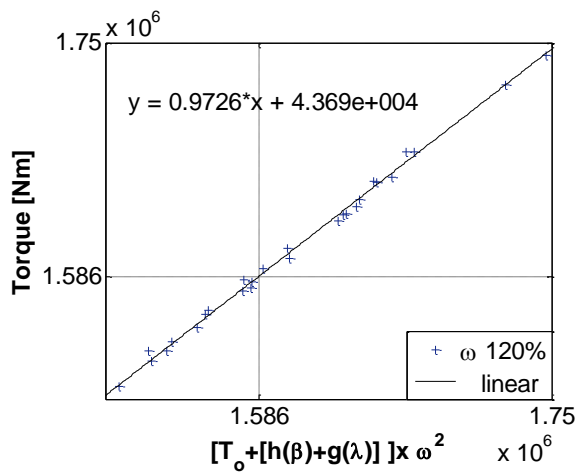


Figure 4-50. Equilibrium points ω 120%

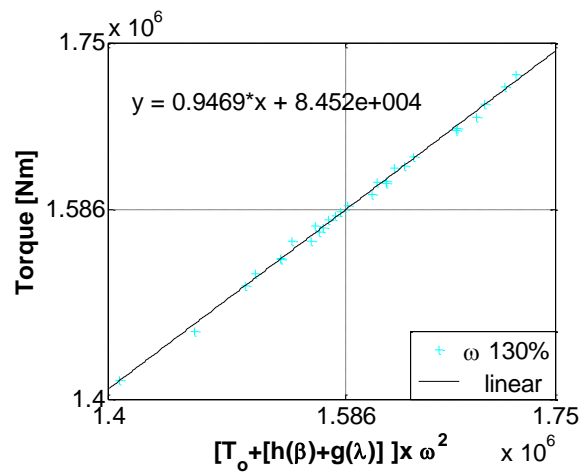


Figure 4-51. Equilibrium points ω 130%

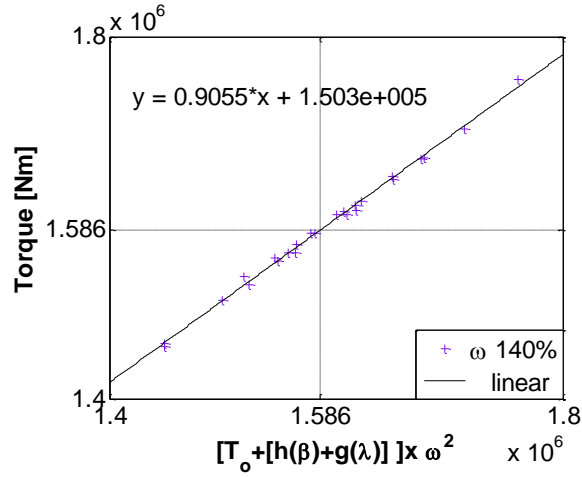


Figure 4-52. Equilibrium points ω 140%

4.4.3. Results for Modified Tip speed Ratio Based Separability

The results for $T = \omega^2 (T_0 + (h(\beta) - g(\lambda)))$ can be seen from Figure 4-53 to Figure 4-59 and for $\frac{T}{\omega^2} = T_0 + (h(\beta) - g(\lambda))$ from Figure 4-56 to Figure 4-62. All results account for the whole set of data for each ω that is represented. The results are discussed in Section 4.5 along with the comparison with the wind speed based Separability.

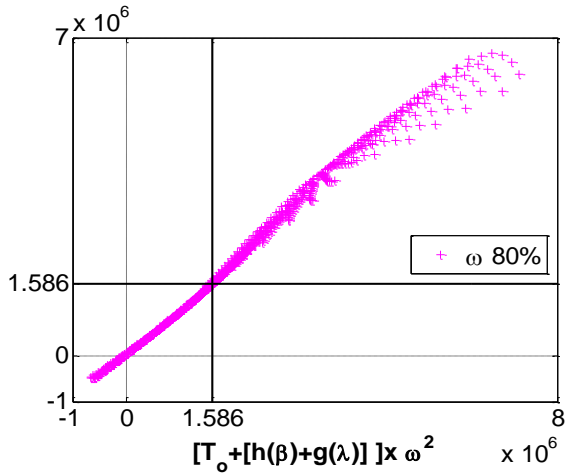


Figure 4-53. Separability in tip speed ratio for T, ω 80%

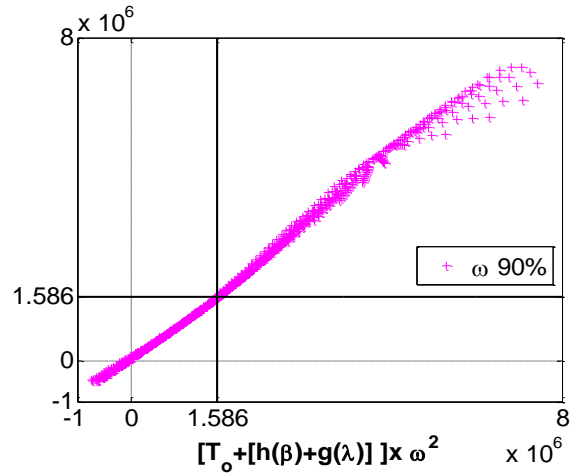


Figure 4-54. Separability in tip speed ratio for T, ω 90%

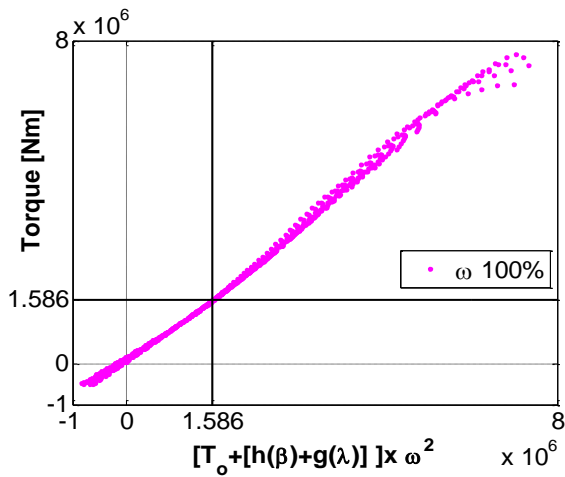


Figure 4-55. Separability in tip speed ratio for T, ω 100%

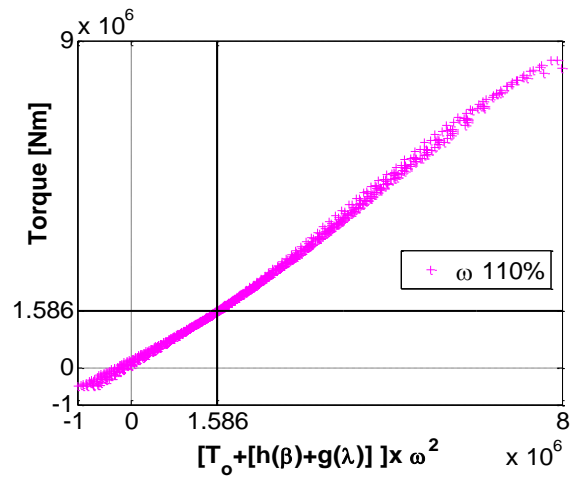


Figure 4-56. Separability in tip speed ratio for T, ω 110%

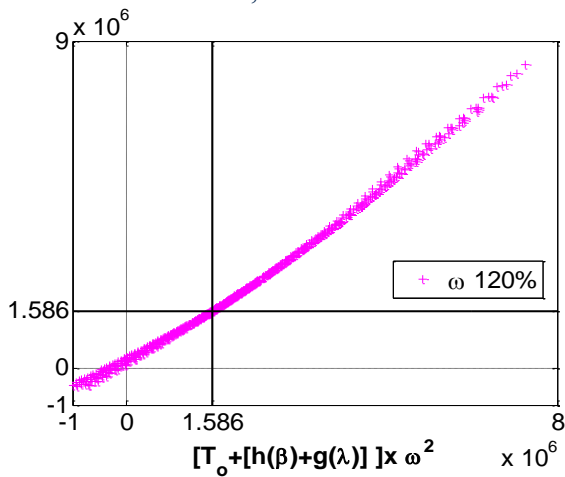


Figure 4-57. Separability in tip speed ratio for T, ω 120%

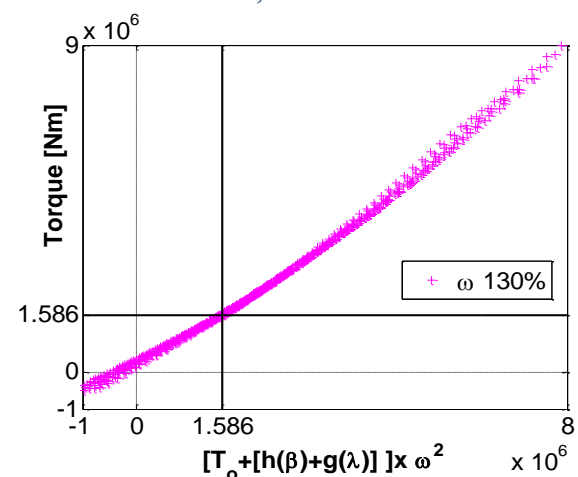


Figure 4-58. Separability in tip speed ratio for T, ω 130%

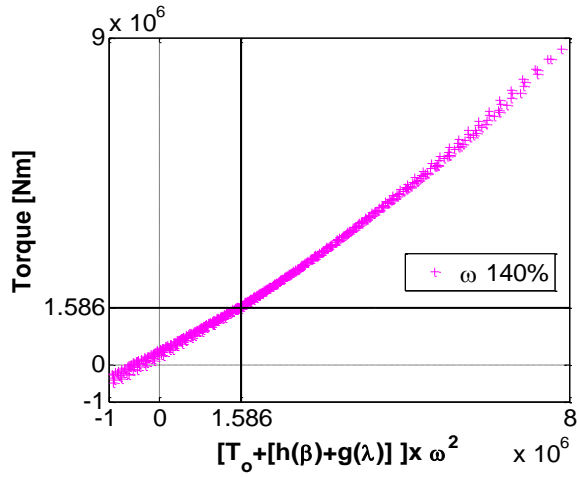


Figure 4-59. Separability in tip speed ratio for T , ω 140%

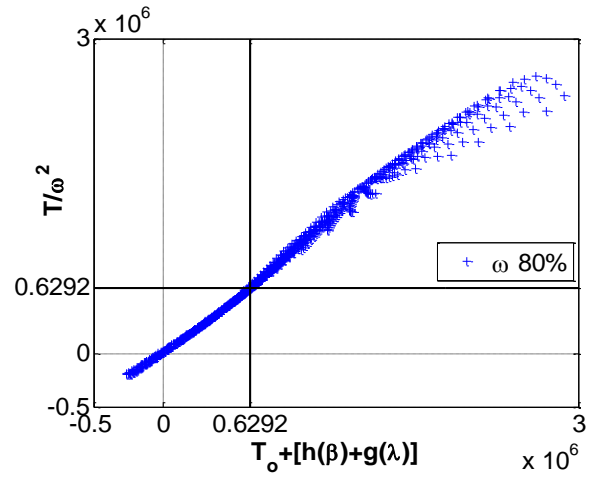


Figure 4-60. Separability in tip speed ratio for T/ω^2 , ω 80%

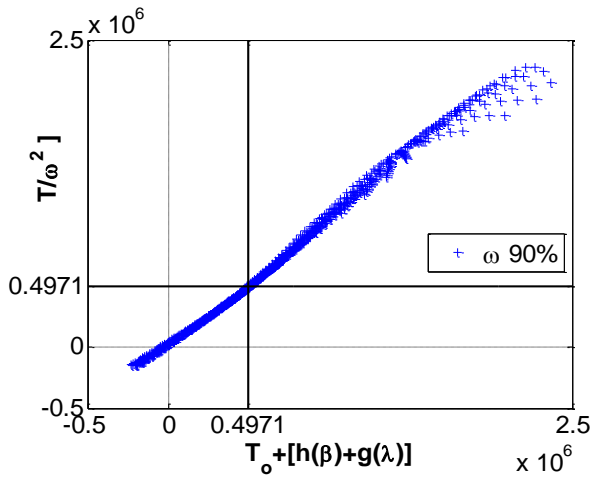


Figure 4-61. Separability in tip speed ratio for T/ω^2 , ω 90%

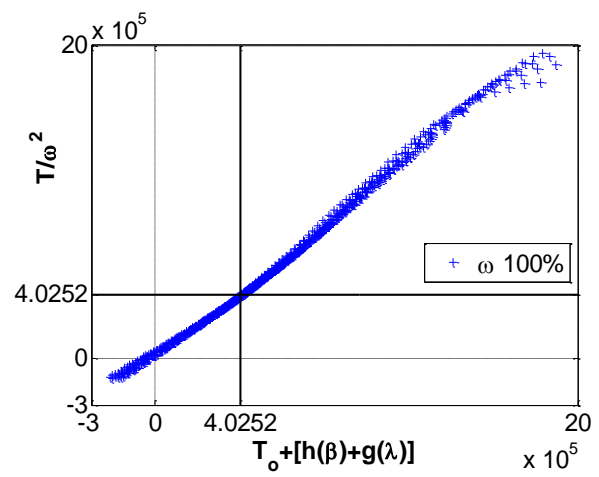


Figure 4-62. Separability in tip speed ratio for T/ω^2 , ω 100%

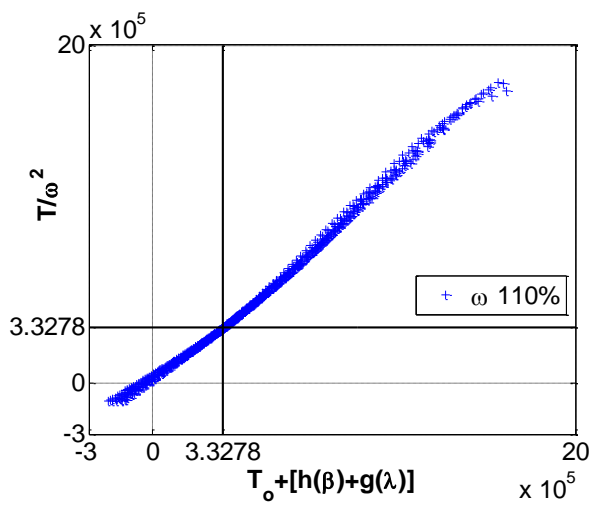


Figure 4-63. Separability in tip speed ratio for T/ω^2 , ω 110%

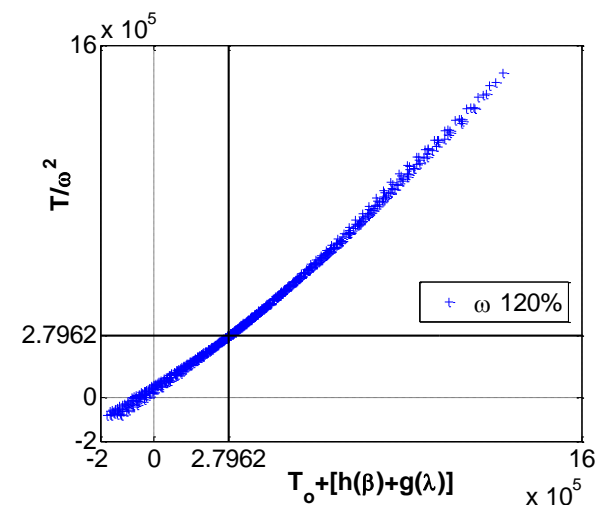


Figure 4-64. Separability in tip speed ratio for T/ω^2 , ω 120%

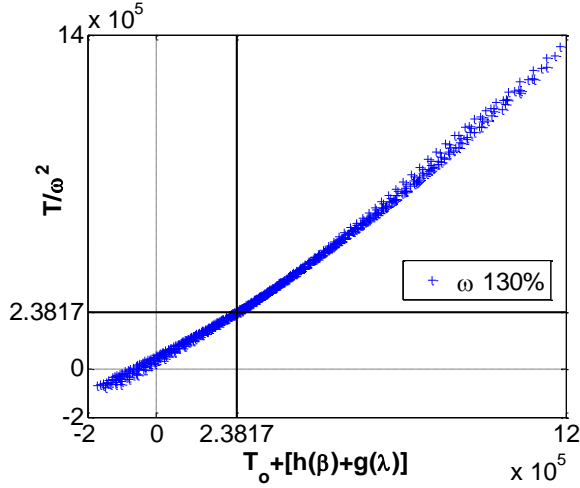


Figure 4-65. Separability in tip speed ratio for T/ω^2 , ω 130%

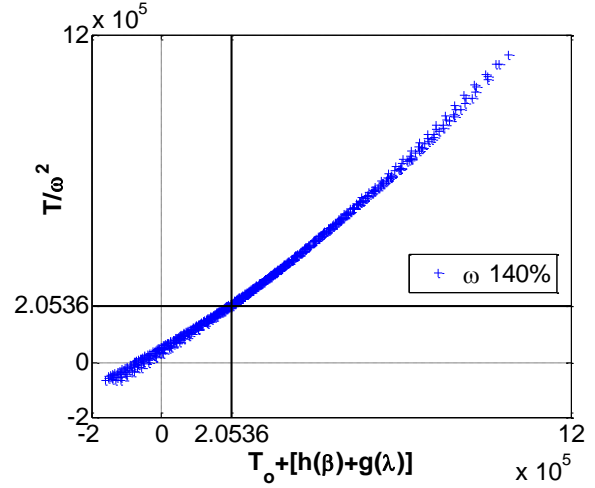


Figure 4-66. Separability in tip speed ratio for T/ω^2 , ω 140%

4.5. Comparison of Wind Speed Based Separability and Tip Speed Ratio Based Separability

In Section 1 and Section 4.4, two different versions of Separability are discussed, specifically, Separation using function $g(\cdot)$ only dependent on wind speed, (4.7), and Separability using tip speed ratio, (4.18), namely,

$$T \approx \tau(T_0 + (h(\omega, \beta) - g(V))) \quad \text{and} \quad T \approx \omega^2 \mu(T_0/\omega_0^2 + (h(\beta) - g(\lambda))) \quad (4.24)$$

For Separability in wind speed, $h(\omega, \beta)$ and $g(V)$ together with optimised polynomial fits, $h(\omega, \beta) = a_\omega \beta^2 + b_\omega \beta + c_\omega$ and $g(V) = aV^2 + bV + c$, are shown in Figure 4-16. For Separability in tip speed ratio, $h(\beta)$ and $g(\lambda)$, together with optimised fits $h(\beta) = K\beta^4 + L\beta^3 + M\beta^2 + N\beta + P$ and $g(\lambda) = A\lambda^{-2} + B\lambda^{-1} + C \ln(\lambda) + D\lambda + E$, are shown in Figure 4-43.

From Figure 4-67 to Figure 4-73 the two versions of Separability are compared directly for rotor speeds of 80%, 90%, 100%, 110%, 120%, 130% and 140% ω_0 , respectively. Neither function $\tau(\cdot)$ nor function $\mu(\cdot)$ have been used. Results show that both types of Separability are good approximations to the aerodynamic torque for large neighbourhoods enclosing the locus of equilibrium points. As would be expected, the 100% ω_0 case exhibits the closest match. The least good is the 80% ω_0 case, but that is not unexpected since its operating points are the closest to stall.

Each Figure is further accompanied by a blow up of the data close to T_0 , i.e. the data local to the equilibrium operating points. It can be seen from these blow up graphs, that there is a small inaccuracy in the tip speed ratio based Separability version. The inaccuracy is particularly clear for the lambda case 140% ω_0 shown in Figure 4-73, where the deviation is at its most severe having a displacement in the order of 5% from the assumed value. The underlying reason for this inaccuracy is the implicit assumption in Section 4.3, that for the data sets for 80%, 90%, 100%, 110%, 120%, 130% and 140% ω_0 the λ fit being based on the Basic Additivity property as in Section 3.1.2, would be as good as the Additivity property in Section 3.2.

For Separability in tip speed ratio, the neighbourhood for which the separated representation of the aerodynamic torque is a close approximation, extends in every case at least from 0 to $2T_0$. This area increases as the set of operating points for the different rotor speeds move away from the stall region, being a particularly good approximation even when $T \gg T_0$.

For Separability in wind speed, the neighbourhood for which the separated representation of the aerodynamic torque is a close approximation, also extends in every case at least from 0 to $2T_0$, and it is particularly good when $T \ll T_0$. Although there is no first principle justification for the simplified wind speed version of Separability, i.e. for a $g(V)$ being independent of ω , the latter even locally to T_0 , is at least as good as Separability in tip speed ratio. In addition, it has a consistent $\tau(\cdot)$ function over the different rotor speeds.

It can be concluded that both versions of Separability provide very good approximations to the aerodynamic torque over extensive neighbourhoods of T_0 , at least from 0 to $2T_0$. If anything, the Separability in wind speed is better but it has the least analytic support being more empirical in nature.

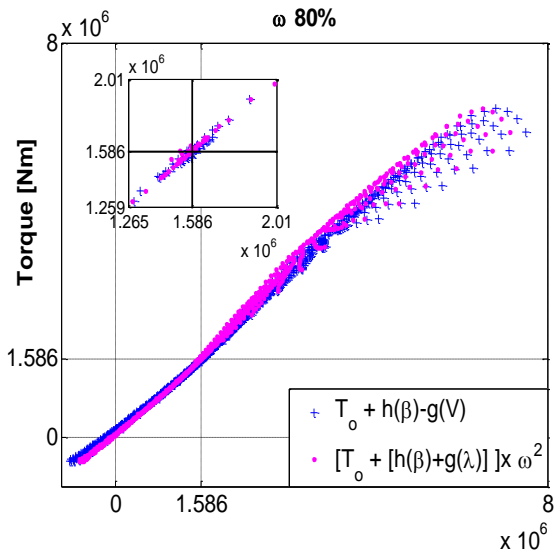


Figure 4-67. Separability comparison ω 80%

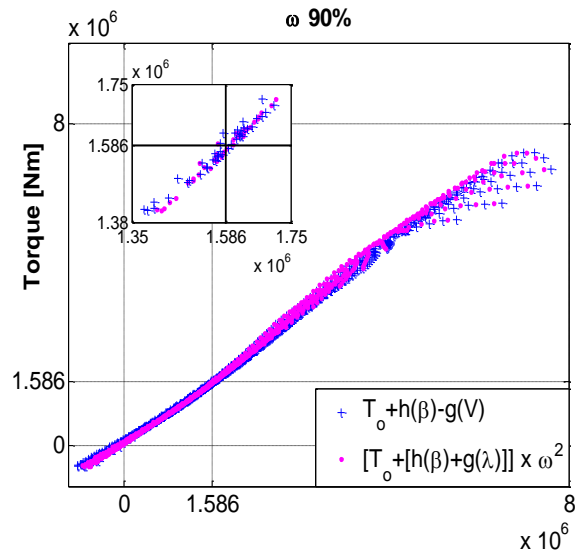


Figure 4-68. Separability comparison ω 90%

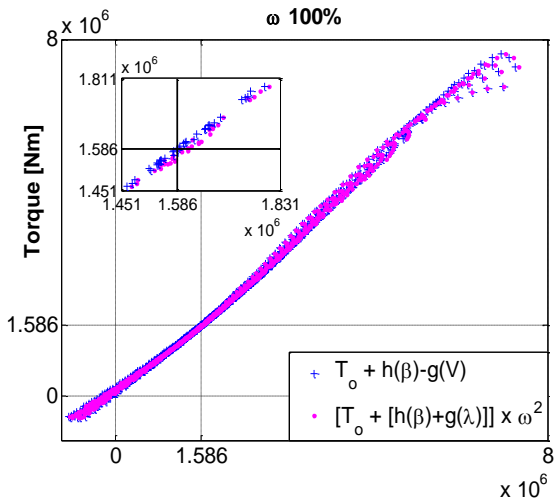


Figure 4-69. Separability comparison ω 100%

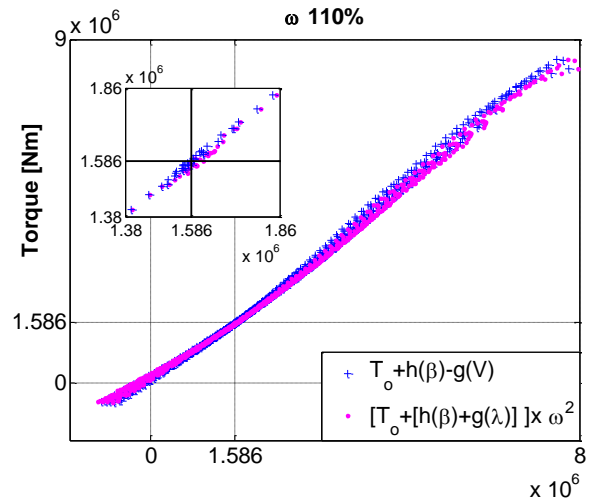


Figure 4-70. Separability comparison ω 110%

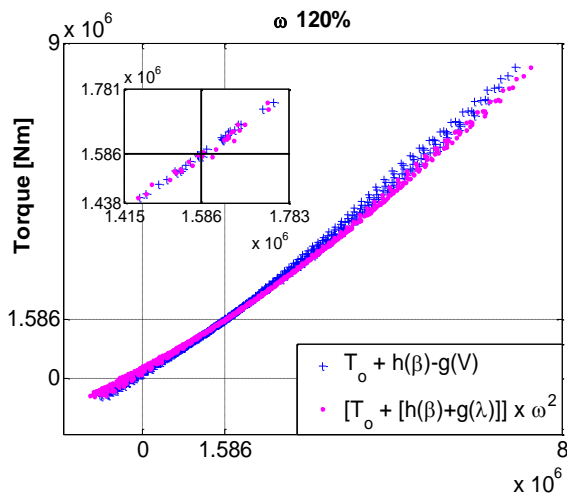


Figure 4-71. Separability comparison ω 120%

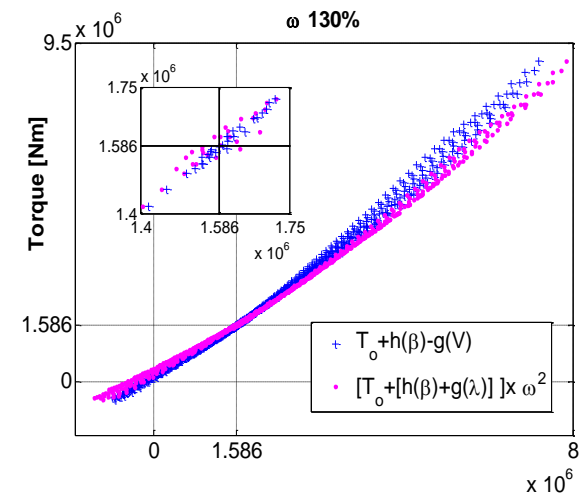


Figure 4-72. Separability comparison ω 130%

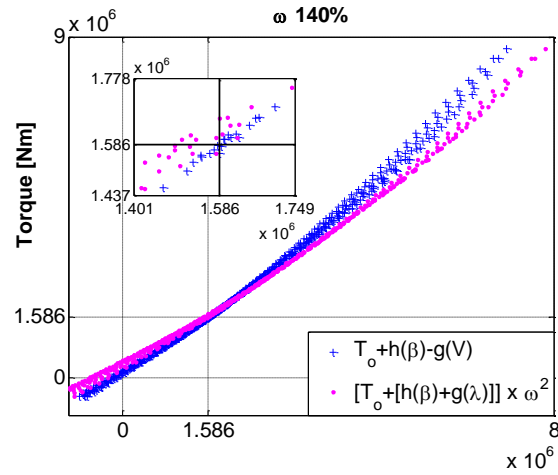


Figure 4-73. Separability comparison ω 140%

4.6. Conclusions

The Separability property is investigated for constant speed WTs and variable speed WTs. The general structure of the Additivity functions $h(\cdot)$ and $g(\cdot)$ for both the wind speed and tip speed ratio based Separability, and their relationship is determined. In particular, the optimised fit for the wind speed based Separability, is found after the best parametric form for the individual equations $h(\cdot)$ and $g(\cdot)$ are identified.

Both the $g(\cdot)$ and $\tau(\cdot)$ functions are proven to be weakly non-linear and can be considered independent from ω . Whereas the $\mu(\cdot)$ function has been confirmed to have both, dependency on ω and more non-linearity, albeit still relatively weakly so. This is largely due to the Basic Additivity property in Section 3.1.2 applying to Separability in tip speed ratio rather than the Additivity property from Section 3.2, an important consequence being that $\mu'(T_0/\omega_0^2) \neq 1$.

It is demonstrated that Separability exists for both constant and variable speed WTs and that it holds for very large neighbourhoods with very good accuracy. In fact, on average, it comfortably covers more than double the rated torque of all WTs explored.

It is established that both, principled Separability based on tip speed ratio and empirical Separability based on a simplified version of wind speed, provide good approximations for the aerodynamic torque with the latter as good as the former. Therefore, when exploiting Separability to develop advanced controllers and other purposes, such as wind speed models, which require good accuracy, the use of the empiric Separability relationship of the form,

$$T \approx \tau\left(T_0 + (h(\omega, \beta) - g(V))\right)$$

is fully justified.

This form of Separability provides with the correct values and derivatives at the equilibrium operating points and the $\tau(\cdot)$ function is invariant with ω .

It is demonstrated in Chapter 4 that representing the aerodynamics in separated form is highly accurate over a very large domain, certainly sufficiently so to support the development of the rotor/wind-field interaction model for variable speed wind turbines.

Chapter 5

Effective Wind-Field Model

Previously in Chapter 3 and Chapter 4, the feasibility of representing the relationship between the statistical characteristics of the wind speeds action on the rotor and the statistical characteristics of the moments and forces induced on the rotor as a linear one, has been explored and validated. Chapter 6 uses this insight to build an effective wind-field model that is suitable for control purposes and that is capable of inducing in the rotor, at least, the correct torque on each blade and the thrust on the tower with the correct correlations over the frequency range up to $6P$.

Since the stochastic and deterministic components of the wind are statistically independent from one another, it is natural to discuss them separately. Accordingly, Chapter 5 is structured as follows: in Section 5.1 the overall structure of the wind-field and aerodynamic model is discussed; in Section 5.2, the stochastic component of the wind is developed; in Section 5.3, the deterministic component (tower shadow, wind shear) is developed. The complete wind-field model is presented in Section 5.4. In Section 5.5 the complete effective wind-field model is validated against Bladed when the WT model used for testing is represented as a stiff structure. In Section 5.6 a Simulink model including the effective wind-field model is compared to Bladed with full structural dynamics and in Section 5.7 a discussion on the outcomes can be found.

5.1. Structure of Wind-Field and Wind Turbine Models

In Chapter 3 and Chapter 4, the Separability property establishes, within its region of validity, a weakly non-linear relationship between the in-plane torque and the wind speed.

On the basis of this relationship, an effective wind-field model is developed with the capacity, in the region of validity of Separability, to induce the correct in-plane moments such as the rotor torque and the in-plane root bending moment (RBM) of a blade. Because of the close relationship between the in-plane and out-of-plane moments and forces, the wind-field model

might also be expected to induce out-of-plane moments but to a lesser degree of accuracy. The validity of this effective wind-field model beyond the in-plane case and beyond the region of validity of Separability, is also explored. The second philosophy introduced in Section 2.2.4.2, which focuses on the outputs of the WT by determining appropriately weighted scalar wind-field components that induce the same spectral properties in the rotor torque or some other scalar force or moment as the wind-field over the rotor disc, is applied to derive the proposed effective wind-field model.

The structure of the proposed wind-field model once sampled, as opposed to prior to sampling, could be thought in a simplistic way to be a number of sinusoids of different frequency and amplitude which when superimposed generate a more complex signal, similarly to a Fourier series, see Figure 5-1. Of course, for the wind-field model, the frequency, amplitude and phase are continuously varying in random manner for all the individual components.

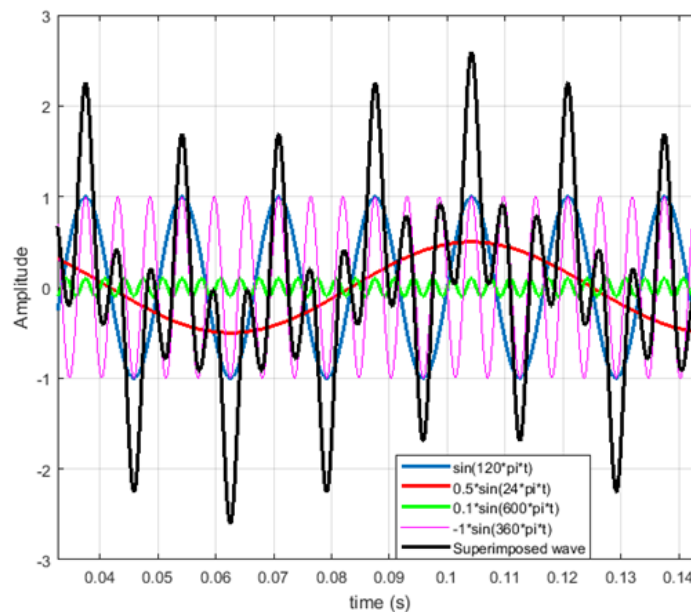


Figure 5-1. Fourier series

In Figure 5-2, a simplified block diagram of the proposed wind-field model is presented; specifically, the structures of *layer P = 0* and *layer P = 1* components of the model are explicitly shown. The *layer P = 2, 3, 4, 5 & 6* components have the same structure as *layer P = 1*. The final wind speed over the wind-field is the addition of all the *layer P* terms and the mean wind speed, V_m . It should be noted that the *P* appearing in the block diagram inside the different elements is simply an integer. The *layer P* component, with $P = n$, is the

wind-field component that gives rise to the nP peak when the effective wind-field is rotationally sampled.

The wind-field model in Figure 5-2, which varies with the azimuthal angle over the rotor disc, has the capability of inducing 0, 1, 2, 3, 4, 5 & 6P stochastic loads using time varying elements named $\text{rrf1f31n}\mathbf{P}$, $\text{rrf2f32n}\mathbf{P}$, $\text{rrf1f31n}\mathbf{Pd}$ and $\text{rrf2f32n}\mathbf{Pd}$ ¹, and deterministic loads through constant elements, wind shear (WS) and tower shadow (TS). The time series for the stochastic elements and the deterministic elements, which are dependent on V_m , are pre-calculated, stored in a file and then read by the simulation when run (see Appendix L for the scripts). It should be noted that the wind-field model in Figure 5-2 generates two different wind signals as the weightings necessary for the correct representation of forces and moments are different. A detailed description of the derivation of the wind-field model is given in Section 5.2 and Section 5.3.

If the effective wind-field model is not valid outside the Separability region, the non-linear nature of the system would manifest itself by distortion of the spectra including leakage, that is, lower frequency components in the wind affecting the higher frequency components. In Section 5.2 and 5.3, leakage affecting the nP peaks is explored. In Section 5.4, the spectra generated by the wind-field model are compared to those generated by Bladed.

In Section 5.2 and 5.3, the presence and impact of leakage is assessed by comparing results from a ‘single’ to a ‘triple’ structure model of interaction between the wind-field and the aerodynamics. What is referred to as ‘single structure’ or model, is the common setup of a wind-field feeding an aerodynamic model as in Figure 5-3. What is referred to as ‘triple structure’ or model, is a less common setup and can be seen in Figure 5-4. There is no difference between the two models as far as the turbulent element of the wind is concerned, only between the nP components; any difference between them would be due to leakage thereby indicating reduced validity of the wind-field model. It is known that, due to the symmetry of the rotor, the rotor loads only exhibit peaks at 0, 3 & 6P, with the disturbances contributing to 1, 2, 4 & 5P peaks cancelling. Nevertheless, due to leakage, frequencies will

¹ Where the bold \mathbf{P} stands to denote that these time varying elements are going to be different for each *layer P* structure

propagate beyond the initial *layer P* that generated them. Consequently, whereas 1, 2, 4, & 5*P* peaks, always disappear due to symmetry²³, the 3 and 6*P* peaks frequencies might be enhanced. As previously stated, by comparing the simple model in Figure 5-3 to the triple structure⁴ in Figure 5-4, it can be determined weather this issue is present.

The results from Section 5.2, Section 5.3 and Section 5.4 give an insight into the validity of the models beyond their natural boundaries and determine which structure, simple or triple, is adequate for inducing the correct load, as far as the *nP* peaks and high frequency components are concerned. The comparison with results from Bladed in Section 5.5 and Section 5.6, provides a further layer of validation to the model, this time by giving an insight to the validity of the model with particular regard to the turbulent components of the wind.

² When there are no imbalances present.

³ Imbalances are not contemplated in this work.

⁴ Each branch of the triple structure is interpreted as representing one of the blades of the rotor. The model as a matter of fact represents 3 rotors and it is the reason why the final signals have to be divided by 3 to obtain the correct magnitude of the moments and forces.

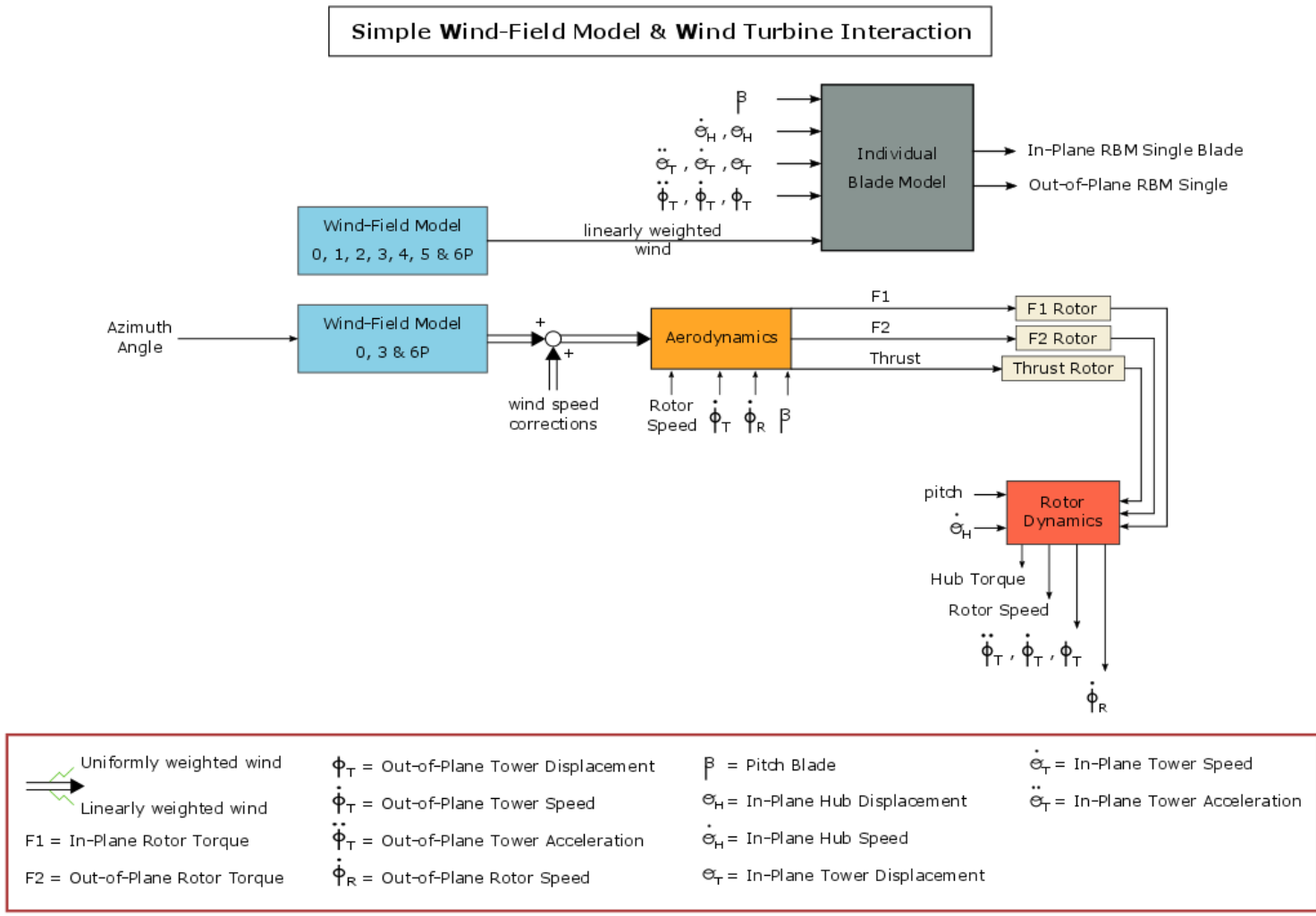


Figure 5-3. Single wind-field and wind turbine interaction

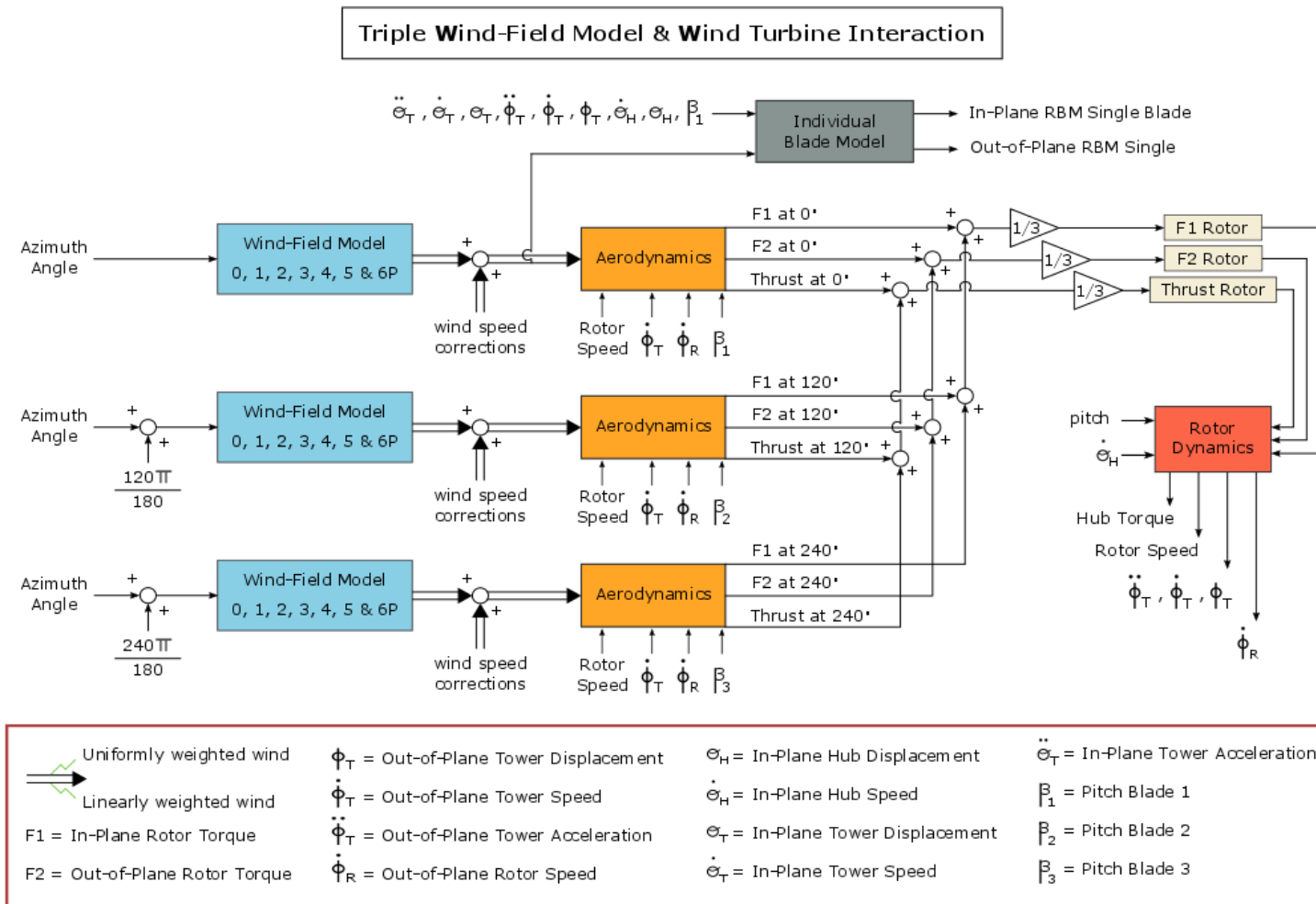


Figure 5-4. Triple wind-field and wind turbine interaction

5.2. Stochastic Component of the Effective Wind-Field Model

In this section, the stochastic components of the effective wind-field model are discussed. Specifically, in Section 5.2 and Section 5.2.1 the theory behind it is explained and in Section 5.2.2, the results relating to the discussion in Section 5.1 about simple and triple structure are discussed.

In Chapter 2, effective wind speed models are introduced and particular attention is given to the model developed in [9] and [13], based on a constant speed WT. The stochastic component of these models is derived by connecting the spectral density function of the torque to the spectral density function of the wind speed. The argument is based on the following assumptions:

- 1) The in-plane force on the blade of a WT is roughly independent of the radius and consequently the aerodynamic torque is approximately linearly dependent on the radial distance from the hub (see Chapter 2, Figure 2-7).
- 2) At low frequencies the timescale of change in the wind-field is comparable or longer than the period of rotation of the rotor.

These assumptions are required so the low frequency components of the torque can then be related to the wind-field over the complete rotor disc.

The relationship between the covariance function for torque, T , and wind speed, V , is⁵,

$$\begin{aligned}
 R_T(t) &= E[(T(t+s) - \bar{T})(T(s) - \bar{T})] \simeq \\
 &\simeq k^2 \int_{A_r} \int_{A_r} E[v(\mathbf{r}_1, t+s)v(\mathbf{r}_2, s)] dA_1 dA_2 = \\
 &= k^2 \int_{A_r} \int_{A_r} R_{v(\mathbf{r}_1)v(\mathbf{r}_2)}(t) dA_1 dA_2
 \end{aligned} \tag{5.1}$$

with, \bar{T} , the mean torque value, A_r , the area of the rotor disc, $R_T(t)$, the torque covariance function, $R_{v(\mathbf{r}_1)v(\mathbf{r}_2)}(t)$, the cross-covariance function between the wind speed at a point \mathbf{r}_1 and the wind speed at a point \mathbf{r}_2 and v , the perturbations about \bar{V} , the mean wind speed of the

⁵ For a detailed discussion of this model refer back to Chapter 2

wind-field impacting on the rotor of the WT for a turbulence intensity that is sufficiently small for Taylor's expansion linearisation to apply. As such the perturbations are defined as,

$$v = V - \bar{V} \quad (5.2)$$

with, V , the wind speed at time t and position \mathbf{r} .

It follows that the power spectral density function of the torque, $S_T(\omega)$, is related to the cross-spectral density function for turbulent wind speed fluctuations at the two points \mathbf{r}_1 and \mathbf{r}_2 , $S_{v(\mathbf{r}_1)v(\mathbf{r}_2)}(\omega)$, by

$$S_T(\omega) = k^2 \int_{A_r} \int_{A_r} S_{v(\mathbf{r}_1)v(\mathbf{r}_2)}(\omega) dA_1 dA_2 = k^2 S_v(\omega) \int_{A_r} \int_{A_r} \chi(\mathbf{r}_1, \mathbf{r}_2, \omega) dA_1 dA_2 \quad (5.3)$$

where $S_v(\omega)$ is the power spectral density function of a point wind speed in space and $\chi(\mathbf{r}_1, \mathbf{r}_2, \omega)$ the coherence function of the wind speed at the two points \mathbf{r}_1 and \mathbf{r}_2 . [9]

A model defined in this way has several limitations. The first limitation is related to the capacity to model higher order frequency components of the wind, caused by assumption 2 which inherently pre-empts the capacity to model frequency components above and including 1P. Assumption 2, thus, restricts the frequency range of the model, because, in reality, the spectral density function induced by the wind-field contains peaks due to rotational sampling of that wind-field at integer multiples of the rotor speed. The effective wind speed model based on assumption 2 cannot reproduce these peaks. This is a significant shortcoming of the model since the peaks at $nP = 0, 3$ and 6 for the rotor and $nP = 0, 1, 2, \dots, 6$ for the blades, are significant and need to be modelled in order to calculate the forces, moments and loads.

The second limitation on the model based on assumptions 1 and 2, comes from using Taylor's expansion linearisation which, by depending on small perturbations of the wind, restricts the magnitude of those perturbations. That is, the need for the Taylor's expansion linearisation to be reasonably accurate restricts the turbulence intensity that can be handled. Moreover, the use of Taylor's expansion linearisation distorts the spectral density functions at higher frequency due to the neglect of leakage. Hence, even without assumption 2, to extend the frequency range of the model to include the nP peaks would require the Taylor's expansion linearisation to be sufficiently accurate, further restricting the turbulence intensity.

To extend the use of effective wind speeds to model out to higher frequencies, requires an approach for which the inherent accuracy is higher than the one that can be assumed for Taylor's series linearisation. Therefore a fitting alternative to the above argument for connecting the spectral density function of the torque to the spectral density function of the wind speed can be based on Separability as follows.

For a rotor, let $(\underline{\beta}, \underline{V})$ be a single operating point for which the contribution to the torque by the blade element at r is

$$\Delta T_r(\underline{\beta}, \underline{V}) = \Delta T_{r_o} \quad (5.4)$$

Integrating over the blades,

$$T(\underline{\beta}, \underline{V}) = \int_{blades} \Delta T_r(\underline{\beta}, \underline{V}) dr = \int_{blades} \Delta T_{r_o} dr = T_o \quad (5.5)$$

The Additivity property Theorem in Section 3.2, implies that

$$T(\beta, V) \approx h_{\underline{V}}(\beta) - g_{\underline{V}}(V) \quad (5.6)$$

to arbitrary accuracy in some neighbourhood of the locus of operating points, (β_o, V_o) , for which

$$T(\beta_o, V_o) = T_o \quad (5.7)$$

Furthermore, the Additivity property Theorem also implies that

$$\Delta T_r(\beta, V_r) \approx h_{r, \underline{V}}(\beta) - g_{r, \underline{V}}(V_r) \quad (5.8)$$

to arbitrary accuracy in some neighbourhood of the locus of operating points, (β_o, V_{r_o}) , for which

$$\Delta T(\beta_o, V_{r_o}) = \Delta T_{r_o} \quad (5.9)$$

Note, that, whilst the pitch angles in (β_o, V_o) and (β_o, V_{r_o}) , are the same, the wind speeds are not necessarily so. Furthermore, the V_{r_o} may change with r .

Provided the neighbourhoods of the loci of operating points, (β_o, V_{r_o}) , are sufficiently small, then it follows that

$$\begin{aligned}
T(\beta(t), V_{sep}(t)) &= \int_{blades} \Delta T_r(\beta(t), V(\mathbf{r}, t)) d\mathbf{r} \approx \\
&\approx \int_{blades} (h_{r,\underline{V}}(\beta(t)) - g_{r,\underline{V}}(V(\mathbf{r}, t))) d\mathbf{r} \approx \\
&\approx \int_{blades} h_{r,\underline{V}}(\beta(t)) - k_{\underline{V}} \int_{blades} k_{r,\underline{V}} V(\mathbf{r}, t) d\mathbf{r} \approx \\
&\approx h_{\underline{V}}(\beta(t)) - g_{\underline{V}} \left(\int_{blades} k_{r,\underline{V}} V(\mathbf{r}, t) d\mathbf{r} \right)
\end{aligned} \tag{5.10}$$

with $k_{\underline{V}}$ the gradient of $g_{\underline{V}}(\cdot)$ and $k_{r,\underline{V}}$ the gradient of $g_{r,\underline{V}}(\cdot)$. To arbitrary accuracy (5.10) is valid for some neighbourhood of the locus of operating points, which includes $(\underline{\beta}, \underline{V})$, where

$$V_{sep}(t) = \int_{blades} k_{r,\underline{V}} V(\mathbf{r}, t) d\mathbf{r} \tag{5.11}$$

However, the neighbourhoods, for which Separability of rotor torque and blade element torque applies, are large, see Chapter 3 and Appendix J, with $g_{r,\underline{V}}(\cdot)$ and $g_{\underline{V}}(\cdot)$ weakly non-linear. Hence, in (5.10), with $V(\mathbf{r}, t)$ the wind speed at (\mathbf{r}, t) due to a turbulent wind-field, $V_{sep}(t)$ is an effective wind speed; that is, $V_{sep}(t)$ can be interpreted as the wind speed uniform over the rotor which induces the same torque as the turbulent wind-field at a time t . Clearly $V_{sep}(t)$ is a weighted linear average of the wind speeds experienced by the blades. Through \mathbf{r} , (5.11) is implicitly dependent on the azimuth angle of the rotor, θ , as explicitly indicated by,

$$V_{sep}(\theta, t) = \int_{blades} k_{r,\underline{V}} V(\mathbf{r}(\theta, r), t) d\mathbf{r} = \int_{blades} W(r) (V(\mathbf{r}(\theta, r), t)) dr \tag{5.12}$$

where $W(r)$ is a weighting function depending solely on the geometry of the blades, and so it is only dependent on r and not θ . Because of the size of the neighbourhoods of validity for Separability and the near linearity of $g(V)$, the spectral density function for torque can be expected to apply for a far larger frequency range including over the spectral peaks than would be expected from the earlier argument, since the effective wind speed, $V_{sep}(\theta, t)$, defined by (5.12) remains dependent on azimuth angle. Moreover, Separability and so the effective wind speed extend to the 3 dimensional case, see Chapter 4, with the inclusion of the rotor speed, ω . To enable direct comparison with the wind speed model in [9] and [13], it is necessary to remove from (5.12) the component in the wind-field giving rise to the higher frequency components by integrating over the azimuth angle,

$$V_e(t) = n \int_0^R W(r) \int_0^{2\pi} V(\mathbf{r}(\theta, r), t) d\theta dr \quad (5.13)$$

because the contribution of each of the n blades is the same as each blade is rotated over one revolution. The weighting function, $W(r)$, is chosen to be linear in r . This derivation of the effective wind speed is much preferred.

How good a wind speed model Separability can justify, is very much dependent on the accuracy of the Separability property itself. The greater the accuracy of Separability the higher the frequencies that the wind-field model can potentially represent correctly. In this chapter, that potential is explored. The accuracy of the Separability results from Chapters 3 and 4 is such as to indicate that a reasonable representation of the interaction of the rotor and the wind-field up to higher frequencies should be expected. Likewise if the results from the wind speed model are good inside the region of applicability of Separability, they would further validate the Separability property.

5.2.1. Stochastic Model

Previously, when discussing effective wind speed models, whether in Chapter 2 or earlier in this chapter, the philosophy has been to determine a scalar effective wind speed that is uniform over the rotor but that induces the same torque as the turbulent wind-field. However, the insight provided by Separability into the very direct relationship of wind speed to torque, see (5.10), (5.11) and (5.12) enables the adoption of a different philosophy wherein the scalar effective wind speed model is replaced by an effective wind-field model; that is, over the rotor, the wind speed varies only with azimuth angle. At time, t , the torque for a blade at azimuth angle, θ , would then be determined using the wind speed at θ . This wind-field model represents the actual flow-field that comes to the turbine such that, when the resulting torques on the blades are calculated, being dependent on the azimuth angle, the loads have the correct correlation between the different blades and the complete rotor.

From (5.12), the perturbations in the effective wind-field at azimuth angle, θ , and time, t , are

$$V(\theta, t) = \int_0^R W(r)v(\mathbf{r}(r, \theta), t)dr \quad ; \quad v(\mathbf{r}(r, \theta), t) = V(\mathbf{r}(r, \theta), t) - \bar{V} \quad (5.14)$$

where \bar{V} is the mean wind speed over the wind-field. To be precise, wind-field here refers to the wind speeds for each point in the rotor disc for each time in some interval. \bar{V} is the mean

over the ensemble of all possible realisations of this wind-field. The average for any single realisation may of course differ from \bar{V} . At any time, t , $V(\theta, t)$ may be considered periodic in θ with Fourier series

$$\begin{aligned} V(\theta, t) &= \sum_{n=-\infty}^{+\infty} A_n(t)e^{jn\theta} = A_0 + \sum_{n=1}^{+\infty} (A_n(t)e^{jn\theta} + A_{-n}(t)e^{-jn\theta}) = \\ &= A_0 + \sum_{n=1}^{+\infty} \{A_n(t)[\cos(n\theta) + jsin(n\theta)] + A_{-n}(t)[\cos(-n\theta) + jsin(-n\theta)]\} \end{aligned} \quad (5.15)$$

$$A_n(t) = \frac{1}{2\pi} \int_{-\pi}^{\pi} V(\theta, t)e^{-jn\theta} d\theta \quad (5.16)$$

Assume the wind-field is homogeneous so that at any point, \mathbf{r} , and time, t , the mean wind speed is the same and thus equal to \bar{V} ; that is, $E[V(\mathbf{r}(r, \theta), t)] = \bar{V}$. Consequently

$$\begin{aligned} E[V(\theta, t)] &= E \left[\int_0^R W(r)v(\mathbf{r}(r, \theta), t) dr \right] = \int_0^R W(r)E[V(\mathbf{r}(r, \theta), t) - \bar{V}] dr = \\ &= \int_0^R W(r)\{E[V(\mathbf{r}(r, \theta), t)] - \bar{V}\} dr = 0 \end{aligned} \quad (5.17)$$

Hence $\bar{A}_n(t)$, the mean of $A_n(t)$ at time, t , is

$$\bar{A}_n(t) = E[A_n(t)] = E \left[\frac{1}{2\pi} \int_{-\pi}^{\pi} V(\theta, t)e^{-jn\theta} d\theta \right] = \frac{1}{2\pi} \int_{-\pi}^{\pi} E[V(\theta, t)]e^{-jn\theta} d\theta = 0 \quad (5.18)$$

The cross-covariance between $A_n(t)$ and $A_m(t)$ is

$$\begin{aligned}
R_{nm}(t) &= E[A_n^*(\tau)A_m(\tau+t)] = E\left[\frac{1}{2\pi}\int_{-\pi}^{\pi}V(\theta_1,\tau)e^{jn\theta_1}d\theta_1\frac{1}{2\pi}\int_{-\pi}^{\pi}V(\theta_2,\tau+t)e^{-jm\theta_2}d\theta_2\right] = \\
&= \frac{1}{4\pi^2}\int_{-\pi}^{\pi}d\theta_1\int_{-\pi}^{\pi}d\theta_2e^{j(n\theta_1-m\theta_2)}E[V(\theta_1,\tau)V(\theta_2,\tau+t)] = \\
&= \frac{1}{4\pi^2}\int_{-\pi}^{\pi}d\theta_1\int_{-\pi}^{\pi}d\theta_2e^{j(n\theta_1-m\theta_2)}E\left[\int_0^R W(r_1)v(\mathbf{r}(r_1,\theta_1),\tau)dr_1\int_0^R W(r_2)v(\mathbf{r}(r_2,\theta_2),\tau+t)dr_2\right] \\
&= \frac{1}{4\pi^2}\int_{-\pi}^{\pi}d\theta_1\int_{-\pi}^{\pi}d\theta_2\int_0^R dr_1\int_0^R dr_2 W(r_1)W(r_2)e^{j(n\theta_1-m\theta_2)}E[v(\mathbf{r}(r_1,\theta_1),\tau)v(\mathbf{r}(r_2,\theta_2),\tau+t)]
\end{aligned} \tag{5.19}$$

It follows that the cross-spectral density function, which is the Fourier transform of the cross-covariance of the associated functions (in this case the Fourier coefficients, $A_n(t)$ and $A_m(t)$), is

$$S_{nm}(\omega) = \frac{1}{4\pi^2}\int_{-\pi}^{\pi}d\theta_1\int_{-\pi}^{\pi}d\theta_2\int_0^R dr_1\int_0^R dr_2 W_1(r_1)W_2(r_2)e^{j(n\theta_1-m\theta_2)}S_{v_1v_2}(\omega) \tag{5.20}$$

The cross-spectral density function for wind speeds at \mathbf{r}_1 and \mathbf{r}_2 , $S_{v_1v_2}(\omega)$, depends only on the distance between the two points, l , as the wind-field is homogeneous. Hence, $e^{j(n\theta_1-m\theta_2)}S_{v_1v_2}(\omega)$ is periodic in θ_1 and θ_2 . The following change of variables can be introduced in $S_{nm}(\omega)$,

$$\psi_1 = \frac{\theta_1 - \theta_2}{2} \quad ; \quad \psi_2 = \frac{\theta_1 + \theta_2}{2} \tag{5.21}$$

$$\theta_1 = 2\psi_1 + \theta_2 = 2\psi_1 + 2\psi_2 - \theta_1 \Rightarrow 2\theta_1 = 2(\psi_1 + \psi_2) \tag{5.22}$$

$$\theta_2 = 2\psi_2 - \theta_1 \Rightarrow \theta_2 = 2\psi_2 - \psi_1 - \psi_2 = -\psi_1 + \psi_2 \tag{5.23}$$

$$\frac{\partial(x,y)}{\partial(u,v)} = \frac{\partial(\theta_1,\theta_2)}{\partial(\psi_1,\psi_2)} = \begin{vmatrix} 1 & 1 \\ -1 & 1 \end{vmatrix} = 1 - (-1) = 2 \tag{5.24}$$

$$d\theta_1 d\theta_2 = 2d\psi_1 d\psi_2 \tag{5.25}$$

with the limits of the integrals changing from $[-\pi, \pi]$ for θ_1 to $[0, \pi]$ for ψ_1 and $[-\pi, \pi]$ for θ_2 being maintained as $[-\pi, \pi]$ for ψ_2 . This has the following explanation

(θ_1, θ_2)	(ψ_1, ψ_2)
$(0,0)$	$(0,0)$
$(\pi, 0)$	$(\frac{\pi}{2}, \frac{\pi}{2})$
$(0, \pi)$	$(-\frac{\pi}{2}, \frac{\pi}{2})$
(π, π)	$(0, \pi)$
$(-\pi, \pi)$	$(-\pi, 0)$
$(\pi, -\pi)$	$(\pi, 0)$
$(-\pi, 0)$	$(-\frac{\pi}{2}, -\frac{\pi}{2})$
$(0, -\pi)$	$(\frac{\pi}{2}, -\frac{\pi}{2})$
$(-\pi, -\pi)$	$(0, -\pi)$

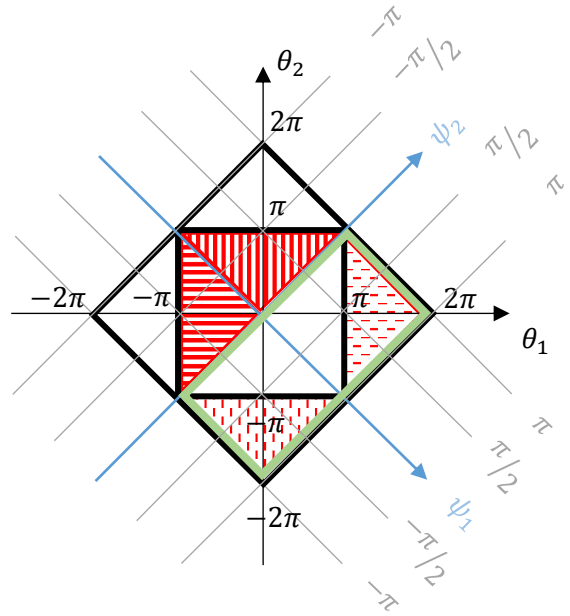


Table 5-1. Change of variable values

Figure 5-5. Integration support

When changing variables it is important to update the area of interpolation. The original area of integration for (θ_1, θ_2) is represented by the black square with limits $[-\pi, \pi]$ for θ_1 and $[-\pi, \pi]$ for θ_2 on Figure 5-5. The lines for constant ψ_1 and ψ_2 (grey lines on Figure 5-5) are determined from (5.21), that is,

$$\psi_1 = \frac{\theta_1 - \theta_2}{2} \Rightarrow \theta_1 = 2\psi_1 + \theta_2 \quad (5.26)$$

$$\psi_2 = \frac{\theta_1 + \theta_2}{2} \Rightarrow \theta_2 = -2\psi_1 + \theta_1 \quad (5.27)$$

From Figure 5-5 it is clear that, when integrating with respect to ψ_1 and ψ_2 , the limits of integration are not fixed. But because the original integrals are periodic on θ_1 and θ_2 , it is possible to displace by 2π the area (or parts of the area) that define the initial area of integration (black square) in both axial directions. This allows for rearrangement of the original area of integration to a more convenient shape with respect to the (ψ_1, ψ_2) axis; that is, one that is rectangular. This process is illustrated in Figure 2 by the red triangles with solid lines indicating the sense of displacement and red triangles with dashed lines representing the final destination.

The new integration area is highlighted by the green rectangle in Figure 5-5 and has limits equal to $[0, \pi]$ for ψ_1 and $[-\pi, \pi]$ for ψ_2 .

Therefore, after the change of variable, $S_{nm}(\omega)$ takes the form

$$S_{nm}(\omega) = \frac{2}{4\pi^2} \int_0^R dr_1 W_1(r_1) \int_0^R dr_2 W_2(r_2) \int_0^\pi d\psi_1 \int_{-\pi}^\pi d\psi_2 e^{j(n+m)\psi_1} e^{j(n-m)\psi_2} S_{v_1 v_2}(\omega) \quad (5.28)$$

With $S_{v_1 v_2}(\omega)$ dependent only on ψ_1 .

- If $n \neq m$,

$$\int_{-\pi}^\pi e^{j(n-m)\psi_2} d\psi_2 = \int_{-\pi}^\pi d\psi_2 [\cos((n-m)\psi_2) + j\sin((n-m)\psi_2)] = 0 \quad (5.29)$$

because the integration is over a complete period of the cosine and sine terms, i.e. $S_{nm}(\omega) = 0$

- If $n = m$, $e^{j(n-m)\psi_2} = 1$ and $\int_{-\pi}^\pi d\psi_2 = 2\pi$,

$$S_{nm}(\omega) = 2\pi \frac{2}{4\pi^2} \int_0^R dr_1 W_1(r_1) \int_0^R dr_2 W_2(r_2) \int_0^\pi d\psi_1 e^{j(n+m)\psi_1} S_{v_1 v_2}(\omega) = \quad (5.30)$$

$$= \frac{1}{\pi} \int_0^R dr_1 W_1(r_1) \int_0^R dr_2 W_2(r_2) \int_0^\pi d\psi_1 [\cos(2n\psi_1) + j\sin(2n\psi_1)] S_{v_1 v_2}(\omega)$$

By introducing the change of variable

$$\theta = 2\psi_1 = \theta_1 - \theta_2 \quad (5.31)$$

$$d\theta = 2d\psi_1 \rightarrow \frac{1}{2}d\theta = d\psi_1 \quad (5.32)$$

The cross-spectral density function becomes

$$S_{nm}(\omega) = \frac{1}{2\pi} \int_0^R dr_1 W_1(r_1) \int_0^R dr_2 W_2(r_2) \left[\int_0^{2\pi} d\theta \cos(n\theta) S_{v_1 v_2}(\omega) + \right. \quad (5.33)$$

$$\left. + j \int_0^{2\pi} d\theta \sin(n\theta) S_{v_1 v_2}(\omega) \right]$$

with θ the angle between the radii to \mathbf{r}_1 and \mathbf{r}_2 ⁶. Since $\sin(n\theta)$ is odd and $S_{v_1 v_2}(\omega)$ even, the integral related to j is zero and the cross-spectral density function for the Fourier coefficients is reduced to

$$S_{nm}(\omega) = \frac{1}{2\pi} \int_0^R dr_1 W_1(r_1) \int_0^R dr_2 W_2(r_2) \left[\int_0^{2\pi} d\theta \cos(n\theta) S_{v_1 v_2}(\omega) \right] \quad (5.34)$$

Note that the cross-spectral density function for the wind speeds at \mathbf{r}_1 and \mathbf{r}_2 , $S_{v_1 v_2}(\omega)$ depends only on $|\theta|$, and is defined as

$$S_{v_1 v_2}(\omega) = S_v(\omega) \frac{S_{v_1 v_2}(\omega)}{\sqrt{S_{v_1 v_1}(\omega) S_{v_2 v_2}(\omega)}} = S_v(\omega) \chi(\mathbf{r}_1, \mathbf{r}_2, \omega) \quad (5.35)$$

with $S_v(\omega)$ the spectrum of a wind speed, $\chi(\mathbf{r}_1, \mathbf{r}_2, \omega)$ the coherence function between the vectors \mathbf{r}_1 and \mathbf{r}_2 and $S_{v_1 v_1}$ and $S_{v_2 v_2}(\omega)$ the auto-spectrum for v_1 and v_2 respectively. Assuming Davenport's coherence function

$$S_{v_1 v_2}(\omega) \approx S_v(\omega) e^{-\gamma l \omega / \bar{v}} = S_v(\omega) e^{-x l} \quad (5.36)$$

with

$$x = \frac{R\gamma\omega}{\bar{v}} = \sigma\omega \quad (5.37)$$

$$l = \sqrt{r_1^2 + r_2^2 - 2r_1 r_2 \cos(\theta)} \quad (5.38)$$

Where γ is the turbulent wind speed decay factor, \bar{v} the mean wind speed, l the separation between \mathbf{r}_1 and \mathbf{r}_2 and θ the angle between \mathbf{r}_1 and \mathbf{r}_2 . Thus,

⁶ It is important to note that θ is **not** the azimuth angle anymore

$$S_{nm}(\omega) = \frac{1}{2\pi} \int_0^R dr_1 W_1(r_1) \int_0^R dr_2 W_2(r_2) \int_0^{2\pi} d\theta \cos(n\theta) e^{-xl} S_v(\omega) \quad (5.39)$$

The integral enclosed by the red rectangle can be solved numerically for the different weighting functions of interest, linear, uniform or mixed. After normalisation, the vectors \mathbf{r}_1 and \mathbf{r}_2 can occupy any position of the unit circle as shown on Figure 5-6,

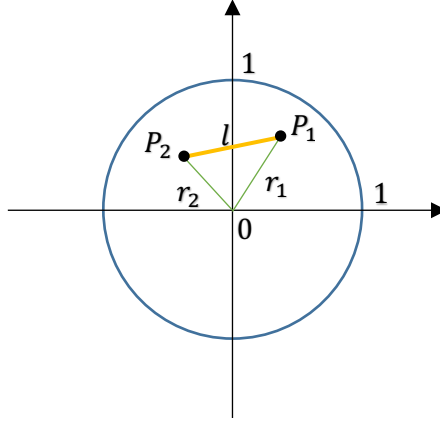


Figure 5-6. Normalised integral space

Since the wind is a real variable,

$$V(\theta, t) = \sum_{n=-\infty}^{+\infty} A_n(t) e^{jn\theta} = A_0 + \sum_{n=1}^{+\infty} (A_n e^{jn\theta} + A_{-n} e^{-jn\theta}) \quad (5.40)$$

and $(A_n e^{jn\theta} + A_{-n} e^{-jn\theta})$ has to be real, making it necessary for $A_{-n}(t) = A_n^*(t)$. Furthermore considering the preceding discussion of $S_{nm}(\omega)$ in the $n = m$ and $n \neq m$ cases, it also follows that $S_{(-n)(-n)}(\omega) = S_{nn}(\omega)$ and $S_{(-n)n}(\omega) = S_{n(-n)}(\omega) = 0$.

Thus an appropriate choice for $A_n(t)$ and $A_{-n}(t)$ is

$$A_n(t) = R_n(t) + jI_n(t) \quad ; \quad A_{-n}(t) = A_n^*(t) = R_n(t) - jI_n(t) \quad (5.41)$$

where $R_n(t)$ and $I_n(t)$ are real, such that

$$S_{R_n R_n}(\omega) = S_{I_n I_n}(\omega) = \frac{1}{2} S_{nn}(\omega) \quad (5.42)$$

$$S_{R_n I_n}(\omega) = S_{I_n R_n}(\omega) = 0 \quad (5.43)$$

All the required spectral properties are met, specifically,

$$S_{(R_n+jI_n)(R_n+jI_n)}(\omega) = S_{R_nR_n}(\omega) + jS_{R_nI_n}(\omega) - jS_{I_nR_n}(\omega) + S_{I_nI_n}(\omega) = S_{nn}(\omega) \quad (5.44)$$

$$\begin{aligned} S_{(R_n-jI_n)(R_n-jI_n)}(\omega) &= S_{R_nR_n}(\omega) - jS_{R_nI_n}(\omega) + jS_{I_nR_n}(\omega) + S_{I_nI_n}(\omega) = S_{nn}(\omega) \\ &= S_{(-n)(-n)}(\omega) \end{aligned} \quad (5.45)$$

$$\begin{aligned} S_{(R_n+jI_n)(R_n-jI_n)}(\omega) &= S_{R_nR_n}(\omega) - jS_{R_nI_n}(\omega) - jS_{I_nR_n}(\omega) - S_{I_nI_n}(\omega) = \\ &= S_{n(-n)}(\omega) = 0 \end{aligned} \quad (5.46)$$

$$\begin{aligned} S_{(R_n-jI_n)(R_n+jI_n)}(\omega) &= S_{R_nR_n}(\omega) + jS_{R_nI_n}(\omega) + jS_{I_nR_n}(\omega) - S_{I_nI_n}(\omega) = \\ &= S_{(-n)n}(\omega) = 0 \end{aligned} \quad (5.47)$$

Thus the contribution of the n^{th} and $(-n)^{th}$ terms in the Fourier series for $V(\theta, t)$ is

$$\begin{aligned} (A_n e^{jn\theta} + A_n^*(t) e^{-jn\theta}) &= \\ &= A_n(t)[\cos(n\theta) + j\sin(n\theta)] + A_n^*(t)[\cos(n\theta) - j\sin(n\theta)] = \\ &= [R_n(t) + jI_n(t)][\cos(n\theta) + j\sin(n\theta)] + \\ &+ [R_n(t) - jI_n(t)][\cos(n\theta) - j\sin(n\theta)] = \\ &= R_n(t)\cos(n\theta) + R_n(t)j\sin(n\theta) + I_n(t)j\cos(n\theta) - \\ &- I_n(t)j\sin(n\theta) + R_n(t)\cos(n\theta) - R_n(t)j\sin(n\theta) - \\ &- I_n(t)j\cos(n\theta) - I_n(t)\sin(n\theta) = \\ &= 2R_n(t)\cos(n\theta) - 2I_n(t)\sin(n\theta) \end{aligned} \quad (5.48)$$

which is real. Hence

$$V(\theta, t) = \sum_{n=-\infty}^{+\infty} A_n(t) e^{jn\theta} = A_0 + \sum_{n=1}^{+\infty} 2(R_n(t)\cos(n\theta) - I_n(t)\sin(n\theta)) \quad (5.49)$$

Let

$$a_n(t) = 2R_n(t) \quad ; \quad b_n(t) = -2I_n(t) \quad ; \quad a_0(t) = A_0 = \frac{1}{2\pi} \int_{-\pi}^{\pi} V(\theta, t) dt \quad (5.50)$$

then

$$S_{a_n a_n}(\omega) = S_{b_n b_n}(\omega) = 2S_{nn}(\omega) \quad (5.51)$$

$$S_{a_n b_n}(\omega) = S_{b_n a_n}(\omega) = 0 \quad (5.52)$$

Thus for the frequency range of interest, equivalent to $0 \leq n \leq 6$, when all the n^{th} and $(-n)^{th}$ terms are combined, the wind speed including the mean \bar{V} is,

$$\begin{aligned} V(\theta, t) = & \bar{V} + a_0(t) + [a_1(t) \cos(\theta) + b_1(t) \sin(\theta)] + \\ & + [a_2(t) \cos(2\theta) + b_2(t) \sin(2\theta)] + \\ & + [a_3(t) \cos(3\theta) + b_3(t) \sin(3\theta)] + \\ & + [a_4(t) \cos(4\theta) + b_4(t) \sin(4\theta)] + \\ & + [a_5(t) \cos(5\theta) + b_5(t) \sin(5\theta)] + \\ & + [a_6(t) \cos(6\theta) + b_6(t) \sin(6\theta)] \end{aligned} \quad (5.53)$$

For the special case when blades rotate at a constant speed, it is possible to extract, from the wind-field, the effective wind speed for the blades. For a generic component in (5.53), $a_n \cos(n\theta) + b_n \sin(n\theta)$ with $\theta = \omega_o t + \delta$, where the ω_o is a constant rotor speed and δ an angular offset, the cross-covariance between two points rotating at ω_o is

$$\begin{aligned} E[(a_n(t) \cos(n\omega_o t + n\delta_1) + b_n(t) \sin(n\omega_o t + n\delta_1)) \\ (a_n(t + \tau) \cos(n\omega_o(t + \tau) + n\delta_2) + b_n(t + \tau) \sin(n\omega_o(t + \tau) + n\delta_2))] = \\ = E[a_n(t) \cos(n\omega_o t + n\delta_1) a_n(t + \tau) \cos(n\omega_o(t + \tau) + n\delta_2)] + \\ + E[b_n(t) \sin(n\omega_o t + n\delta_1) b_n(t + \tau) \sin(n\omega_o(t + \tau) + n\delta_2)] = \\ = \cos(n\omega_o t + n\delta_1) \cos(n\omega_o(t + \tau) + n\delta_2) R_{a_n a_n}(\tau) + \\ + \sin(n\omega_o t + n\delta_1) \sin(n\omega_o(t + \tau) + n\delta_2) R_{b_n b_n}(\tau) = \\ = \cos(n\omega_o \tau + n(\delta_2 - \delta_1)) R_{a_n a_n}(\tau) \end{aligned} \quad (5.54)$$

Since (5.54) is stationary the cross-spectral density function (Fourier transform of the cross-covariance), can be obtained such

$$\frac{1}{2\pi} \mathcal{F}[\cos(n\omega_o\tau + n(\delta_2 - \delta_1))] * 2S_{nn}(\omega) = \quad (5.55)$$

$$\begin{aligned} &= \frac{1}{\pi} \cos(n\delta_2 - n\delta_1) \mathcal{F}[\cos(n\omega_o\tau)] * S_{nn}(\omega) - \\ &- \frac{1}{\pi} \sin(n\delta_2 - n\delta_1) \mathcal{F}[\sin(n\omega_o\tau)] * S_{nn}(\omega) = \\ &= \cos(n\delta_2 - n\delta_1)[S_{nn}(\omega + n\omega_o) + S_{nn}(\omega - n\omega_o)] + \\ &+ j\sin(n\delta_2 - n\delta_1)[-S_{nn}(\omega + n\omega_o) + S_{nn}(\omega - n\omega_o)] = \\ &= e^{-jn(\delta_2 - \delta_1)} S_{nn}(\omega + n\omega_o) + e^{jn(\delta_2 - \delta_1)} S_{nn}(\omega - n\omega_o) = \\ &= e^{j(-n)(\delta_2 - \delta_1)} S_{(-n)(-n)}(\omega + n\omega_o) + e^{jn(\delta_2 - \delta_1)} S_{nn}(\omega - n\omega_o) \end{aligned}$$

Hence, the summation over the terms, with $n = 0, \dots, 6$, with $\Delta\delta = \delta_2 - \delta_1$, becomes

$$S_{V_1V_2}(\omega, \Delta\delta) = \sum_{n=0}^6 S_{nn}(\omega - n\omega_o) e^{jn(\Delta\delta)} \quad (5.56)$$

which, with $n = -\infty, \dots, \infty$, is the same as the spectra proposed in [28] namely,

$$S_{V_1V_2}(\omega, \Delta\delta) = \sum_{n=-\infty}^{\infty} S_{nn}(\omega - n\omega_o) e^{jn(\Delta\delta)} = \sum_{n=-\infty}^{\infty} \tilde{S}_{nn}^e(\omega - n\omega_r) e^{in\Delta\psi} = S^e(\omega, \Delta\psi) \quad (5.57)$$

Whereas [28] then proceeded with the spectral factorisation of the blade effective wind speeds, here the spectra for the wind-field components themselves are spectrally factorised. Having obtained this wind-field spectral factorisation, it can be applied to blades at any position whether stationary or varying rotor speed.

5.2.1.1. Spectral Factorisation

The $S_{nn}(\omega)$ from (5.39) is determined for two different weighting functions. This is because the effective wind speeds that induce forces on the WT are better described by a uniform weighting, denoted in here with the suffix xx , whereas for torques and bending moments a linear weighting is more appropriate, denoted in here by suffix yy . The forces and moments clearly cross-correlate, with the cross terms being denoted by suffix xy . Hence, it is appropriate to consider a 2×2 matrix which requires spectral factorisation.

When accounting for the appropriate weighting functions, $S_{nn}(\omega)$ takes the following forms

- Both weighting functions are uniform

$$\begin{aligned}
S_{xx}(\omega) &= \left[\frac{1}{2\pi} \int_0^R dr_1 W_1(r_1) \int_0^R dr_2 W_2(r_2) \int_0^{2\pi} d\theta \cos(n\theta) e^{-xl} \right] S_v(\omega) = & (5.58) \\
&= \left[\frac{2}{2\pi} \int_0^R dr_1 \frac{1}{R} \int_0^R dr_2 \frac{1}{R} \int_0^\pi d\theta \cos(n\theta) e^{-xl} \right] S_v(\omega) = \\
&= \left[\frac{1}{\pi R^2} \int_0^R dr_1 \int_0^R dr_2 \int_0^\pi d\theta \cos(n\theta) e^{-xl} \right] S_v(\omega) = \\
&= \left[\frac{R^2}{\pi R^2} \int_0^1 d\bar{r}_1 \int_0^1 d\bar{r}_2 \int_0^\pi d\theta \cos(n\theta) e^{-x\bar{l}} \right] S_v(\omega)
\end{aligned}$$

- Both weighting function are linear

$$\begin{aligned}
S_{yy}(\omega) &= \left[\frac{1}{2\pi} \int_0^R dr_1 W_1(r_1) \int_0^R dr_2 W_2(r_2) \int_0^{2\pi} d\theta \cos(n\theta) e^{-xl} \right] S_v(\omega) = & (5.59) \\
&= \left[\frac{2}{2\pi} \int_0^R dr_1 \frac{2r_1}{R^2} \int_0^R dr_2 \frac{2r_2}{R^2} \int_0^\pi d\theta \cos(n\theta) e^{-xl} \right] S_v(\omega) = \\
&= \left[\frac{4}{\pi R^4} \int_0^R r_1 dr_1 \int_0^R r_2 dr_2 \int_0^\pi d\theta \cos(n\theta) e^{-xl} \right] S_v(\omega) = \\
&= \left[\frac{4R^2 R^2}{\pi R^4} \int_0^1 \bar{r}_1 d\bar{r}_1 \int_0^1 \bar{r}_2 d\bar{r}_2 \int_0^\pi d\theta \cos(n\theta) e^{-x\bar{l}} \right] S_v(\omega)
\end{aligned}$$

- One weighting function is uniform and one is linear

$$\begin{aligned}
S_{xy}(\omega) &= \left[\frac{1}{2\pi} \int_0^R dr_1 W_1(r_1) \int_0^R dr_2 W_2(r_2) \int_0^{2\pi} d\theta \cos(n\theta) e^{-xl} \right] S_v(\omega) = & (5.60) \\
&= \left[\frac{2}{2\pi} \int_0^R dr_1 \frac{2r_1}{R^2} \int_0^R dr_2 \frac{1}{R} \int_0^\pi d\theta \cos(n\theta) e^{-xl} \right] S_v(\omega) = \\
&= \left[\frac{2}{\pi R^3} \int_0^R r_1 dr_1 \int_0^R dr_2 \int_0^\pi d\theta \cos(n\theta) e^{-xl} \right] S_v(\omega) = \\
&= \left[\frac{2R^2 R}{\pi R^3} \int_0^1 \bar{r}_1 d\bar{r}_1 \int_0^1 d\bar{r}_2 \int_0^\pi d\theta \cos(n\theta) e^{-x\bar{l}} \right] S_v(\omega)
\end{aligned}$$

The standard method of generating correlated wind speeds for simulating a wind-field model follows the Veers algorithm [37] which is based on the Shinozuka cross-spectral density function algorithm [38]. This method is frequently found in literature and exploited by commercial codes such as TurbSim by NREL [39][40].

It essentially follows the principle that for a given spectral density function matrix, $S(\omega)$, a matrix $H(\omega)$, can be determined by spectrally factorising $S(\omega)$, such that

$$[S(\omega)] = H(\omega) H^T(\omega) \quad (5.61)^7$$

Consistently with $S(\omega)$ being real, $H(\omega)$ has been chosen to be real and therefore $H(\omega) = H^*(\omega)$. Here, the elements of the matrix H of size 2×2 are:

$$\begin{aligned} H_{11} &= S_{11}^{1/2} \\ H_{12} &= 0 \\ H_{21} &= \frac{S_{21}}{H_{11}} \\ H_{22} &= (S_{22} - H_{21}^2)^{1/2} \end{aligned} \quad (5.62)$$

Using the H matrix as a frequency response function matrix, with an input consisting of a vector of 2 independent frequency representations of white noise, $\Omega_1(\omega)$ and $\Omega_2(\omega)$, it yields 2 correlated turbulent wind speeds $V_1(\omega)$ and $V_2(\omega)$.

Therefore when discretising time, t , in the frequency domain, indexed by $i = 1, \dots, N$, the turbulent wind speeds $V_1(\omega)$, $V_2(\omega)$ and the frequency response elements $H_{11}(\omega)$, $H_{21}(\omega)$ and $H_{22}(\omega)$ all become vectors, with the values of the elements corresponding to the discretisation,

$$V_1(\omega_i) = H_{11}(\omega_i) \Omega_1(\omega_i) + H_{12}(\omega_i) \Omega_2(\omega_i) \quad (5.63)$$

$$V_2(\omega_i) = H_{21}(\omega_i) \Omega_1(\omega_i) + H_{22}(\omega_i) \Omega_2(\omega_i)$$

⁷ the T in (5.61) stands for Hermitian, not transpose. complex conjugated and transposed

$$\Omega_k(\omega_i) = \begin{bmatrix} e^{-j\theta_{i=1}} \\ e^{-j\theta_2} \\ \vdots \\ e^{-j\theta_N} \end{bmatrix}$$

where, $k = 1, 2$. For each k , θ_i , is a uniformly distributed random variable with domain $[0, 2\pi]$. By taking the inverse fast Fourier transform (iFFT) of $V_1(\omega)$ and $V_2(\omega)$, the turbulent wind speeds time series are computed. [40][41]

Whilst the above standard form of spectral factorisation suffices for generating wind speed time series with the correct characteristics, the $H(\omega_i)$ are by necessity non-causal in nature since they have been chosen to be real. Hence, the $H(\omega_i)$ defined in this way are not suitable for incorporation into dynamic models used when designing controllers or observers. Consequently transfer function based models of the wind speeds/wind-field are required since these can be chosen causal⁸ and stable⁹. This approach [9][13], is described below.

Following (5.39), the auto-spectrum and cross-spectrum can be reformulated as

$$S_{xx}(\omega) = \phi_{xx}^R(x)S_v(\omega) \quad (5.64)$$

$$S_{yy}(\omega) = \phi_{yy}^R(x)S_v(\omega) \quad (5.65)$$

$$S_{xy}(\omega) = \phi_{xy}^R(x)S_v(\omega) \quad (5.66)$$

where the ϕ^R are the terms in the square brackets in (5.58), (5.59) and (5.60). By definition the spectrums $S_{xx}(\omega)$, $S_{xy}(\omega)$ and $S_{yy}(\omega)$ are real.

The uniform and linear wind can be represented by the spectral matrix

$$\begin{bmatrix} S_{xx}(\omega) & S_{xy}(\omega) \\ S_{xy}(\omega) & S_{yy}(\omega) \end{bmatrix} = \begin{bmatrix} \phi_{xx}^R(x)S_v(\omega) & \phi_{xy}^R(x)S_v(\omega) \\ \phi_{xy}^R(x)S_v(\omega) & \phi_{yy}^R(x)S_v(\omega) \end{bmatrix} \quad (5.67)$$

with the most general spectral factorisation of (5.67) having the form

$$V_{uniform}(s) = f_1(s)\omega_1 + (f_3(s)f_4(s))\omega_3 = f_1(s)\omega_1 + f_{31}(s)\omega_3 \quad (5.68)$$

⁸ A system is causal if its outputs only depends on the past and present inputs

⁹ A system is stable if its output is absolutely integrable

$$V_{linear}(s) = f_2(s)\omega_2 + \frac{f_3(s)}{f_4(-s)}\omega_3 = f_2(s)\omega_2 + f_{32}(s)\omega_3 \quad (5.69)$$

where ω_1 , ω_2 and ω_3 are independent frequency domain representations of point wind speeds all with spectra $S_v(\omega)$. The spectral factorisation is done such that the filters f_1 , f_2 and f_3 are stable and causal¹⁰ and such that $f_4(s)$ and $f_4^{-1}(s)$ are stable and proper. Note the negative sign on the denominator of (5.69), this is a correction applied to (2.65). It follows that,

$$|f_1(j\omega)|^2 = \phi_{xx}^R(x) - \phi_{xy}^R(x) \psi(x) \quad (5.70)$$

$$|f_2(j\omega)|^2 = \phi_{yy}^R(x) - \frac{\phi_{xy}^R(x)}{\psi(x)} \quad (5.71)$$

$$|f_3(j\omega)|^2 = \phi_{xy}^R(x) \quad (5.72)$$

$$|f_4(j\omega)|^2 = \psi(x) \quad (5.73)$$

where the spectrum $\psi(x)$ is chosen so $\psi(0) = 1$ and (3.70) and (3.71) are greater than zero for all x .

The discretised independent point wind speeds are calculated making sure that they will be real and symmetric about the midpoint of $[1, N]$. This is done by making the double-sided Kaimal spectrum periodic between the negative of the Nyquist rate and the Nyquist rate. Its spectral factorisation, discretised over $[1, N]$, is then multiplied by the FFT of a randomly generated set of values of white noise. Finally by applying the iFFT, the point wind speeds are brought back to the time domain.

For an n^{th} term in (5.53), the wind speed in the frequency domain corresponding to uniform weighting is derived from (5.68), that is,

$$V_{uniform}(t) = a_{n\ uniform}(t)\cos(n\theta) + b_{n\ uniform}(t)\sin(n\theta) \quad (5.74)$$

where $a_{n\ uniform}(t)$ and $b_{n\ uniform}(t)$ in the frequency domain are

¹⁰ It is obvious that f_1 and f_2 will have to account in their definitions for the presence of the cross-term f_3 and thus by introducing f_4 directly in the cross-term, it is effectively also being introduced into f_1 and f_2

$$a_{n \text{ uniform frequency}} = f_1(s)\omega_1 + f_{31}(s)\omega_3 \quad (5.75)$$

$$b_{n \text{ uniform frequency}} = f_1(s)\omega_4 + f_{31}(s)\omega_6 \quad (5.76)$$

with $\omega_1, \omega_3, \omega_4$ and ω_6 independent point wind speeds.

Similarly, the wind speed corresponding to the linear weighting is derived from (5.69) such,

$$V_{linear}(t) = a_{n \text{ linear}}(t)\cos(n\theta) + b_{n \text{ linear}}(t)\sin(n\theta) \quad (5.77)$$

where $a_{n \text{ linear}}(t)$ and $b_{n \text{ linear}}(t)$ in the frequency domain are

$$a_{n \text{ linear frequency}} = f_2(s)\omega_2 + f_{32}(s)\omega_3 \quad (5.78)$$

$$b_{n \text{ linear frequency}} = f_2(s)\omega_5 + f_{32}(s)\omega_6 \quad (5.79)$$

with $\omega_2, \omega_3, \omega_5$ and ω_6 independent point wind speeds.

Note that the cross terms f_{31} and f_{32} share the same point wind speed, that is ω_3 for the $a(\cdot)$ coefficients and ω_6 for the $b(\cdot)$ coefficients.

The derivation of the filters f_1, f_2, f_3 and f_4 is achieved by following the procedure reported in [9] and can be found in Appendix B.

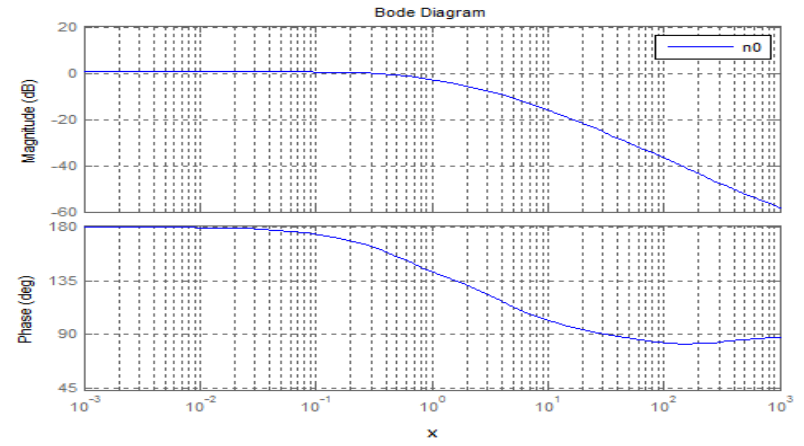
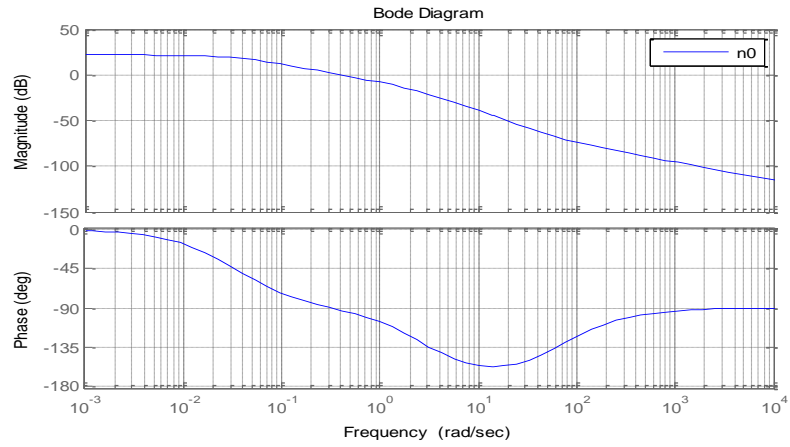
The full set of transfer functions corresponding to the wind-field model are given below in generic form, Table 5-2 to Table 5-8, together with the spectrum and illustrative time series for a wind with mean speed of 15m/s and 10% of turbulence intensity, after being rotationally sampled by a rotor with radius of 63m. For *layer P* = 0 the spectrum and time series for linear weighting is shown in Figure 5-8 and Figure 5-9, and for uniform weighting in Figure 5-10 and Figure 5-11. The corresponding figures for *layer P* = 1 are shown in Figure 5-12, Figure 5-13, Figure 5-14 and Figure 5-15. For *layer P* = 2 in Figure 5-16, Figure 5-17, Figure 5-18 and Figure 5-19. For *layer P* = 3 in Figure 5-20, Figure 5-21, Figure 5-22 and Figure 5-23. For *layer P* = 4 in Figure 5-24, Figure 5-25, Figure 5-26 and Figure 5-27. For *layer P* = 5 in Figure 5-28, Figure 5-29, Figure 5-30 and Figure 5-31. Finally, for *layer P* = 6 in Figure 5-32, Figure 5-33, Figure 5-34 and to Figure 5-35.

These spectra and time series effectively represent the stochastic component of the wind only¹¹, as WS and TS are treated as a further addition to it as seen in Figure 5-2. For the illustrative examples $\sigma = 5.46$ and the azimuth angle that drives the effective wind-field model is generated by a 5MW WT simulation. The data used in the spectrum of the wind have not been detrended.

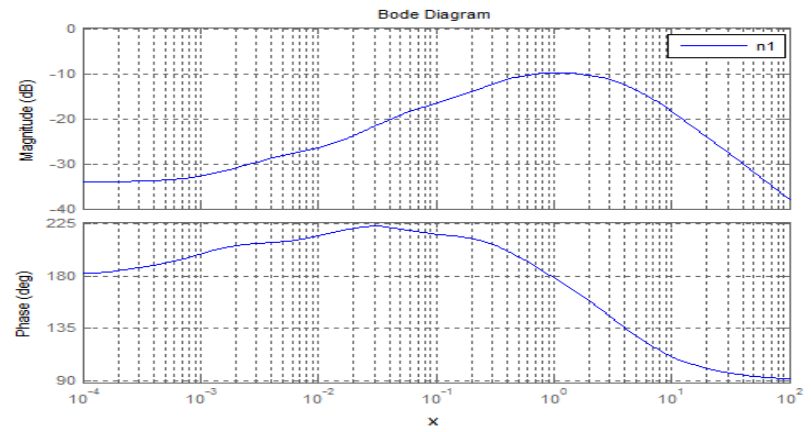
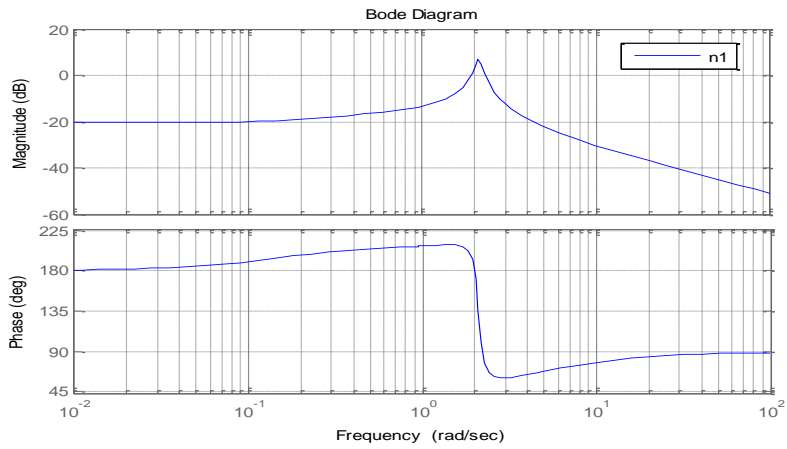
Following the discussion at the end of Section 5.2.1, it is interesting at this point to compare the gains for the frequency response functions proposed by [28] (as reported in Section 2.2.4.2.3) with their counterparts in the proposed effective wind-field model, see Figure 5-7. The frequency response functions from [28] generate effective wind speeds for a rotating blade with corresponding spectral density functions proportional to their magnitude squared. The frequency response functions developed here, generate an effective wind-field with corresponding double-sided spectral density functions. When this wind-field is sampled by a blade rotating at constant rotational velocity, the centre of the double-sided spectrum for the n^{th} -layer component is shifted to nP ; that is, the spectral peaks induced by rotational sampling are now double peaks, symmetric about their centre, rather than the single peaks in [28]. Figure 5-7 shows the single-sided spectra.

From Figure 5-7, it can be seen that the roll-off rates for the frequency response functions from [28] are in the range 40 to 50dB per decade whereas in the proposed effective wind-field model the roll-off rates are 20dB per decade.

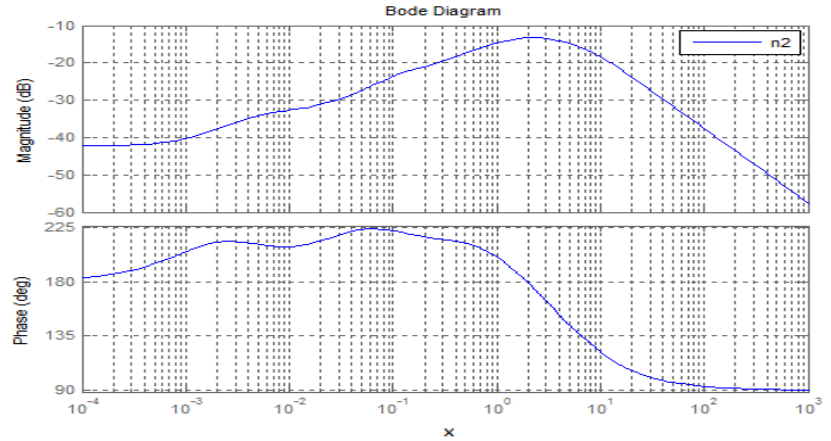
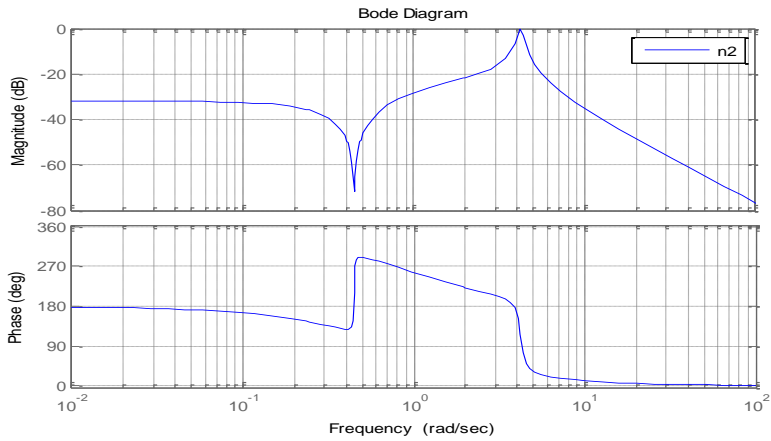
¹¹ Remember that the linear weighting is used in the stochastic component of the wind to induce moments and the uniform weighting to induce forces, most specifically the thrust.



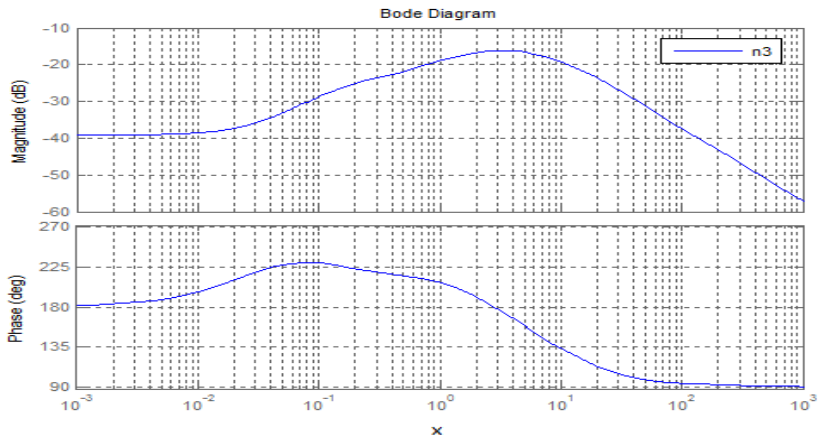
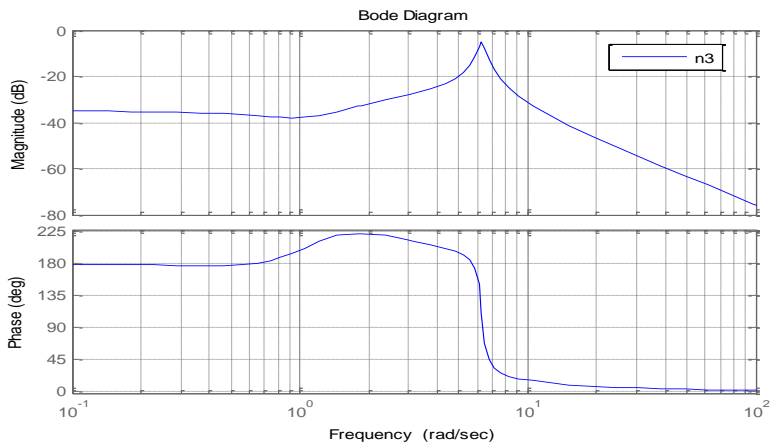
a)



b)



c)



d)

Figure 5-7. Comparison between the transfer functions proposed by [28] in the left hand-side column and their counterpart transfer functions in the proposed effective wind-field model in the right hand-side column for: a) $n = 0$, b) $n = 1$, c) $n = 2$, d) $n = 3$

$n = 0$	
f_1	$\frac{2.1132 (\sigma s + 137.8) (\sigma s + 31.62) (\sigma s + 8.867) (\sigma s + 3) (\sigma s + 0.2285) (\sigma s + 0.01795) (\sigma s + 0.001795)}{(\sigma s + 167.3) (\sigma s + 36.06) (\sigma s + 12.33) (\sigma s + 4.123) (\sigma s + 3.162) (\sigma s + 0.5476) (\sigma s + 0.06327) (\sigma s + 0.003077)}$
f_{31}	$\frac{1.2063 (\sigma s + 173.2) (\sigma s + 1.414)}{(\sigma s + 132.3) (\sigma s + 3.162) (\sigma s + 0.7069)}$
f_{32}	$\frac{1.2063 (\sigma s + 173.2) (\sigma s + 1.414)}{(\sigma s + 132.3) (\sigma s + 3.162) (\sigma s + 0.7069)}$
f_2	$\frac{14.009 (\sigma s + 6.11) (\sigma s + 4.472) (\sigma s + 0.3504) (\sigma s + 0.02414) (\sigma s + 0.002414)}{(\sigma s + 47.96) (\sigma s + 3.873) (\sigma s + 3.162) (\sigma s + 3) (\sigma s + 0.7069) (\sigma s + 0.08369) (\sigma s + 0.005119)}$

Table 5-2. Transfer function terms for *layer P* corresponding to $n = 0$

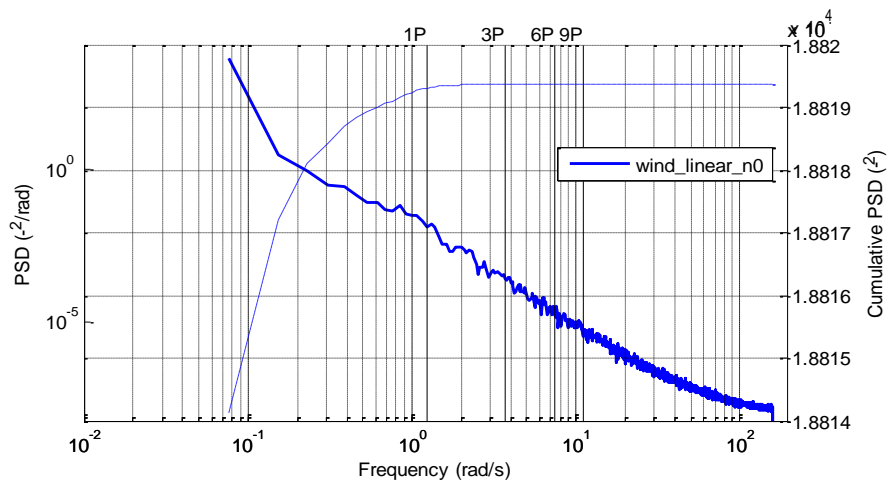


Figure 5-8. Spectrum for *layer P* corresponding to $n = 0$ with linear weighting

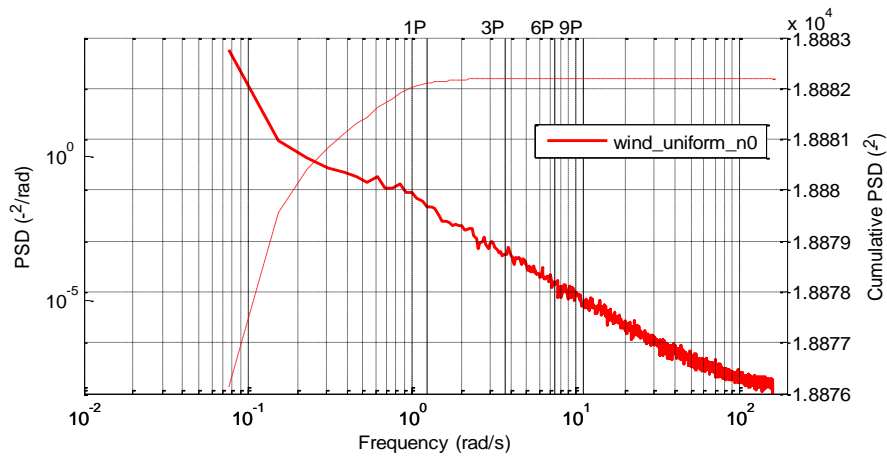


Figure 5-10. Spectrum for *layer P* corresponding to $n = 0$ with uniform weighting

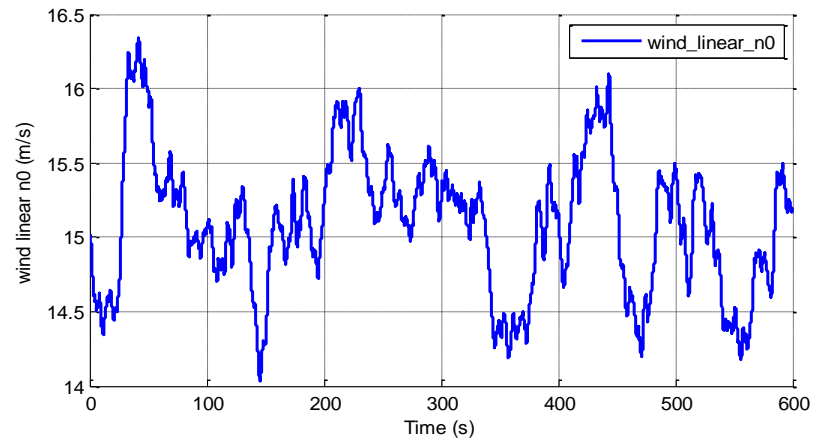


Figure 5-9. Time series for *layer P* corresponding to $n = 0$ with linear weighting

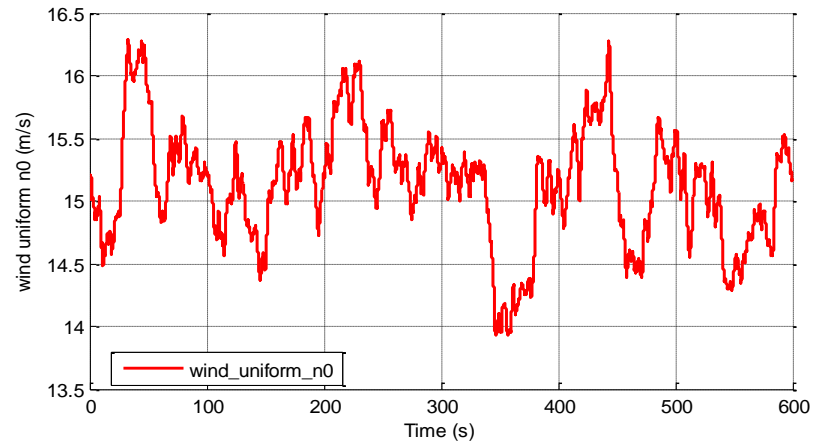


Figure 5-11. Time series for *layer P* corresponding to $n = 0$ with uniform weighting

$n = 1$	
f_1	$\frac{1.6432 (\sigma s + 31.62) (\sigma s + 1.949)^4 (\sigma s + 0.04958) (\sigma s + 0.0006246)}{(\sigma s + 67.06) (\sigma s + 7.556) (\sigma s + 5) (\sigma s + 4.399) (\sigma s + 1.437) (\sigma s + 0.942) (\sigma s + 0.38) (\sigma s + 0.0038)}$
f_{31}	$\frac{1.2894 (\sigma s - 7.112) (\sigma s - 1.414) (\sigma s + 0.1588) (\sigma s + 0.0143) (\sigma s + 0.00143)}{(\sigma s + 7.681) (\sigma s + 3.873) (\sigma s + 1.517) (\sigma s + 0.3956) (\sigma s + 0.05101) (\sigma s + 0.003476)}$
f_{32}	$\frac{1.2069 (\sigma s - 7.681) (\sigma s - 1.517) (\sigma s + 0.1588) (\sigma s + 0.0143) (\sigma s + 0.00143)}{(\sigma s + 7.112) (\sigma s + 3.873) (\sigma s + 1.414) (\sigma s + 0.3956) (\sigma s + 0.05101) (\sigma s + 0.002934)}$
f_2	$\frac{0.39122 (\sigma s + 0.6478) (\sigma s + 0.2832) (\sigma s + 0.2646) (\sigma s + 0.01564) (\sigma s + 0.001564)}{(\sigma s + 4) (\sigma s + 1.622) (\sigma s + 1.614) (\sigma s + 0.1093) (\sigma s + 0.06327) (\sigma s + 0.003618)}$

Table 5-3. Transfer function terms for layer P corresponding to $n = 1$

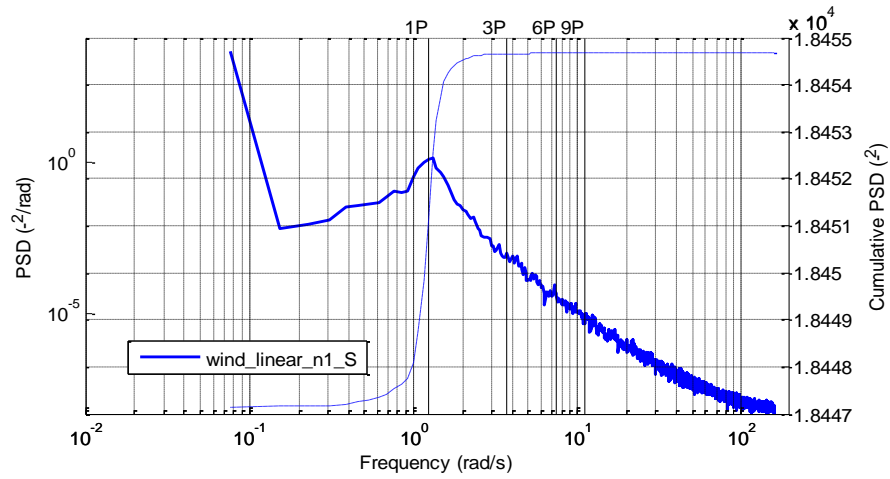


Figure 5-12. Spectrum for *layer P* corresponding to $n = 1$ with linear weighting

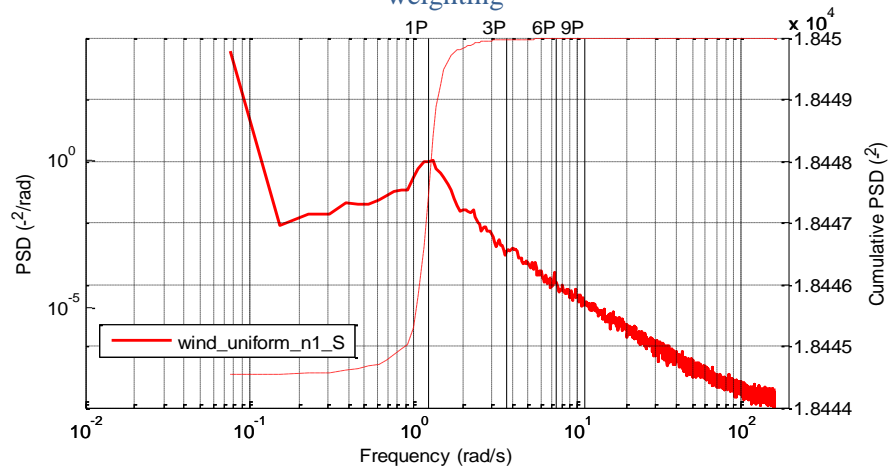


Figure 5-14. Spectrum for *layer P* corresponding to $n = 1$ with uniform weighting

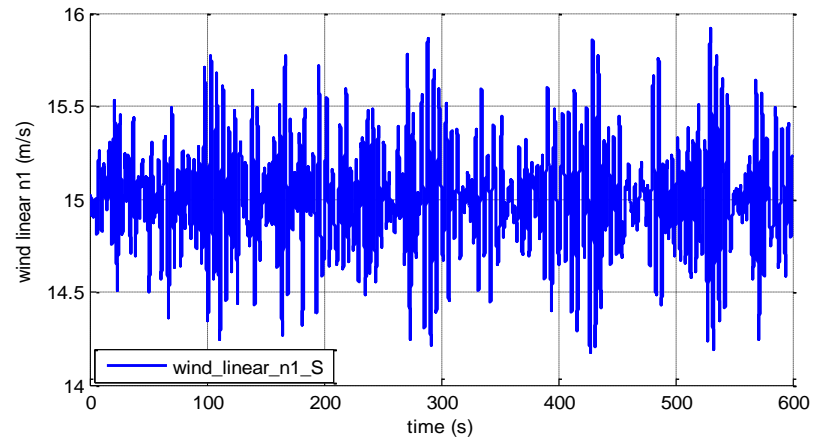


Figure 5-13. Time series for *layer P* corresponding to $n = 1$ with linear weighting

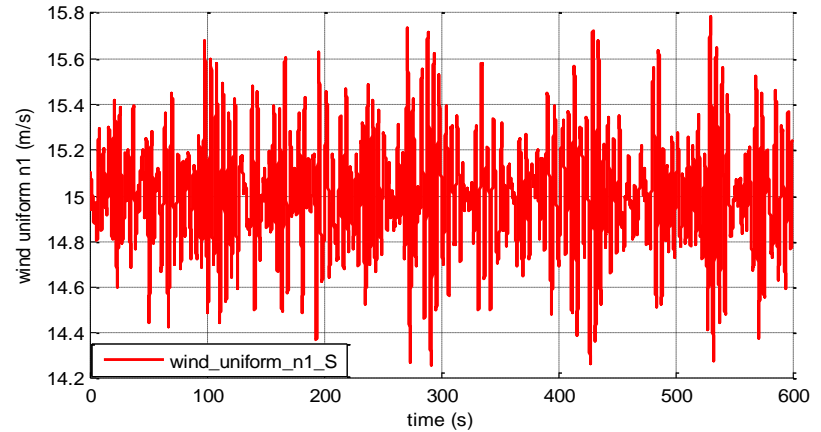


Figure 5-15. Time series for *layer P* corresponding to $n = 1$ with uniform weighting

$n = 2$	
f_1	$\frac{2.3069 (\sigma s + 352.1) (\sigma s + 0.9793) (\sigma s + 0.01085)}{(\sigma s + 650) (\sigma s + 35.5) (\sigma s + 2.198) (\sigma s + 0.1671)}$
f_{31}	$\frac{1.3419 (\sigma s - 11.62) (\sigma s - 5.568) (\sigma s + 11.62) (\sigma s + 5.569) (\sigma s + 0.3811) (\sigma s + 0.02888) (\sigma s + 0.001263)}{(\sigma s + 12.25) (\sigma s + 11.62) (\sigma s + 6.44) (\sigma s + 5.655) (\sigma s + 5.568) (\sigma s + 1.074) (\sigma s + 0.1139) (\sigma s + 0.003808)}$
f_{32}	$\frac{1.1923 (\sigma s - 12.25) (\sigma s - 6.442) (\sigma s + 12.25) (\sigma s + 6.44) (\sigma s + 0.3811) (\sigma s + 0.02888) (\sigma s + 0.001263)}{(\sigma s + 12.25) (\sigma s + 11.62) (\sigma s + 6.442) (\sigma s + 5.655) (\sigma s + 5.569) (\sigma s + 1.074) (\sigma s + 0.1139) (\sigma s + 0.003808)}$
f_2	$\frac{0.56648 (\sigma s + 0.8087) (\sigma s + 0.02453) (\sigma s + 0.002453)}{(\sigma s + 6.327) (\sigma s + 5.292) (\sigma s + 0.1094) (\sigma s + 0.00552)}$

Table 5-4. Transfer function terms for layer P corresponding to $n = 2$

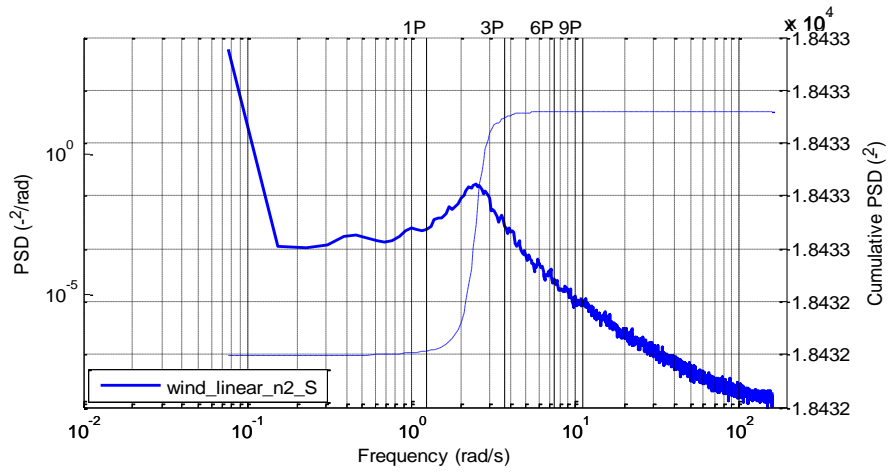


Figure 5-16. Spectrum for *layer P* corresponding to $n = 2$ with linear weighting

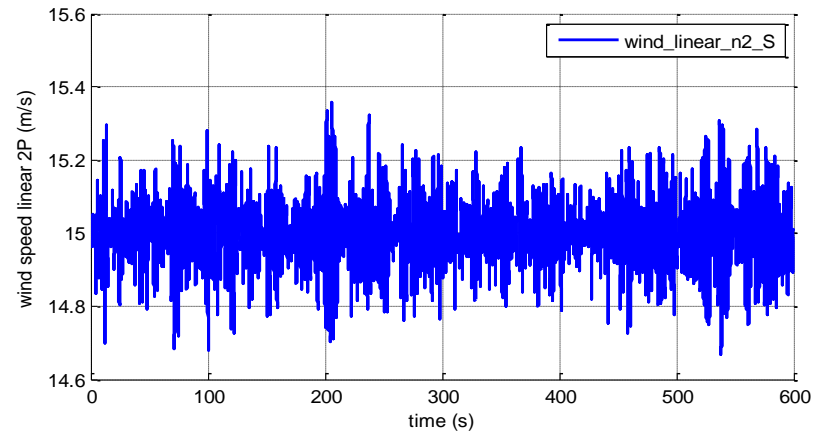


Figure 5-17. Time series for *layer P* corresponding to $n = 2$ with linear weighting

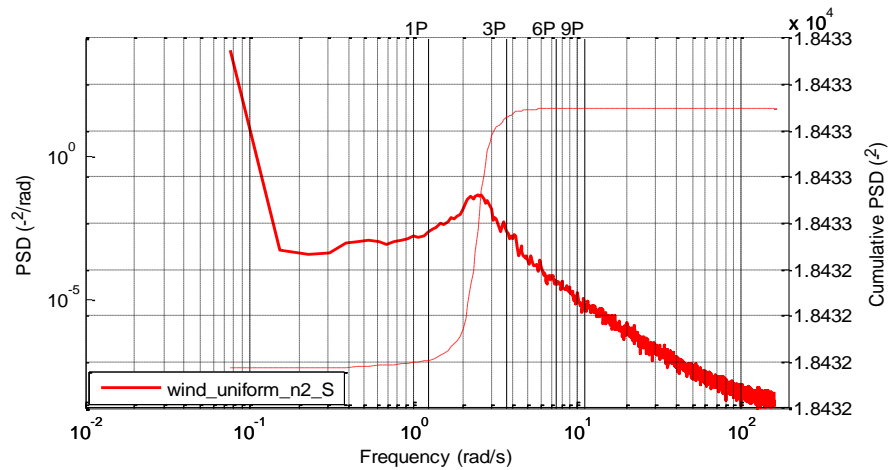


Figure 5-18. Spectrum for *layer P* corresponding to $n = 2$ with uniform weighting

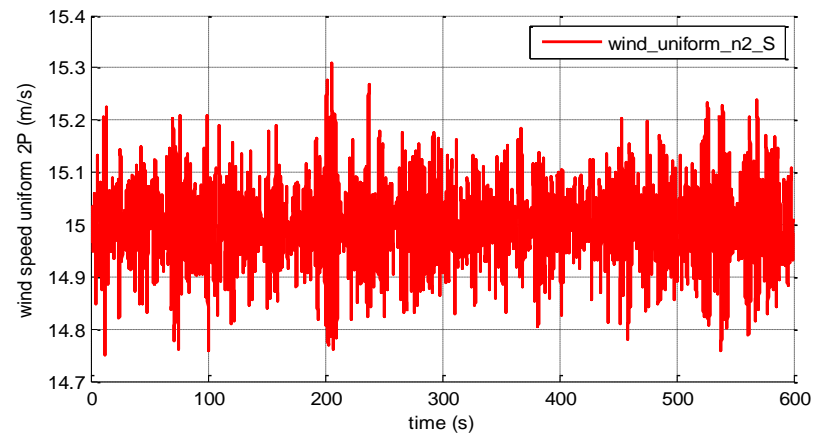


Figure 5-19. Time series for *layer P* corresponding to $n = 2$ with uniform weighting

$n = 3$	
f_1	$\frac{1.241 s (\sigma s + 0.3873) ((\sigma s)^2 + 25.21 \sigma s + 192.6)}{(\sigma s + 61.64) (\sigma s + 20) (\sigma s + 7.071) (\sigma s + 1.619) (\sigma s + 0.08944)}$
f_{31}	$\frac{1.4318 (\sigma s - 15.3) (\sigma s - 6.403) (\sigma s + 6.403) (\sigma s + 15.3) (\sigma s + 0.5897) (\sigma s + 0.02828)}{(\sigma s + 18.71) (\sigma s + 15.3) (\sigma s + 7.746) (\sigma s + 7.106) (\sigma s + 6.403) (\sigma s + 1.619) (\sigma s + 0.1732)}$
f_{32}	$\frac{1.2649 (\sigma s - 17.32) (\sigma s - 7.106) (\sigma s + 7.106) (\sigma s + 15.81) (\sigma s + 0.5897) (\sigma s + 0.02828)}{(\sigma s + 17.32) (\sigma s + 15.3) (\sigma s + 7.746) (\sigma s + 7.106) (\sigma s + 6.403) (\sigma s + 1.619) (\sigma s + 0.1732)}$
f_2	$\frac{0.57446 s (\sigma s + 3) (\sigma s + 0.5725) ((\sigma s)^2 + 163 \sigma s + 8746)}{(\sigma s + 128.5) (\sigma s + 52.92) (\sigma s + 15.3) (\sigma s + 5.675) (\sigma s + 1.619) (\sigma s + 0.1448)}$

Table 5-5. Transfer function terms for layer P corresponding to $n = 3$

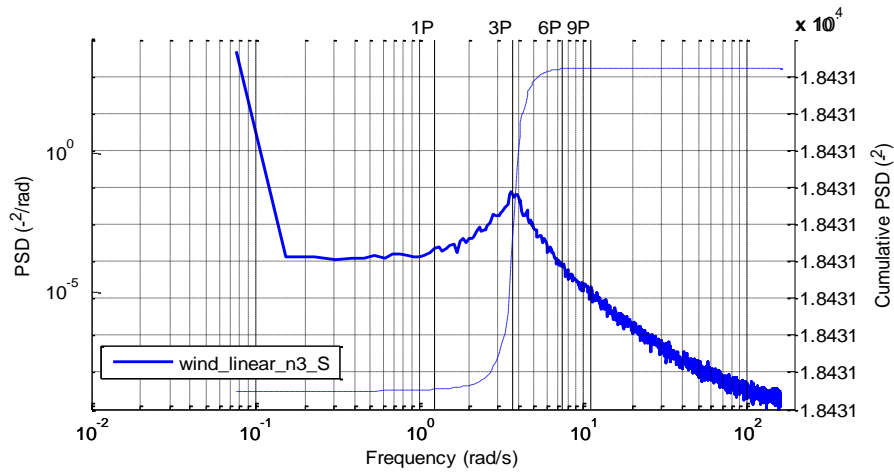


Figure 5-20. Spectrum for *layer P* corresponding to $n = 3$ with linear weighting

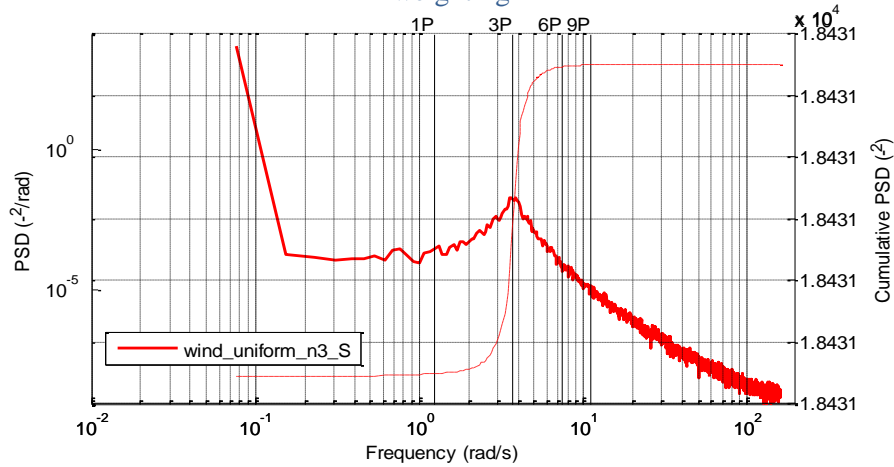


Figure 5-22. Spectrum for *layer P* corresponding to $n = 3$ with uniform weighting

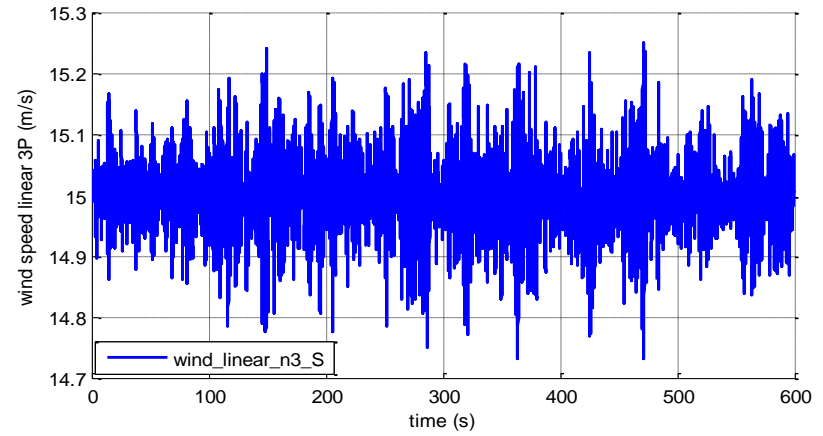


Figure 5-21. Time series for *layer P* corresponding to $n = 3$ with linear weighting

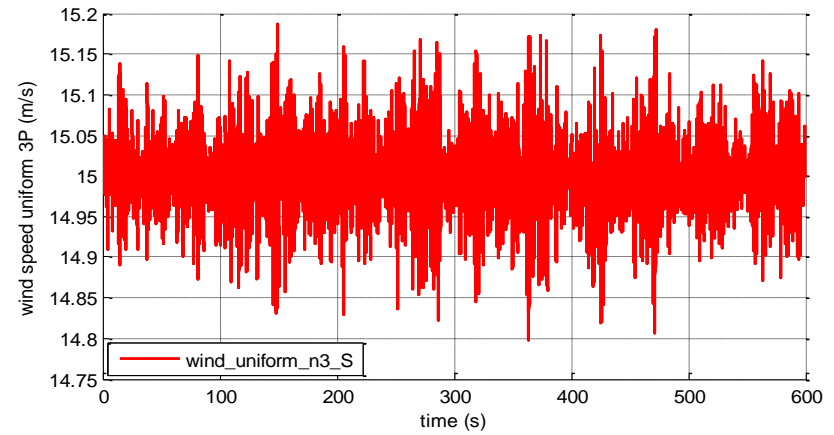


Figure 5-23. Time series for *layer P* corresponding to $n = 3$ with uniform weighting

$n = 4$	
f_1	$\frac{1.3237 (\sigma s + 59.15) (\sigma s + 9.902) (\sigma s + 9.43) (\sigma s + 6.858) (\sigma s + 0.6841) (\sigma s + 0.05877) (\sigma s + 0.005877)}{(\sigma s + 134.2) (\sigma s + 24.14) (\sigma s + 12.65) (\sigma s + 11.18) (\sigma s + 4.142) (\sigma s + 2.97) (\sigma s + 0.2098) (\sigma s + 0.01556)}$
f_{31}	$\frac{1.4408 (\sigma s - 38.73) (\sigma s - 8.829) (\sigma s + 0.6061) (\sigma s + 0.04064) (\sigma s + 0.00244)}{(\sigma s + 44.72) (\sigma s + 10.72) (\sigma s + 9.999) (\sigma s + 1.766) (\sigma s + 0.1762) (\sigma s + 0.006787)}$
f_{32}	$\frac{1.179 (\sigma s - 44.72) (\sigma s - 9.999) (\sigma s + 0.6061) (\sigma s + 0.04064) (\sigma s + 0.004064)}{(\sigma s + 38.73) (\sigma s + 10.72) (\sigma s + 8.829) (\sigma s + 1.766) (\sigma s + 0.1762) (\sigma s + 0.0122)}$
f_2	$\frac{0.61479 \sigma s (\sigma s + 42.43) (\sigma s + 2.09) (\sigma s + 0.1433)}{(\sigma s + 52.92) (\sigma s + 13.42) (\sigma s + 5.817) (\sigma s + 0.5412) (\sigma s + 0.03742)}$

Table 5-6. Transfer function terms for *layer P* corresponding to $n = 4$

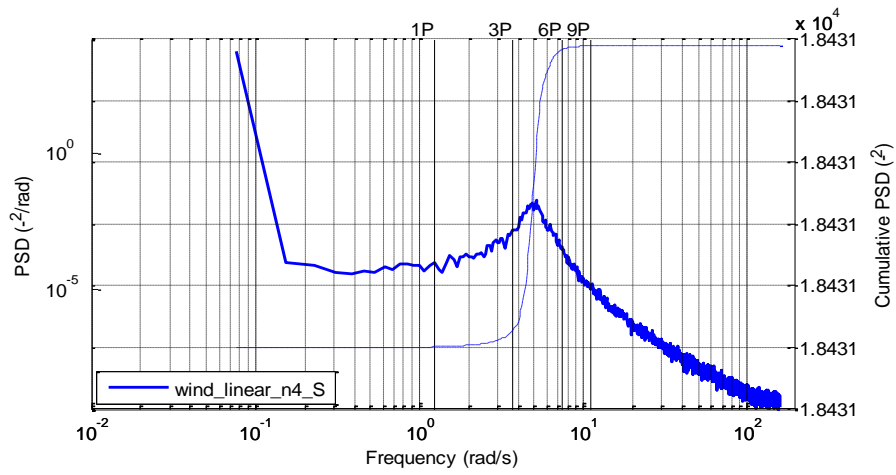


Figure 5-24. Spectrum for *layer P* corresponding to $n = 4$ with linear weighting

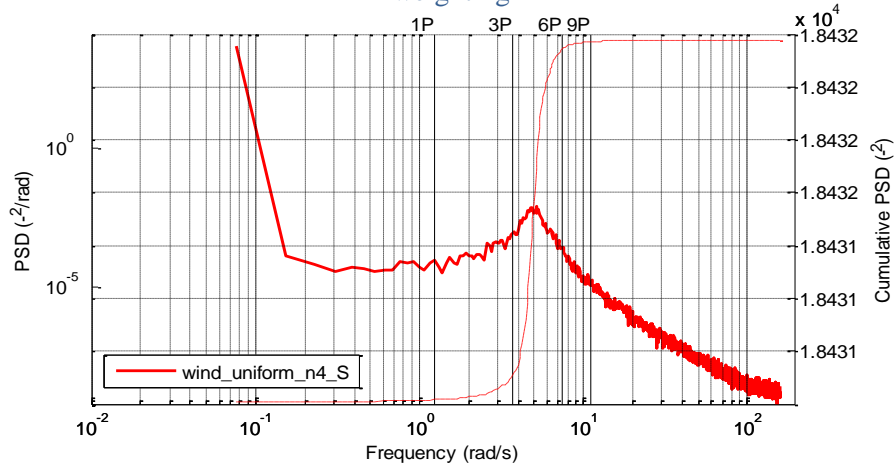


Figure 5-26. Spectrum for *layer P* corresponding to $n = 4$ with uniform weighting

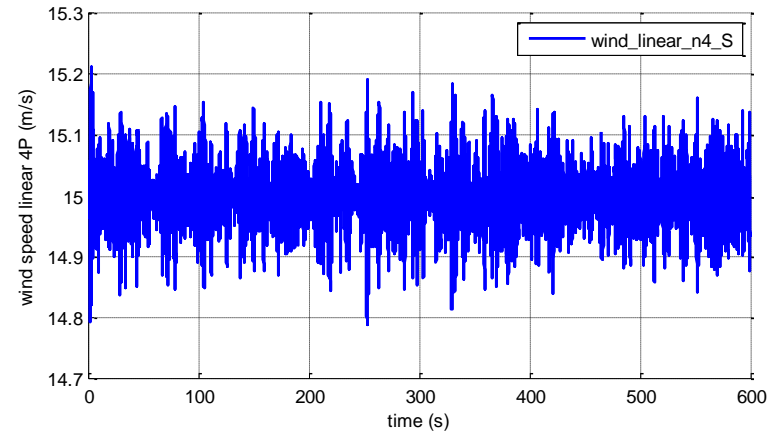


Figure 5-25. Time series for *layer P* corresponding to $n = 4$ with linear weighting

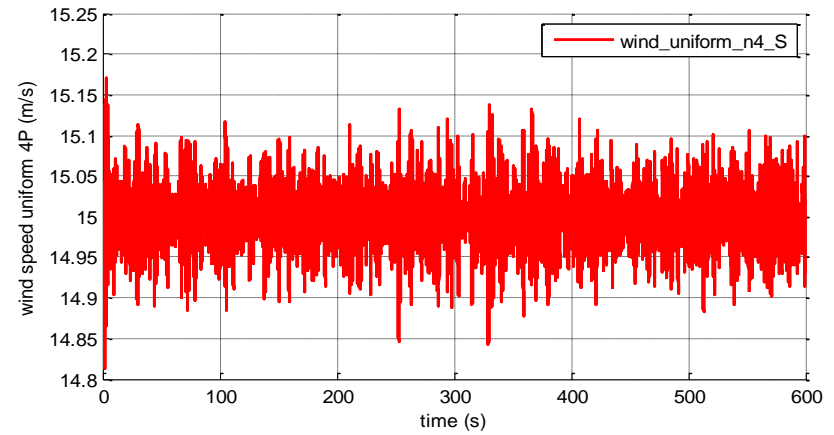


Figure 5-27. Time series for *layer P* corresponding to $n = 4$ with uniform weighting

$n = 5$	
f_1	$\frac{1.2209 \sigma s (\sigma s + 42.43) (\sigma s + 7.584) (\sigma s + 0.7925) (\sigma s + 0.07226)}{(\sigma s + 110.9) (\sigma s + 17.6) (\sigma s + 12.84) (\sigma s + 2.371) (\sigma s + 0.2469) (\sigma s + 0.01871)}$
f_{31}	$\frac{1.3884 \sigma s (\sigma s - 34.64) (\sigma s - 8.829) (\sigma s + 0.7925) (\sigma s + 0.07226)}{(\sigma s + 41.23) (\sigma s + 12.65) (\sigma s + 9.539) (\sigma s + 2.371) (\sigma s + 0.2469) (\sigma s + 0.01871)}$
f_{32}	$\frac{1.1909 \sigma s (\sigma s - 41.23) (\sigma s - 9.539) (\sigma s + 0.7925) (\sigma s + 0.07226)}{(\sigma s + 34.64) (\sigma s + 12.65) (\sigma s + 8.829) (\sigma s + 2.371) (\sigma s + 0.2469) (\sigma s + 0.01871)}$
f_2	$\frac{0.58333 \sigma s (\sigma s + 41.23) (\sigma s + 11) (\sigma s + 0.9631) (\sigma s + 0.07226)}{(\sigma s + 56.55) (\sigma s + 15.66) (\sigma s + 13.04) (\sigma s + 2.97) (\sigma s + 0.2664) (\sigma s + 0.01871)}$

Table 5-7. Transfer function terms for *layer P* corresponding to $n = 5$

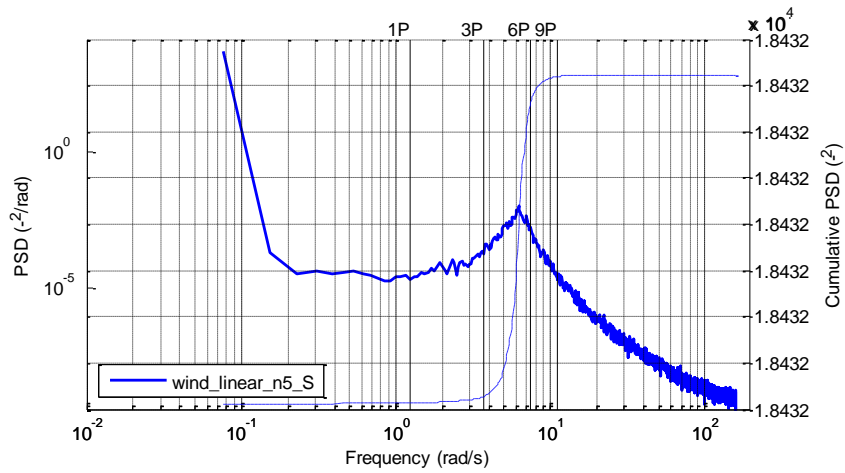


Figure 5-28. Spectrum for *layer P* corresponding to $n = 5$ with linear weighting

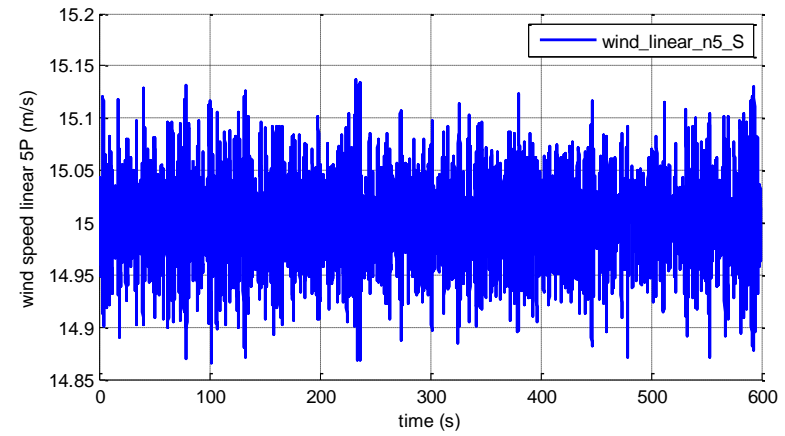


Figure 5-29. Time series for *layer P* corresponding to $n = 5$ with linear weighting

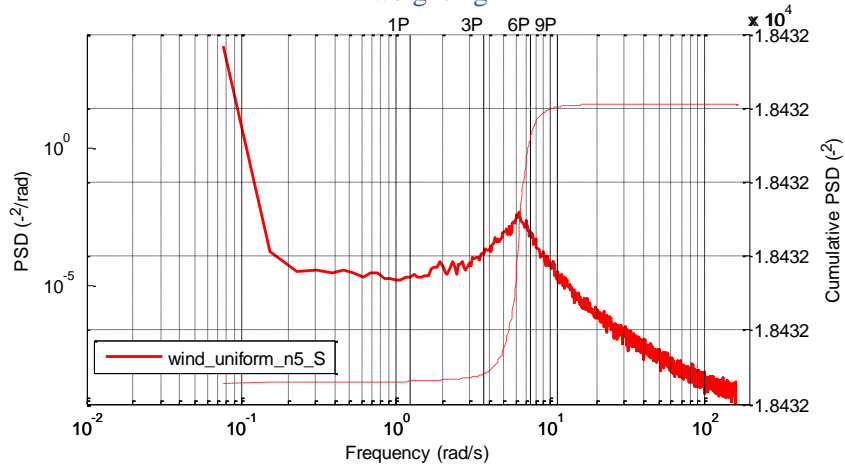


Figure 5-30. Spectrum for *layer P* corresponding to $n = 5$ with uniform weighting

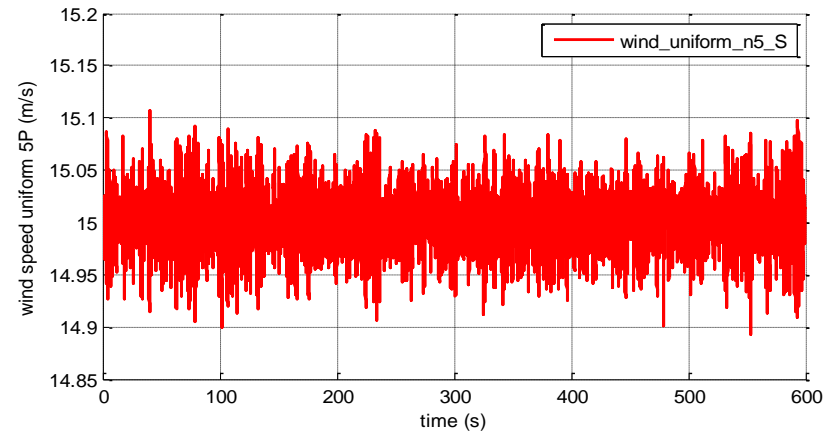


Figure 5-31. Time series for *layer P* corresponding to $n = 5$ with uniform weighting

$n = 6$	
f_1	$\frac{1.3229 (\sigma s + 63.27) (\sigma s + 1.098) (\sigma s + 0.07031)}{(\sigma s + 144.9) (\sigma s + 33.17) (\sigma s + 4.463) (\sigma s + 0.2738)}$
f_{31}	$\frac{1.4268 (\sigma s - 41.83) (\sigma s - 11.66) (\sigma s + 0.9506) (\sigma s + 0.09702)}{(\sigma s + 48.99) (\sigma s + 15.49) (\sigma s + 12.67) (\sigma s + 2.731) (\sigma s + 0.3037)}$
f_{32}	$\frac{1.2627 (\sigma s - 48.99) (\sigma s - 12.67) (\sigma s + 0.9506) (\sigma s + 0.09702)}{(\sigma s + 41.83) (\sigma s + 15.49) (\sigma s + 11.66) (\sigma s + 2.731) (\sigma s + 0.3037)}$
f_2	$\frac{5.4772 \times 10^5 (\sigma s + 22.22) (\sigma s + 7.507) (\sigma s + 0.9447) (\sigma s + 0.06105)}{(\sigma s + 999.9) (\sigma s + 894.3) (\sigma s + 51.91) (\sigma s + 11.66) (\sigma s + 9.593) (\sigma s + 2.976) (\sigma s + 0.2289)}$

Table 5-8. Transfer function terms for layer P corresponding to $n = 6$

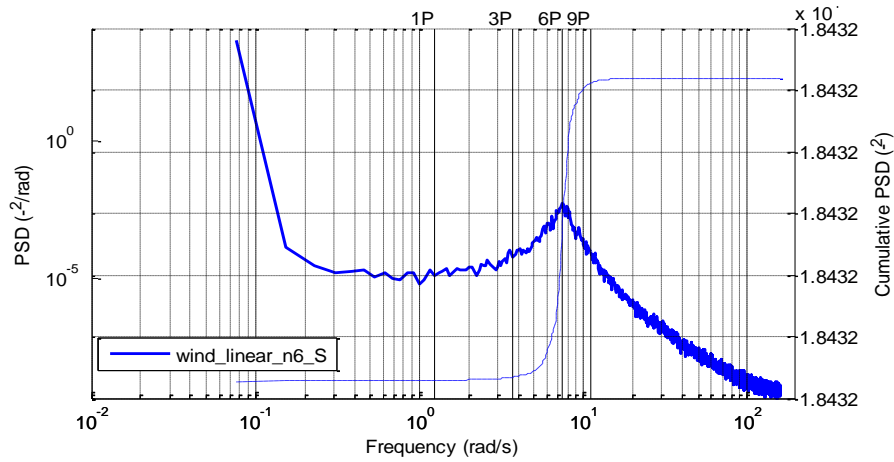


Figure 5-32. Spectrum for *layer P* corresponding to $n = 6$ with linear weighting

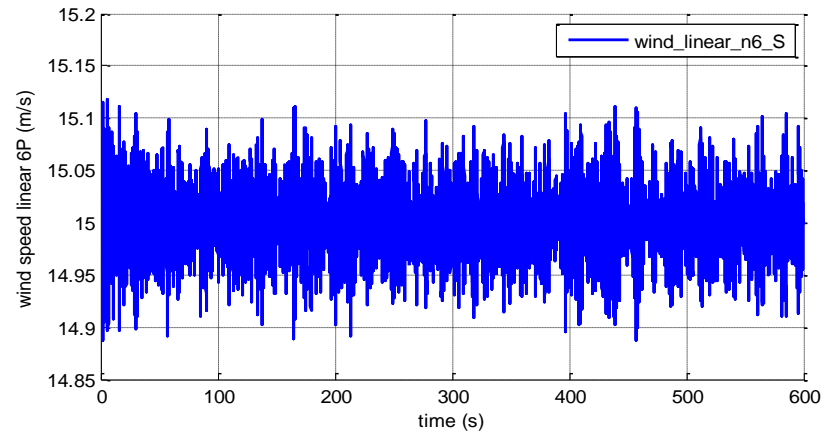


Figure 5-33. Time series for *layer P* corresponding to $n = 6$ with linear weighting

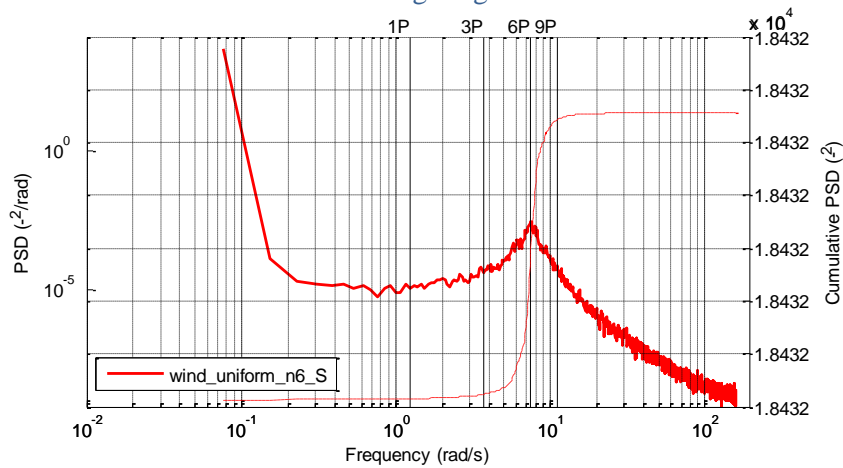


Figure 5-34. Spectrum for *layer P* corresponding to $n = 6$ with uniform weighting

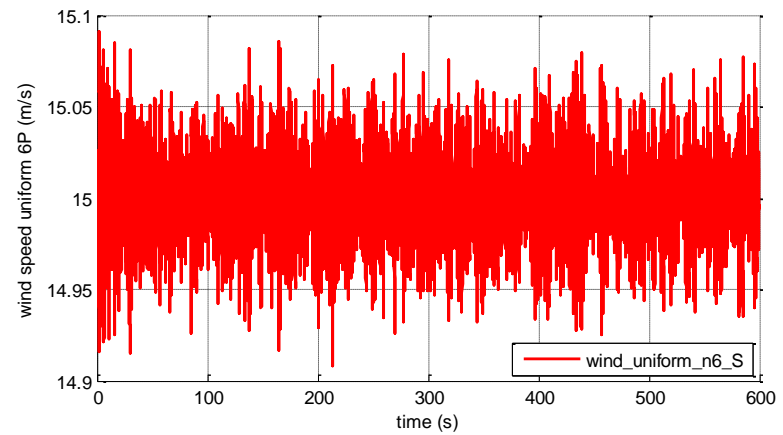


Figure 5-35. Time series for *layer P* corresponding to $n = 6$ with uniform weighting

5.2.2. Results for the Stochastic Component of the Effective Wind-Field Model

Before analysing the results for the induced moments and forces by the stochastic component of the wind-field, the spectra and time series of the stochastic component of the wind-field itself, for both the rotor and single blade, are presented for a wind-field with 15m/s mean and 10% TI.

The spectrum of the stochastic component of the wind-field with linear weighting and its time series (used for inducing moments) can be found in Figure 5-36 and Figure 5-37. Similarly, the spectrum and time series for uniform weighting (used for inducing thrust) can be found in Figure 5-38 and Figure 5-39. Both cases contain all the necessary *layer P* structures for the rotor in the simple model (which induces 0, 3 and 6P) and their time series¹². The data used in the spectrum of the wind have not been detrended.

¹² The rotor in the triple structure uses 3 wind-field models like the one that drives the single blade, each one of which has a 120 degree of azimuthal offset with respect to each other, in order to represent the three blades.

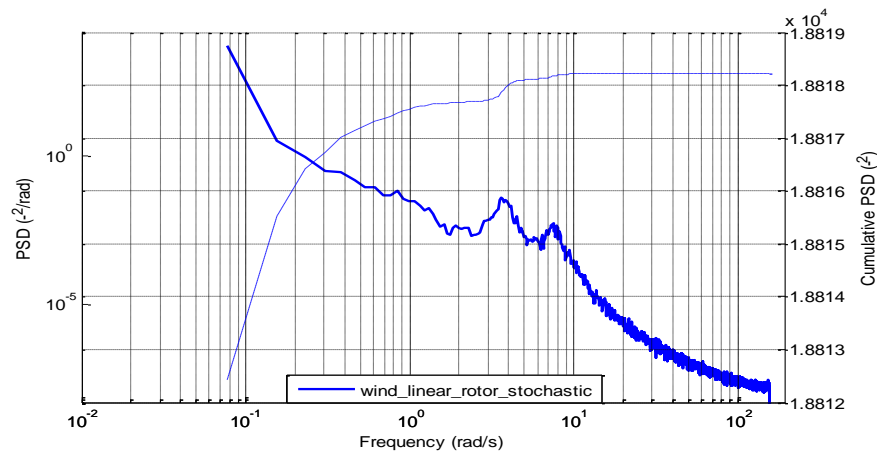


Figure 5-36. Spectrum of the stochastic component of wind-field for inducing moments at the rotor by the simple model

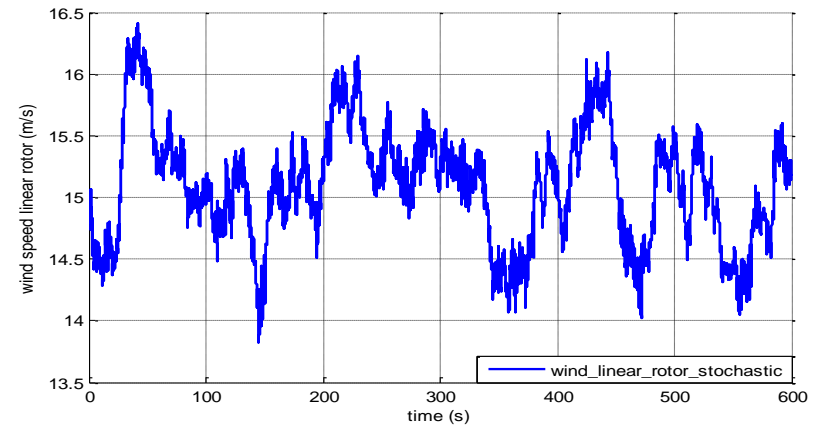


Figure 5-37. Time series of the stochastic component of wind-field for inducing moments at the rotor by the simple model

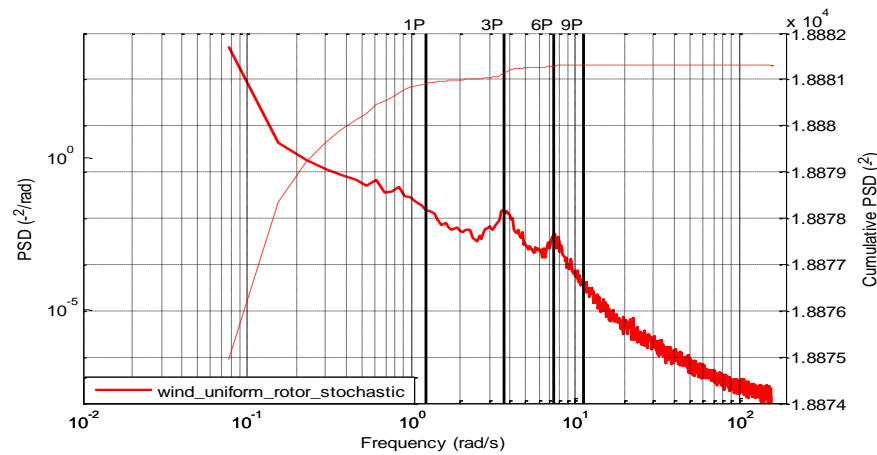


Figure 5-38. Spectrum of the stochastic component of wind-field for inducing thrust at the rotor by the simple model

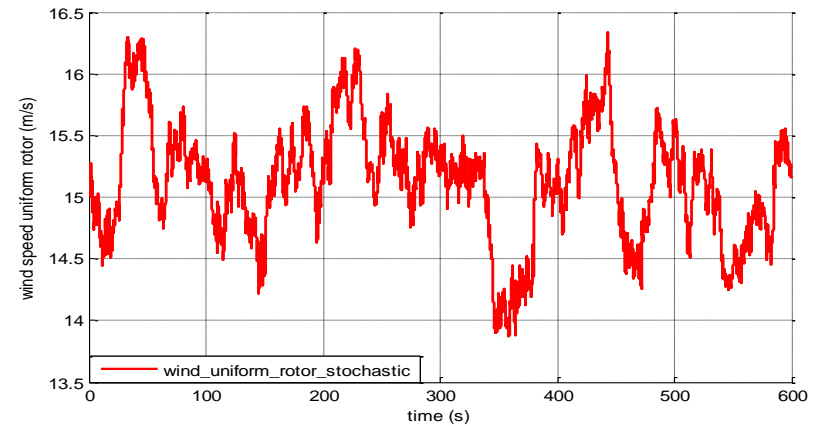


Figure 5-39. Time series of the stochastic component of wind-field for inducing thrust at the rotor by the simple model

From Figure 5-40 to Figure 6-39, the spectrum of the wind with linear and uniform weighting, containing all the necessary *layer P* structures for the single blade (inducing 0, 1, 2, 3, 4, 5 and 6P) and their time series can be seen.

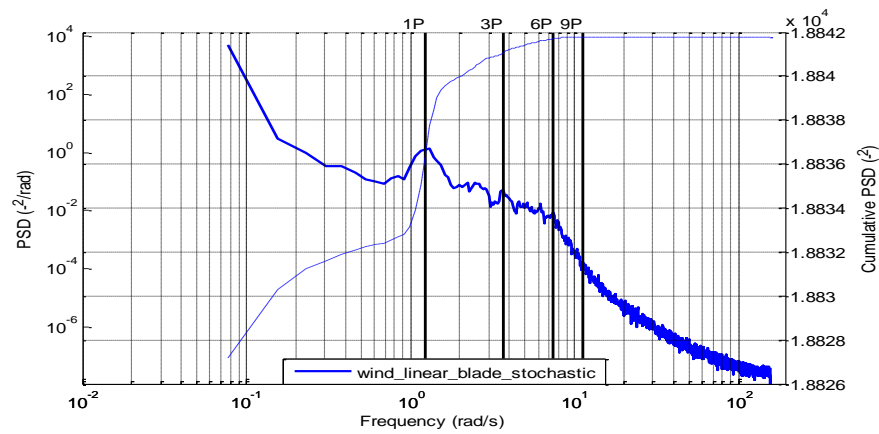


Figure 5-40. Spectrum of the stochastic component of wind-field for inducing moments at a single blade

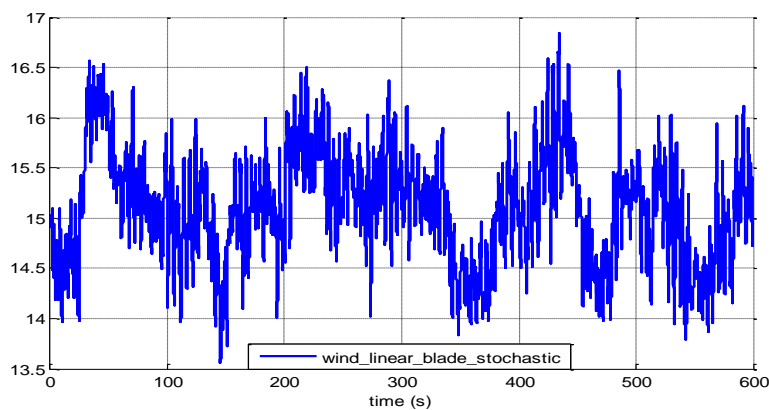


Figure 5-41. Time series of the stochastic component of wind-field for inducing moments at a single blade

As expected, the shape of the induced nP peaks are consistent with the characteristic shape of a stochastic signal as described in Chapter 2.

In the following, the results for a representative moment for which Separability applies, that is in-plane hub torque and for a representative moment for which Separability does not apply, that is out-of-plane RBM of a blade, are analysed for the stochastic component of the wind-field. In Appendix C the results for the thrust force, the in-plane RBM of the blade, the edgewise moment of the blade, M_e , the flapwise moment of the blade, M_f , the rotor speed and the pitch angle of the blades, can be found. Unless otherwise stated, the dynamics of the WT have been suppressed to better understand the impact of the effective wind-field model.

The in-plane hub torque and out-of-plane RBM are both considered within the domain Separability applies, that is the above rated wind speed 15m/s, and outside the domain, that is the below rated wind speed 8m/s. The scenario of 15m/s with 18 degrees of pitch offset, which is on the boundaries of Separability and is subject to the non-linearity effects of $\tau(\cdot)$, is also explored as part of the region of applicability of Separability as the WT should be able to return to the point of equilibrium when such a disturbance is applied. At this stage, the gravity component is switched off in the models to allow for a clearer visualisation of the results from the simulations.

When looking at the results for the in-plane hub torque, which is the moment for which Separability applies, it is clear that in the two cases, for which the wind speed lies within the region of applicability of Separability, that is Figure 5-42 to Figure 5-44 for the 15m/s case and Figure 5-45 to Figure 5-47 for the 15m/s with 18 degrees of pitch offset, the match between the simple and triple model is remarkable, especially for the 15m/s with no pitch offset case. Overall, no leakage is observed as expected as a consequence of Separability. When interrogating the region outside the region of applicability of Separability, that is 8m/s, the results, Figure 5-48 to Figure 5-49, indicate that for the in-plane hub torque in the stochastic case, there is no presence of leakage. An explanation for good results while tracking the $C_{p \max}$ tracking curve is that in this region there is only one variable left in the definition of torque, that is, the wind speed. In addition, the perturbations about the λ are small with $V = \bar{V} + \Delta V$ and everything else is constant. Therefore, using Taylor's series expansion

$$T = \frac{1}{2} \rho A V^2 R \frac{C_p(\lambda, \beta)}{\lambda} = k V^2 = k \bar{V}^2 \left(1 + \frac{2\Delta V}{\bar{V}} + \left(\frac{\Delta V}{\bar{V}} \right)^2 \right) \quad (5.80)$$

There is still a form of separation, albeit not that of the Separability property being exploited here. Furthermore, the squared term in the expansion is small and can be discounted, giving an approximately linear relationship between the torque and the wind speed,

$$T \cong k \bar{V}^2 \left(1 + \frac{2\Delta V}{\bar{V}} \right) \quad (5.81)$$

The out-of-plane RBM of the blade has been selected as the representative moment, for which Separability does not apply, because it clearly displays all the nP peaks. Since this moment by its nature is *a priori* not covered by Separability, there is no initial expectation for it to be

correctly induced by the wind-field model. Nevertheless, since effective wind speeds obtained independently for the in-plane RBM and the out-of-plane RBM for a blade must be strongly correlated, good results for the in-plane RBM would imply good results for the out-of-plane RBM even if Separability does not directly cover the later. The results for the out-of-plane RBM of the blade can be seen from Figure 5-51 to Figure 5-53 for the 15m/s case, from Figure 5-54 to Figure 5-56 for the 15m/s with 18 degrees of pitch offset and from Figure 5-57 to Figure 5-59 for the 8m/s case. It is striking how closely the simple and triple model follow for all of them, providing no signs of leakage for the 15m/s and 15m/s with 18deg of pitch offset and only a minor discrepancy in the cumulative value for the 8m/s case, whist the spectrum looks virtually identical. The data used in the spectrum of the moments and forces have been detrended.

After analysis of all the results for the stochastic component of the wind-field, including the ones present in Appendix C, it can be concluded that overall, no leakage is observed for the stochastic component of the wind-field and that the simple model should suffice to induce moments and forces as far as the stochastic component of the wind-field is concerned.

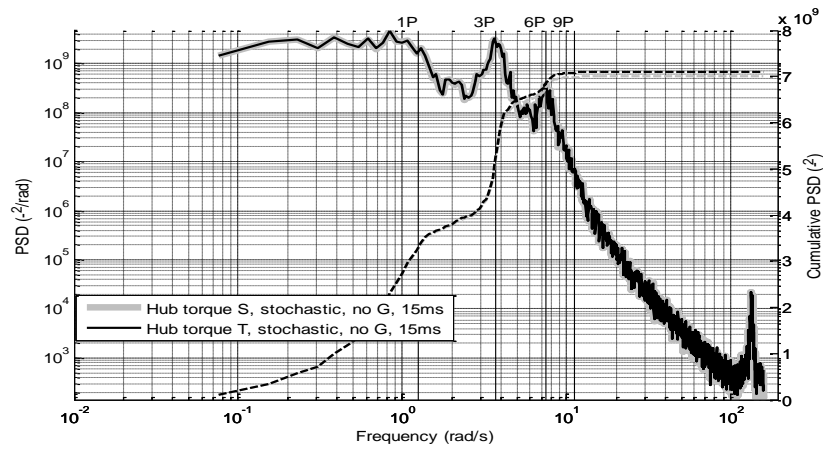


Figure 5-42. Hub torque spectrum comparison between simple and triple structure for the stochastic component of the wind-field with mean 15m/s

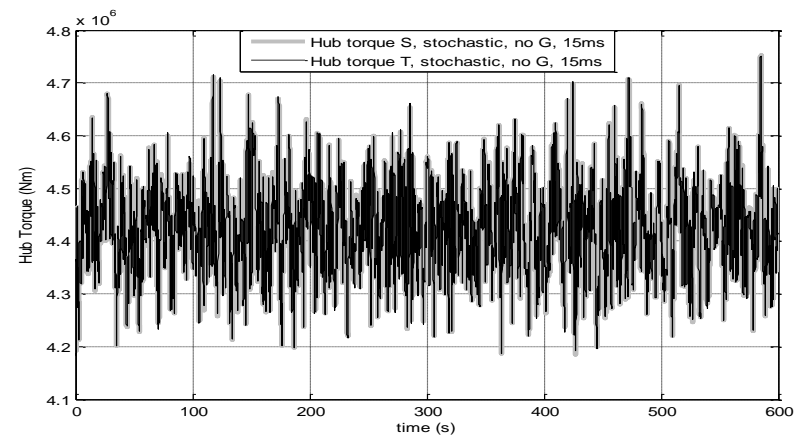


Figure 5-43. Hub torque time series comparison between simple and triple structure for the stochastic component of the wind-field with mean 15m/s

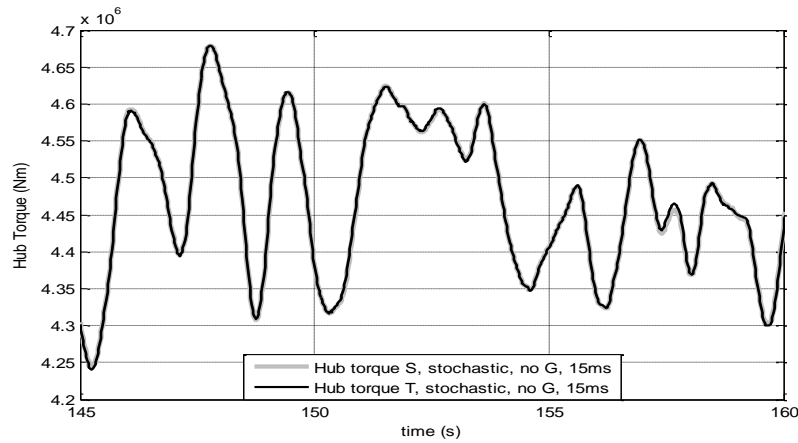


Figure 5-44. Hub torque extract time series comparison between simple and triple structure for the stochastic component of the wind-field with mean 15m/s

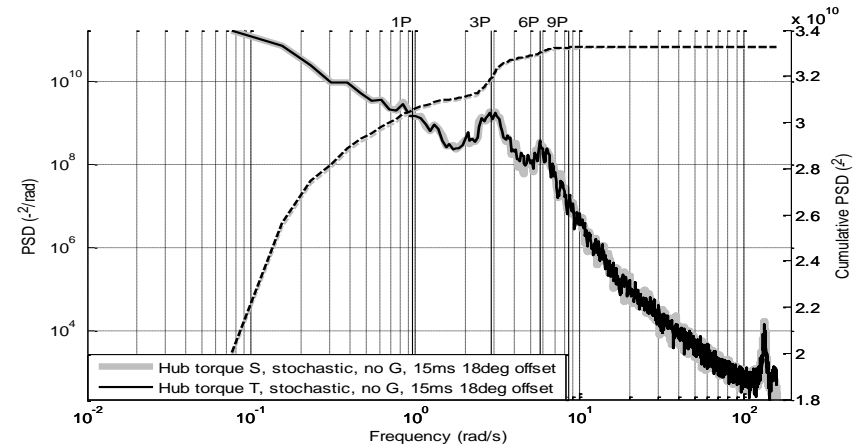


Figure 5-45. Hub torque spectrum comparison between simple and triple structure for the stochastic component of the wind-field with mean 15m/s and 18 degrees of pitch offset

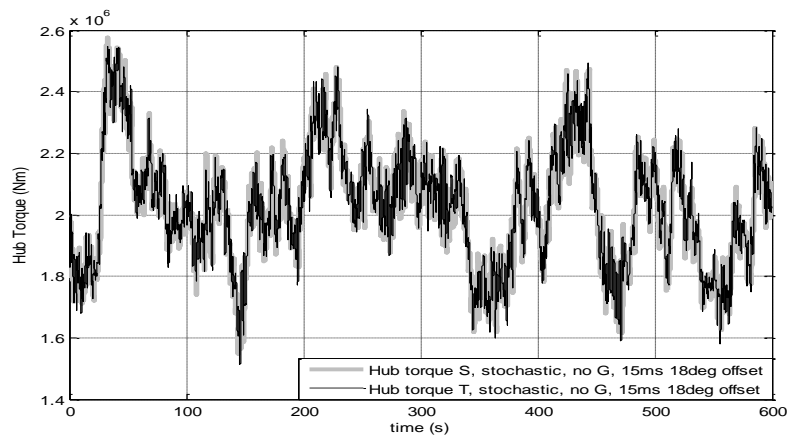


Figure 5-46. Hub torque time series comparison between simple and triple structure for the stochastic component of the wind-field with mean 15m/s and 18 degrees of pitch offset

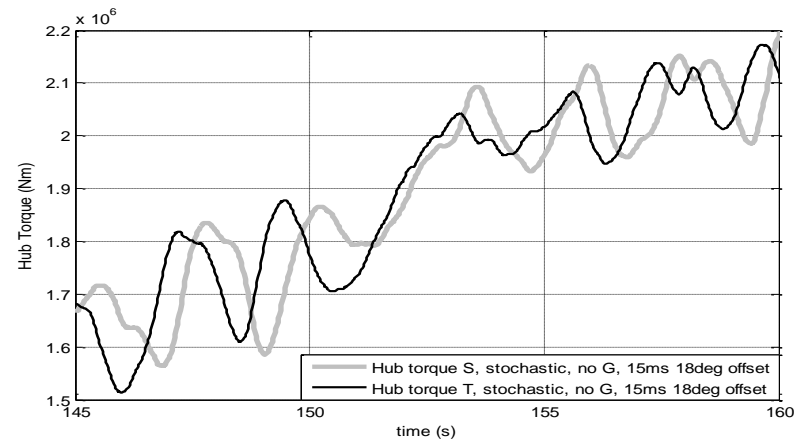


Figure 5-47. Hub torque extract time series comparison between simple and triple structure for the stochastic component of the wind-field with mean 15m/s and 18 degrees of pitch offset

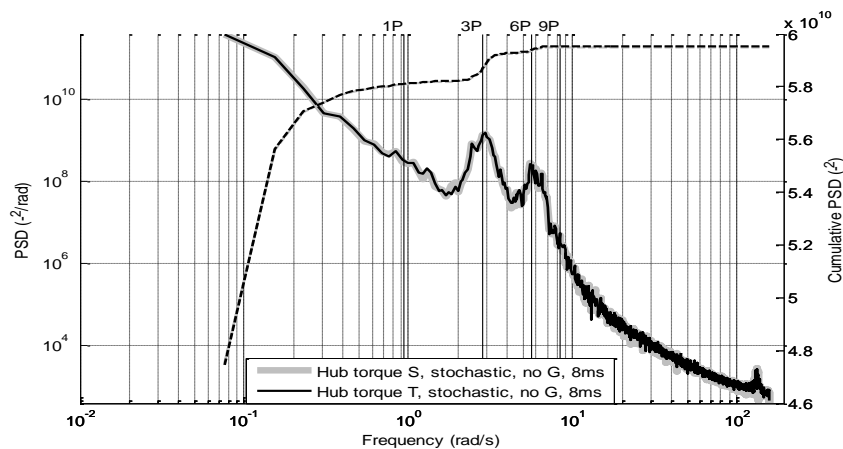


Figure 5-48. Hub torque spectrum comparison between simple and triple structure for the stochastic component of the wind-field with mean 8m/s

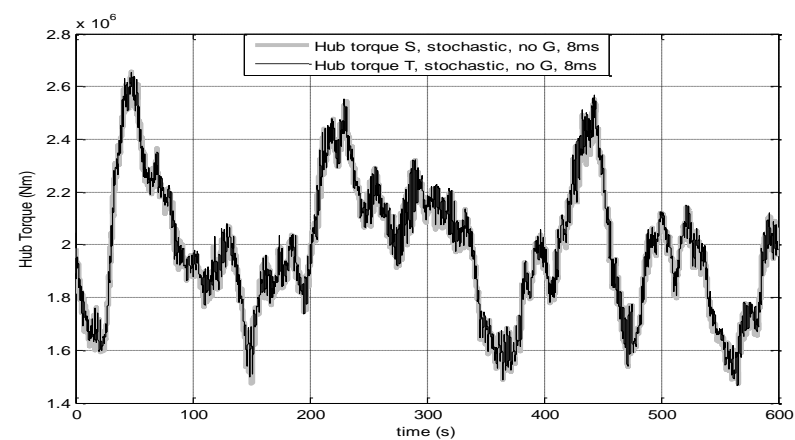


Figure 5-49. Hub torque time series comparison between simple and triple structure for the stochastic component of the wind-field with mean 8m/s

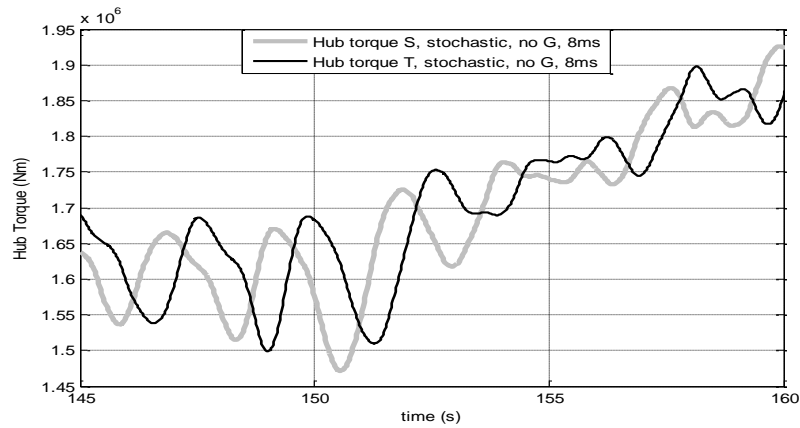


Figure 5-50. Hub torque extract time series comparison between simple and triple structure for the stochastic component of the wind-field with mean 8m/s

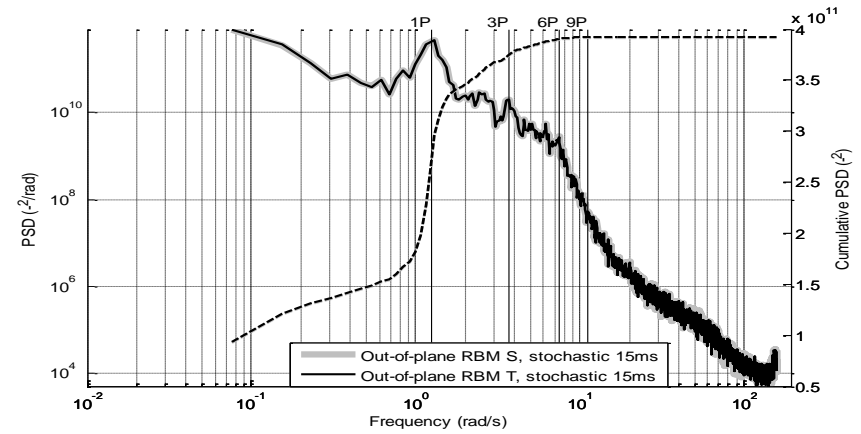


Figure 5-51. Out-of-plane blade RBM spectrum comparison between simple and triple structure for the stochastic component of the wind-field with mean 15m/s

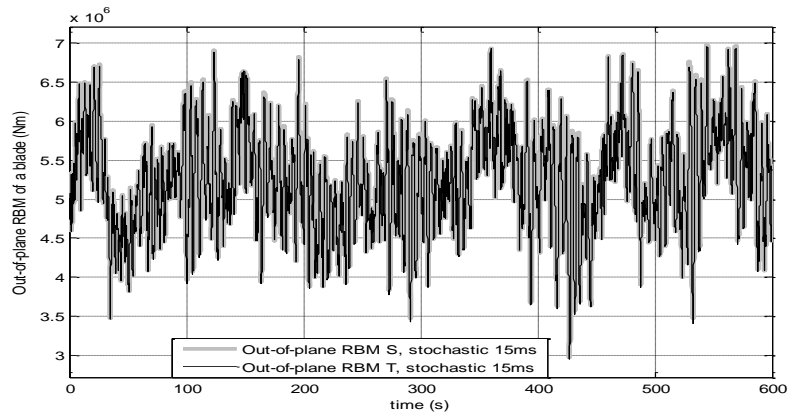


Figure 5-52. Out-of-plane blade RBM time series comparison between simple and triple structure for the stochastic component of the wind-field with mean 15m/s

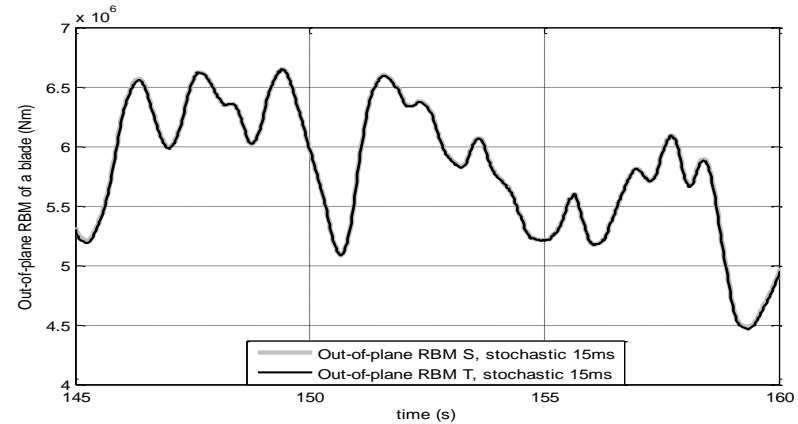


Figure 5-53. Out-of-plane blade RBM extract time series comparison between simple and triple structure for the stochastic component of the wind-field with mean 15m/s

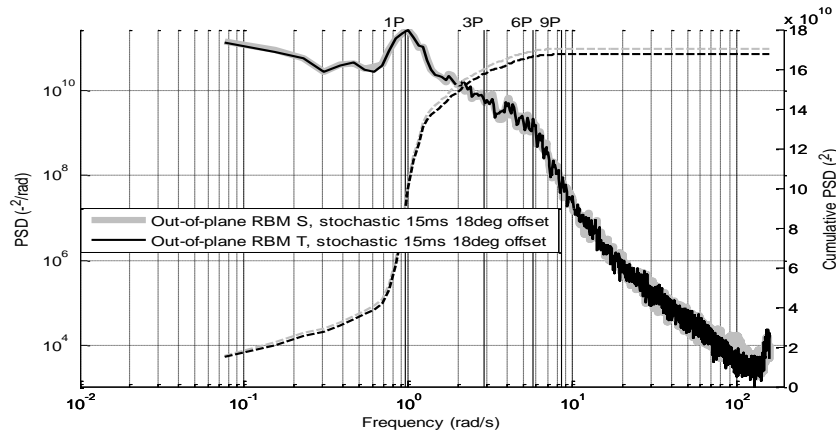


Figure 5-54. Out-of-plane blade RBM spectrum comparison between simple and triple structure for stochastic component of wind-field with mean 15m/s and 18 degrees pitch offset

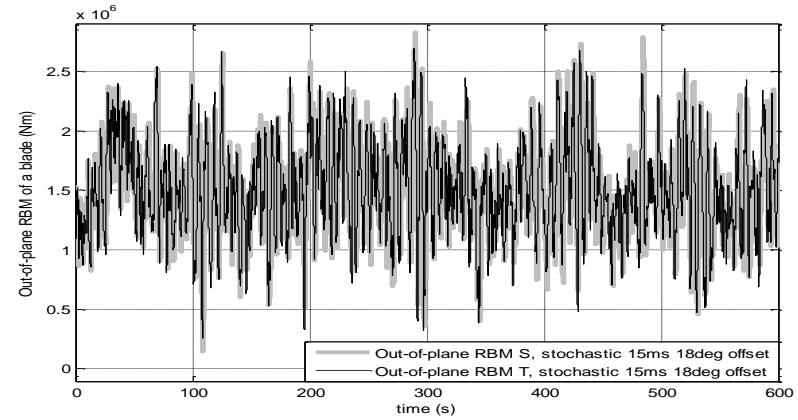


Figure 5-55. Out-of-plane blade RBM time series comparison between simple and triple structure for stochastic component of wind-field with mean 15m/s and 18 degrees pitch offset

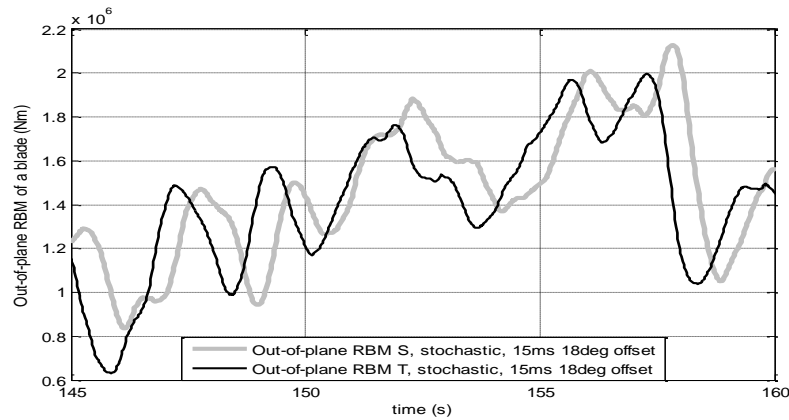


Figure 5-56. Out-of-plane blade RBM time series comparison between simple and triple structure for stochastic component of wind-field with mean 15m/s and 18 degrees pitch offset

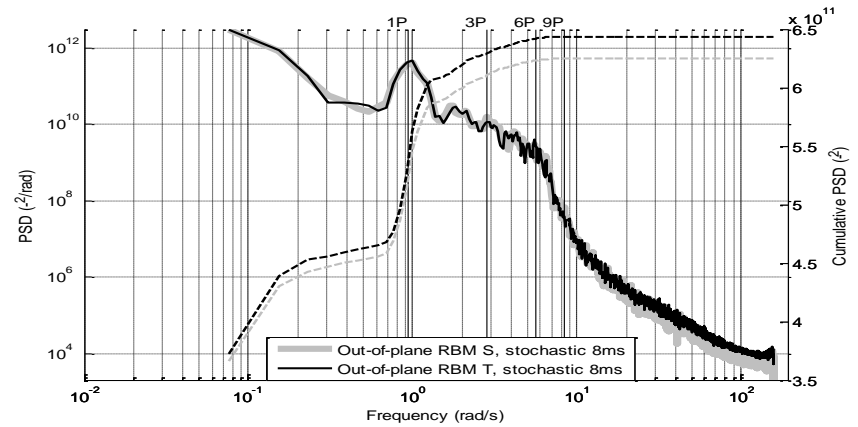


Figure 5-57. Out-of-plane blade RBM spectrum comparison between simple and triple structure for the stochastic component of the wind-field with mean 8m/s

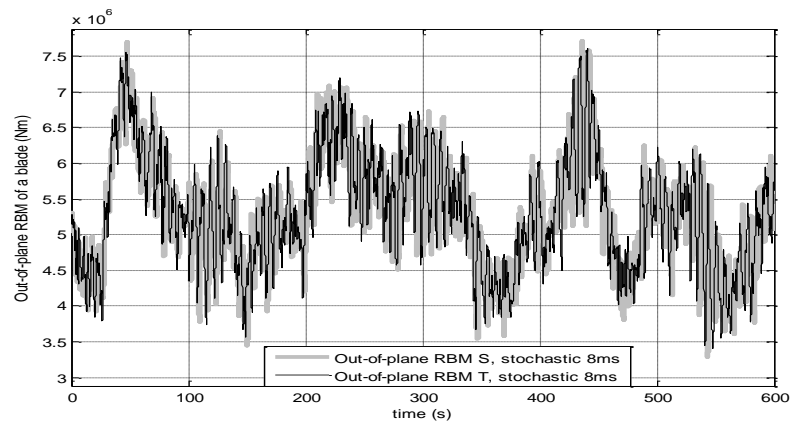


Figure 5-58. Out-of-plane blade RBM time series comparison between simple and triple structure for the stochastic component of wind-field with mean 8m/s

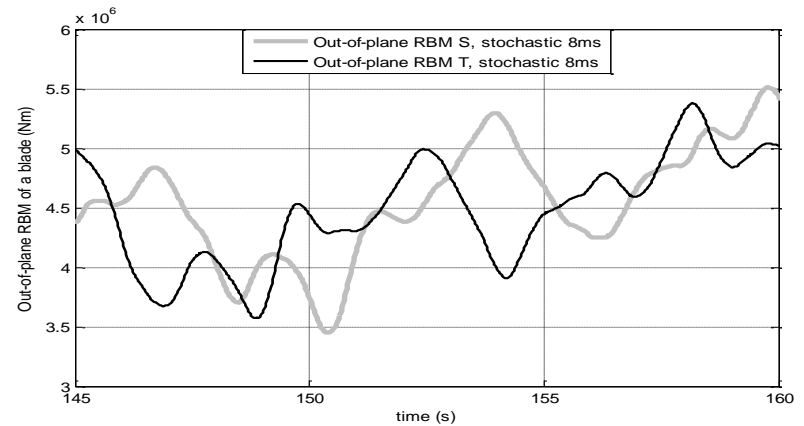


Figure 5-59. Out-of-plane blade RBM time series comparison between simple and triple structure for the stochastic component of wind-field with mean 8m/s

		Cumulative Value		
		Simple Model	Triple Model	
Stochastic Component of the Wind-field	Torque	15m/s	7.0008e+009	7.0959e+009
		15m/s + 18 deg offset	3.3215e+010	3.3269e+010
		8m/s	5.9506e+010	5.9545e+010
	Out-of-plane RBM	15m/s	3.9119e+011	3.9215e+011
		15m/s + 18 deg offset	1.704e+011	1.6758e+011
		8m/s	6.2477e+011	6.4349e+011

Table 5-9. Cumulative PSD value for hub torque and blade out-of-plane RBM for case study of 15m/s, 15m/s with 18 degree pitch offset and 8m/s for the simple and triple structure for the stochastic component of the wind. The force of gravity is not taken into account.

5.3. Deterministic Component of the Effective Wind-Field Model

In Section 2.2 of Chapter 2 the deterministic components of the wind are introduced, specifically the WS and TS effects are explicitly described in Section 2.2.3 and Section 2.2.3 respectively. In the current section, the theory for the deterministic components of the wind-field are presented, that is the WS in isolation and TS in isolation, together with the hub torque and out-of-plane RBM they induce. For the full set of the different *layer P* structures of the wind-field, including the results for the combined WS and TS, refer to Appendix D and for the full set of results for the induced forces and masses for the three cases (WS, TS and WS & TS), refer to Appendix E.

5.3.1. Wind Shear Results

The wind shear contribution to each *layer P* of the wind-field is defined as a series of WSa_{nP} and WSb_{nP} Fourier coefficients with the appropriate weighting coefficient, wc , for the induction of moments (M) and thrust (F), as seen in Figure 5-2, are expressed from manipulating (3.39) as:

$$WS a_{nP} = \frac{1}{\pi} \left(\frac{wc + 1}{R^{wc+1}} \right) V_m \int_0^{2\pi} f_{WS}(\theta) \cos(n\theta) d\theta \quad (5.82)$$

$$WS b_{nP} = \frac{1}{\pi} \left(\frac{wc + 1}{R^{wc+1}} \right) V_m \int_0^{2\pi} f_{WS}(\theta) \sin(n\theta) d\theta = 0 \quad (5.83)$$

$$f_{WS}(\theta) = \int_0^R \frac{\ln \left(\frac{h + r \cos \theta}{z_o} \right)}{\ln \left(\frac{h}{z_o} \right)} r^{wc} dr \quad (5.84)$$

where R is the radius of the WT, r , the position on the length of the blade, h , the hub height, z_o , the surface roughness length, n , an integer corresponding to the *layer P* being considered, θ , the azimuth angle and V_m , the mean wind speed.

There is room for further simplification by rendering integral (5.84) dimensionless,

$$f_{WS}(\theta) = \frac{R^{wc+1}}{wc + 1} + \frac{R^{wc+1}}{\ln\left(\frac{h}{z_o}\right)} \int_0^1 \ln\left(1 + \bar{r} \left(\frac{R}{h} \cos\theta\right)\right) \bar{r}^{wc} d\bar{r} \quad (5.85)$$

with $\bar{r} = \frac{r}{R}$

The weighting coefficient for the WS contribution to the wind-field responsible for the induction of moments is 0.65 and the coefficient used for the induction of thrust is 0. These values have been determined by deriving the wind traces from the in-plane RBM moment and thrust force from Bladed, when a constant wind with only wind shear is applied, and determining the Fourier series description of the same. The Fourier series of the theoretical equation for the wind shear phenomena is then generated. The theoretical equation has a weighting factor applied to it, the value of which is modified until the Bladed results and the theoretical description of the wind shear coincide.

In Table 5-10, the value of the $WS a_{nP}$ and $WS b_{nP}$ contributions to the wind-field for each *layer P*, for both the moments and the thrust for a wind-field with mean wind speed 15m/s, can be found¹³. These coefficients will change with the wind speed. In Table 5-11, the $WS a_{nP}$ coefficients for moments are given in generic form for *layer P*, level 0 to 6, and a selection of R/h ratios. Similarly, in Table 5-12, the $WS a_{nP}$ coefficients in generic form for forces can be found.

¹³ For this example $R = 63\text{m}$, $h = 90\text{m}$ and $z_o = 0.001$

	Moments		Forces (Thrust)	
	$WS a_{nP}$	$WS b_{nP}$	$WS a_{nP}$	$WS b_{nP}$
layer $P = 0$	0	0	0	0
layer $P = 1$	0.6222	0	0.4945	0
layer $P = 2$	-0.0880	0	-0.0640	0
layer $P = 3$	0.0182	0	0.0126	0
layer $P = 4$	-0.0045	0	-0.0030	0
layer $P = 5$	0.0012	0	0.0008	0
layer $P = 6$	-0.0004	0	-0.0002	0

Table 5-10. Fourier coefficients for the characterisation of wind shear for a 15m/s wind speed.

From Table 5-10 it can be seen that for the wind shear, the magnitude of the Fourier coefficients decreases with the increase of the *layer P* level.

From Figure 5-60 to Figure 5-63 it can be seen that the spectrum of the wind-field containing only WS with all the necessary *layer P* structures for the rotor in the simple model (inducing 0, 3 and 6P) and their time series, for the induction of the moments and thrust. Likewise for the triple structure rotor, from Figure 5-64 to Figure 5-67 it can be seen the spectrum of the wind with only WS present, for the induction of the moments and thrust, containing all the necessary *layer P* structures (inducing 0, 1, 2, 3, 4, 5 and 6P) and their time series. The spectrum in Figure 5-66, with its correspondent time series in Figure 5-67, is also used to induce the associated moments is the single blade in both models.

As expected the peaks in the spectra have the sharp and narrow profile characteristic of deterministic signals. The figures suggest that the wind for inducing moments has a slightly bigger magnitude than the one for inducing thrust. The data used in the spectrum of the wind have not been detrended.

	<i>layer P</i> = 0	<i>layer P</i> = 1	<i>layer P</i> = 2	<i>layer P</i> = 3	<i>layer P</i> = 4	<i>layer P</i> = 5	<i>layer P</i> = 6
$\frac{R}{h} = 0.60$	0	$\frac{1.65}{\pi \ln\left(\frac{h}{z_o}\right)} V_m[0.7534]$	$\frac{1.65}{\pi \ln\left(\frac{h}{z_o}\right)} V_m[-0.0884]$	$\frac{1.65}{\pi \ln\left(\frac{h}{z_o}\right)} V_m[0.0151]$	$\frac{1.65}{\pi \ln\left(\frac{h}{z_o}\right)} V_m[-0.0031]$	$\frac{1.65}{\pi \ln\left(\frac{h}{z_o}\right)} V_m[0.0007]$	$\frac{1.65}{\pi \ln\left(\frac{h}{z_o}\right)} V_m[-0.0002]$
$\frac{R}{h} = 0.65$	0	$\frac{1.65}{\pi \ln\left(\frac{h}{z_o}\right)} V_m[0.8257]$	$\frac{1.65}{\pi \ln\left(\frac{h}{z_o}\right)} V_m[-0.1065]$	$\frac{1.65}{\pi \ln\left(\frac{h}{z_o}\right)} V_m[0.0200]$	$\frac{1.65}{\pi \ln\left(\frac{h}{z_o}\right)} V_m[-0.0045]$	$\frac{1.65}{\pi \ln\left(\frac{h}{z_o}\right)} V_m[0.0011]$	$\frac{1.65}{\pi \ln\left(\frac{h}{z_o}\right)} V_m[-0.0003]$
$\frac{R}{h} = 0.70$	0	$\frac{1.65}{\pi \ln\left(\frac{h}{z_o}\right)} V_m[0.9010]$	$\frac{1.65}{\pi \ln\left(\frac{h}{z_o}\right)} V_m[-0.1274]$	$\frac{1.65}{\pi \ln\left(\frac{h}{z_o}\right)} V_m[0.0264]$	$\frac{1.65}{\pi \ln\left(\frac{h}{z_o}\right)} V_m[-0.0065]$	$\frac{1.65}{\pi \ln\left(\frac{h}{z_o}\right)} V_m[0.0018]$	$\frac{1.65}{\pi \ln\left(\frac{h}{z_o}\right)} V_m[-0.0005]$
$\frac{R}{h} = 0.75$	0	$\frac{1.65}{\pi \ln\left(\frac{h}{z_o}\right)} V_m[0.9801]$	$\frac{1.65}{\pi \ln\left(\frac{h}{z_o}\right)} V_m[-0.1515]$	$\frac{1.65}{\pi \ln\left(\frac{h}{z_o}\right)} V_m[0.0344]$	$\frac{1.65}{\pi \ln\left(\frac{h}{z_o}\right)} V_m[-0.0093]$	$\frac{1.65}{\pi \ln\left(\frac{h}{z_o}\right)} V_m[0.0028]$	$\frac{1.65}{\pi \ln\left(\frac{h}{z_o}\right)} V_m[-0.0009]$
$\frac{R}{h} = 0.80$	0	$\frac{1.65}{\pi \ln\left(\frac{h}{z_o}\right)} V_m[1.0639]$	$\frac{1.65}{\pi \ln\left(\frac{h}{z_o}\right)} V_m[-0.1797]$	$\frac{1.65}{\pi \ln\left(\frac{h}{z_o}\right)} V_m[0.0447]$	$\frac{1.65}{\pi \ln\left(\frac{h}{z_o}\right)} V_m[-0.0133]$	$\frac{1.65}{\pi \ln\left(\frac{h}{z_o}\right)} V_m[0.0044]$	$\frac{1.65}{\pi \ln\left(\frac{h}{z_o}\right)} V_m[-0.0016]$
$\frac{R}{h} = 0.85$	0	$\frac{1.65}{\pi \ln\left(\frac{h}{z_o}\right)} V_m[1.1540]$	$\frac{1.65}{\pi \ln\left(\frac{h}{z_o}\right)} V_m[-0.2131]$	$\frac{1.65}{\pi \ln\left(\frac{h}{z_o}\right)} V_m[0.0582]$	$\frac{1.65}{\pi \ln\left(\frac{h}{z_o}\right)} V_m[-0.0191]$	$\frac{1.65}{\pi \ln\left(\frac{h}{z_o}\right)} V_m[0.0070]$	$\frac{1.65}{\pi \ln\left(\frac{h}{z_o}\right)} V_m[-0.0027]$
$\frac{R}{h} = 0.90$	0	$\frac{1.65}{\pi \ln\left(\frac{h}{z_o}\right)} V_m[1.2525]$	$\frac{1.65}{\pi \ln\left(\frac{h}{z_o}\right)} V_m[-0.2538]$	$\frac{1.65}{\pi \ln\left(\frac{h}{z_o}\right)} V_m[0.0766]$	$\frac{1.65}{\pi \ln\left(\frac{h}{z_o}\right)} V_m[-0.0279]$	$\frac{1.65}{\pi \ln\left(\frac{h}{z_o}\right)} V_m[0.0113]$	$\frac{1.65}{\pi \ln\left(\frac{h}{z_o}\right)} V_m[-0.0049]$

Table 5-11. *WS* a_{nP} coefficients for moments, resolved in generic form for *layer P* from 0 to 6 and a selection of R/h ratios

	<i>layer P</i> = 0	<i>layer P</i> = 1	<i>layer P</i> = 2	<i>layer P</i> = 3	<i>layer P</i> = 4	<i>layer P</i> = 5	<i>layer P</i> = 6
$\frac{R}{h} = 0.60$	0	$\frac{1}{\pi \ln\left(\frac{h}{z_o}\right)} V_m[0.9911]$	$\frac{1}{\pi \ln\left(\frac{h}{z_o}\right)} V_m[-0.1065]$	$\frac{1}{\pi \ln\left(\frac{h}{z_o}\right)} V_m[0.0174]$	$\frac{1}{\pi \ln\left(\frac{h}{z_o}\right)} V_m[-0.0034]$	$\frac{1}{\pi \ln\left(\frac{h}{z_o}\right)} V_m[0.0007]$	$\frac{1}{\pi \ln\left(\frac{h}{z_o}\right)} V_m[-0.0002]$
$\frac{R}{h} = 0.65$	0	$\frac{wc + 1}{\pi \ln\left(\frac{h}{z_o}\right)} V_m[1.0845]$	$\frac{1}{\pi \ln\left(\frac{h}{z_o}\right)} V_m[-0.1281]$	$\frac{1}{\pi \ln\left(\frac{h}{z_o}\right)} V_m[0.0230]$	$\frac{1}{\pi \ln\left(\frac{h}{z_o}\right)} V_m[-0.0050]$	$\frac{1}{\pi \ln\left(\frac{h}{z_o}\right)} V_m[0.0012]$	$\frac{1}{\pi \ln\left(\frac{h}{z_o}\right)} V_m[-0.0003]$
$\frac{R}{h} = 0.70$	0	$\frac{wc + 1}{\pi \ln\left(\frac{h}{z_o}\right)} V_m[1.1814]$	$\frac{1}{\pi \ln\left(\frac{h}{z_o}\right)} V_m[-0.1529]$	$\frac{1}{\pi \ln\left(\frac{h}{z_o}\right)} V_m[0.0302]$	$\frac{1}{\pi \ln\left(\frac{h}{z_o}\right)} V_m[-0.0072]$	$\frac{1}{\pi \ln\left(\frac{h}{z_o}\right)} V_m[0.0019]$	$\frac{1}{\pi \ln\left(\frac{h}{z_o}\right)} V_m[-0.0006]$
$\frac{R}{h} = 0.75$	0	$\frac{1}{\pi \ln\left(\frac{h}{z_o}\right)} V_m[1.2826]$	$\frac{1}{\pi \ln\left(\frac{h}{z_o}\right)} V_m[-0.1813]$	$\frac{1}{\pi \ln\left(\frac{h}{z_o}\right)} V_m[0.0392]$	$\frac{1}{\pi \ln\left(\frac{h}{z_o}\right)} V_m[-0.0103]$	$\frac{1}{\pi \ln\left(\frac{h}{z_o}\right)} V_m[0.0030]$	$\frac{1}{\pi \ln\left(\frac{h}{z_o}\right)} V_m[-0.0010]$
$\frac{R}{h} = 0.80$	0	$\frac{1}{\pi \ln\left(\frac{h}{z_o}\right)} V_m[1.3890]$	$\frac{1}{\pi \ln\left(\frac{h}{z_o}\right)} V_m[-0.2144]$	$\frac{1}{\pi \ln\left(\frac{h}{z_o}\right)} V_m[0.0509]$	$\frac{1}{\pi \ln\left(\frac{h}{z_o}\right)} V_m[-0.0147]$	$\frac{1}{\pi \ln\left(\frac{h}{z_o}\right)} V_m[0.0048]$	$\frac{1}{\pi \ln\left(\frac{h}{z_o}\right)} V_m[-0.0017]$
$\frac{R}{h} = 0.85$	0	$\frac{1}{\pi \ln\left(\frac{h}{z_o}\right)} V_m[1.5023]$	$\frac{1}{\pi \ln\left(\frac{h}{z_o}\right)} V_m[-0.2532]$	$\frac{1}{\pi \ln\left(\frac{h}{z_o}\right)} V_m[0.0660]$	$\frac{1}{\pi \ln\left(\frac{h}{z_o}\right)} V_m[-0.0210]$	$\frac{1}{\pi \ln\left(\frac{h}{z_o}\right)} V_m[0.0075]$	$\frac{1}{\pi \ln\left(\frac{h}{z_o}\right)} V_m[-0.0029]$
$\frac{R}{h} = 0.90$	0	$\frac{1}{\pi \ln\left(\frac{h}{z_o}\right)} V_m[1.6249]$	$\frac{1}{\pi \ln\left(\frac{h}{z_o}\right)} V_m[-0.3001]$	$\frac{1}{\pi \ln\left(\frac{h}{z_o}\right)} V_m[0.0864]$	$\frac{1}{\pi \ln\left(\frac{h}{z_o}\right)} V_m[-0.0305]$	$\frac{1}{\pi \ln\left(\frac{h}{z_o}\right)} V_m[0.0122]$	$\frac{1}{\pi \ln\left(\frac{h}{z_o}\right)} V_m[-0.0053]$

Table 5-12. *WS a_{nP}* coefficients for forces, resolved in generic form for *layer P* from 0 to 6 and a selection of R/h ratios

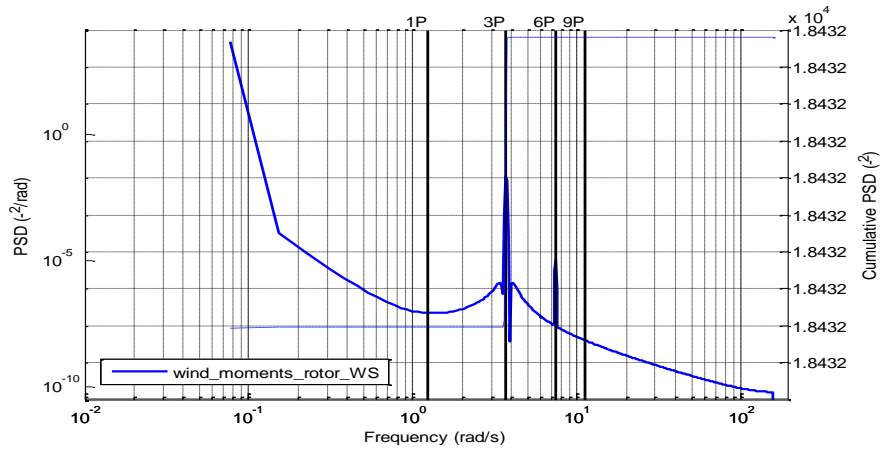


Figure 5-60. Spectrum of the deterministic component of wind-field WS for inducing moments at the rotor by the simple model

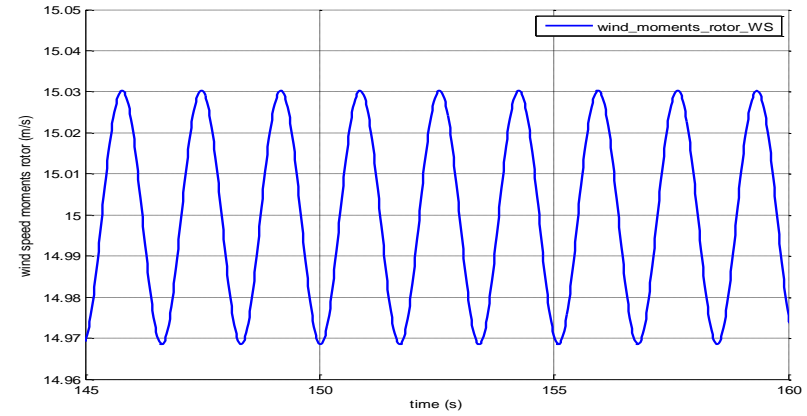


Figure 5-61. Time series of the deterministic component of wind-field WS for inducing moments at the rotor by the simple model

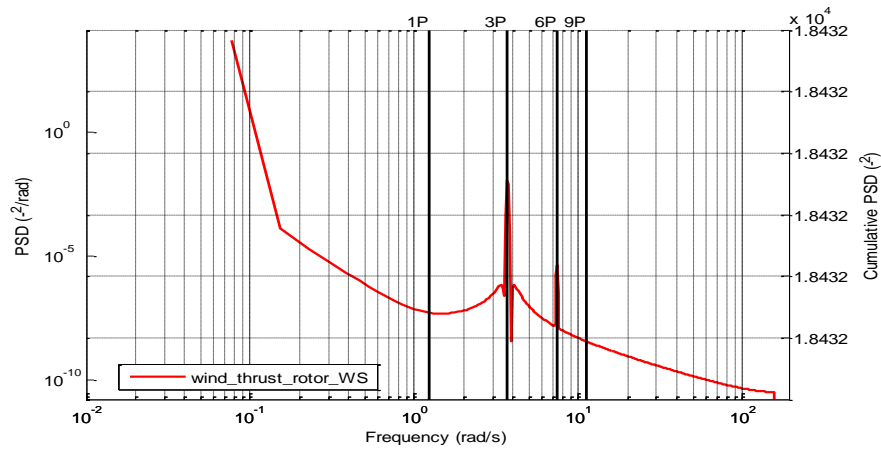


Figure 5-62. Spectrum of the deterministic component of wind-field WS for inducing thrust at the rotor by the simple model

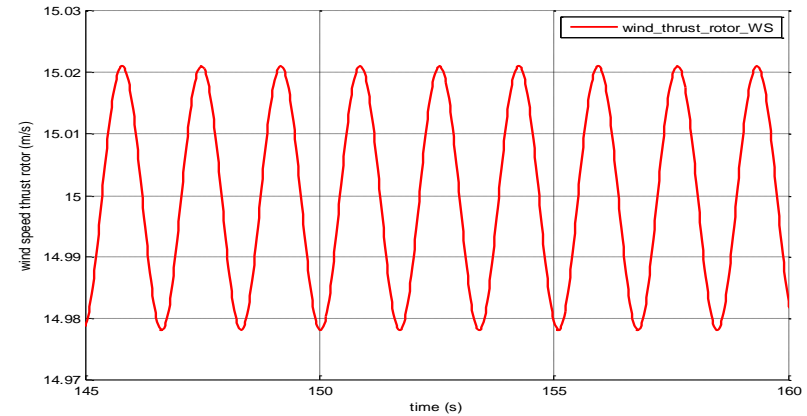


Figure 5-63. Time series of the deterministic component of wind-field WS for inducing thrust at the rotor by the simple model

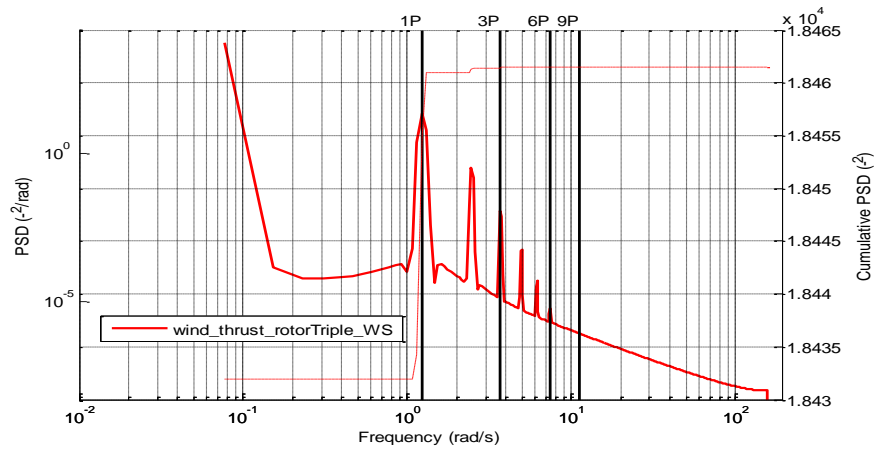


Figure 5-64. Spectrum for the deterministic component of wind-field WS used for inducing thrust at the rotor by triple model

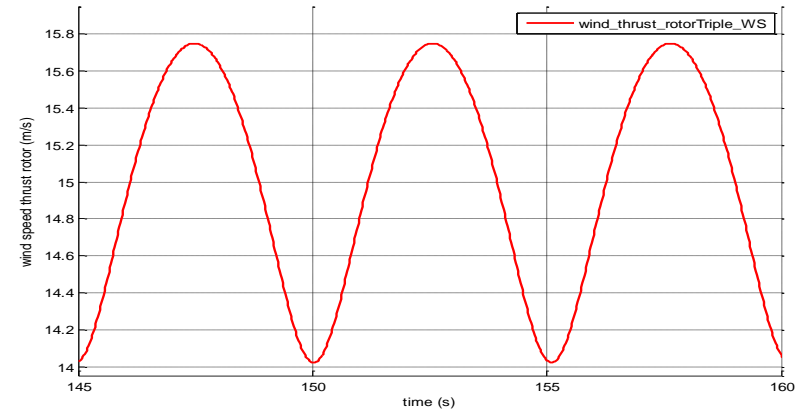


Figure 5-65. Time series for the deterministic component of wind-field WS used for inducing thrust at the rotor by triple model

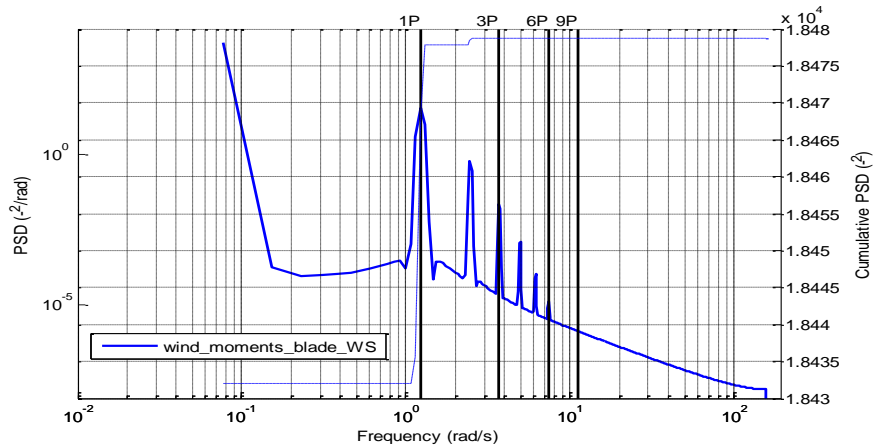


Figure 5-66. Spectrum for deterministic component of wind-field WS used for inducing moments at a single blade by simple and triple model. Also used for inducing moments at the rotor by triple model

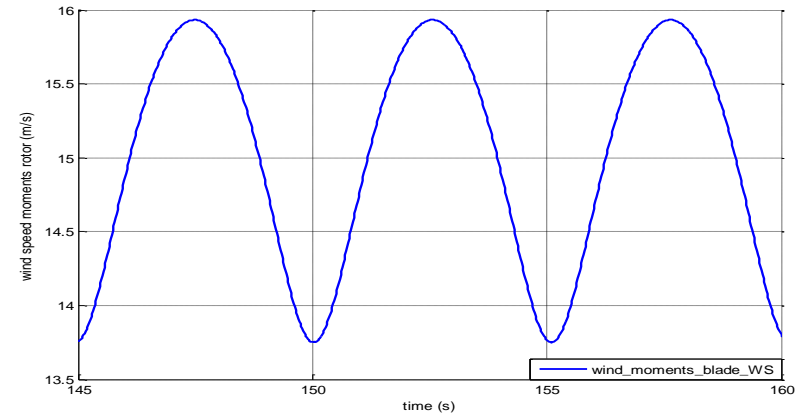


Figure 5-67. Time series for deterministic component of wind-field WS used for inducing moments at a single blade by simple and triple model. Also used for inducing moments at the rotor by triple model

Similarly to the stochastic component in Section 5.2.2, the results for the in-plane hub torque and out-of-plane RBM of a blade are analysed with only the presence of the deterministic component WS for a 15m/s wind, 15m/s wind with 18 deg offset and a 8m/s wind, all of them with a 10% TI. The results for the in-plane RBM of the blade, the edgewise moment of the blade, M_e , the flapwise moment of the blade, M_f , and the thrust force can be found in Appendix E.

When looking at the results for the in-plane hub torque, which is the moment for which Separability applies, see Figure 5-68 to Figure 5-69 for the 15m/s case, Figure 5-70 to Figure 5-71 for the 15m/s with 18 degrees of pitch offset case and Figure 5-72 to Figure 5-73 for the 8mm/s case, leakage can clearly be seen in the spectrum of the three cases, especially for the 15m/s with 18 degree offset and 8m/s cases, in the form of the presence of extra spectral peaks. The presence of leakage is also clearly seen in Table 5-13. For the time series of the 15m/s and 18 degree offset cases, a difference in the hub torque mean can be observed.

The presence of leakage in the hub torque even at wind speeds in the above rated region is significant, perhaps, not in magnitude but in its existence *per se*. It would seem to raise a question over the region of validity of Separability. The hub torque is effectively the summation of the in-plane RBM of each one of the three blades of the WT (results for which can be found in Appendix E), which leads to the cancellation by symmetry of all the nP peaks but the 3P and 6P.

When looking in detail into the spectra of the in-plane RBM of the blade in Appendix E, some leakage is seen at the 3P peak, with an indisputable dominant 1P. The result of adding the in-plane RBM of the blades together is that all of the sudden, the 3P and 6P peaks are the only surviving peaks, the 1P peak disappears, and that only the small contribution from 1P to 3P and even smaller contribution to 6P, remain. These differences are now important. As such, due to the relative size of the 3P to the 1P, the hub torque is quite sensitive to even weak leakage from 1P into the 3P peak in the in-plane RBM.

The presence of some weak non-linearity induces some leakage, but because of the shape and magnitude of the peaks (of 10^{10} in the in-plane RBM and 10^7 in the hub torque), the leakage present in the in-plane RBM is clearly visible but is small and does not have implications for the validity of Separability. In other words, the leakage seen in the hub torque in Figure 5-68, Figure 5-70 and Figure 5-72, stems from 3P and 6P, mainly 3P, in the in-plane RBM

components contributing to hub torque, see Appendix E. In addition, the numbers in Table 5-13 are the square of the amplitude, by square rooting them the impact of the differences decrease significantly.

On the other hand, for the out-of-plane RBM of the blade, the 1P is not so dominant. Looking at Figure 5-74 to Figure 5-75 for the 15m/s case, Figure 5-76 to Figure 5-77 for the 15m/s with 18 degrees of pitch offset and Figure 5-78 to Figure 5-79 for the 8m/s case, the match between the triple and simple model is remarkably close and no significant differences can be appreciated.

Furthermore, it should be observed that for both hub torque and out-of-plane RBM, there is a steeply decreasing trend, for the energy involved in the spectrum, representing the effect of the WS in higher frequencies. The data used in the spectrum of the moments and forces have been detrended.

After analysis of the results regarding the deterministic component WS of the wind-field, including the results present in Appendix E, it can be stated that overall leakage is observed, especially at the rotor. However, this leakage is not due to shortcoming in the Separability property. As a conclusion, the simple model would not suffice to induce moments and forces as far as the WS component of the wind-field above is concerned.

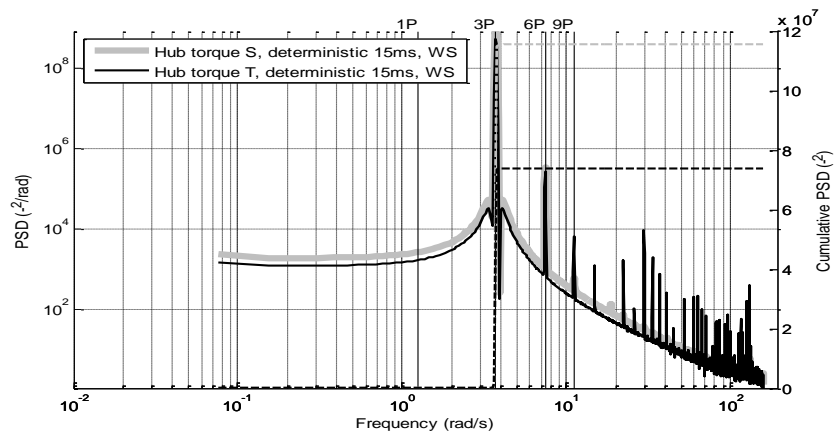


Figure 5-68. Hub torque spectrum comparison between simple and triple structure for the deterministic component of wind-field WS, with mean 15m/s

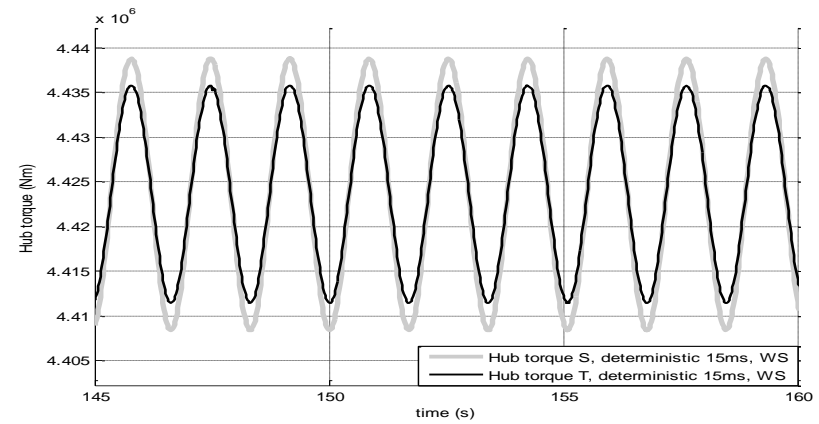


Figure 5-69. Hub torque time series comparison between simple and triple structure for the deterministic component of wind-field WS, with mean 15m/s

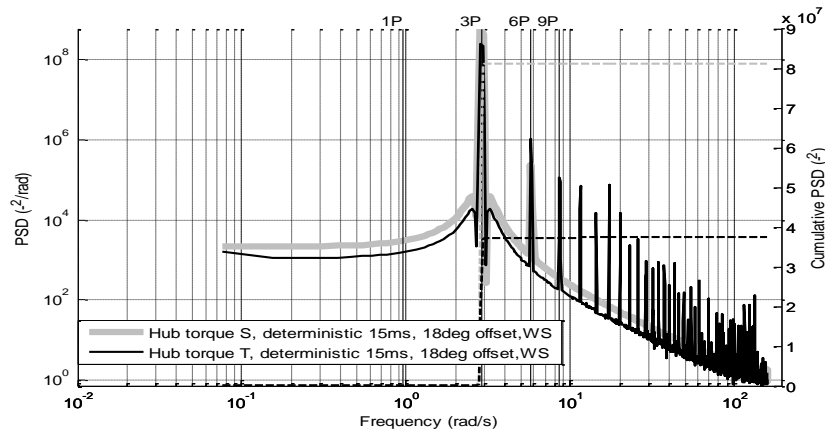


Figure 5-70. Hub torque spectrum comparison between simple and triple structure for the deterministic component of wind-field WS, with mean 15m/s and 18 degrees of pitch offset

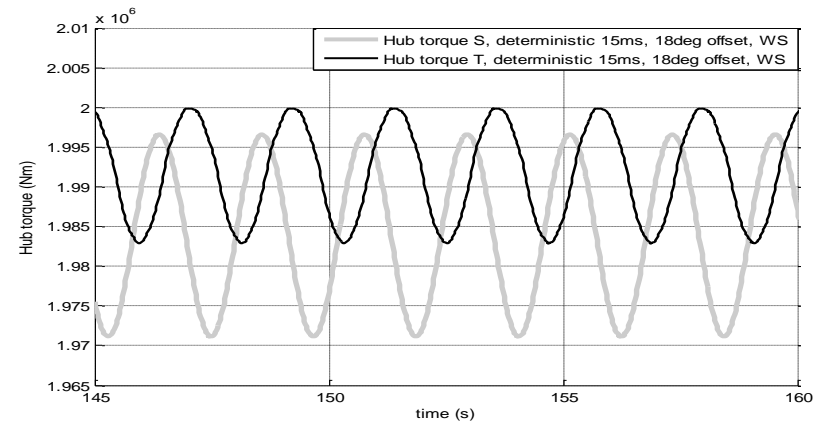


Figure 5-71. Hub torque time series comparison between simple and triple structure for the deterministic component of wind-field WS, with mean 15m/s and 18 degrees of pitch offset

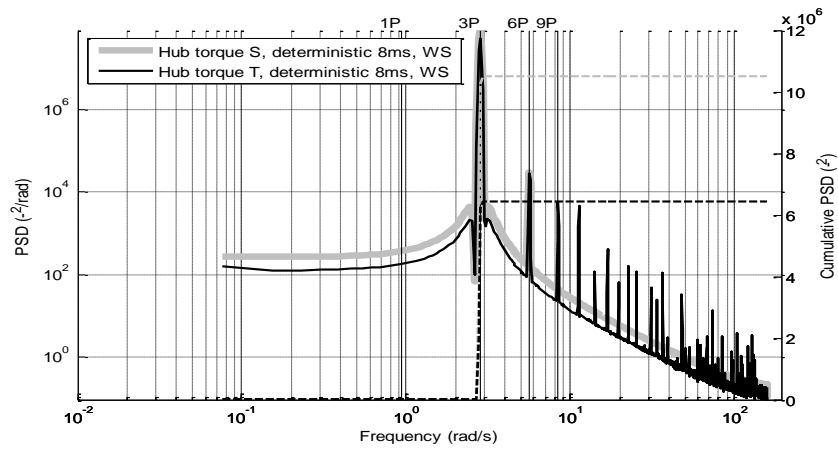


Figure 5-72. Hub torque spectrum comparison between simple and triple structure for the deterministic component of wind-field WS, with mean 8m/s

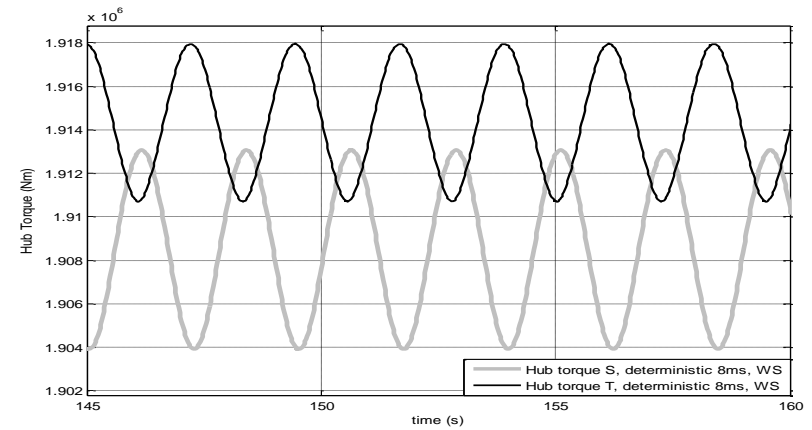


Figure 5-73. Hub torque time series comparison between simple and triple structure for the deterministic component of wind-field WS, mean 8m/s

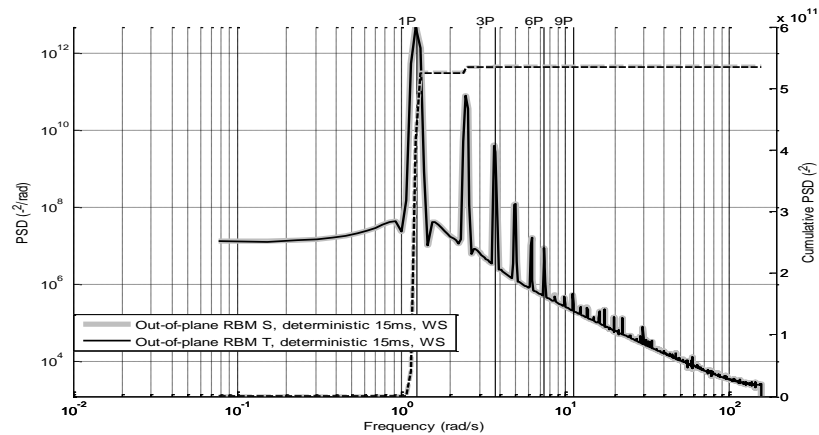


Figure 5-74. Out-of-plane blade RBM spectrum comparison between simple and triple structure for the deterministic component of wind-field WS, with mean 15m/s

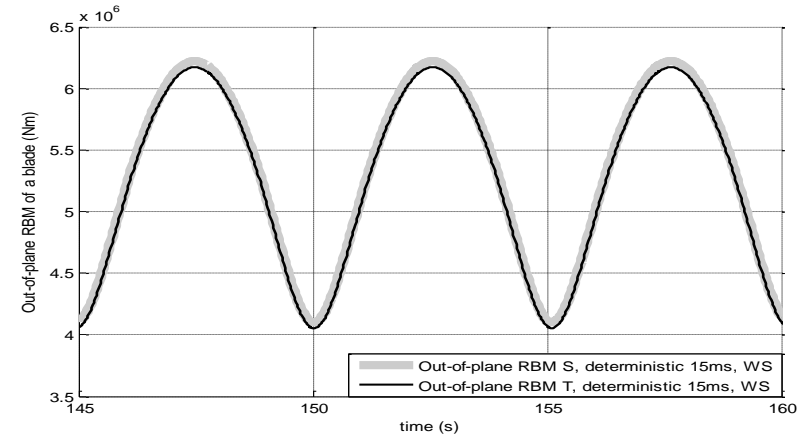


Figure 5-75. Out-of-plane blade RBM time series comparison between simple and triple structure for the deterministic component of wind-field WS, with mean 15m/s

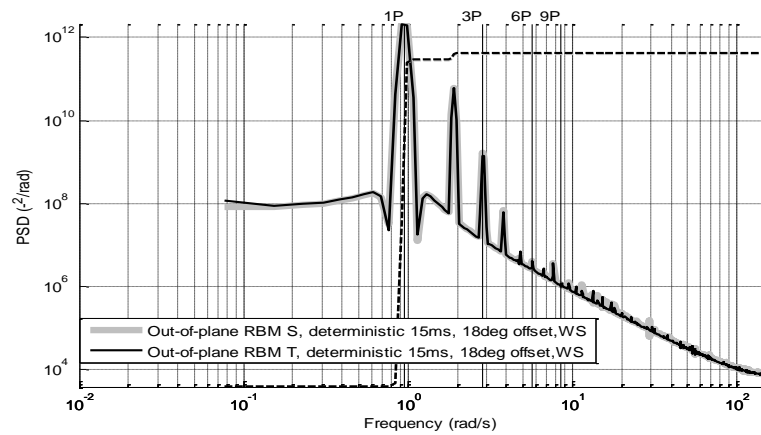


Figure 5-76. Out-of-plane blade RBM spectrum comparison between simple and triple structure for the deterministic component of wind-field WS, with mean 15m/s and 18 degrees of pitch offset

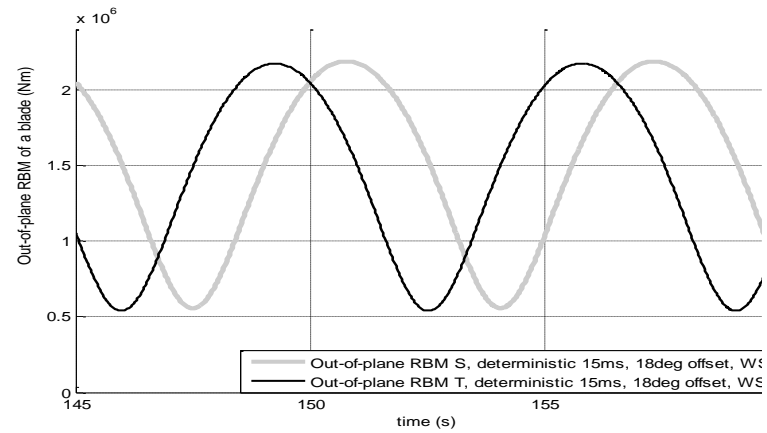


Figure 5-77. Out-of-plane blade RBM time series comparison between simple and triple structure for the deterministic component of wind-field WS, with mean 15m/s and 18 degrees of pitch offset

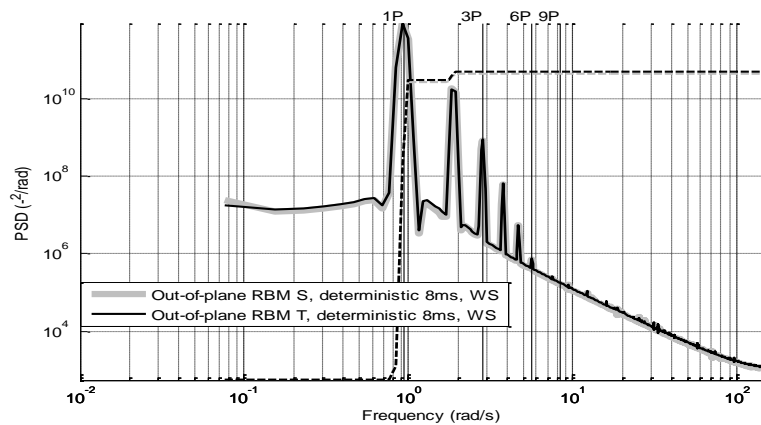


Figure 5-78. Out-of-plane blade RBM spectrum comparison between simple and triple structure for the deterministic component of wind-field WS, with mean 8m/s

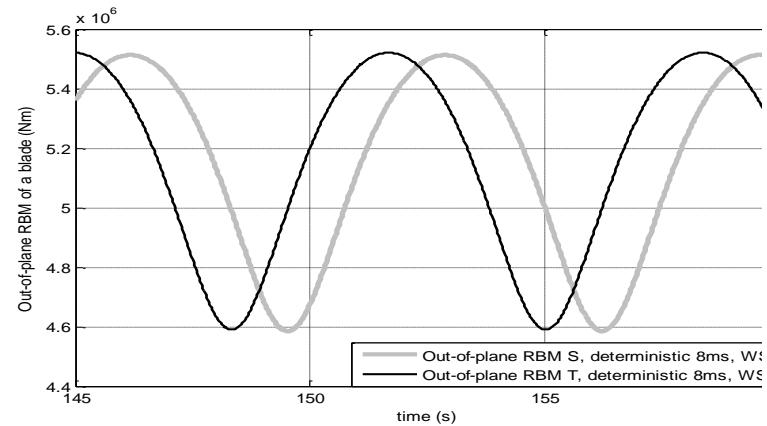


Figure 5-79. Out-of-plane blade RBM time series comparison between simple and triple structure for the deterministic component of wind-field WS, with mean 8m/s

			Cumulative Value	
			Simple Model	Triple Model
WS	Torque	15m/s	1.155e+008	7.3829e+007
		15m/s + 18 deg offset	8.1113e+007	3.7387e+007
		8m/s	1.0508e+007	6.4392e+006
	Out-of-plane RBM	15m/s	5.3589e+011	5.3473e+011
		15m/s + 18 deg offset	3.2097e+011	3.2211e+011
		8m/s	1.0306e+011	1.0375e+011

Table 5-13. Cumulative PSD value for hub torque and blade out-of-plane RBM for case study of 15m/s, 15m/s with 18 degree pitch offset and 8m/s for the simple and triple structure for the deterministic component of the wind WS.

5.3.2. Tower Shadow Results

The tower shadow contribution to each *layer P* of the wind-field has been defined as a series of $TS a_{nP}$ and $TS b_{nP}$ Fourier coefficients as seen in Figure 5-2. The Fourier series has the appropriate weighting coefficient, wc , for the induction of moments (M) and thrust (F), as necessary. It is identified that the tower shadow is significantly impacted on by the shape of the tower when its diameter, R_T , narrows towards the hub. To characterise this variation with respect to the position on the length of the blade, r , a linear representation is found to suffice¹⁴ in this case. The tower shadow equation, (3.12), is accordingly modified as follows,

$$TS a_{nP} = \frac{1}{\pi} \left(\frac{wc + 1}{R^{wc+1}} \right) V_m \int_{\pi/2}^{3\pi/2} f_{TS}(\theta) \cos(n\theta) \quad (5.86)$$

$$TS b_{nP} = \frac{1}{\pi} \left(\frac{wc + 1}{R^{wc+1}} \right) V_m \int_{\pi/2}^{3\pi/2} f_{TS}(\theta) \sin(n\theta) \quad (5.87)$$

$$f_{TS}(\theta) = \int_0^R \frac{(ar + b)^2 (r^2 \sin^2 \theta - X^2)}{(r^2 \sin^2 \theta + X^2)^2} r^{wc} dr \quad (5.88)$$

¹⁴ For the specific turbine used, this variation has the values: $R_T = ar + b = 0.013197r + 1.8295$

where R is the radius of the WT, r , the position on the length of the blade, n , an integer corresponding to the *layer P* level, wc , the appropriate weighting coefficient for the induction of moments and thrust, X , the overhang, a , the slope of the linear description of the variation of R_T , b , the constant of the linear description of the variation of R_T and θ , the azimuth angle.

Simplifying to make the integral (5.88) dimensionless,

$$f_{TS}(\theta) = R^{wc+1} \int_0^1 \frac{\left(a\bar{r} + \frac{b}{R}\right)^2 \left(\bar{r}^2 \sin^2 \theta - \frac{X^2}{R^2}\right)}{\left(\bar{r}^2 \sin^2 \theta + \frac{X^2}{R^2}\right)^2} \bar{r}^{wc} d\bar{r} = \quad (5.89)$$

$$= R^{wc+1} a^2 \int_0^1 \bar{r}^2 \frac{\left(\bar{r}^2 \sin^2 \theta - \frac{X^2}{R^2}\right)}{\left(\bar{r}^2 \sin^2 \theta + \frac{X^2}{R^2}\right)^2} \bar{r}^{wc} d\bar{r} + \quad (5.90)$$

$$+ R^{wc} 2ab \int_0^1 \bar{r} \frac{\left(\bar{r}^2 \sin^2 \theta - \frac{X^2}{R^2}\right)}{\left(\bar{r}^2 \sin^2 \theta + \frac{X^2}{R^2}\right)^2} \bar{r}^{wc} d\bar{r} +$$

$$+ \frac{1}{R} b^2 \int_0^1 \frac{\left(\bar{r}^2 \sin^2 \theta - \frac{X^2}{R^2}\right)}{\left(\bar{r}^2 \sin^2 \theta + \frac{X^2}{R^2}\right)^2} \bar{r}^{wc} d\bar{r}$$

with $\bar{r} = \frac{r}{R}$.

The weighting coefficient for the TS contribution to the wind-field is 3 for moments and 2 for thrust. These values have been determined by deriving the wind traces from the in-plane RBM moment and thrust force from Bladed when a constant wind with only tower shadow is applied and determining the Fourier series description of the same. The Fourier series of the theoretical equation for the tower shadow phenomena is then generated.

The theoretical equation has a weighting factor, wc , applied to it, as seen in (5.86), (5.87) and (5.88), the value of which is modified until the Bladed results and the theoretical description of the tower shadow coincide.

In Table 5-14, the value of the $TS a_{nP}$ and $TS b_{nP}$ contributions to the wind-field for each *layer P*, for both the moments and the thrust for a wind-field with mean wind speed 15m/s can be found.

	Moments		Forces (Thrust)	
	$TS a_{nP}$	$TS b_{nP}$	$TS a_{nP}$	$TS b_{nP}$
<i>layer P = 0</i>	0	0	0	0
<i>layer P = 1</i>	0.0268	0	0.0336	0
<i>layer P = 2</i>	-0.0695	0	-0.0812	0
<i>layer P = 3</i>	0.0981	0	0.1112	0
<i>layer P = 4</i>	-0.1065	0	-0.1173	0
<i>layer P = 5</i>	0.1132	0	0.1217	0
<i>layer P = 6</i>	-0.1260	0	-0.1337	0

Table 5-14. Fourier coefficients for the characterisation of tower shadow.

From Figure 5-80 to Figure 5-83, the spectrum and time series of the wind-field for the simple model with only TS present can be found. It contains all the necessary *layer P* structures for the rotor in the simple model to induce the correct moments and thrust (inducing 0, 3 and 6P peaks only). Likewise for the triple structure rotor, from Figure 5-84 to Figure 5-87, the spectrum and time series of the wind-field for the induction of the moments and thrust, containing all the necessary *layer P* structures (inducing 0, 1, 2, 3, 4, 5 and 6P peaks) can be seen. The spectrum in Figure 5-86 with its corresponding time series in Figure 5-87 is also used to induce the associated moments on the single blade in both models.

As expected, the peaks in the spectra have the sharp and narrow profile characteristic of deterministic signals. It would seem that the signal for the induction of moments has a slightly bigger magnitude than the one for the induction of thrust. The data used in the spectrum of the wind have not been detrended.

	<i>layer P</i> = 0	<i>layer P</i> = 1	<i>layer P</i> = 2	<i>layer P</i> = 3	<i>layer P</i> = 4	<i>layer P</i> = 5	<i>layer P</i> = 6
$\frac{X}{R} = 0.13$	0	$\frac{4}{\pi} V_m a^2 [0.4999]$	$\frac{4}{\pi} V_m a^2 [-1.53940]$	$\frac{4}{\pi} V_m a^2 [2.4173]$	$\frac{4}{\pi} V_m a^2 [-2.9882]$	$\frac{4}{\pi} V_m a^2 [3.5901]$	$\frac{4}{\pi} V_m a^2 [-4.3605]$
$\frac{X}{R} = 0.11$	0	$\frac{4}{\pi} V_m a^2 [0.4991]$	$\frac{4}{\pi} V_m a^2 [-1.4767]$	$\frac{4}{\pi} V_m a^2 [2.2585]$	$\frac{4}{\pi} V_m a^2 [-2.7028]$	$\frac{4}{\pi} V_m a^2 [3.1491]$	$\frac{4}{\pi} V_m a^2 [-3.73670]$
$\frac{X}{R} = 0.09$	0	$\frac{4}{\pi} V_m a^2 [0.4975]$	$\frac{4}{\pi} V_m a^2 [-1.4146]$	$\frac{4}{\pi} V_m a^2 [2.1084]$	$\frac{4}{\pi} V_m a^2 [-2.4439]$	$\frac{4}{\pi} V_m a^2 [2.7621]$	$\frac{4}{\pi} V_m a^2 [-3.2052]$
$\frac{X}{R} = 0.07$	0	$\frac{4}{\pi} V_m a^2 [0.4952]$	$\frac{4}{\pi} V_m a^2 [-1.3533]$	$\frac{4}{\pi} V_m a^2 [1.9667]$	$\frac{4}{\pi} V_m a^2 [-2.2091]$	$\frac{4}{\pi} V_m a^2 [2.4225]$	$\frac{4}{\pi} V_m a^2 [-2.7515]$
$\frac{X}{R} = 0.05$	0	$\frac{4}{\pi} V_m a^2 [0.4922]$	$\frac{4}{\pi} V_m a^2 [-1.2930]$	$\frac{4}{\pi} V_m a^2 [1.8332]$	$\frac{4}{\pi} V_m a^2 [-1.9963]$	$\frac{4}{\pi} V_m a^2 [2.1244]$	$\frac{4}{\pi} V_m a^2 [-2.3637]$
$\frac{X}{R} = 0.03$	0	$\frac{4}{\pi} V_m a^2 [0.4885]$	$\frac{4}{\pi} V_m a^2 [-1.2340]$	$\frac{4}{\pi} V_m a^2 [1.7076]$	$\frac{4}{\pi} V_m a^2 [-1.8037]$	$\frac{4}{\pi} V_m a^2 [1.8628]$	$\frac{4}{\pi} V_m a^2 [-2.0318]$
$\frac{X}{R} = 0.01$	0	$\frac{4}{\pi} V_m a^2 [0.4843]$	$\frac{4}{\pi} V_m a^2 [-1.1764]$	$\frac{4}{\pi} V_m a^2 [1.5897]$	$\frac{4}{\pi} V_m a^2 [-1.6293]$	$\frac{4}{\pi} V_m a^2 [1.6333]$	$\frac{4}{\pi} V_m a^2 [-1.7477]$

Table 5-15. First integral term of $TS a_{nP}$ coefficient for moments, resolved in generic form for *layer P* from 0 to 6 and a selection of R/h ratios

	<i>layer P</i> = 0	<i>layer P</i> = 1	<i>layer P</i> = 2	<i>layer P</i> = 3	<i>layer P</i> = 4	<i>layer P</i> = 5	<i>layer P</i> = 6
$\frac{X}{R} = 0.13$	0	$\frac{4}{\pi R} V_m 2ab [0.6665]$	$\frac{4}{\pi R} V_m 2ab [-2.0473]$	$\frac{4}{\pi R} V_m 2ab [3.2099]$	$\frac{4}{\pi R} V_m 2ab [-3.9604]$	$\frac{4}{\pi R} V_m 2ab [4.7498]$	$\frac{4}{\pi R} V_m 2ab [-5.7614]$
$\frac{X}{R} = 0.11$	0	$\frac{4}{\pi R} V_m 2ab [0.6650]$	$\frac{4}{\pi R} V_m 2ab [-1.9538]$	$\frac{4}{\pi R} V_m 2ab [2.9755]$	$\frac{4}{\pi R} V_m 2ab [-3.5433]$	$\frac{4}{\pi R} V_m 2ab [4.1098]$	$\frac{4}{\pi R} V_m 2ab [-4.8615]$
$\frac{X}{R} = 0.09$	0	$\frac{4}{\pi R} V_m 2ab [0.6620]$	$\frac{4}{\pi R} V_m 2ab [-1.8617]$	$\frac{4}{\pi R} V_m 2ab [2.7573]$	$\frac{4}{\pi R} V_m 2ab [-3.1728]$	$\frac{4}{\pi R} V_m 2ab [3.5624]$	$\frac{4}{\pi R} V_m 2ab [-4.1160]$
$\frac{X}{R} = 0.07$	0	$\frac{4}{\pi R} V_m 2ab [0.6579]$	$\frac{4}{\pi R} V_m 2ab [-1.7717]$	$\frac{4}{\pi R} V_m 2ab [2.5542]$	$\frac{4}{\pi R} V_m 2ab [-2.8427]$	$\frac{4}{\pi R} V_m 2ab [3.0917]$	$\frac{4}{\pi R} V_m 2ab [-3.4936]$
$\frac{X}{R} = 0.05$	0	$\frac{4}{\pi R} V_m 2ab [0.6526]$	$\frac{4}{\pi R} V_m 2ab [-1.6841]$	$\frac{4}{\pi R} V_m 2ab [2.3653]$	$\frac{1.65}{\pi R} V_m 2ab [-2.5483]$	$\frac{4}{\pi R} V_m 2ab [2.6858]$	$\frac{4}{\pi R} V_m 2ab [-2.9714]$
$\frac{X}{R} = 0.03$	0	$\frac{4}{\pi R} V_m 2ab [0.6464]$	$\frac{4}{\pi R} V_m 2ab [-1.5991]$	$\frac{4}{\pi R} V_m 2ab [2.1897]$	$\frac{4}{\pi R} V_m 2ab [-2.2854]$	$\frac{4}{\pi R} V_m 2ab [2.3350]$	$\frac{4}{\pi R} V_m 2ab [-2.5316]$
$\frac{X}{R} = 0.01$	0	$\frac{4}{\pi R} V_m 2ab [0.6392]$	$\frac{4}{\pi R} V_m 2ab [-1.5170]$	$\frac{4}{\pi R} V_m 2ab [2.0264]$	$\frac{4}{\pi R} V_m 2ab [-2.0504]$	$\frac{4}{\pi R} V_m 2ab [2.0313]$	$\frac{4}{\pi R} V_m 2ab [-2.1601]$

Table 5-16. Second integral term of $TS a_{nP}$ coefficient for moments, resolved in generic form for *layer P* from 0 to 6 and a selection of R/h ratios

	<i>layer P</i> = 0	<i>layer P</i> = 1	<i>layer P</i> = 2	<i>layer P</i> = 3	<i>layer P</i> = 4	<i>layer P</i> = 5	<i>layer P</i> = 6
$\frac{X}{R} = 0.13$	0	$\frac{4}{\pi R^2} V_m b^2 [0.9991]$	$\frac{4}{\pi R^2} V_m b^2 [-3.0486]$	$\frac{4}{\pi R^2} V_m b^2 [4.7604]$	$\frac{4}{\pi R^2} V_m b^2 [-5.8459]$	$\frac{4}{\pi R^2} V_m b^2 [6.9813]$	$\frac{4}{\pi R^2} V_m b^2 [-8.4424]$
$\frac{X}{R} = 0.11$	0	$\frac{4}{\pi R^2} V_m b^2 [0.9937]$	$\frac{4}{\pi R^2} V_m b^2 [-2.8699]$	$\frac{4}{\pi R^2} V_m b^2 [4.3299]$	$\frac{1.65}{\pi R^2} V_m b^2 [-5.1014]$	$\frac{1.65}{\pi R^2} V_m b^2 [5.8620]$	$\frac{4}{\pi R^2} V_m b^2 [-6.8916]$
$\frac{X}{R} = 0.09$	0	$\frac{4}{\pi R^2} V_m b^2 [0.9850]$	$\frac{4}{\pi R^2} V_m b^2 [-2.7008]$	$\frac{4}{\pi R^2} V_m b^2 [3.9482]$	$\frac{4}{\pi R^2} V_m b^2 [-4.4778]$	$\frac{4}{\pi R^2} V_m b^2 [4.9647]$	$\frac{4}{\pi R^2} V_m b^2 [-5.6920]$
$\frac{X}{R} = 0.07$	0	$\frac{4}{\pi R^2} V_m b^2 [0.9739]$	$\frac{4}{\pi R^2} V_m b^2 [-2.5407]$	$\frac{4}{\pi R^2} V_m b^2 [3.6059]$	$\frac{4}{\pi R^2} V_m b^2 [-3.9453]$	$\frac{4}{\pi R^2} V_m b^2 [4.2273]$	$\frac{4}{\pi R^2} V_m b^2 [-4.7357]$
$\frac{X}{R} = 0.05$	0	$\frac{4}{\pi R^2} V_m b^2 [0.9609]$	$\frac{4}{\pi R^2} V_m b^2 [-2.3894]$	$\frac{4}{\pi R^2} V_m b^2 [3.2971]$	$\frac{4}{\pi R^2} V_m b^2 [-3.4856]$	$\frac{4}{\pi R^2} V_m b^2 [3.6131]$	$\frac{4}{\pi R^2} V_m b^2 [-3.9608]$
$\frac{X}{R} = 0.03$	0	$\frac{4}{\pi R^2} V_m b^2 [0.9464]$	$\frac{4}{\pi R^2} V_m b^2 [-2.2465]$	$\frac{4}{\pi R^2} V_m b^2 [3.0174]$	$\frac{4}{\pi R^2} V_m b^2 [-3.0862]$	$\frac{4}{\pi R^2} V_m b^2 [3.0971]$	$\frac{4}{\pi R^2} V_m b^2 [-3.3263]$
$\frac{X}{R} = 0.01$	0	$\frac{4}{\pi R^2} V_m b^2 [0.9308]$	$\frac{4}{\pi R^2} V_m b^2 [-2.1116]$	$\frac{4}{\pi R^2} V_m b^2 [2.7633]$	$\frac{4}{\pi R^2} V_m b^2 [-2.7373]$	$\frac{4}{\pi R^2} V_m b^2 [2.6609]$	$\frac{4}{\pi R^2} V_m b^2 [-2.8029]$

Table 5-17. Third integral term of *TS* a_{nP} coefficient for moments, resolved in generic form for *layer P* from 0 to 6 and a selection of R/h ratios

	<i>layer P</i> = 0	<i>layer P</i> = 1	<i>layer P</i> = 2	<i>layer P</i> = 3	<i>layer P</i> = 4	<i>layer P</i> = 5	<i>layer P</i> = 6
$\frac{X}{R} = 0.13$	0	$\frac{3}{\pi} V_m a^2 [0.6665]$	$\frac{3}{\pi} V_m a^2 [-2.0473]$	$\frac{3}{\pi} V_m a^2 [3.2099]$	$\frac{3}{\pi} V_m a^2 [-3.9604]$	$\frac{3}{\pi} V_m a^2 [4.7498]$	$\frac{3}{\pi} V_m a^2 [-5.7614]$
$\frac{X}{R} = 0.11$	0	$\frac{3}{\pi} V_m a^2 [0.6650]$	$\frac{3}{\pi} V_m a^2 [-1.9538]$	$\frac{3}{\pi} V_m a^2 [2.9755]$	$\frac{3}{\pi} V_m a^2 [-3.5433]$	$\frac{3}{\pi} V_m a^2 [4.1098]$	$\frac{3}{\pi} V_m a^2 [-4.8615]$
$\frac{X}{R} = 0.09$	0	$\frac{3}{\pi} V_m a^2 [0.6620]$	$\frac{3}{\pi} V_m a^2 [-1.8617]$	$\frac{3}{\pi} V_m a^2 [2.7573]$	$\frac{3}{\pi} V_m a^2 [-3.1728]$	$\frac{3}{\pi} V_m a^2 [3.5624]$	$\frac{3}{\pi} V_m a^2 [-4.1160]$
$\frac{X}{R} = 0.07$	0	$\frac{3}{\pi} V_m a^2 [0.6579]$	$\frac{3}{\pi} V_m a^2 [-1.7717]$	$\frac{3}{\pi} V_m a^2 [2.5542]$	$\frac{3}{\pi} V_m a^2 [-2.8427]$	$\frac{3}{\pi} V_m a^2 [3.0917]$	$\frac{3}{\pi} V_m a^2 [-3.4936]$
$\frac{X}{R} = 0.05$	0	$\frac{3}{\pi} V_m a^2 [0.6526]$	$\frac{3}{\pi} V_m a^2 [-1.6841]$	$\frac{3}{\pi} V_m a^2 [2.3653]$	$\frac{3}{\pi} V_m a^2 [-2.5483]$	$\frac{3}{\pi} V_m a^2 [2.6858]$	$\frac{3}{\pi} V_m a^2 [-2.9714]$
$\frac{X}{R} = 0.03$	0	$\frac{3}{\pi} V_m a^2 [0.6464]$	$\frac{3}{\pi} V_m a^2 [-1.5991]$	$\frac{3}{\pi} V_m a^2 [2.1897]$	$\frac{3}{\pi} V_m a^2 [-2.2854]$	$\frac{3}{\pi} V_m a^2 [2.3350]$	$\frac{3}{\pi} V_m a^2 [-2.5316]$
$\frac{X}{R} = 0.01$	0	$\frac{3}{\pi} V_m a^2 [0.6392]$	$\frac{3}{\pi} V_m a^2 [-1.5170]$	$\frac{3}{\pi} V_m a^2 [2.0264]$	$\frac{3}{\pi} V_m a^2 [-2.0504]$	$\frac{3}{\pi} V_m a^2 [2.0313]$	$\frac{3}{\pi} V_m a^2 [-2.1601]$

Table 5-18. First integral term of $TS a_{nP}$ coefficient for forces, resolved in generic form for *layer P* from 0 to 6 and a selection of R/h ratios

	<i>layer P</i> = 0	<i>layer P</i> = 1	<i>layer P</i> = 2	<i>layer P</i> = 3	<i>layer P</i> = 4	<i>layer P</i> = 5	<i>layer P</i> = 6
$\frac{X}{R} = 0.13$	0	$\frac{3}{\pi R} V_m 2ab [0.9991]$	$\frac{3}{\pi R} V_m 2ab [-3.0486]$	$\frac{3}{\pi R} V_m 2ab [4.7604]$	$\frac{3}{\pi R} V_m 2ab [-5.8459]$	$\frac{3}{\pi R} V_m 2ab [6.9813]$	$\frac{3}{\pi R} V_m 2ab [-8.4424]$
$\frac{X}{R} = 0.11$	0	$\frac{3}{\pi R} V_m 2ab [0.9937]$	$\frac{3}{\pi R} V_m 2ab [-2.8699]$	$\frac{3}{\pi R} V_m 2ab [4.3299]$	$\frac{3}{\pi R} V_m 2ab [-5.1014]$	$\frac{3}{\pi R} V_m 2ab [5.8620]$	$\frac{3}{\pi R} V_m 2ab [-6.8916]$
$\frac{X}{R} = 0.09$	0	$\frac{3}{\pi R} V_m 2ab [0.9850]$	$\frac{3}{\pi R} V_m 2ab [-2.7008]$	$\frac{3}{\pi R} V_m 2ab [3.9482]$	$\frac{3}{\pi R} V_m 2ab [-4.4778]$	$\frac{3}{\pi R} V_m 2ab [4.9647]$	$\frac{3}{\pi R} V_m 2ab [-5.6920]$
$\frac{X}{R} = 0.07$	0	$\frac{3}{\pi R} V_m 2ab [0.9739]$	$\frac{3}{\pi R} V_m 2ab [-2.5407]$	$\frac{3}{\pi R} V_m 2ab [3.6059]$	$\frac{3}{\pi R} V_m 2ab [-3.9453]$	$\frac{3}{\pi R} V_m 2ab [4.2273]$	$\frac{3}{\pi R} V_m 2ab [-4.7357]$
$\frac{X}{R} = 0.05$	0	$\frac{3}{\pi R} V_m 2ab [0.9609]$	$\frac{3}{\pi R} V_m 2ab [-2.3894]$	$\frac{3}{\pi R} V_m 2ab [3.2971]$	$\frac{3}{\pi R} V_m 2ab [-3.4856]$	$\frac{3}{\pi R} V_m 2ab [3.6131]$	$\frac{3}{\pi R} V_m 2ab [-3.9608]$
$\frac{X}{R} = 0.03$	0	$\frac{3}{\pi R} V_m 2ab [0.9464]$	$\frac{3}{\pi R} V_m 2ab [-2.2465]$	$\frac{3}{\pi R} V_m 2ab [3.0174]$	$\frac{3}{\pi R} V_m 2ab [-3.0862]$	$\frac{3}{\pi R} V_m 2ab [3.0971]$	$\frac{3}{\pi R} V_m 2ab [-3.3263]$
$\frac{X}{R} = 0.01$	0	$\frac{3}{\pi R} V_m 2ab [0.9308]$	$\frac{3}{\pi R} V_m 2ab [-2.1116]$	$\frac{3}{\pi R} V_m 2ab [2.7633]$	$\frac{3}{\pi R} V_m 2ab [-2.7373]$	$\frac{3}{\pi R} V_m 2ab [2.6609]$	$\frac{3}{\pi R} V_m 2ab [-2.8029]$

Table 5-19. Second integral term of TS a_{nP} coefficient for forces, resolved in generic form for *layer P* from 0 to 6 and a selection of R/h ratios

	<i>layer P</i> = 0	<i>layer P</i> = 1	<i>layer P</i> = 2	<i>layer P</i> = 3	<i>layer P</i> = 4	<i>layer P</i> = 5	<i>layer P</i> = 6
$\frac{X}{R} = 0.13$	0	$\frac{3}{\pi R^2} V_m b^2 [1.9688]$	$\frac{3}{\pi R^2} V_m b^2 [-5.8152]$	$\frac{3}{\pi R^2} V_m b^2 [8.9346]$	$\frac{3}{\pi R^2} V_m b^2 [-10.7846]$	$\frac{3}{\pi R^2} V_m b^2 [12.6928]$	$\frac{3}{\pi R^2} V_m b^2 [-15.2034]$
$\frac{X}{R} = 0.11$	0	$\frac{3}{\pi R^2} V_m b^2 [1.9076]$	$\frac{3}{\pi R^2} V_m b^2 [-5.1899]$	$\frac{3}{\pi R^2} V_m b^2 [7.6191]$	$\frac{3}{\pi R^2} V_m b^2 [-8.7298]$	$\frac{3}{\pi R^2} V_m b^2 [9.7997]$	$\frac{3}{\pi R^2} V_m b^2 [-11.3600]$
$\frac{X}{R} = 0.09$	0	$\frac{3}{\pi R^2} V_m b^2 [1.8479]$	$\frac{3}{\pi R^2} V_m b^2 [-4.7014]$	$\frac{3}{\pi R^2} V_m b^2 [6.6517]$	$\frac{3}{\pi R^2} V_m b^2 [-7.3024]$	$\frac{3}{\pi R^2} V_m b^2 [7.8781]$	$\frac{3}{\pi R^2} V_m b^2 [-8.8927]$
$\frac{X}{R} = 0.07$	0	$\frac{3}{\pi R^2} V_m b^2 [1.7899]$	$\frac{3}{\pi R^2} V_m b^2 [-4.2901]$	$\frac{3}{\pi R^2} V_m b^2 [5.8736]$	$\frac{3}{\pi R^2} V_m b^2 [-6.2058]$	$\frac{3}{\pi R^2} V_m b^2 [6.4558]$	$\frac{3}{\pi R^2} V_m b^2 [-7.1168]$
$\frac{X}{R} = 0.05$	0	$\frac{3}{\pi R^2} V_m b^2 [1.7334]$	$\frac{3}{\pi R^2} V_m b^2 [-3.9326]$	$\frac{3}{\pi R^2} V_m b^2 [5.2236]$	$\frac{3}{\pi R^2} V_m b^2 [-5.3267]$	$\frac{3}{\pi R^2} V_m b^2 [5.3535]$	$\frac{3}{\pi R^2} V_m b^2 [-5.7742]$
$\frac{X}{R} = 0.03$	0	$\frac{3}{\pi R^2} V_m b^2 [1.6785]$	$\frac{3}{\pi R^2} V_m b^2 [-3.6166]$	$\frac{3}{\pi R^2} V_m b^2 [4.6688]$	$\frac{3}{\pi R^2} V_m b^2 [-4.6041]$	$\frac{3}{\pi R^2} V_m b^2 [4.4764]$	$\frac{3}{\pi R^2} V_m b^2 [-4.7306]$
$\frac{X}{R} = 0.01$	0	$\frac{3}{\pi R^2} V_m b^2 [1.6252]$	$\frac{3}{\pi R^2} V_m b^2 [-3.3341]$	$\frac{3}{\pi R^2} V_m b^2 [4.1886]$	$\frac{3}{\pi R^2} V_m b^2 [-4.0008]$	$\frac{3}{\pi R^2} V_m b^2 [3.7664]$	$\frac{3}{\pi R^2} V_m b^2 [-3.9040]$

Table 5-20. Third integral term of $TS a_{nP}$ coefficient for forces, resolved in generic form for *layer P* from 0 to 6 and a selection of R/h ratios

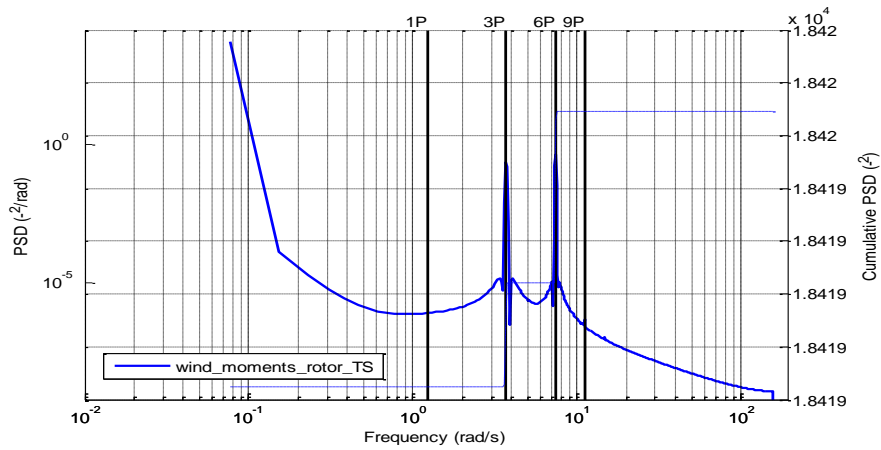


Figure 5-80. Spectrum of the deterministic component of wind-field TS for inducing moments at the rotor by the simple model

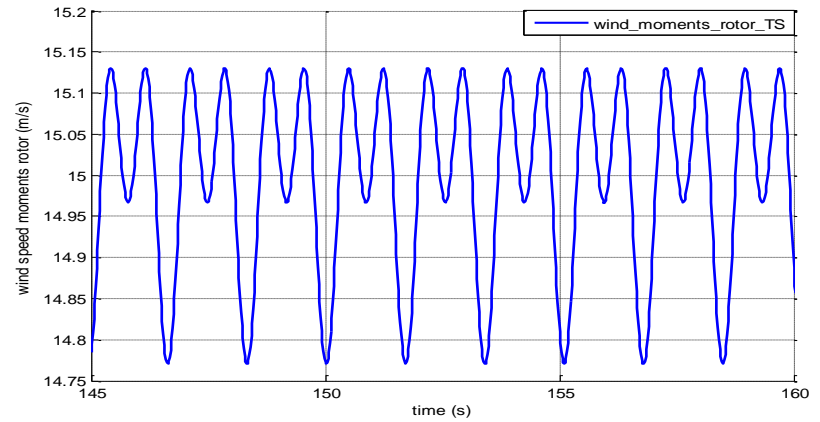


Figure 5-81. Time series of the deterministic component of wind-field TS for inducing moments at the rotor by the simple model

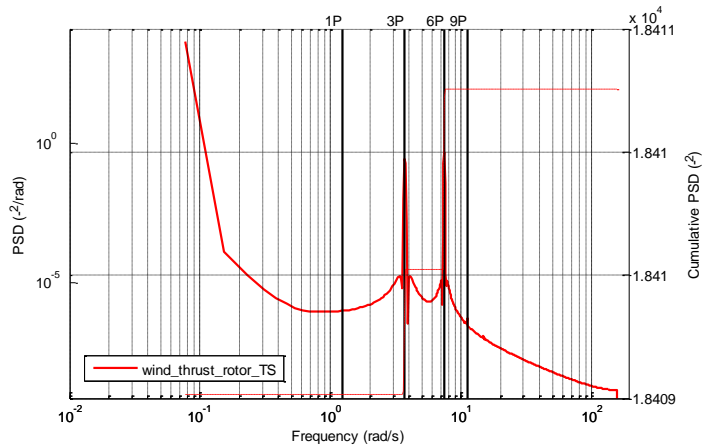


Figure 5-82. Spectrum of the deterministic component of wind-field TS for inducing thrust at the rotor by the simple model

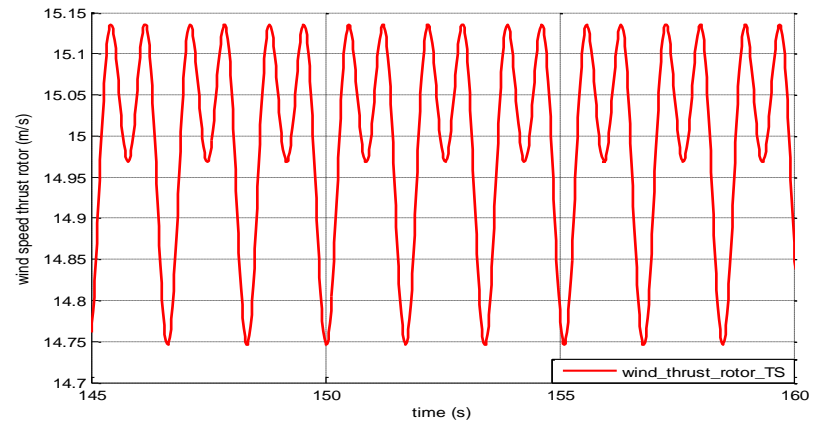


Figure 5-83. Time series of the deterministic component of wind-field TS for inducing thrust at the rotor by the simple model

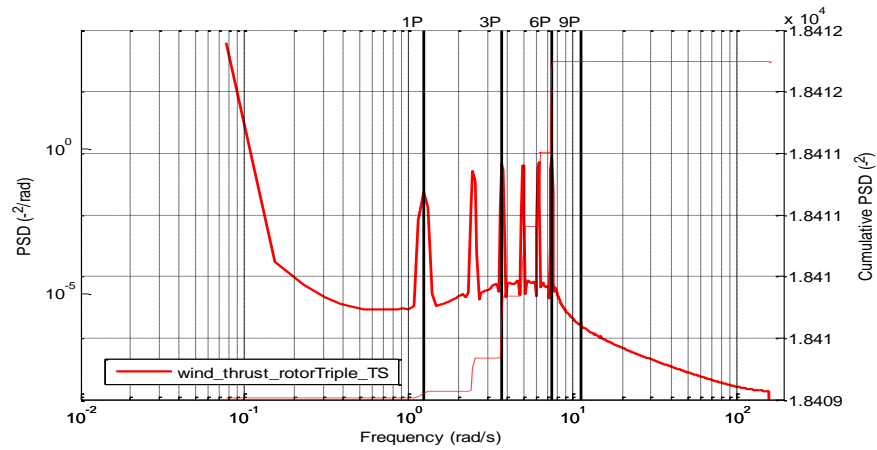


Figure 5-84. Spectrum for the deterministic component of wind-field TS used for inducing thrust at the rotor by triple model

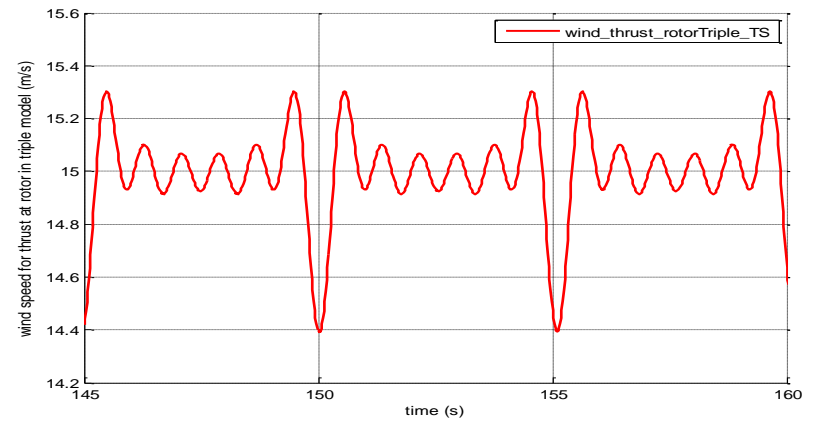


Figure 5-85. Time series for the deterministic component of wind-field TS used for inducing thrust at the rotor by triple model

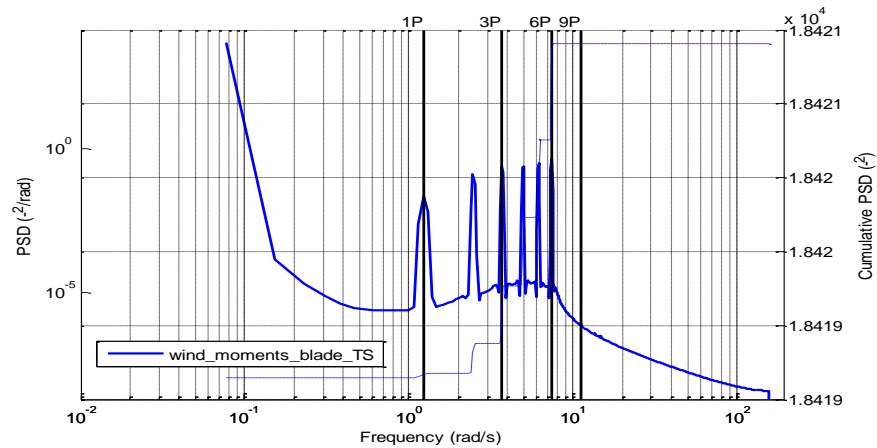


Figure 5-86. Spectrum of deterministic component of wind-field TS, for inducing moments at a single blade by simple and triple model. Also used for inducing moments at the rotor by triple model

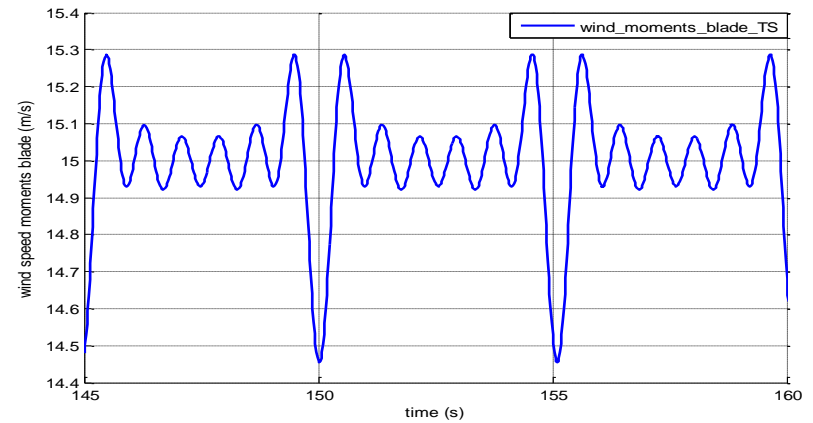


Figure 5-87. Time series of deterministic component of wind-field TS, for inducing moments at a single blade by simple and triple model. Also used for inducing moments at the rotor by triple model

Similarly to the stochastic component in Section 5.2.2 and WS in Section 5.3.1, the results for the in-plane hub torque and out-of-plane RBM of a blade are analysed with only the deterministic component TS present, for a 15m/s wind, 15m/s wind with 18 degrees offset and a 8m/s wind, all of them with a 10% TI. The results for the in-plane RBM of the blade, the edgewise moment of the blade, M_e , the flapwise moment of the blade, M_f , and the thrust force can be found in Appendix E.

When looking at the results of the in-plane hub torque, see Figure 5-88 to Figure 5-89 for the 15m/s case, Figure 5-90 to Figure 5-91 for the 15m/s with 18 degree of pitch offset case and Figure 5-92 to Figure 5-93 for the 8m/s case, leakage can be seen in all three cases, albeit small in overall magnitude. By examining the values for the cumulative spectra in Table 5-21 for the same results, it is confirmed that the impact of this leakage is negligible.

In similar fashion, in the out-of-plane RBM of the blade found, see Figure 5-94 to Figure 5-95 for the 15m/s case, Figure 5-96 to Figure 5-97 for the 15m/s with 18 degrees of pitch offset and Figure 5-98 to Figure 5-99 for the 8m/s case, leakage is clearly present but of an even smaller impact than on the hub torque.

The match between the triple and simple model for both the hub torque and the out-of-plane RBM is notably close and no significant differences can be observed in the nP peaks and in the general trend of the spectrum. The trend of the spectrum further shows that the impact of the TS increases with frequency, which is especially noticeable in the out-of-plane RBM. This trend is also observed in the other results related to the TS, see Appendix E. The data used in the spectrum of the moments and forces have been detrended.

After analysing the results regarding the deterministic component TS of the wind-field, including the results present in Appendix E, it can be stated that overall leakage is observed in the spectrum, but when looking at the magnitude of the amplitude, its impact is negligible, and that the simple model should suffice to induce moments and forces as far as the TS component of the wind-field is concerned.

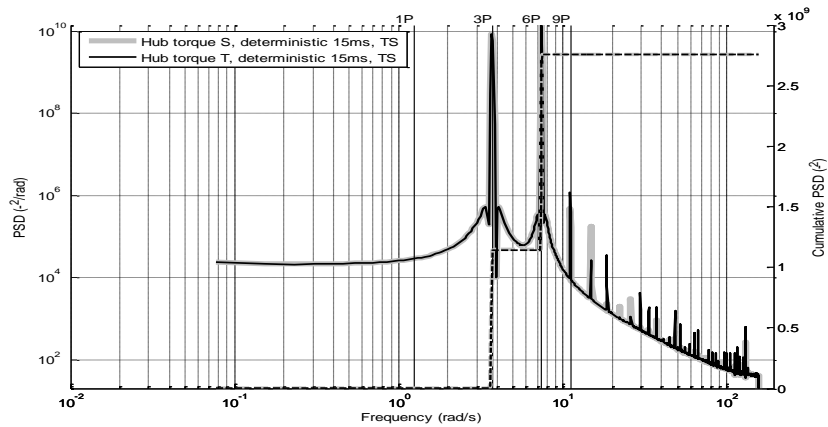


Figure 5-88. Hub torque spectrum comparison between simple and triple structure for the deterministic component of wind-field TS, with mean 15m/s

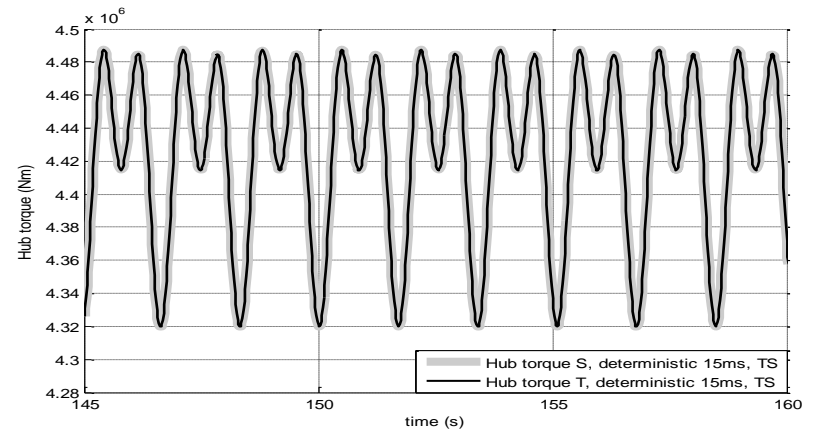


Figure 5-89. Hub torque time series comparison between simple and triple structure for the deterministic component of wind-field TS, with mean 15m/s

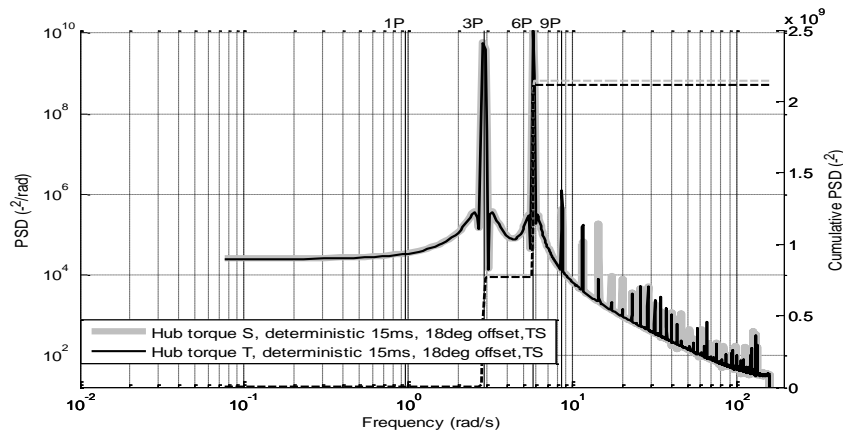


Figure 5-90. Hub torque spectrum comparison between simple and triple structure for the deterministic component of wind-field TS, with mean 15m/s and 18 degrees of pitch offset

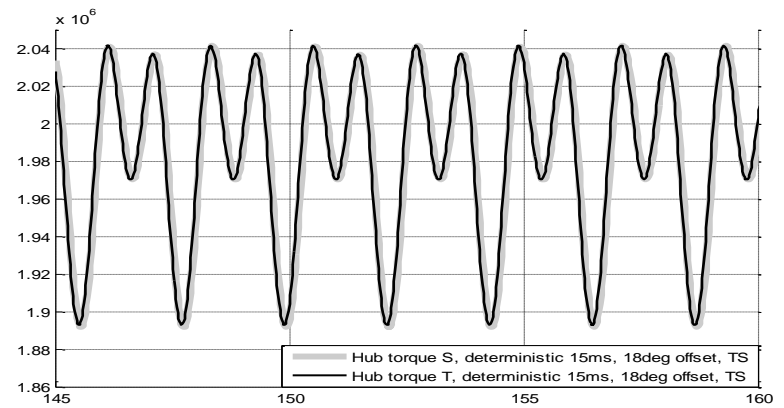


Figure 5-91. Hub torque time series comparison between simple and triple structure for the deterministic component of wind-field TS, with mean 15m/s and 18 degrees of pitch offset

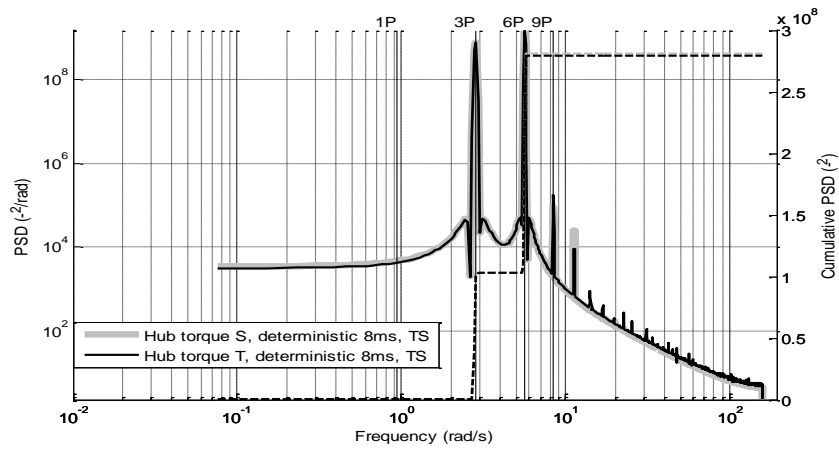


Figure 5-92. Hub torque spectrum comparison between simple and triple structure for the deterministic component of wind-field TS, with mean 8m/s

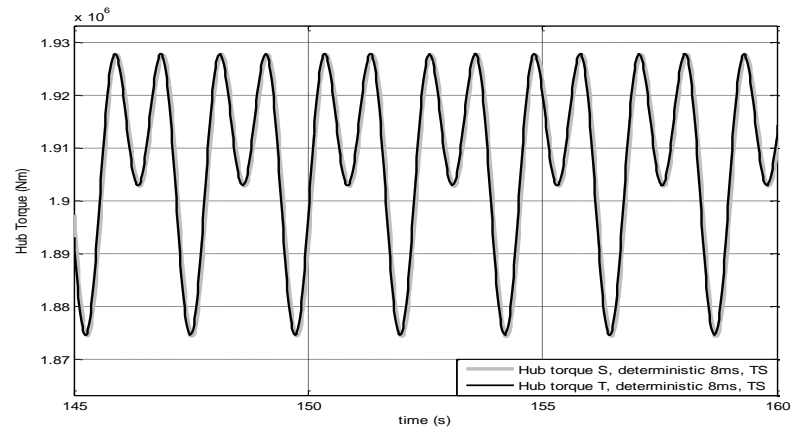


Figure 5-93. Hub torque time series comparison between simple and triple structure for the deterministic component of wind-field TS, with mean 8m/s

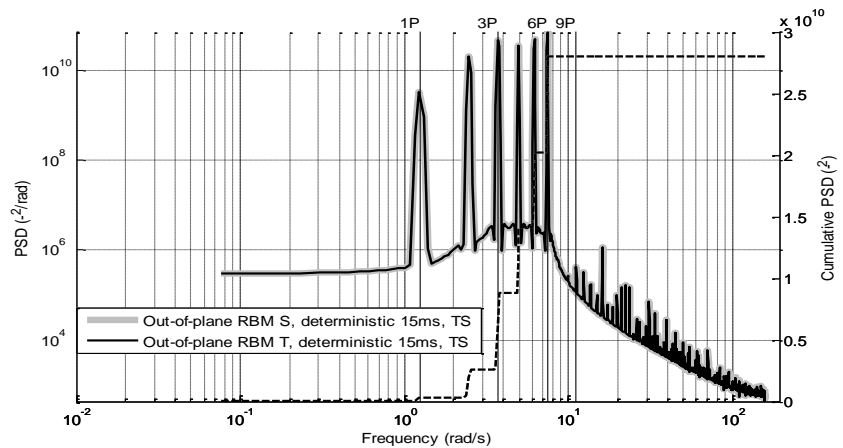


Figure 5-94. Out-of-plane blade RBM spectrum comparison between simple and triple structure for the deterministic component of wind-field TS, with mean 15m/s

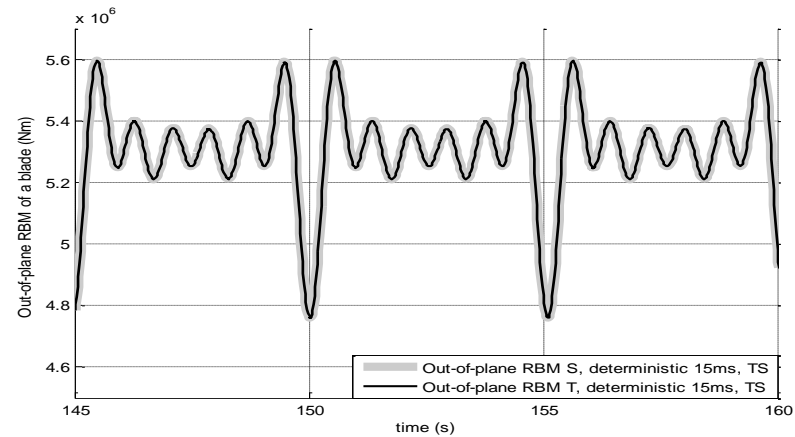


Figure 5-95. Out-of-plane blade RBM time series comparison between simple and triple structure for the deterministic component of wind-field TS, with mean 15m/s

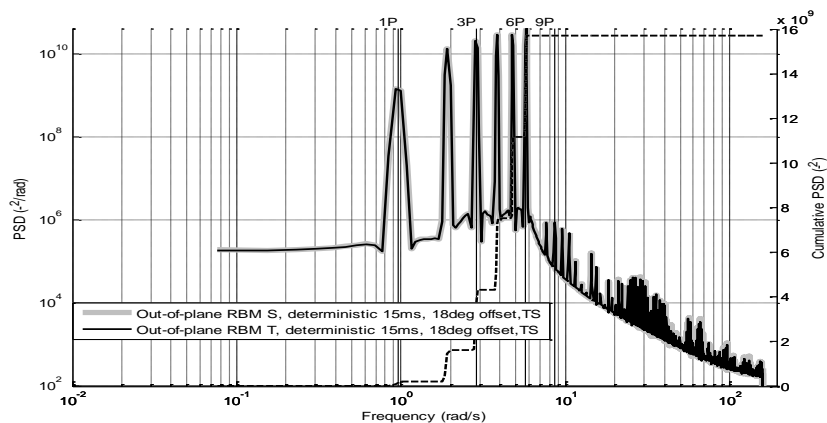


Figure 5-96. Out-of-plane blade RBM spectrum comparison between simple and triple structure for the deterministic component of wind-field TS, with mean 15m/s and 18 degrees of pitch offset

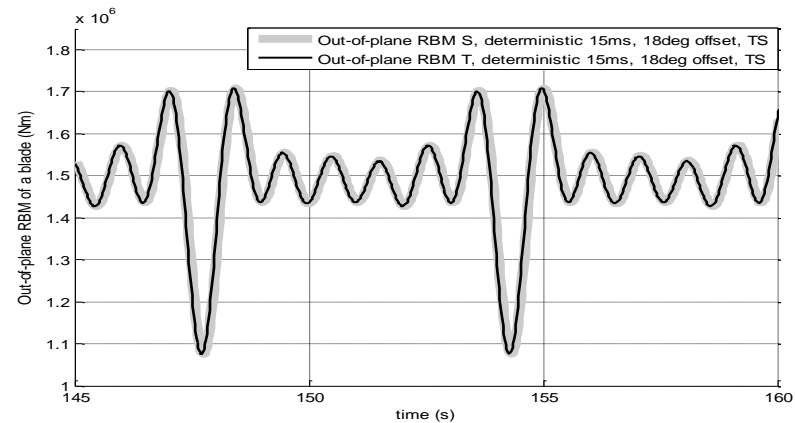


Figure 5-97. Out-of-plane blade RBM time series comparison between simple and triple structure for the deterministic component of wind-field TS, with mean 15m/s and 18 degrees of pitch offset

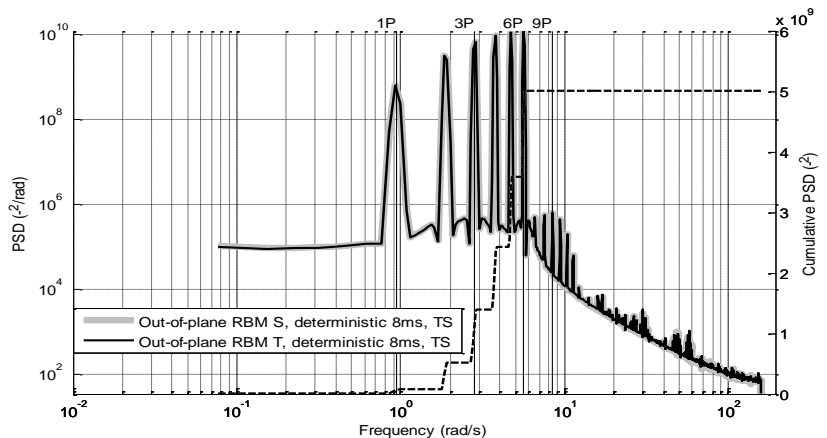


Figure 5-98. Out-of-plane blade RBM spectrum comparison between simple and triple structure for the deterministic component of wind-field TS, with mean 8m/s

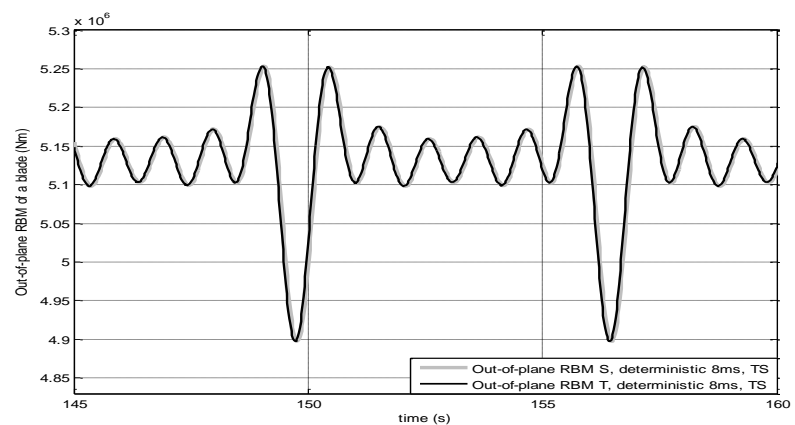


Figure 5-99. Out-of-plane blade RBM time series comparison between simple and triple structure for the deterministic component of wind-field TS, with mean 8m/s

			Cumulative Value	
			Simple Model	Triple Model
TS	Torque	15m/s	2.7599e+009	2.7564e+009
		15m/s + 18 deg offset	2.1466e+009	2.1147e+009
		8m/s	2.8117e+008	2.7973e+008
	Out-of-plane RBM	15m/s	2.8017e+010	2.8013e+010
		15m/s + 18 deg offset	1.5699e+010	1.5702e+010
		8m/s	5.0147e+009	5.0156e+009

Table 5-21 Cumulative PSD value for hub torque and blade out-of-plane RBM for case study of 15m/s, 15m/s with 18 degree pitch offset and 8m/s for the simple and triple structure for the deterministic component of the wind TS.

5.3.3. Combined Wind Shear and Tower Shadow Results

Before merging the stochastic and deterministic components of the wind, it is interesting, and important, to examine the synergies present, or not, when the two deterministic components of the wind-field are integrated together.

As per previous sections before looking into the impact on the forces and moments of interest the spectrum related to the wind generated only by the components under study is presented. Accordingly, from Figure 5-100 to Figure 5-103, the spectrum of the combined TS & WS containing all the necessary *layer P* structures for the rotor in the simple model (inducing 0, 3 and 6P) and their time series, for the induction of the moments and thrust, can be found. Likewise for the triple structure rotor, from Figure 5-104 to Figure 5-107 the spectrum of the wind for the induction of the moments and thrust, containing all the necessary *layer P* structures (inducing 0, 1, 2, 3, 4, 5 and 6P) and their time series can be seen. The spectrum in Figure 5-106, with its corresponding time series in Figure 5-107, corresponds to the wind-field component used to induce the blade moments in both models.

As expected, the peaks in the spectra have the sharp and narrow profile characteristic of deterministic signals. It would seem that the wind-field components for inducing moments and those for inducing thrust in the combined WS & TS case have magnitudes closer in value than when considering the WS and TS separately. The data used in the spectrum of the wind have not been detrended.

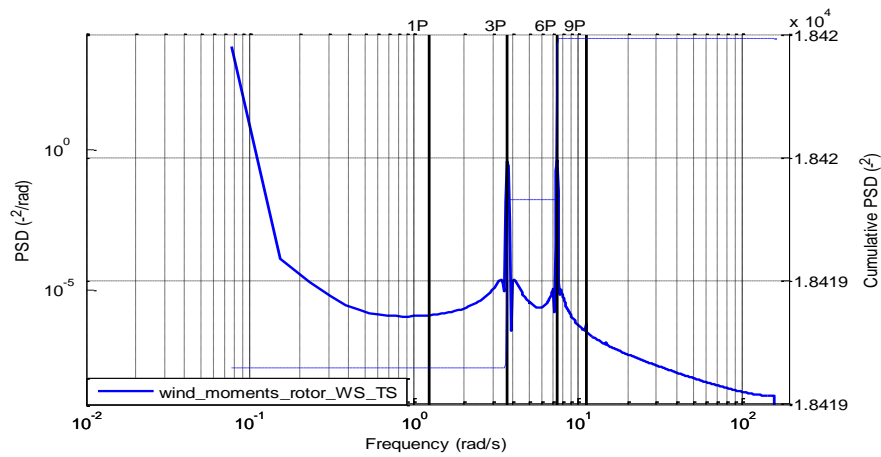


Figure 5-100. Spectrum for the complete deterministic component of wind-field used for inducing moments at the rotor by the simple model

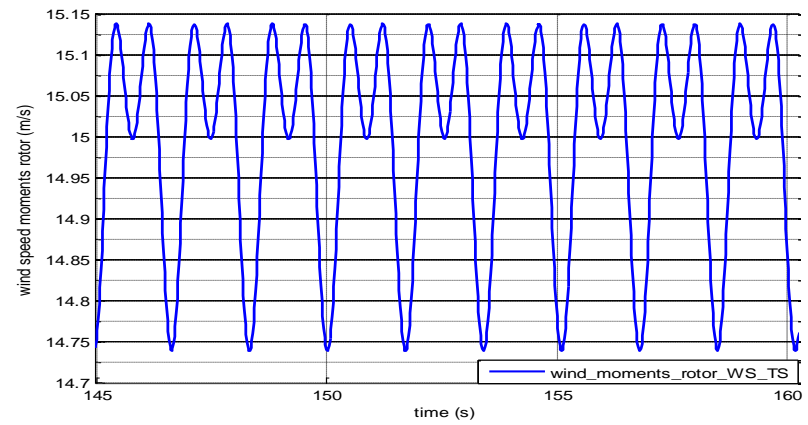


Figure 5-101. Time series extract for the complete deterministic component of wind-field used for inducing moments at the rotor by the simple model

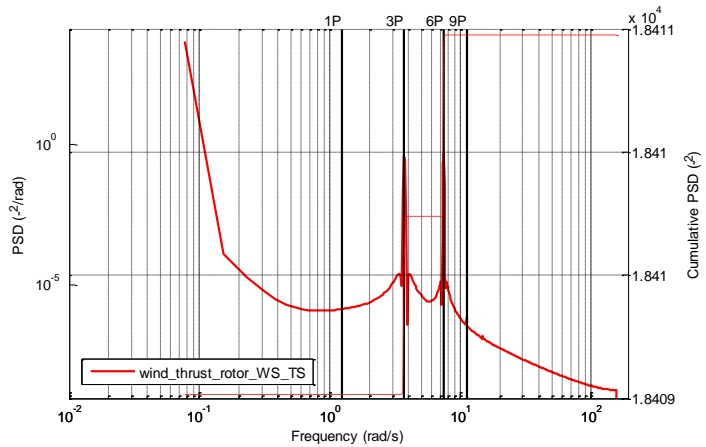


Figure 5-102. Spectrum for the complete deterministic component of wind-field used for inducing thrust at the rotor by the simple model

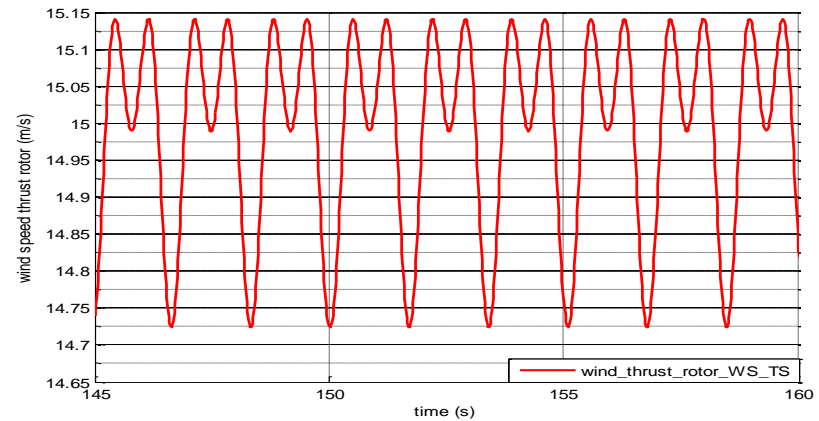


Figure 5-103. Time series extract for the complete deterministic component of wind-field used for inducing thrust at the rotor by the simple model

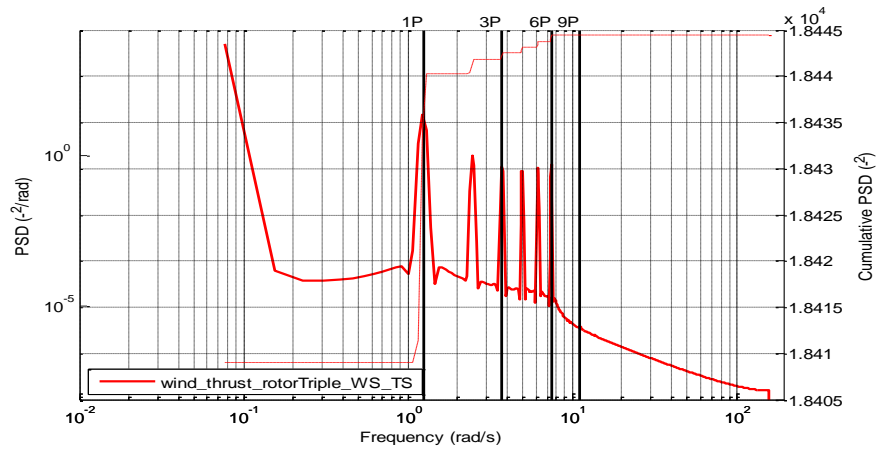


Figure 5-104. Spectrum for the complete deterministic component of wind-field used for inducing thrust at the rotor by triple model

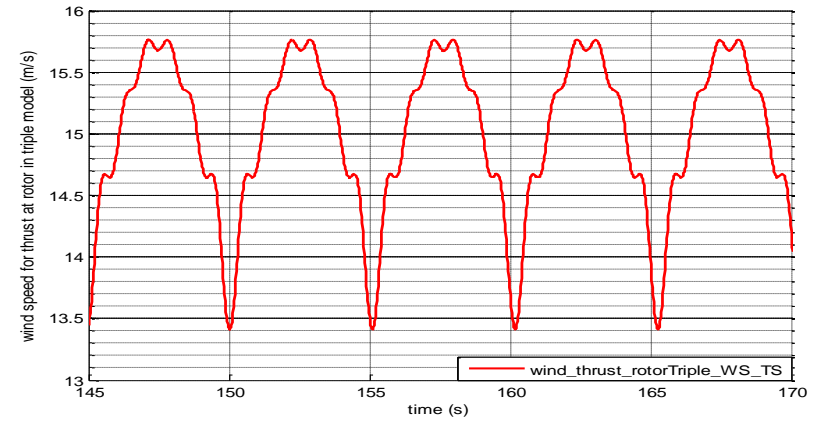


Figure 5-105. Time series extract for the complete deterministic component of wind-field used for inducing thrust at the rotor by triple model

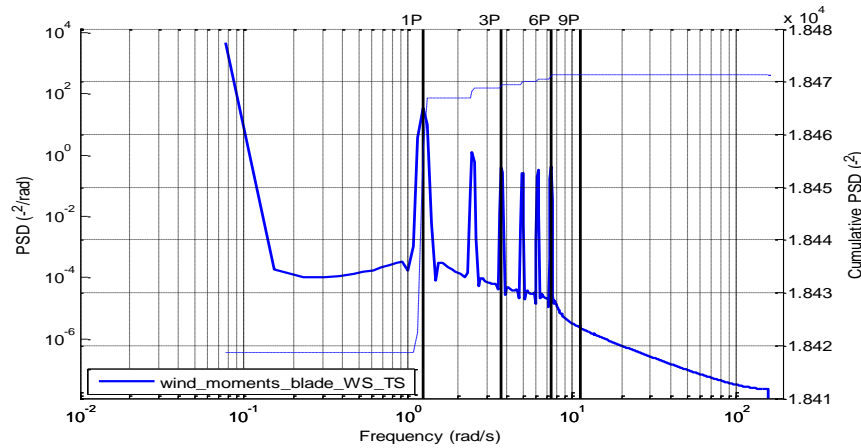


Figure 5-106. Spectrum for the complete deterministic component of wind-field used for inducing moments at the single blade by simple and triple model. Also used for inducing moments at the rotor by triple model

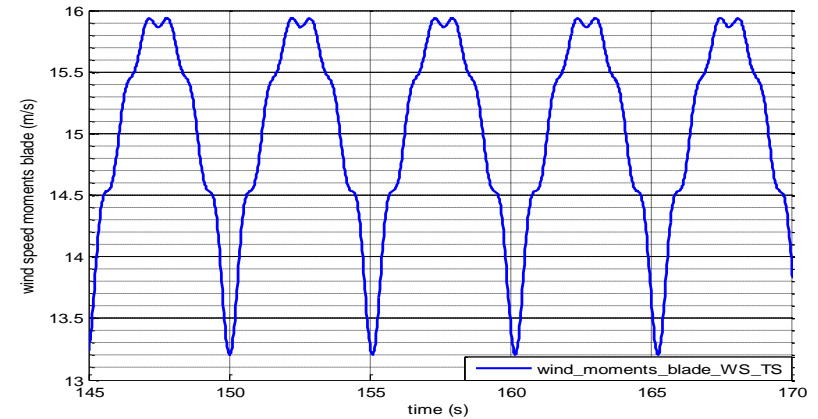


Figure 5-107. Time series extract for the complete deterministic component of wind-field used for inducing moments at the single blade by simple and triple model. Also used for inducing moments at the rotor by triple model

When considering the hub torque results, see Figure 5-108 to Figure 5-109 for 15m/s case, Figure 5-110 to Figure 5-111 for 15m/s and 18 degrees of pitch offset, Figure 5-112 to Figure 5-113 for the 8m/s case and Table 5-22, it is clearly noticeable that there are some discrepancies present between the triple and simple models and that there is leakage present in the higher frequencies; albeit small and with no significant contribution to the cumulative values. If these differences were to be taken in isolation it would be tempting, if not natural, to question the validity of the Separability property. In reality, to fully understand the results for the combined WS & TS components of the hub torque, which is nothing else than the addition of the in-plane RBM of each one of the three blades, it is necessary to spend some time analysing the latter, looking at the individual contributions of the WS and TS to be able to correctly interpret the hub torque when both, the WS and TS, are present.

When considering the in-plane RBM results in Appendix E, for the WS and TS individually, Figure E-1 to Figure E-12, there does not seem to be much discrepancy between the simple and triple model apart from some leakage on the 3P peak, this is true for both components. The 1P peak is clearly the dominant contribution for the WS but, as the frequency goes higher, the impact of the WS diminishes and the impact of the TS increases. Due to the magnitude, trend and shape of the peaks present on both components, when combined, the resultant spectrum, Figure E-13 to Figure E-18, is much more homogenous in shape than the WS and TS contributions taken individually. However, it would seem that ultimately the WS has the biggest impact on the appearance of the combined spectrum, with the 1P still dominant. The contribution from 3P, 4P, 5P and 6P peaks have a considerably bigger magnitude than for the WS component alone and are mainly due to the contribution from the TS component.

When combining 3 in-plane RBMs to obtain the hub torque, by symmetry only the 3P and 6P peaks remain, see Figure 5-108, Figure 5-110 and Figure 5-112. However, for one of the in-plane RBM, the 3P and 6P are not the dominant nP peaks and have significantly smaller magnitudes than the dominant 1P peak, see Figure E-13, Figure E-15 and E-17. Consequently, when considering the hub torque, even weak leakage from 1P into 3P and 6P, is still significant in some cases, see Figure 5-108, Figure 5-110 and Figure 5-112.

In other words, there are indeed small non-linear effects present, otherwise there would be no leakage. However, this leakage is not strong, thereby supporting the validity of the Separability

property. They rather are the outcome of the peculiar combination of the magnitude and trends in the individual deterministic components of the wind, WS and TS.

Furthermore, it needs to be remembered that the numbers present in Table 5-22 are not the amplitude but their square. As such, if the square root of those numbers were tabulated instead, the difference in the numbers would be less.

The results for the out-of-plane RBM of the blade are presented in Figure 5-114 to Figure 5-115 for the 15m/s case, Figure 5-116 to Figure 5-117 for the 15m/s and 18 degrees of pitch offset, Figure 5-118 to Figure 5-119 for the 8m/s case and in Table 5-22. *A priori*, the Separability property is not valid for the out-of-plane RBM of the blade. Yet, the results still exhibit a close match between the simple and triple structure, most likely due to the correlation between in-plane and out-of-plane moments as previously explained. The data used in the spectrum of the moments and forces have been detrended.

After analysing the results for the combined effect of the deterministic components of the wind WS and TS, including the results in Appendix E, it can be concluded that the simple model should suffice for inducing the moments and forces when modelling the wind with only WS and TS components present.

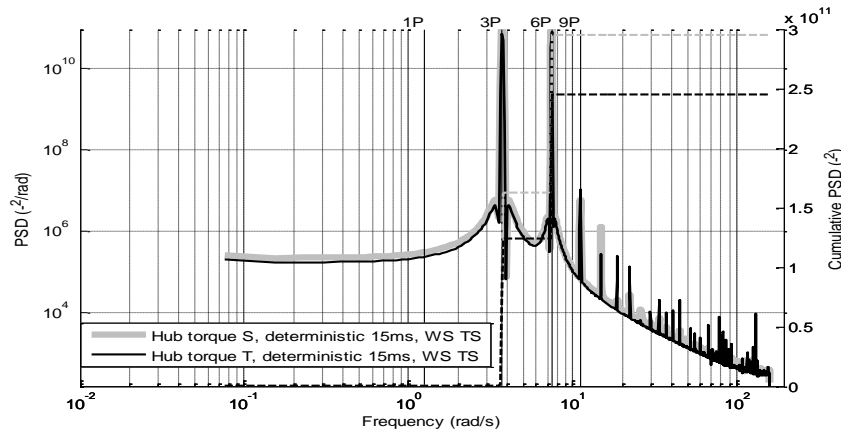


Figure 5-108. Hub torque spectrum comparison between simple and triple structure for the deterministic component of the wind-field with mean 15m/s, WS TS active

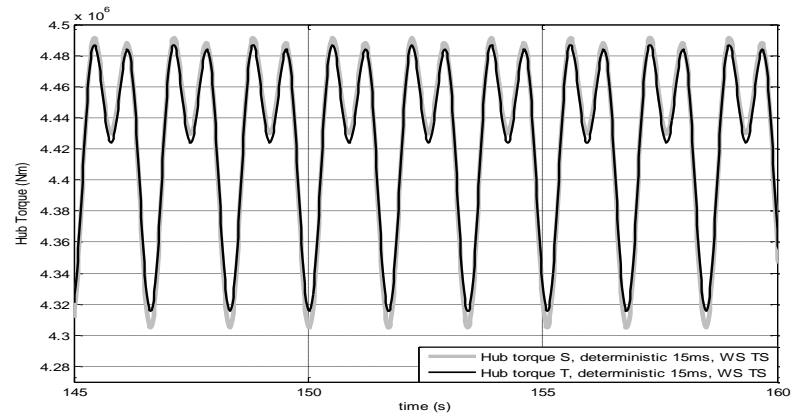


Figure 5-109. Hub torque time series comparison between simple and triple structure for the deterministic component of the wind-field with mean 15m/s, WS TS active

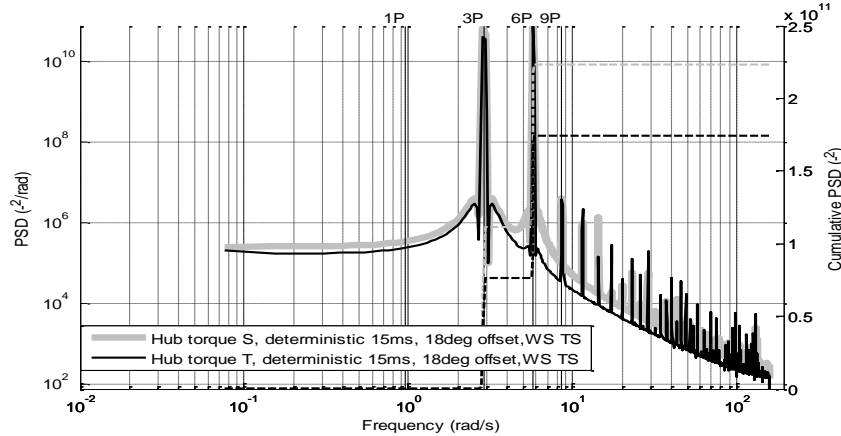


Figure 5-110. Hub torque spectrum comparison between simple and triple structure for the deterministic component of the wind-field with mean 15m/s and 18 degrees of pitch offset, WS TS active

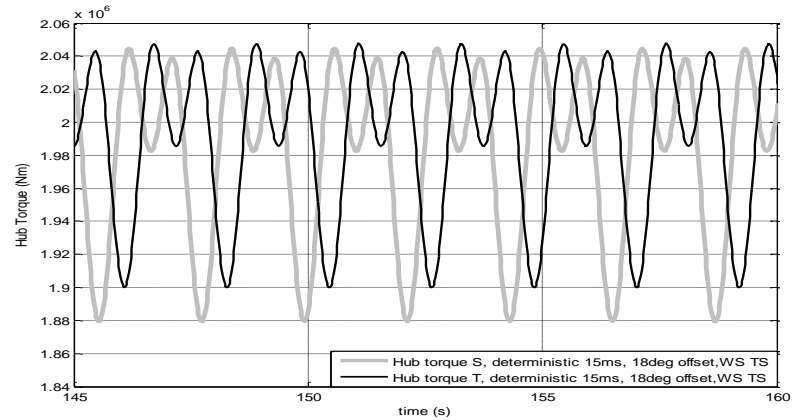


Figure 5-111. Hub torque time series comparison between simple and triple structure for the deterministic component of the wind-field with mean 15m/s and 18 degrees of pitch offset, WS TS active

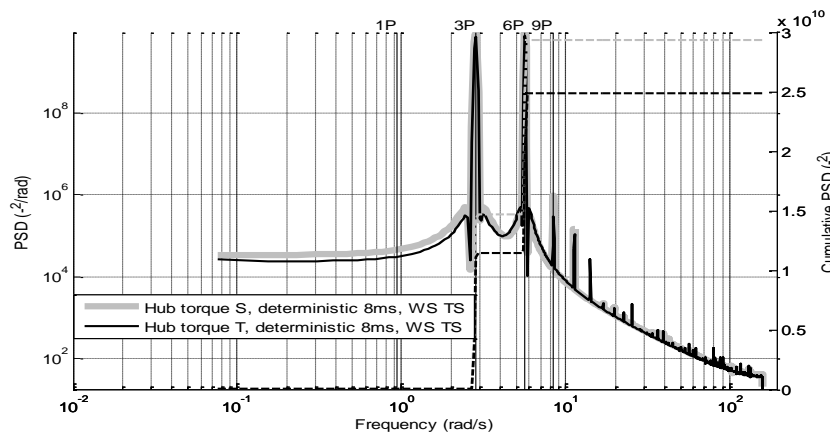


Figure 5-112. Hub torque spectrum comparison between simple and triple structure for the deterministic component of the wind-field with mean 8m/s, WS TS active

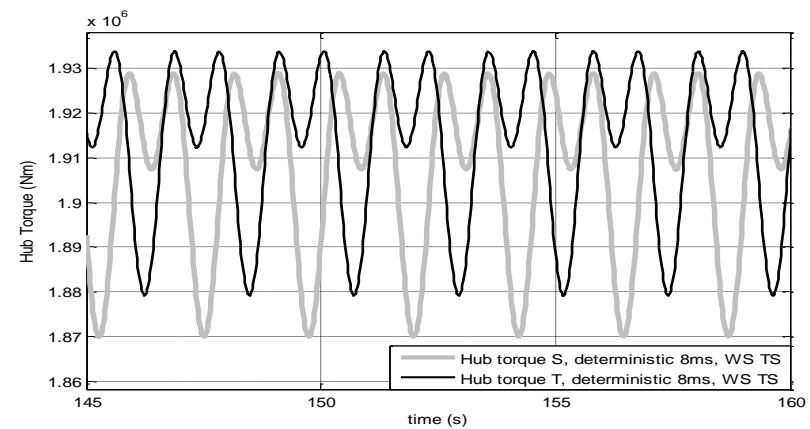


Figure 5-113. Hub torque time series comparison between simple and triple structure for the deterministic component of the wind-field with mean 8m/s, WS TS active

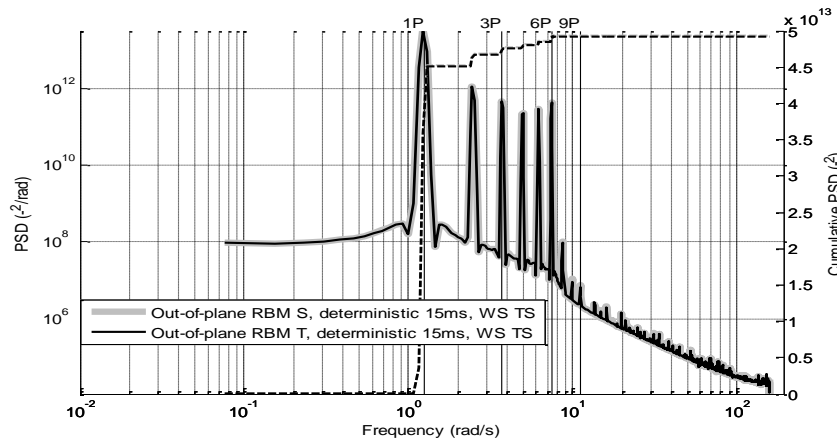


Figure 5-114. Out-of-plane RBM spectrum comparison between simple and triple structure for the deterministic component of the wind-field with mean 15m/s, WS TS active

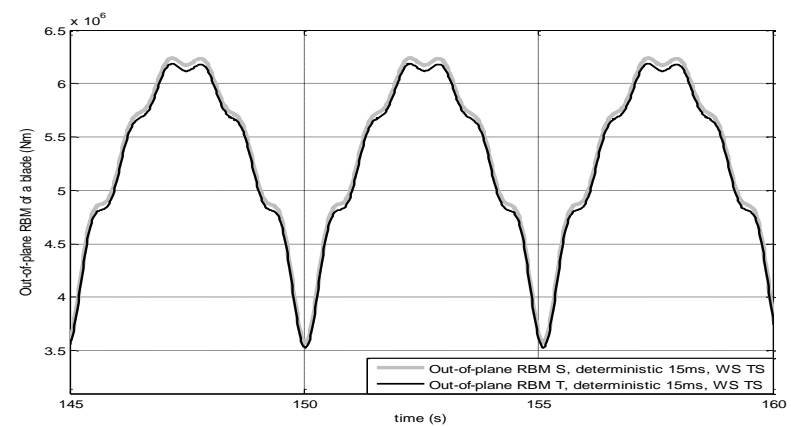


Figure 5-115. Out-of-plane RBM time series comparison between simple and triple structure for the deterministic component of the wind-field with mean 15m/s, WS TS active

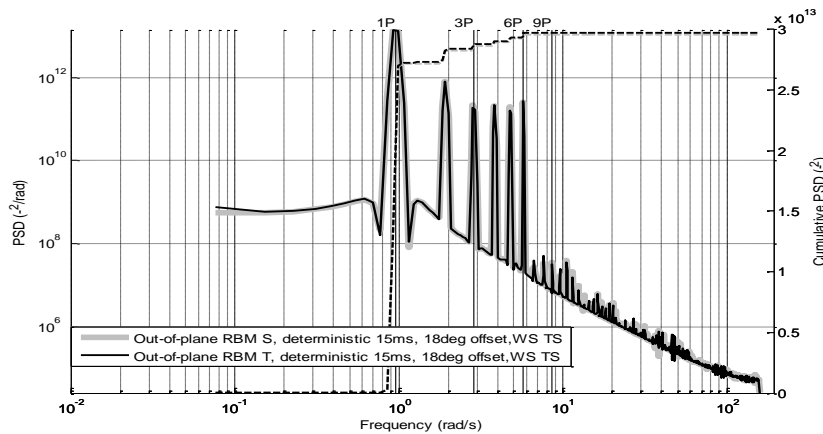


Figure 5-116. Out-of-plane RBM spectrum comparison between simple and triple structure for the deterministic component of the wind-field with mean 15m/s and 18 degrees of pitch offset, WS TS active

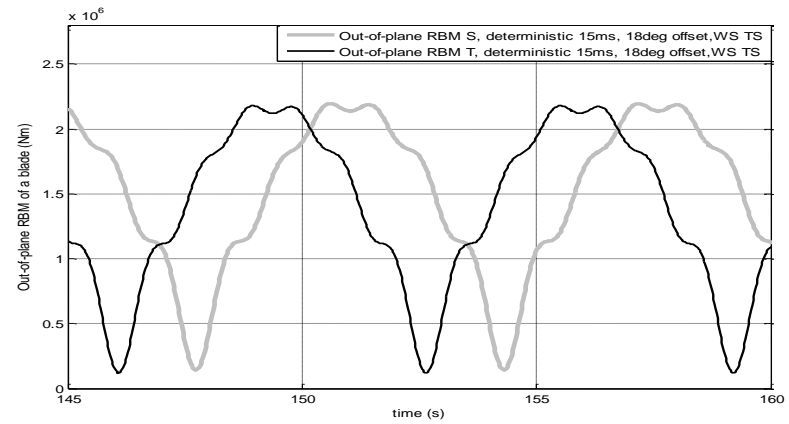


Figure 5-117. Out-of-plane RBM time series comparison between simple and triple structure for the deterministic component of the wind-field with mean 15m/s and 18 degrees of pitch offset, WS TS active

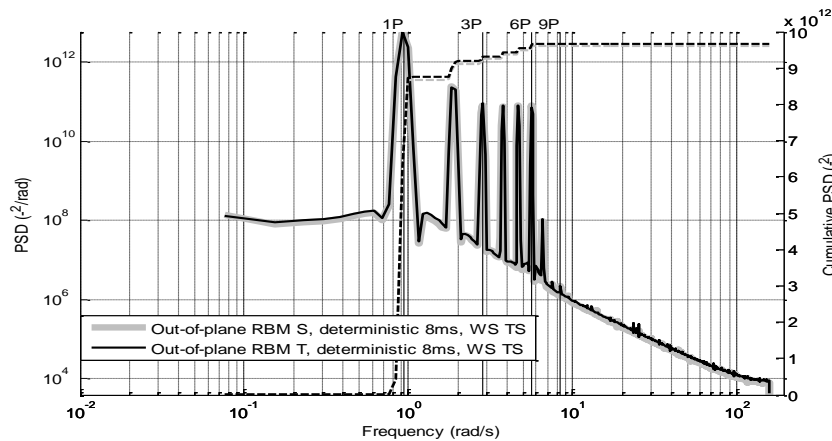


Figure 5-118. Out-of-plane RBM spectrum comparison between simple and triple structure for the deterministic component of the wind-field with mean 8m/s, WS TS active

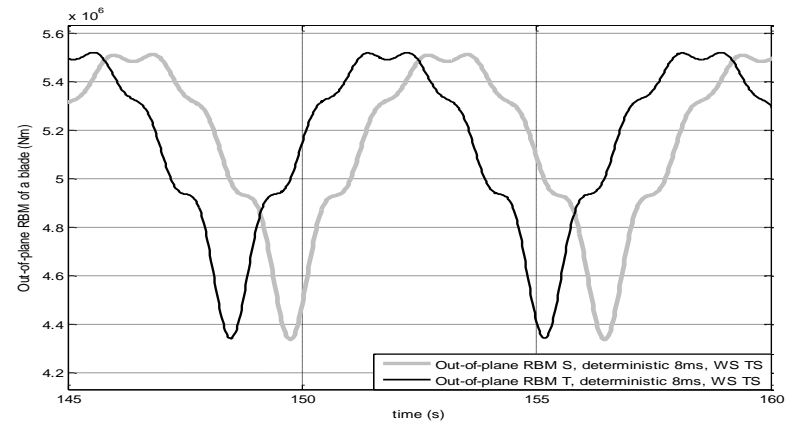


Figure 5-119. Out-of-plane RBM time series comparison between simple and triple structure for the deterministic component of the wind-field with mean 8m/s, WS TS active

			Cumulative Value	
			Simple Model	Triple Model
WS & TS	Torque	15m/s	3.6048e+009	2.989e+009
		15m/s + 18 deg offset	2.7241e+009	2.1258e+009
		8m/s	3.5773e+008	3.032e+008
	Out-of-plane RBM	15m/s	6.0165e+011	6e+011
		15m/s + 18 deg offset	3.613e+011	3.6316e+011
		8m/s	1.1727e+011	1.1806e+011

Table 5-22. Cumulative PSD value for hub torque and blade out-of-plane RBM for case study of 15m/s, 15m/s with 18 degree pitch offset and 8m/s for the simple and triple structure of the complete deterministic component of the wind. The force of gravity is not taken into account.

5.4. Complete Effective Wind-Field Model

The impact of leakage needs to be further assessed by looking at the results when both the stochastic and deterministic components of the wind are incorporated into the wind-field model. It should be noted that the effect of gravity force is not included in order to not affect considerations on leakage. In the current section, as per the previous sections, the results for the in-plane hub torque and out of plane RBM of the blade will be analysed and the full set of results for the complete effective wind-field model can be found in and Appendix G.

Before analysing the signals that are induced by the complete effective wind-field model, as per previous sections, the spectrum related to the wind generated only by the components under study is presented. Since it is the complete wind-field model that is evaluated in this section, an extra graph showing the complete 600s time series has been included in addition to the usual 15s extracted plot. For the rotor in the simple model, from Figure 5-120 to Figure 5-122 for the induction of the moments and from Figure 5-123 to Figure 5-125 for the induction of the thrust, the spectrum of the complete effective wind-field model, containing all the necessary *layer P* structures (inducing 0, 3 and 6P) and their time series, can be found. Likewise for the triple structure rotor, from Figure 5-126 to Figure 5-128 for the induction of the moments and from Figure 5-129 to Figure 5-131 for the induction of the thrust, the spectrum of the wind containing all the necessary *layer P* structures (inducing 0, 1, 2, 3, 4, 5 and 6P) and their time series, can be seen. The spectrum in Figure 5-129, with its corresponding time series in Figure 5-130 and Figure 5-131, is further used to induce the associated moments to the single blade for both models.

The signals clearly show simultaneously the characteristics of both their stochastic and deterministic components by the nP peaks having a broad base endowed by the former and with a narrow top as a result of the latter. As in previous sections it would look like the thrust inducing wind signals are of slightly bigger magnitude than the moment inducing ones. The data used in the spectrum of the wind have not been detrended.

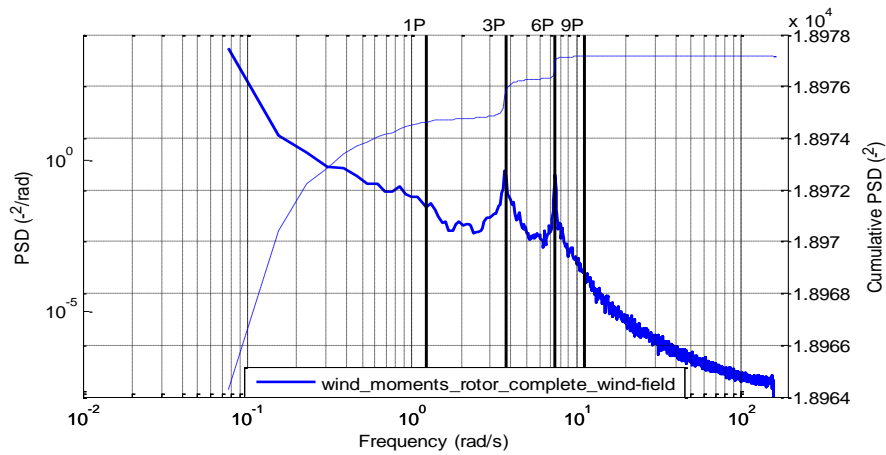


Figure 5-120. Spectrum of the complete wind-field with 15m/s mean, used for inducing moments at the rotor by the simple model

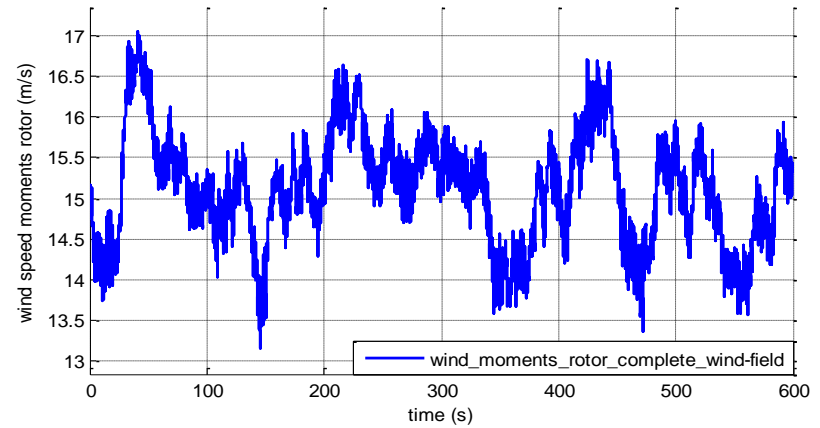


Figure 5-121. Time series of the complete wind-field with 15m/s mean, used for inducing moments at the rotor by the simple model

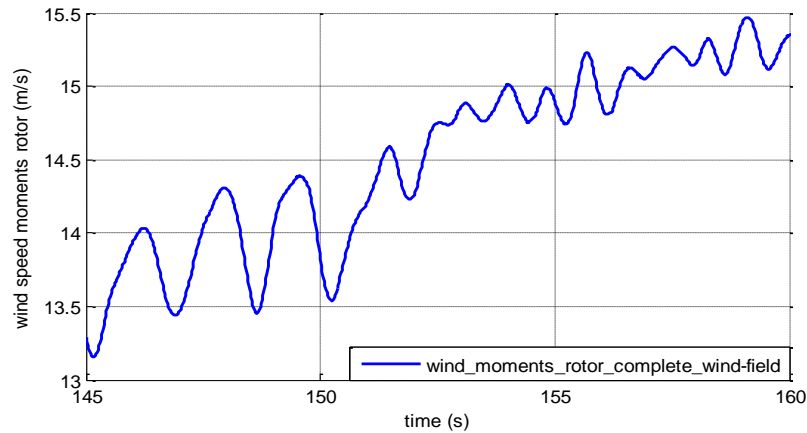


Figure 5-122. Time series extract of the complete wind-field with 15m/s mean, used for inducing moments at the rotor by the simple model

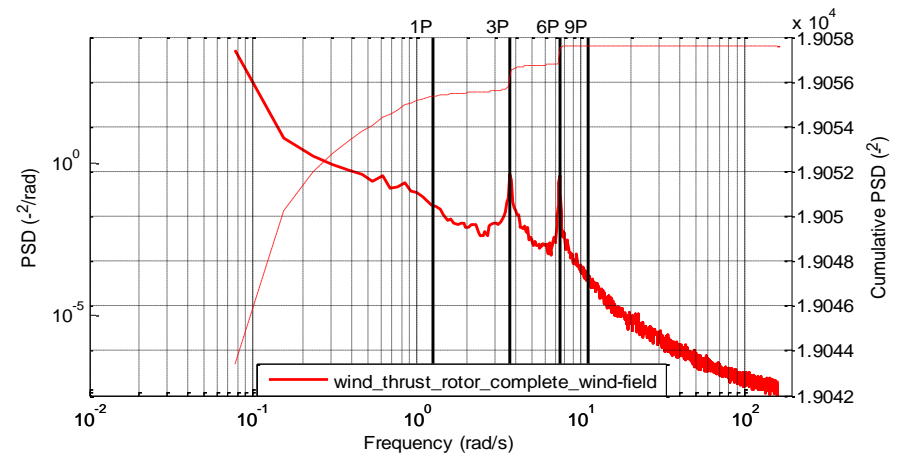


Figure 5-123. Spectrum of the complete wind-field with 15m/s mean, used for inducing thrust at the rotor by the simple model

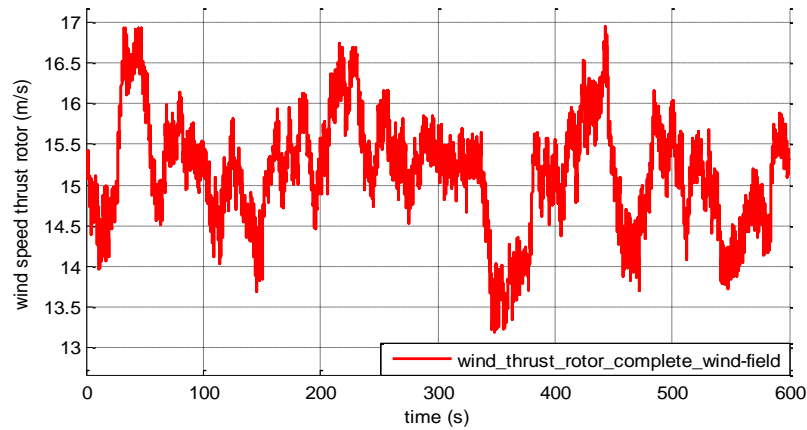


Figure 5-124. Time series of the complete wind-field with 15m/s mean, used for inducing thrust at the rotor by the simple model

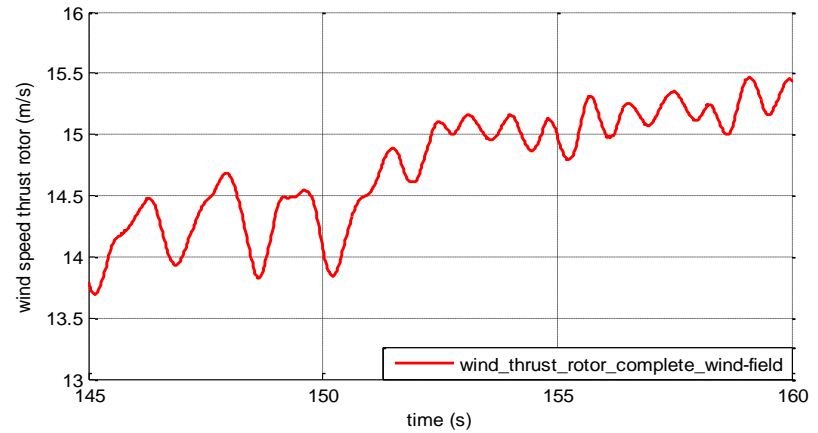


Figure 5-125. Time series extract of the complete wind-field with 15m/s mean, used for inducing thrust at the rotor by the simple model

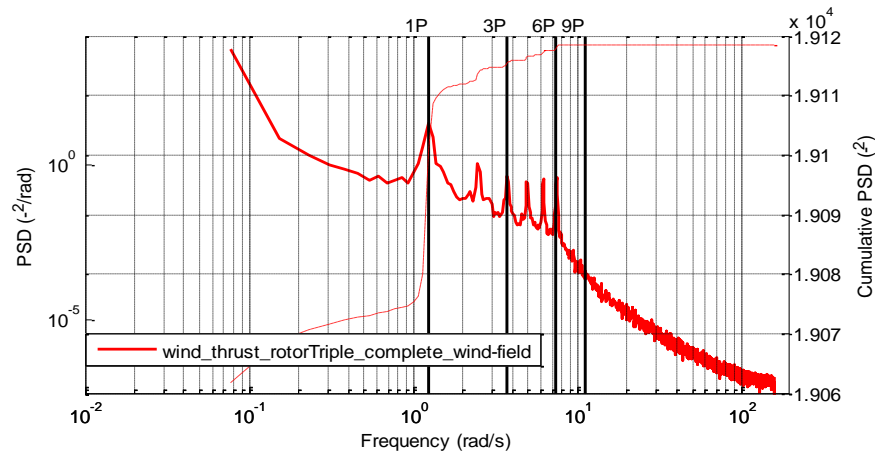


Figure 5-126. Spectrum of the complete wind-field with 15m/s mean, used for inducing thrust at the rotor by triple model

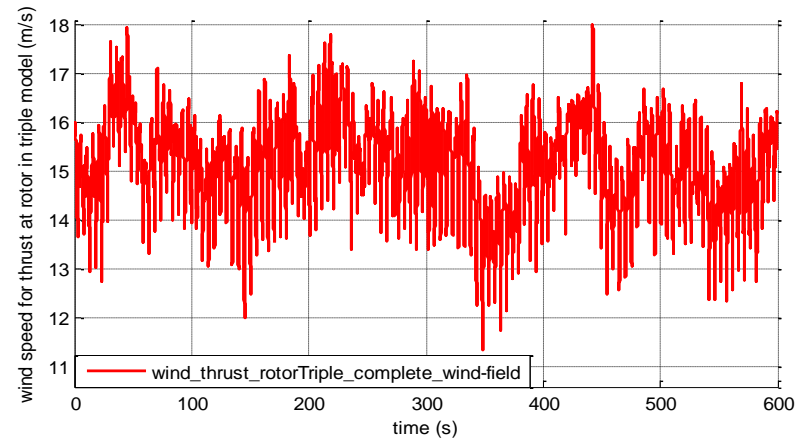


Figure 5-127. Time series of the complete wind-field with 15m/s mean, used for inducing thrust at the rotor by triple model

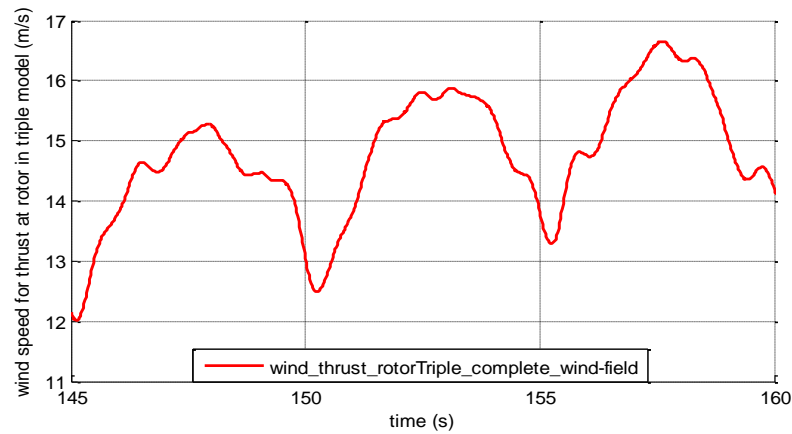


Figure 5-128. Time series extract of the complete wind-field with 15m/s mean, used for inducing thrust at the rotor by triple model

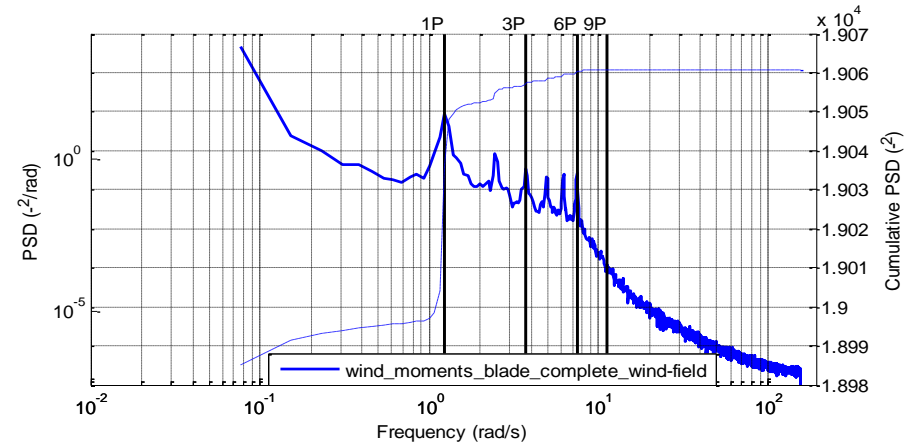


Figure 5-129. Spectrum of complete wind-field with 15m/s mean, used for inducing moments at the single blade by simple and triple model. Also used for inducing moments at the rotor by triple model

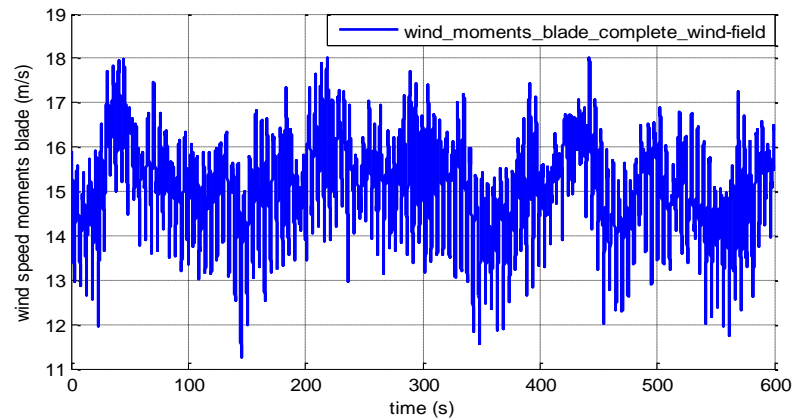


Figure 5-130. Time series of complete wind-field with 15m/s mean, used for inducing moments at the single blade by simple and triple model. Also used for inducing moments at the rotor by triple model

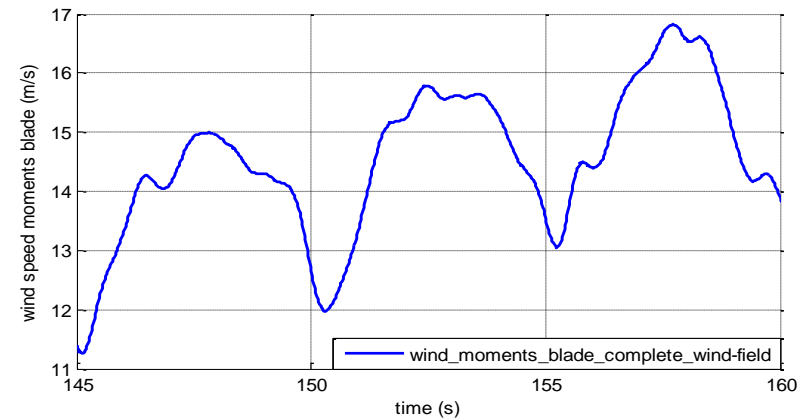


Figure 5-131. Time series extract of complete wind-field with 15m/s mean, used by simple and triple model for inducing moments at single blade and for inducing moments at the rotor by triple model

When considering the hub torque results, see Figure 5-132 to Figure 5-134 for the 15m/s case, Figure 5-135 to Figure 5-137 for the 15m/s and 18 degrees pitch offset and Figure 5-138 to Figure 5-140 for the 8m/s case, it is immediately obvious that the triple and single structure have a very close match. There is a small deviation in the cumulative spectrum in Figure 5-132 and Figure 5-135, for the 15m/s and 15m/s with 18deg offset which arises from the 3P peak. For the 8m/s case, the deviation in the cumulative spectra in Figure 5-138 arises from the lower frequencies. This would indicate the presence of some leakage which is worse in the 8m/s case, as would be expected as it is farthest away from the region of applicability of Separability. However, the impact of this leakage, as can be seen from the spectrum itself and the values in Table 6-23, is negligible. By looking at the cumulative spectrum from Figure 5-132, Figure 5-135, Figure 5-138, Table 5-22, the behaviour of the spectrum and time series for the isolated stochastic component of the wind-field and the isolated deterministic component of the wind-field, it is clear that the dynamics are going to be dominated by the stochastic component of the wind-field. Effectively, this is what is observed on the results of the complete effective wind-field model.

Similar observations can be made while looking at the out-of-plane RBM of the blade, see Figure 5-141 to Figure 5-143 for the 15m/s case, Figure 5-144 to Figure 5-146 for the 15m/s with 18 degrees of pitch offset and Figure 5-147 to Figure 5-149 for the 8m/s case, and their correspondent cumulative spectra. There is a very close match of the spectrum of the out-of-plane RBM between the single and triple model especially for the 15 m/s and 15m/s with 18deg pitch offset. It is in fact a closer match than for the hub torque for these two cases with the 8m/s case study having a small degree of deviation. As with previous tests, this behaviour is rather unexpected as the out-of-plane RBM is not supported by Separability. As expected the worse results come from the 8m/s case, but they are not bad. The data used in the spectrum of the moments and forces have been detrended.

The main conclusion that can be drawn from looking at the results for the torque (in-plane moment supported by Separability) and out-of-plane RBM of the blade (out-of-plane moment not supported by Separability) is that when the wind model is used in its complete form, the difference between the simple and triple structures and the leakage is such that it can be considered negligible and thus ignored. The cumulative values in Table 5-23 provide further support for this conclusion and the simple model should suffice to induce acceptable moments and forces.

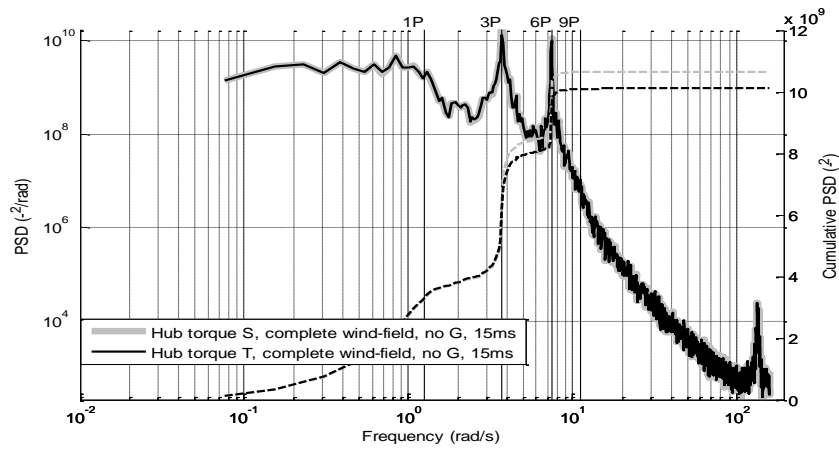


Figure 5-132. Hub torque spectrum comparison between simple and triple structure for the complete wind-field with mean 15m/s

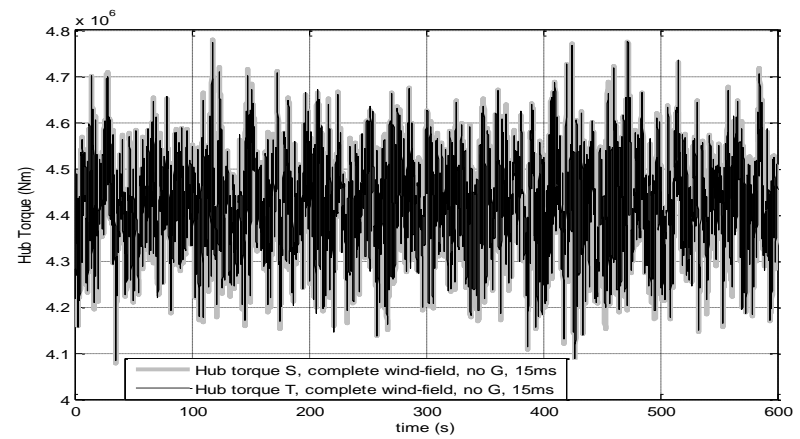


Figure 5-133. Hub torque time series comparison between simple and triple structure for the complete wind-field with mean 15m/s. Duration 600s

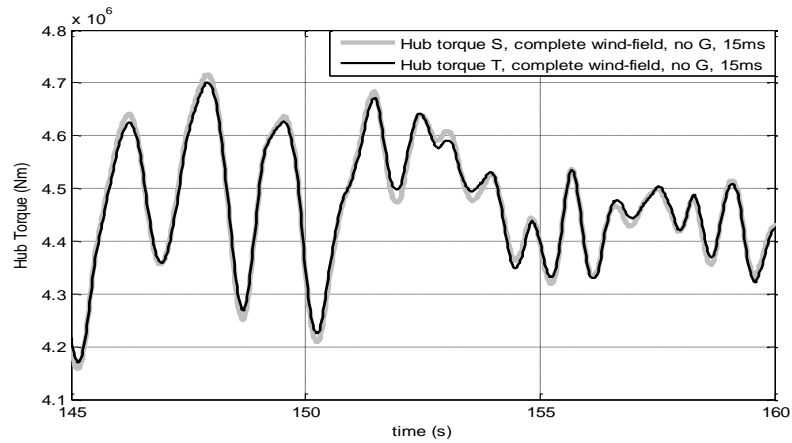


Figure 5-134. Hub torque 15s extract time series comparison between simple and triple structure for the complete wind-field with mean 15m/s

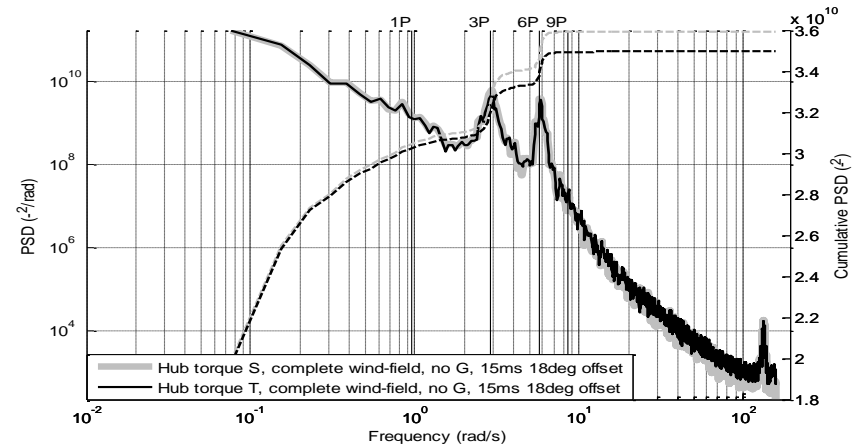


Figure 5-135. Hub torque spectrum comparison between simple and triple structure for the complete wind-field with mean 15m/s and 18 degrees of pitch offset

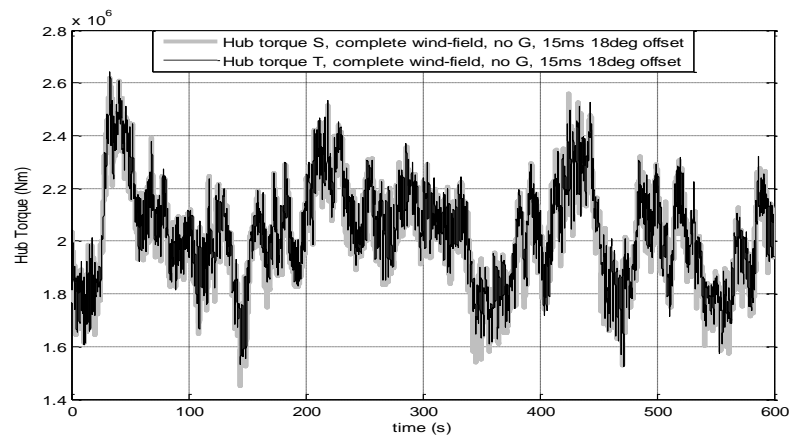


Figure 5-136. Hub torque time series comparison between simple and triple structure for the complete wind-field with mean 15m/s and 18 degrees of pitch offset. Duration 600s

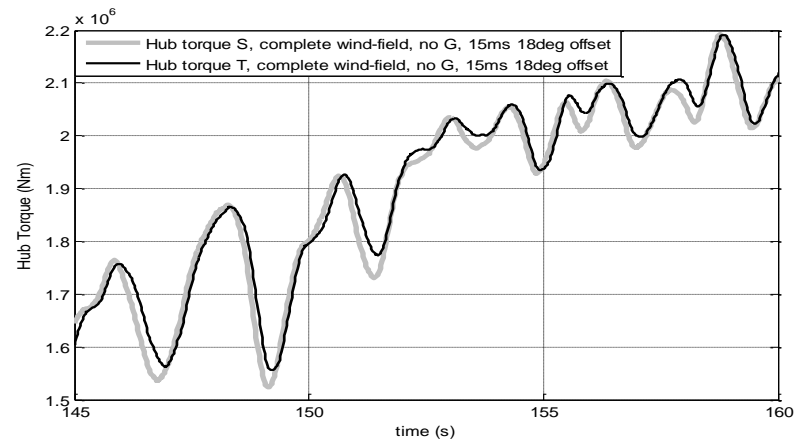


Figure 5-137. Hub torque 15s extract time series comparison between simple and triple structure for the complete wind-field with mean 15m/s and 18 degrees of pitch offset

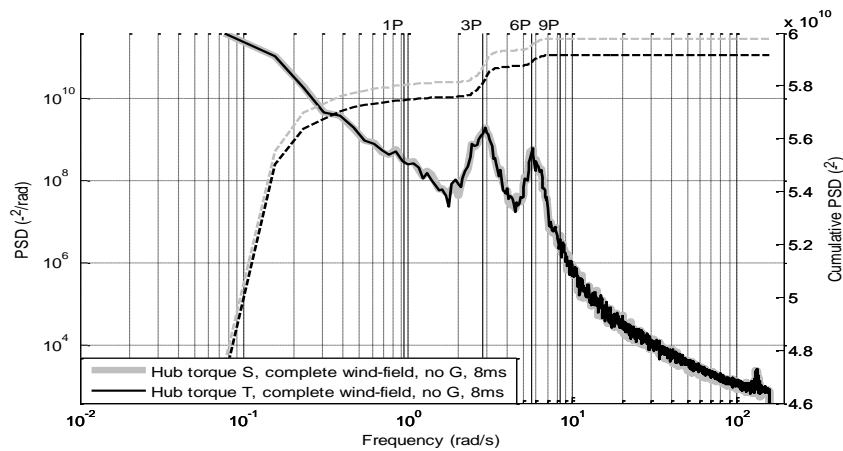


Figure 5-138. Hub torque spectrum comparison between simple and triple structure for the complete wind-field with mean 8m/s

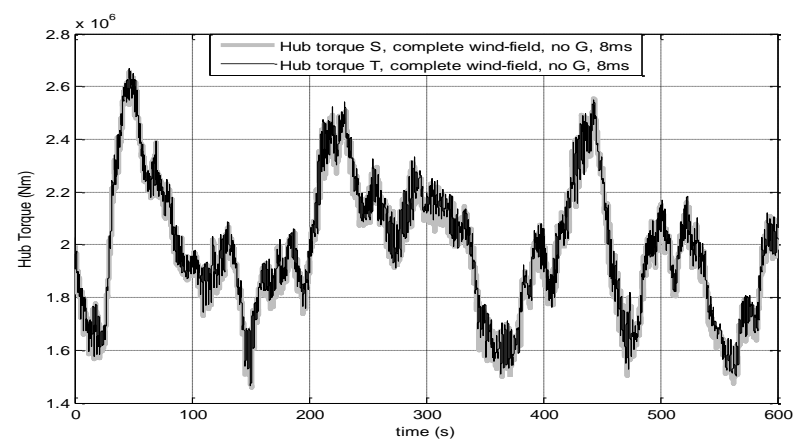


Figure 5-139. Hub torque time series comparison between simple and triple structure for the complete wind-field with mean 8m/s. Duration 600s

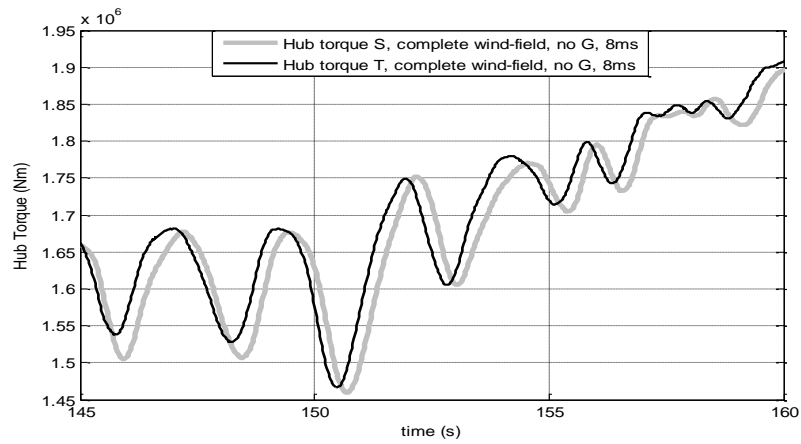


Figure 5-140. Hub torque 15s extract time series comparison between simple and triple structure for the complete wind-field with mean 8m/s

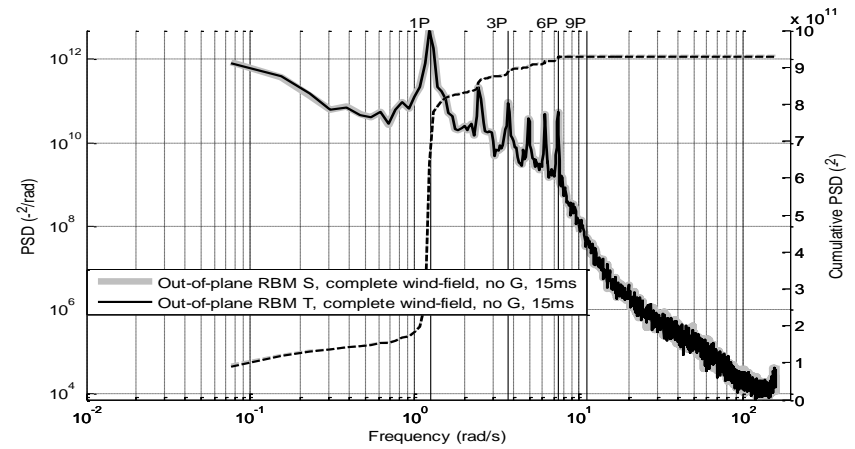


Figure 5-141. Out-of-plane RBM spectrum comparison between simple and triple structure for the complete wind-field with mean 15m/s

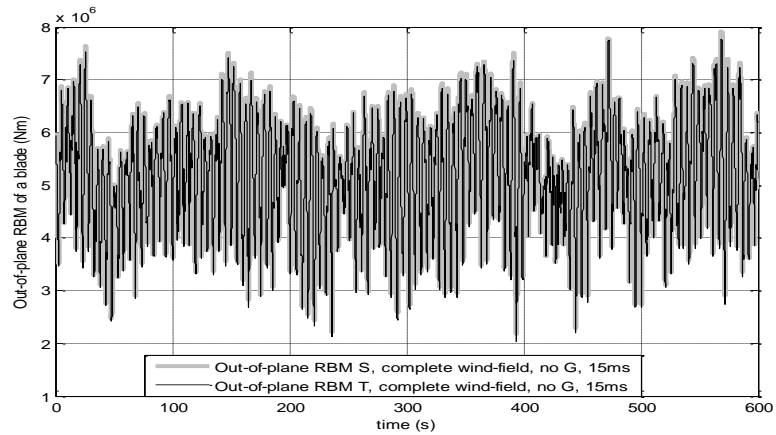


Figure 5-142. Out-of-plane RBM time series comparison between simple and triple structure for the complete wind-field with mean 15m/s. Duration 600s

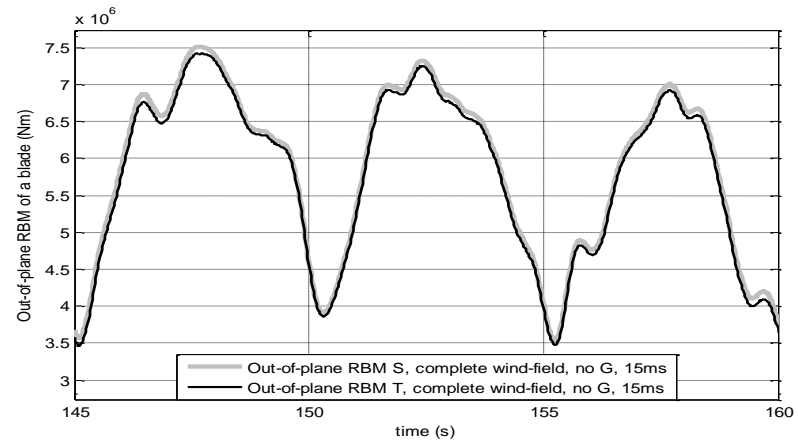


Figure 5-143. Out-of-plane RBM 15s extract time series comparison between simple and triple structure for the complete wind-field with mean 15m/s

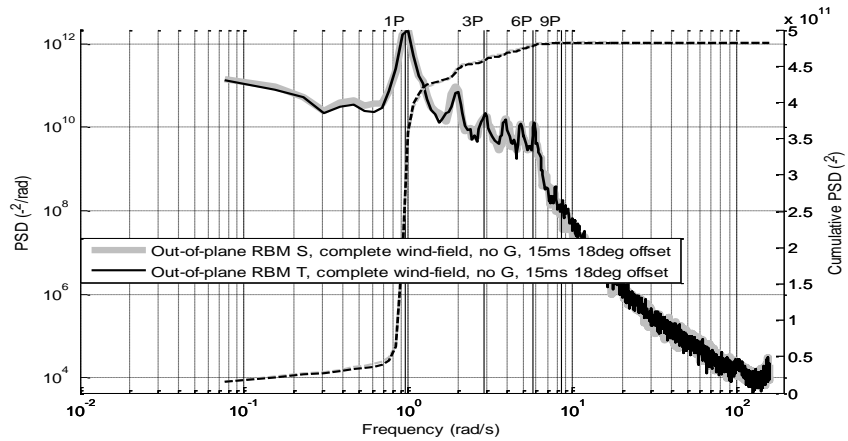


Figure 5-144. Out-of-plane RBM spectrum comparison between simple and triple structure for the complete wind-field with mean 15m/s and 18 degrees of pitch offset

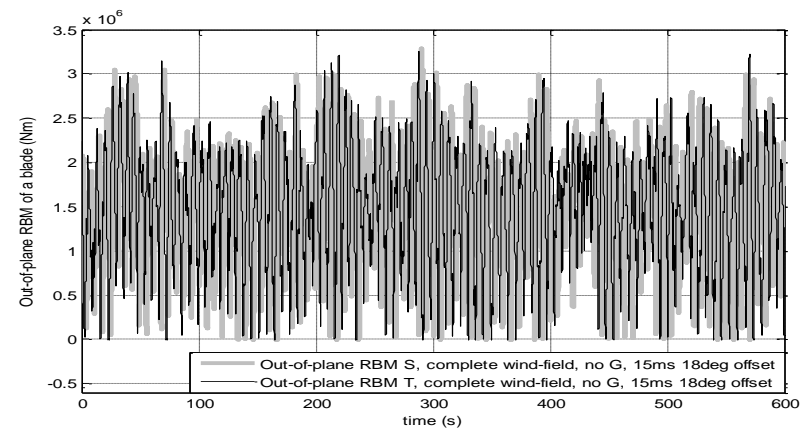


Figure 5-145. Out-of-plane RBM time series comparison between simple and triple structure for the complete wind-field with mean 15m/s and 18 degrees of pitch offset. Duration 600s

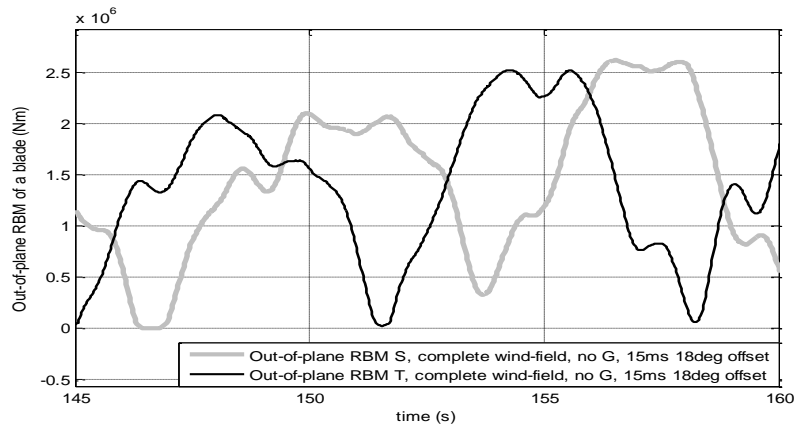


Figure 5-146. Out-of-plane RBM 15s extract time series comparison between simple and triple structure for the complete wind-field with mean 15m/s and 18 degrees of pitch offset

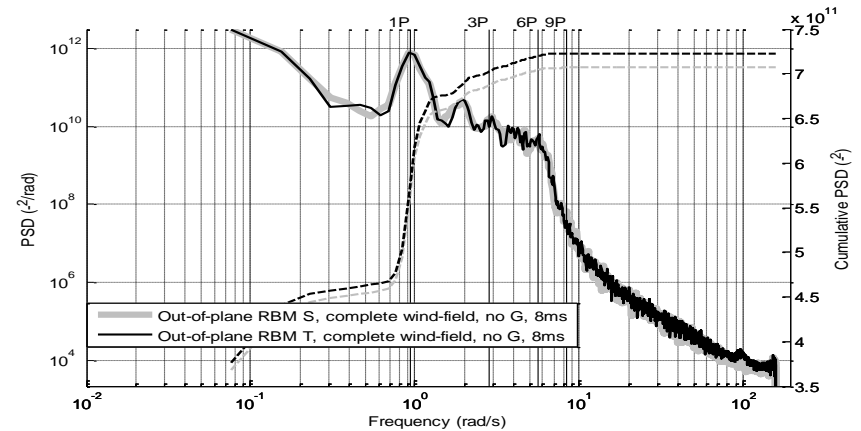


Figure 5-147. Out-of-plane RBM spectrum comparison between simple and triple structure for the complete wind-field with mean 8m/s

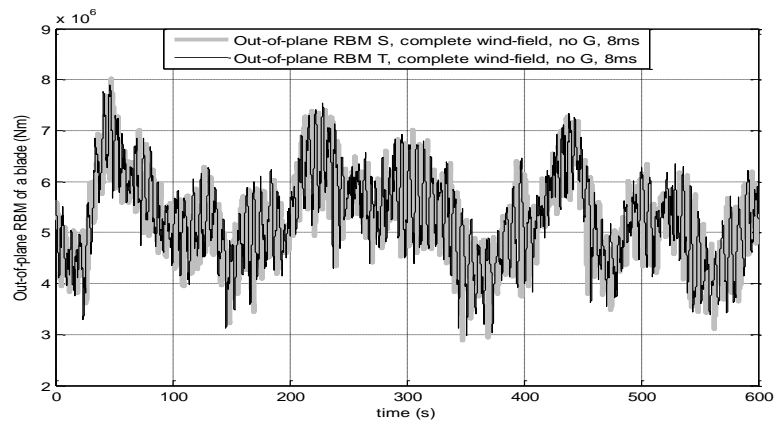


Figure 5-148. Out-of-plane RBM time series comparison between simple and triple structure for the complete wind-field with mean 8m/s. Duration 600s

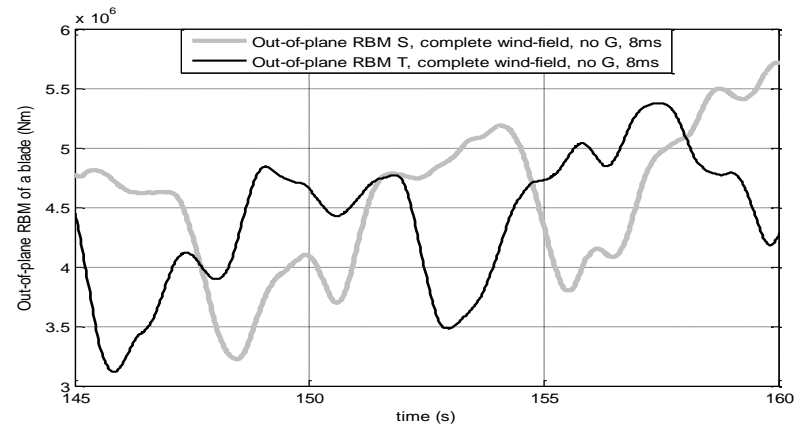


Figure 5-149. Out-of-plane RBM 15s extract time series comparison between simple and triple structure for the complete wind-field with mean 8m/s

			Cumulative Value	
			Simple Model	Triple Model
Complete wind-field	Torque	15m/s	1.0664e+010	1.0108e+010
		15m/s + 18 deg offset	3.5939e+010	3.4952e+010
		8m/s	5.979e+010	5.9166e+010
	Out-of-plane RBM	15m/s	9.304e+011	9.2874e+011
		15m/s + 18 deg offset	4.828e+011	4.8148e+011
		8m/s	7.068e+011	7.2246e+011

Table 5-23. Cumulative PSD value for hub torque and blade out-of-plane RBM for case study of 15m/s, 15m/s with 18 degree pitch offset and 8m/s for the simple and triple structure for the complete wind-field. The force of gravity is not taken into account.

5.5. Comparison to Bladed with Stiff Structural Dynamics

In order to verify the ability of the proposed effective wind-field model to induce the correct moments and forces on a WT, a direct comparison of performance against the industry standard program Bladed is made.

The structure of the verification compares the results from the effective wind-field model integrated into a Simulink model of a 5MW turbine to a Bladed model for a WT with the same characteristics and with a comparable wind input generated by Bladed itself. Both WT have the same controller. Nevertheless, the Bladed and Simulink WT models have differences that are not related to the input coming from the wind-field model *per se*. Rather these differences arise from the differences in the WT model dynamics and representation of the wind. Such differences can be magnified by the controller.

To minimise the impact of these and have a clearer and fairer comparison, the following actions have been taken,

- 1) To use the Bladed capacity to generate a wind series on the basis of empiric data to generate a Bladed turbulent wind file based on the common component in the uniform and linear *layer $nP = 0$* level of the proposed effective wind-field model. The common component in *layer $nP = 0$* is chosen because it has the biggest impact on the wind characteristics. The 2 representations cannot be the same but should have similar statistical properties.
- 2) To make the WT structure much stiffer to reduce the impact from the differences in representation of the WT dynamics between Bladed and the Simulink model.

In this section the results for the hub torque and the out-of-plane RBM of the blade are analysed whereas the full set of results can be found on Appendix H. The effective wind-field in these examples has a TI of 10% and 3 different mean wind speeds have been tested: 15m/s (above rated region), 15m/s with 18 degrees offset (below rated) and 8m/s (below rated C_p tracking region). The data used in the spectrum of the moments and forces have been detrended. In Figure 5-150 the operating strategy of the WT can be seen. The nominal generator torque of this 5MW WT is around 4.3×10^6 Nm.

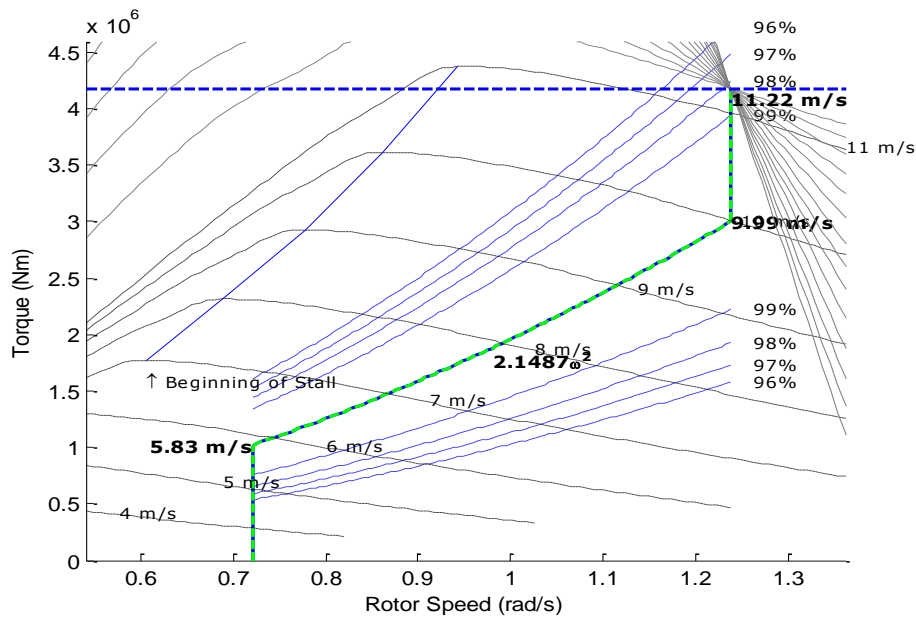


Figure 5-150. Operational strategy of the 5MW WT used for testing

In Figure 5-151 to Figure 5-152 for the 15m/s case, Figure 5-153 to Figure 5-154 for the 15m/s with 18 degrees offset case and Figure 5-155 to Figure 5-156 for the 8m/s case, the hub torque spectrum and its time series can be seen. From Figure 5-157 to Figure 5-158 for the 15m/s case, from Figure 5-159 to Figure 5-160 for the 15m/s with 18 degrees of pitch offset and from Figure 5-161 to Figure 5-162 for the 8m/s case, the out-of-plane RBM of the blade spectrum and its time series can be seen. The Bladed results are presented with the thin black line whereas the Simulink results are presented with a bold grey line. The proposed effective wind-field model is designed to only induce moments and forces up to 6P and components above 6P are not included the Simulink model.

In the case of hub torque, which is supported by the Separability property, all three cases have closely matching spectrum for Simulink and Bladed, even for the 8m/s case. The 15m/s with 18deg of pitch offset presents a small deviation in the 3P peak with the Simulink model inducing a slightly smaller peak, still this difference is not considered significant.

As expected, the results of the out-of-plane RBM are of a lesser quality when compared to the hub torque, since the out-of-plane RBM is not supported by the Separability property. The differences being more acute perhaps at the 1P peak. Regardless of this, the overall match is still very good especially for the 8m/s and 15m/s cases. From a more detailed comparison, the discrepancies seen at the 15m/s with 18deg offset and the improvement of the match when

moving to 8m/s would suggest that these discrepancies might be caused by the pitch offset being too aggressive and leading to the WT entering the 1st constant speed region and the controller being unable to cater appropriately with all the resulting switching of modes. In addition, the results in the above rated wind speed region are not as good as those below rated. Similar behaviour is also observed on other signals, see Appendix H, Section 5.6 and Appendix I. These discrepancies are in part due to differences in behaviour of the controllers in the Bladed and Simulink simulations, since it is in below rated conditions that the impact of the controller is at its minimum. Although these control related issues have no impact on the validity of the effective wind-field model, they should be taken into consideration during comparison of Simulink and Bladed model results, especially when the WT is not stiffened.

When considering the time traces for hub torque and out-of-plane RBM, it is quite clear that the wind traces in the time domain are similar but not the same. Still, both time series induce satisfactorily similar spectra which is the purpose of the proposed effective wind-field model.

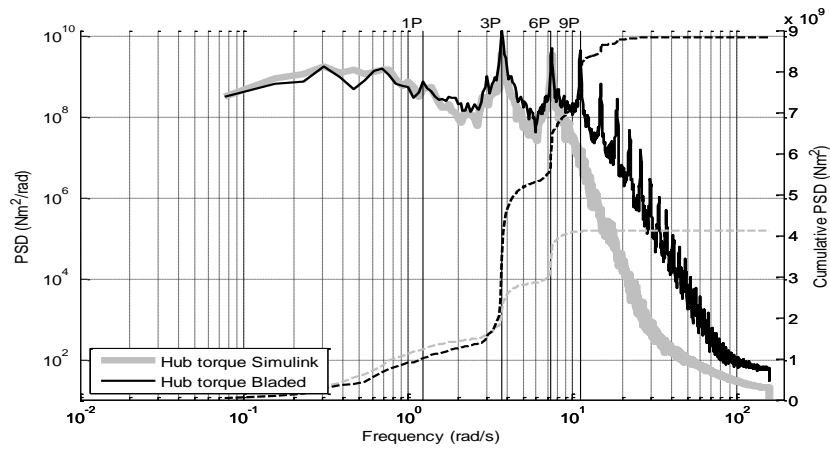


Figure 5-151. Hub torque spectrum comparison between Simulink and Bladed for the complete wind-field with mean 15m/s

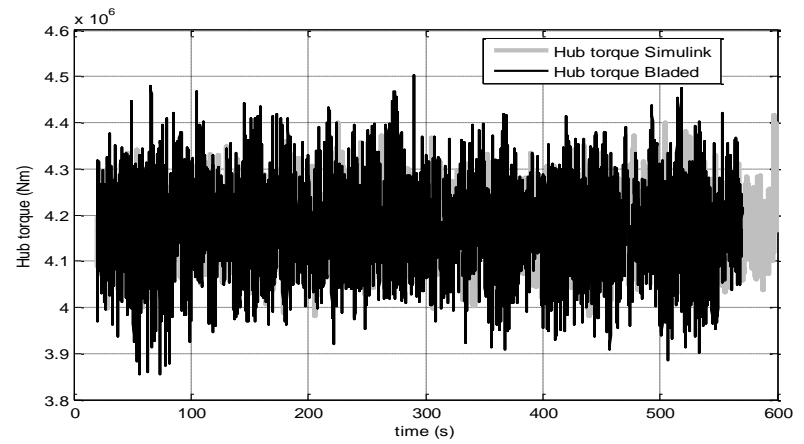


Figure 5-152. Hub torque time series comparison between Simulink and Bladed for the complete wind-field with mean 15m/s. Duration 600s

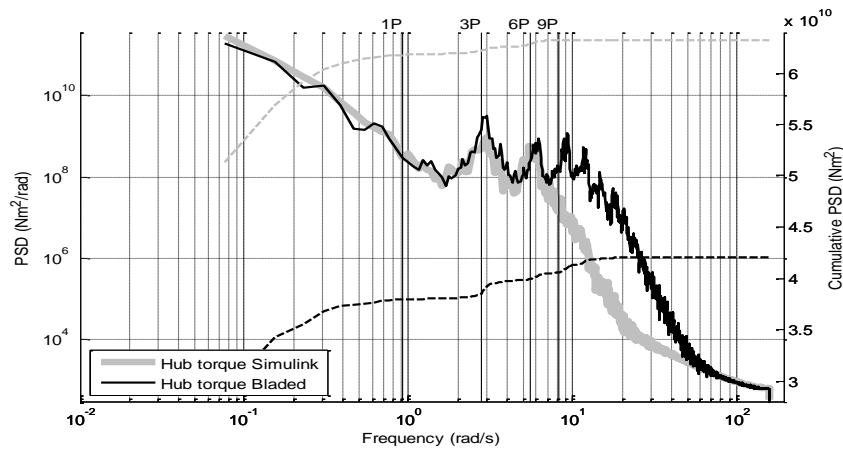


Figure 5-153. Hub torque spectrum comparison between Simulink and Bladed for the complete wind-field with mean 15m/s and 18 degrees of pitch offset

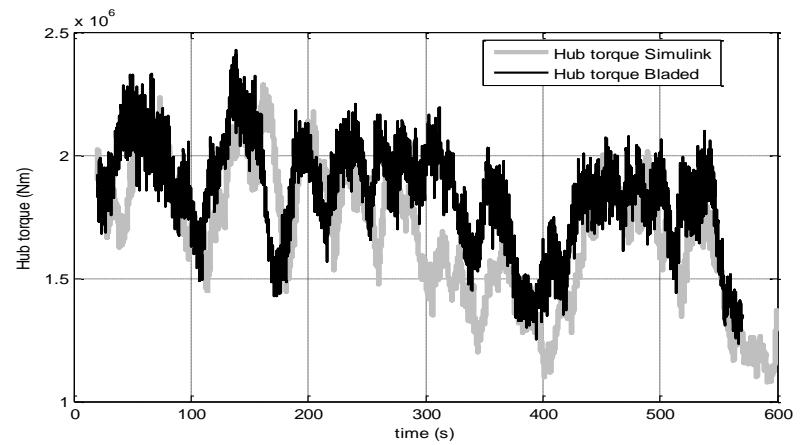


Figure 5-154. Hub torque time series comparison between Simulink and Bladed for the complete wind-field with mean 15m/s and 18 degrees of pitch offset. Duration 600s

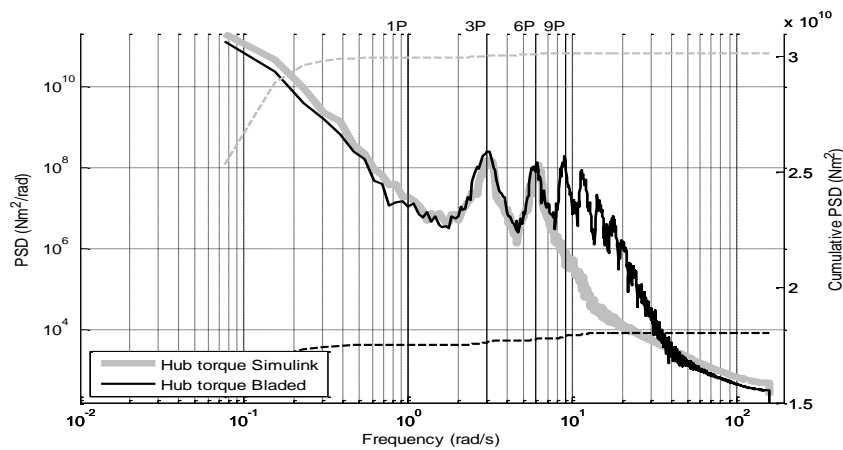


Figure 5-155. Hub torque spectrum comparison between Simulink and Bladed for the complete wind-field with mean 8m/s

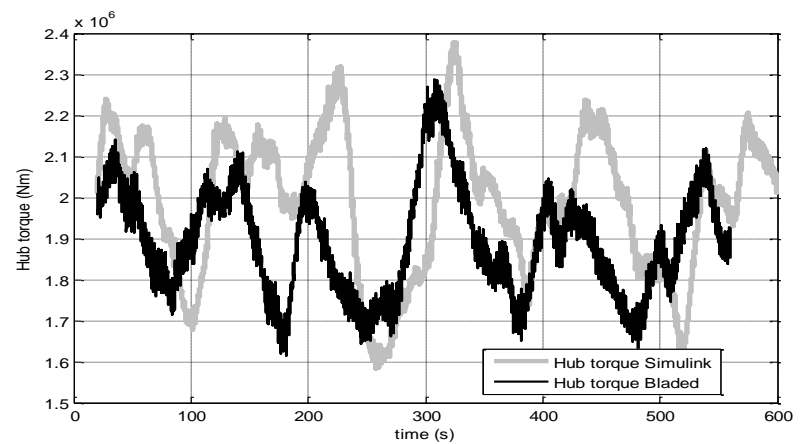


Figure 5-156. Hub torque time series comparison between Simulink and Bladed for the complete wind-field with mean 8m/s. Duration 600s

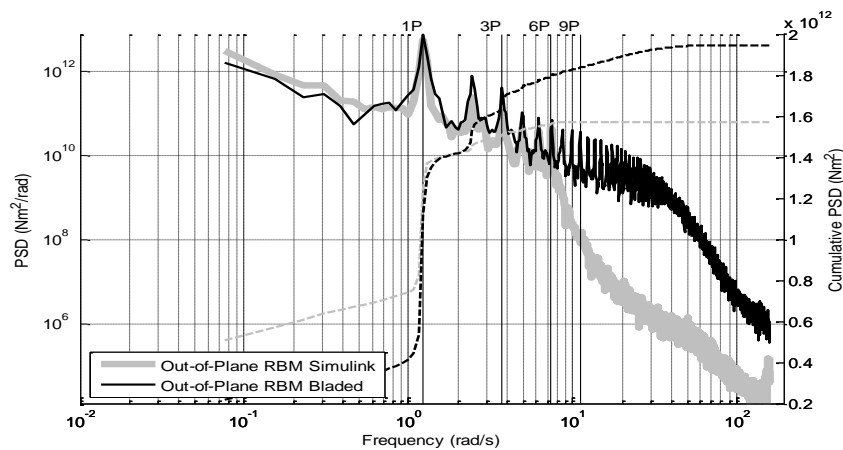


Figure 5-157. Out-of-plane RBM spectrum comparison between Simulink and Bladed for the complete wind-field with mean 15m/s

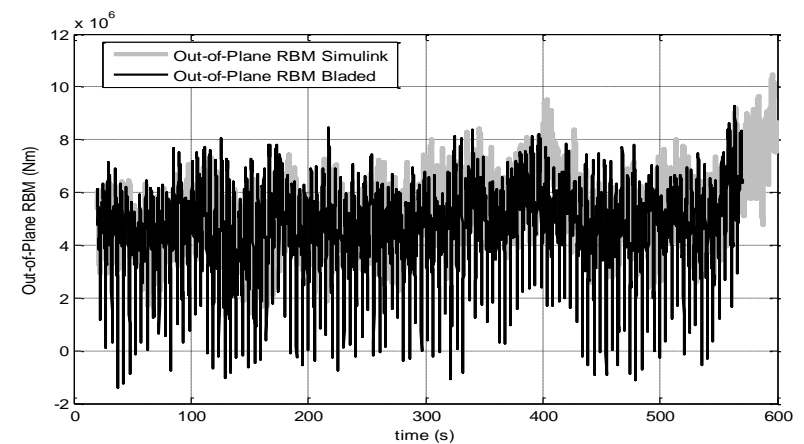


Figure 5-158. Out-of-plane RBM time series comparison between Simulink and Bladed for the complete wind-field with mean 15m/s. Duration 600s

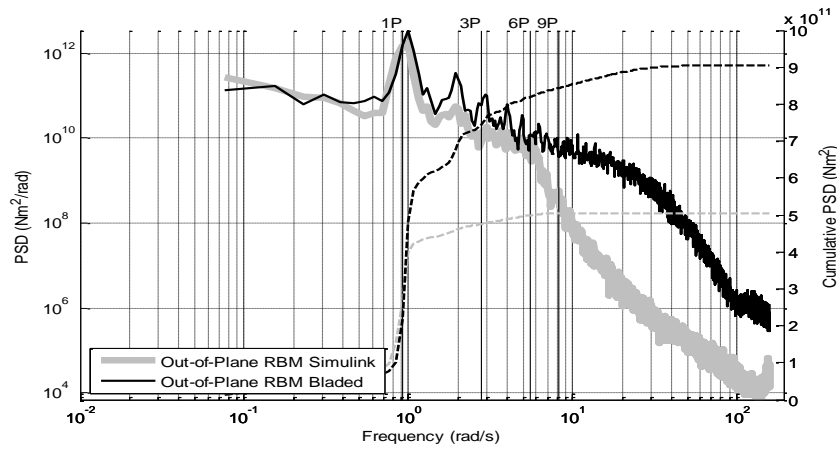


Figure 5-159. Out-of-plane RBM spectrum comparison between Simulink and Bladed for the complete wind-field with mean 15m/s and 18 degrees of pitch offset

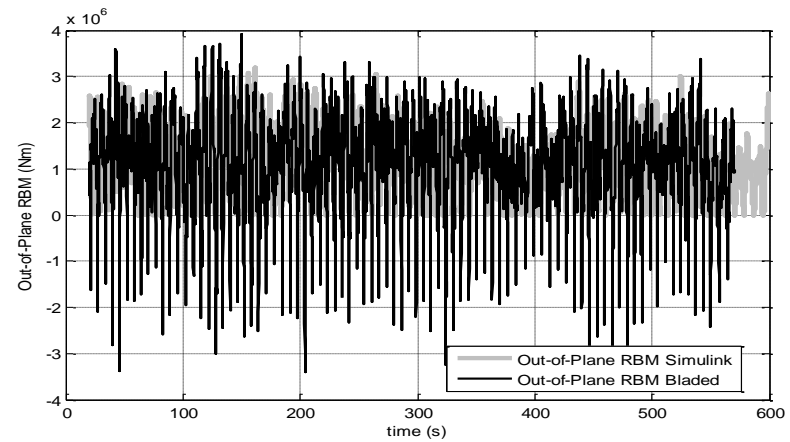


Figure 5-160. Out-of-plane RBM time series comparison between Simulink and Bladed for the complete wind-field with mean 15m/s and 18 degrees of pitch offset. Duration 600s

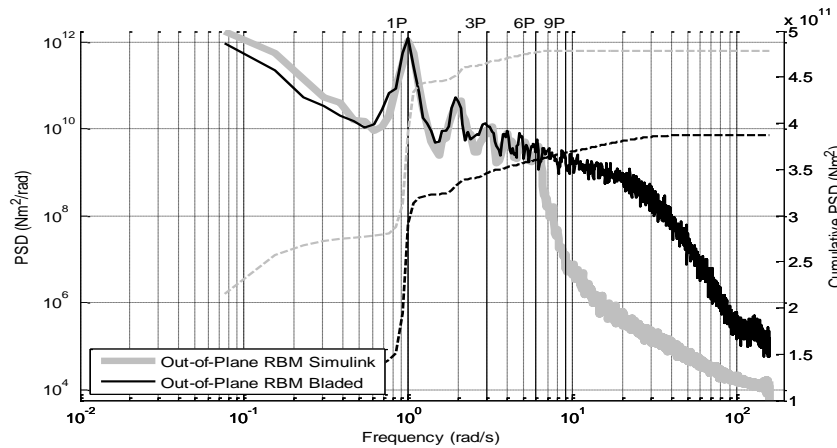


Figure 5-161. Out-of-plane RBM spectrum comparison between Simulink and Bladed for the complete wind-field with mean 8m/s

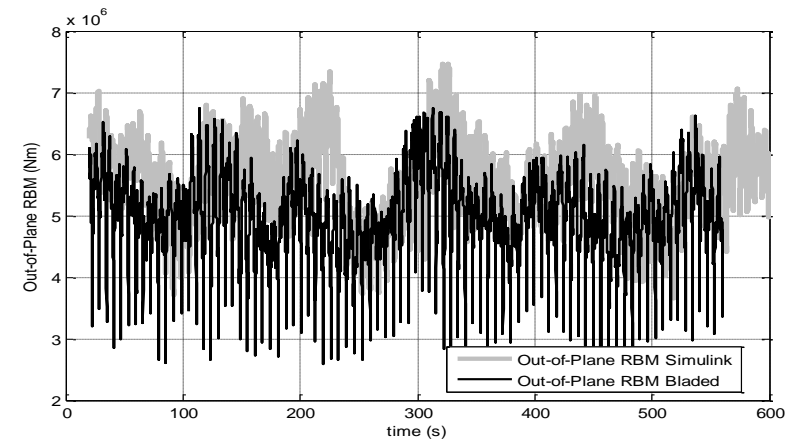


Figure 5-162. Out-of-plane RBM time series comparison between Simulink and Bladed for the complete wind-field with mean 8m/s. Duration 600s

5.6. Comparison to Bladed with Structural Dynamics

The effective wind-field model is compared to Bladed, with the dynamic modes of the WT active to provide a more realistic context.

The same 10% TI wind-field as in Section 5.5 has been used. Besides hub torque and out-of-plane RBM, thrust and in-plane RBM are also present in this set of results for the 15m/s and 8m/s cases. Results for the hub torque are shown from Figure 5-163 to Figure 5-164 for the 15m/s case and from Figure 5-165 to Figure 5-166 for the 8m/s case. Results for the thrust are shown from Figure 5-167 to Figure 5-168 for the 15m/s case and from Figure 5-169 to Figure 5-170 for the 8m/s case. Results for the in-plane RBM are shown from Figure 5-171 to Figure 5-172 for the 15m/s case and from Figure 5-173 to Figure 5-174 for the 8m/s case. Finally, results for the out-of-plane RBM are shown from Figure 5-175 to Figure 5-176 for the 15m/s case and from Figure 5-177 to Figure 5-178 for the 8m/s case. In Appendix I an equivalent set, including generator speed, can be found for a wind-field with turbulence intensity of 15% and 20%.

The comparison between Bladed and Simulink in this more realistic scenario shows that the proposed effective wind-field model is capable of successfully inducing forces and moments in a way that is meaningful for control purposes and that this capability applies to forces, e.g. thrust, and moments, e.g. out-of-plane RBM of the blade, which are not directly supported by the Separability theory.

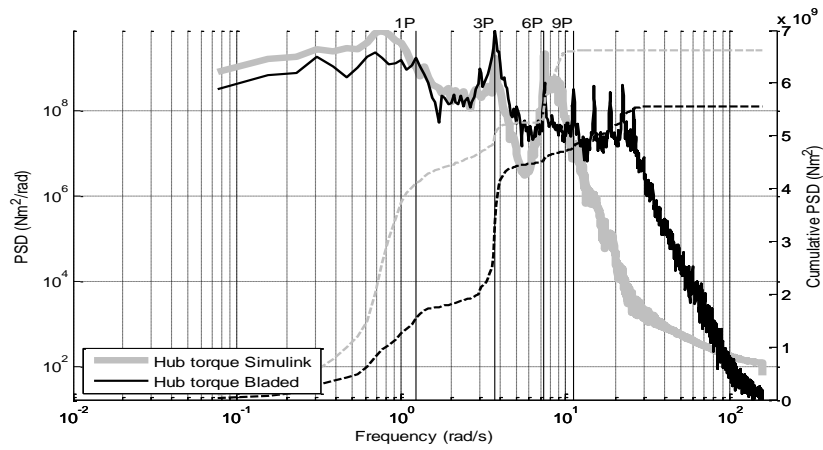


Figure 5-163. Hub torque spectrum comparison between Simulink and Bladed for the complete wind-field with mean 15m/s and a flexible WT

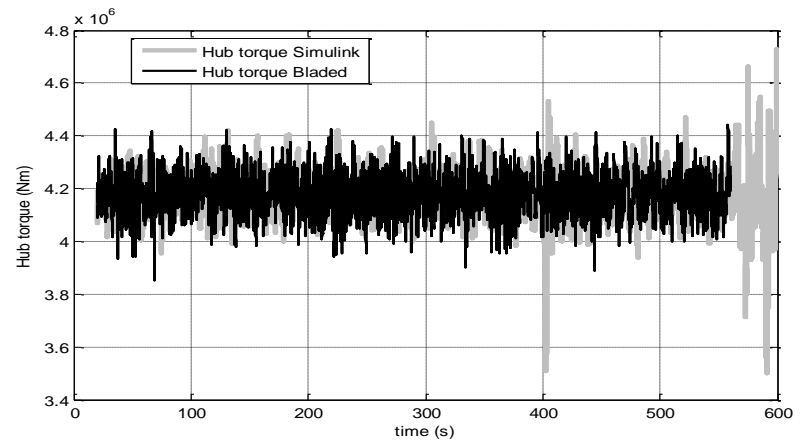


Figure 5-164. Hub torque time series comparison between Simulink and Bladed for the complete wind-field with mean 15m/s and a flexible WT.

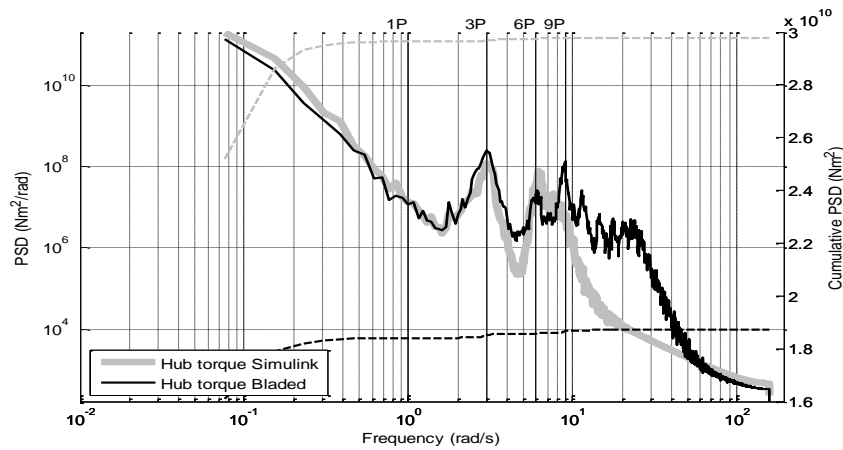


Figure 5-165. Hub torque spectrum comparison between Simulink and Bladed for the complete wind-field with mean 8m/s and a flexible WT

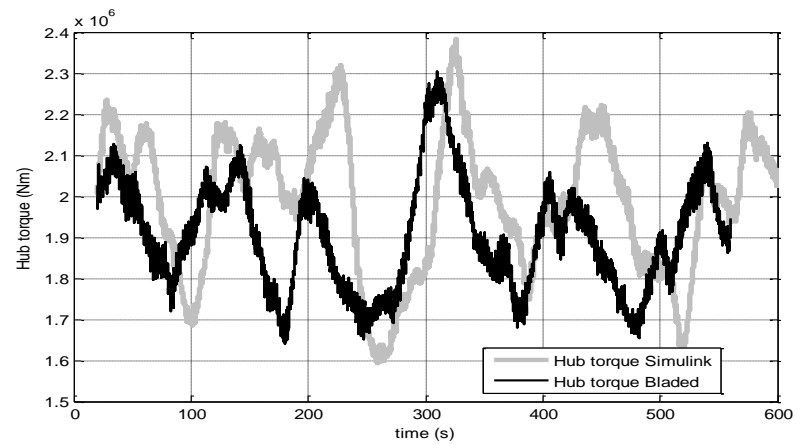


Figure 5-166. Hub torque time series comparison between Simulink and Bladed for the complete wind-field with mean 8m/s and a flexible WT

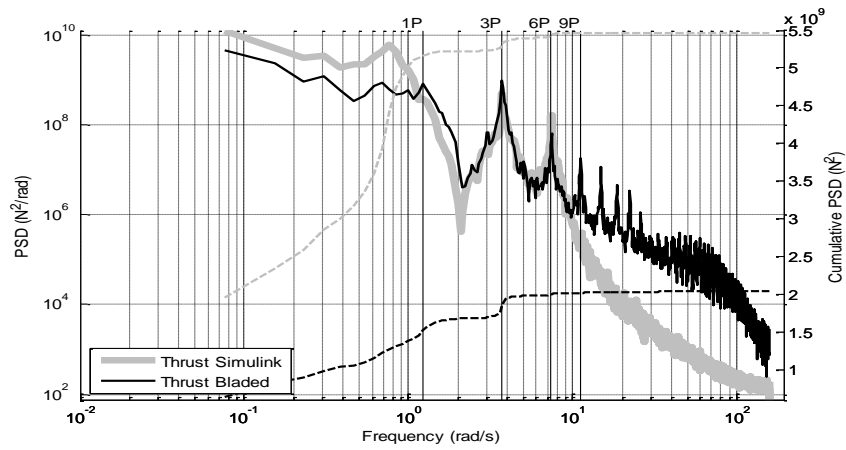


Figure 5-167. Thrust spectrum comparison between Simulink and Bladed for the complete wind-field with mean 15m/s and a flexible WT

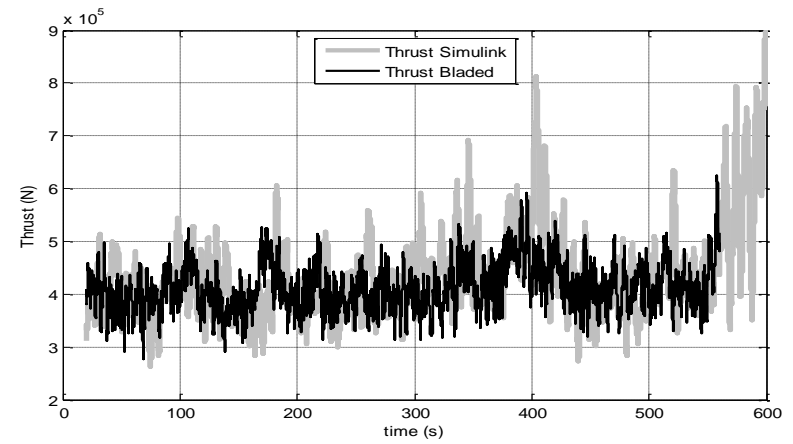


Figure 5-168. Thrust time series comparison between Simulink and Bladed for the complete wind-field with mean 15m/s and a flexible WT

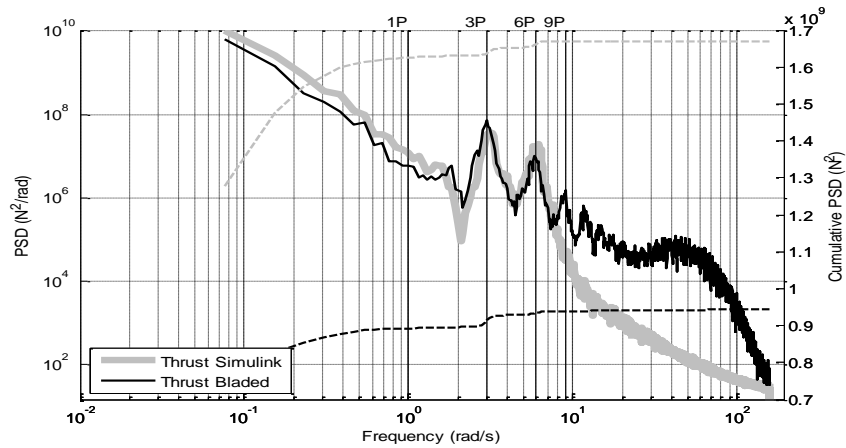


Figure 5-169. Thrust spectrum comparison between Simulink and Bladed for the complete wind-field with mean 8m/s and a flexible WT

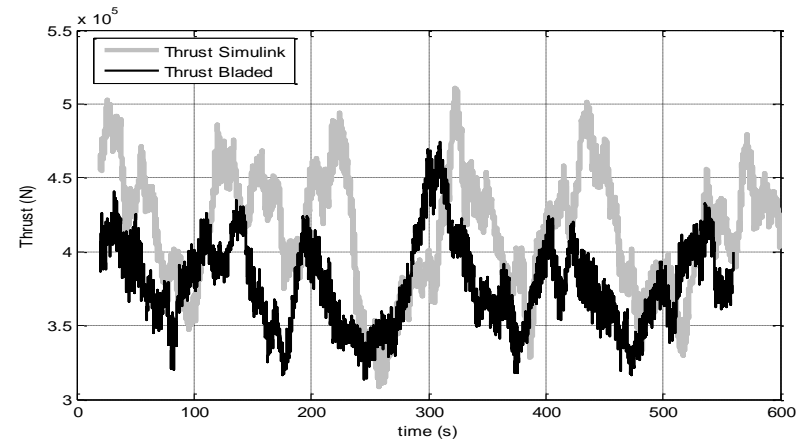


Figure 5-170. Thrust time series comparison between Simulink and Bladed for the complete wind-field with mean 8m/s and a flexible WT

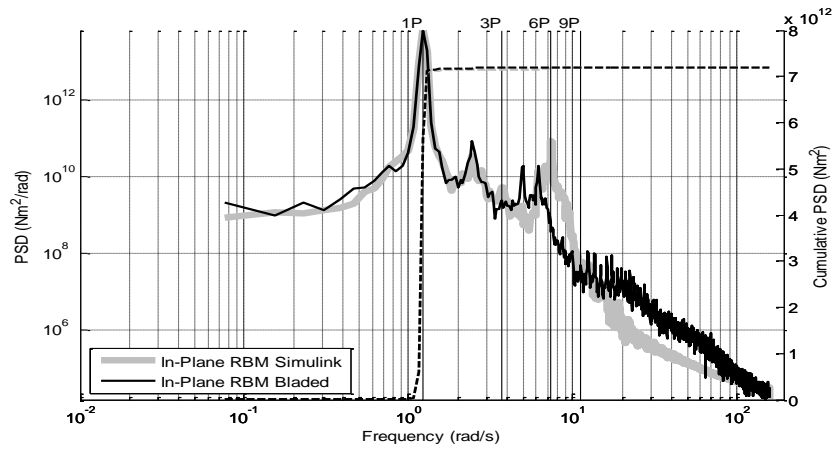


Figure 5-171. In-plane RBM spectrum comparison between Simulink and Bladed for the complete wind-field with mean 15m/s and a flexible WT

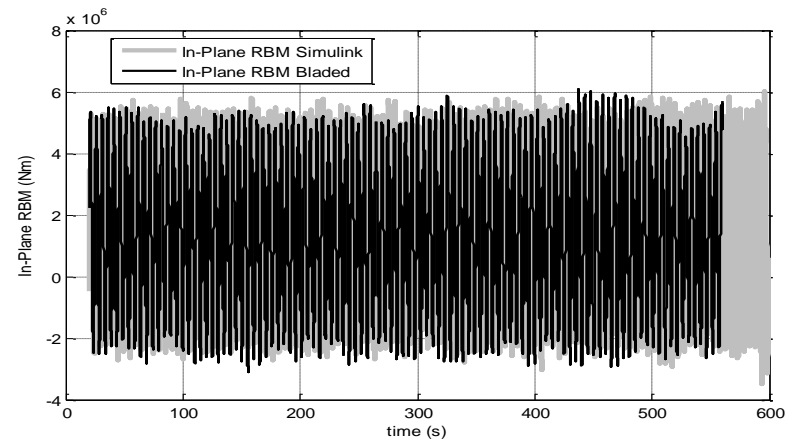


Figure 5-172. In-plane RBM time series comparison between Simulink and Bladed for the complete wind-field with mean 15m/s and a flexible WT

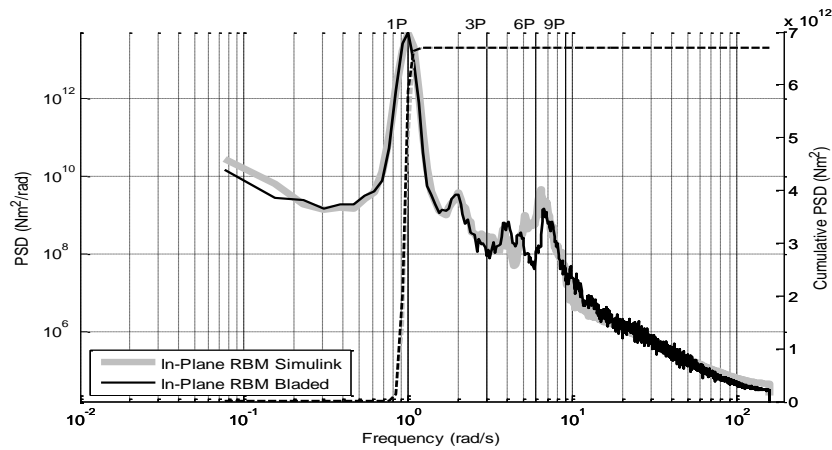


Figure 5-173. In-plane RBM spectrum comparison between Simulink and Bladed for the complete wind-field with mean 8m/s and a flexible WT

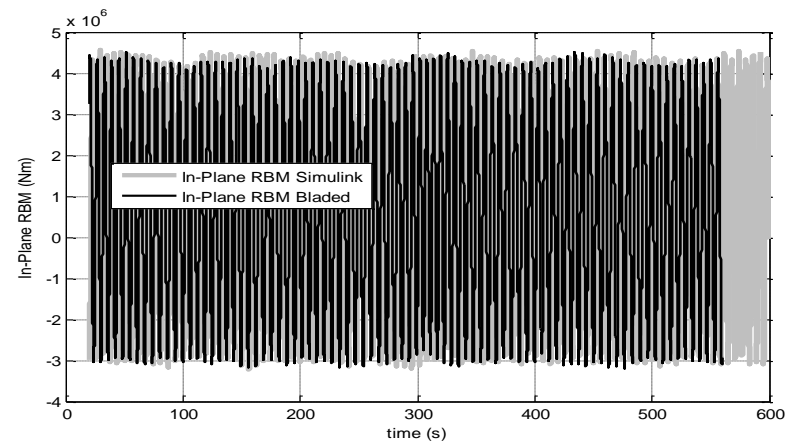


Figure 5-174. In-plane RBM time series comparison between Simulink and Bladed for the complete wind-field with mean 8m/s and a flexible WT

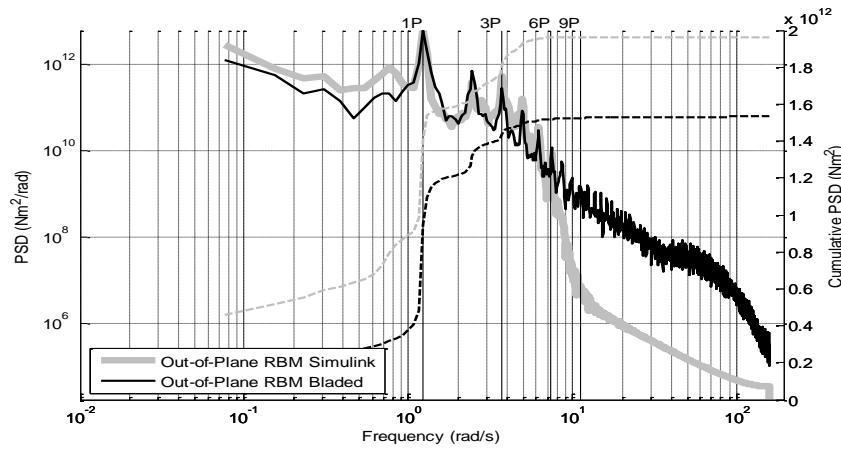


Figure 5-175. Out-of-plane RBM spectrum comparison between Simulink and Bladed for the complete wind-field with mean 15m/s and a flexible WT

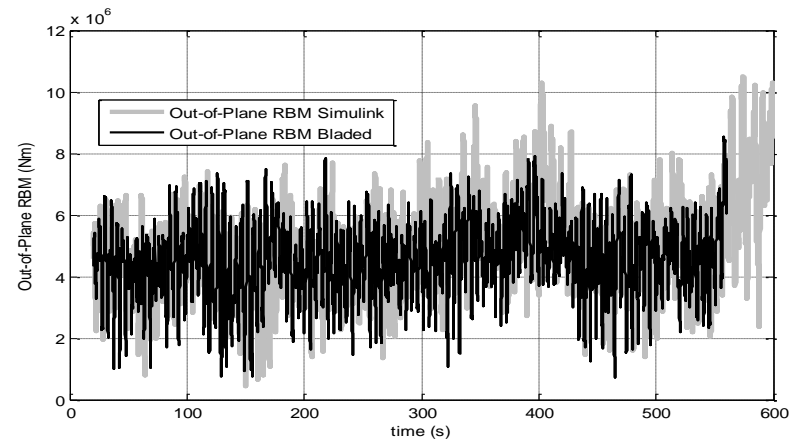


Figure 5-176. Out-of-plane RBM time series comparison between Simulink and Bladed for the complete wind-field with mean 15m/s and a flexible WT

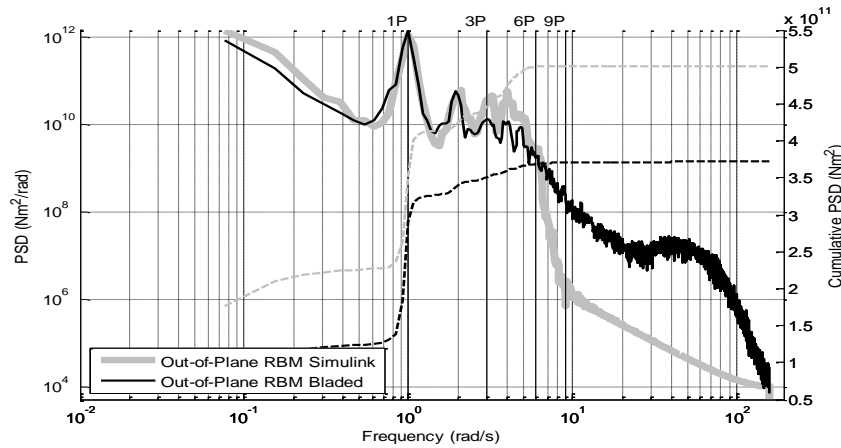


Figure 5-177. Out-of-plane RBM spectrum comparison between Simulink and Bladed for the complete wind-field with mean 8m/s and a flexible WT

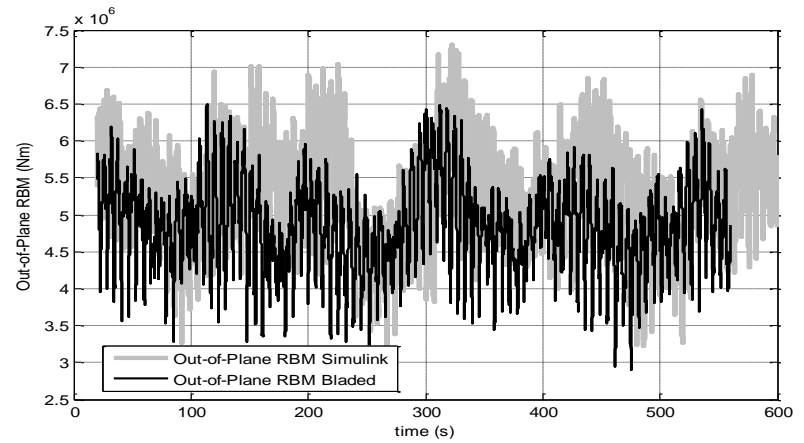


Figure 5-178. Out-of-plane RBM time series comparison between Simulink and Bladed for the complete wind-field with mean 8m/s and a flexible WT

5.7. Discussion on Wind-Field Modelling and Separability

The proposed effective wind-field model is tested systematically for two configurations of the model, triple and simple structure, see Section 5.1. The wind-field model consists of a number of components which are studied individually to assess the impact of leakage, were the Separability property invalid, see Section 5.2 and Section 5.3. The proposed effective wind-field model relies on the Separability property to be accurate. After the single components of the wind-field model are studied, the complete model is constructed in a step by step manner, see Section 5.4. To generate forces and moments the effective wind-field model is incorporated into a Simulink 5MW WT representation.

From the analysis, the outcomes regarding the presence of non-linear effects seen in leakage and the suitability of the triple and simple structure models for inducing forces and moments are the following:

- For the stochastic component of the wind-field the simple structure model should suffice.
- For the WS component of the wind-field modelled alone, the simple structure model may not suffice.
- For the TS component of the wind-field modelled alone, the simple structure model should suffice.
- For the deterministic component of the wind-field, as WS and TS components together, the simple structure model should suffice.
- For the complete effective wind-field model, composed of the complete stochastic component and a deterministic component containing WS and TS, the simple structure model should suffice.

The complete effective wind-field model, with the simple structure incorporated into a Simulink 5MW WT representation, is used for direct comparison with Bladed simulation for validation purposes. The WT Bladed model is defined with the same characteristics and with a comparable wind input generated by Bladed itself, as specified in Section 5.5. Both WT models, defined in Simulink and Bladed, have the same controller. Nevertheless, the Bladed and Simulink WT models have differences that are not related to the input coming from the wind-field model *per se*. Rather these differences arise from the differences in the WT model dynamics and representation of the wind. Such differences can be magnified by the controller.

Therefore, the comparison is firstly done with stiff WT structural dynamics to minimise the impact of these differences and focus on the effectiveness of the proposed effective wind-field model. Results in Section 5.5 provide a good match between the proposed effective wind-field model and Bladed.

Further comparison is pursued by activating the WT structural dynamics. Results in Section 5.6 suggest that in this more realistic scenario, the proposed effective wind-field model is capable of successfully inducing forces and moments in a way that is meaningful for control analysis and design purposes and that this capability applies to forces, e.g. thrust, and moments, e.g. out-of-plane RB of the blade, which are not directly supported by the Separability theory.

Consequently, it can be concluded that the wind-field model developed as per Figure 5-2 is a reasonable representation of the wind-field and is sufficiently validated to establish its suitability for control analysis and design purposes. If the assumption that Separability applied over the operating region of the WT were not valid, then that would have been clear from the results.

Furthermore, the detailed investigation in this chapter supports and provides strong additional evidence that Separability is valid over the operational envelope of the WT.

Chapter 6

Conclusions

The Separability property is investigated for constant speed WTs and variable speed WTs. The general structure of the Additivity functions $h(\cdot)$ and $g(\cdot)$ for both the wind speed and tip speed ratio based Separability, and their relationship is determined. In particular, the optimised fit for the wind speed based Separability, is found after the best parametric form for the individual equations $h(\cdot)$ and $g(\cdot)$ are identified.

Both the $g(\cdot)$ and $\tau(\cdot)$ functions are proven to be weakly non-linear and can be considered independent from ω . Whereas the $\mu(\cdot)$ function has been confirmed to have both dependency on ω and more non-linearity, albeit still relatively weakly so. This is largely due to the Basic Additivity property in Section 3.1.2 applying to Separability in tip speed ratio rather than the Additivity property from Section 3.2, an important consequence being that $\mu'(T_0/\omega_0^2) \neq 1$.

It is demonstrated that Separability exists for both constant and variable speed WTs and that it holds for very large neighbourhoods with very good accuracy. In fact, on average, it comfortably covers more than double the rated torque of all WTs explored.

It is established that both, principled Separability based on tip speed ratio and empirical Separability based on a simplified version of wind speed, provide good approximations for the aerodynamic torque with the latter as good as the former. Therefore, when exploiting Separability to develop advanced controllers and other purposes, such as wind speed models, which require good accuracy, the use of the empiric Separability relationship of the form,

$$T \approx \tau\left(T_0 + (h(\omega, \beta) - g(V))\right)$$

is fully justified.

This form of Separability provides with the correct values and derivatives at the equilibrium operating points and the $\tau(\cdot)$ function is invariant with ω .

Exploiting Separability, an effective wind-field model is proposed. It is tested systematically for two configurations of the model, triple and simple structure, see Section 5.1. The wind-field

model consists of a number of components which are studied individually to assess the impact of leakage, were the Separability property invalid, see Section 5.2 and Section 5.3. The proposed effective wind-field model relies on the Separability property to be accurate. After the single components of the wind-field model are studied, the complete model is constructed in a step by step manner, see Section 5.4. To generate forces and moments the effective wind-field model is incorporated into a Simulink 5MW WT representation.

From the analysis, the outcomes regarding the presence of non-linear effects seen in leakage and the suitability of the triple and simple structure models for inducing forces and moments are the following:

- For the stochastic component of the wind-field the simple structure model should suffice.
- For the WS component of the wind-field modelled alone, the simple structure model may not suffice.
- For the TS component of the wind-field modelled alone, the simple structure model should suffice.
- For the deterministic component of the wind-field, as WS and TS components together, the simple structure model should suffice.
- For the complete effective wind-field model, composed of the complete stochastic component and a deterministic component containing WS and TS, the simple structure model should suffice.

The complete effective wind-field model, with the simple structure incorporated into a Simulink 5MW WT representation, is used for direct comparison with Bladed simulation for validation purposes. The WT Bladed model is defined with the same characteristics and with a comparable wind input generated by Bladed itself, as specified in Section 5.5. Both WT models, defined in Simulink and Bladed, have the same controller. Nevertheless, the Bladed and Simulink WT models have differences that are not related to the input coming from the wind-field model *per se*. Rather these differences arise from the differences in the WT model dynamics and representation of the wind. Such differences can be magnified by the controller. Therefore, the comparison is firstly done with stiff WT structural dynamics to minimise the impact of these differences and focus on the effectiveness of the proposed effective wind-field model. Results in Section 5.5 provide a good match between the proposed effective wind-field model and Bladed.

Further comparison is pursued by activating the WT structural dynamics. Results in Section 5.6 suggest that in this more realistic scenario, the proposed effective wind-field model is capable of successfully inducing forces and moments in a way that is meaningful for control analysis and design purposes and that this capability applies to forces, e.g. thrust, and moments, e.g. out-of-plane RB of the blade, which are not directly supported by the Separability theory.

Consequently, it can be concluded that the wind-field model developed as per Figure 5-1 is a reasonable representation of the wind-field and is sufficiently validated to establish its suitability for control analysis and design purposes. If the assumption that Separability applied over the operating region of the WT were not valid, then that would have been clear from the results.

Furthermore, the detailed investigation in Chapter 5 supports and provides strong additional evidence that Separability is valid over the operational envelope of the WT.

6.1. Future Work

The following actions have been identified as the natural next steps for further work.

Whereas the accuracy and domain of validity of the Separability property has been extensively explored in this thesis and successfully applied to the above rated region, advanced controllers would benefit from further refinement of the Separability property such that the below rated region of the operating strategy is fully explored. This should be done in such a way that the validity regions are meticulously defined as they would improve the confidence in and accuracy of the fits for operating points further away from the locus of operating points.

The research presented in this thesis, shows that there is a relationship between the accuracy of Separability of the aerodynamics and the rotor design, as the accuracy of Separability changes with the different rotor design explored. Further exploration on this aerodynamics-Separability-rotor design relationship would further the understanding of the property as well as possibly shedding light on the aerodynamics themselves and the rotor design.

The proposed effective wind-field model could be further refined through an exploration of the effective wind-field model's weightings, which in this thesis have been chosen on general principles to be uniform for forces and linear for moments. The benefit would be to advance control designs that use the wind-field models. Furthermore, to account for certain control

complexities at high frequencies, that arise under particular circumstance for big WTs, the wind-field model could be expanded from $n = 1, \dots, 6$ to $n = 1, \dots, 12$.

Finally, whereas the capacity of designing an effective wind-field model provides an advancements in knowledge per se, it is the exploitation of the proposed effective wind-field model which will bring the biggest benefits.

Chapter 7

References

- [1] University of Strathclyde Archive Records.
- [2] What Causes Wind? UK Met Office, accessed March 2015,
<<http://www.metoffice.gov.uk/learning/wind/what-causes-wind>>
- [3] Starr, J. R., ‘*Source Book to the Forecasters’ reference book*’, The Meteorological Office, Berkshire, 1997.
- [4] US FAA Flight Standards Service, US National Weather Service. ‘*Aviation Weather for Pilots and Flight Operations Personnel*’, asa Publications, Washington, 1975.
- [5] Burton T., Sharpe D., Jenkins N., Bossanyi E., ‘*Wind Energy Handbook*’, 8th ed, Wiley Chichester, 2008.
- [6] Munteanu, I., Bractcu, A. I., Cutululis, N.-A, Ceanga, E. ‘*Optimal control of wind energy Systems. Towards a global approach*’, Springer-Verlag London, 2008.
- [7] Thresher R., Robinson M., Veers, P. ‘*The Future of Wind Energy Technology in the United States*’, Proc. of World Renewable Energy Congress, Glasgow, Scotland, October 2008.
- [8] Neilson V. W. ‘*Individual Blade Control for Fatigue Load Reduction of Large-scaled Wind Turbines: Theory and Modelling*’, Master’s Thesis, University of Strathclyde, March 2010.
- [9] Robb D. M. ‘*Model Based Predictive Control with Application to Renewable Energy Systems*’, PhD Thesis, University of Strathclyde, 2000.
- [10] Cook M.V. ‘*Flight Dynamics Principles: A Linear Systems Approach to Aircraft Stability and Control*’, 3rd ed, Elsevier Ltd Waltham, 2012.

- [11] Martin O., Hansen L. ‘*Aerodynamics of Wind Turbines*’, 2nd ed, Earthscan Oxon, 2008.
- [12] Troen, I. and Petersen, E. L. ‘*European Wind Atlas*’, Riso National Laboratory, 1989.
- [13] Leithead, W.E. ‘*Effective Wind Speed Models for Simple Wind Turbine Simulations*’, Proc. BWEA, Nottingham, pp 321-326, March 1992.
- [14] Gavriluta C., Spataru S., Mosincat I., Citro C., Candela I., Rodriguez P. ‘*Complete methodology on generating realistic wind speed profiles based on measurements*’, International Conference on Renewable Energies and Power Quality (ICREPQ’ 12) Santiago de Compostela Spain 2012.
- [15] Krause, D.C., Man, D.T. ‘*Transient behaviour of a class of turbine generators during electrical disturbances*’, I.E.E.E. Trans. of Power Appr. and Syst., V.PAS-100, pp. 2202-2210, 1981.
- [16] Anderson P.M., Bose A. ‘*Stability simulation of a wind turbine*’, I.E.E.E. Trans. of Power Appr. and Syst., V.PAS-102, pp. 791-3795, 1983.
- [17] Vaicaitis, Rimas, Masanoba Shinozuka, and Masaru Takeno. ‘*Parameters Study of Wind Loading on Structures*’, J. of the Structural Div., ASCE, pp. 453-468, Mar. 1973.
- [18] Leithead WE, De la Salle S, Reardon D. ‘*Role and Objectives of Control for Wind Turbines*’, IEE Proceedings-C 138(2):135-148, 1991.
- [19] Nichita C., Dragos L., Dakyo B., Ceanga E. ‘*Large band simulation of the wind speed for real time wind turbine simulators*’, I.E.E.E. Trans. on Energy Conversion, VOL. 17, NO. 4, December 2002.
- [20] Welfonder E, Neifer R, Spanner M. ‘*Development and experimental identification of dynamic models for wind turbines*’, Control Engineering Practice 5(1):63-73, 1997.
- [21] Madsen, P.H., Frandsen, S. ‘*Pitch Angle Control for Power Limitation*’, Proc. of European Wind Energy Conference, Hamburg, pp. 612-919, 1984.

- [22] Leithead, W.E., de la Salle, S.A., Reardon, D., Grimble, M. J. ‘*Wind Turbine Control Systems Modelling and Design -Phase I + II*’, Report prepared for Dept. of Energy, University of Strathclyde, 1991.
- [23] Davenport, A. G. ‘*The Spectrum of Horizontal Gustiness near the Ground in High Winds*’, Q. J. R. Meteorol. Soc., 87, pp. 194-211, 1961.
- [24] Leithead, W.E., de la Salle, S.A., Reardon, D. ‘*Classical Control of Active Pitch Regulation of Constant Speed Horizontal Axis Wind Turbines*’, Int. J. of Control, Vol. 55, No. 4, pp 845-876, 1992.
- [25] Bosanyi, E.A., Smith, E.J., Leithead, W.E., Agius, P.R.D. ‘*Design and Testing of a Classical Controller for MS-3 Wind Turbine*’, UK Dept. Energy Report, WN/6033, 1992.
- [26] De La Salle S. A., Reardon D., Leithead W. E., Grimble M.J. ‘*Review of Wind Turbine Control*’, International Journal of Control 52(6):1295-1310, 1990.
- [27] Leithead, W.E. ‘*Lecture 5. Rotor Drive Train*’, Course Notes, Centre for Doctoral Training in Wind Energy Systems, University of Strathclyde, 2010.
- [28] Thomsen, S.C., Niemann H., Poulsen N. K., ‘*Stochastic Wind Turbine Modeling for Individual Pitch Control*’, Proceedings of the European Control Conference, Budapest, Hungary, August 23-26, 2009
- [29] Leithead, W.E., Rogers, M. C. M., Agius, P., ‘*Dynamic Analysis of the Compliant Tip*’. University of Strathclyde, Report prepared for A.E.A. Technology, May 1992.
- [30] Leithead, W.E., Rogers, M.C.M., Leith, D.J., Connor B., ‘*Design of Wind Turbine Controllers*’, Proceedings of EURACO workshop ‘Recent Results in Robust and Adaptive Control’ Florence, Italy, 1995
- [31] Leithead, W.E., Leith, D., Harden, F., Markou, H., ‘*Global Gain-Scheduling Control for Variable Speed Wind Turbines*’, EWEC, Nice, France, 1999
- [32] Leithead, W.E., Harden, F., Leith, D., ‘*Identification of Aerodynamics and Drive-Train Dynamics for Variable Speed Wind Turbines*’, EWEC, Madrid, Spain, July 2003

- [33] Stock, A., ‘*Augmented Control for Flexible Operation of Wind Turbines*’, PhD Thesis, University of Strathclyde, 2014.
- [34] Private communication with Professor W. Leithead of the University of Strathclyde.
- [35] Leithead W.E., D.J. Leith, ‘*On the Separability of Wind Turbine Rotor Aerodynamics*’ . Internal Report, University of Strathclyde, 2000
- [36] Gala Santos M.L., Leithead W.E., Jamieson P., ‘*Aerodynamic Separability in Tip Speed Ratio and Separability in Wind - a Comparison*’, Torque 2012
- [37] Paul S. Veers, ‘*Three-Dimensional Wind Simulations*’, Sandia Report, SAND-0152, 1988.
- [38] M. Shinozuka, ‘*Simulation of Multivariate and Multidimensional Random Processes*’, J. Acoust. Soc. Am., no. 1, pp. 357-368, 1971.
- [39] B.J. Jonkman and L. Kilcher, ‘*TurbSim User’s Guide: Version 1.06.00*’, NREL Technical Report, 2012.
- [40] S. Poushpas, ‘*Wind Farm Simulation Modelling and Control*’, PhD Thesis, University of Strathclyde, 2016.
- [41] V. Spudic, M. Jelavic, M. Baotic, M. Vasak, and N. Peric, ‘*Reconfigurable control extension*’, AEOLUS, deliverable 3.3, University of Zagreb, 2010.
- [42] Jamieson, P., Leithead, W.E., Gala Santos, M.L., ‘*The Aerodynamic Basis of a Torque Separability Property*’. Proceedings of EWEA 2011, Brussels, 2011

Appendix A

Wind Turbine Models

In the following, the Bladed report description of the three wind turbines used in the study of the Separability property, namely Demo, Demo-modified and PJ9, can be found. The C_q tables for the same can be found in the USB stick accompanying this thesis.

A.1 Rotor PJ9

Project Name	Base 100m
Date	12 Oct 2006
Engineer	FM
Notes	
20 Feb 06 - DVW:	
Adjusted optimal mode gain	
- TSR of 9.0	
Re-tuned controller	
3MW	
Version	3.82
Project file	

GENERAL CHARACTERISTICS OF ROTOR AND TURBINE

Rotor diameter	100	m
Number of blades	3	
Teeter hinge	No	
Hub height	81.11	m
Offset of hub to side of tower centre	0	m
Tower height	79	m
Tilt angle of rotor to horizontal	6	deg
Cone angle of rotor	0	deg
Blade set angle	0	deg
Rotor overhang	4.33	m
Rotational sense of rotor, viewed from upwind	Clockwise	
Position of rotor relative to tower	Upwind	
Transmission	Gearbox	
Aerodynamic control surfaces	Pitch	
Fixed / Variable speed	Variable	
Diameter of spinner	4.444	m
Radial position of root station	1.33	m
Extension piece diameter	2.684	m
Extension piece drag coefficient	1	
Cut in windspeed	4	m/s
Cut out windspeed	25	m/s

BLADE GEOMETRY

Blade name	LM43.8P
Blade length	48.67 m
Pre-bend at tip	1.667 m
Pitch control	Full span

Distance from root (m)	Chord (m)	Twist (deg)	Twist Axis (% chord)	Thickness (% chord)	Pitch Axis (% chord)	Pre-bend (m)	Aero-dynamic control	Aerofoil section reference
0	2.68	5	25	100	50	0	Pitchable	1
2.22	2.76	5.38	25	96.412	49	0	Pitchable	2
4.44	2.94	6.695	25	80.537	48	1.E-03	Pitchable	2
6.67	3.13	8.093	25	65.08	47	0.007	Pitchable	2
8.89	3.31	9.37	25	51.689	46	0.02	Pitchable	3
11.11	3.48	10.215	25	40.327	45	0.052	Pitchable	3
13.33	3.52	9.39	25	32.55	44	0.062	Pitchable	3
15.56	3.33	7.17	25	28.4	42	0.042	Pitchable	3
17.78	3.1	5.42	25	25.62	41	0.043	Pitchable	3
20	2.86	4.326	25	23.769	41	0.072	Pitchable	3
22.22	2.65	3.499	25	22.248	40	0.117	Pitchable	3
24.44	2.46	2.859	25	20.99	40	0.172	Pitchable	4
26.67	2.29	2.31	25	20.034	40	0.229	Pitchable	4
28.89	2.13	1.762	25	19.405	40	0.32	Pitchable	5
31.11	2	1.281	25	19.027	40	0.413	Pitchable	5
33.33	1.86	0.893	25	18.785	40	0.521	Pitchable	5
35.56	1.73	0.559	25	18.642	40	0.642	Pitchable	5
37.78	1.62	0.3	25	18.61	40	0.779	Pitchable	5
40	1.52	0.12	25	18.52	40	0.929	Pitchable	5
42.22	1.41	-0.04	25	18.36	40	1.096	Pitchable	5
44.44	1.25	-0.22	25	18.17	40	1.277	Pitchable	5
46.67	0.96	-0.334	25	17.39	40	1.476	Pitchable	6
47.78	0.63	0.591	25	16.309	40	1.579	Pitchable	6
48.22	0.44	2.043	25	15.605	40	1.623	Pitchable	6
48.67	0.01	5.8	25	14.84	40	1.667	Pitchable	7

Blade Mass Integrals (No ice)

Blade Mass	8218.03	kg
First Mass Moment	121311	kgm
Second Mass Moment	3.206E+06	kgm ²
Blade inertia about shaft	3.544E+06	kgm ²

BLADE STIFFNESS DISTRIBUTION

Radial Position (m)	Flapwise stiffness (Nm ²)	Edgewise stiffness (Nm ²)
0	9.66E+09	9.66E+09
2.22	4.83E+09	7.51E+09
4.44	2.7E+09	4.83E+09
6.67	1.9E+09	4.51E+09
8.89	1.45E+09	3.69E+09
11.11	1.1E+09	3.25E+09
13.33	8.5E+08	2.85E+09
15.56	6.6E+08	2.39E+09
17.78	4.93E+08	1.8E+09
20	3.83E+08	1.4E+09
22.22	3.01E+08	1.44E+09
24.44	2.3E+08	1.27E+09
26.67	1.72E+08	1.05E+09
28.89	1.24E+08	1.02E+09
31.11	8.69E+07	7.94E+08
33.33	5.89E+07	6.1E+08
35.56	3.79E+07	3.9E+08
37.78	2.29E+07	2.36E+08
40	1.27E+07	1.46E+08
42.22	6.23E+06	1.14E+08
44.44	2.47E+06	6.19E+07
46.67	664000	2.5E+07
47.78	73600	3.37E+06
48.22	2840	1.83E+06
48.67	1.23	152

HUB MASS AND INERTIA

Mass of hub	45267.5	kg
Mass centre of hub	-0.1	m
Hub inertia: about shaft	60966.3	kgm ²
perpendicular to shaft	60966.3	kgm ²
Total Rotor Mass	69921.6	kg
Total Rotor Inertia	1.069E+07	kgm ²

A.2 Rotor Demo

Project Name Demo_a
Date 5 Sept 2001
Engineer EAB
Notes Generic 2MW Offshore turbine

Version 3.82

Project file

GENERAL CHARACTERISTICS OF ROTOR AND TURBINE

Rotor diameter	80	m
Number of blades	3	
Teeter hinge	No	
Hub height	61.5	m
Offset of hub to side of tower centre	0	m
Tower height	60	m
Tilt angle of rotor to horizontal	4	deg
Cone angle of rotor	0	deg
Blade set angle	0	deg
Rotor overhang	3.7	m
Rotational sense of rotor, viewed from upwind	Clockwise	
Position of rotor relative to tower	Upwind	
Transmission	Gearbox	
Aerodynamic control surfaces	Pitch	
Fixed / Variable speed	Variable	
Diameter of spinner	2.5	m
Radial position of root station	1.25	m
Extension piece diameter	1.9	m
Extension piece drag coefficient	0.8	
Cut in windspeed	4	m/s
Cut out windspeed	25	m/s

BLADE GEOMETRY

Blade length	38.75	m
Pre-bend at tip	0	m
Pitch control	Full span	

Distance from root (m)	Chord (m)	Twist (deg)	Twist Axis (% chord)	Thickness (% chord)	Pitch Axis (% chord)	Pre-bend (m)	Aero-dynamic control	Aerofoil section reference
0	2.06667	0	50	100	50	0	Pitchable	1
1.14815	2.06667	0	50	100	50	0	Pitchable	1
3.44444	2.75556	9	35	64	38	0	Pitchable	1
5.74074	3.44444	13	25	40	29	0	Pitchable	2
9.18519	3.44444	11	25	30	29	0	Pitchable	2
16.0741	2.75556	7.8	25	22	29	0	Pitchable	2
26.4074	1.83704	3.3	25	15	29	0	Pitchable	3
35.5926	1.14815	0.3	25	13	29	0	Pitchable	4
38.2333	0.688889	2.75	25	13	29	0	Pitchable	4
38.75	0.028704	4	25	13	29	0	Pitchable	4

BLADE MASS DISTRIBUTION

Distance from root (m)	Centre of Mass (% chord)	Mass/unit length (kg/m)
0	50	1084.77
1.14815	50	369.809
3.44444	38	277.356
5.74074	29	234.212
9.18519	29	209.558
16.0741	29	172.577
26.4074	29	103.546
35.5926	29	55.4713
38.2333	29	40.6789
38.75	29	24.6539

Blade Mass Integrals (No ice)

Blade Mass	6546.72	kg
First Mass Moment	84218.6	kgm
Second Mass Moment	1.785E+06	kgm ²
Blade inertia about shaft	2.006E+06	kgm ²

BLADE STIFFNESS DISTRIBUTION

Radial Position (m)	Flapwise stiffness (Nm ²)	Edgewise stiffness (Nm ²)
0	7.472E+09	7.472E+09
1.14815	2.433E+09	2.607E+09
3.44444	1.408E+09	2.085E+09
5.74074	8.341E+08	1.425E+09
9.18519	5.561E+08	1.286E+09
16.0741	2.085E+08	5.648E+08
26.4074	2.954E+07	1.216E+08
35.5926	2.259E+06	2.433E+07
38.2333	113824	4.518E+06
38.75	3127.98	8167.51

HUB MASS AND INERTIA

Mass of hub	14000	kg
Mass centre of hub	0	m
Hub inertia: about shaft	12000	kgm ²
perpendicular to shaft	0	kgm ²
Total Rotor Mass	33640.2	kg
Total Rotor Inertia	6.029E+06	kgm ²

A.3 Rotor Demo-Modified

Project Name Demo-modified
Date 5 Sept 2001
Engineer EAB
Notes Generic 2MW Offshore turbine

Version 3.80

Project file

GENERAL CHARACTERISTICS OF ROTOR AND TURBINE

Rotor diameter	80	m
Number of blades	3	
Teeter hinge	No	
Hub height	61.5	m
Offset of hub to side of tower centre	0	m
Tower height	60	m
Tilt angle of rotor to horizontal	4	deg
Cone angle of rotor	0	deg
Blade set angle	0	deg
Rotor overhang	3.7	m
Rotational sense of rotor, viewed from upwind	Clockwise	
Position of rotor relative to tower	Upwind	
Transmission	Gearbox	
Aerodynamic control surfaces	Pitch	
Fixed / Variable speed	Variable	
Diameter of spinner	2.5	m
Radial position of root station	1.25	m
Extension piece diameter	1.9	m
Extension piece drag coefficient	0.8	
Cut in windspeed	4	m/s
Cut out windspeed	25	m/s

BLADE GEOMETRY

Blade length	38.75	m
Pre-bend at tip	0	m
Pitch control	Full span	

Distance from root (m)	Chord (m)	Twist (deg)	Twist Axis (% chord)	Thickness (% chord)	Pitch Axis (% chord)	Pre-bend (m)	Aero-dynamic control	Aerofoil section reference
0	2.02361	0	50	100	29	0	Pitchable	1
1.14815	2.02361	0	50	100	29	0	Pitchable	1
3.44444	2.02361	0	35	64	29	0	Pitchable	1
5.74074	2.02361	0	25	40	29	0	Pitchable	2
9.18519	2.02361	0	25	30	29	0	Pitchable	2
16.0741	2.02361	0	25	22	29	0	Pitchable	2
26.4074	2.02361	0	25	15	29	0	Pitchable	3
35.5926	2.02361	0	25	13	29	0	Pitchable	4
38.2333	2.02361	0	25	13	29	0	Pitchable	4
38.75	2.02361	0	25	13	29	0	Pitchable	4

BLADE MASS DISTRIBUTION

Distance from root (m)	Centre of Mass (% chord)	Mass/unit length (kg/m)
0	50	1084.77
1.14815	50	369.809
3.44444	38	277.356
5.74074	29	234.212
9.18519	29	209.558
16.0741	29	172.577
26.4074	29	103.546
35.5926	29	55.4713
38.2333	29	40.6789
38.75	29	24.6539

Blade Mass Integrals (No ice)

Blade Mass	6546.72	kg
First Mass Moment	84218.6	kgm
Second Mass Moment	1.785E+06	kgm ²
Blade inertia about shaft	2.006E+06	kgm ²

BLADE STIFFNESS DISTRIBUTION

Radial Position (m)	Flapwise stiffness (Nm ²)	Edgewise stiffness (Nm ²)
0	7.472E+09	7.472E+09
1.14815	2.433E+09	2.607E+09
3.44444	1.408E+09	2.085E+09
5.74074	8.341E+08	1.425E+09
9.18519	5.561E+08	1.286E+09
16.0741	2.085E+08	5.648E+08
26.4074	2.954E+07	1.216E+08
35.5926	2.259E+06	2.433E+07
38.2333	113824	4.518E+06
38.75	3127.98	8167.51

HUB MASS AND INERTIA

Mass of hub	14000	kg
Mass centre of hub	0	m
Hub inertia: about shaft	12000	kgm ²
perpendicular to shaft	0	kgm ²
Total Rotor Mass	33640.2	kg
Total Rotor Inertia	6.029E+06	kgm ²

Appendix B

Wind-Field Model Transfer Functions Design

The transfer functions used in the effective wind-field model developed in Chapter 5, have been obtained following a procedure introduced in [9], to which minor but important, modifications to equations and nomenclature have been applied, as per Chapter 5. This procedure, including the abovementioned adaptations, is recalled below directly from [9]:

The functions ϕ_{xx}^R , ϕ_{yy}^R and ϕ_{xy}^R from (5.64), (5.65) and (5.66) are reformulated as functions of x^2 , rather than x , and suitable fits ϕ_{xx} , ϕ_{yy} and ϕ_{xy} respectively, determined. The fits must have the following properties.

- a) ϕ_{xx} , ϕ_{yy} and ϕ_{xy} must be proper rational expressions in x^2
- b) None of the roots of the numerator and denominators of ϕ_{xx} , ϕ_{yy} and ϕ_{xy} must lie in the right-half of the complex x^2 plane.

Requirements a) and b) can be met in a relatively simple manner provided that the fitted functions roll off in x^2 as an integer multiple of -20dB/decade. Since the correlation factor, μ , defined by

$$\mu = \frac{\phi_{xy}^R}{\sqrt{\phi_{xx}^R \phi_{yy}^R}} \quad (\text{B. 1})$$

is the most important measure of cross-correlation it must be fitted with the greatest accuracy.

Unfortunately, both $\sqrt{\phi_{xx}^R}$ and $\sqrt{\phi_{yy}^R}$ roll off at -10dB/decade. However, A and B, where

$$A = \sqrt{\phi_{xx}^R \phi_{yy}^R} \quad ; \quad B = \sqrt{\phi_{yy}^R / \phi_{xx}^R} \quad (\text{B. 2})$$

Roll off at -20dB/decade and 0dB/decade, respectively. Consequently, the most appropriate way to represent the numerical calculated data is by the fits μ_{fit} , A_{fit} and B_{fit} , to μ , A and B, respectively. Subsequently ϕ_{xx} , ϕ_{yy} and ϕ_{xy} are determined from

$$\phi_{xx} = A_{fit}/B_{fit} \quad ; \quad \phi_{yy} = A_{fit}B_{fit} \quad ; \quad \phi_{xy} = \mu_{fit}A_{fit} \quad (\text{B. 3})$$

Clearly from

$$V_{uniform} = f_1(s)\omega_1 + (f_3(s)f_4(s))\omega_3 = f_1(s)\omega_1 + f_{31}(s)\omega_3 \quad (\text{B. 4})$$

$$V_{linear} = f_2(s)\omega_2 + \frac{f_3(s)}{f_4(-s)}\omega_3 = f_2(s)\omega_2 + f_{32}(s)\omega_3 \quad (\text{B. 5})$$

it follows,

$$|f_3(j\omega)|^2 = \phi_{xy} = \mu A \quad (\text{B. 6})$$

$$|f_4(j\omega)|^2 = \psi \quad (\text{B. 7})$$

$$|f_1(j\omega)|^2 = \phi_{xx} - \phi_{xy}\psi = \phi_{xx} \left(1 - \frac{\phi_{xy}\psi}{\phi_{xx}}\right) = \frac{A}{B}(1 - \mu B\psi) \quad (\text{B. 8})$$

$$|f_2(j\omega)|^2 = \phi_{yy} - \frac{\phi_{xy}}{\psi} = \phi_{yy} \left(1 - \frac{\phi_{xy}}{\phi_{yy}\psi}\right) = AB \left(1 - \frac{\mu}{B\psi}\right) \quad (\text{B. 9})$$

$$|f_{31}(j\omega)|^2 = |f_3(j\omega)|^2 |f_4(j\omega)|^2 = \phi_{xy}\psi = \mu A\psi \quad (\text{B. 10})$$

$$|f_{32}(j\omega)|^2 = \frac{|f_3(j\omega)|^2}{|f_4(j\omega)|^2} = \frac{\phi_{xy}}{\psi} = \frac{\mu A}{\psi} \quad (\text{B. 11})$$

Where ψ has the properties a) and b) such the magnitude of $\psi(0) = 1$ and the degree of the numerator and denominator are the same. The spectrum of $\psi(x)$ is chosen to ensure that both $|f_1(j\omega)|^2$ and $|f_2(j\omega)|^2$ have no roots in the right-half complex x^2 plane. By the Nyquist stability criterion (see any control text), this requirement is met provided the magnitude of both $\phi_{xy}\psi/\phi_{xx}$ and $\phi_{xy}/\phi_{yy}\psi$ are less than one for all x , since

$$\left| \frac{\phi_{xy}^2}{\phi_{xx}\phi_{yy}} \right| \approx \left| \frac{(\phi_{xy}^R)^2}{\phi_{xx}^R\phi_{yy}^R} \right| \leq 1 \quad (\text{B. 12})$$

It is straightforward to find a suitable $\psi(x)$ using standard control methods.

The transfer functions for $f_1(s), \dots, f_4(s)$ are determined by factorising the right-hand side of the expressions of $|f_1(j\omega)|^2, \dots, |f_4(j\omega)|^2$, respectively; that is, the overall gain, K^2 , corresponds to gain, K , in the transfer function, each factor of $(x^2 + a^2)$ corresponds to a factor $(\sigma s + a)$ in the transfer function and each factor $((x^2)^2 + ux^2 + v^2)$ corresponds to a factor

$(\sigma^2 s^2 + \sqrt{u + 2v}\sigma s + v)$ in the transfer function. Because of the number of steps involved, the filters $f_1(s)$ to $f_4(s)$ can be high order, but low order approximations for each can be readily determined using standard control methods. However, rather than $f_3(s)$ and $f_4(s)$, themselves, low order approximations $f_{31}(s)$ and $f_{32}(s)$ are directly determined for $f_3(s)f_4(s)$ and $f_3(s)/f_4(-s)$ respectively. Of course the filters $f_{31}(s)$ and $f_{32}(s)$ tend to one and $f_1(s)$ and $f_2(s)$ tend to zero on the limit as s tends to zero.

B.1 Design Procedure for Lump Parameter Subsystem Models. An Illustrated Example

The previous process is now illustrated for the case $n = 4$. To be noted, that for simplicity this method does not deal with phase since it would unnecessarily complicate the process of retrieving the expressions for the filters. Instead the phase is adjusted a posteriori and only before final modelling. This is the easiest way to assure the right gain and phase in the final model.

In order, from Figure B-1 to Figure B-3, the approximations A_{fit} , B_{fit} and μ_{fit} can be found plotted against their associated original values (from numerically solving the respective integrals), and are of the form,

$$A_{fit} = \frac{2.5741 x^2 (x^2 + 1960)(x^2 + 0.4677)(x^2 + 0.00352)}{(x^2 + 2800)(x^2 + 115)(x^2 + 3.821)(x^2 + 0.04296)(x^2 + 0.00024)} \quad (\text{B. 13})$$

$$B_{fit} = \frac{0.65236 (x^2 + 9.9e04) (x^2 + 1.8e04) (x^2 + 2000) (x^2 + 100)}{(x^2 + 8.9e04) (x^2 + 1.6e04) (x^2 + 1500) (x^2 + 78)} \quad (\text{B. 14})$$

$$\mu_{fit} = \frac{0.62107 (x^2 + 9.2e04) (x^2 + 6300) (x^2 + 260)}{(x^2 + 7.6e04) (x^2 + 5500) (x^2 + 230)} \quad (\text{B. 15})$$

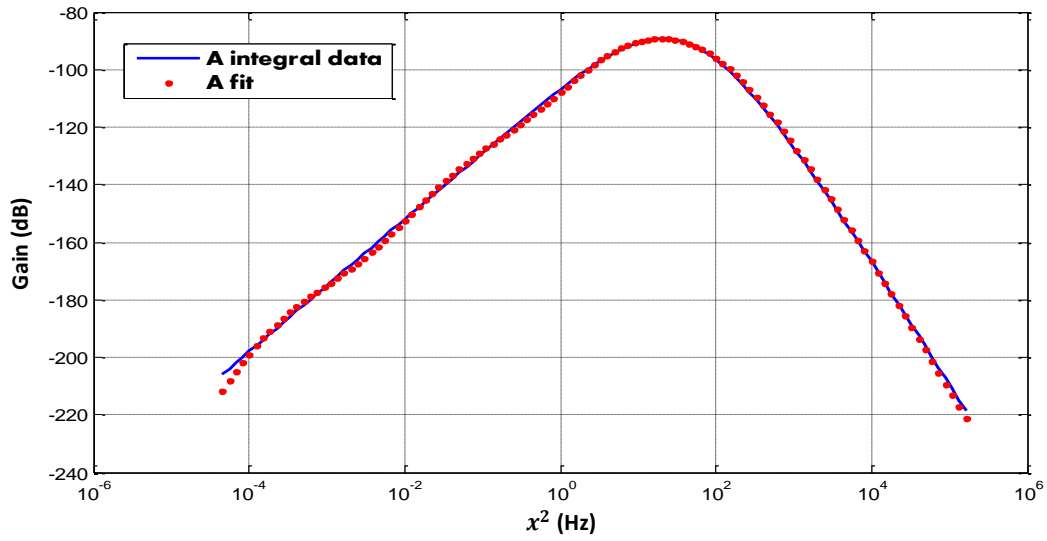


Figure B-1. Comparison between fit for A and A from integral data, $n = 4$

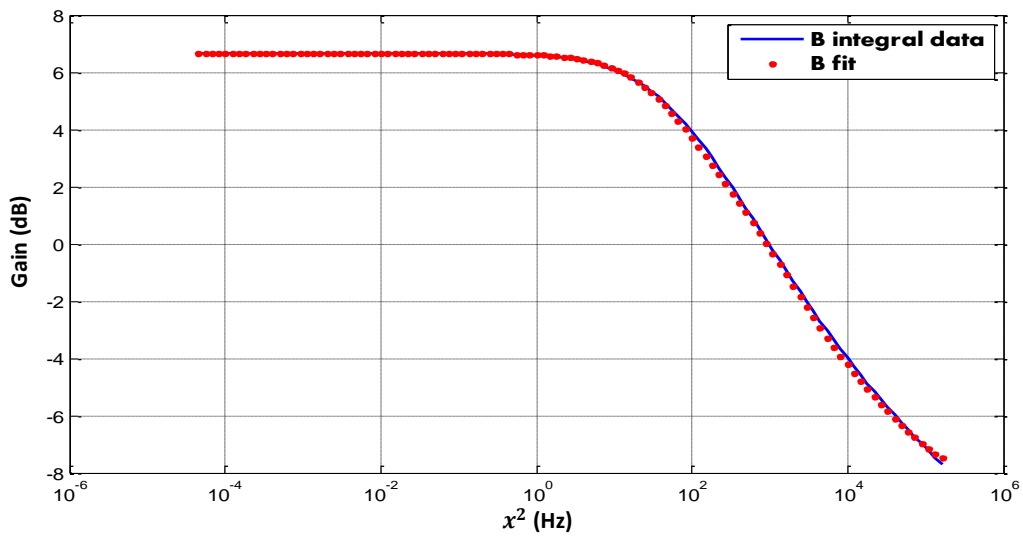


Figure B-2. Comparison between fit for B and B from integral data, $n = 4$

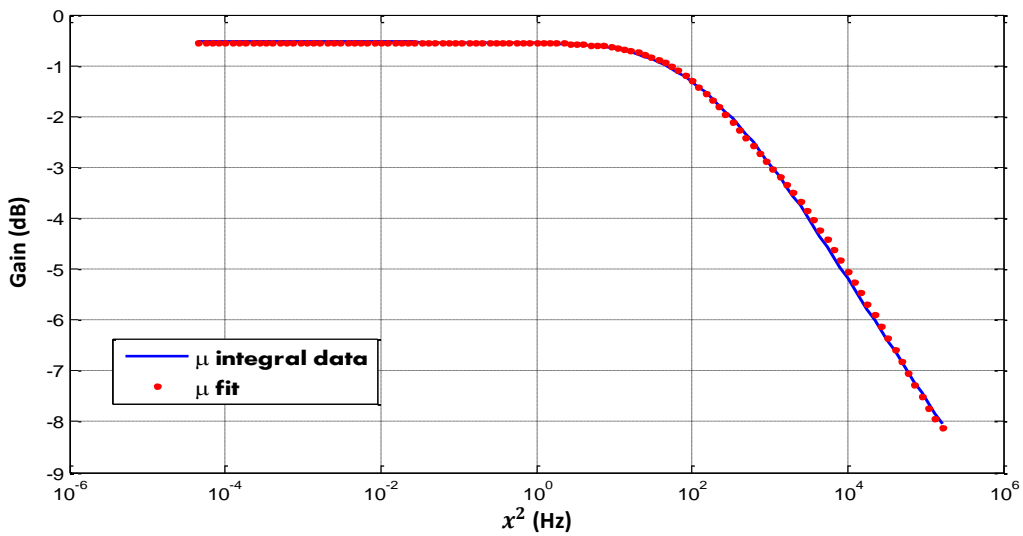


Figure B-3. Comparison between fit for μ and μ from integral data, $n = 4$

It follows that $\phi_{xx}fit$, $\phi_{yy}fit$ and $\phi_{xy}fit$, which can be found in Figure B-4, Figure B-5 and Figure B-6 respectively, are of the form

$$\phi_{xx}fit = \frac{3.9458x^2 (x^2 + 1960)(x^2 + 1500)(x^2 + 1.6e04)(x^2 + 8.9e04)}{(x^2 + 2800)(x^2 + 2000)(x^2 + 1.8e04)(x^2 + 9.9e04)(x^2 + 115)} \quad (\text{B. 16})$$

$$\frac{(x^2 + 78) (x^2 + 0.4677) (x^2 + 0.00352)}{(x^2 + 100) (x^2 + 3.821) (x^2 + 0.04296) (x^2 + 0.00024)}$$

$$\phi_{yy}fit = \frac{1.6792 x^2 (x^2 + 1960) (x^2 + 2000) (x^2 + 1.8e04) (x^2 + 9.9e04)}{(x^2 + 2800) (x^2 + 1500) (x^2 + 1.6e04) (x^2 + 8.9e04) (x^2 + 115)} \quad (\text{B. 17})$$

$$\frac{(x^2 + 100)(x^2 + 0.4677) (x^2 + 0.00352)}{(x^2 + 78)(x^2 + 3.821) (x^2 + 0.04296) (x^2 + 0.00024)}$$

$$\phi_{xy}fit = \frac{1.5987 s (s + 9.2e04) (s + 6300) (s + 1960) (s + 260) (s + 0.4677)}{(s + 7.6e04) (s + 5500) (s + 2800) (s + 230) (s + 115) (s + 3.821)} \quad (\text{B. 18})$$

$$\frac{(s + 0.00352)}{(s + 0.04296) (s + 0.00024)}$$

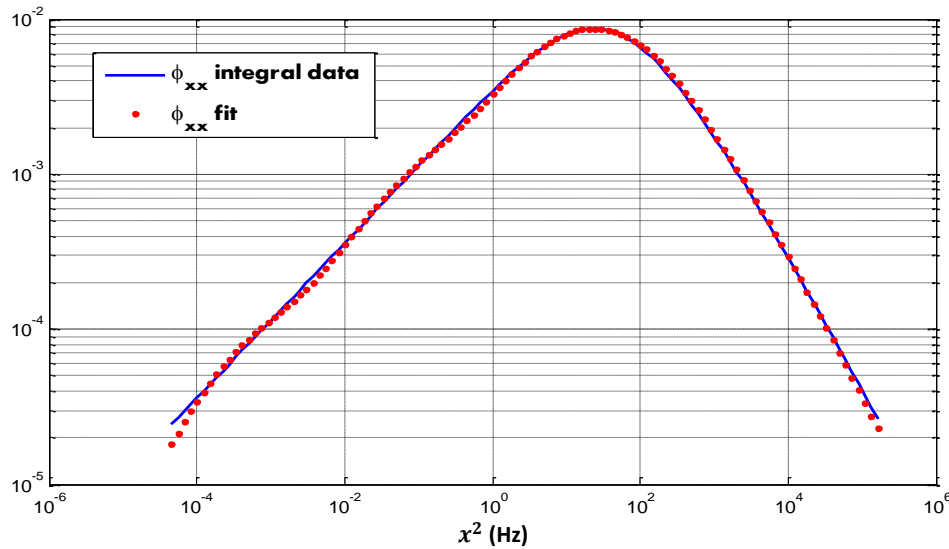


Figure B-4. Comparison between fit for function ϕ_{xx} and ϕ_{xx} from integral data, $n = 4$

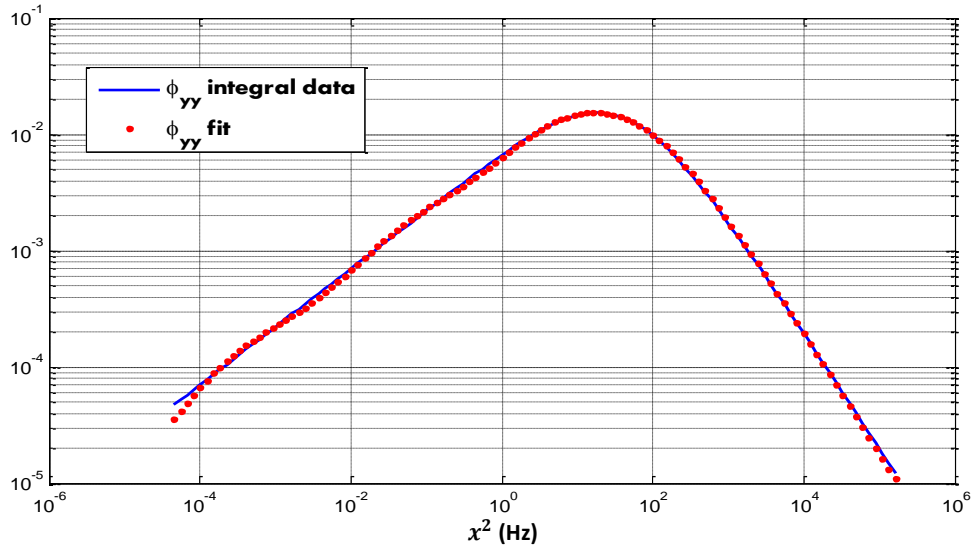


Figure B-5. Comparison between fit for function ϕ_{yy} and ϕ_{yy} from integral data, $n = 4$

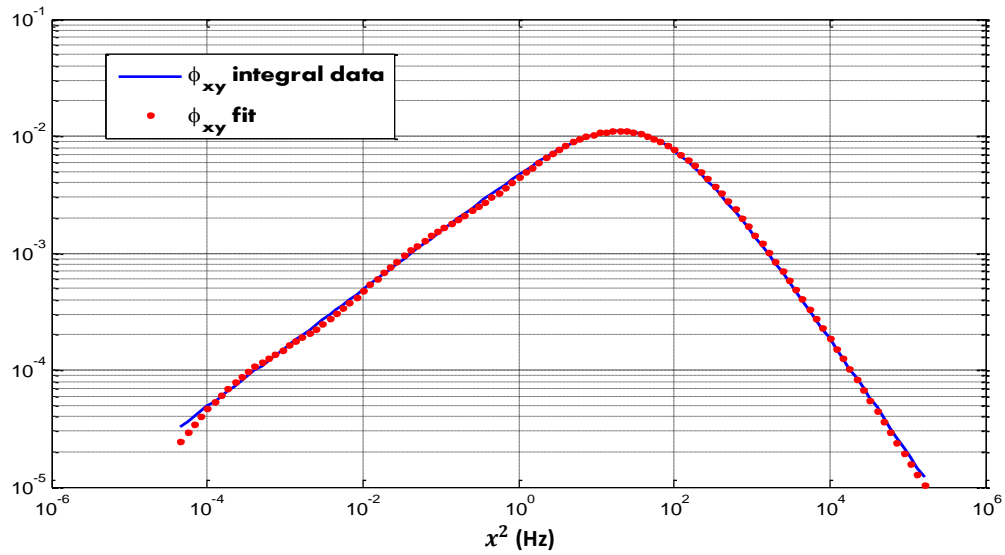


Figure B-6. Comparison between fit for function ϕ_{xy} and ϕ_{xy} from integral data, $n = 4$

And as can be seen in Figure B-7, $\left| \frac{\phi_{xy}^2}{\phi_{xx}\phi_{yy}} \right| \approx \left| \frac{(\phi_{xy}^R)^2}{\phi_{xx}^R\phi_{yy}^R} \right| \leq 1$ as required.

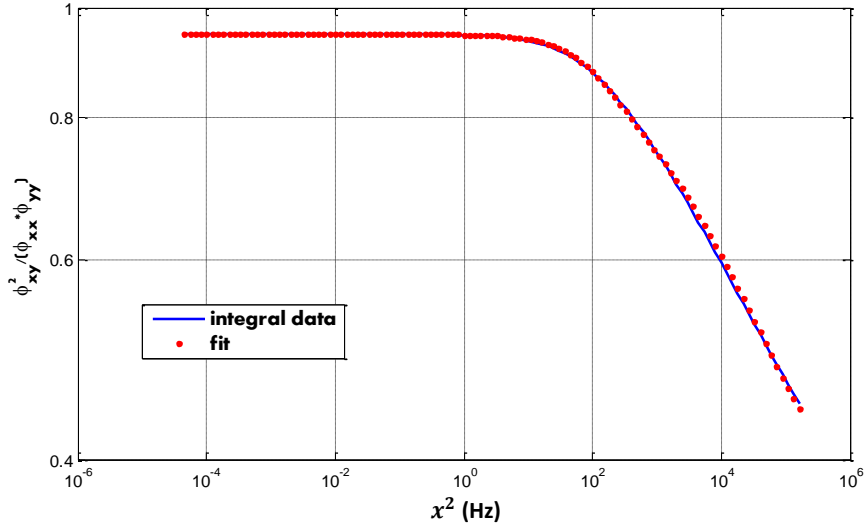


Figure B-7. Confirmation that $\left| \frac{\phi_{xy}^2}{\phi_{xx}\phi_{yy}} \right| \leq 1, n = 4$

From the definition of f_1 and f_2 , it is clear that $\psi(x)$ needs to exist between the following limits (see Figure B-8),

$$\text{Ratio 1} = \frac{\phi_{xx}}{\phi_{xy}} \tag{B. 19}$$

$$\text{Ratio 2} = \frac{\phi_{xy}}{\phi_{yy}} \tag{B. 20}$$

And for $n = 4$, $\psi(x)$ takes the form of,

$$\psi(x) = \frac{1.222 (x^2 + 1500) (x^2 + 78)}{(x^2 + 2000) (x^2 + 100)} \tag{B. 21}$$

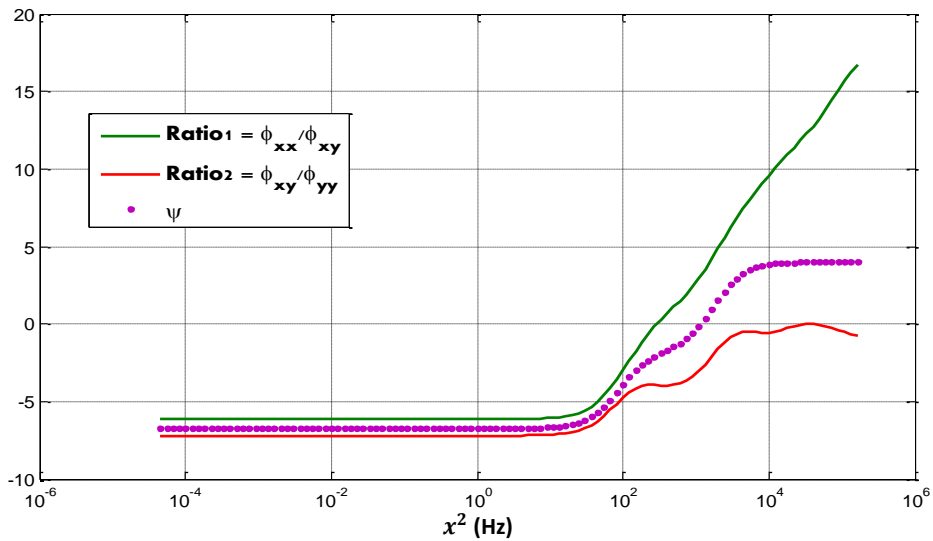


Figure B-8. Ratio 1, Ratio 2 and ψ function, $n = 4$

The corresponding un-factorised and un-modified filters that follow can be found from Figure B-9 to Figure B-12. It can be clearly appreciated from f_1 and f_2 in Figure B-9 and Figure B-10 respectively, that in certain cases the transfer functions need to be tweaked to better match the integral values. The transfer functions before any manipulation are,

$$f_1 \text{ unfactorised} = \tag{B. 22}$$

$$= \frac{1.9922 x^2 (x^2 + 8.973e04)(x^2 + 5.311e04)(x^2 + 1.271e04)(x^2 + 2864)}{(x^2 + 9.9e04) (x^2 + 7.6e04) (x^2 + 1.8e04) (x^2 + 5500)(x^2 + 2800)(x^2 + 2000)}$$

$$\frac{(x^2 + 1960)(x^2 + 1500)(x^2 + 78) (x^2 + 45.04) (x^2 + 0.4677)(x^2 + 0.00352)}{(x^2 + 230) (x^2 + 115)(x^2 + 100) (x^2 + 3.821)(x^2 + 0.04296)(x^2 + 0.00024)}$$

$$f_2 \text{ unfactorised} = \tag{B. 23}$$

$$= \frac{0.37099 x^2 (x^2 + 1.042e05) (x^2 + 4.191e04)(x^2 + 3.219e04)(x^2 + 3360)}{(x^2 + 8.9e04) (x^2 + 7.6e04) (x^2 + 1.6e04)(x^2 + 5500)(x^2 + 2800)(x^2 + 1500)}$$

$$\frac{(x^2 + 2000) (x^2 + 1960) (x^2 + 100) (x^2 + 39.68)(x^2 + 0.4677)(x^2 + 0.00352)}{(x^2 + 230) (x^2 + 115) (x^2 + 78)(x^2 + 3.821) (x^2 + 0.04296) (x^2 + 0.00024)}$$

$$f_{31} \text{ unfactorised} = \tag{B. 24}$$

$$= \frac{1.9537x^2 (x^2 + 9.2e04) (x^2 + 6300) (x^2 + 1960)(x^2 + 1500)(x^2 + 260)}{(x^2 + 7.6e04) (x^2 + 5500)(x^2 + 2800) (x^2 + 2000)(x^2 + 230)(x^2 + 115)}$$

$$\frac{(x^2 + 78) (x^2 + 0.4677)(x^2 + 0.00352)}{(x^2 + 100) (x^2 + 3.821) (x^2 + 0.04296) (x^2 + 0.00024)}$$

$$f_{32} \text{ unfactorised} = \tag{B. 25}$$

$$= \frac{1.3082 x^2 (x^2 + 9.2e04) (x^2 + 6300) (x^2 + 2000)}{(x^2 + 7.6e04) (x^2 + 5500) (x^2 + 2800) (x^2 + 1500)}$$

$$\frac{(x^2 + 1960)(x^2 + 260) (x^2 + 100) (x^2 + 0.4677) (x^2 + 0.00352)}{(x^2 + 230)(x^2 + 115) (x^2 + 78) (x^2 + 3.821) (x^2 + 0.04296) (x^2 + 0.00024)}$$

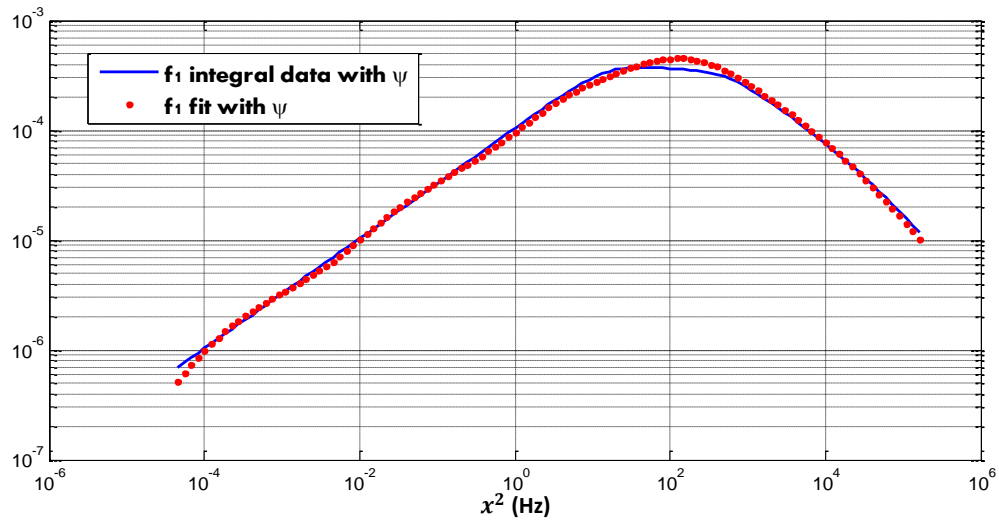


Figure B-9. Filter f_1 prior to factorisation for $n = 4$

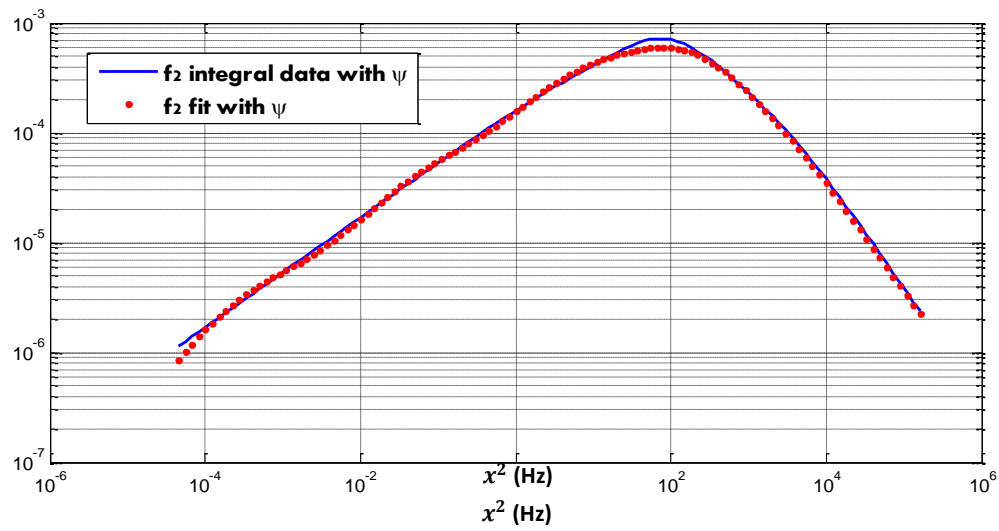


Figure B-10. Filter f_2 prior to factorisation for $n = 4$

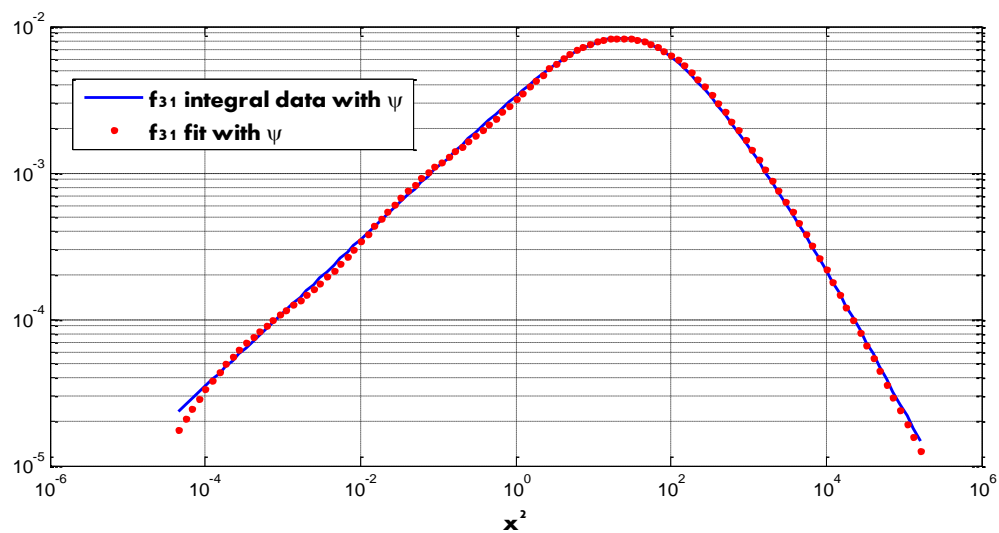


Figure B-11. Filter f_{31} prior to factorisation for $n = 4$

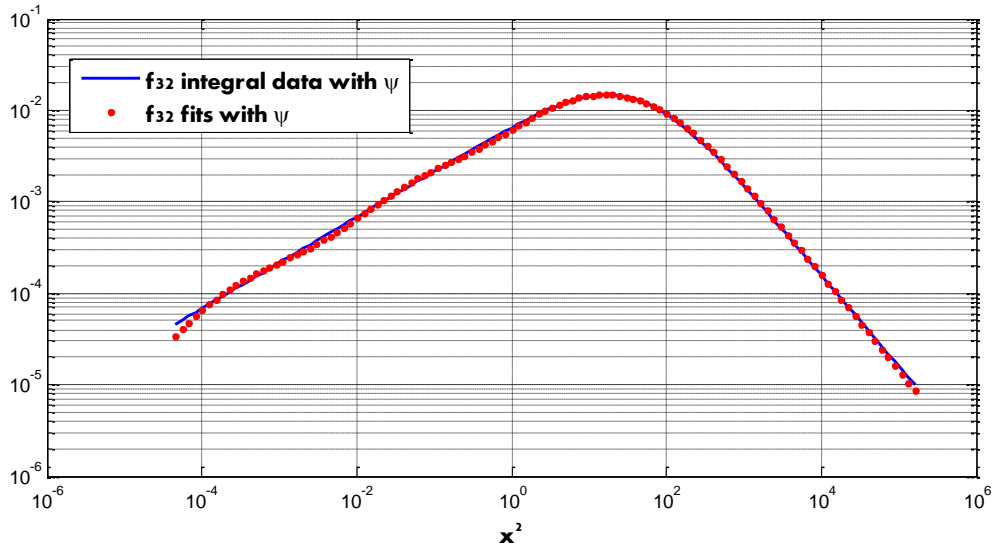


Figure B-12. Filter f_{32} prior to factorisation for $n = 4$

When approaching the creation of the transfer functions and any modifications to them, it is of special importance that for the middle frequencies the match with the numerical values is the best possible. Whereas both, the very high and low frequency ranges can be sacrificed for the sake of a leaner transfer function, as can be seen from Figure B-13 to Figure B-16. Following that line, the resulting transfer functions for $n = 4$ are acceptable lower order approximations of the form (still un-factorised),

$$f_1 \text{ modified} = \tag{B. 26}$$

$$= \frac{1.7522 (x^2 + 3500) (x^2 + 98) (x^2 + 88.98) (x^2 + 47.04)(x^2 + 0.4677)}{(x^2 + 1.8e04)(x^2 + 582.8)(x^2 + 17.16) (x^2 + 17.16) (x^2 + 8.821)}$$

$$\frac{(x^2 + 0.003452)}{(x^2 + 0.044)}$$

$$f_2 \text{ modified} \tag{B. 27}$$

$$= \frac{0.378 x^2 (x^2 + 1800) (x^2 + 4.368) (x^2 + 0.02052)}{(x^2 + 2800) (x^2 + 180) (x^2 + 33.82) (x^2 + 0.293) (x^2 + 0.0014)}$$

$$f_{31} \text{ modified} \tag{B. 28}$$

$$= \frac{2.0759 (x^2 + 1500) (x^2 + 78) (x^2 + 0.3677) (x^2 + 0.001652)}{(x^2 + 2000) (x^2 + 115) (x^2 + 100) (x^2 + 3.121) (x^2 + 0.03104)}$$

f_{32} modified

(B. 29)

$$= \frac{1.3901 (x^2 + 2000) (x^2 + 100) (x^2 + 0.3677) (x^2 + 0.001652)}{(x^2 + 1500) (x^2 + 115) (x^2 + 78) (x^2 + 3.121) (x^2 + 0.03104)}$$

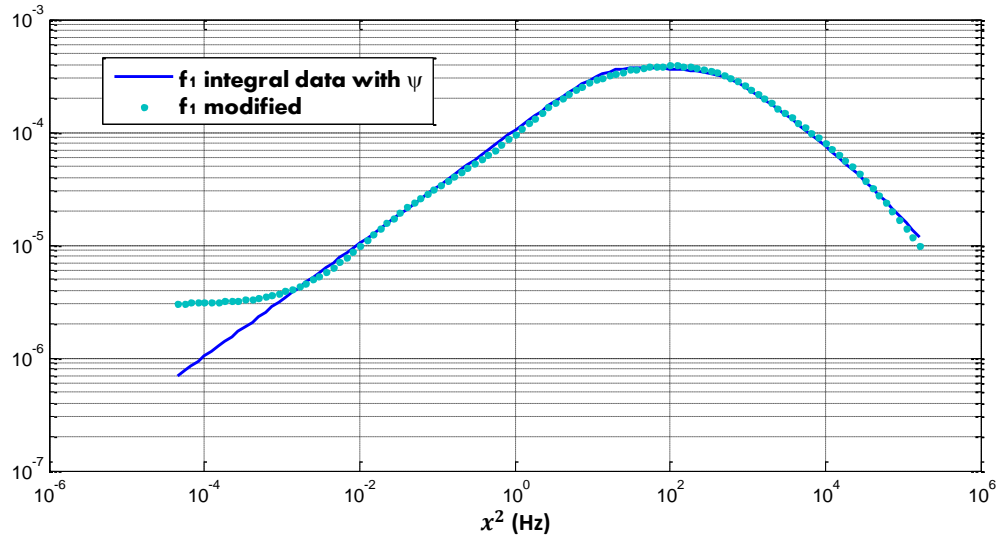


Figure B-13. Filter f_1 simplified prior to factorisation for $n = 4$

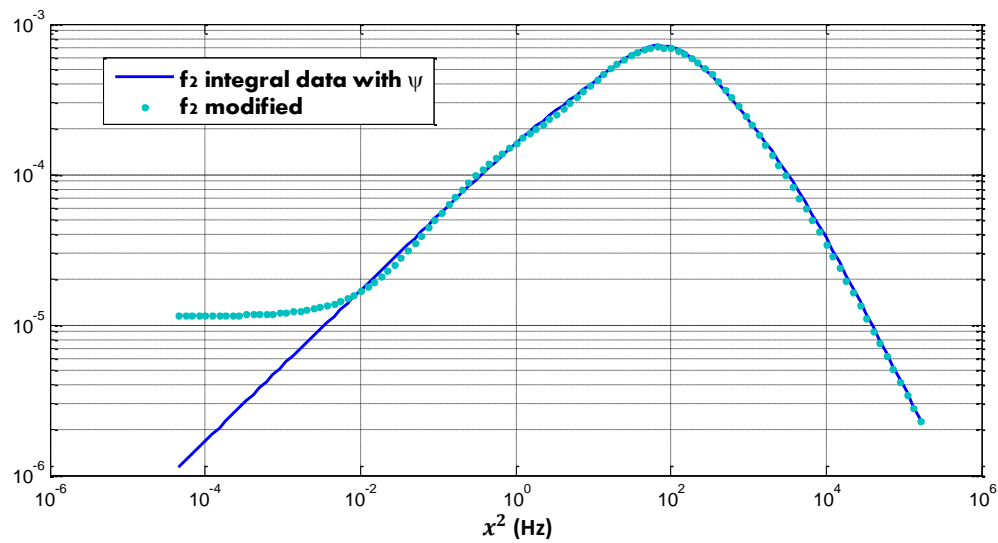


Figure B-14. Filter f_2 simplified prior to factorisation for $n = 4$

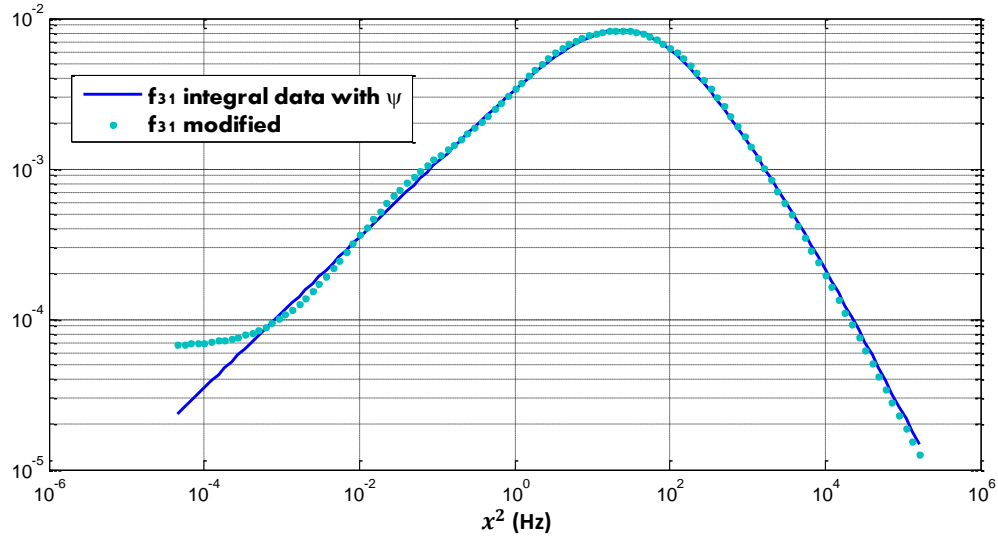


Figure B-15. Filter f_{31} simplified prior to factorisation for $n = 4$

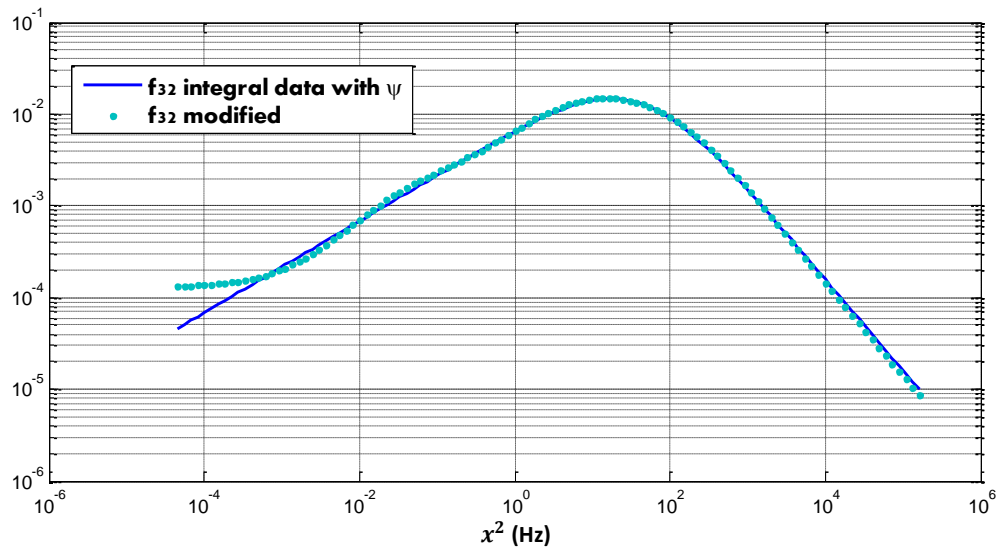


Figure B-16. Filter f_{32} simplified prior to factorisation for $n = 4$

After factorisation, as can be seen from to Figure B-20, the filters may need a final adjustment to ensure that the transfer function has at least a decade of margin between the middle frequencies and the rolling off (not necessary for f_2 in this case). It follows that the final, factorised transfer functions for f_1 , f_2 , f_{31} and f_{32} , are of the form

$$f_1 \text{ factorised} = \tag{B. 30}$$

$$= \frac{0.24438 (s + 10.92)(s + 1.828)(s + 1.741)(s + 1.266)(s + 0.1263)}{(s + 24.77)(s + 4.457)(s + 2.335)(s + 2.064)(s + 0.7648)(s + 0.5483)}$$

$$\frac{(s + 0.01085) (s + 0.001085)}{(s + 0.03873)(s + 0.002873)}$$

$$f_2 \text{ factorised} = \tag{B. 31}$$

$$= \frac{0.1135 s (s + 7.833) (s + 0.3858) (s + 0.02645)}{(s + 9.769) (s + 2.477) (s + 1.074) (s + 0.09992) (s + 0.006908)}$$

$$f_{31} \text{ factorised} = \tag{B. 32}$$

$$= \frac{0.26599(s + 7.15)(s + 1.63)(s + 0.1119)(s + 0.007504)(s + 0.0004504)}{(s + 8.256)(s + 1.98) (s + 1.846)(s + 0.3261)(s + 0.03253)(s + 0.001253)}$$

$$f_{32} \text{ factorised} = \tag{B. 33}$$

$$= \frac{0.21766 (s + 8.256)(s + 1.846)(s + 0.1119)(s + 0.007504)(s + 0.0007504)}{(s + 7.15)(s + 1.98)(s + 1.63)(s + 0.3261) (s + 0.03253)(s + 0.002253)}$$

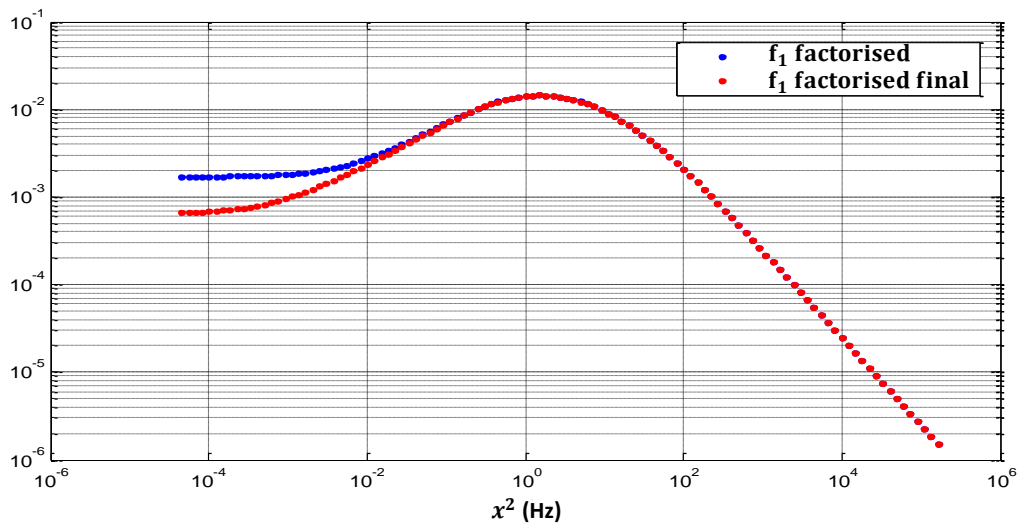


Figure B-17. Filter f_1 for $n = 4$

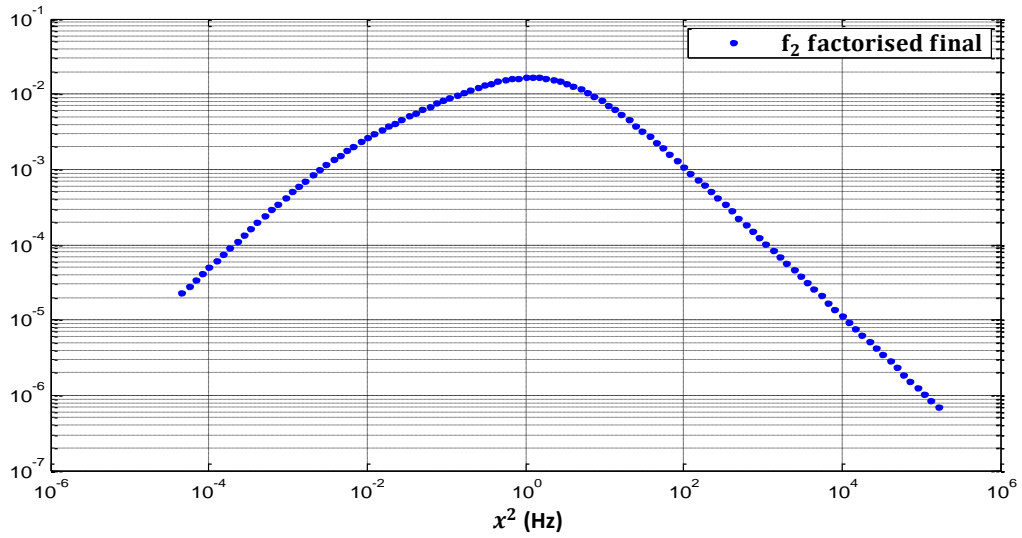


Figure B-18. Filter f_2 for $n = 4$

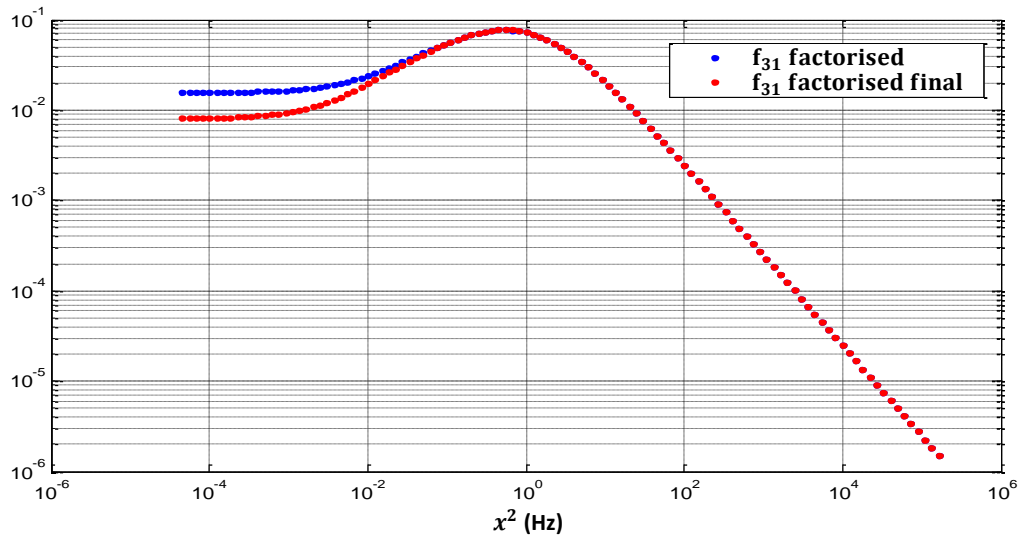


Figure B-19. Filter f_{31} for $n = 4$

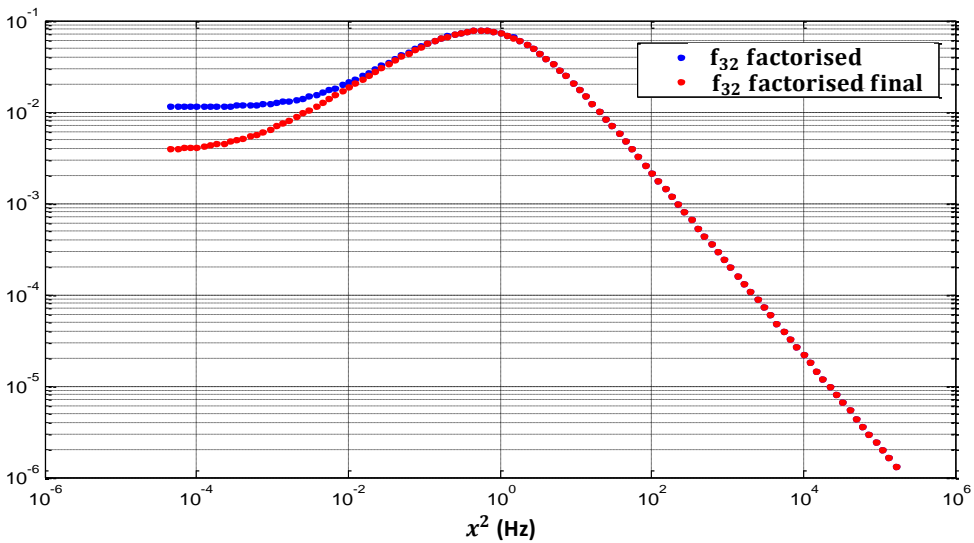


Figure B-20. Filter f_{32} for $n = 4$

Due to the intensive modifications, a final sanity check on the appropriateness of the resulting transfer functions is of order. The verification consists on the de-factorisation of the final filters in order to retrieve the associated ϕ_{xx} , ϕ_{yy} and ϕ_{xy} and directly compare them with the numerical results of the integrals. As appreciated from results shown from Figure B-21, Figure B-22 and Figure B-23, the transfer functions do provide a good fit to the original data.

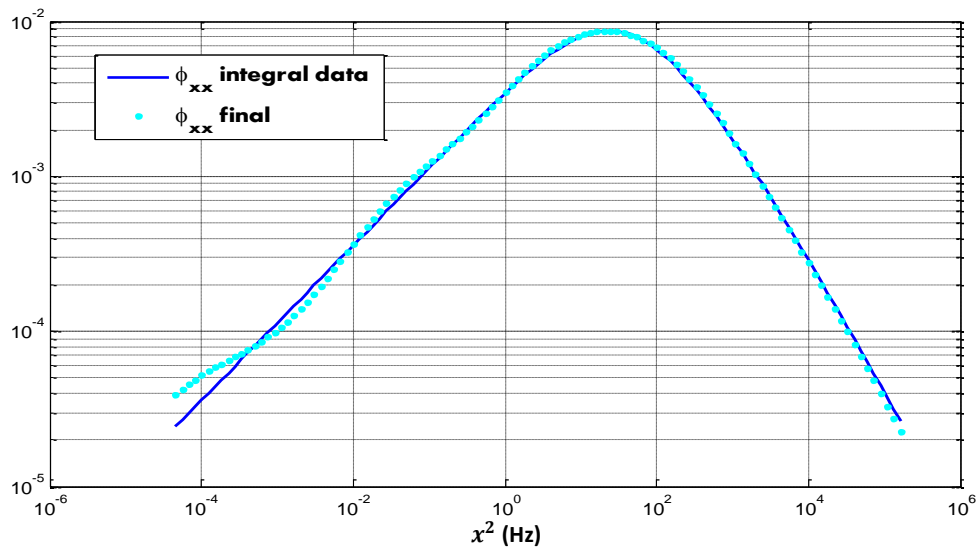


Figure B-21. Sanity check against initial data for ϕ_{xx} , $n = 4$

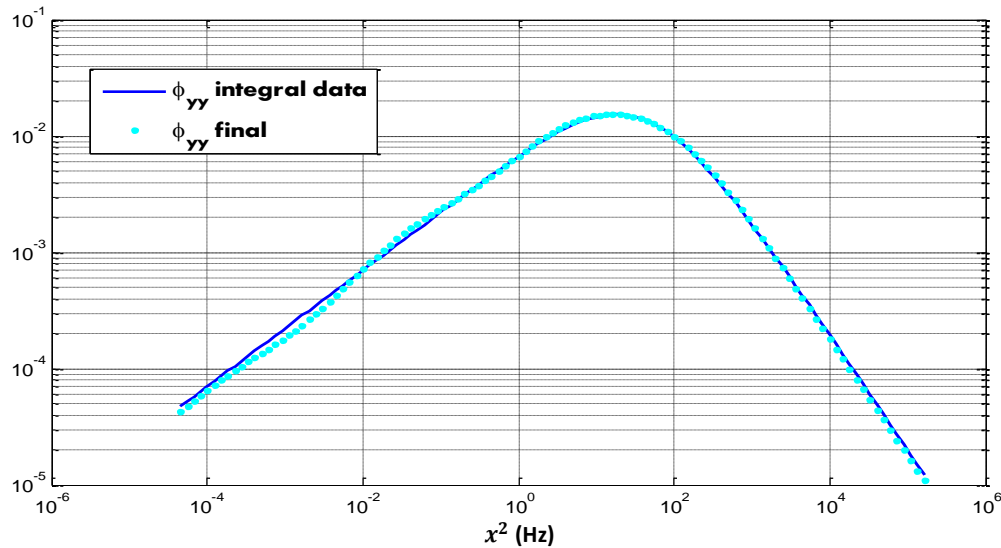


Figure B-22. Sanity check against initial data for ϕ_{yy} , $n = 4$

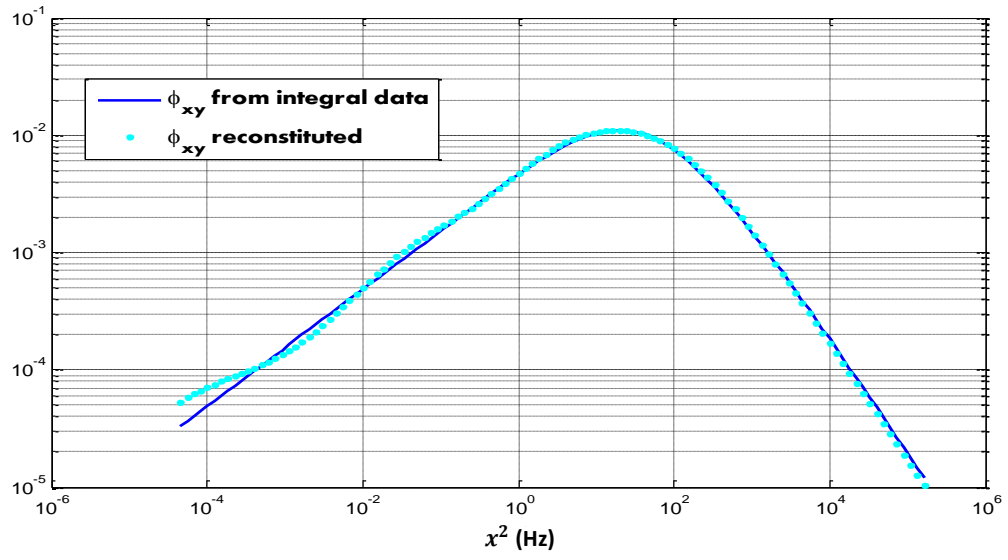


Figure B-23. Sanity check against initial data for ϕ_{xy} , $n = 4$

Appendix C

Wind-Field Stochastic Component Results

In the following can be found the results¹ for thrust force, the in-plane RBM of the blade, the edgewise moment of the blade, M_e , the flapwise moment of the blade, M_f , the rotor speed and the pitch angle of the blade for the stochastic component of the wind-field. To be noted that the induced forces and moments in these results do not account for the force of gravity in order to better appreciate the outcomes induced by the wind-field. The results are for both the simple and triple structure and for three different case studies: 15m/s, 15m/s with 18deg of pitch offset and 8m/s.

Likewise for the hub torque and out-of-plane RBM results seen in section 6.2, the full set of results in this appendix points, as far as the stochastic component of the wind is concerned, to the simple wind-field model as an acceptable compromise to induce the loads and moment of the rotor and blades as there is no sign of significant leakage.

¹ Results have not been detrended before spectrum is taken

- Thrust Force

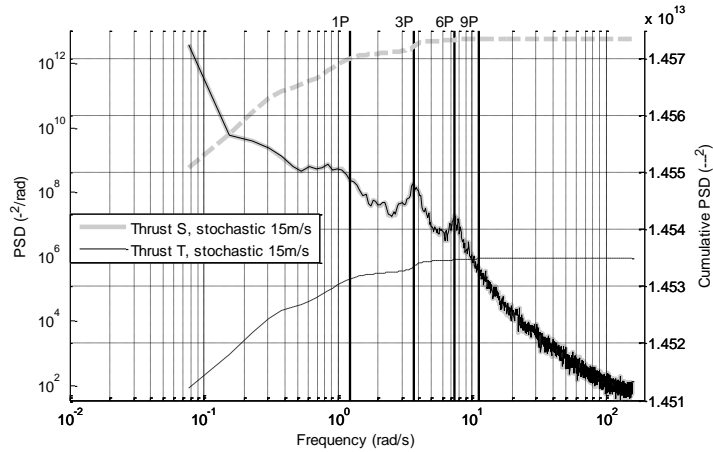


Figure C-1. Thrust force spectrum comparison between simple and triple structure for the stochastic component of the wind-field with mean 15m/s

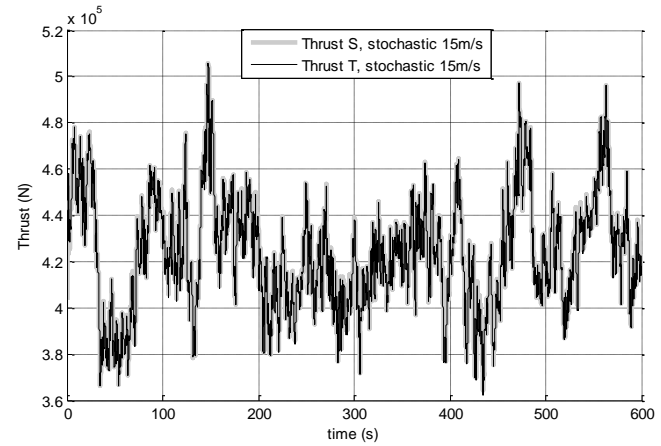


Figure C-2. Thrust force time series comparison between simple and triple structure for the stochastic component of the wind-field with mean 15m/s

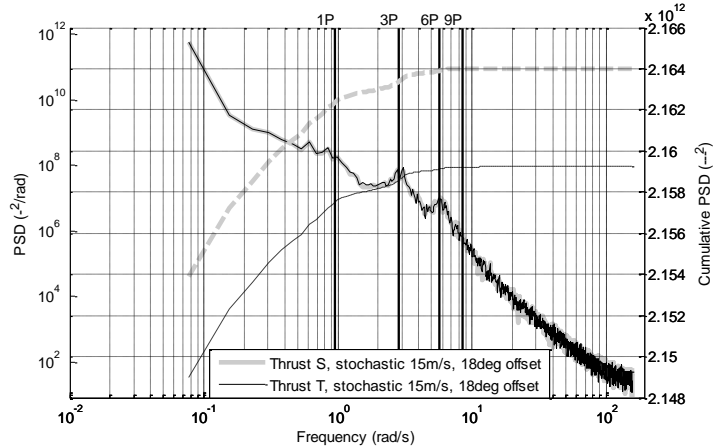


Figure C-3. Thrust force spectrum comparison between simple and triple structure for the stochastic component of the wind-field with mean 15m/s and 18 degrees of pitch offset

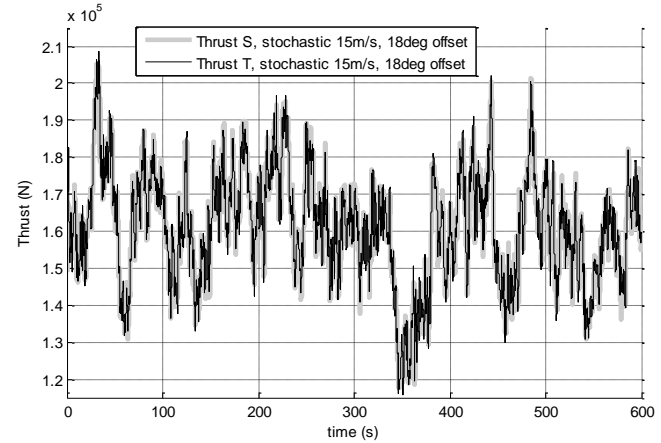


Figure C-4. Thrust force time series comparison between simple and triple structure for the stochastic component of the wind-field with mean 15m/s and 18 degrees of pitch offset

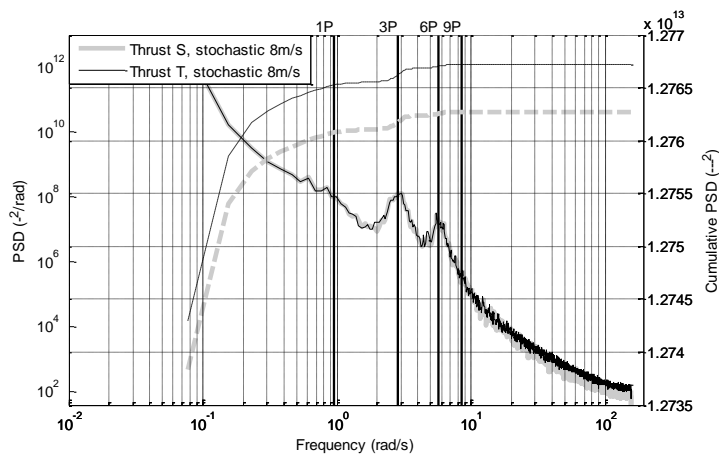


Figure C-5. Thrust force spectrum comparison between simple and triple structure for the stochastic component of the wind-field with mean 8m/s

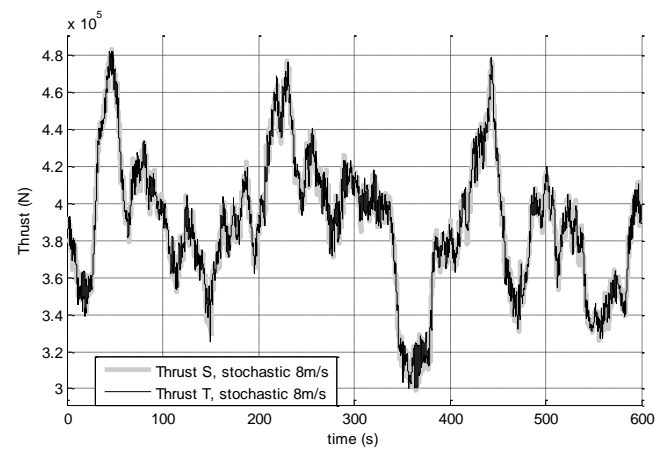


Figure C-6. Thrust force time series comparison between simple and triple structure for the stochastic component of the wind-field with mean 8m/s

- In-plane RBM of the blade

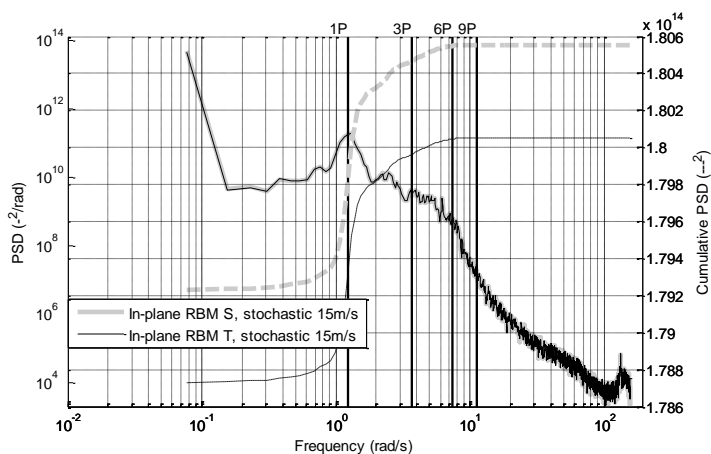


Figure C-7. In-plane RBM spectrum comparison between simple and triple structure for the stochastic component of the wind-field with mean 15m/s

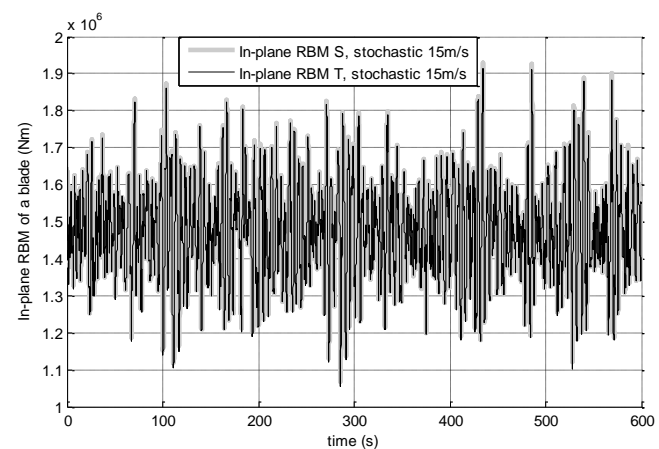


Figure C-8. In-plane RBM time series comparison between simple and triple structure for the stochastic component of the wind-field with mean 15m/s

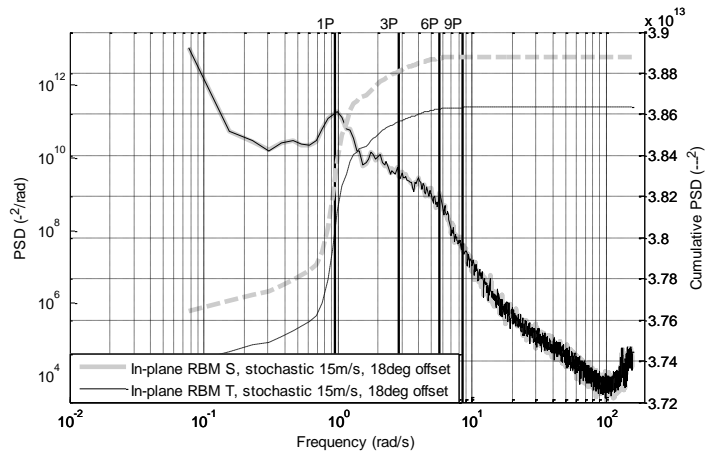


Figure C-9. In-plane RBM spectrum comparison between simple and triple structure for the stochastic component of the wind-field with mean 15m/s and 18 degrees of pitch offset

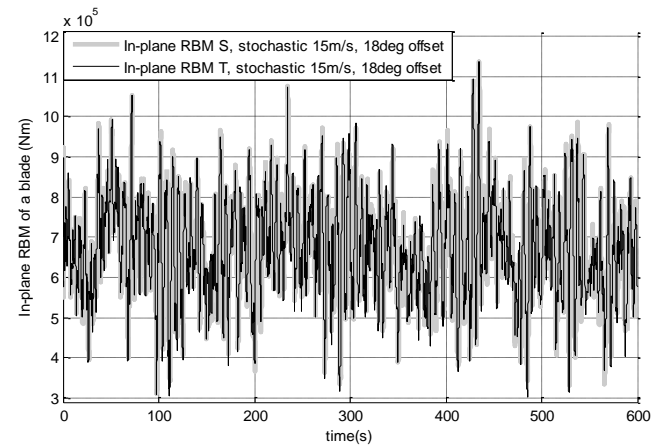


Figure C-10. In-plane RBM time series comparison between simple and triple structure for the stochastic component of the wind-field with mean 15m/s and 18 degrees of pitch offset

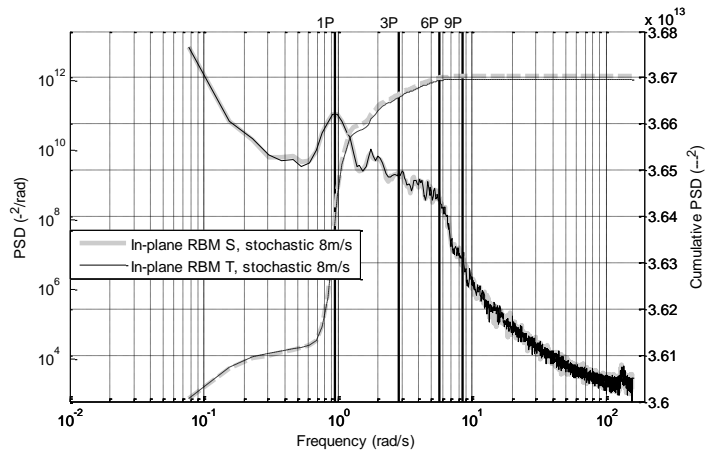


Figure C-11. In-plane RBM spectrum comparison between simple and triple structure for the stochastic component of the wind-field with mean 8m/s

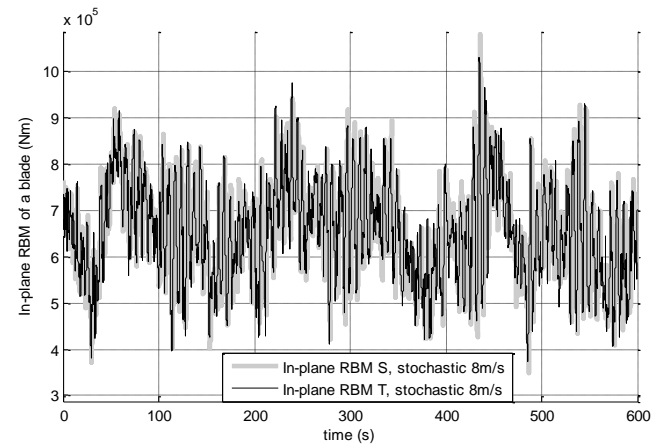


Figure C-12. In-plane RBM time series comparison between simple and triple structure for the stochastic component of the wind-field with mean 8m/s

- Edgewise moment of the blade, M_e

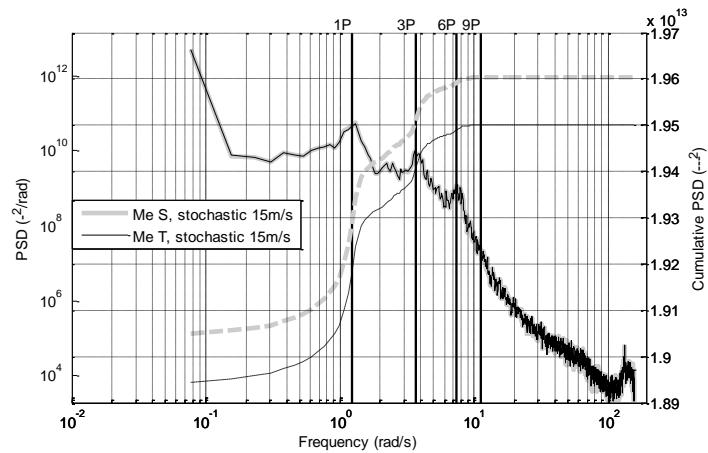


Figure C-13. M_e spectrum comparison between simple and triple structure for stochastic component of the wind-field with mean 15m/s

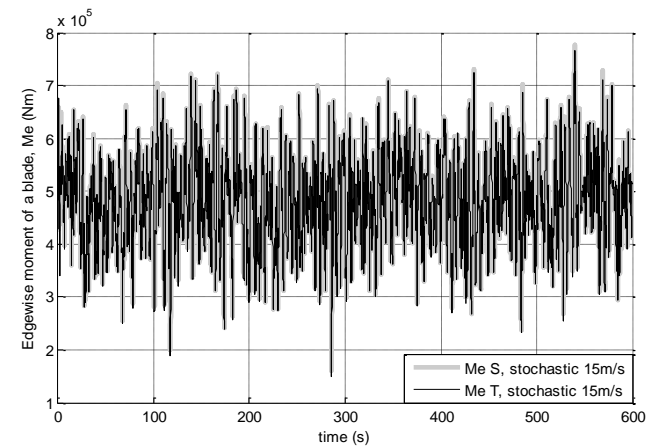


Figure C-14. M_e time series comparison between simple and triple structure for the stochastic component of the wind-field with mean 15m/s

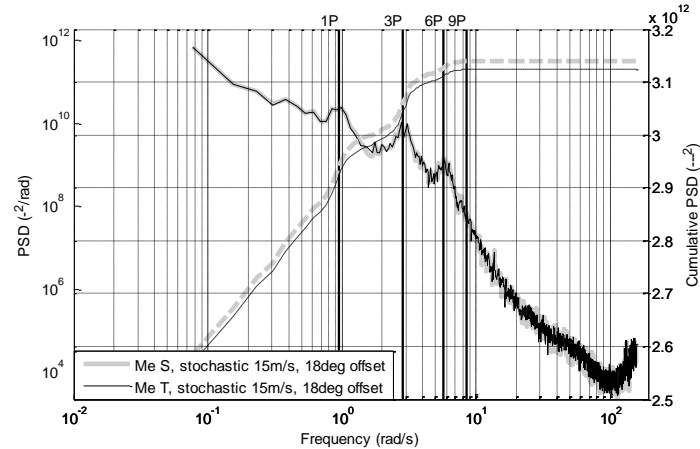


Figure C-15. M_e spectrum comparison between simple and triple structure for the stochastic component of the wind-field with mean 15m/s and 18 degrees of pitch offset

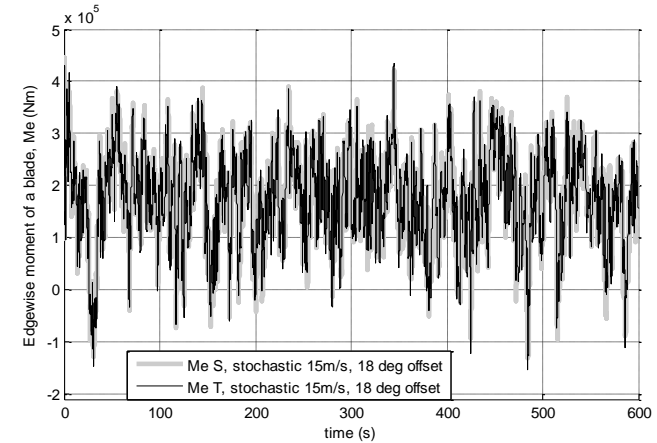


Figure C-16. M_e time series comparison between simple and triple structure for the stochastic component of the wind-field with mean 15m/s and 18 degrees of pitch offset

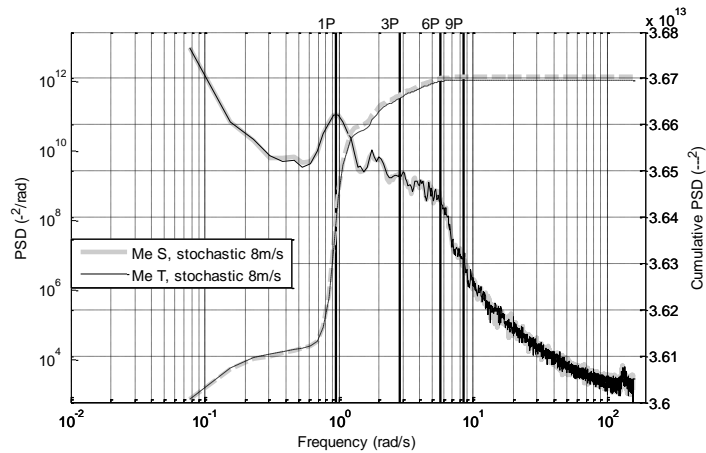


Figure C-17. M_e spectrum comparison between simple and triple structure for the stochastic component of the wind-field with mean 8m/s

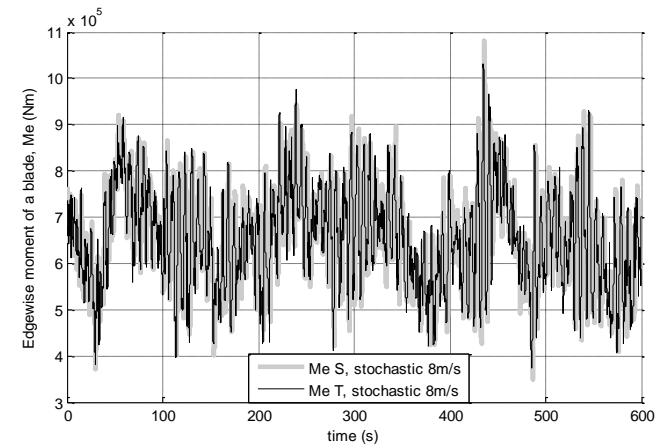


Figure C-18. M_e time series comparison between simple and triple structure for the stochastic component of the wind-field with mean 8m/s

- Flapwise moment of the blade, M_f

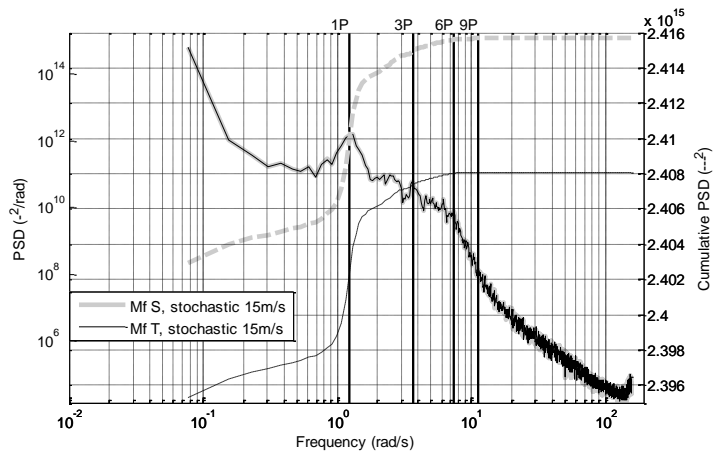


Figure C-19. M_f spectrum comparison between simple and triple structure for the stochastic component of the wind-field with mean 15m/s

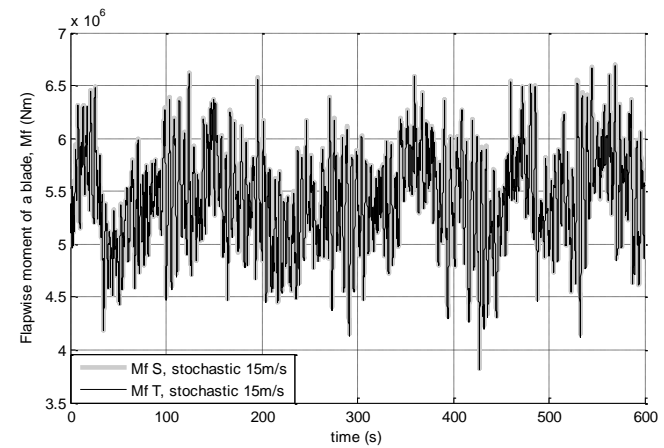


Figure C-20. M_f time series comparison between simple and triple structure for the stochastic component of the wind-field with mean 15m/s

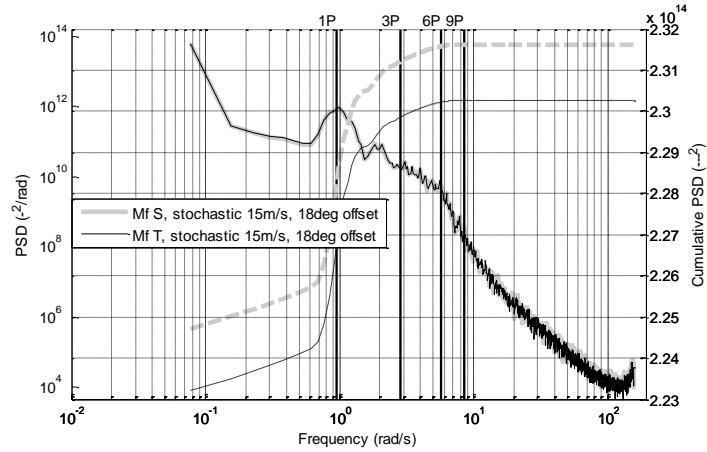


Figure C-21. M_f spectrum comparison between simple and triple structure for the stochastic component of the wind-field with mean 15m/s and 18 degrees of pitch offset

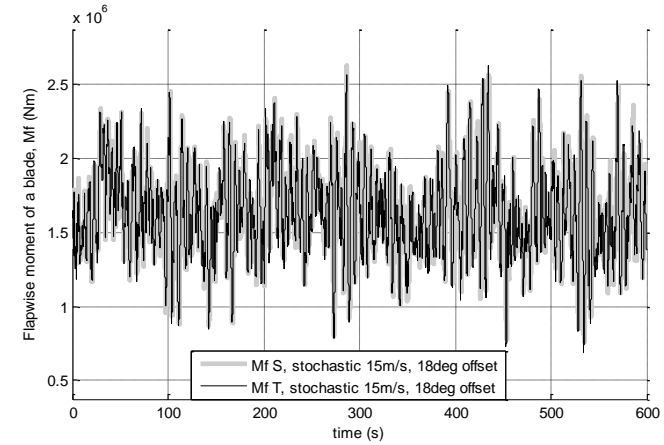


Figure C-22. M_f time series comparison between simple and triple structure for the stochastic component of the wind-field with mean 15m/s and 18 degrees of pitch offset

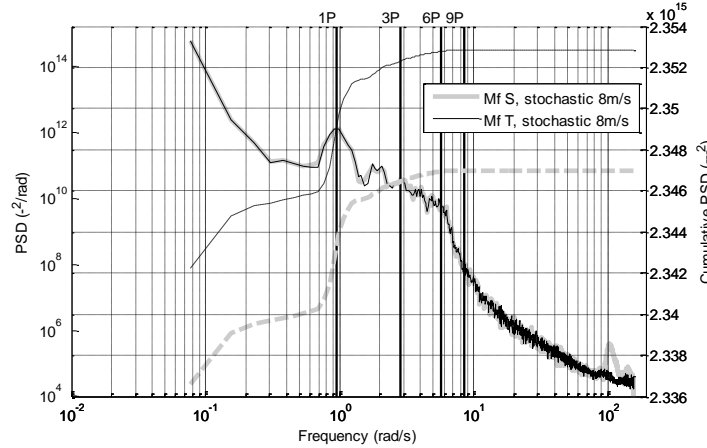


Figure C-23. M_f spectrum comparison between simple and triple structure for the stochastic component of the wind-field with mean 8m/s

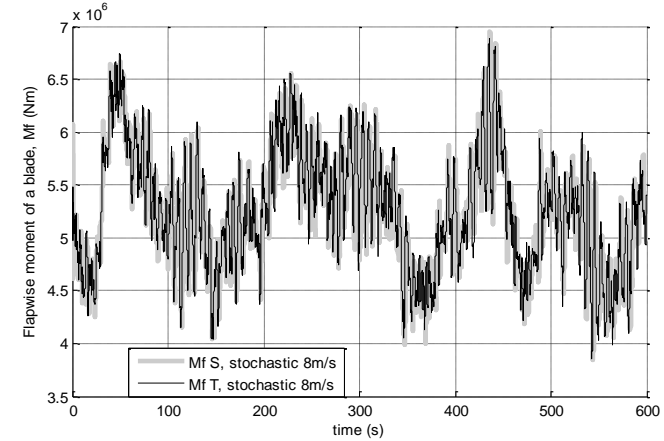


Figure C-24. M_f time series comparison between simple and triple structure for the stochastic component of the wind-field with mean 8m/s

- Rotor speed

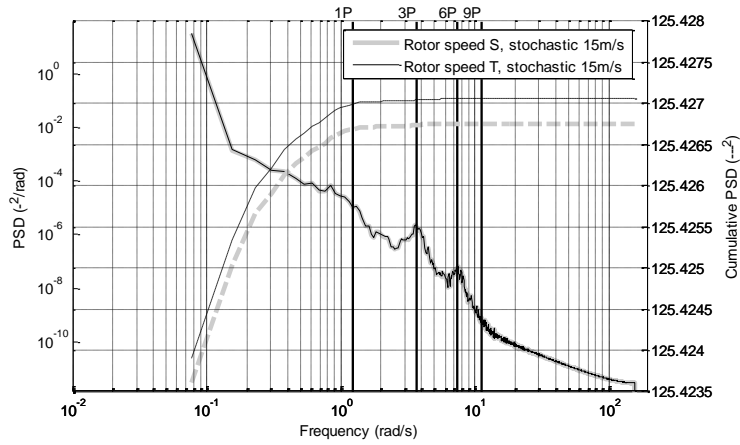


Figure C-25. Rotor speed spectrum comparison between simple and triple structure for the stochastic component of the wind-field with mean 15m/s

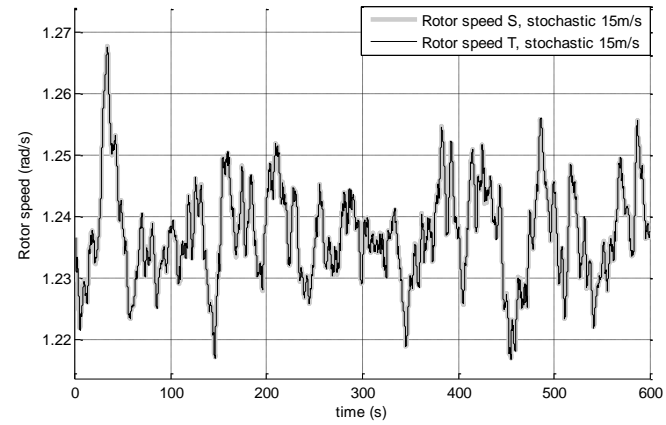


Figure C-26. Rotor speed time series comparison between simple and triple structure for the stochastic component of the wind-field with mean 15m/s

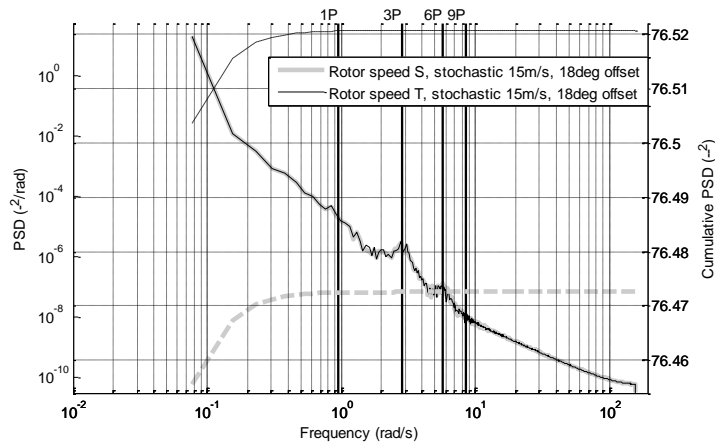


Figure C-27. Rotor speed spectrum comparison between simple and triple structure for the stochastic component of the wind-field with mean 15m/s and 18 degrees of pitch offset

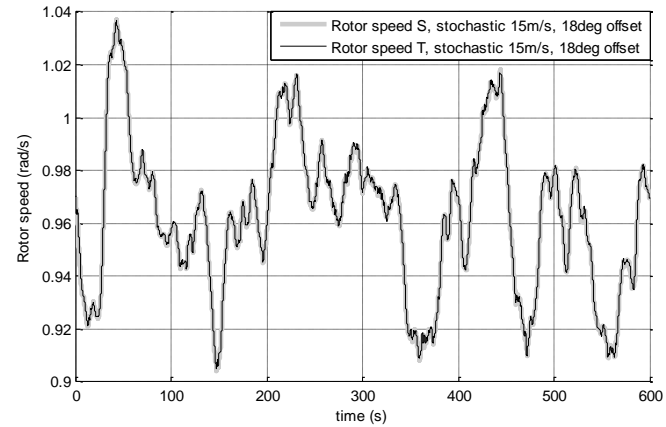


Figure C-28. Rotor speed time series comparison between simple and triple structure for the stochastic component of the wind-field with mean 15m/s and 18 degrees of pitch offset

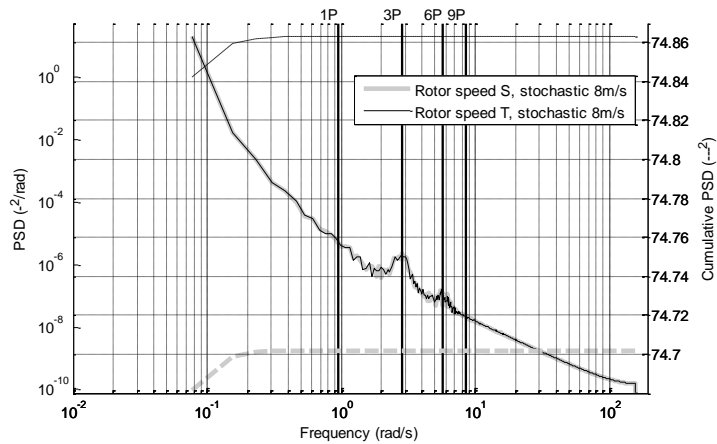


Figure C-29. Rotor speed spectrum comparison between simple and triple structure for the stochastic component of the wind-field with mean 8m/s

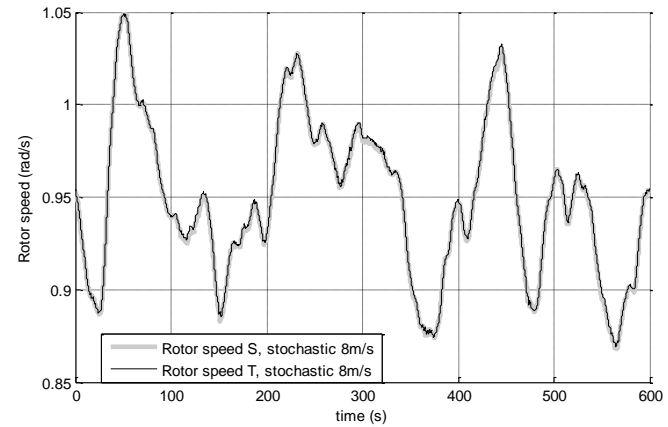


Figure C-30. Rotor speed time series comparison between simple and triple structure for the stochastic component of the wind-field with mean 8m/s

- Pitch angle of the blade

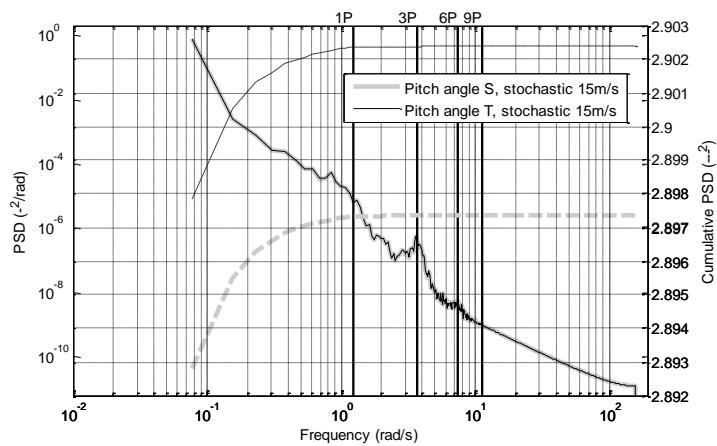


Figure C-31. Pitch angle spectrum comparison between simple and triple structure for the stochastic component of the wind-field with mean 15m/s

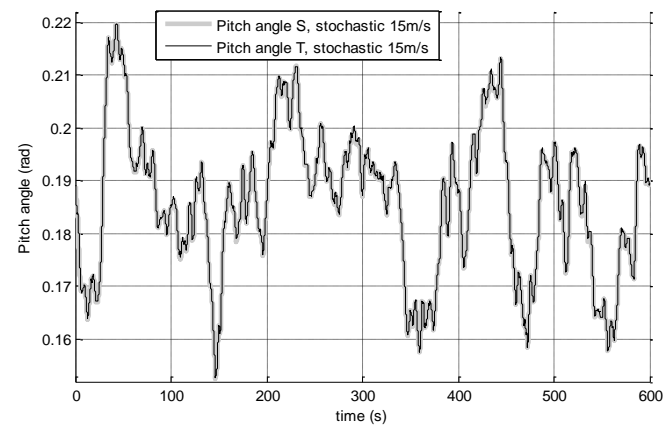


Figure C-32. Pitch angle time series comparison between simple and triple structure for the stochastic component of the wind-field with mean 15m/s

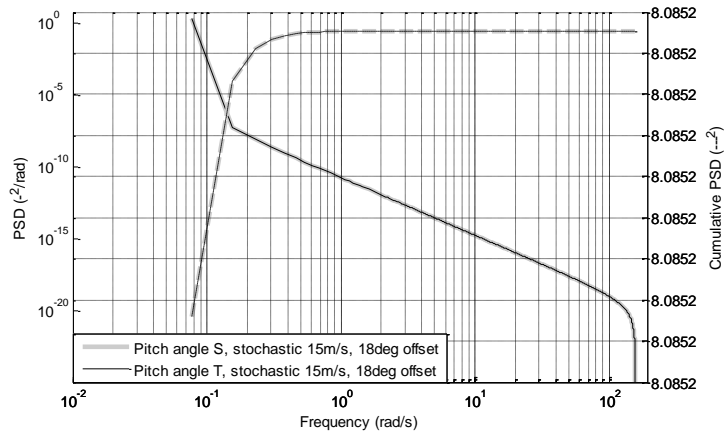


Figure C-33. Pitch angle spectrum comparison between simple and triple structure for the stochastic component of the wind-field with mean 15m/s and 18 degrees of pitch offset

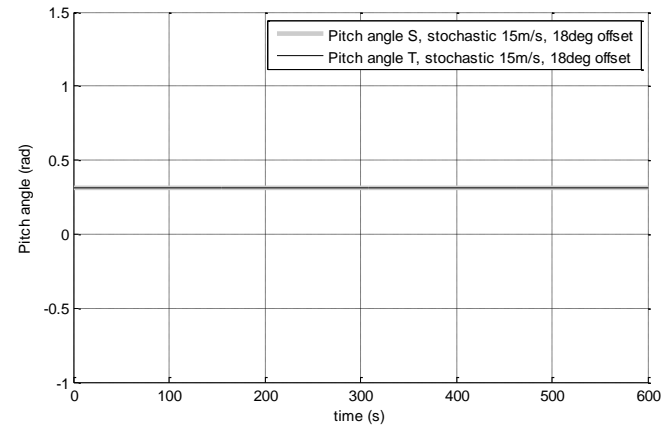


Figure C-34. Pitch angle time series comparison between simple and triple structure for the stochastic component of the wind-field with mean 15m/s and 18 degrees of pitch offset

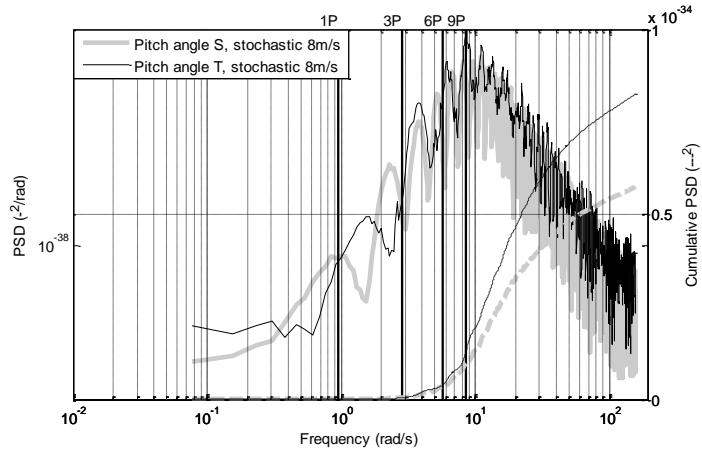


Figure C-35. Pitch angle spectrum comparison between simple and triple structure for the stochastic component of the wind-field with mean 8m/s

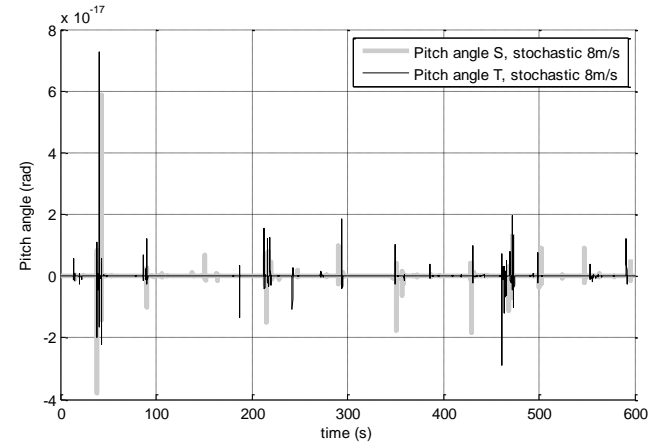


Figure C-36. Pitch angle time series comparison between simple and triple structure for the stochastic component of the wind-field with mean 8m/s

Appendix D

Wind Traces of Wind-Field Deterministic Component

In this appendix the results completing the sets of wind traces of section 6.3.1 and 6.3.2 can be found. The results cover the spectrum and time series generated by each *layer P* for the wind shear (WS) only case, tower shadow (TS) only case and complete deterministic component of the wind-field model (WS and TS together) for a wind-field with mean speed of 15m/s after being rotationally sampled by a 5MW wind turbine. For the complete deterministic case (WS and TS) the spectrum and time series of the wind-field as applied to the rotor and blade are also presented¹.

¹ Results have not been detrended before spectrum is taken

- Wind traces for WS

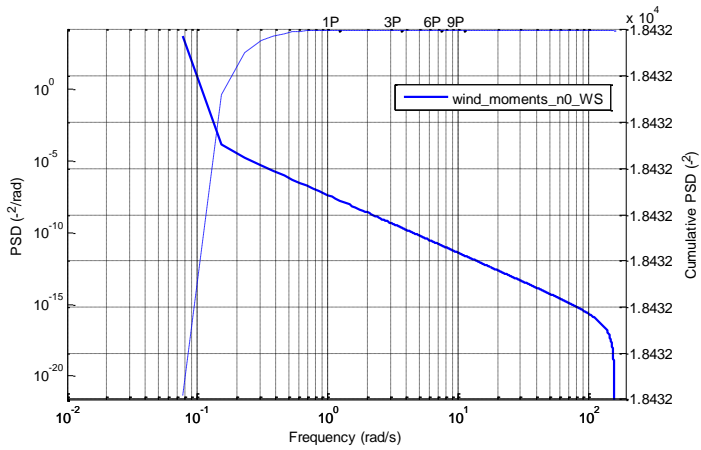


Figure D-1. Spectrum for *layer P* corresponding to $n = 0$ of the deterministic component of wind-field WS used for inducing moments

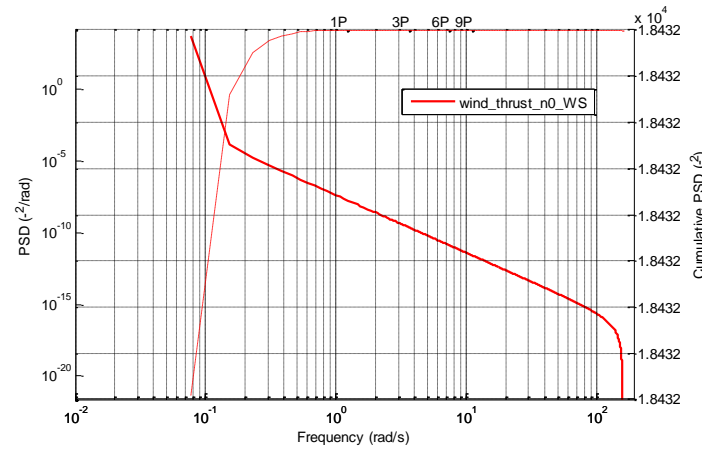


Figure D-2. Spectrum for *layer P* corresponding to $n = 0$ of the deterministic component of wind-field WS used for inducing thrust

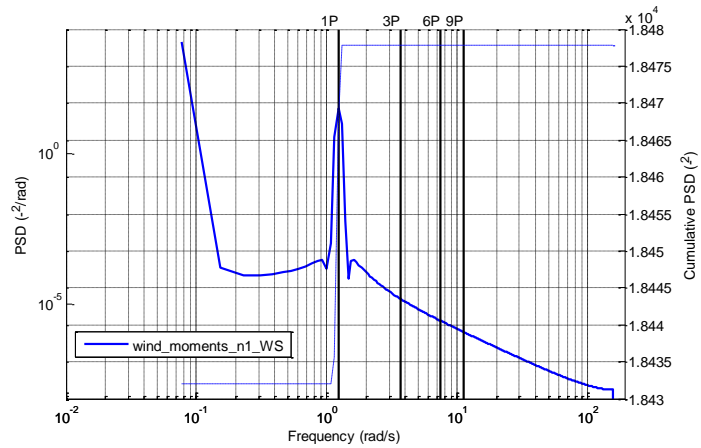


Figure D-3. Spectrum for *layer P* corresponding to $n = 1$ of the deterministic component of wind-field WS used for inducing moments

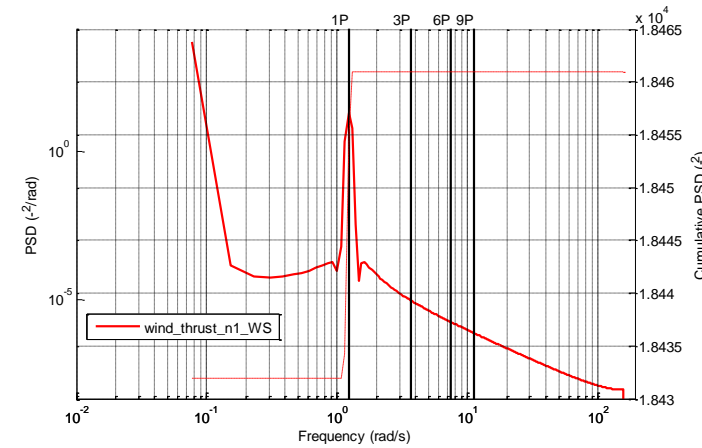


Figure D-4. Spectrum for *layer P* corresponding to $n = 1$ of the deterministic component of wind-field WS used for inducing thrust

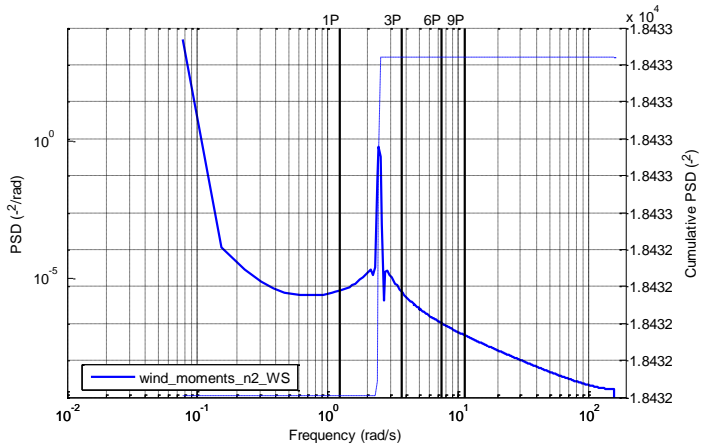


Figure D-5. Spectrum for *layer P* corresponding to $n = 2$ of the deterministic component of wind-field WS used for inducing moments

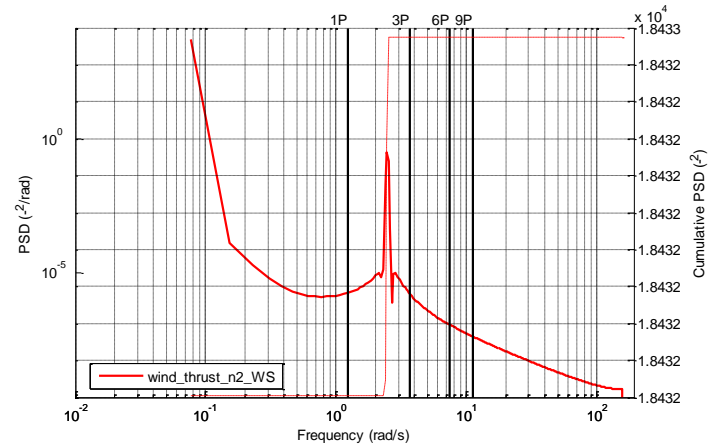


Figure D-6. Spectrum for *layer P* corresponding to $n = 2$ of the deterministic component of wind-field WS used for inducing thrust

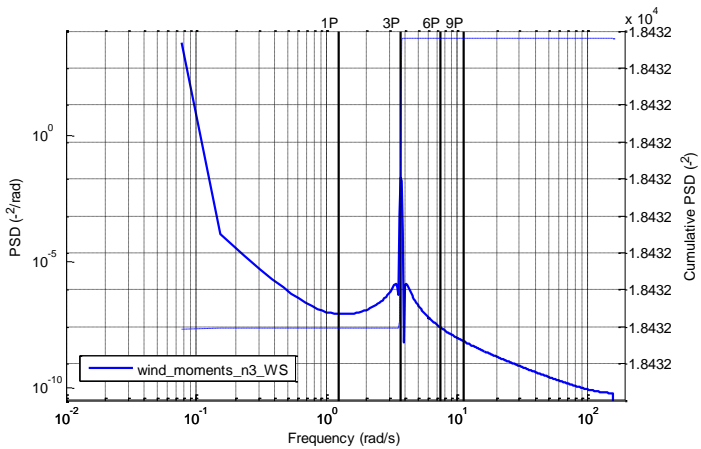


Figure D-7. Spectrum for *layer P* corresponding to $n = 3$ of the deterministic component of wind-field WS used for inducing moments

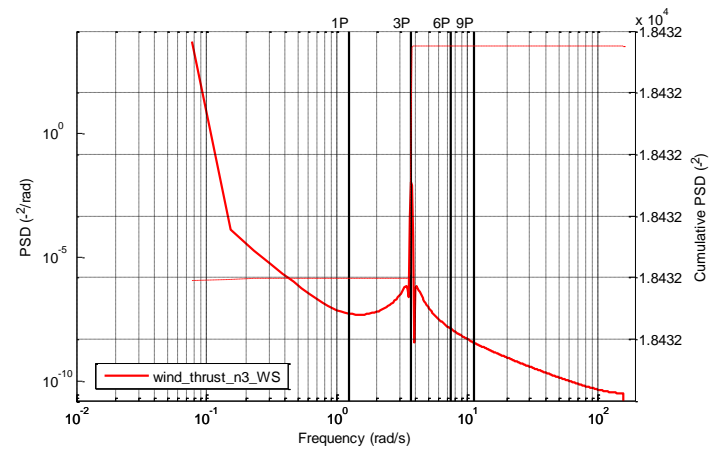


Figure D-8. Spectrum for *layer P* corresponding to $n = 3$ of the deterministic component of wind-field WS used for inducing thrust

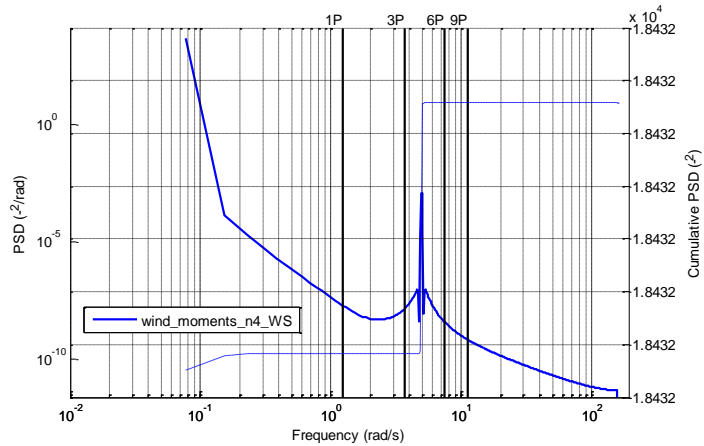


Figure D-9. Spectrum for **layer P** corresponding to $n = 4$ of the deterministic component of wind-field WS used for inducing moments

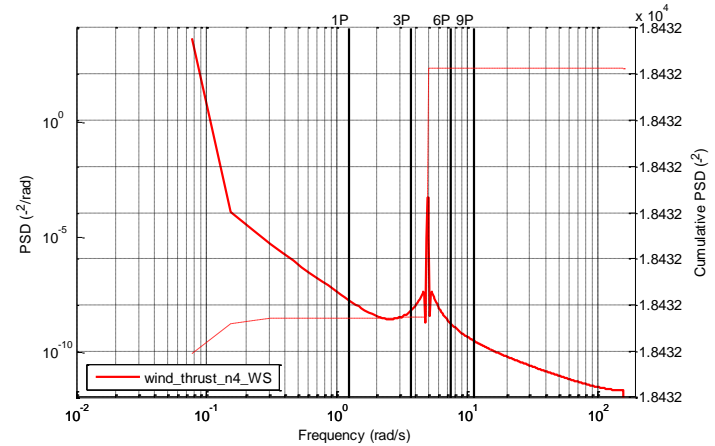


Figure D-10. Spectrum for **layer P** corresponding to $n = 4$ of the deterministic component of wind-field WS used for inducing thrust

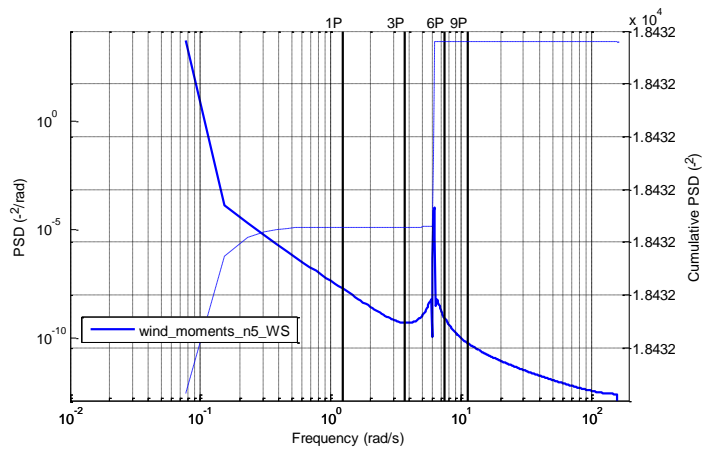


Figure D-11. Spectrum for **layer P** corresponding to $n = 5$ of the deterministic component of wind-field WS used for inducing moments

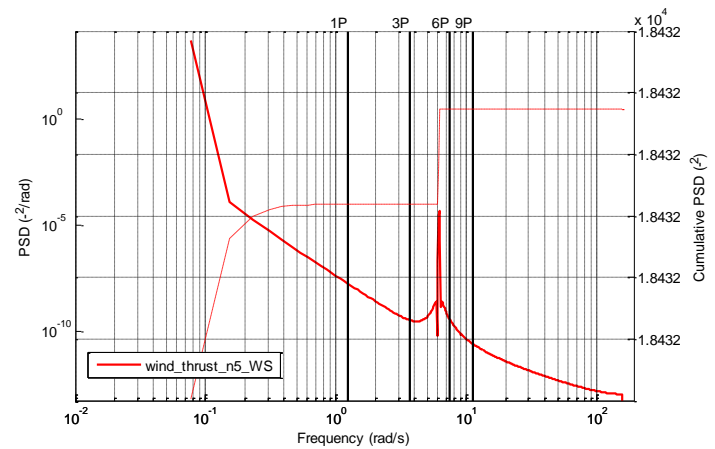


Figure D-12. Spectrum for **layer P** corresponding to $n = 5$ of the deterministic component of wind-field WS used for inducing thrust

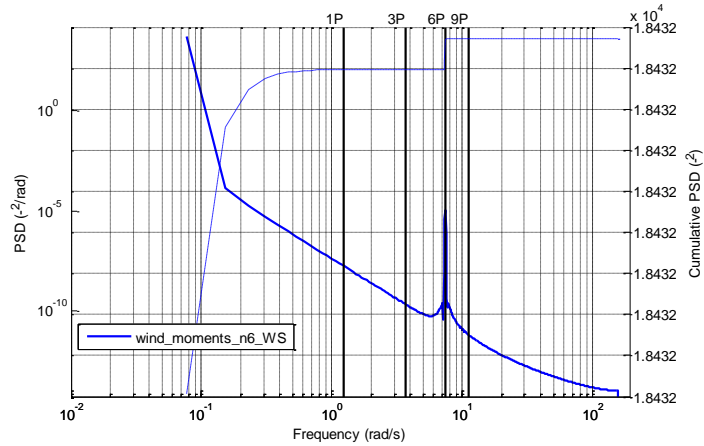


Figure D-13. Spectrum for *layer P* corresponding to $n = 6$ of the deterministic component of wind-field WS used for inducing moments

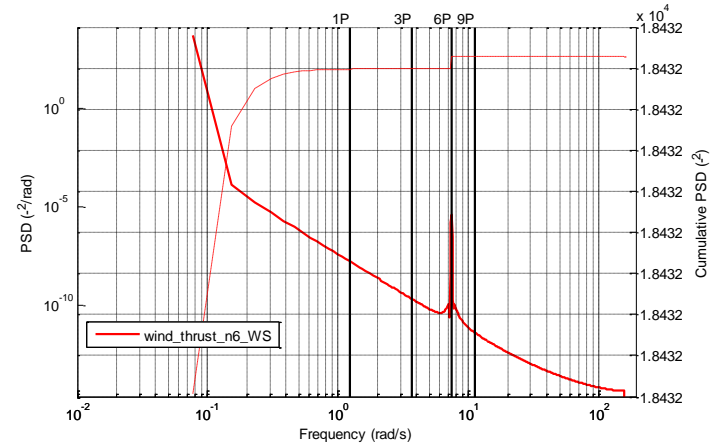


Figure D-14. Spectrum for *layer P* corresponding to $n = 6$ of the deterministic component of wind-field WS used for inducing thrust

WS	Moments			Forces (Thrust)		
	min	max	Amplitude	min	max	Amplitude
<i>layer P</i> = 0	15	15	0	15	15	0
<i>layer P</i> = 1	13.9417	16.0583	1.0583	14.1590	15.8410	0.8410
<i>layer P</i> = 2	14.8504	15.1496	0.1496	14.8912	15.1088	0.1088
<i>layer P</i> = 3	14.9691	15.0309	0.0309	14.9785	15.0215	0.0215
<i>layer P</i> = 4	14.9914	15.0076	0.0076	14.9949	15.0051	0.0051
<i>layer P</i> = 5	14.9979	15.0021	0.0021	14.9986	15.0014	0.0014
<i>layer P</i> = 6	14.9994	15.0006	0.0006	14.9996	15.0004	0.0004

Table D-1. Range of wind speed in the time series for every *layer P* when the WS phenomena is the only addition to a 15m/s wind

- Wind traces for TS

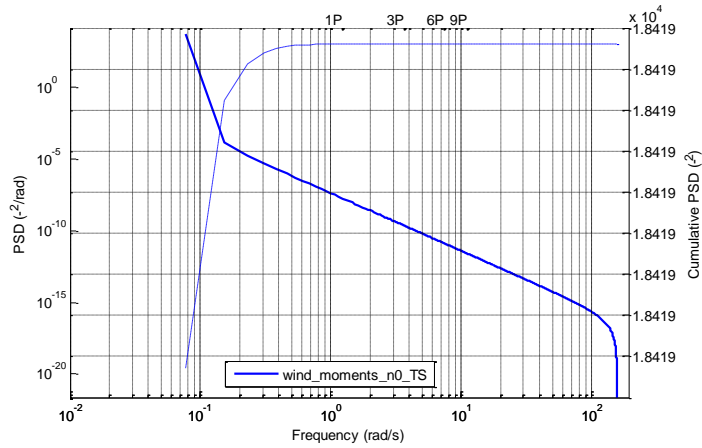


Figure D-15. Spectrum for *layer P* corresponding to $n = 0$ of the deterministic component of wind-field TS used for inducing moments

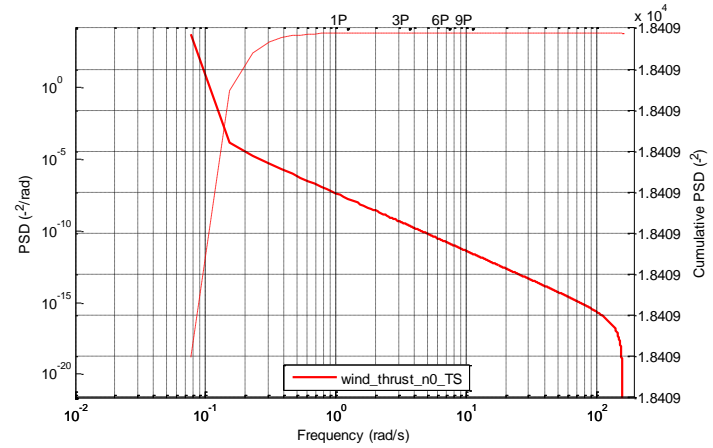


Figure D-16. Spectrum for *layer P* corresponding to $n = 0$ of the deterministic component of wind-field TS used for inducing thrust

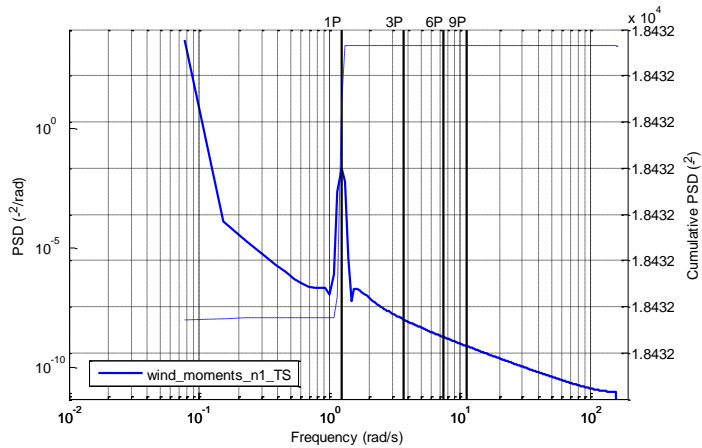


Figure D-17. Spectrum for *layer P* corresponding to $n = 1$ of the deterministic component of wind-field TS used for inducing moments

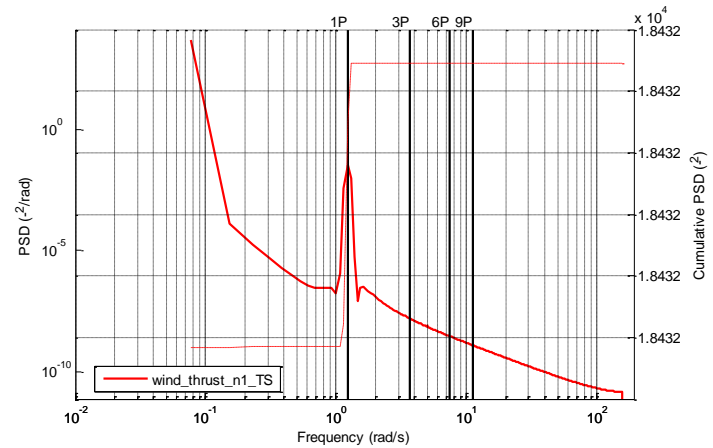


Figure D-18. Spectrum for *layer P* corresponding to $n = 1$ of the deterministic component of wind-field TS used for inducing thrust

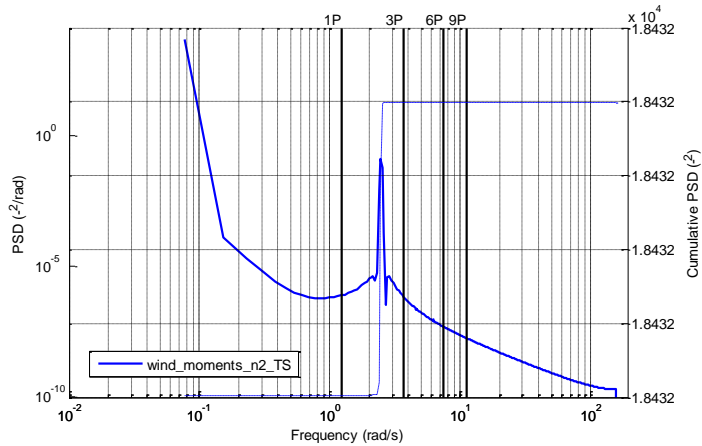


Figure D-19. Spectrum for *layer P* corresponding to $n = 2$ of the deterministic component of wind-field TS used for inducing moments

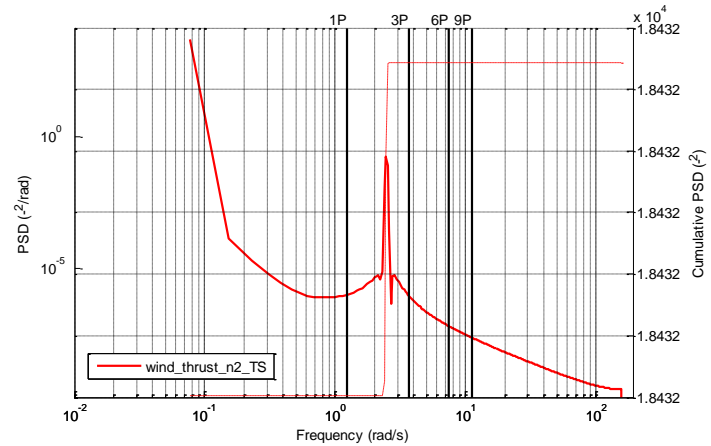


Figure D-20. Spectrum for *layer P* corresponding to $n = 2$ of the deterministic component of wind-field TS used for inducing thrust

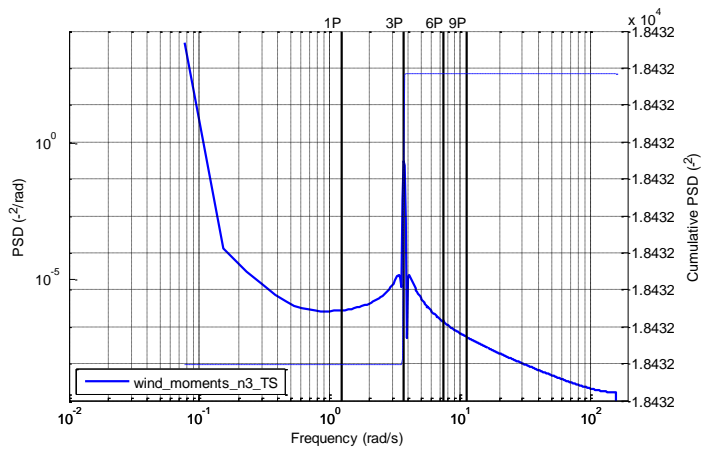


Figure D-21. Spectrum for *layer P* corresponding to $n = 3$ of the deterministic component of wind-field TS used for inducing moments

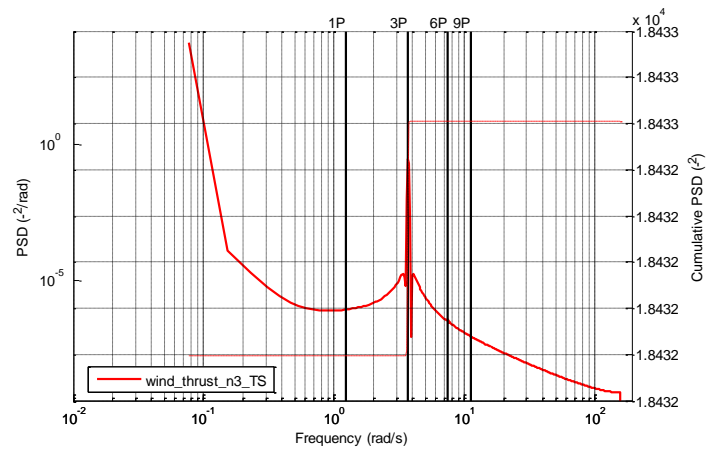


Figure D-22. Spectrum for *layer P* corresponding to $n = 3$ of the deterministic component of wind-field TS used for inducing thrust

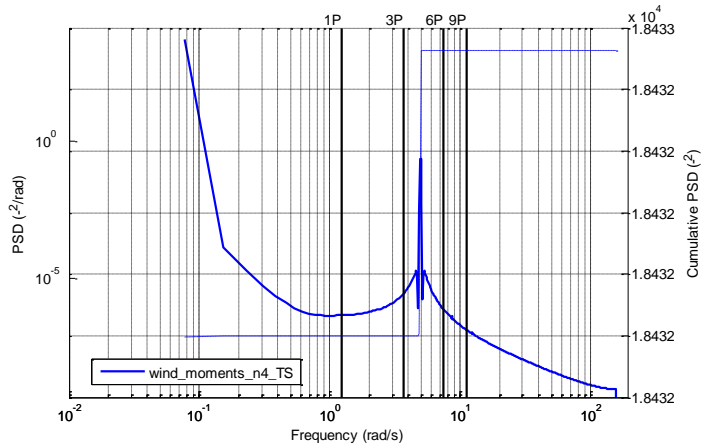


Figure D-23. Spectrum for *layer P* corresponding to $n = 4$ of the deterministic component of wind-field TS used for inducing moments

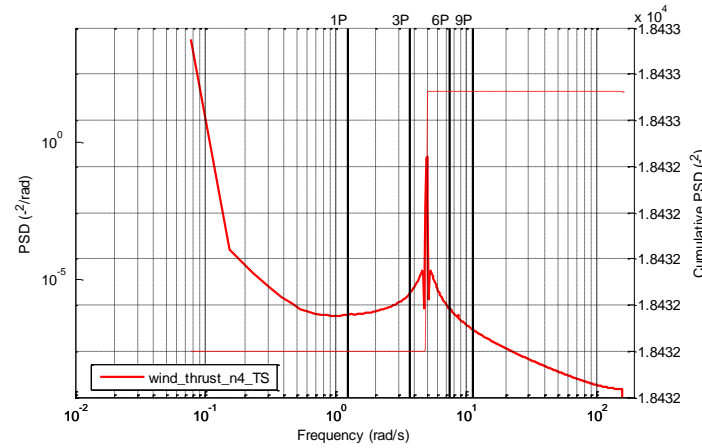


Figure D-24. Spectrum for *layer P* corresponding to $n = 4$ of the deterministic component of wind-field TS used for inducing thrust

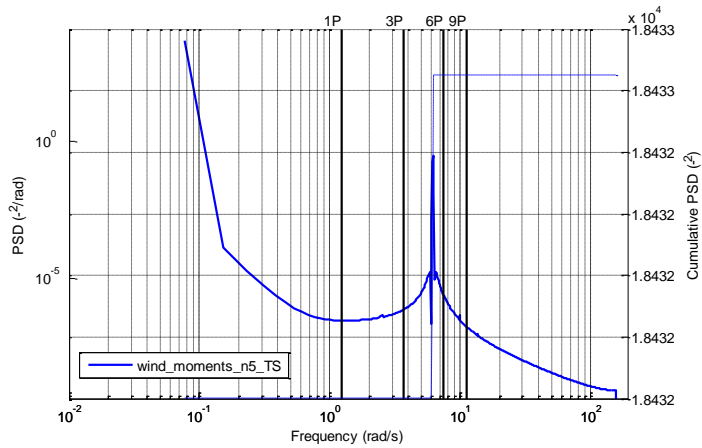


Figure D-25. Spectrum for *layer P* corresponding to $n = 5$ of the deterministic component of wind-field TS used for inducing moments

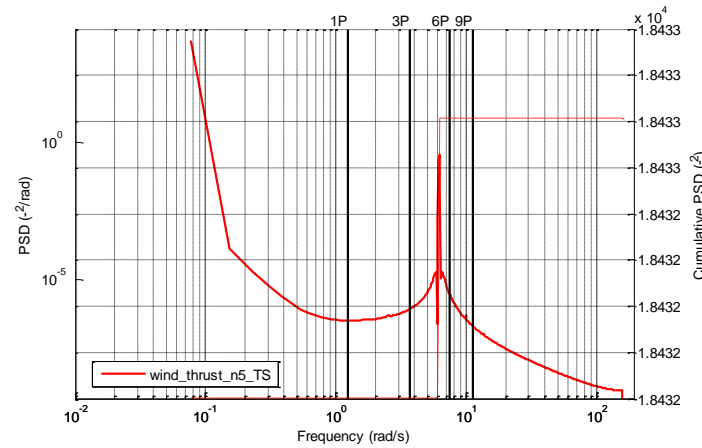


Figure D-26. Spectrum for *layer P* corresponding to $n = 5$ of the deterministic component of wind-field TS used for inducing thrust

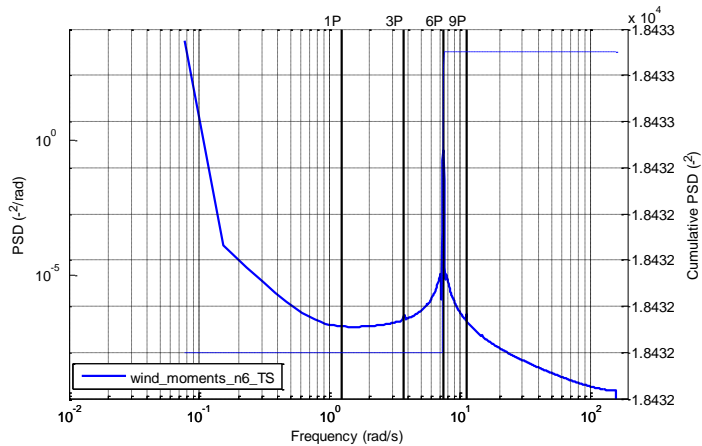


Figure D-27. Spectrum for *layer P* corresponding to $n = 6$ of the deterministic component of wind-field TS used for inducing moments

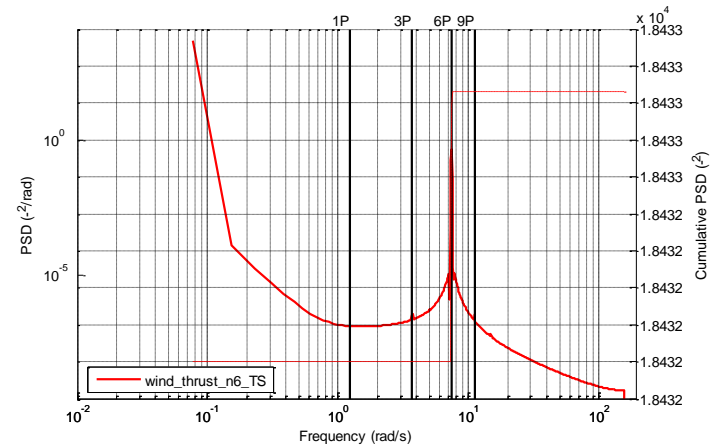


Figure D-28. Spectrum for *layer P* corresponding to $n = 6$ of the deterministic component of wind-field TS used for inducing thrust

TS	Moments			Forces (Thrust)		
	min	max	Amplitude	min	max	Amplitude
<i>layer P</i> = 0	14.9946	15.0054	0.0054	14.9906	15.0094	0.0094
<i>layer P</i> = 1	14.9732	15.0268	0.0268	14.9664	15.0336	0.0336
<i>layer P</i> = 2	14.9305	15.0695	0.0695	14.9188	15.0812	0.0812
<i>layer P</i> = 3	14.9019	15.0981	0.0981	14.8888	15.1112	0.1112
<i>layer P</i> = 4	14.8935	15.1065	0.1065	14.8827	15.1173	0.1173
<i>layer P</i> = 5	14.8868	15.1132	0.1132	14.8783	15.1217	0.1217
<i>layer P</i> = 6	14.8740	15.1260	0.1260	14.8663	15.1337	0.1337

Table D-2. Range of wind speed in the time series for every *layer P* when the TS phenomena is the only addition to a 15m/s wind

- Wind traces for WS and TS together

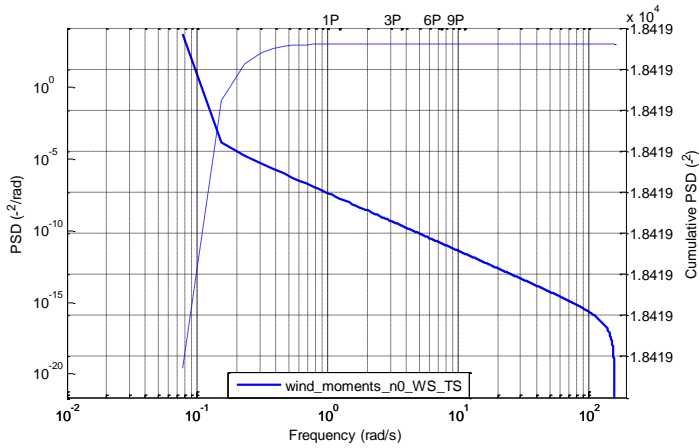


Figure D-29. Spectrum for *layer P* corresponding to $n = 0$ of the complete deterministic component of wind-field used for inducing moments

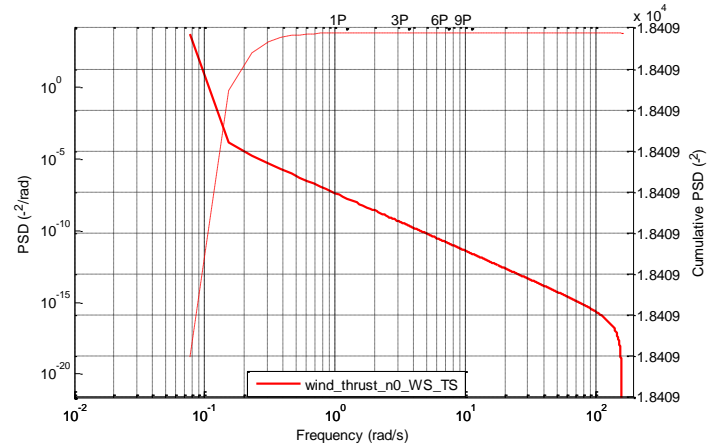


Figure D-30. Spectrum for *layer P* corresponding to $n = 0$ of the complete deterministic component of wind-field used for inducing thrust

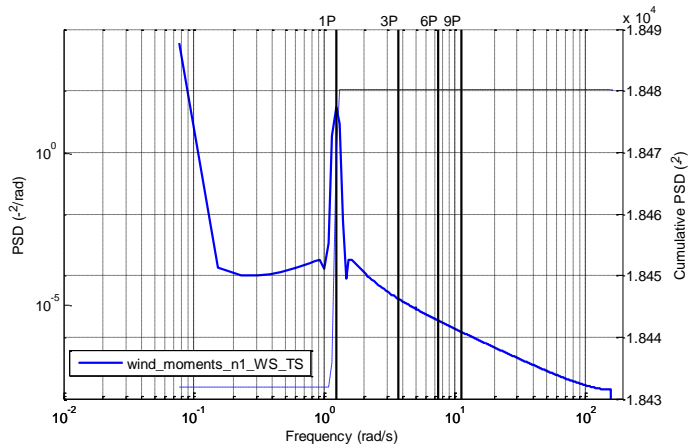


Figure D-31. Spectrum for *layer P* corresponding to $n = 1$ of the complete deterministic component of wind-field used for inducing moments

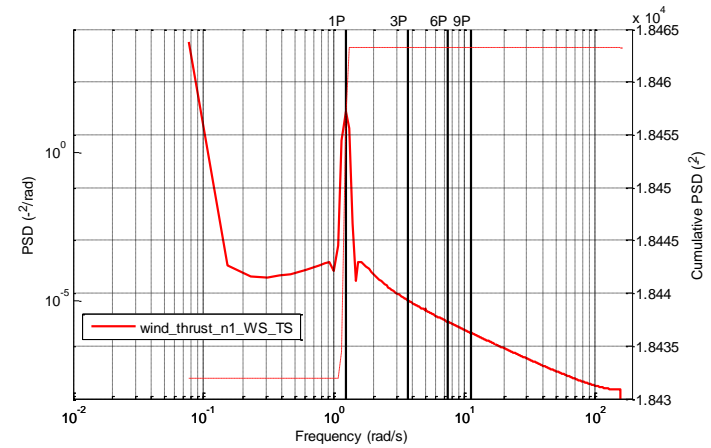


Figure D-32. Spectrum for *layer P* corresponding to $n = 1$ of the complete deterministic component of wind-field used for inducing thrust

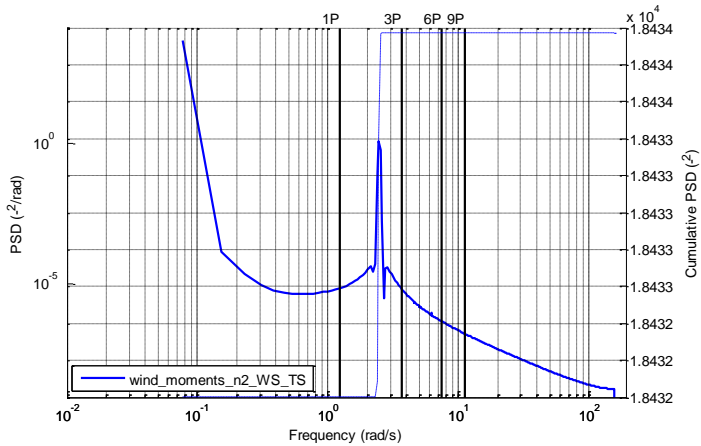


Figure D-33. Spectrum for *layer P* corresponding to $n = 2$ of the complete deterministic component of wind-field used for inducing moments

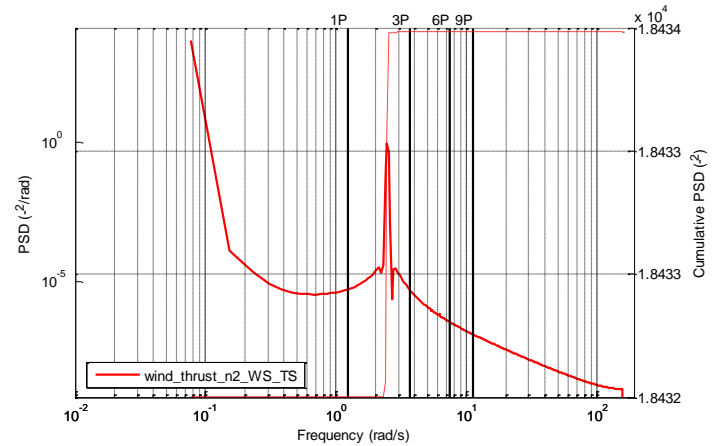


Figure D-34. Spectrum for *layer P* corresponding to $n = 2$ of the complete deterministic component of wind-field used for inducing thrust

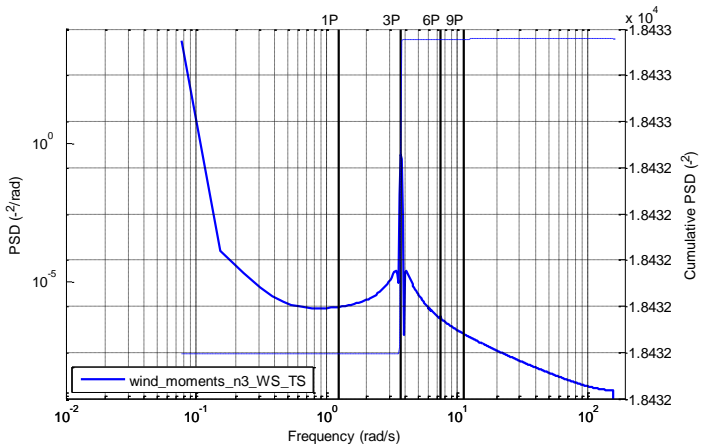


Figure D-35. Spectrum for *layer P* corresponding to $n = 3$ of the complete deterministic component of wind-field used for inducing moments

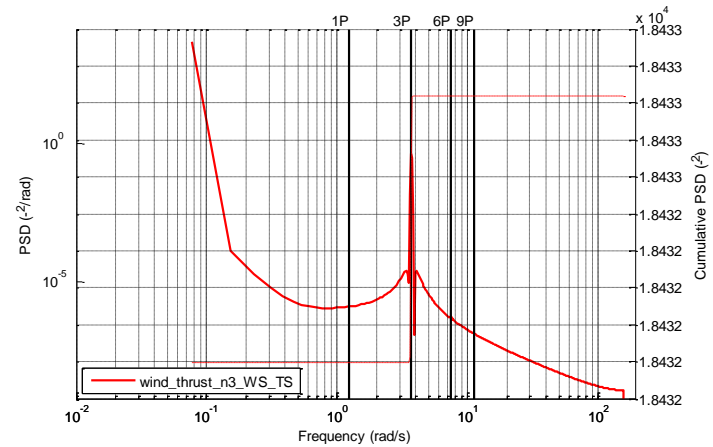


Figure D-36. Spectrum for *layer P* corresponding to $n = 3$ of the complete deterministic component of wind-field used for inducing thrust

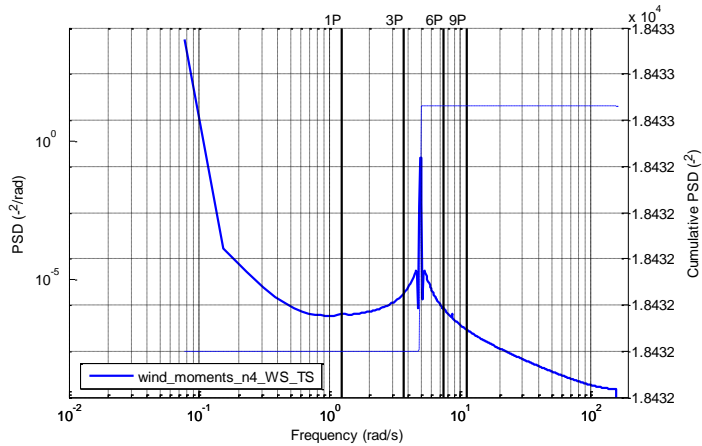


Figure D-37. Spectrum for *layer P* corresponding to $n = 4$ of the complete deterministic component of wind-field used for inducing moments

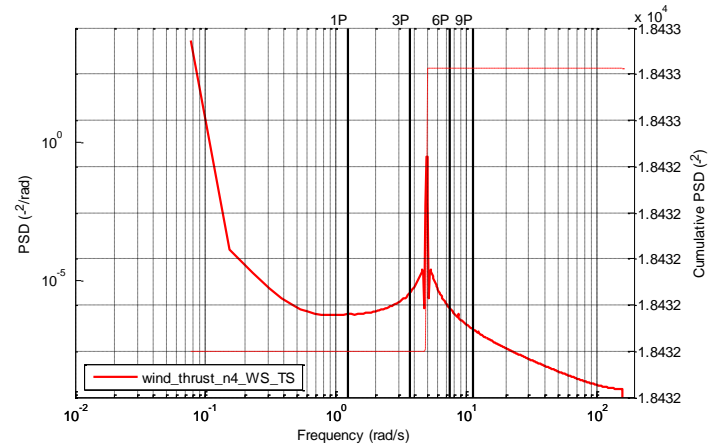


Figure D-38. Spectrum for *layer P* corresponding to $n = 4$ of the complete deterministic component of wind-field used for inducing thrust

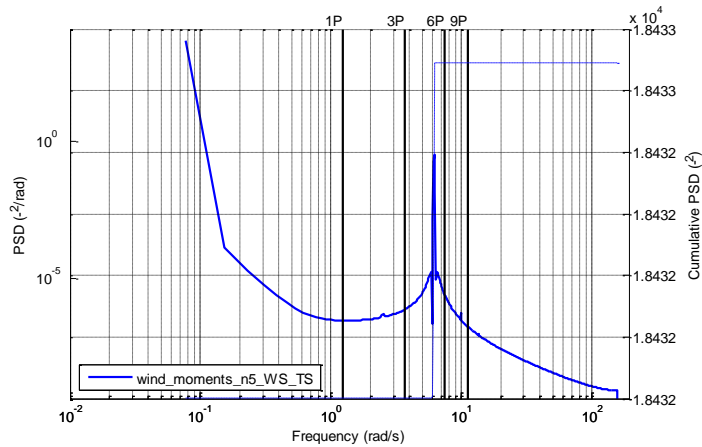


Figure D-39. Spectrum for *layer P* corresponding to $n = 5$ of the complete deterministic component of wind-field used for inducing moments

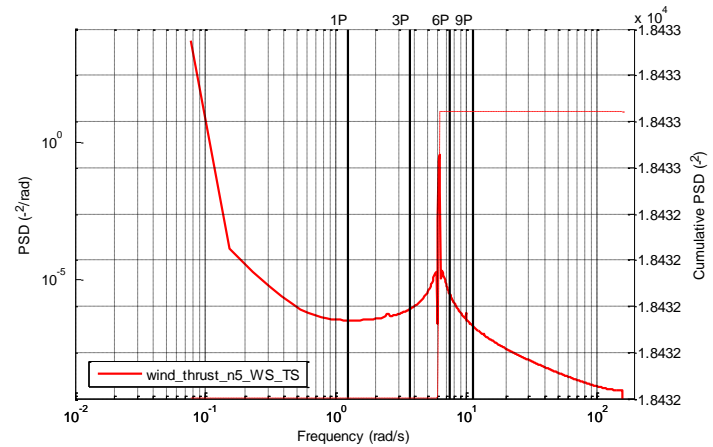


Figure D-40. Spectrum for *layer P* corresponding to $n = 5$ of the complete deterministic component of wind-field used for inducing thrust

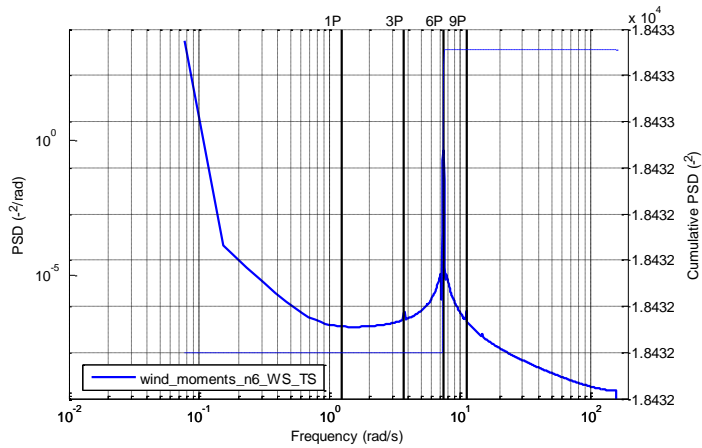


Figure D-41. Spectrum for *layer P* corresponding to $n = 6$ of the complete deterministic component of wind-field used for inducing moments

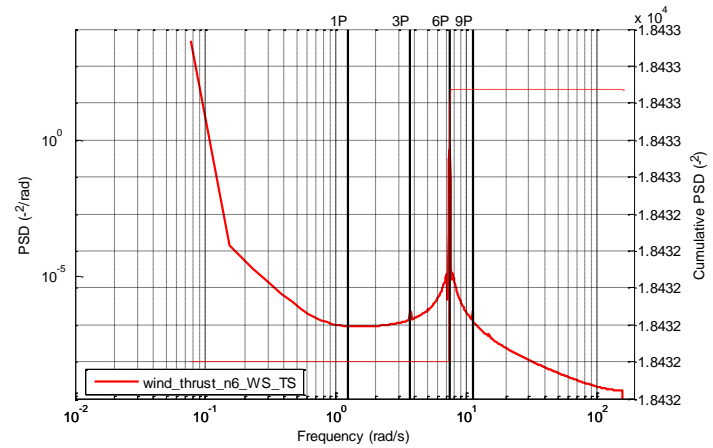


Figure D-42. Spectrum for *layer P* corresponding to $n = 6$ of the complete deterministic component of wind-field used for inducing thrust

WS & TS	Moments			Forces (Thrust)		
	min	max	range	min	max	range
<i>layer P</i> = 0	14.9946	15.0054	0.0054	14.9906	15.0094	0.0094
<i>layer P</i> = 1	13.9149	16.0851	1.0851	14.1254	15.8746	0.8746
<i>layer P</i> = 2	14.7809	15.2191	0.2191	14.8100	15.1900	0.1900
<i>layer P</i> = 3	14.8710	15.1290	0.1290	14.8673	15.1327	0.1327
<i>layer P</i> = 4	14.8859	15.1141	0.1141	14.8776	15.1224	0.1224
<i>layer P</i> = 5	14.8847	15.1153	0.1153	14.8770	15.1231	0.1231
<i>layer P</i> = 6	14.8734	15.1266	0.1266	14.8659	15.1341	0.1341

Table D-3. Range of wind speed in the time series for every *layer P* when the WS and TS phenomena are the only addition to a 15m/s wind

Appendix E

Wind-Field Deterministic Component Results

In the following can be found the results¹ for the in-plane RBM of the blade, edgewise moment of the blade, M_e , flapwise moment of the blade, M_f , and thrust force for the deterministic component of the wind-field. To be noted that the induced forces and moments in these results do not account for the force of gravity in order to better appreciate the outcomes induced by the wind-field. The results are for both the simple and triple structure, showing the WS and TS phenomena individually and in combination, for three different case studies. 15m/s, 15m/s with 18deg of pitch offset and 8m/s.

Likewise for the hub torque and out-of-plane RBM results seen in Section 6.3, the full set of results in this appendix for the deterministic component of the wind shows the presence of leakage. The impact of this leakage needs to be further assessed by looking at the results when both the stochastic and deterministic components of the wind are incorporated into the wind-field model. These results can be found in Section 6.4 and Appendix G.

While looking into the results for the in-plane RBM of the blade from Figure E-1 to Figure E-18 and Table E-1, it can be seen that the numbers and graphs for the single and triple models match closely, as expected since separability is justified for this moment. The only difference is a small discrepancy at the 3P peak for the WS case. It is interesting to note that when looking at spectral peaks for the wind shear case, Figure E-1, Figure E-3 and Figure E-5, the shape and magnitude of the same decrease as the frequency increases and that the 1P peak is dominant having the biggest amount of energy associated to it. On the other hand when looking at the TS case, Figure E-7, Figure E-9 and Figure E-11, the opposite can be appreciated with the steps in the cumulative related to each peak becoming increasingly bigger as the spectrum moves to higher frequencies. This opposite trend together with the order of magnitude associated to the

¹ The time series are presented as a 15s extract.

WS case and the TS case, means that when combined together on Figure E-13, Figure E-15 and Figure E-17, the low frequency spectral peaks are dominated by the WS component and the high frequency components of the spectrum by the TS component. The same observations are true for M_e (Figure E-19 to Figure E-36) and can be extended to M_f (Figure E-37 to Figure E-54) with exception to the point justifying the good match between the triple and single structure being due to separability. This is because whereas it was expected that M_e would have a good match due to separability also applying to it, M_f is not justified by the Separability property as is an out-of-plane moment. That said, there is a small discrepancy between the triple and single model for the M_e results of the WS & TS combined case at 15m/s + 18 deg of offset, (see Table E-1 and Figure E-33) for which there is no current explanation.

When looking into the thrust component of the wind, Figure E-55 to Figure E-72, which likewise the M_f and the out-of-plane RBM of the blade, is not covered by the Separability property, there is no expectation for a close match between the results from the simple and triple structure. Nevertheless a close match is what it is observed and the same opposite trend for the WS and TS is also present. Perhaps the biggest difference is that for the WS instead of the 3P peak, is the 6P peak that shows a discrepancy, significant in its context of WS only context, and with its biggest deviation at 8m/s which is a zone that separability would unlikely cover even if it was an appropriate in-plane moment/force that was being examined. When looking at the combined WS & TS results, Figure E-67 to Figure E-72, the only significant deviation is present in Figure E-70 on the frequencies leading up to the 6P peak.

Overall some small degree of leakage can be appreciated, especially on the thrust force, but it is of not great significance as the cumulative values shown are the square of the amplitude, not the amplitude per se. If the amplitude was to be calculated by square rooting of the values present in Table E-1, these deviations would be even smaller.

- In-plane RBM of the blade, WS

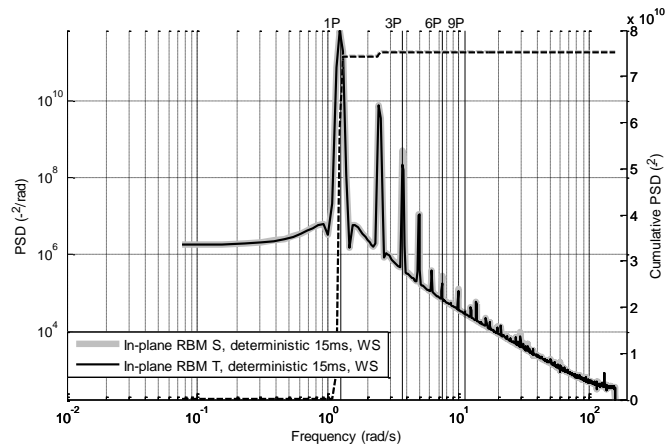


Figure E-1. In-plane RBM spectrum comparison between simple and triple structure for deterministic component of wind-field with mean 15m/s, WS active

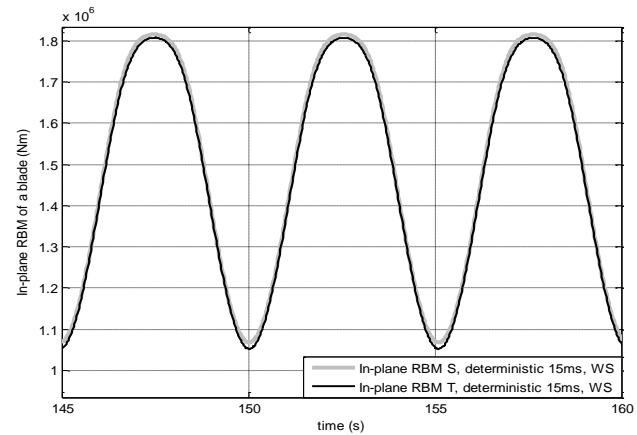


Figure E-2. In-plane RBM time series comparison between simple and triple structure for deterministic component of wind-field with mean 15m/s, WS active

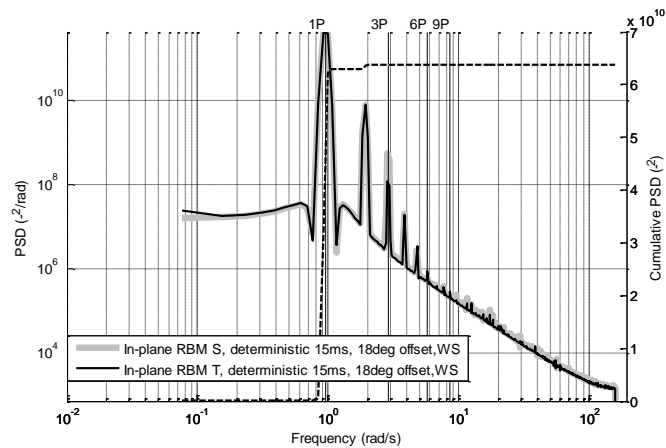


Figure E-3. In-plane RBM spectrum comparison between simple and triple structure for the deterministic component of the wind-field with mean 15m/s and 18 degrees of pitch offset, WS active

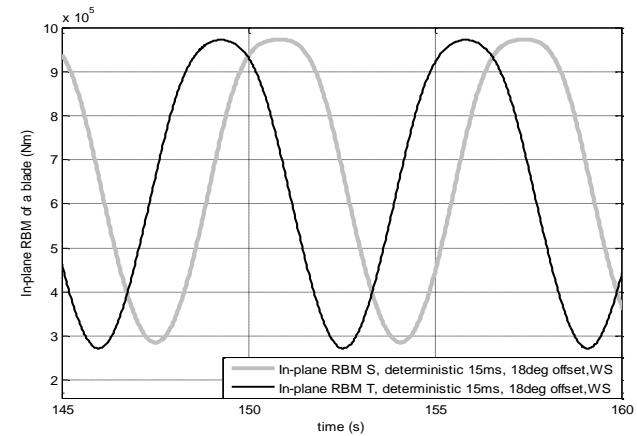


Figure E-4. In-plane RBM time series comparison between simple and triple structure for the deterministic component of the wind-field with mean 15m/s and 18 degrees of pitch offset, WS active

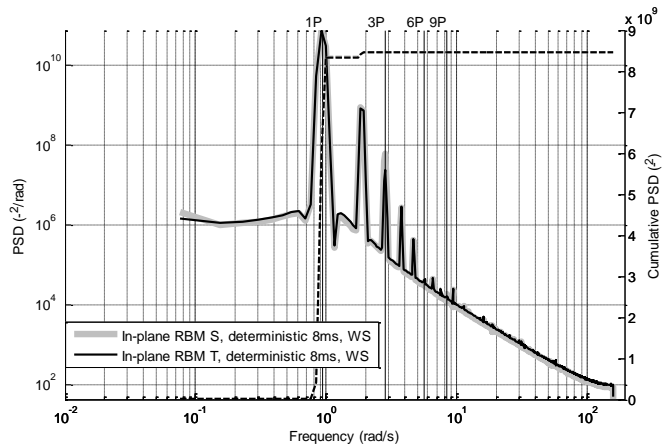


Figure E-5. In-plane RBM spectrum comparison between simple and triple structure for the deterministic component of the wind-field with mean 8m/s, WS active

- In-plane RBM of the blade, TS

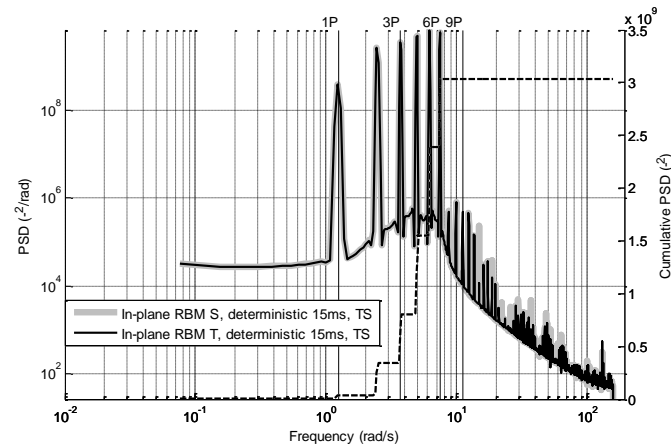


Figure E-7. In-plane RBM spectrum comparison between simple and triple structure for deterministic component of wind-field with mean 15m/s, TS active

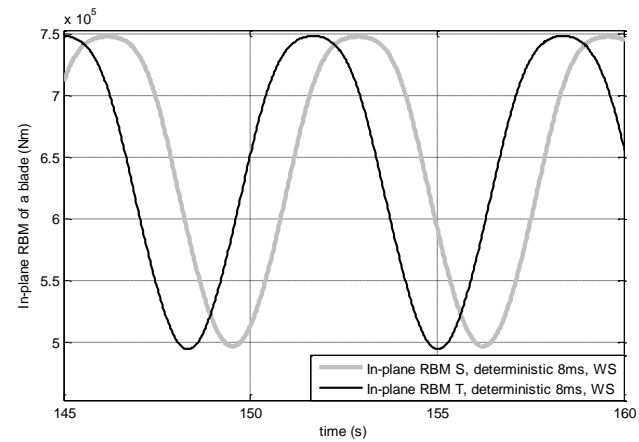


Figure E-6. In-plane RBM time series comparison between simple and triple structure for the deterministic component of the wind-field with mean 8m/s, WS active

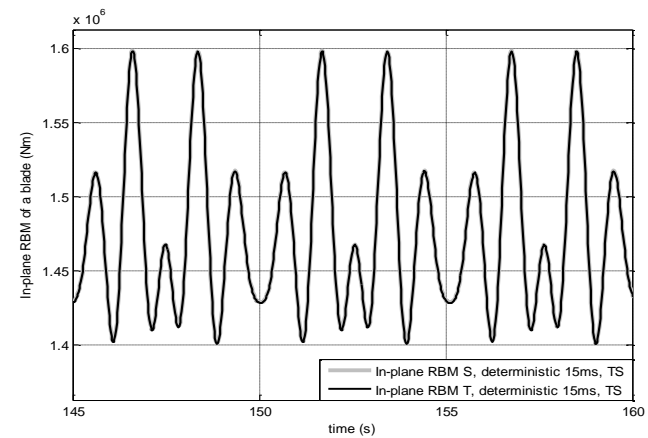


Figure E-8. In-plane RBM time series comparison between simple and triple structure for deterministic component of wind-field with mean 15m/s, TS active

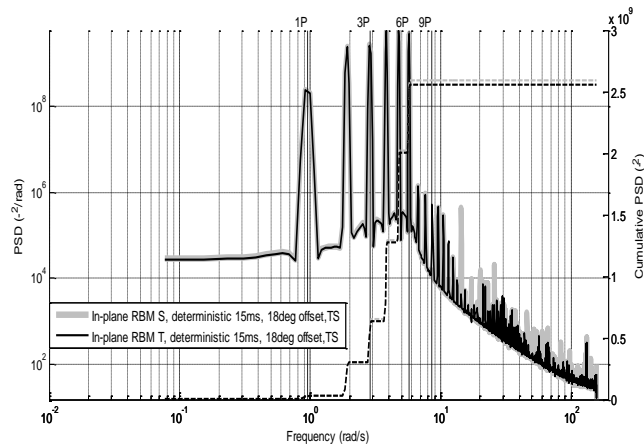


Figure E-9. In-plane RBM spectrum comparison between simple and triple structure for deterministic component of wind-field with mean 15m/s and 18 degrees of pitch offset, TS active

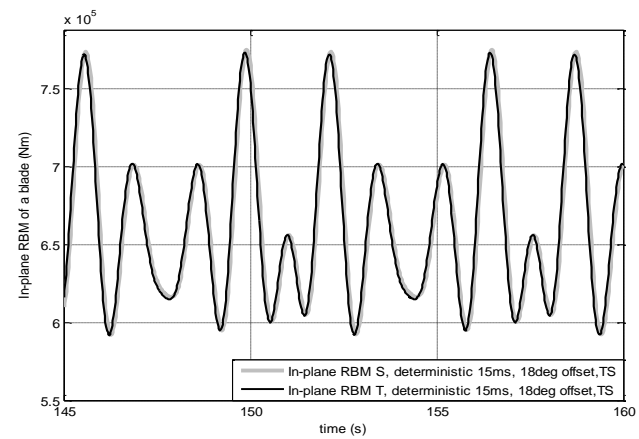


Figure E-10. In-plane RBM time series comparison between simple and triple structure for deterministic component of wind-field with mean 15m/s and 18 degrees of pitch offset, TS active

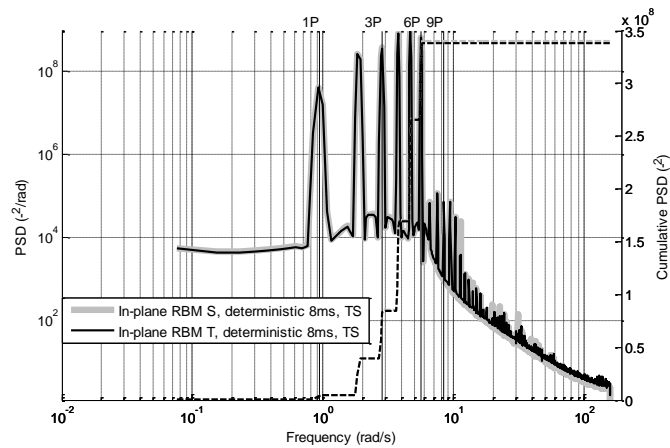


Figure E-11. In-plane RBM spectrum comparison between simple and triple structure for deterministic component of wind-field with mean 8m/s, TS active

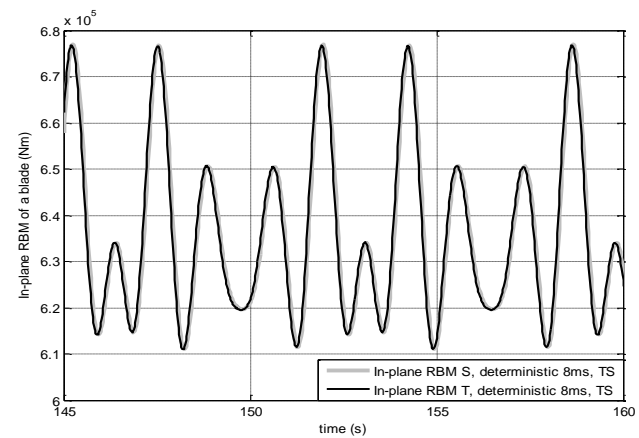


Figure E-12. In-plane RBM time series comparison between simple and triple structure for deterministic component of wind-field with mean 8m/s, TS active

- In-plane RBM of the blade, WS & TS

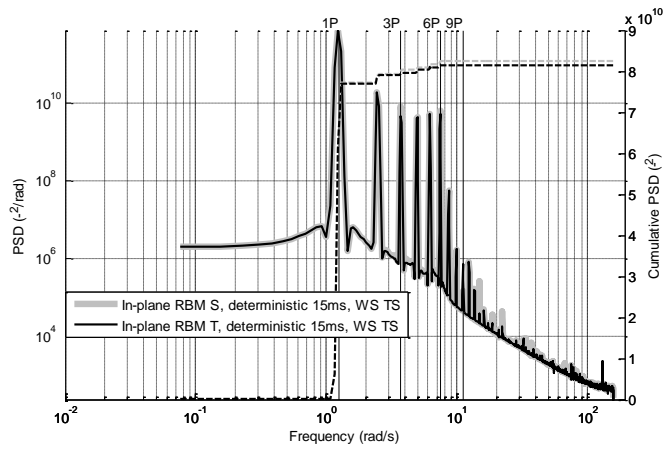


Figure E-13. In-plane RBM spectrum comparison between simple and triple structure for deterministic component of wind-field with mean 15m/s, WS TS active

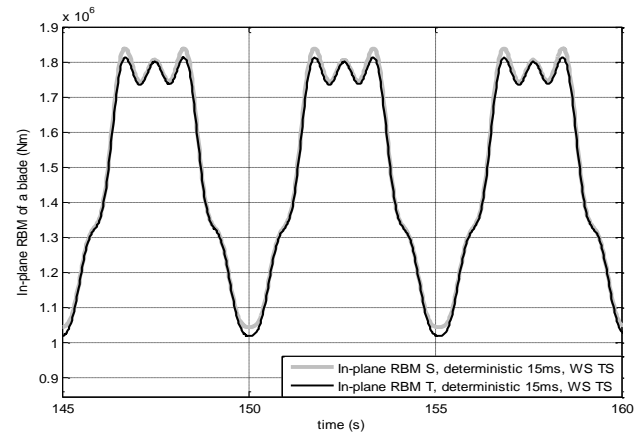


Figure E-14. In-plane RBM time series comparison between simple and triple structure for deterministic component of wind-field with mean 15m/s, WS TS active

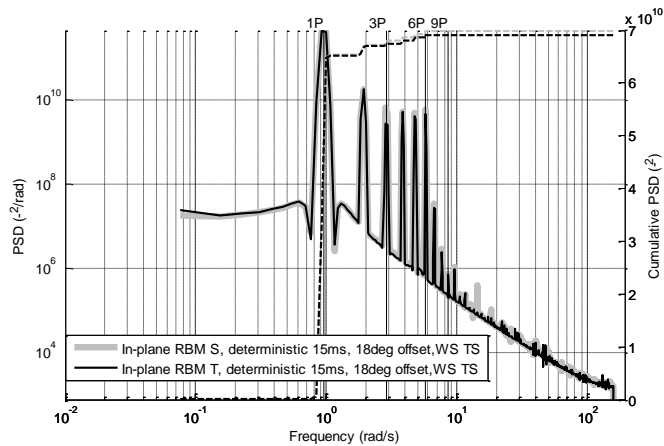


Figure E-15. In-plane RBM spectrum comparison between simple and triple structure for deterministic component of wind-field with mean 15m/s and 18 degrees of pitch offset, WS TS active

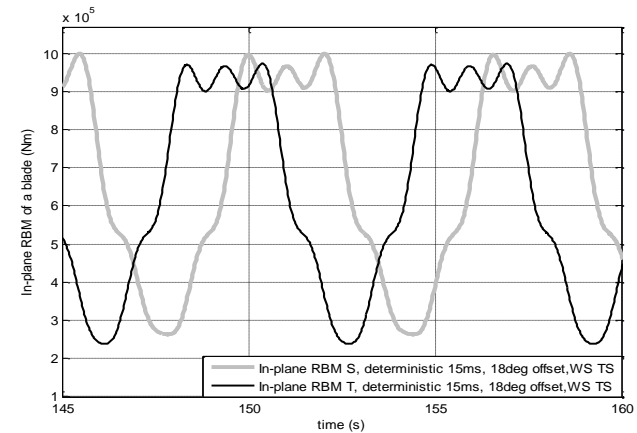


Figure E-16. In-plane RBM time series comparison between simple and triple structure for deterministic component of wind-field with mean 15m/s and 18 degrees of pitch offset, WS TS active

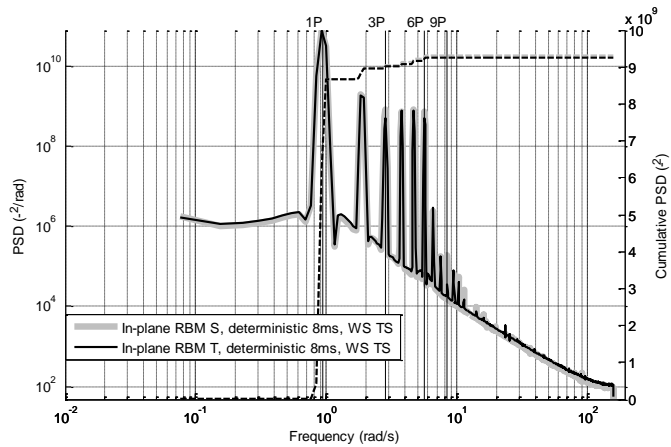


Figure E-17. In-plane RBM spectrum comparison between simple and triple structure for deterministic component of wind-field with mean 8m/s, WS TS active

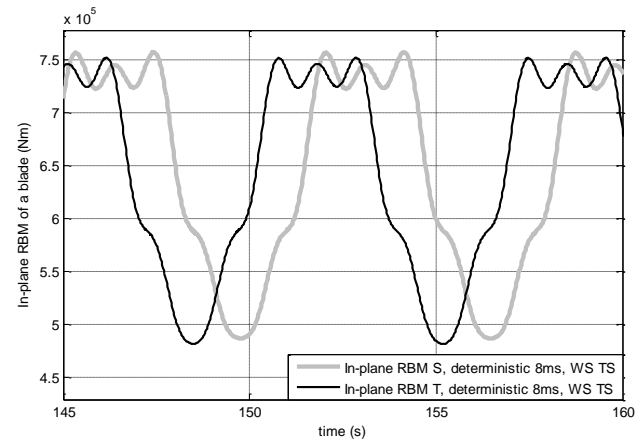


Figure E-18. In-plane RBM time series comparison between simple and triple structure for deterministic component of wind-field with mean 8m/s, WS TS active

- Edgewise moment of the blade, Me, WS

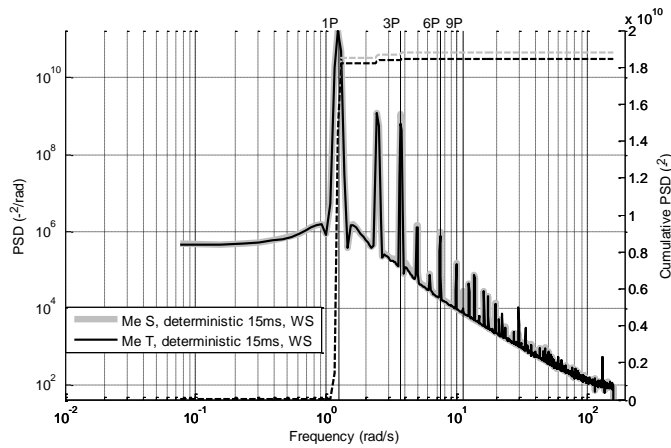


Figure E-19. Me spectrum comparison between simple and triple structure for the deterministic component of the wind-field with mean 15m/s, WS active

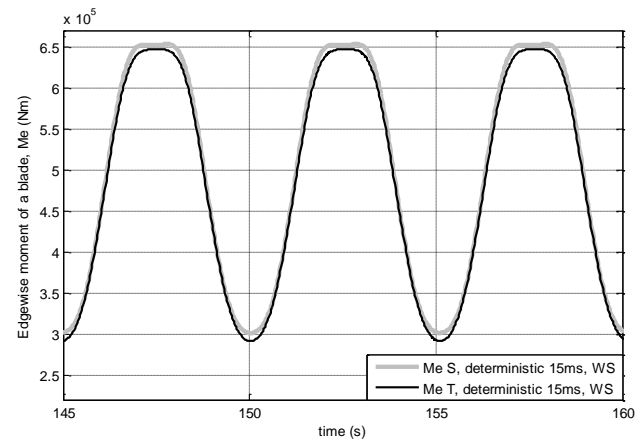


Figure E-20. Me time series comparison between simple and triple structure for the deterministic component of the wind-field with mean 15m/s, WS active

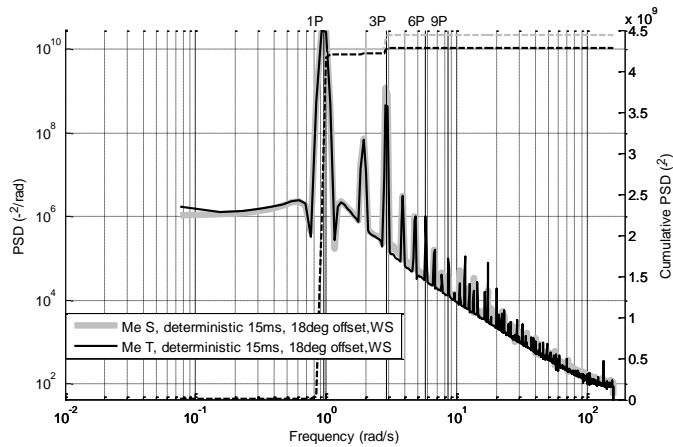


Figure E-21. Me spectrum comparison between simple and triple structure for the deterministic component of the wind-field with mean 15m/s and 18 degrees of pitch offset, WS active

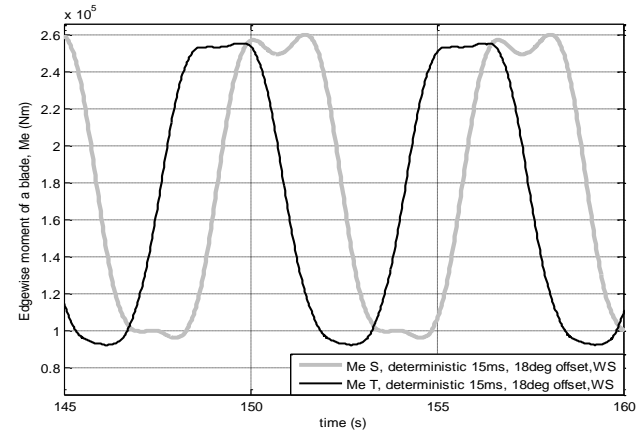


Figure E-22. Me time series comparison between simple and triple structure for the deterministic component of the wind-field with mean 15m/s and 18 degrees of pitch offset, WS active

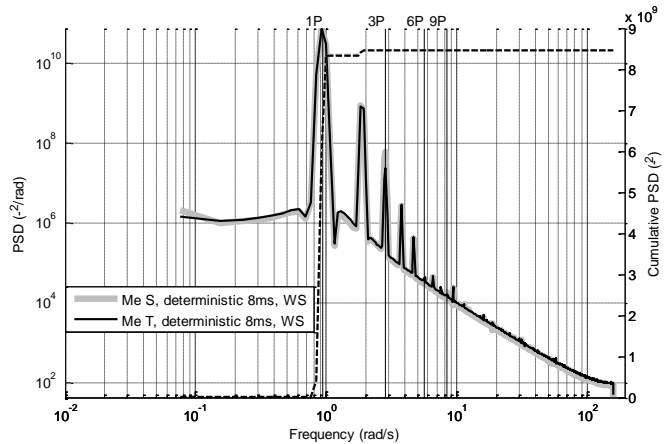


Figure E-23. Me spectrum comparison between simple and triple structure for the deterministic component of the wind-field with mean 8m/s, WS active

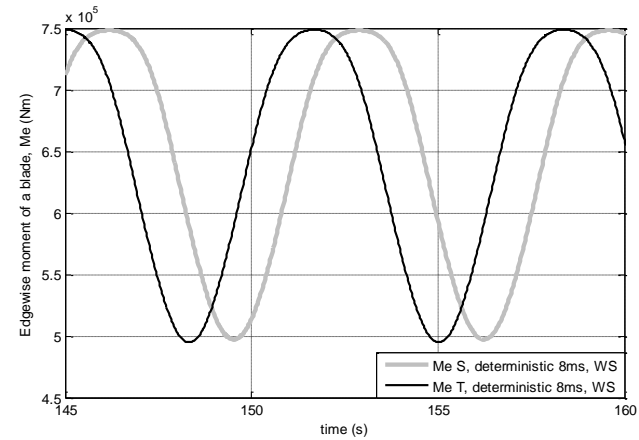


Figure E-24. Me time series comparison between simple and triple structure for the deterministic component of the wind-field with mean 8m/s, WS active

- Edgewise moment of the blade, Me, TS

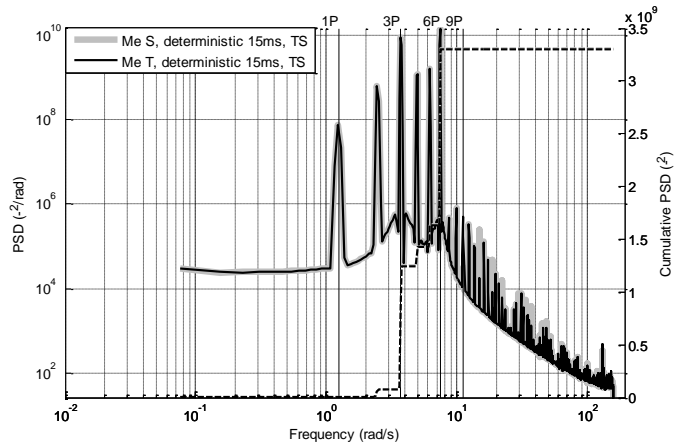


Figure E-25. Me spectrum comparison between simple and triple structure for the deterministic component of the wind-field with mean 15m/s, TS active

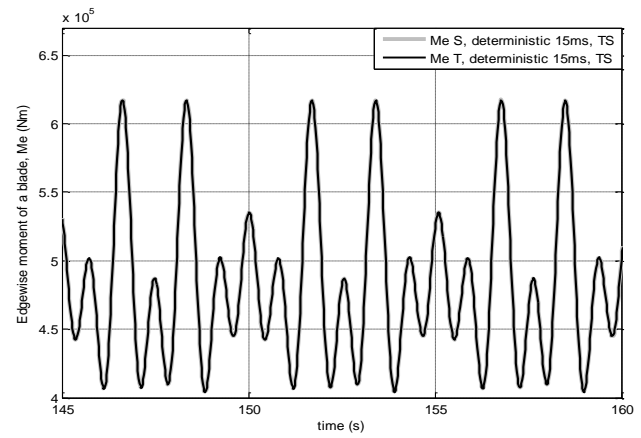


Figure E-26. Me time series comparison between simple and triple structure for the deterministic component of the wind-field with mean 15m/s, TS active

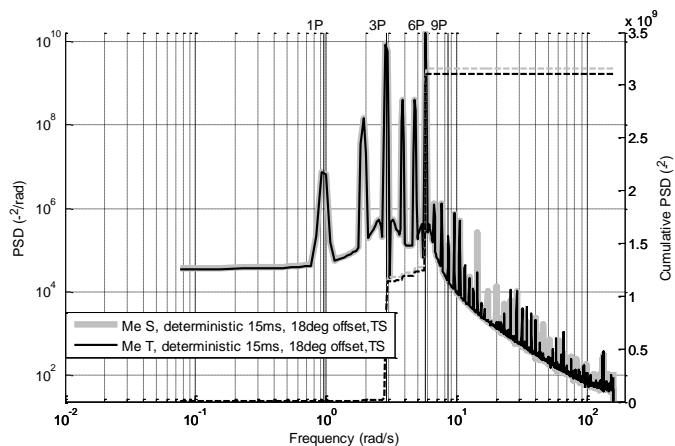


Figure E-27. Me spectrum comparison between simple and triple structure for the deterministic component of the wind-field with mean 15m/s and 18 degrees of pitch offset, TS active

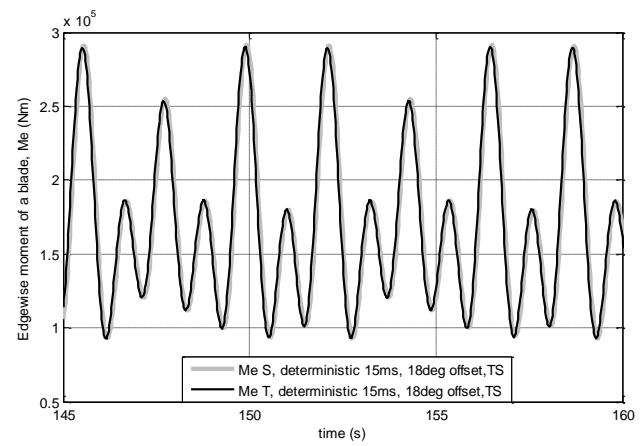


Figure E-28. Me time series comparison between simple and triple structure for the deterministic component of the wind-field with mean 15m/s and 18 degrees of pitch offset, TS active

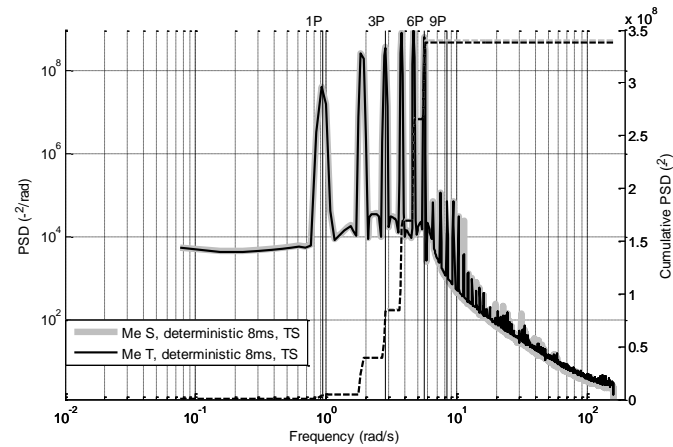


Figure E-29. Me spectrum comparison between simple and triple structure for the deterministic component of the wind-field with mean 8m/s, TS active

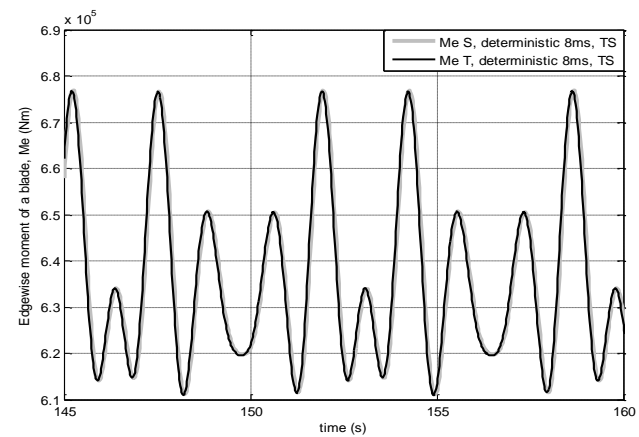


Figure E-30. Me time series comparison between simple and triple structure for the deterministic component of the wind-field with mean 8m/s, TS active

- Edgewise moment of the blade, Me, WS & TS

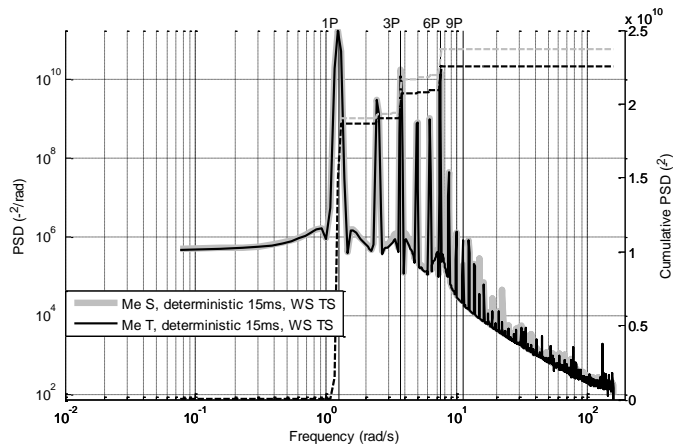


Figure E-31. Me spectrum comparison between simple and triple structure for the deterministic component of the wind-field with mean 15m/s, WS TS active

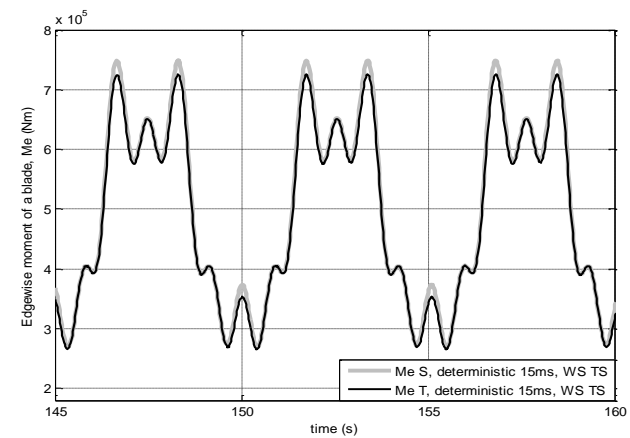


Figure E-32. Me time series comparison between simple and triple structure for the deterministic component of the wind-field with mean 15m/s, WS TS active

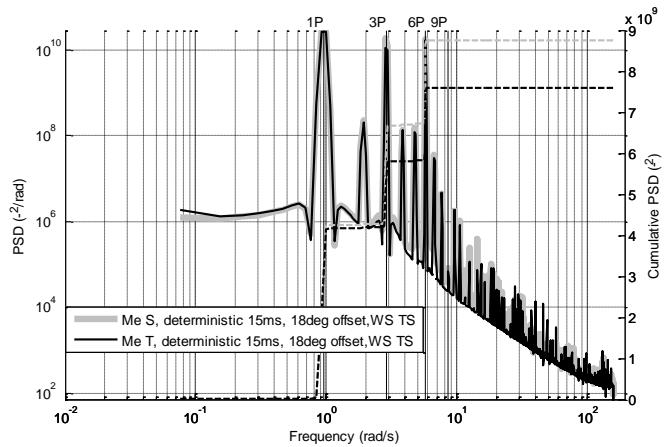


Figure E-33. Me spectrum comparison between simple and triple structure for the deterministic component of the wind-field with mean 15m/s and 18 degrees of pitch offset, WS TS active

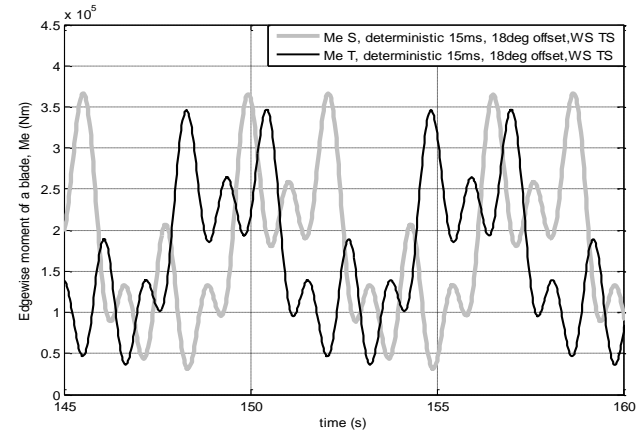


Figure E-34. Me time series comparison between simple and triple structure for the deterministic component of the wind-field with mean 15m/s and 18 degrees of pitch offset, WS TS active

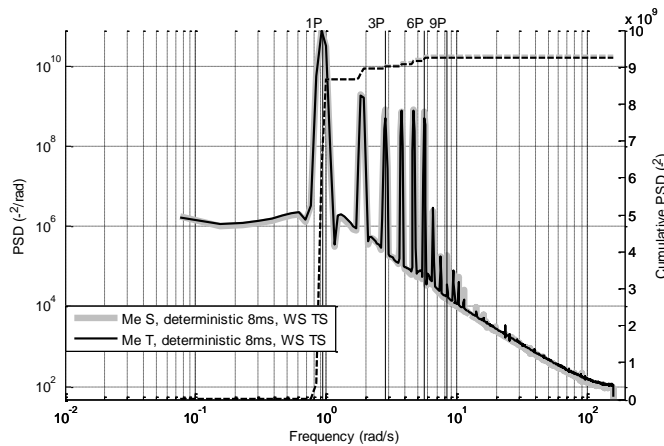


Figure E-35. Me spectrum comparison between simple and triple structure for the deterministic component of the wind-field with mean 8m/s, WS TS active

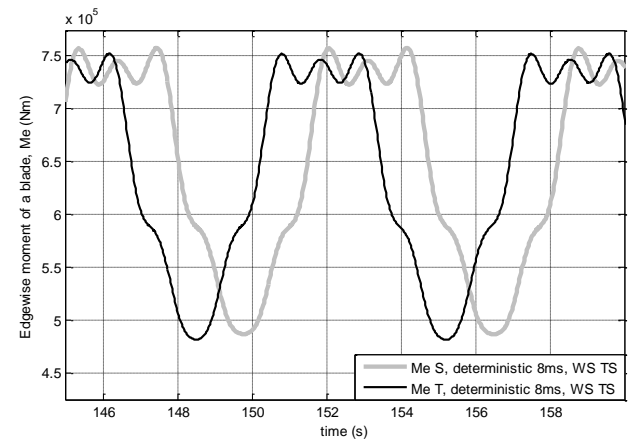


Figure E-36. Me time series comparison between simple and triple structure for the deterministic component of the wind-field with mean 8m/s, WS TS active

- Flapwise moment of the blade, Mf, WS

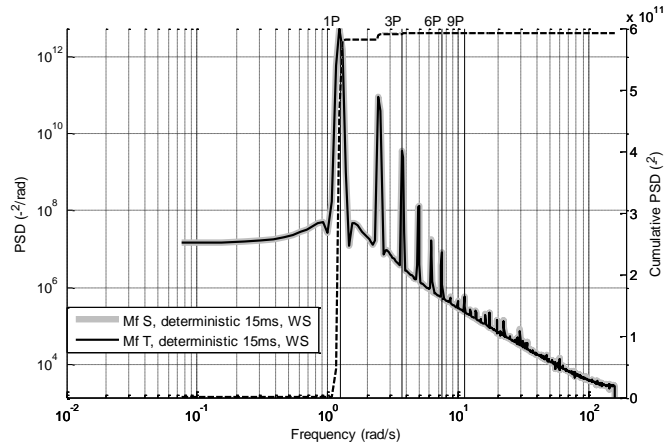


Figure E-37. Mf force spectrum comparison between simple and triple structure for the deterministic component of the wind-field with mean 15m/s, WS active

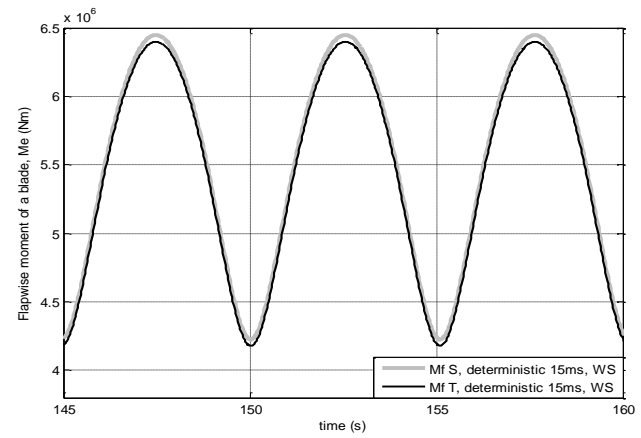


Figure E-38. Mf time series comparison between simple and triple structure for the deterministic component of the wind-field with mean 15m/s, WS active

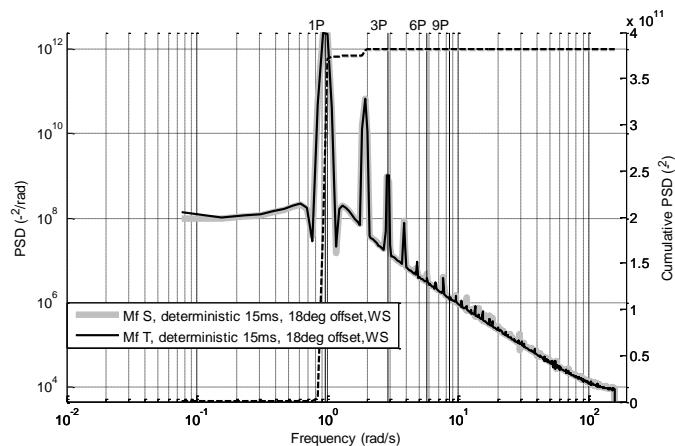


Figure E-39. Mf force spectrum comparison between simple and triple structure for the deterministic component of the wind-field with mean 15m/s and 18 degrees of pitch offset, WS active

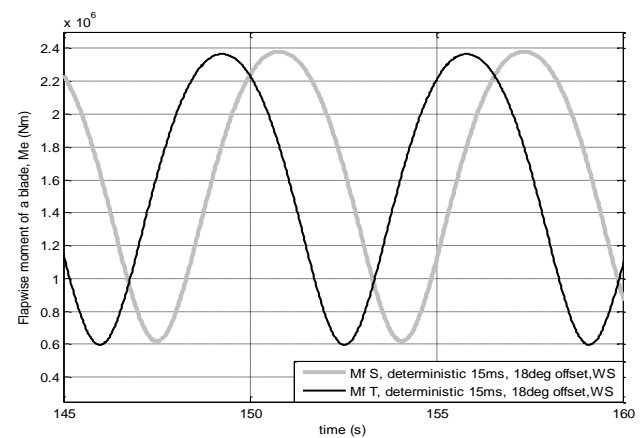


Figure E-40. Mf time series comparison between simple and triple structure for the deterministic component of the wind-field with mean 15m/s and 18 degrees of pitch offset, WS active

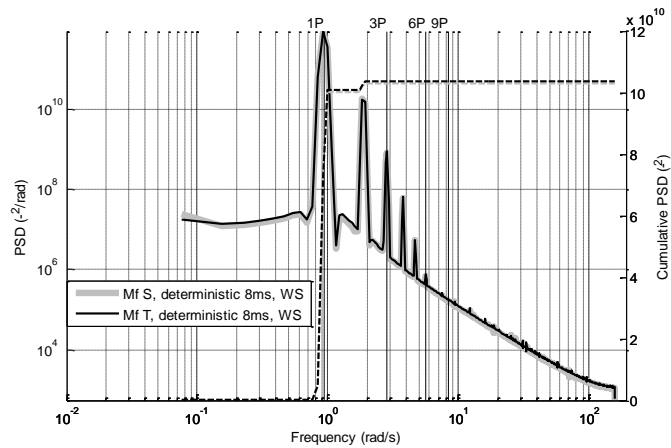


Figure E-41. Mf force spectrum comparison between simple and triple structure for the deterministic component of the wind-field with mean 8m/s, WS active

- Flapwise moment of the blade, Mf, TS

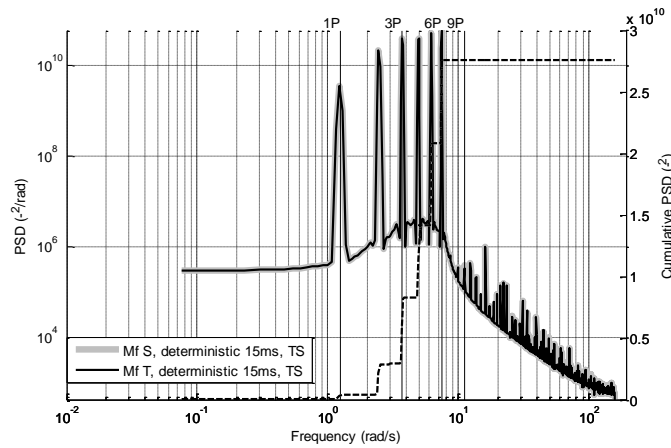


Figure E-43. Mf force spectrum comparison between simple and triple structure for the deterministic component of the wind-field with mean 15m/s, TS active

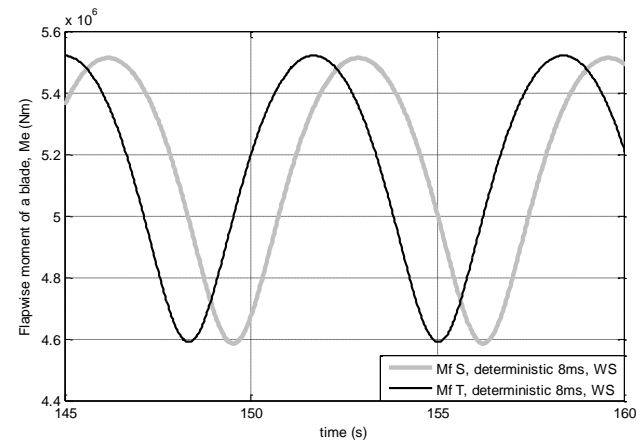


Figure E-42. Mf time series comparison between simple and triple structure for the deterministic component of the wind-field with mean 8m/s, WS active

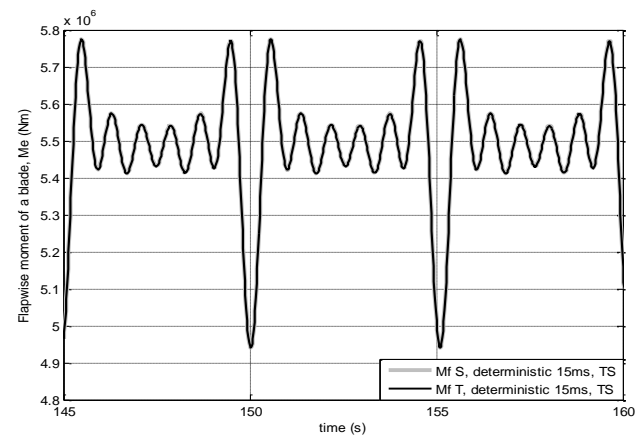


Figure E-44. Mf time series comparison between simple and triple structure for the deterministic component of the wind-field with mean 15m/s, TS active

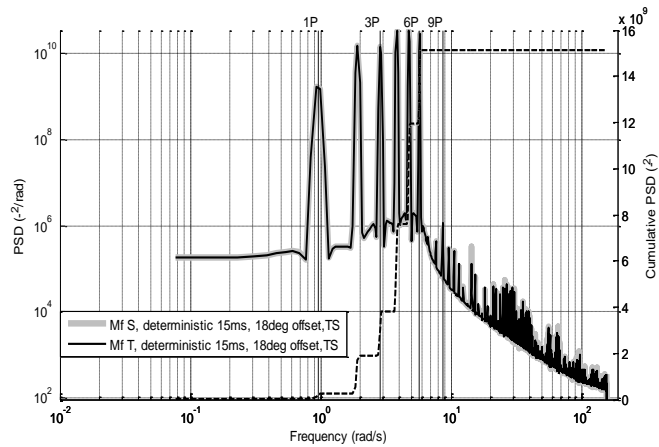


Figure E-45. Mf force spectrum comparison between simple and triple structure for the deterministic component of the wind-field with mean 15m/s and 18 degrees of pitch offset, TS active

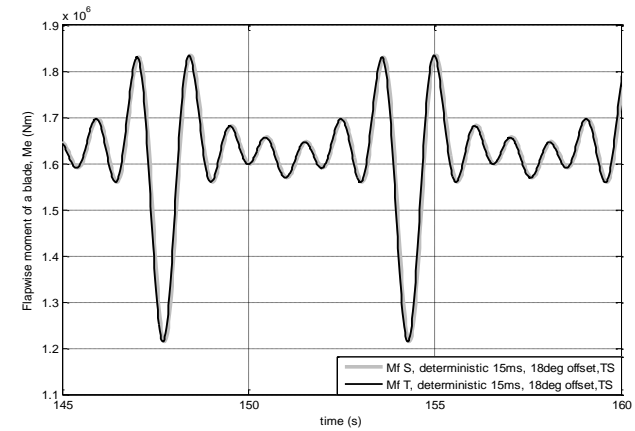


Figure E-46. Mf time series comparison between simple and triple structure for the deterministic component of the wind-field with mean 15m/s and 18 degrees of pitch offset, TS active

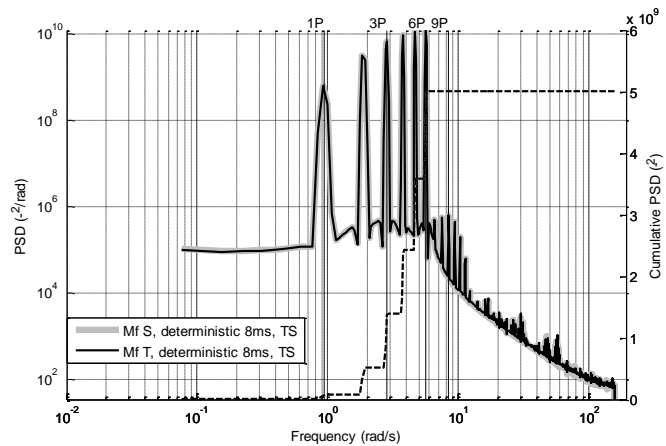


Figure E-47. Mf force spectrum comparison between simple and triple structure for the deterministic component of the wind-field with mean 8m/s, TS active

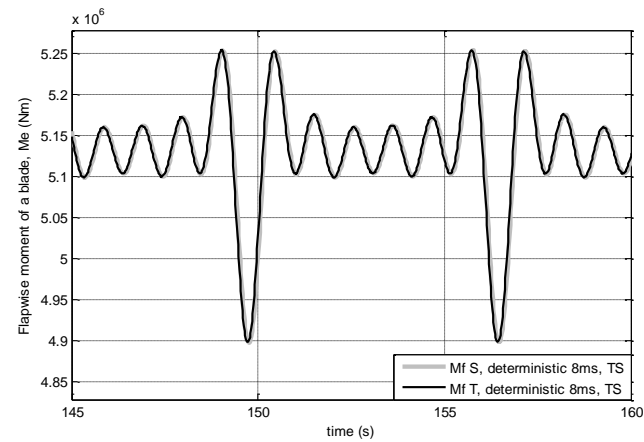


Figure E-48. Mf time series comparison between simple and triple structure for the deterministic component of the wind-field with mean 8m/s, TS active

- Flapwise moment of the blade, Mf, WS & TS

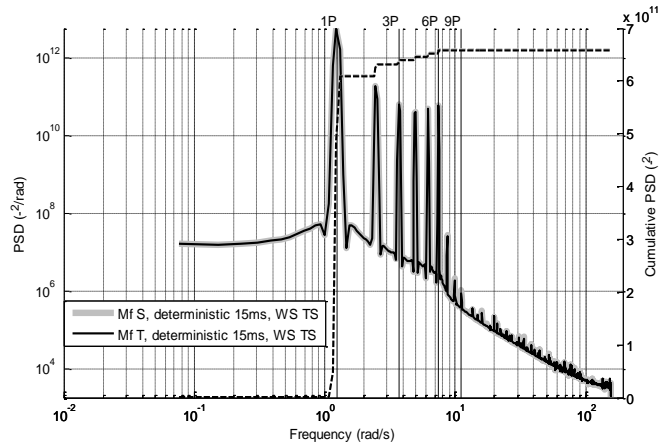


Figure E-49. Mf force spectrum comparison between simple and triple structure for the deterministic component of the wind-field with mean 15m/s, WS TS active

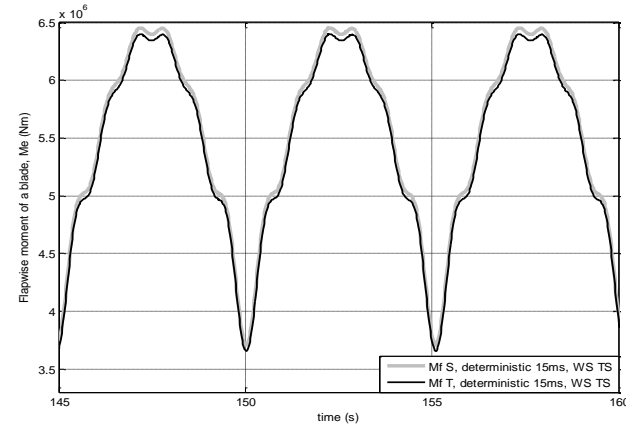


Figure E-50. Mf time series comparison between simple and triple structure for the deterministic component of the wind-field with mean 15m/s, WS TS active

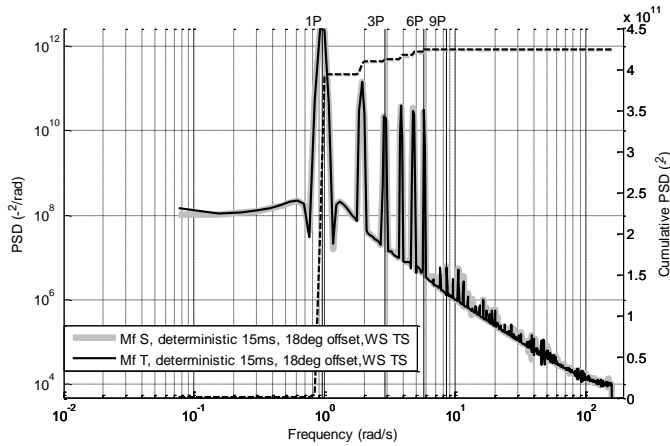


Figure E-51. Mf force spectrum comparison between simple and triple structure for the deterministic component of the wind-field with mean 15m/s and 18 degrees of pitch offset, WS TS active

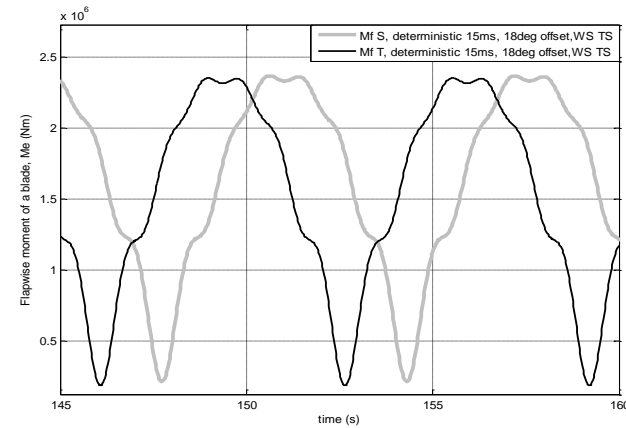


Figure E-52. Mf time series comparison between simple and triple structure for the deterministic component of the wind-field with mean 15m/s and 18 degrees of pitch offset, WS TS active

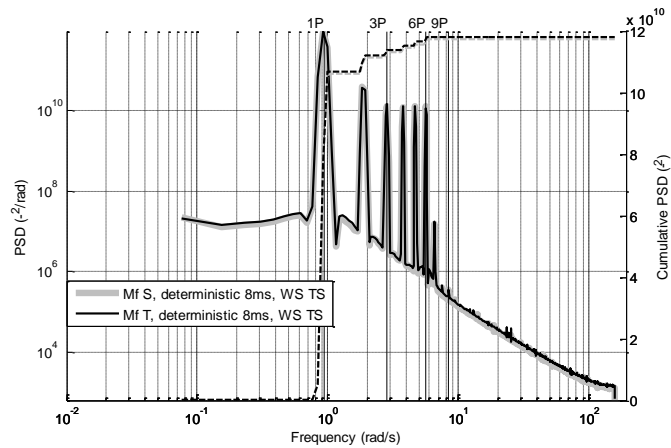


Figure E-53. Mf force spectrum comparison between simple and triple structure for the deterministic component of the wind-field with mean 8m/s, WS TS active

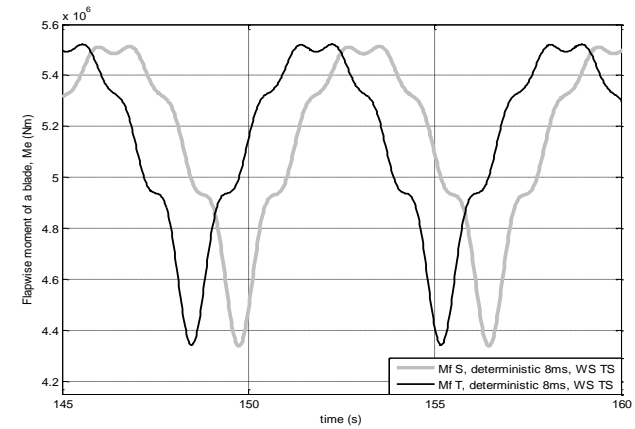


Figure E-54. Mf time series comparison between simple and triple structure for the deterministic component of the wind-field with mean 8m/s, WS TS active

- Thrust Force, WS

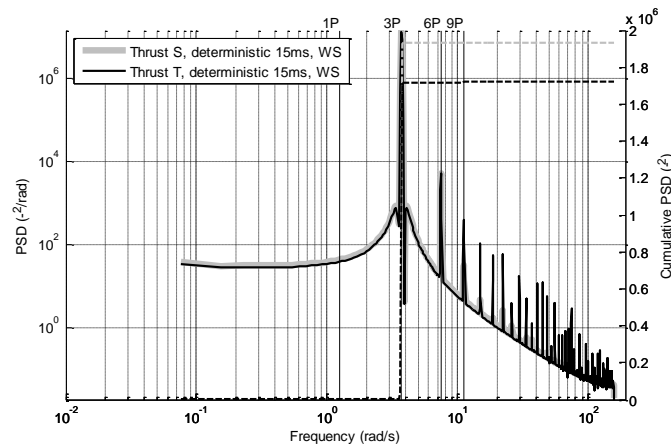


Figure E-55. Thrust force spectrum comparison between simple and triple structure for the deterministic component of the wind-field with mean 15m/s, WS active

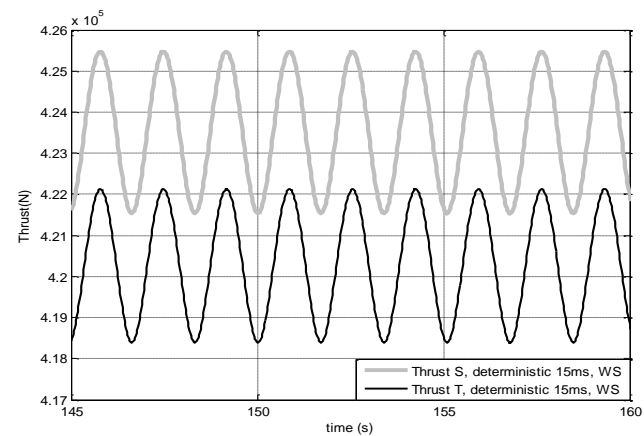


Figure E-56. Thrust force time series comparison between simple and triple structure for the deterministic component of the wind-field with mean 15m/s, WS active

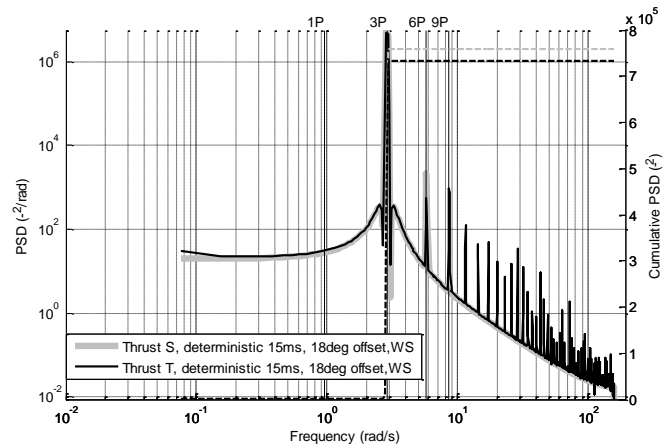


Figure E-57. Thrust force spectrum comparison between simple and triple structure for the deterministic component of the wind-field with mean 15m/s and 18 degrees of pitch offset, WS active

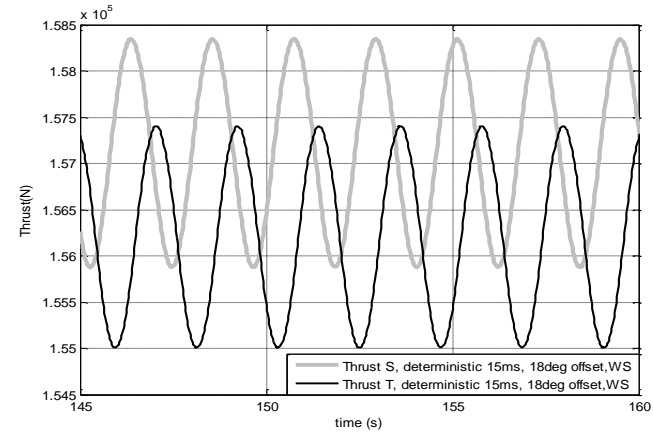


Figure E-58. Thrust force time series comparison between simple and triple structure for the deterministic component of the wind-field with mean 15m/s and 18 degrees of pitch offset, WS active

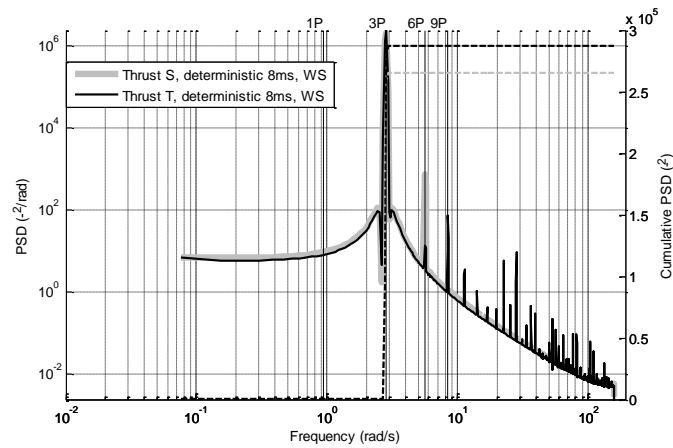


Figure E-59. Thrust force spectrum comparison between simple and triple structure for the deterministic component of the wind-field with mean 8m/s, WS active

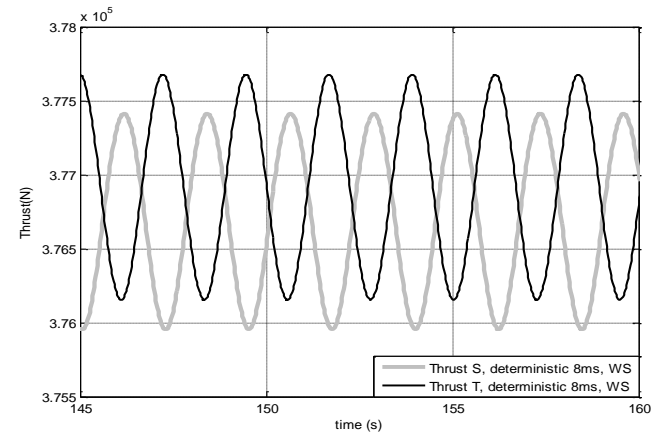


Figure E-60. Thrust force time series comparison between simple and triple structure for the deterministic component of the wind-field with mean 8m/s, WS active

- Thrust Force, TS

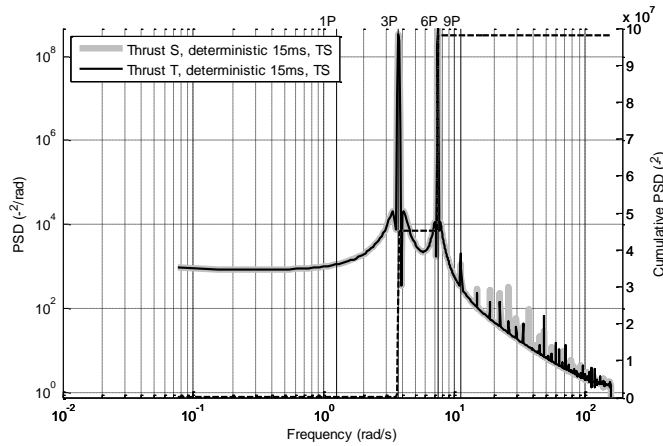


Figure E-61. Thrust force spectrum comparison between simple and triple structure for the deterministic component of the wind-field with mean 15m/s, TS active

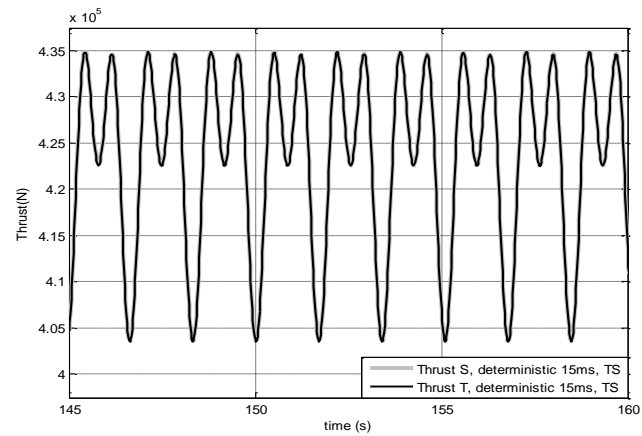


Figure E-62. Thrust force time series comparison between simple and triple structure for the deterministic component of the wind-field with mean 15m/s, TS active

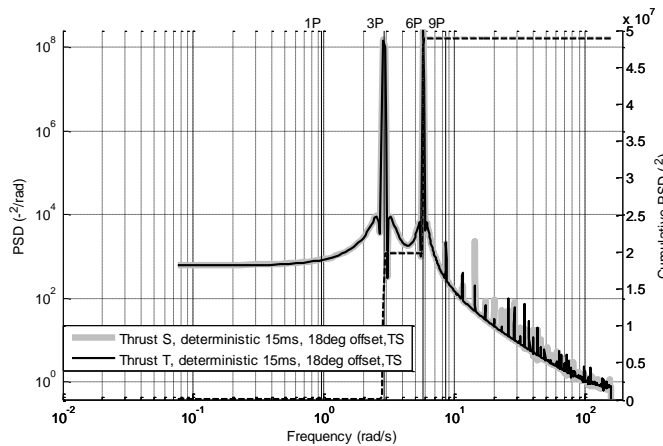


Figure E-63. Thrust force spectrum comparison between simple and triple structure for the deterministic component of the wind-field with mean 15m/s and 18 degrees of pitch offset, TS active

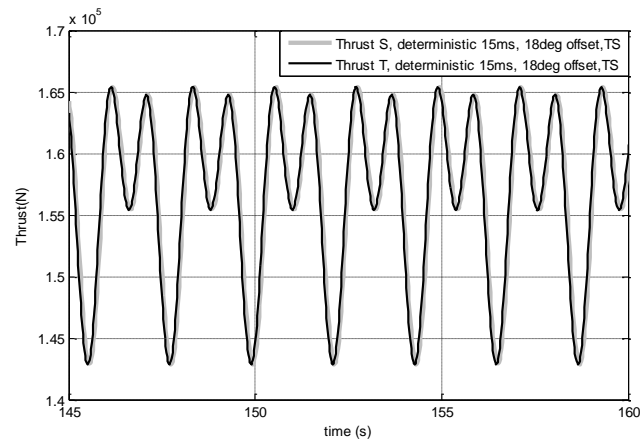


Figure E-64. Thrust force time series comparison between simple and triple structure for the deterministic component of the wind-field with mean 15m/s and 18 degrees of pitch offset, TS active

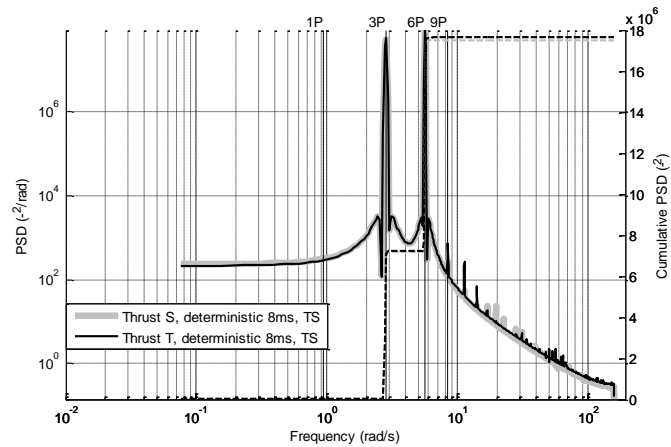


Figure E-65. Thrust force spectrum comparison between simple and triple structure for the deterministic component of the wind-field with mean 8m/s, TS active

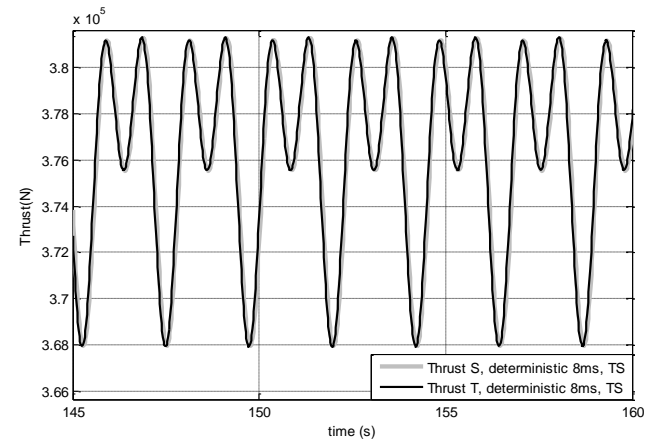


Figure E-66. Thrust force time series comparison between simple and triple structure for the deterministic component of the wind-field with mean 8m/s, TS active

- Thrust Force, WS & TS

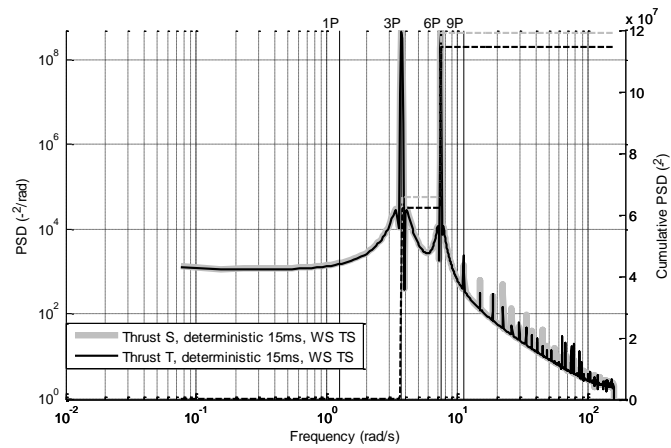


Figure E-67. Thrust force spectrum comparison between simple and triple structure for the deterministic component of the wind-field with mean 15m/s, WS TS active

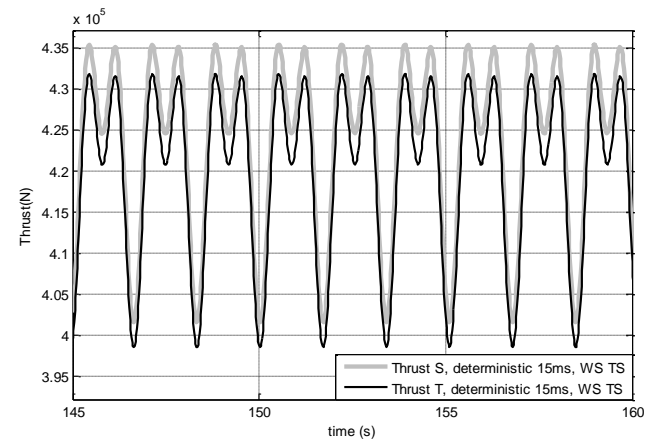


Figure E-68. Thrust force time series comparison between simple and triple structure for the deterministic component of the wind-field with mean 15m/s, WS TS active

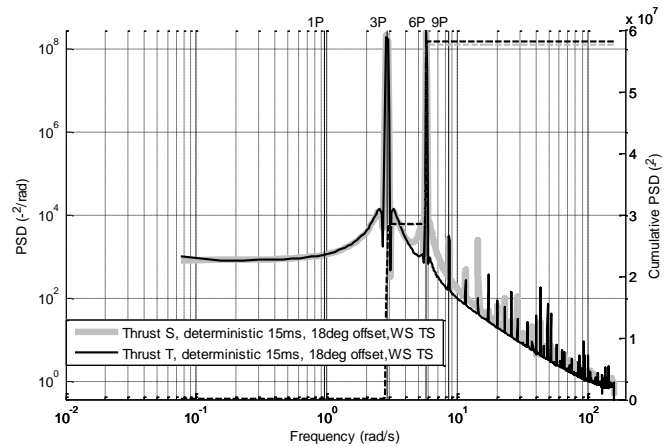


Figure E-69. Thrust force spectrum comparison between simple and triple structure for the deterministic component of the wind-field with mean 15m/s and 18 degrees of pitch offset, WS TS active

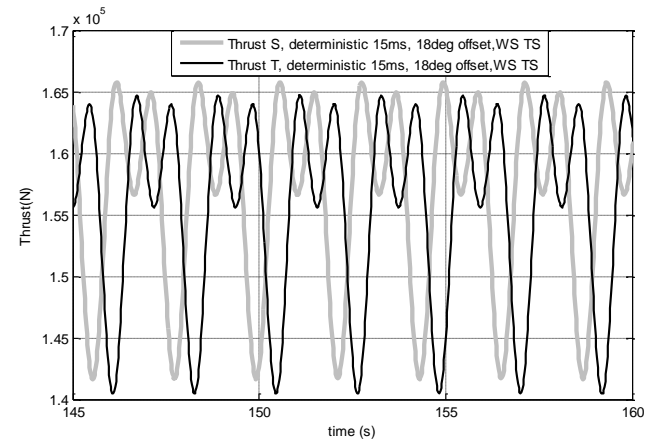


Figure E-70. Thrust force time series comparison between simple and triple structure for the deterministic component of the wind-field with mean 15m/s and 18 degrees of pitch offset, WS TS active

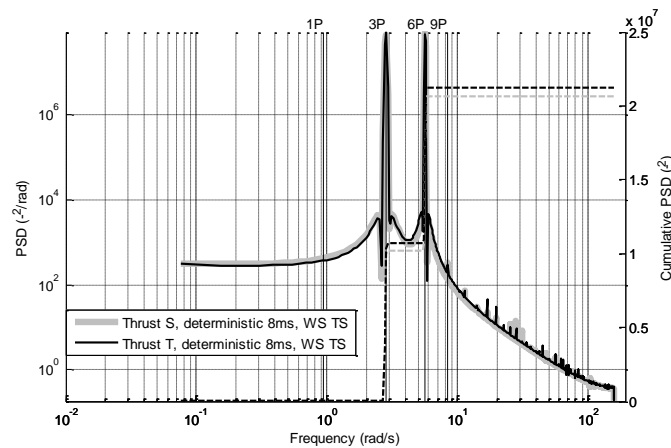


Figure E-71. Thrust force spectrum comparison between simple and triple structure for the deterministic component of the wind-field with mean 8m/s, WS TS active

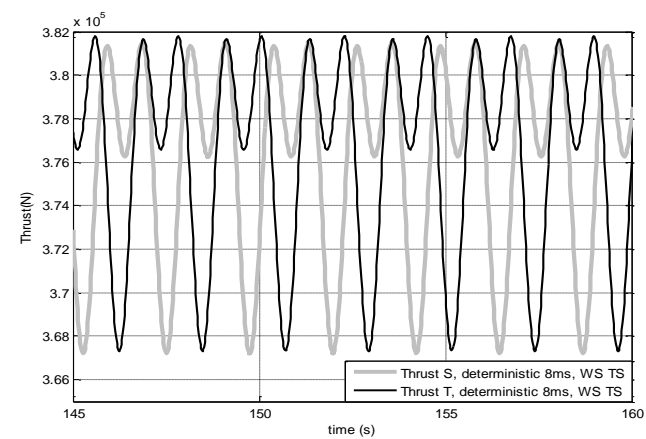


Figure E-72. Thrust force time series comparison between simple and triple structure for the deterministic component of the wind-field with mean 8m/s, WS TS active

			Cumulative Value	
			Simple Model	Triple Model
In-plane RBM	WS	15m/s	7.5483e+010	7.5152e+010
		15m/s + 18 deg offset	6.3848e+010	6.3703e+010
		8m/s	8.4728e+009	8.4647e+009
	TS	15m/s	3.0377e+009	3.0347e+009
		15m/s + 18 deg offset	2.5897e+009	2.5583e+009
		8m/s	3.401e+008	3.387e+008
	WS & TS	15m/s	8.2446e+010	8.1547e+010
		15m/s + 18 deg offset	6.9887e+010	6.9149e+010
		8m/s	9.3037e+009	9.2442e+009
Me	WS	15m/s	1.8818e+010	1.8456e+010
		15m/s + 18 deg offset	4.4359e+009	4.2845e+009
		8m/s	8.4728e+009	8.4647e+009
	TS	15m/s	3.3091e+009	3.3044e+009
		15m/s + 18 deg offset	3.1584e+009	3.1045e+009
		8m/s	3.401e+008	3.387e+008
	WS & TS	15m/s	2.3756e+010	2.2535e+010
		15m/s + 18 deg offset	8.7593e+009	7.5912e+009
		8m/s	9.3037e+009	9.2442e+009
Mf	WS	15m/s	5.9255e+011	5.9142e+011
		15m/s + 18 deg offset	3.8038e+011	3.8153e+011
		8m/s	1.0306e+011	1.0375e+011
	TS	15m/s	2.7626e+010	2.7624e+010
		15m/s + 18 deg offset	1.513e+010	1.5156e+010
		8m/s	5.0147e+009	5.0156e+009
	WS & TS	15m/s	6.6013e+011	6.5886e+011
		15m/s + 18 deg offset	4.2243e+011	4.2471e+011
		8m/s	1.1727e+011	1.1806e+011

Thrust	WS	15m/s	1.9334e+006	1.7194e+006
		15m/s + 18 deg offset	7.5946e+005	7.3326e+005
		8m/s	2.6564e+005	2.8721e+005
	TS	15m/s	9.813e+007	9.8131e+007
		15m/s + 18 deg offset	4.9066e+007	4.8933e+007
		8m/s	1.7516e+007	1.7633e+007
	WS & TS	15m/s	1.1906e+008	1.1456e+008
		15m/s + 18 deg offset	5.7587e+007	5.8177e+007
		8m/s	2.0626e+007	2.126e+007

Table E-1. Cumulative PSD value for the forces and loads explored in the case study of 15m/s, 15m/s plus 18 degree pitch offset and 8m/s for the simple and triple structure for the deterministic component of the wind, presented as WS alone, TS alone and combined WS & TS

Appendix F

Wind Traces of Complete Wind-Field

In this appendix the results completing the sets of wind traces of section 5.4 for the complete wind-field (stochastic and deterministic components) can be found. The results cover the spectrum and time series generated by each *layer P* for a complete wind-field with mean speed of 15m/s and 10% of turbulence intensity after being rotationally sampled by a 5MW wind turbine.

- n_0

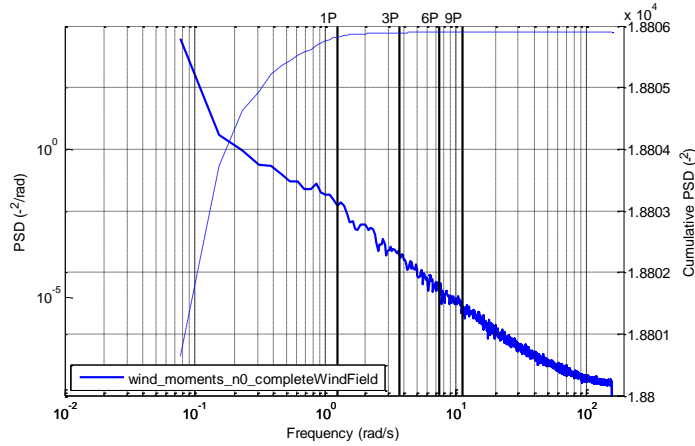


Figure F-1. Spectrum for *layer P* corresponding to $n = 0$ of the complete wind-field used for inducing moments

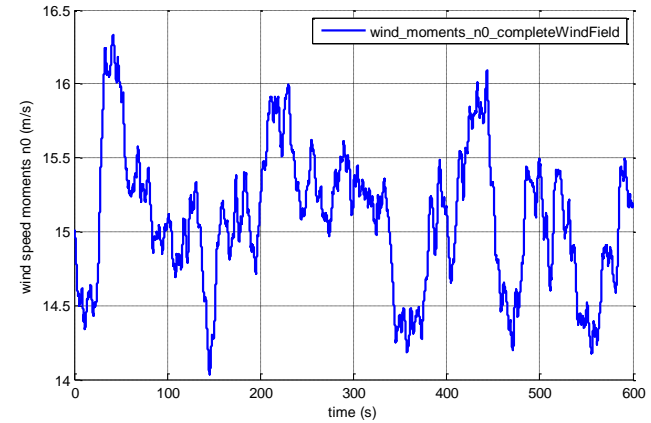


Figure F-2. Time series for *layer P* corresponding to $n = 0$ of the complete wind-field used for inducing moments

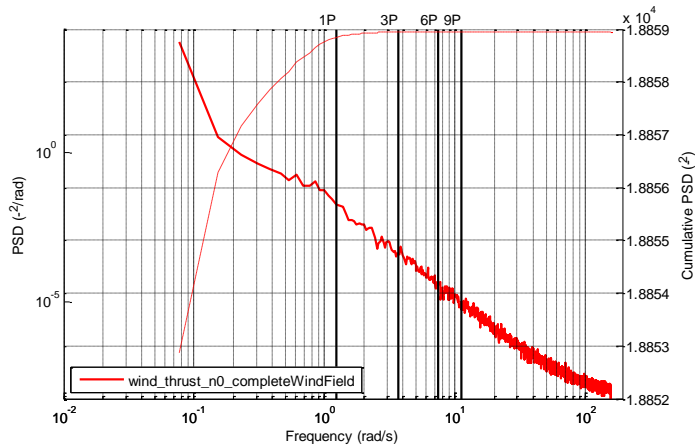


Figure F-3. Spectrum for *layer P* corresponding to $n = 0$ of the complete wind-field used for inducing thrust

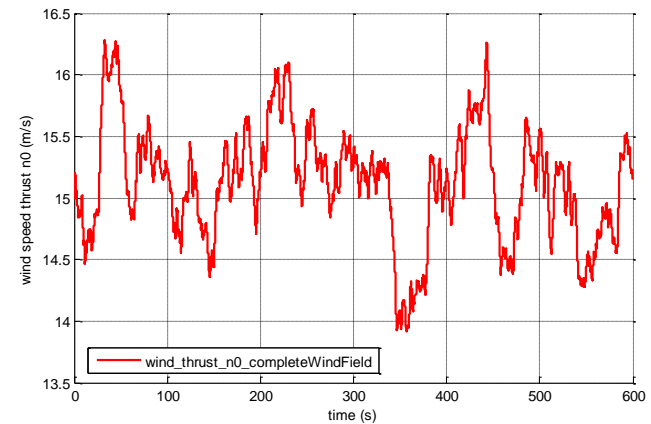


Figure F-4. Time series for *layer P* corresponding to $n = 0$ of the complete wind-field used for inducing thrust

- n1

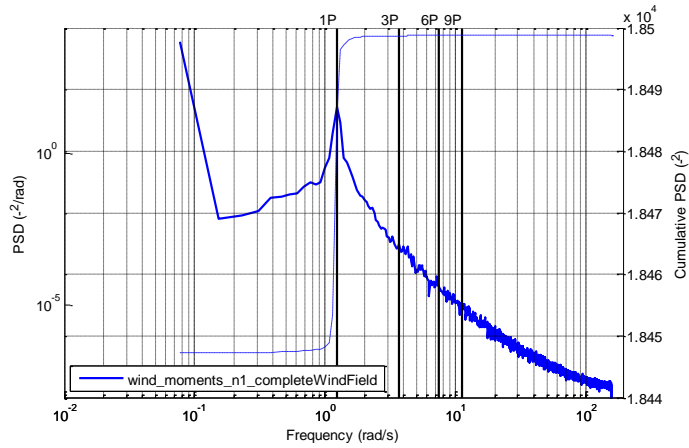


Figure F-5. Spectrum for *layer P* corresponding to $n = 1$ of the complete wind-field used for inducing moments

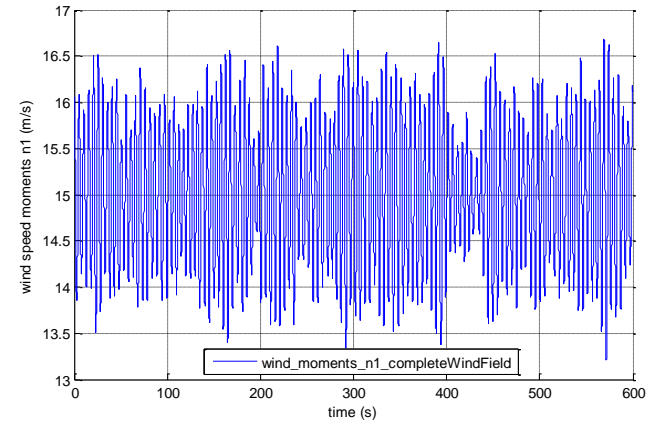


Figure F-6. Time series for *layer P* corresponding to $n = 1$ of the complete wind-field used for inducing moments

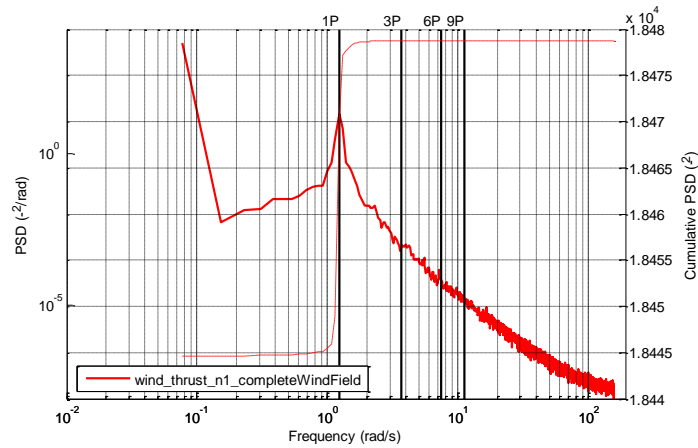


Figure F-7. Spectrum for *layer P* corresponding to $n = 1$ of the complete wind-field used for inducing thrust

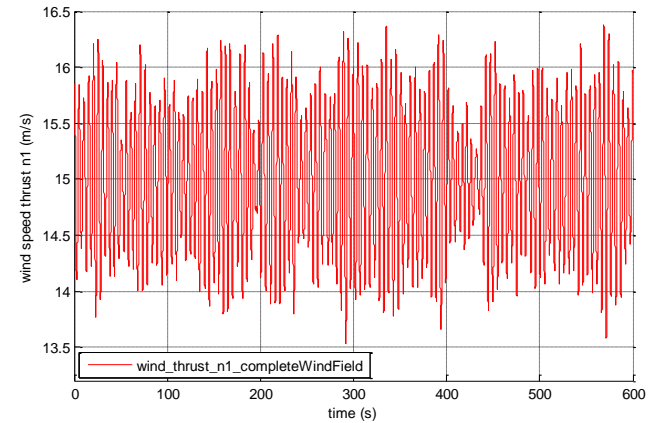


Figure F-8. Time series for *layer P* corresponding to $n = 1$ of the complete wind-field used for inducing thrust

- n2

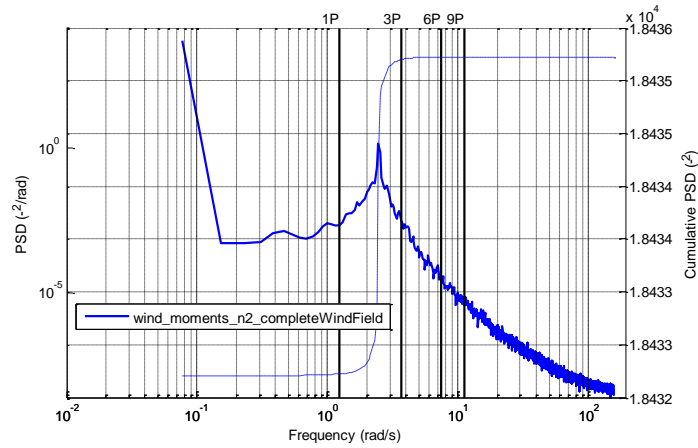


Figure F-9. Spectrum for *layer P* corresponding to $n = 2$ of the complete wind-field used for inducing moments

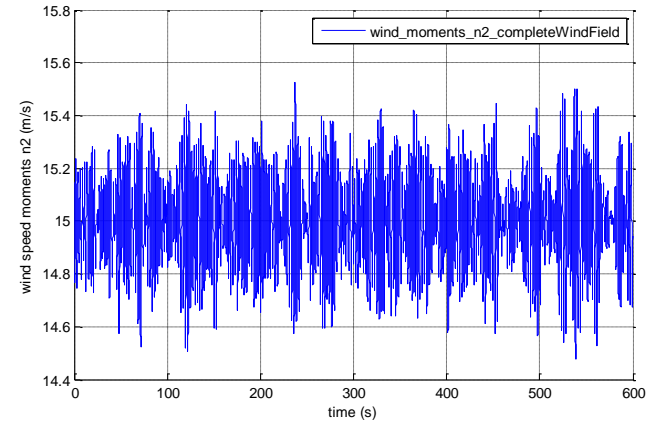


Figure F-10. Time series for *layer P* corresponding to $n = 2$ of the complete wind-field used for inducing moments

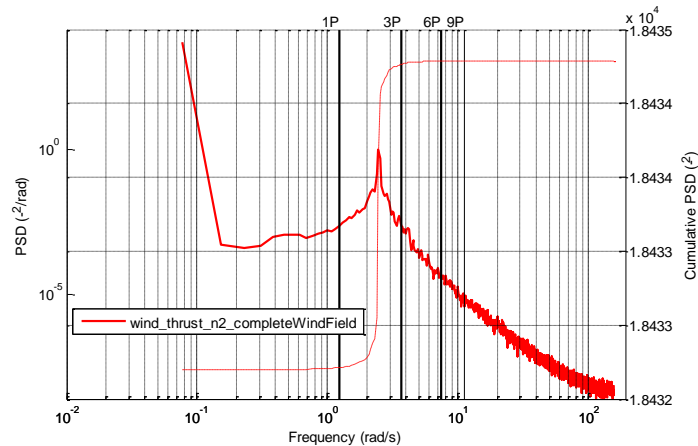


Figure F-11. Spectrum for *layer P* corresponding to $n = 2$ of the complete wind-field used for inducing thrust

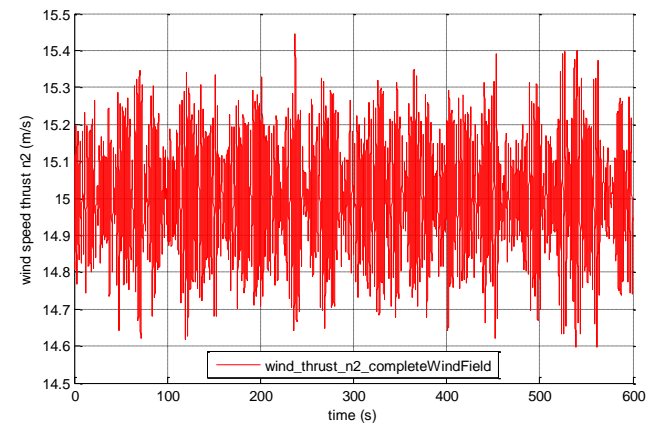


Figure F-12. Time series for *layer P* corresponding to $n = 2$ of the complete wind-field used for inducing thrust

- n3

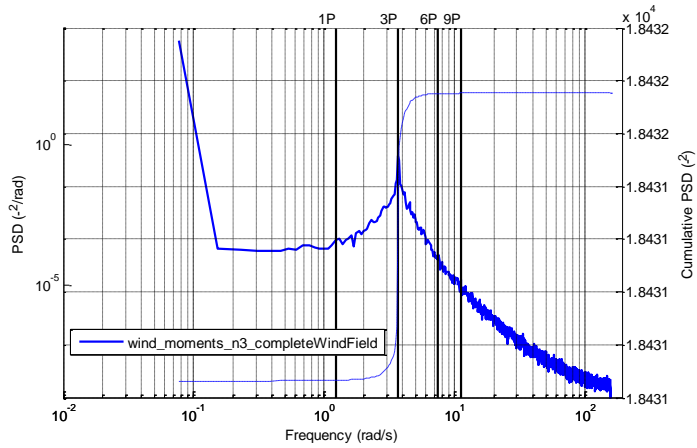


Figure F-13. Spectrum for *layer P* corresponding to $n = 3$ of the complete wind-field used for inducing moments

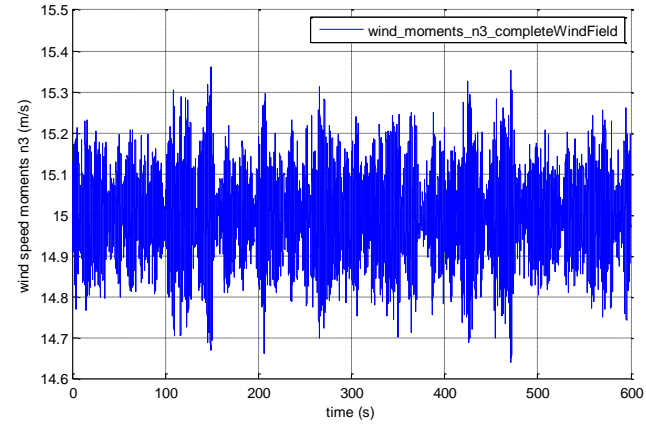


Figure F-14. Time series for *layer P* corresponding to $n = 3$ of the complete wind-field used for inducing moments

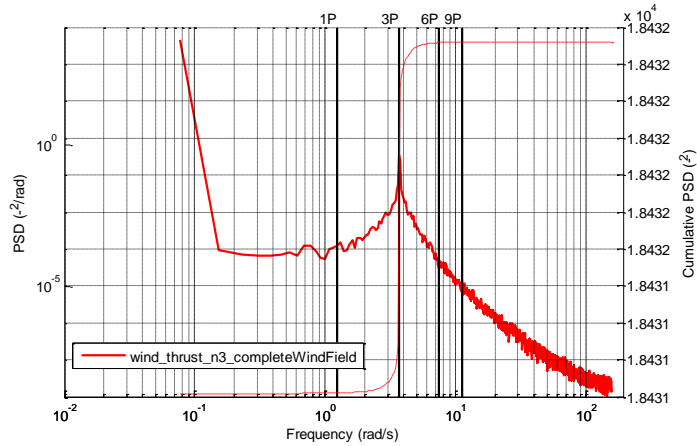


Figure F-15. Spectrum for *layer P* corresponding to $n = 3$ of the complete wind-field used for inducing thrust

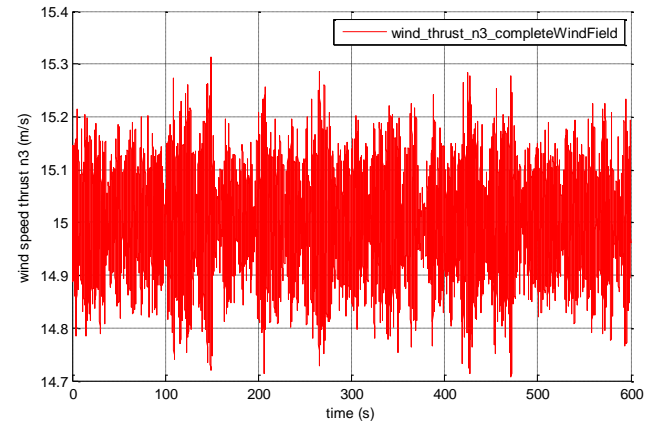


Figure F-16. Time series for *layer P* corresponding to $n = 3$ of the complete wind-field used for inducing thrust

- n4

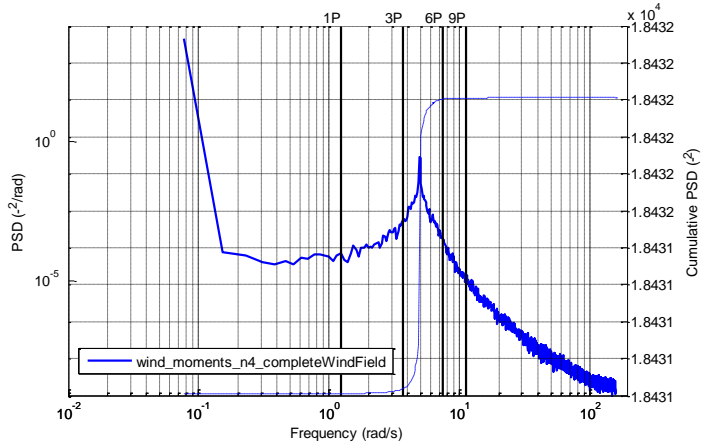


Figure F-17. Spectrum for *layer P* corresponding to $n = 4$ of the complete wind-field used for inducing moments

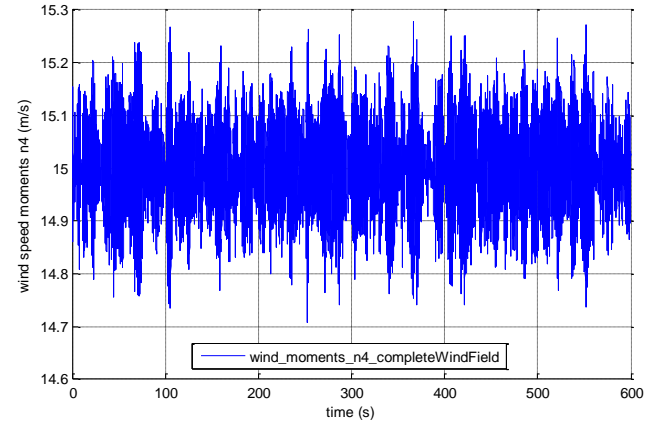


Figure F-18. Time series for *layer P* corresponding to $n = 4$ of the complete wind-field used for inducing moments

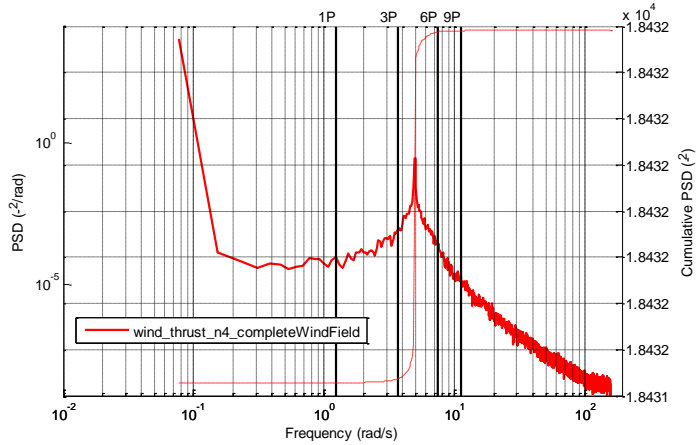


Figure F-19. Spectrum for *layer P* corresponding to $n = 4$ of the complete wind-field used for inducing thrust

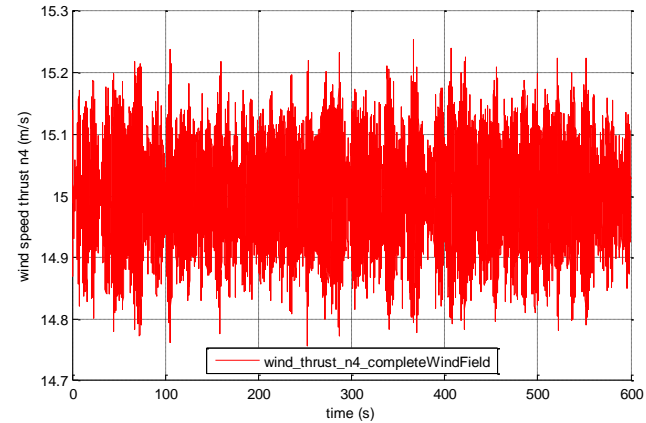


Figure F-20. Time series for *layer P* corresponding to $n = 4$ of the complete wind-field used for inducing thrust

- n5

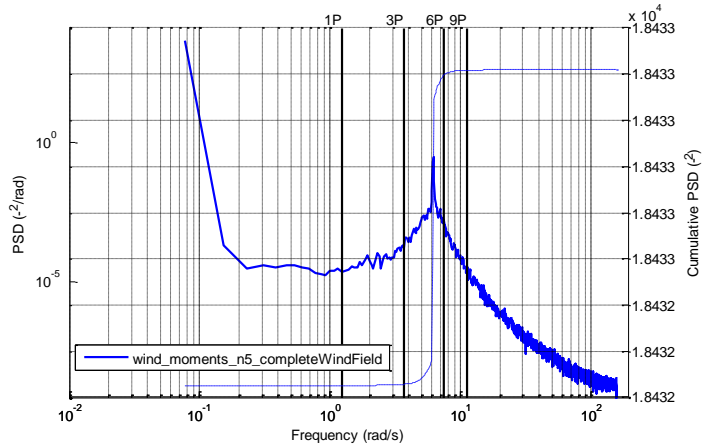


Figure F-21. Spectrum for *layer P* corresponding to $n = 5$ of the complete wind-field used for inducing moments

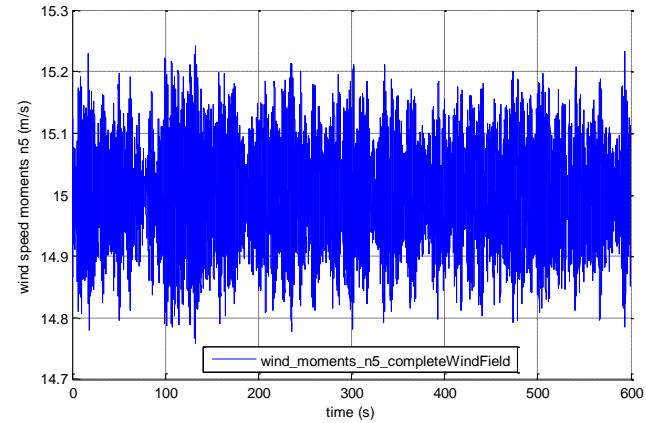


Figure F-22. Time series for *layer P* corresponding to $n = 5$ of the complete wind-field used for inducing moments

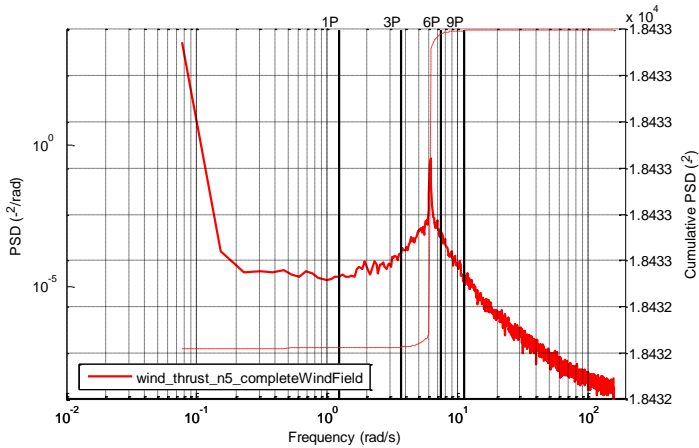


Figure F-23. Spectrum for *layer P* corresponding to $n = 5$ of the complete wind-field used for inducing thrust

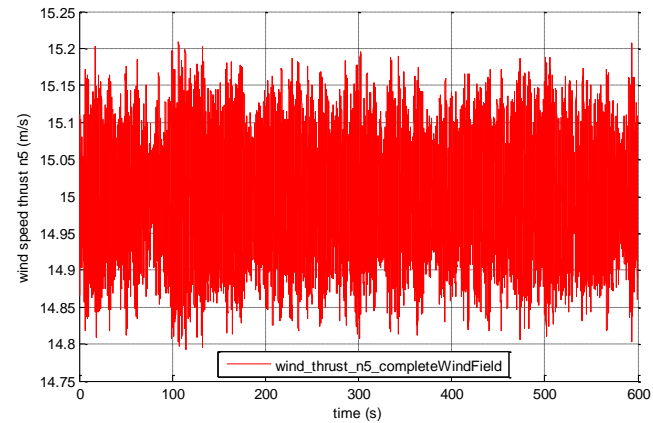


Figure F-24. Time series for *layer P* corresponding to $n = 5$ of the complete wind-field used for inducing thrust

- n6

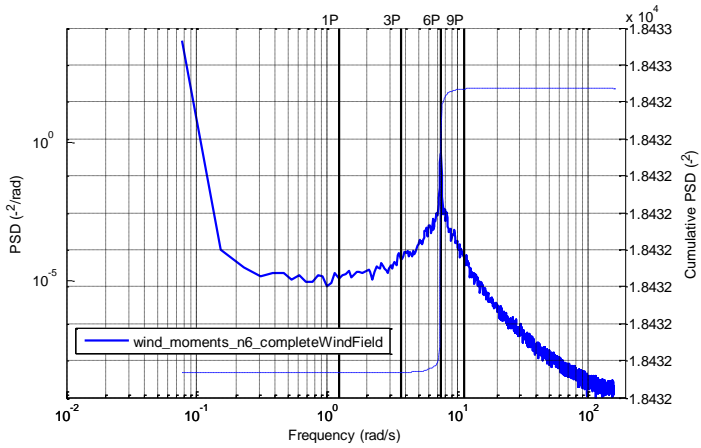


Figure F-25. Spectrum for *layer P* corresponding to $n = 6$ of the complete wind-field used for inducing moments

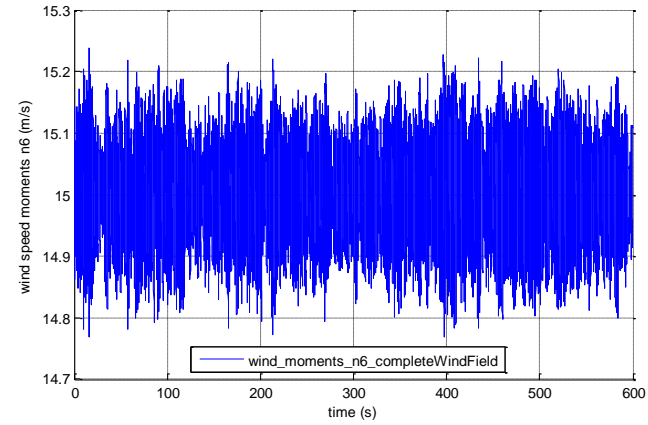


Figure F-26. Time series for *layer P* corresponding to $n = 6$ of the complete wind-field used for inducing moments

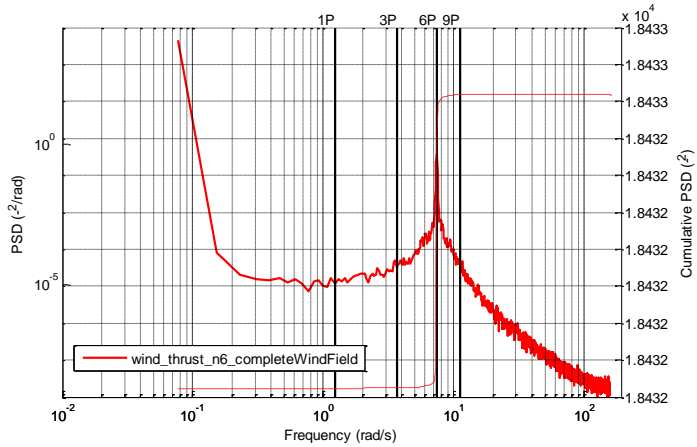


Figure F-27. Spectrum for *layer P* corresponding to $n = 6$ of the complete wind-field used for inducing thrust

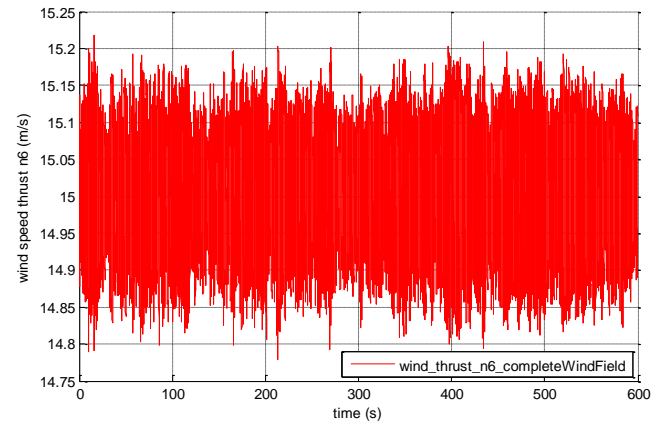


Figure F-28. Time series for *layer P* corresponding to $n = 6$ of the complete wind-field used for inducing thrust

- All *layer P* for rotor and blade, complete wind-field

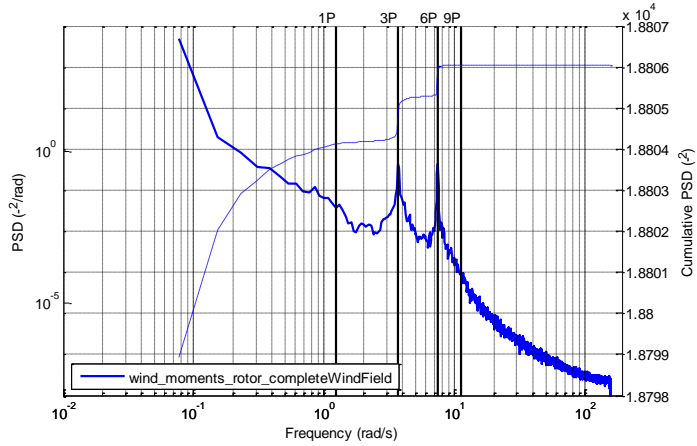


Figure F-29. Spectrum for the complete wind-field used for inducing moments at the rotor by the simple model

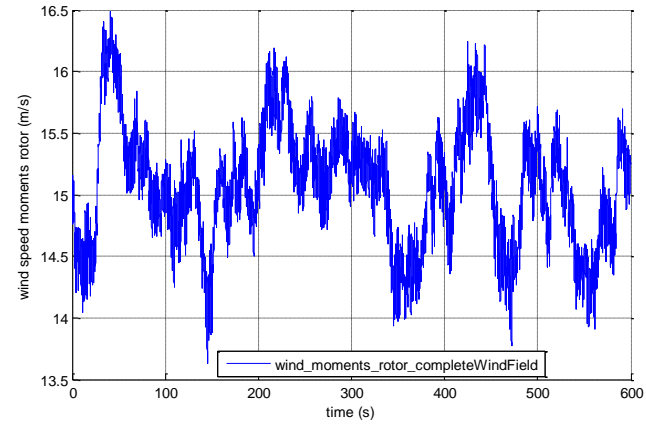


Figure F-30. Time series for the complete wind-field used for inducing moments at the rotor by the simple model

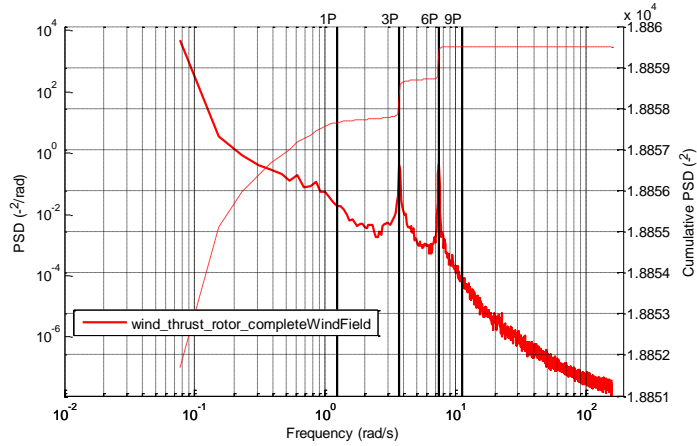


Figure F-31. Spectrum for the complete wind-field used for inducing thrust at the rotor by the simple model

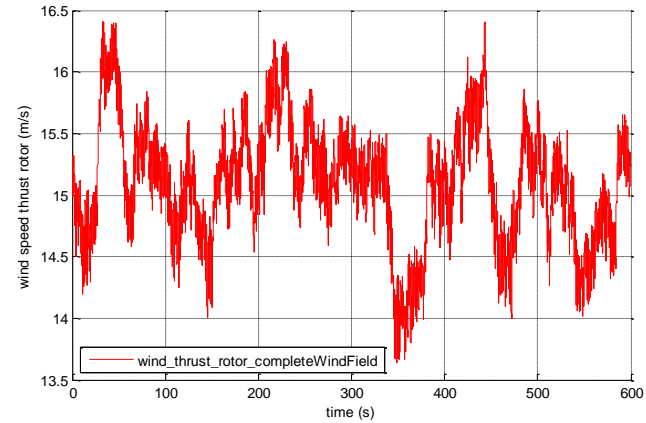


Figure F-32. Time series for the complete wind-field used for inducing thrust at the rotor by the simple model

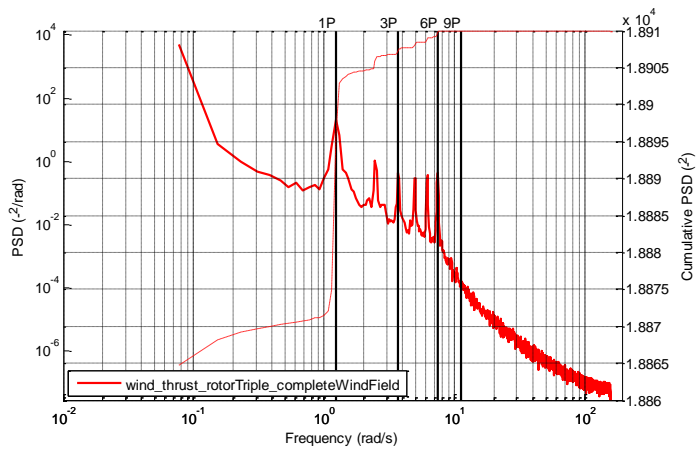


Figure F-33. Spectrum for the complete wind-field used for inducing thrust at the rotor by triple model

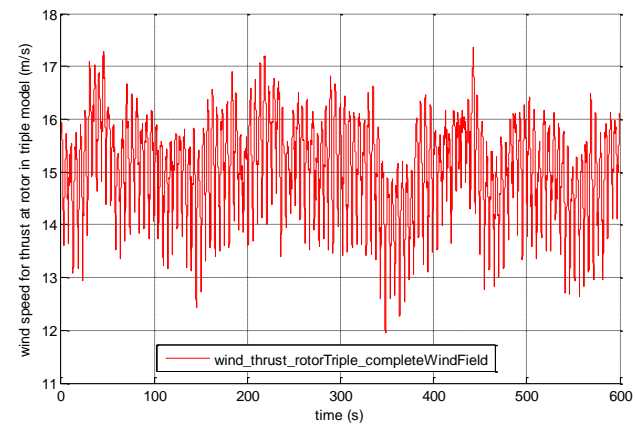


Figure F-34. Time series for the complete wind-field used for inducing thrust at the rotor by triple model

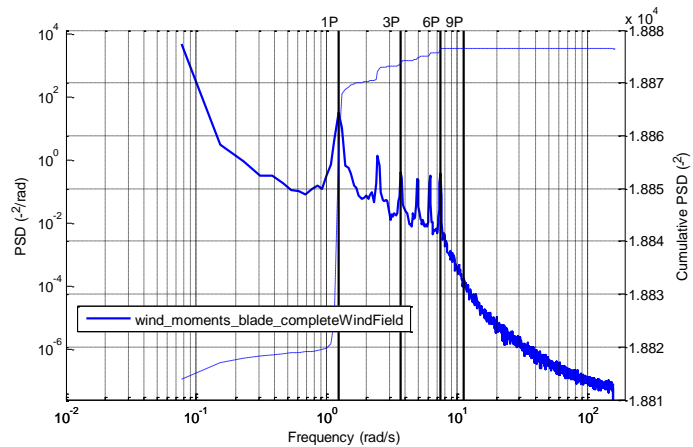


Figure F-35. Spectrum for the complete wind-field used for inducing moments at the single blade by simple and triple model. Also used for inducing moments at the rotor by the triple model

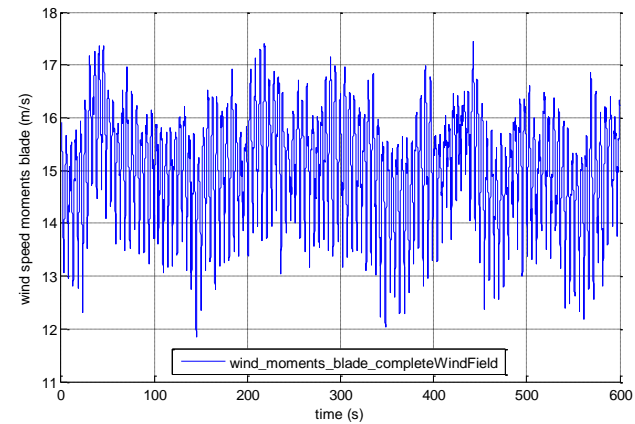


Figure F-36. Time series for the complete wind-field used for inducing moments at the single blade by simple and triple model. Also used for inducing moments at the rotor by the triple model

Appendix G

Complete Wind-Field Results

In the following can be found the results for the thrust force, the in-plane RBM of the blade, the edgewise moment of the blade, M_e , the flapwise moment of the blade, M_f , the rotor speed and the pitch angle of the blade for the complete wind-field, both stochastic and deterministic components are present. To be noted that the induced forces and moments in these results do not account for the force of gravity in order to better appreciate the outcomes induced by the wind-field. The results are for both the simple and triple structure and for three different case studies: 15m/s, 15m/s with 18deg of pitch offset and 8m/s.

Likewise for the hub torque and out-of-plane RBM results seen in section 5.4, the full set of results in this appendix points to the simple wind-field model as an acceptable compromise to induce the loads and moment of the rotor and blades. On the grounds that when the full-wind field model is used, the leakage previously observed arising from the deterministic component of the wind-field becomes not significant overall.

- Thrust Force

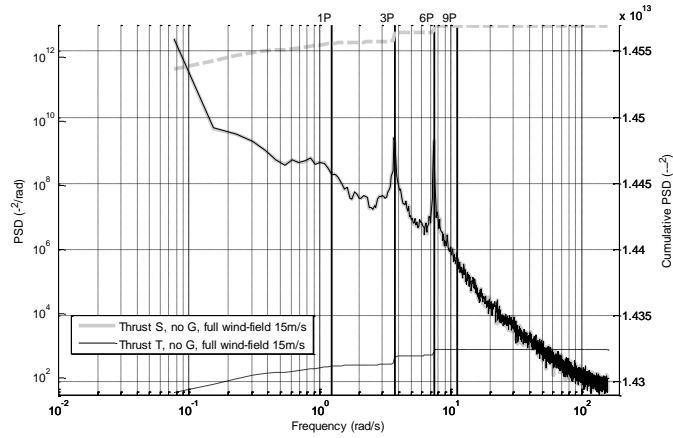


Figure G-1. Thrust force spectrum comparison between simple and triple structure for the complete wind-field with mean 15m/s

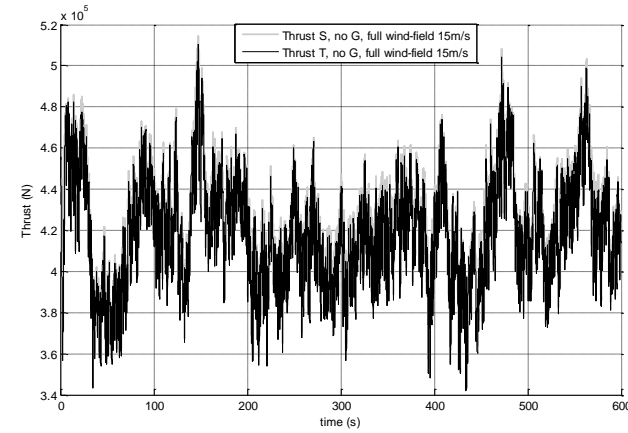


Figure G-2. Thrust force time series comparison between simple and triple structure for the complete wind-field with mean 15m/s

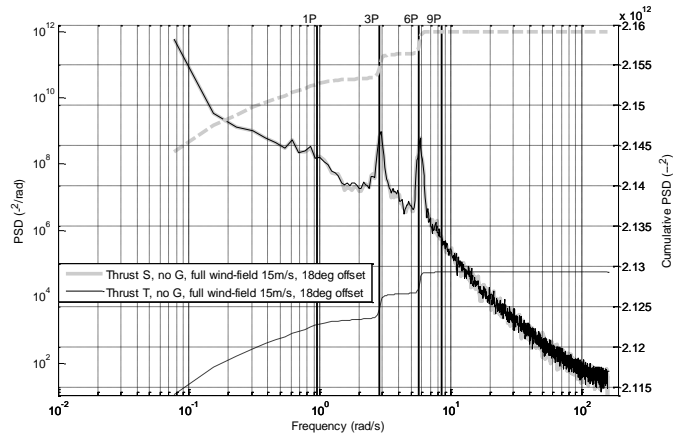


Figure G-3. Thrust force spectrum comparison between simple and triple structure for the complete wind-field with mean 15m/s and 18 degrees of pitch offset

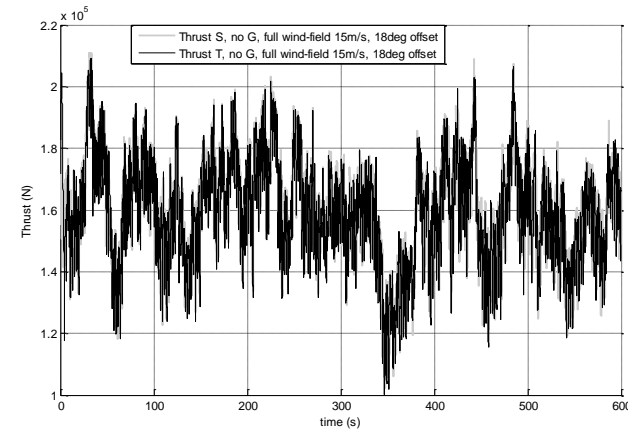


Figure G-4. Thrust force time series comparison between simple and triple structure for the complete wind-field with mean 15m/s and 18 degrees of pitch offset

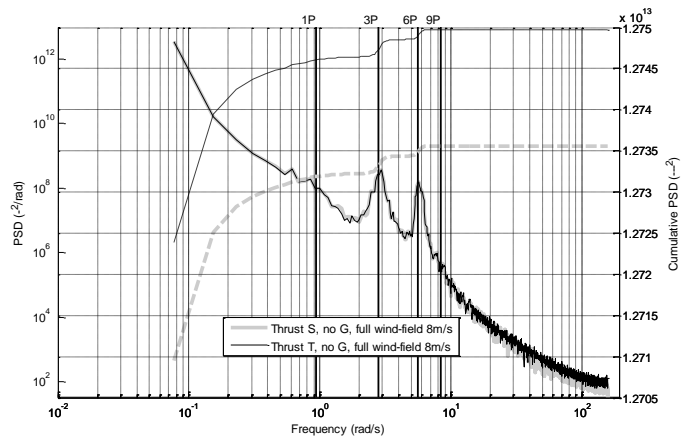


Figure G-5. Thrust force spectrum comparison between simple and triple structure for the complete wind-field with mean 8m/s

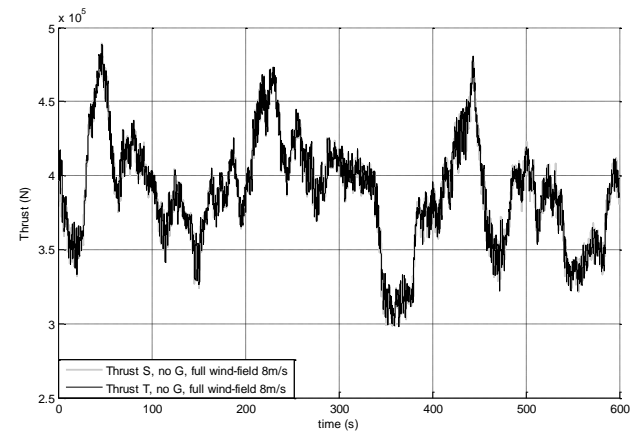


Figure G-6. Thrust force time series comparison between simple and triple structure for the complete wind-field with mean 8m/s

- In-plane RBM of the blade

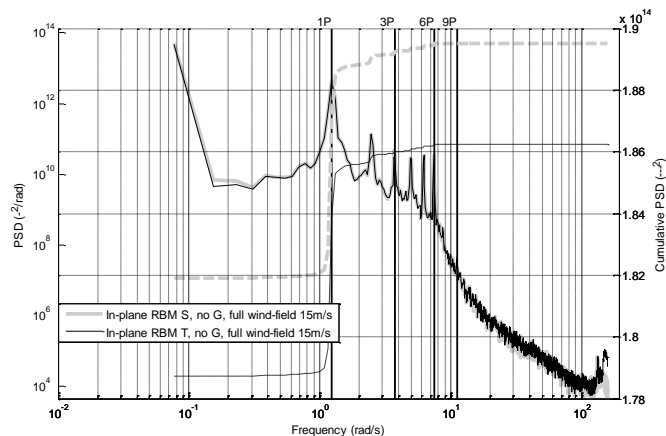


Figure G-7. In-plane RBM spectrum comparison between simple and triple structure for the complete wind-field with mean 15m/s

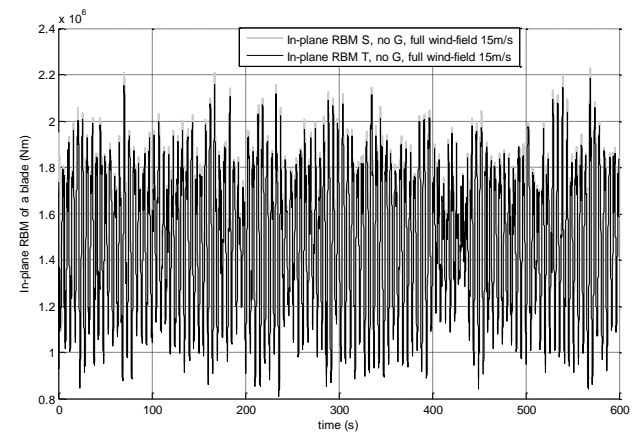


Figure G-8. In-plane RBM time series comparison between simple and triple structure for the complete wind-field with mean 15m/s

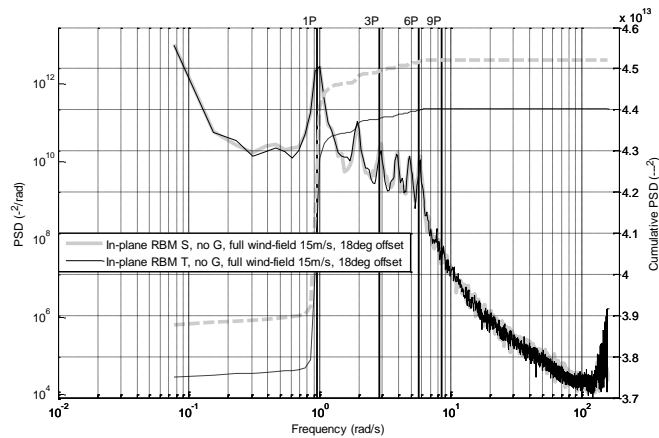


Figure G-9. In-plane RBM spectrum comparison between simple and triple structure for the complete wind-field with mean 15m/s and 18 degrees of pitch offset

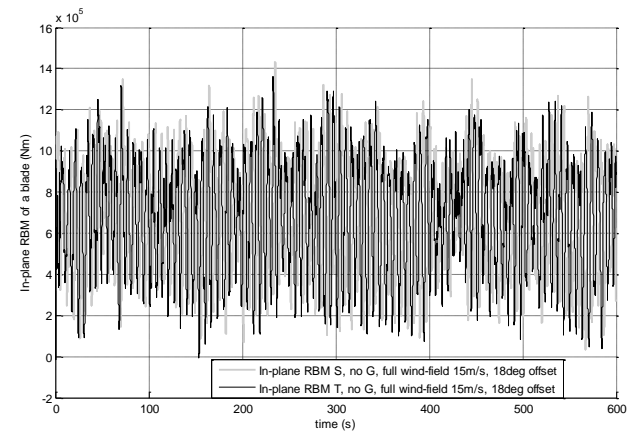


Figure G-10. In-plane RBM time series comparison between simple and triple structure for the complete wind-field with mean 15m/s and 18 degrees of pitch offset

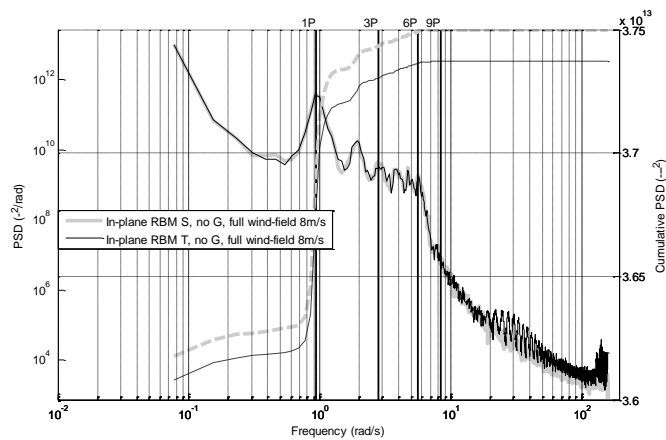


Figure G-11. In-plane RBM spectrum comparison between simple and triple structure for the complete wind-field with mean 8m/s

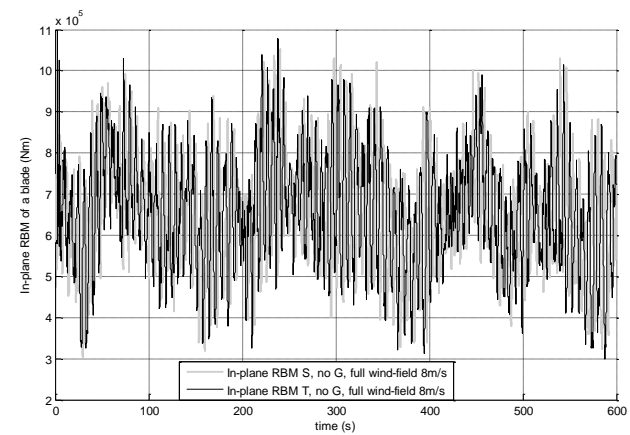


Figure G-12. In-plane RBM time series comparison between simple and triple structure for the complete wind-field with mean 8m/s

- Edgewise moment of the blade, M_e

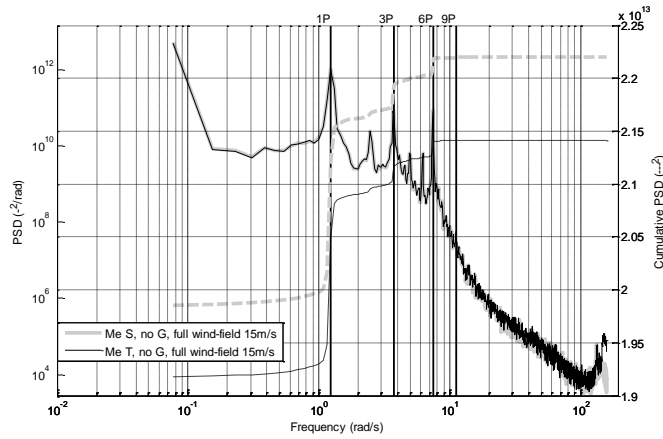


Figure G-13. M_e spectrum comparison between simple and triple structure for the complete wind-field with mean 15m/s

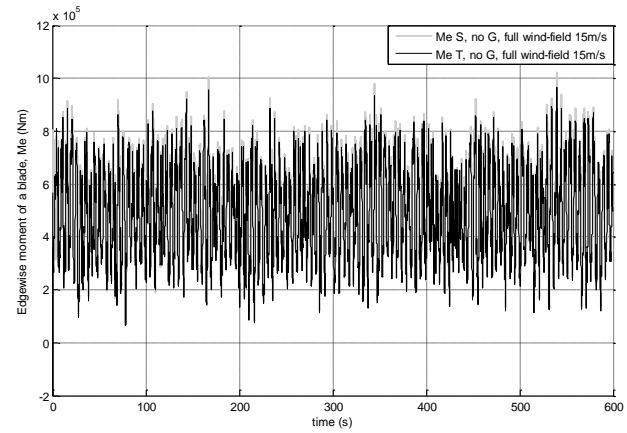


Figure G-14. M_e time series comparison between simple and triple structure for the complete wind-field with mean 15m/s

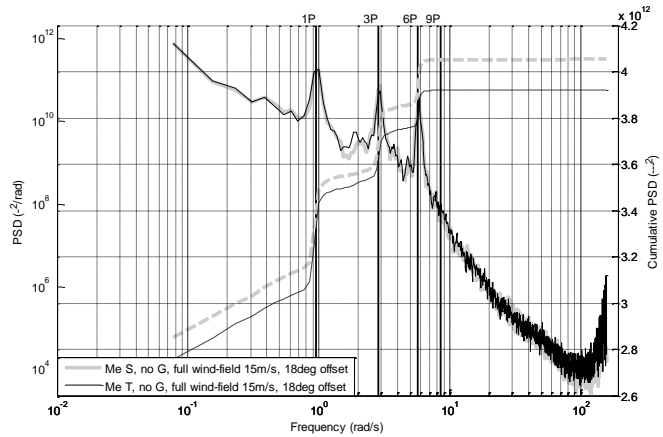


Figure G-15. M_e spectrum comparison between simple and triple structure for the complete wind-field with mean 15m/s and 18 degrees of pitch offset

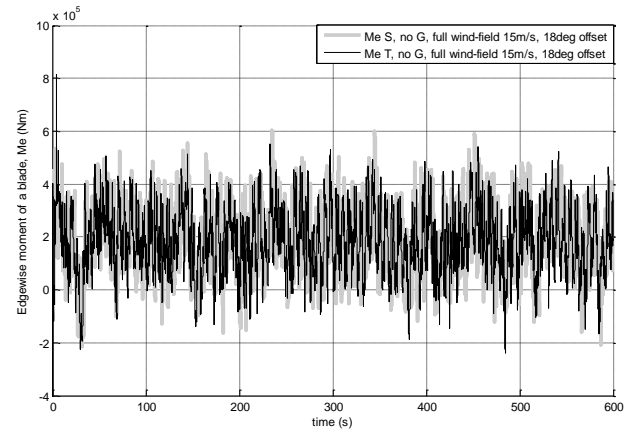


Figure G-16. M_e time series comparison between simple and triple structure for the complete wind-field with mean 15m/s and 18 degrees of pitch offset

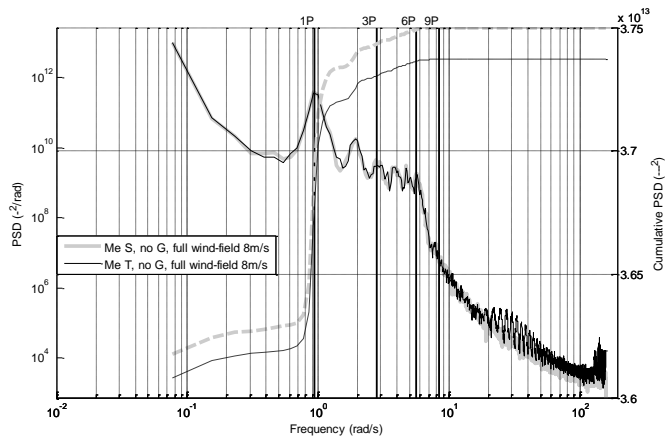


Figure G-17. M_e spectrum comparison between simple and triple structure for the complete wind-field with mean 8m/s

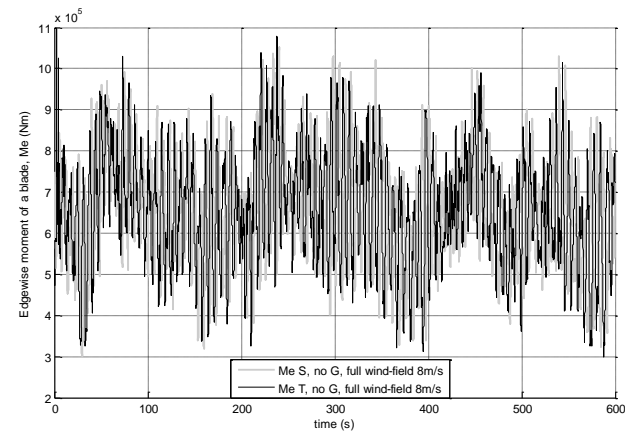


Figure G-18. M_e time series comparison between simple and triple structure for the complete wind-field with mean 8m/s

- Flapwise moment of the blade, M_f

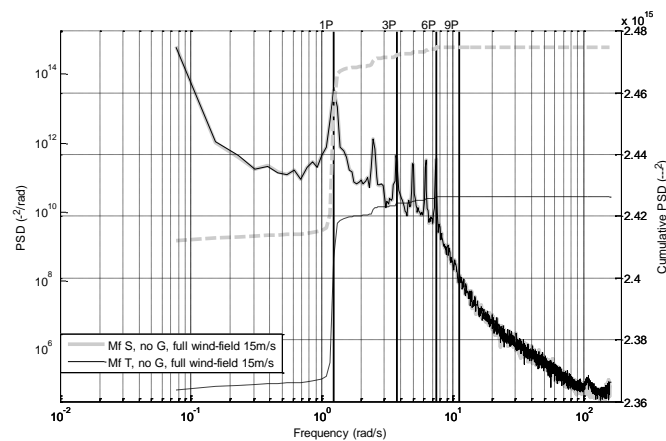


Figure G-19. M_f spectrum comparison between simple and triple structure for the complete wind-field with mean 15m/s

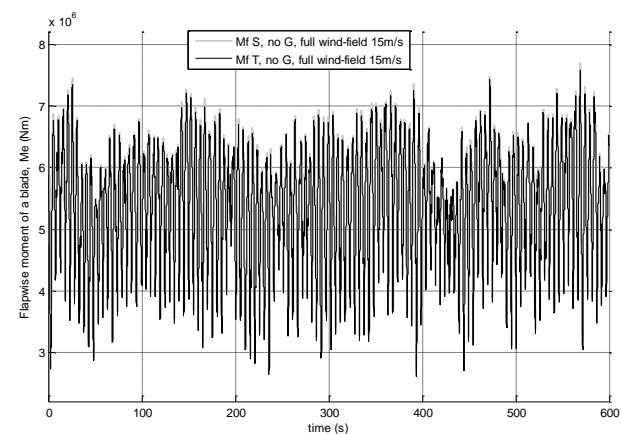


Figure G-20. M_f time series comparison between simple and triple structure for the complete wind-field with mean 15m/s

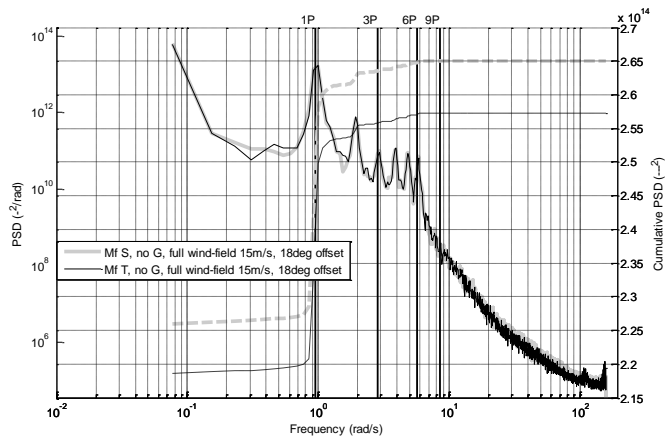


Figure G-21. M_f spectrum comparison between simple and triple structure for the complete wind-field with mean 15m/s and 18 degrees of pitch offset

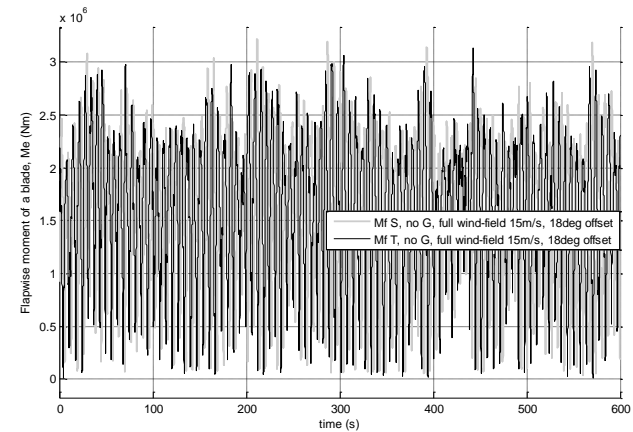


Figure G-22. M_f time series comparison between simple and triple structure for the complete wind-field with mean 15m/s and 18 degrees of pitch offset

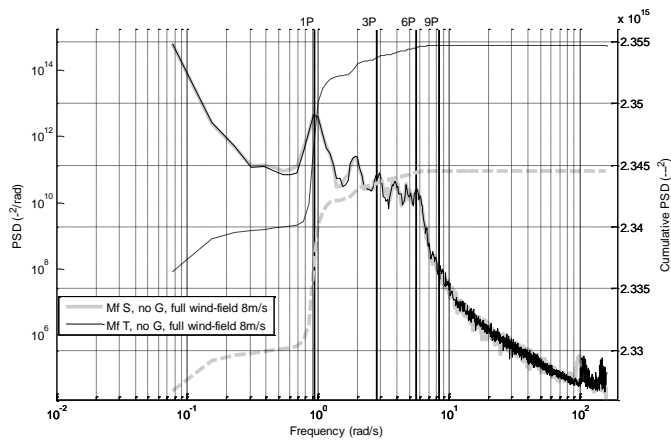


Figure G-23. M_f spectrum comparison between simple and triple structure for the complete wind-field with mean 8m/s

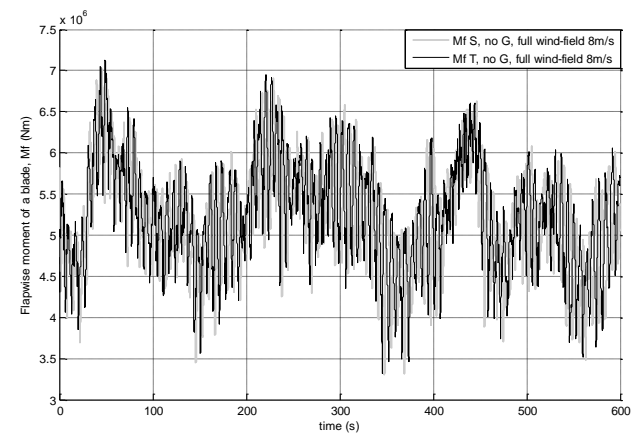


Figure G-24. M_f time series comparison between simple and triple structure for the complete wind-field with mean 8m/s

- Rotor speed

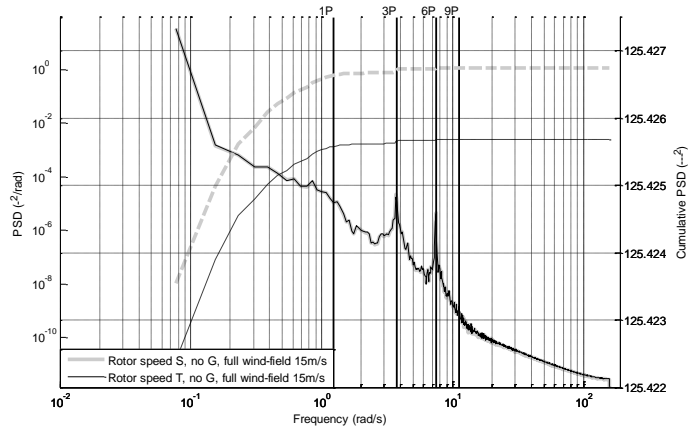


Figure G-25. Rotor speed spectrum comparison between simple and triple structure for the complete wind-field with mean 15m/s

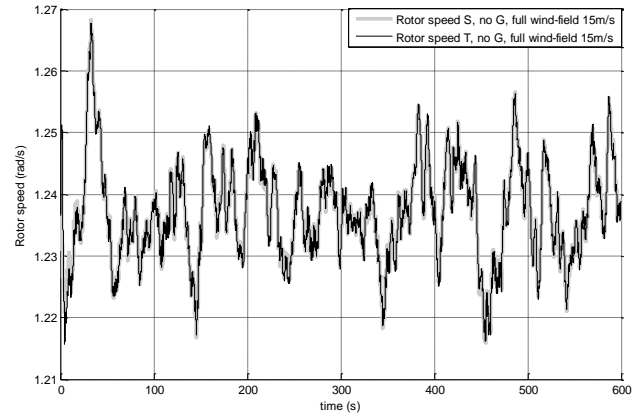


Figure G-26. Rotor speed time series comparison between simple and triple structure for the complete wind-field with mean 15m/s

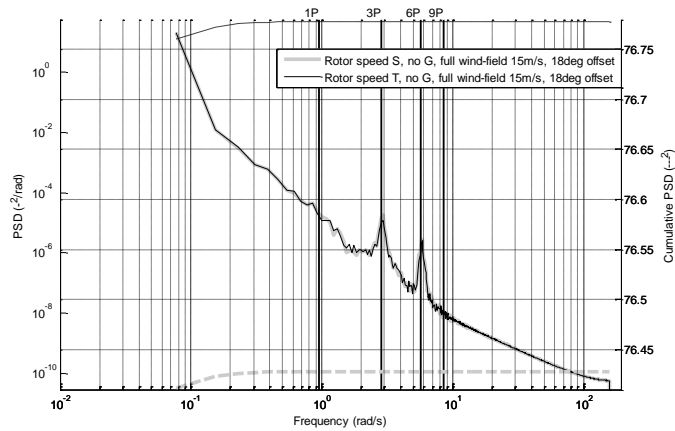


Figure G-27. Rotor speed spectrum comparison between simple and triple structure for the complete wind-field with mean 15m/s and 18 degrees of pitch offset

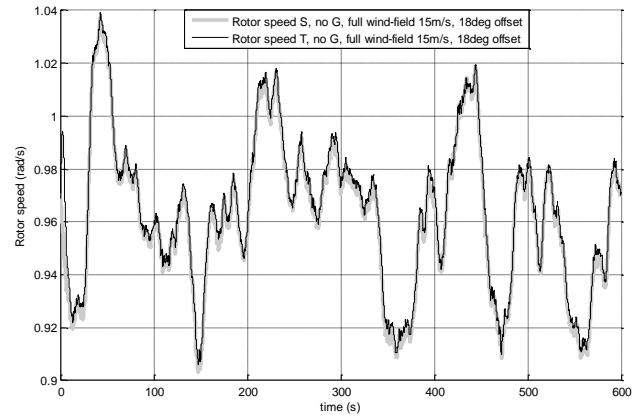


Figure G-28. Rotor speed time series comparison between simple and triple structure for the complete wind-field with mean 15m/s and 18 degrees of pitch offset

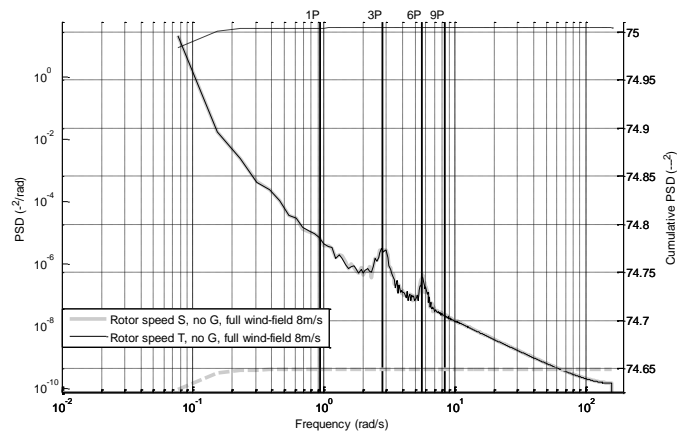


Figure G-29. Rotor speed spectrum comparison between simple and triple structure for the complete wind-field with mean 8m/s

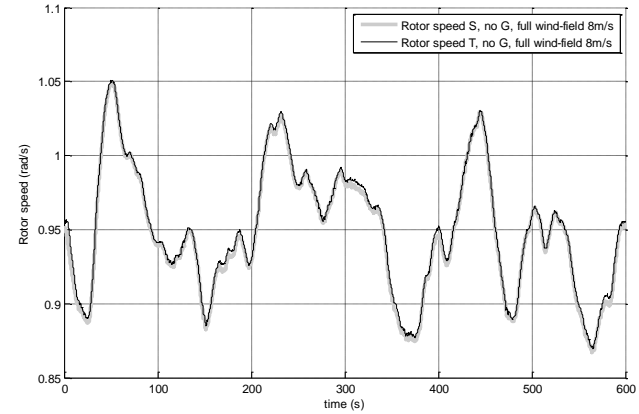


Figure G-30. Rotor speed time series comparison between simple and triple structure for the complete wind-field with mean 8m/s

- Pitch angle of the blade

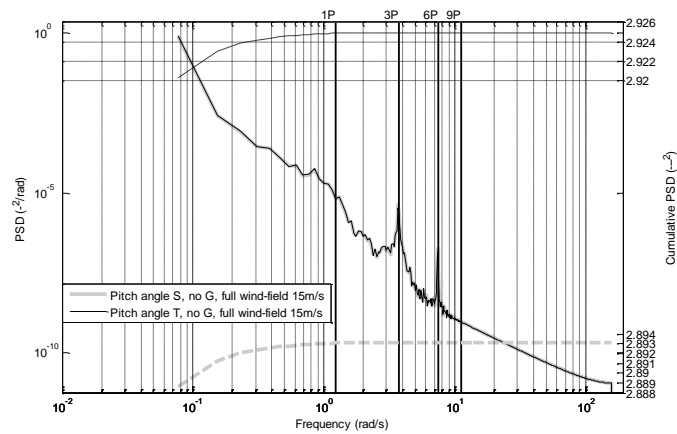


Figure G-31. Pitch angle spectrum comparison between simple and triple structure for the complete wind-field with mean 15m/s

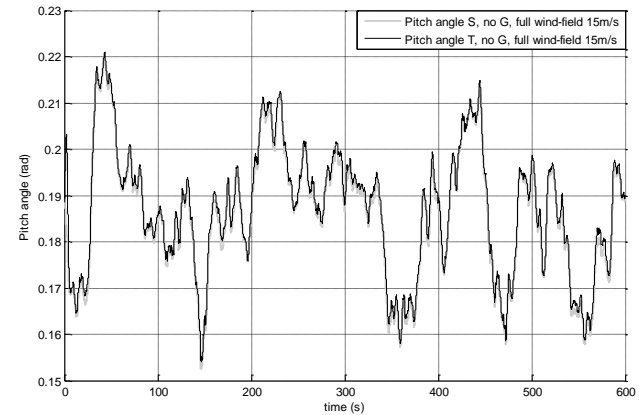


Figure G-32. Pitch angle time series comparison between simple and triple structure for the complete wind-field with mean 15m/s

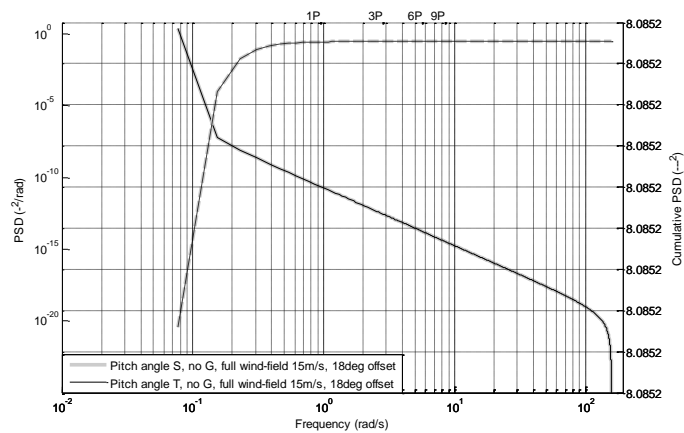


Figure G-33. Pitch angle spectrum comparison between simple and triple structure for the complete wind-field with mean 15m/s and 18 degrees of pitch offset

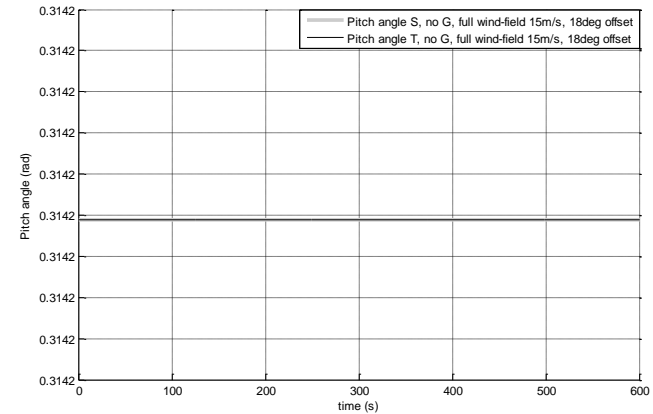


Figure G-34. Pitch angle time series comparison between simple and triple structure for the complete wind-field with mean 15m/s and 18 degrees of pitch offset

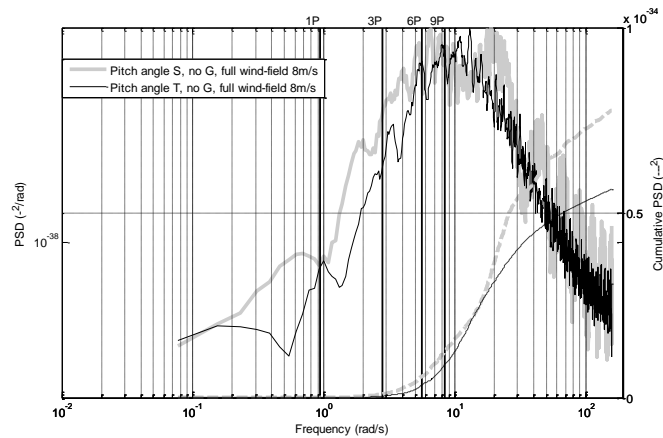


Figure G-35. Pitch angle spectrum comparison between simple and triple structure for the complete wind-field with mean 8m/s

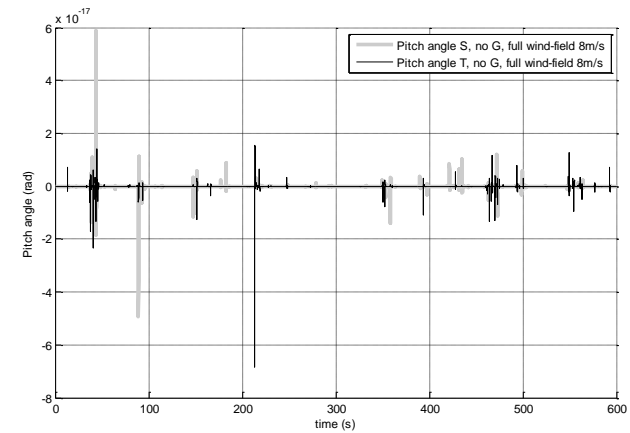


Figure G-36. Pitch angle time series comparison between simple and triple structure for the complete wind-field with mean 8m/s

Appendix H

Bladed Comparison. Stiff Structural Dynamics

In the following can be found the results for the thrust force, the in-plane RBM of the blade and the generator speed for the comparison between the proposed effective wind-field model and WT setting as per Section 5.5 and Bladed. The results are for three different case studies: 15m/s, 15m/s with 18deg of pitch offset and 8m/s, with TI of 10%.

- Thrust Force

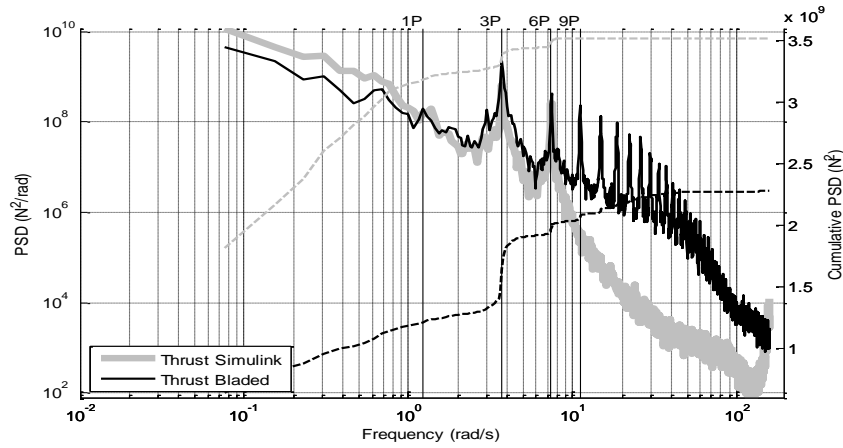


Figure H-1. Thrust PSD comparison between Simulink and Bladed with mean 15m/s

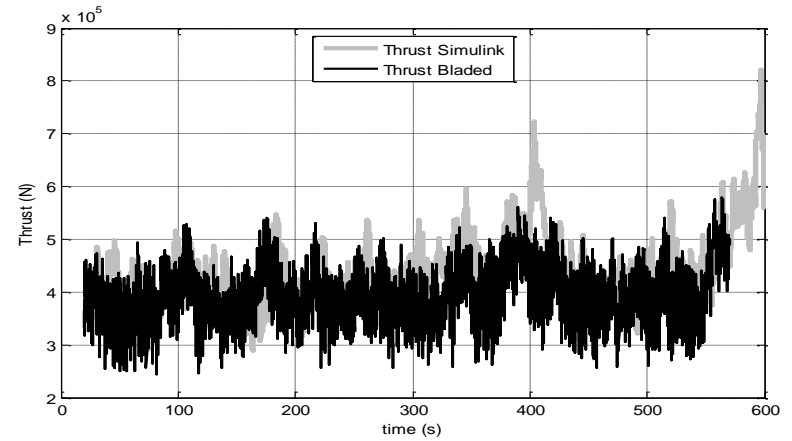


Figure H-2. Thrust time series comparison between Simulink and Bladed with mean 15m/s

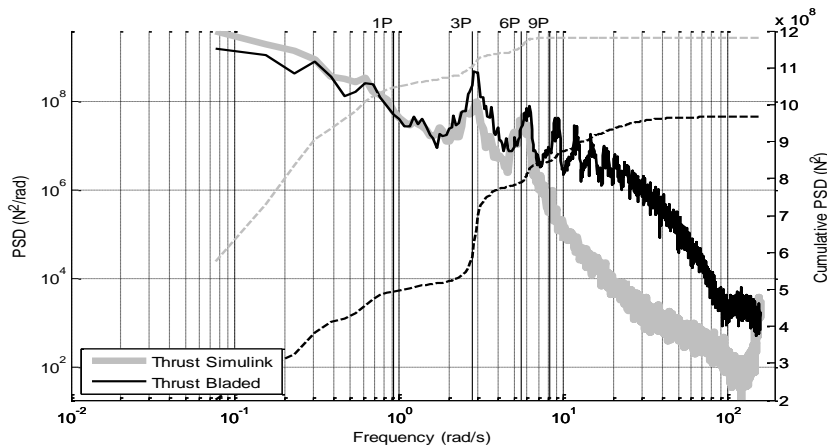


Figure H-3. Thrust PSD comparison between Simulink and Bladed with mean 15m/s and 18 degrees of pitch offset

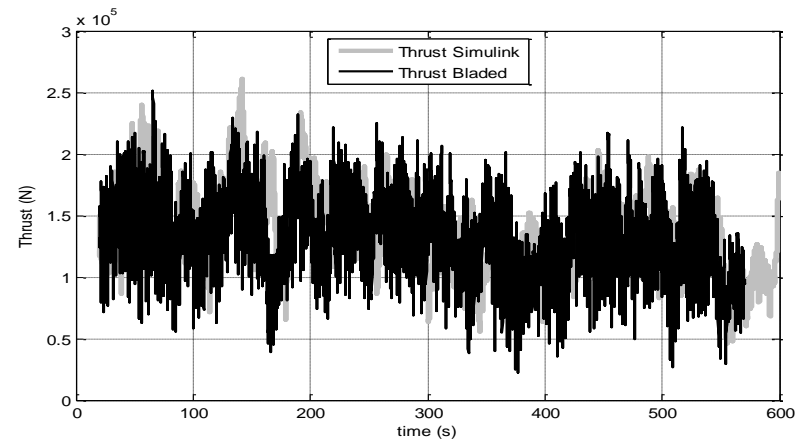


Figure H-4. Thrust time series comparison between Simulink and Bladed with mean 15m/s and 18 degrees of pitch offset

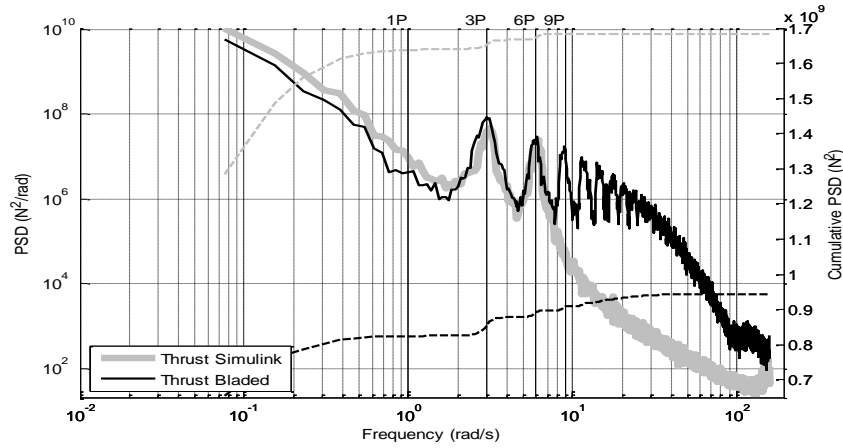


Figure H-5. Thrust PSD comparison between Simulink and Bladed with mean 8m/s

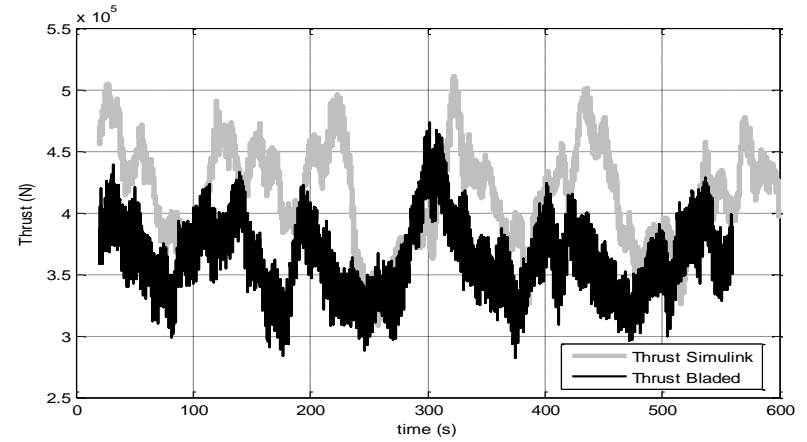


Figure H-6. Thrust time series comparison between Simulink and Bladed with mean 8m/s

- In-plane RBM of the blade

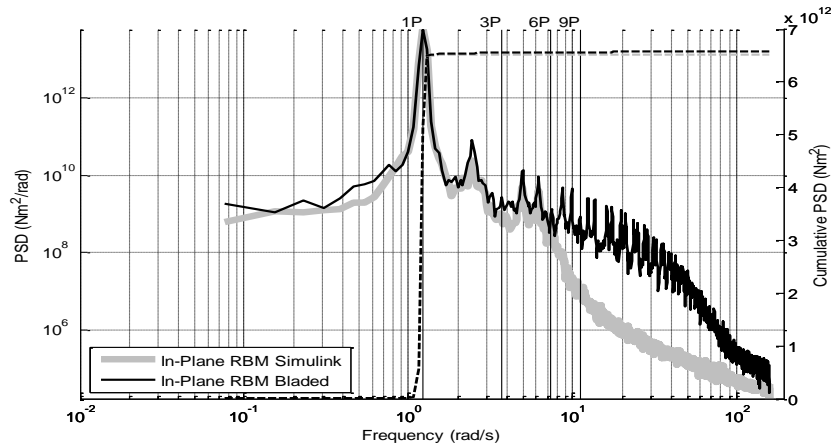


Figure H-7. In-Plane RBM PSD comparison between Simulink and Bladed with mean 15m/s

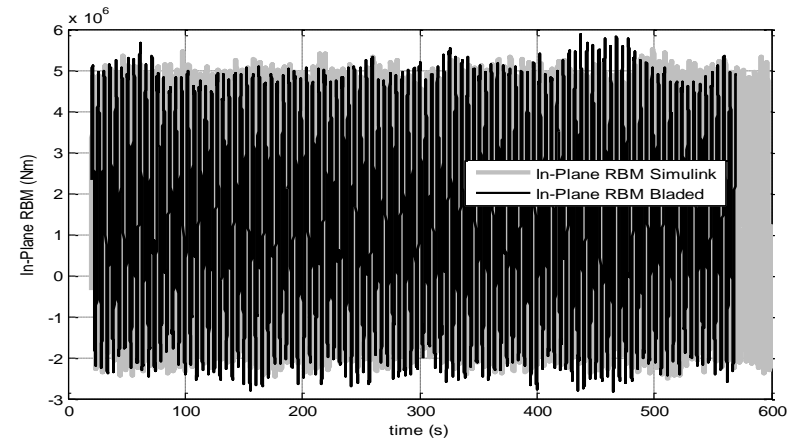


Figure H-8. In-Plane RBM time series comparison between Simulink and Bladed with mean 15m/s

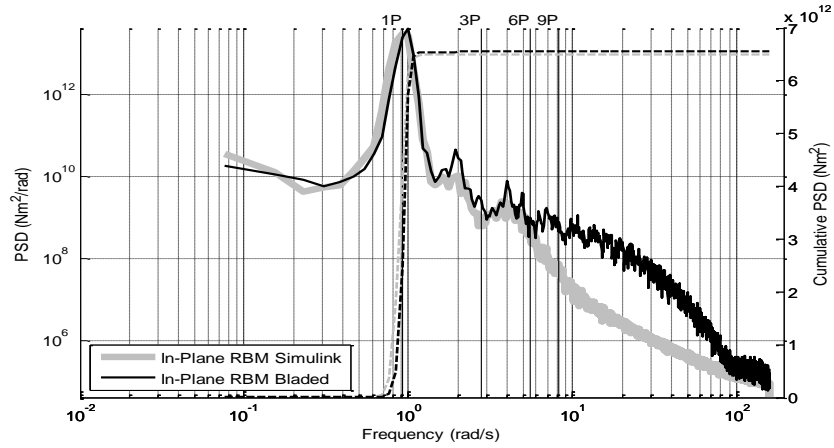


Figure H-9. . In-Plane RBM PSD comparison between Simulink and Bladed with mean 15m/s and 18 degrees of pitch offset

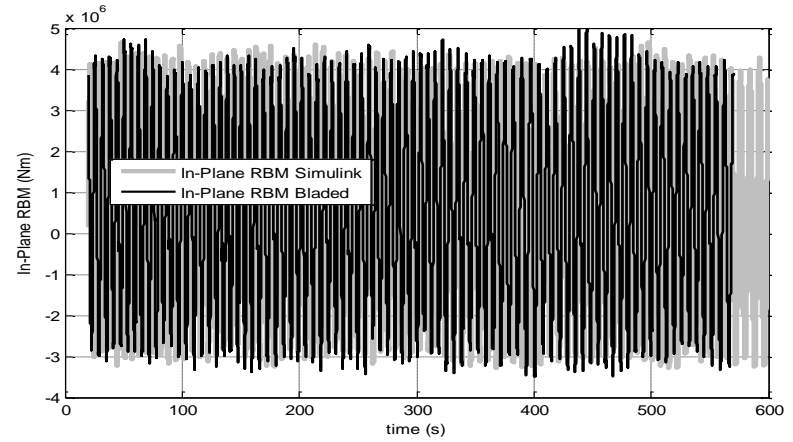


Figure H-10. In-Plane RBM time series comparison between Simulink and Bladed with mean 15m/s and 18 degrees of pitch offset

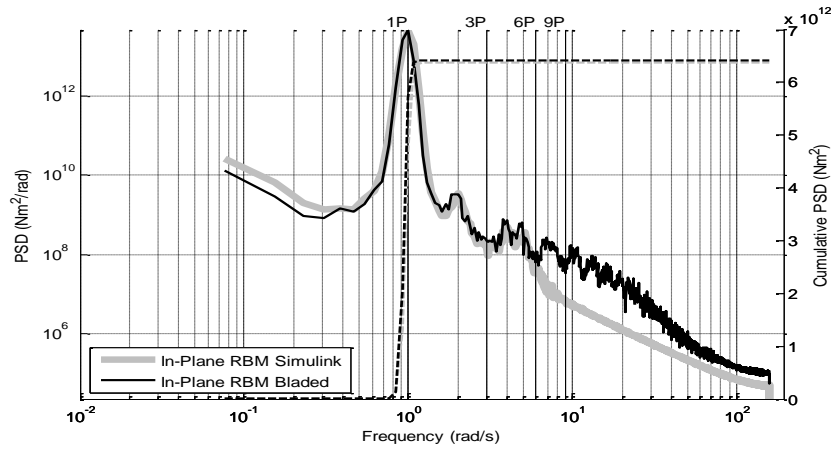


Figure H-11. . In-Plane RBM PSD comparison between Simulink and Bladed with mean 8m/s

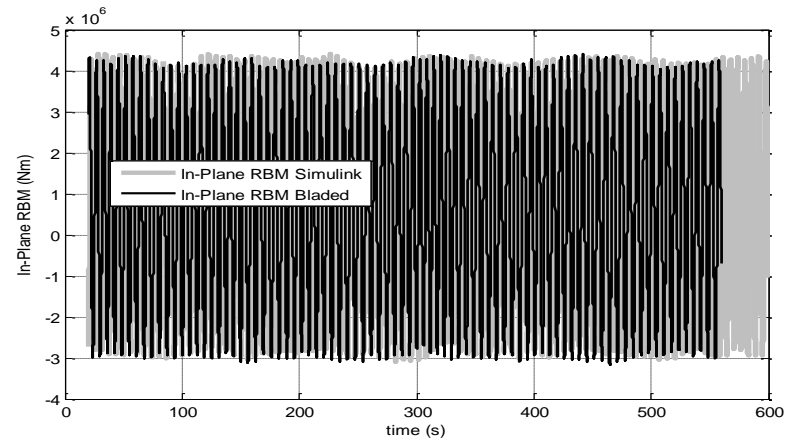


Figure H-12. In-Plane RBM time series comparison between Simulink and Bladed with mean 8m/s

- Generator speed

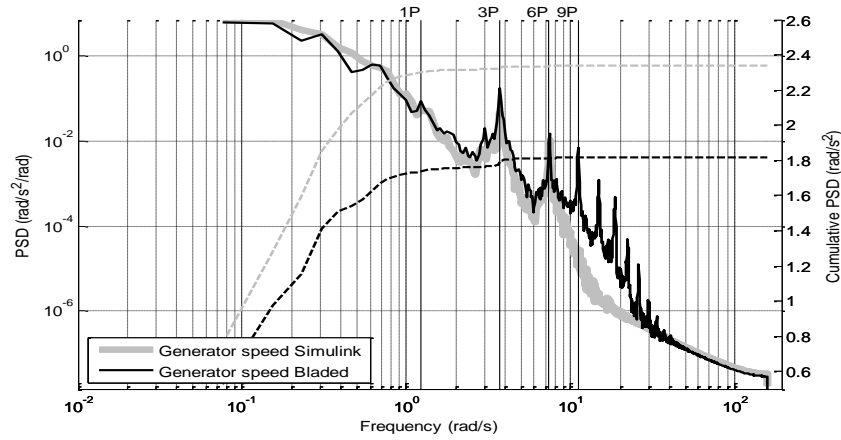


Figure H-13. Generator speed PSD comparison between Simulink and Bladed with mean 15m/s

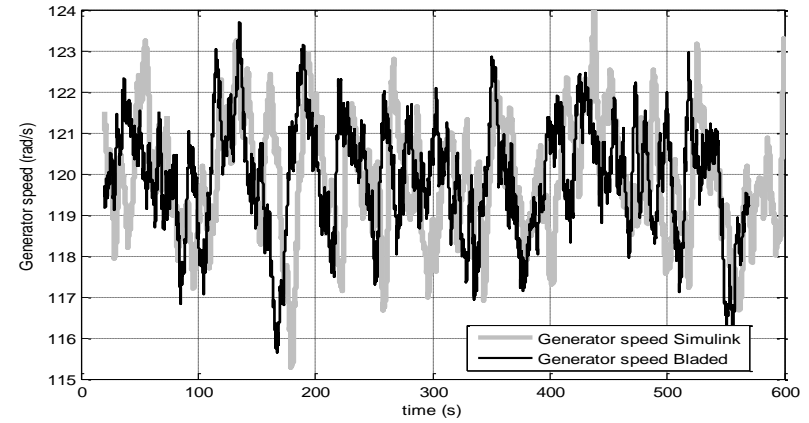


Figure H-14. Generator speed time series comparison between Simulink and Bladed with mean 15m/s

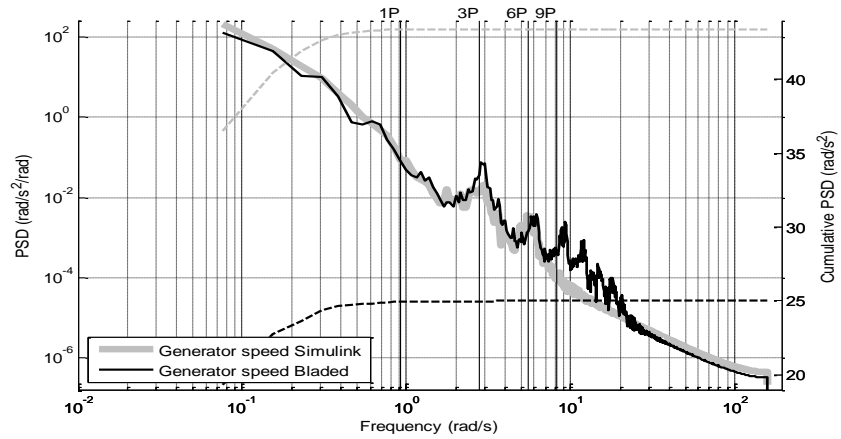


Figure H-15. Generator speed PSD comparison between Simulink and Bladed with mean 15m/s and 18 degrees of pitch offset

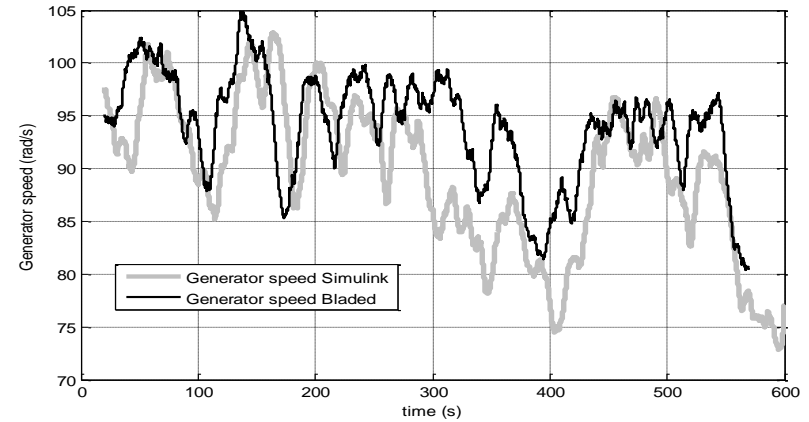


Figure H-16. Generator speed time series comparison between Simulink and Bladed with mean 15m/s and 18 degrees of pitch offset

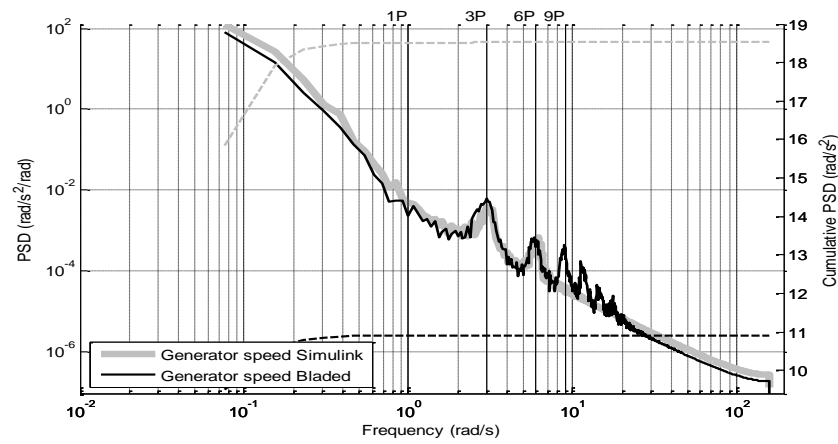


Figure H-17. Generator speed PSD comparison between Simulink and Bladed with mean 8m/s

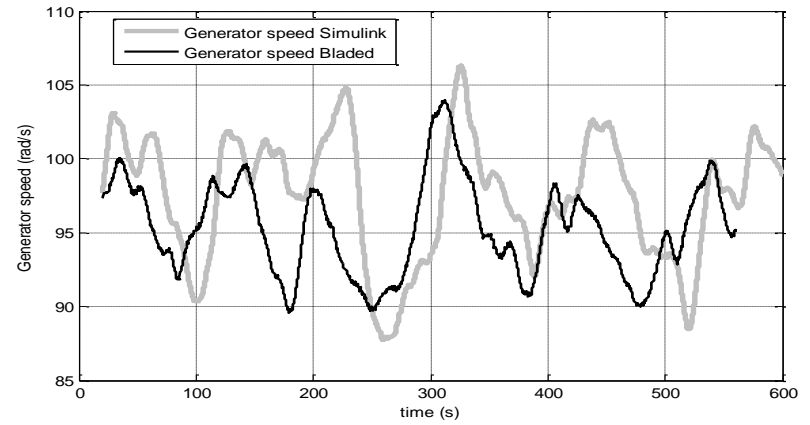


Figure H-18. Generator speed time series comparison between Simulink and Bladed with mean 8m/s

Appendix I

Bladed Comparison. Active Structural Dynamics

In the following can be found the results for the hub torque, thrust force, in-plane RBM of the blade, out-of-plane RBM of the blade and generator speed, for the comparison between the proposed effective wind-field model and WT setting as per Section 5.6 and Bladed. The results are for two different case studies, 15m/s and 8m/s, at two different TI values, 15% and 20%. The generator speed results also include the outputs from 10% TI.

- Hub torque

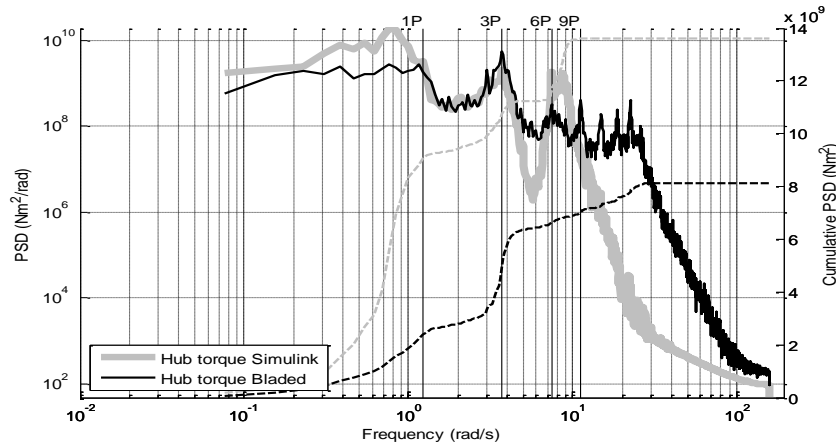


Figure I-1. Hub torque PSD comparison between Simulink and Bladed with mean 15m/s, TI 15%

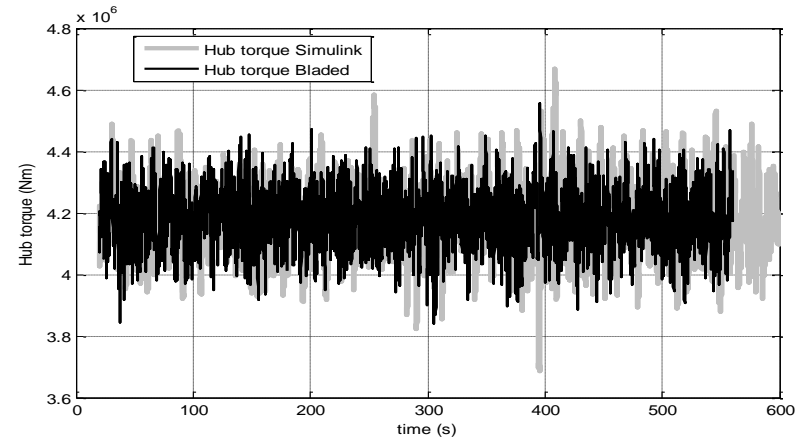


Figure I-2. Hub torque time series comparison between Simulink and Bladed with mean 15m/s, TI 15%

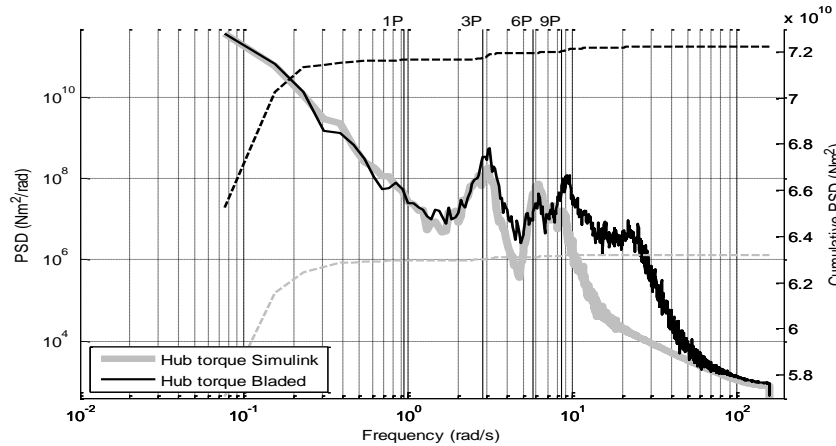


Figure I-3. Hub torque PSD comparison between Simulink and Bladed with mean 8m/s, TI 15%

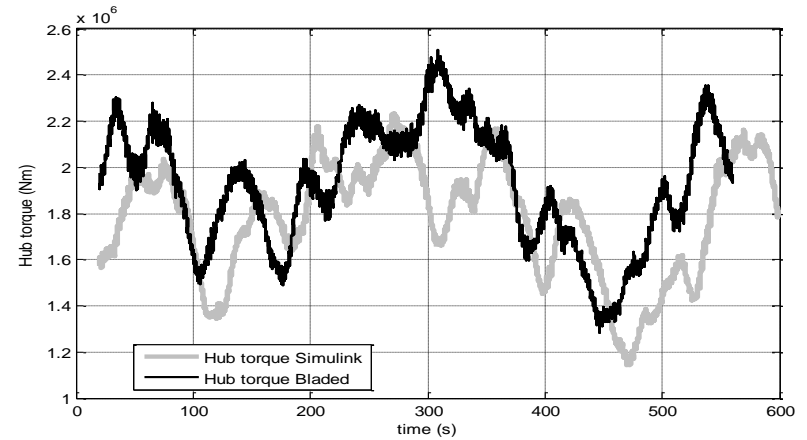


Figure I-4. Hub torque time series comparison between Simulink and Bladed with mean 8m/s, TI 15%

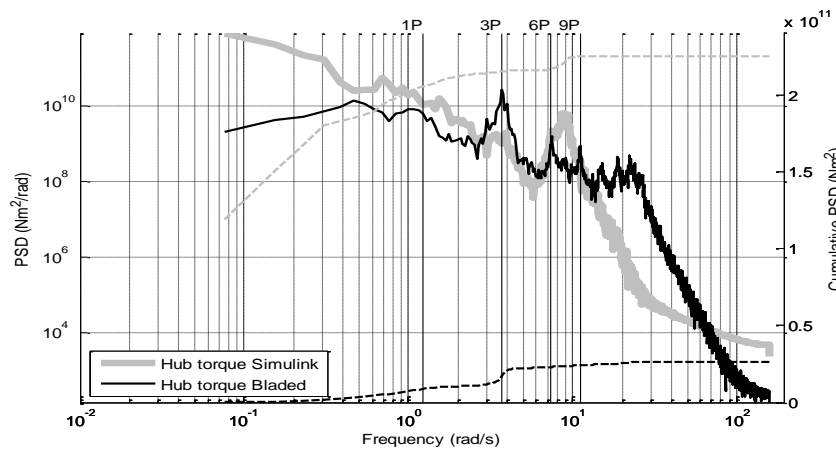


Figure I-5. Hub torque PSD comparison between Simulink and Bladed with mean 15m/s, TI 20%

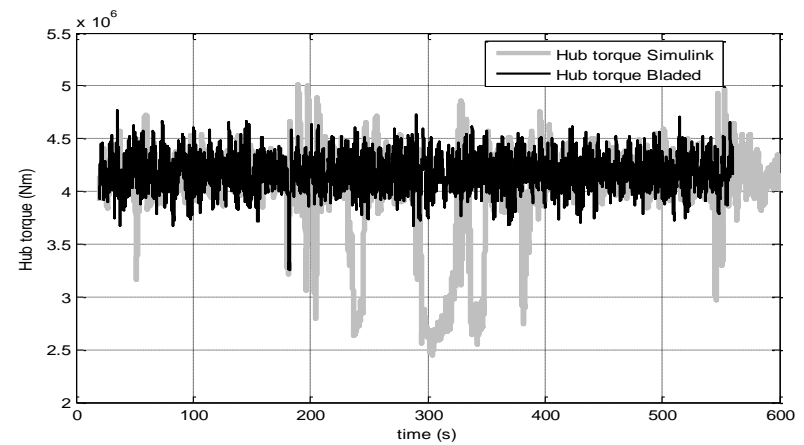


Figure I-6. Hub torque time series comparison between Simulink and Bladed with mean 15m/s, TI 20%

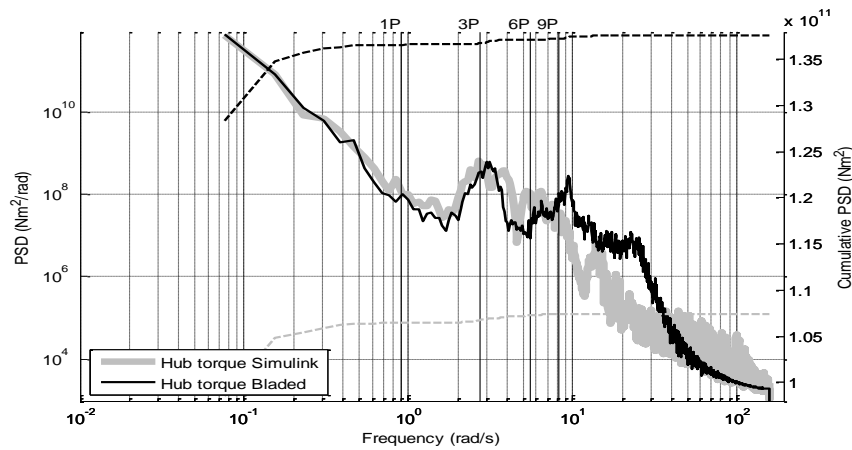


Figure I-7. Hub torque PSD comparison between Simulink and Bladed with mean 8m/s, TI 20%

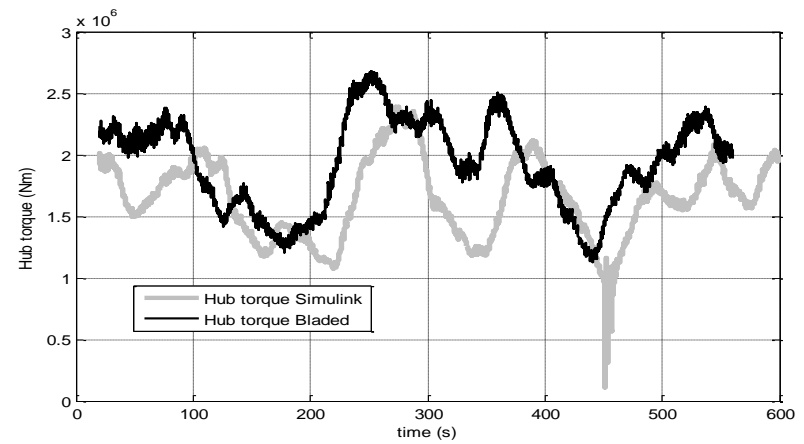


Figure I-8. Hub torque time series comparison between Simulink and Bladed with mean 8m/s, TI 20%

- Thrust Force

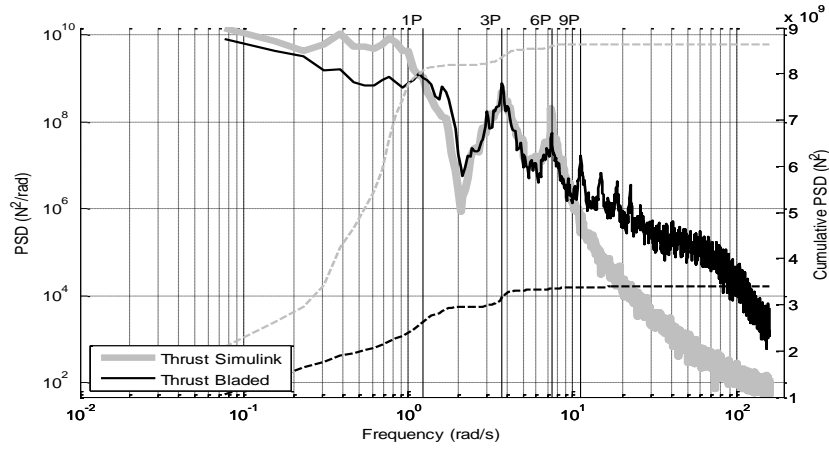


Figure I-9. Thrust PSD comparison between Simulink and Bladed with mean 15m/s, TI 15%

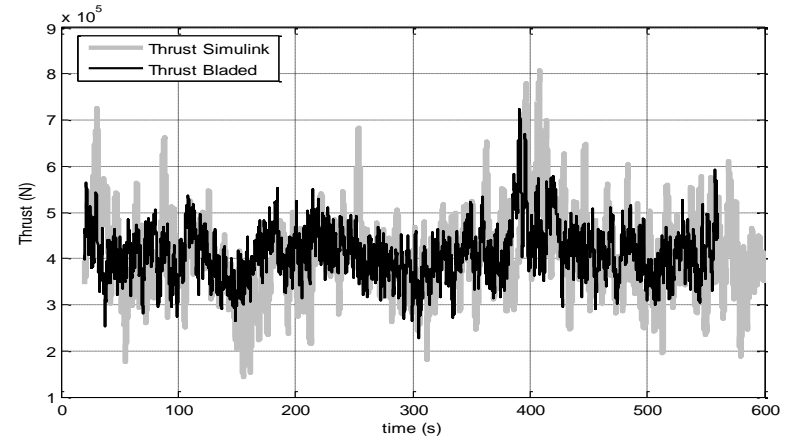


Figure I-10. Thrust time series comparison between Simulink and Bladed with mean 15m/s, TI 15%

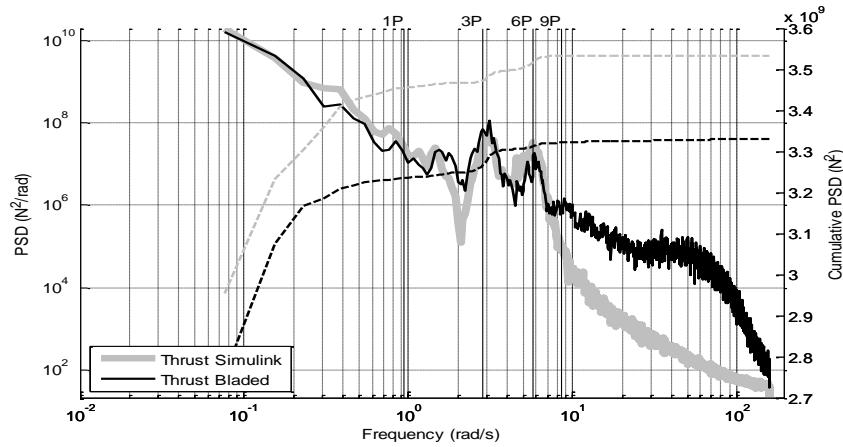


Figure I-11. Thrust PSD comparison between Simulink and Bladed with mean 8m/s, TI 15%

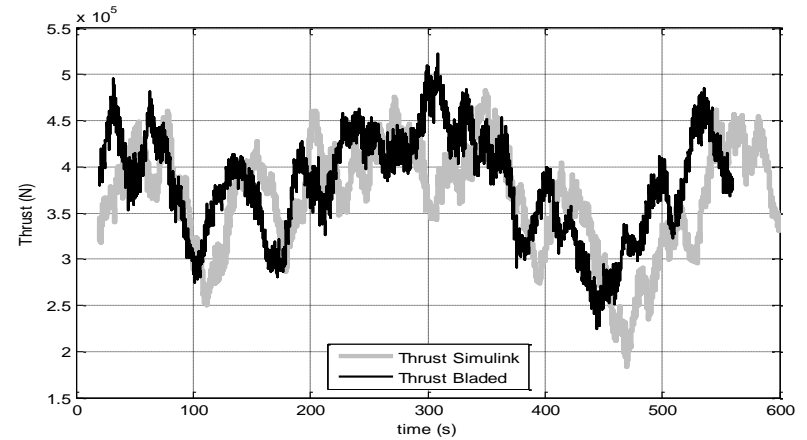


Figure I-12. Thrust time series comparison between Simulink and Bladed with mean 8m/s, TI 15%

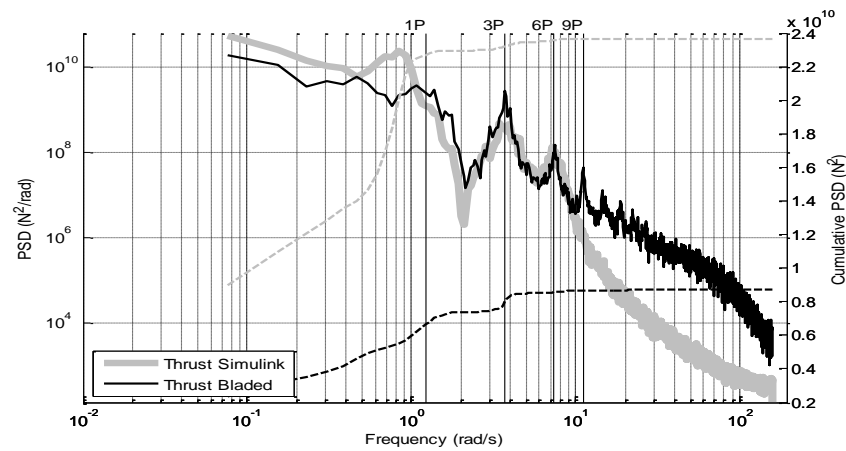


Figure I-13. Thrust PSD comparison between Simulink and Bladed with mean 15m/s, TI 20%

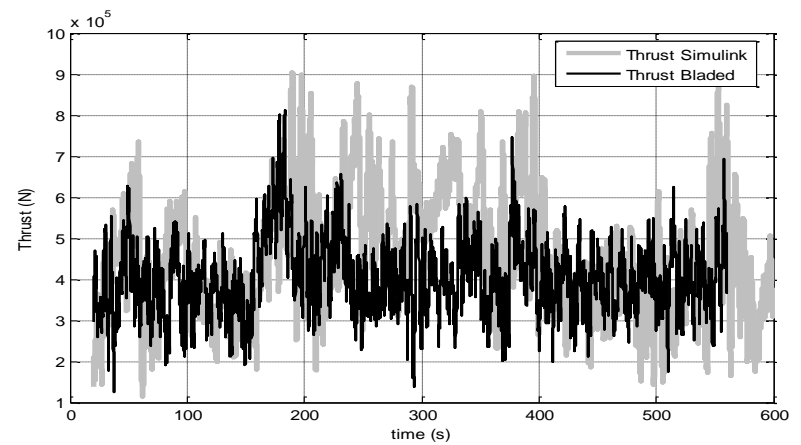


Figure I-14. Thrust time series comparison between Simulink and Bladed with mean 15m/s, TI 20%

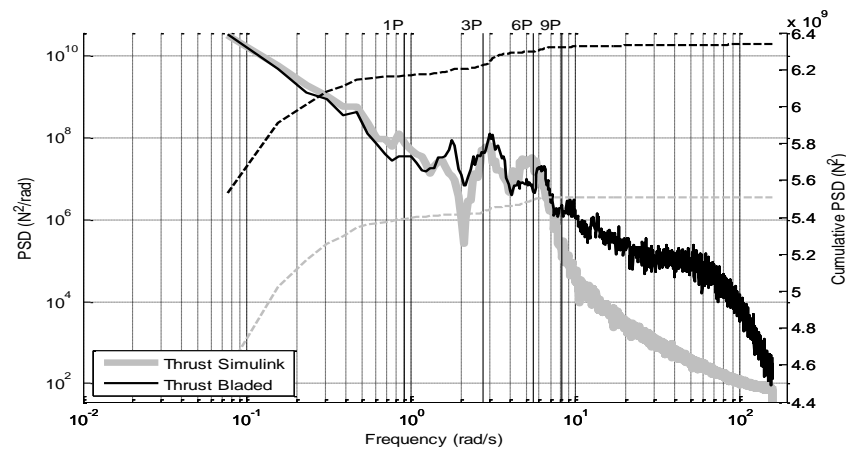


Figure I-15. Thrust PSD comparison between Simulink and Bladed with mean 8m/s, TI 20%

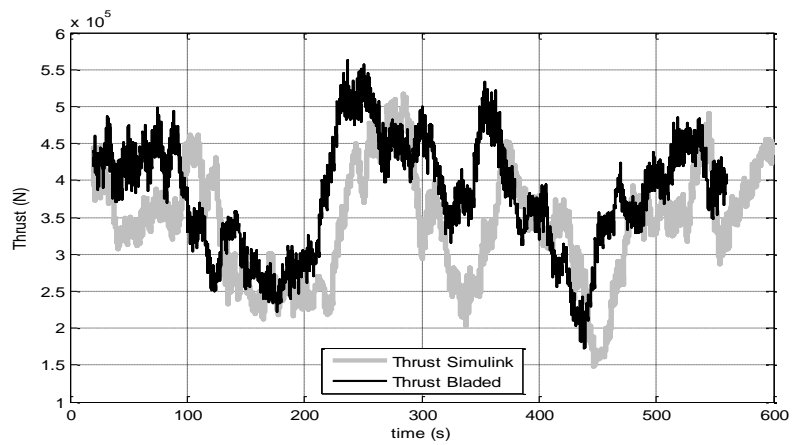


Figure I-16. Thrust time series comparison between Simulink and Bladed with mean 8m/s, TI 20%

- In-plane RBM of the blade

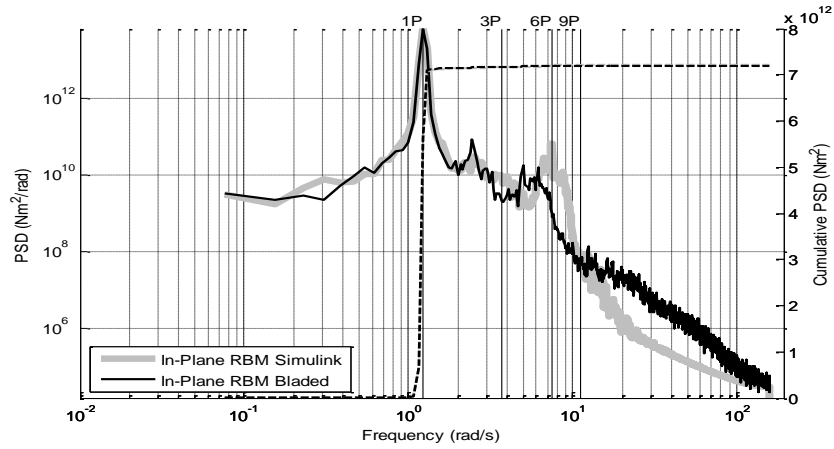


Figure I-17. In-plane RBM PSD comparison between Simulink and Bladed with mean 15m/s, TI 15%

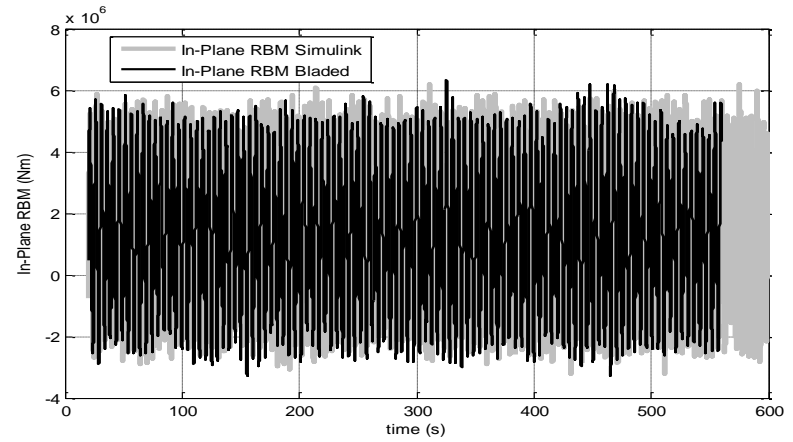


Figure I-18. In-plane RBM time series comparison between Simulink and Bladed with mean 15m/s, TI 15%

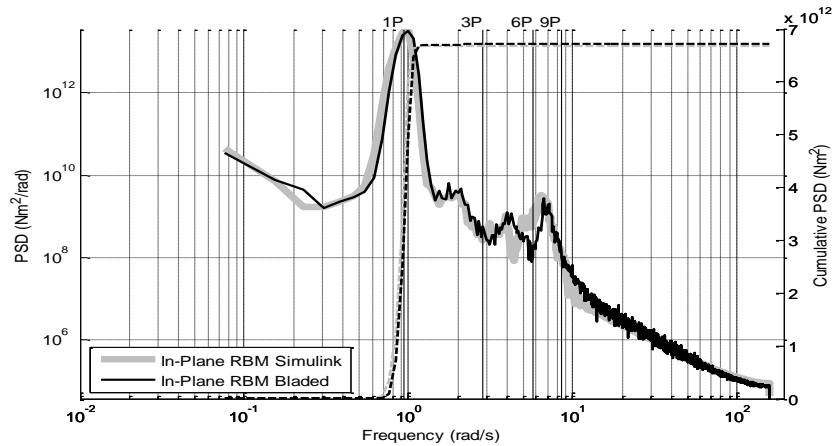


Figure I-19. In-plane RBM PSD comparison between Simulink and Bladed with mean 8m/s, TI 15%

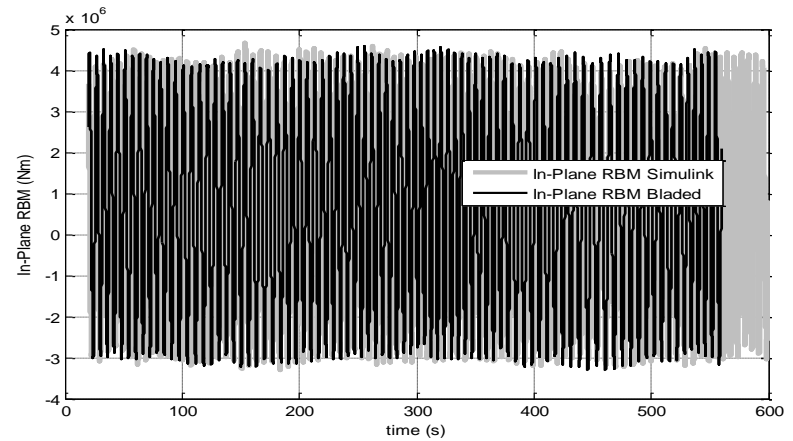


Figure I-20. In-plane RBM time series comparison between Simulink and Bladed with mean 8m/s, TI 15%

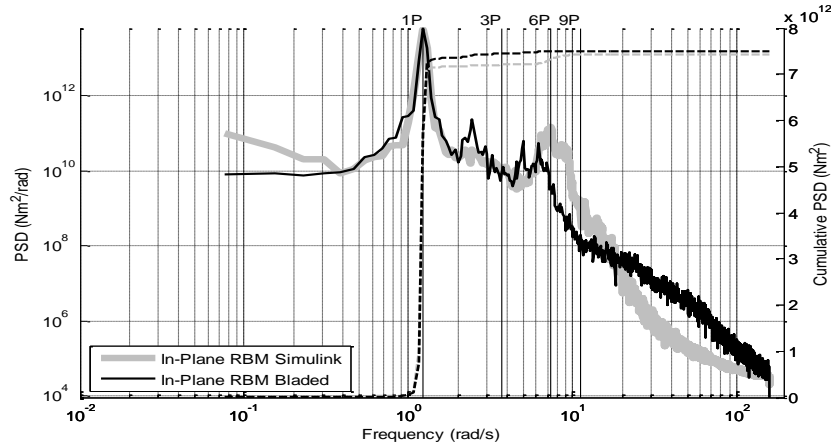


Figure I-21. In-plane RBM PSD comparison between Simulink and Bladed with mean 15m/s, TI 20%

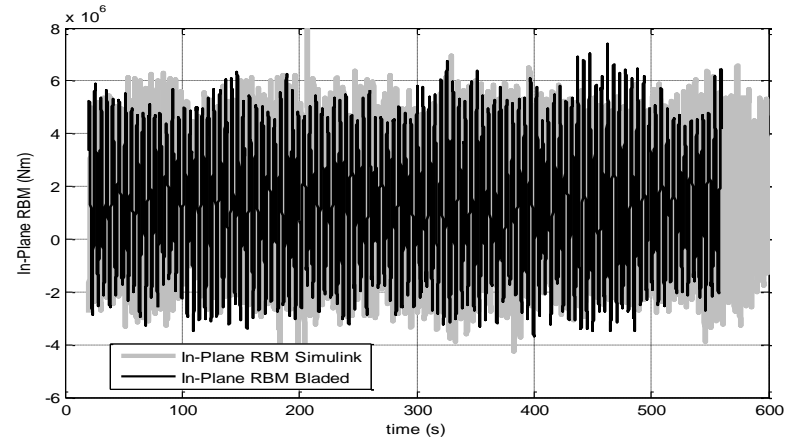


Figure I-22. In-plane RBM time series comparison between Simulink and Bladed with mean 15m/s, TI 20%

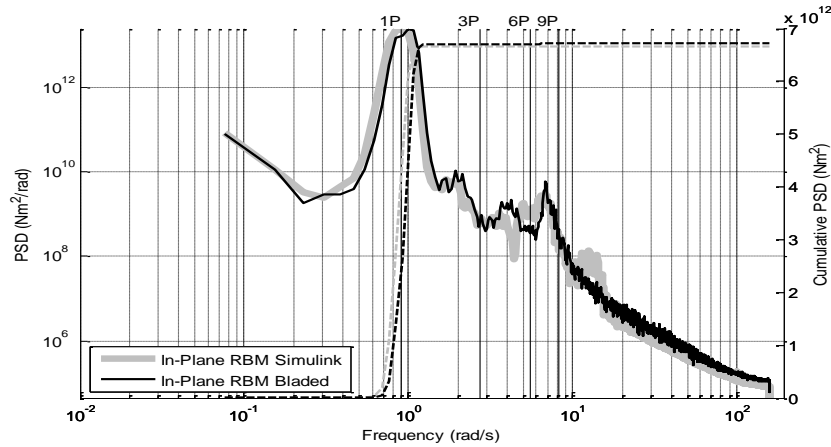


Figure I-23. In-plane RBM PSD comparison between Simulink and Bladed with mean 8m/s, TI 20%

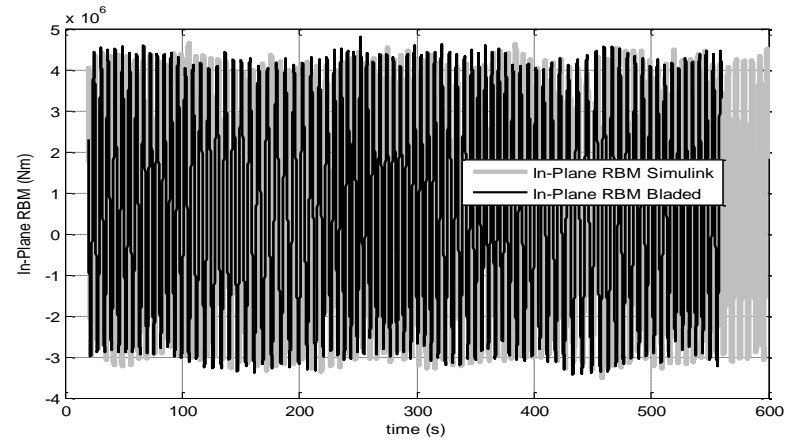


Figure I-24. In-plane RBM time series comparison between Simulink and Bladed with mean 8m/s, TI 20%

- Out-of-plane RBM of the blade

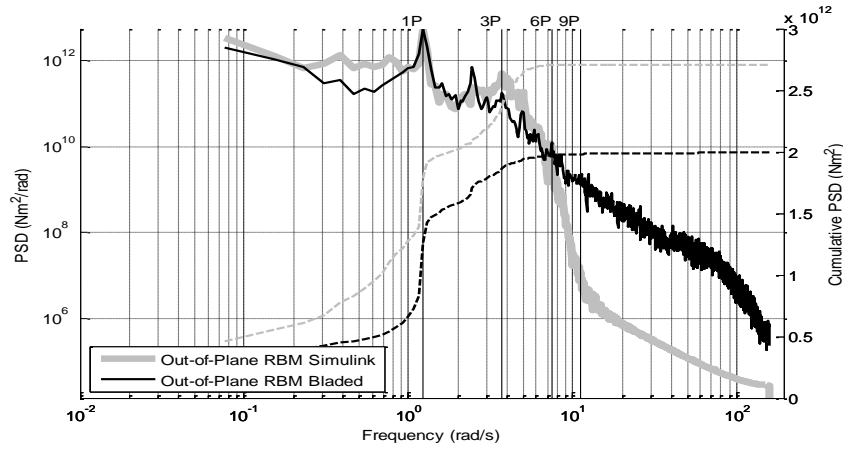


Figure I-25. Out-of-Plane RBM PSD comparison between Simulink and Bladed with mean 15m/s, TI 15%

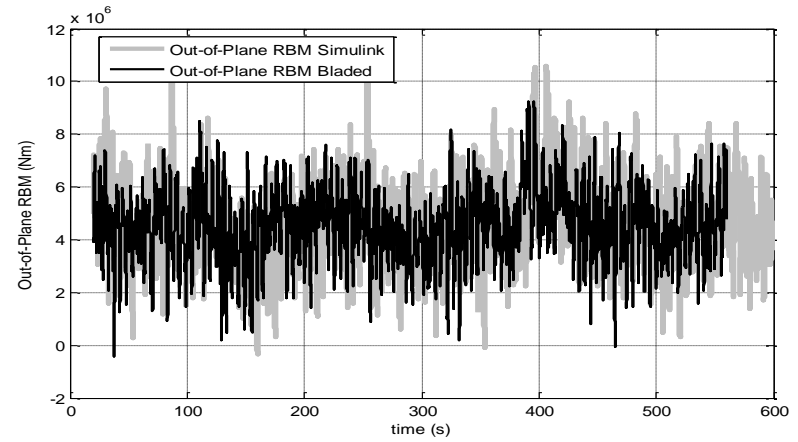


Figure I-26. Out-of-Plane RBM time series comparison between Simulink and Bladed with mean 15m/s, TI 15%

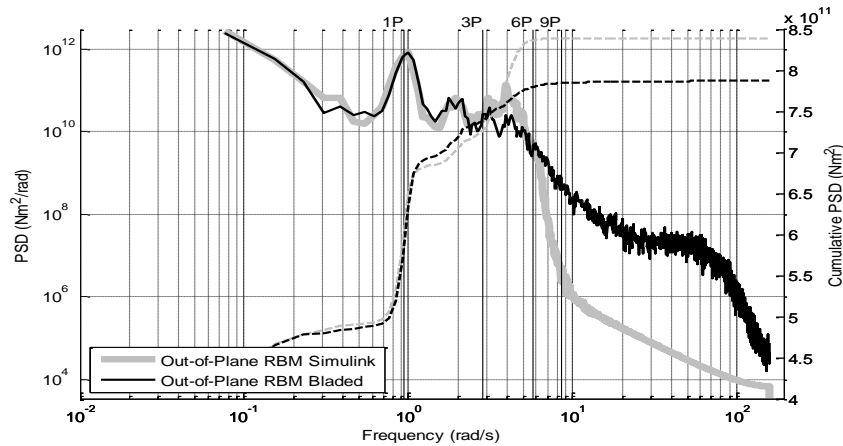


Figure I-27. Out-of-Plane RBM PSD comparison between Simulink and Bladed with mean 8m/s, TI 15%

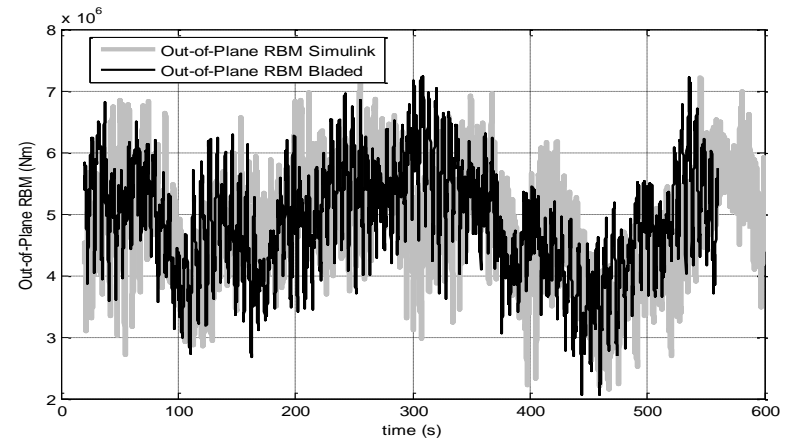


Figure I-28. Out-of-Plane RBM time series comparison between Simulink and Bladed with mean 8m/s, TI 15%

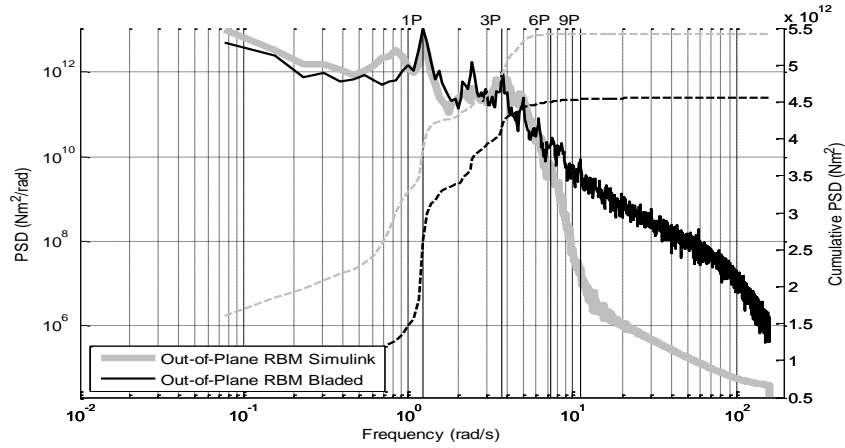


Figure I-29. Out-of-Plane RBM PSD comparison between Simulink and Bladed with mean 15m/s, TI 20%

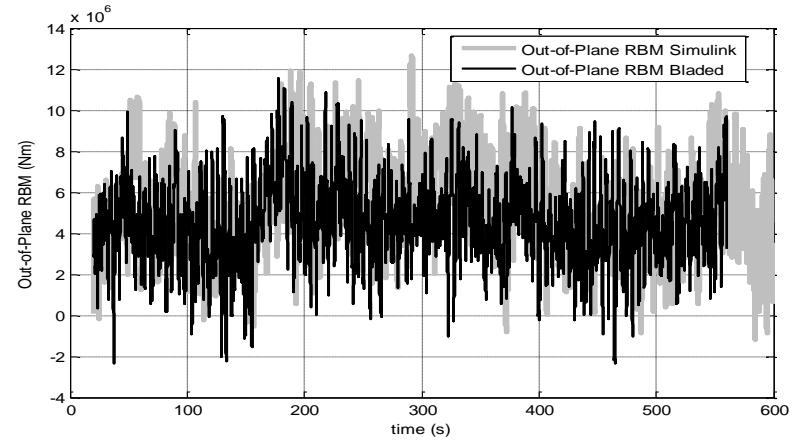


Figure I-30. Out-of-Plane RBM time series comparison between Simulink and Bladed with mean 15m/s, TI 20%

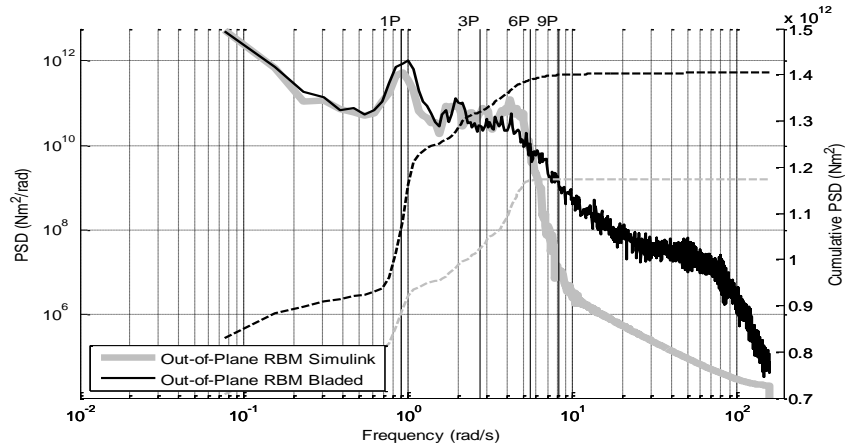


Figure I-31. Out-of-Plane RBM PSD comparison between Simulink and Bladed with mean 8m/s, TI 20%

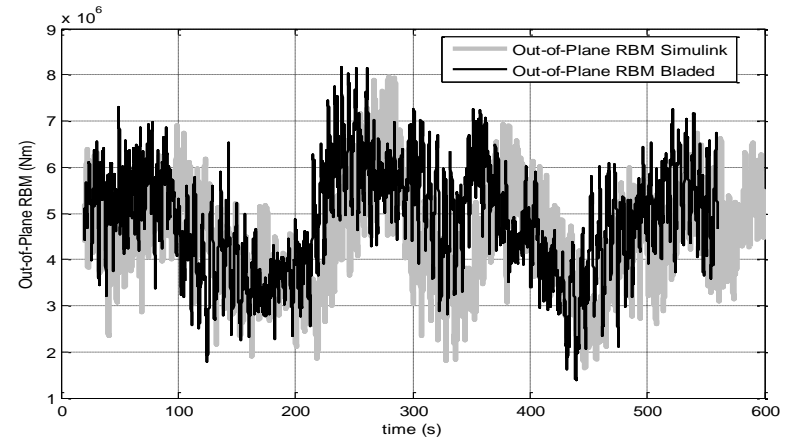


Figure I-32. Out-of-Plane RBM time series comparison between Simulink and Bladed with mean 8m/s, TI 20%

- Generator Speed

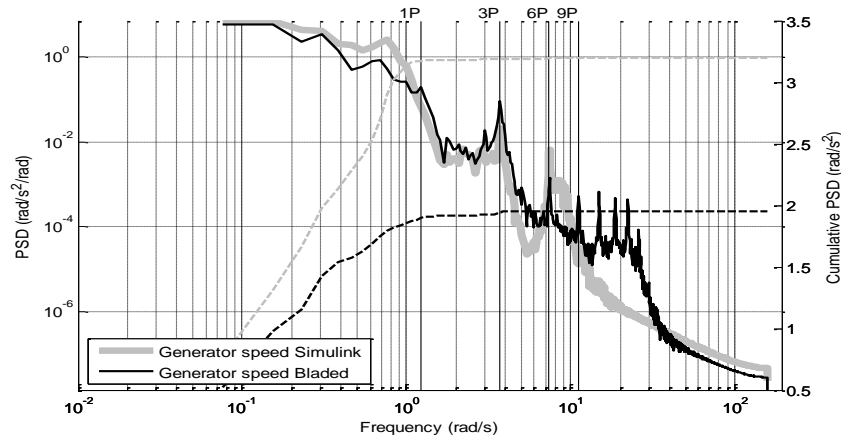


Figure I-33. Generator speed PSD comparison between Simulink and Bladed with mean 15m/s, TI 10%

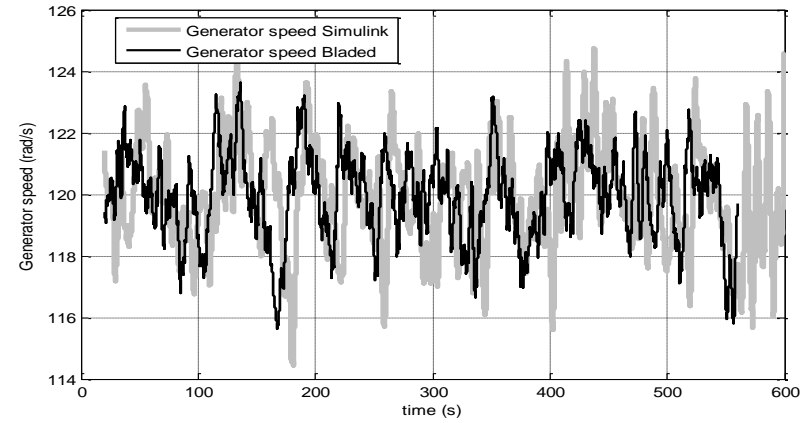


Figure I-34. Generator speed time series comparison between Simulink and Bladed with mean 15m/s, TI 10%

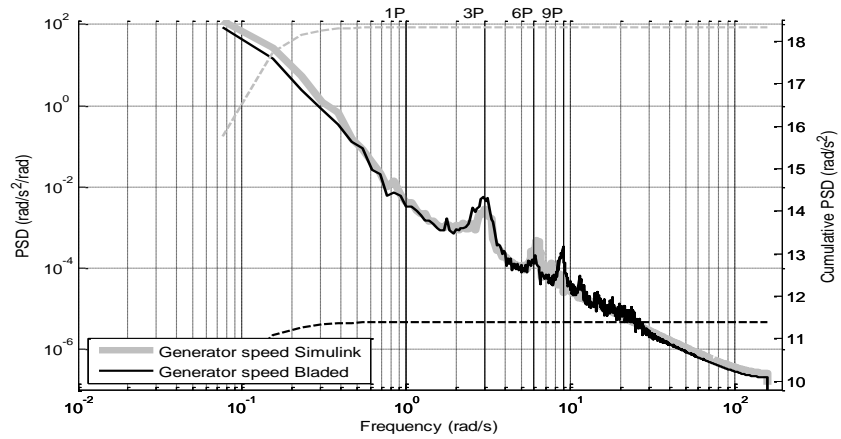


Figure I-35. Generator speed PSD comparison between Simulink and Bladed with mean 8m/s, TI 10%

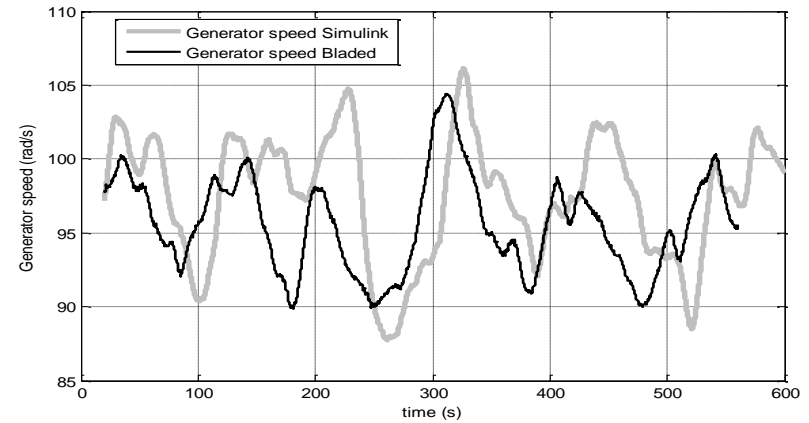


Figure I-36. Generator speed time series comparison between Simulink and Bladed with mean 8m/s, TI 10%

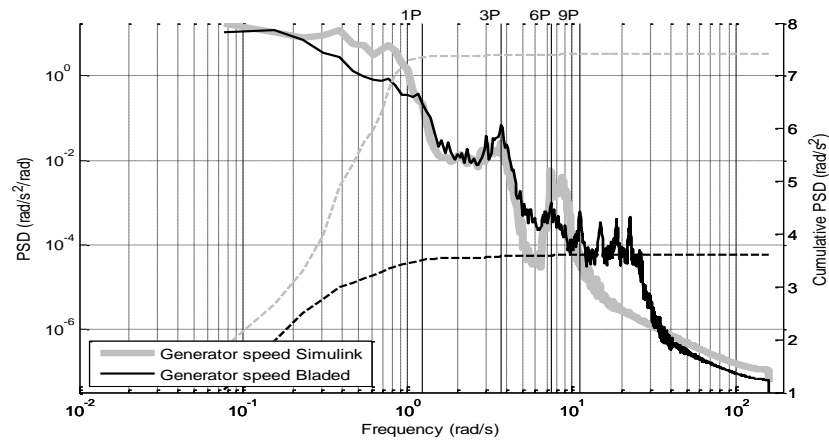


Figure I-37. Generator speed PSD comparison between Simulink and Bladed with mean 15m/s, TI 15%

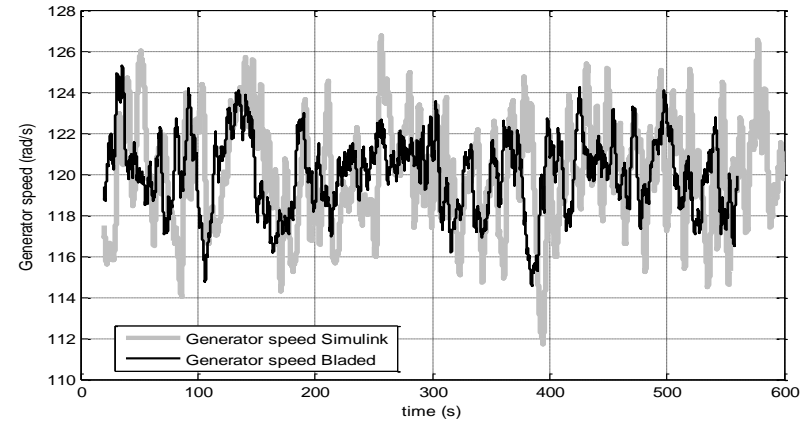


Figure I-38. Generator speed time series comparison between Simulink and Bladed with mean 15m/s, TI 15%

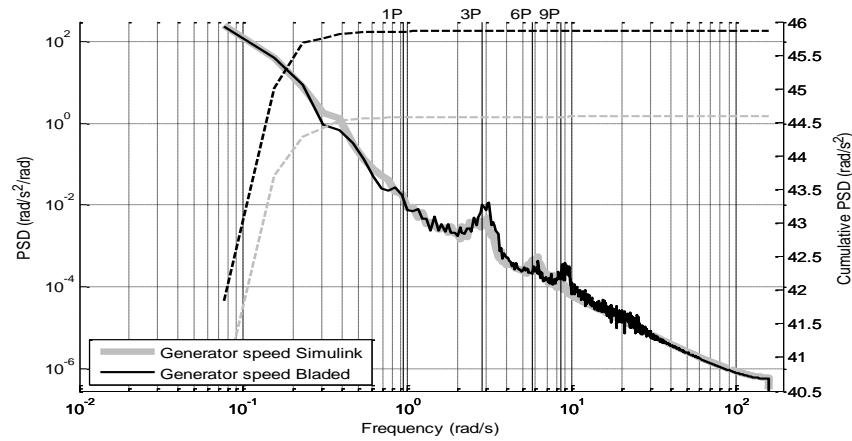


Figure I-39. Generator speed PSD comparison between Simulink and Bladed with mean 8m/s, TI 15%

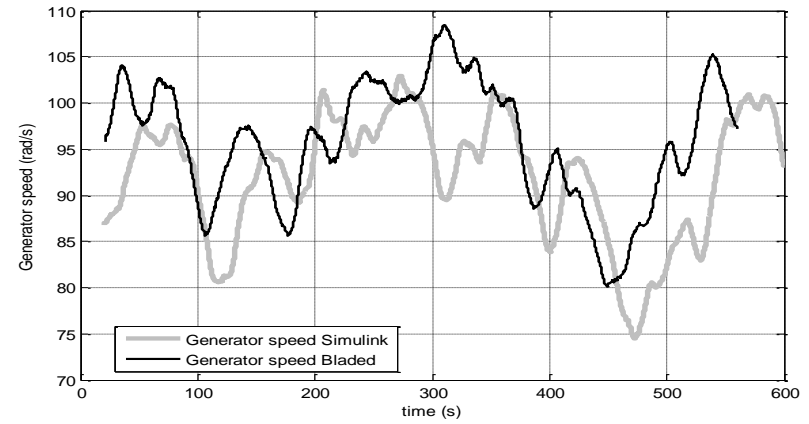


Figure I-40. Generator speed time series comparison between Simulink and Bladed with mean 8m/s, TI 15%

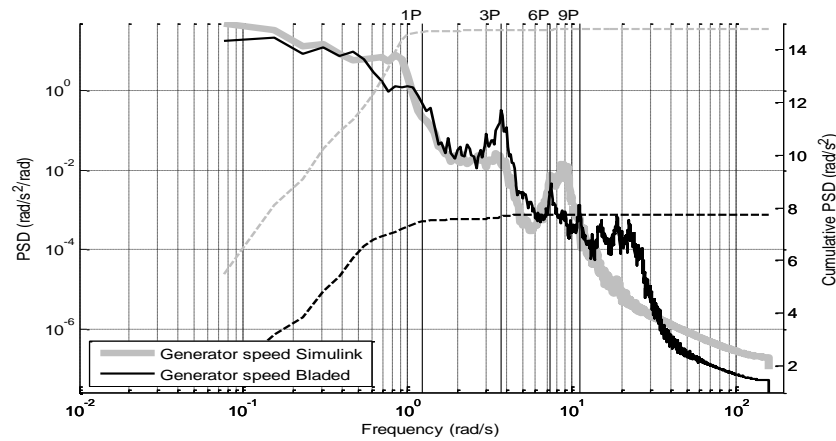


Figure I-41. Generator speed PSD comparison between Simulink and Bladed with mean 15m/s, TI 20%

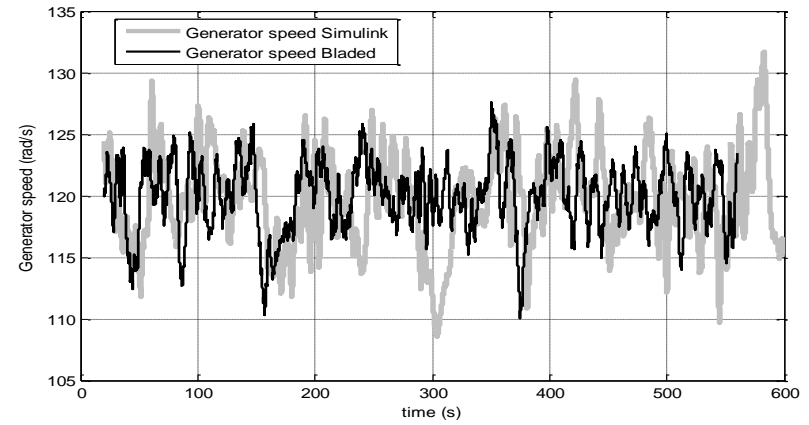


Figure I-42. Generator speed time series comparison between Simulink and Bladed with mean 15m/s, TI 20%

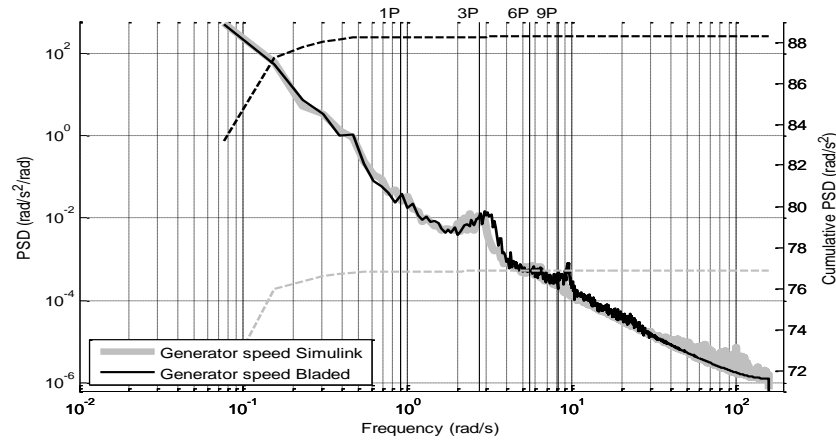


Figure I-43. Generator speed PSD comparison between Simulink and Bladed with mean 8m/s, TI 20%

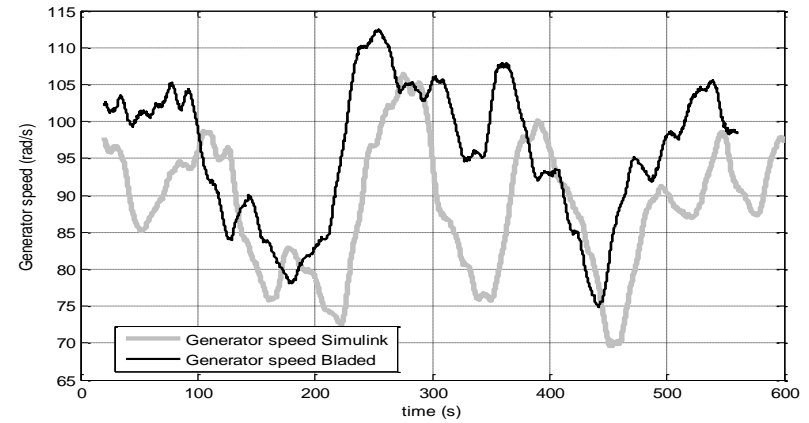


Figure I-44. Generator speed time series comparison between Simulink and Bladed with mean 8m/s, TI 20%

Appendix J

Single Blade Element Separability

The Separability for the individual blade elements of the rotor PJ9 at the blade station of 50%, 75% and 90% from the root of the blade, has been explored for rotors speeds of 90%, 100 and 110% of rated ω_0 . The results can be seen from Figure H-1 to Figure H-9 and confirm the existence of Separability for the single blade elements.

- Rotor speed 90% ω_0

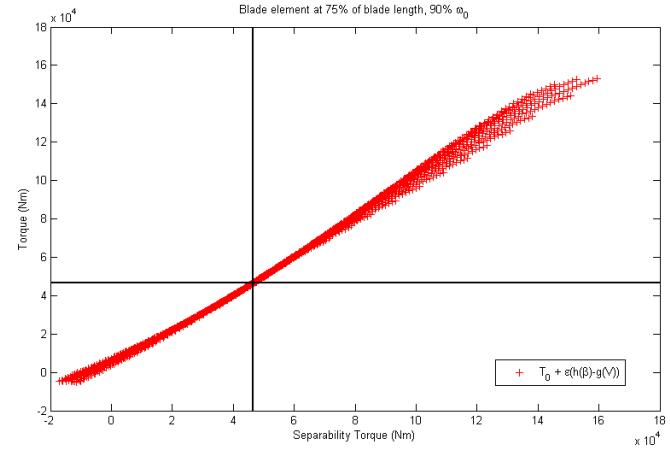
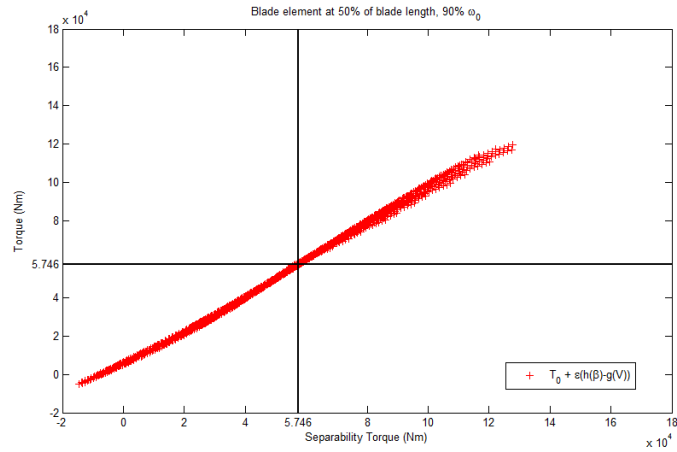


Figure H-1. Separability for a blade element situated at 50% from the root of the blade for 90% ω_0 rotor speed

Figure H-2. Separability for a blade element situated at 75% from the root of the blade for 90% ω_0 rotor speed

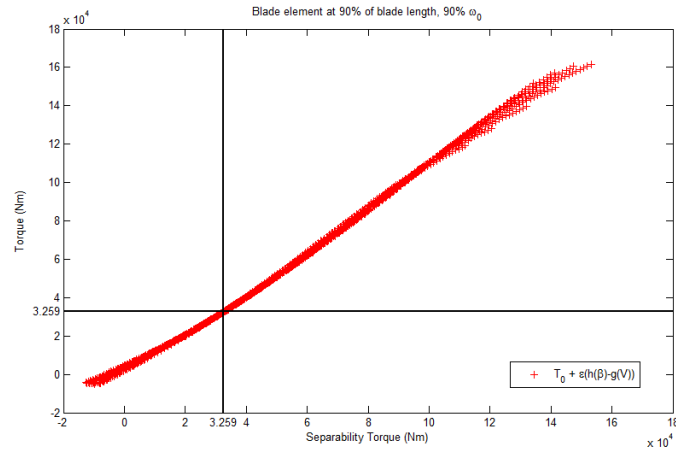


Figure H-3. Separability for a blade element situated at 90% from the root of the blade for 90% ω_0 rotor speed

- Rotor speed 100% ω_0

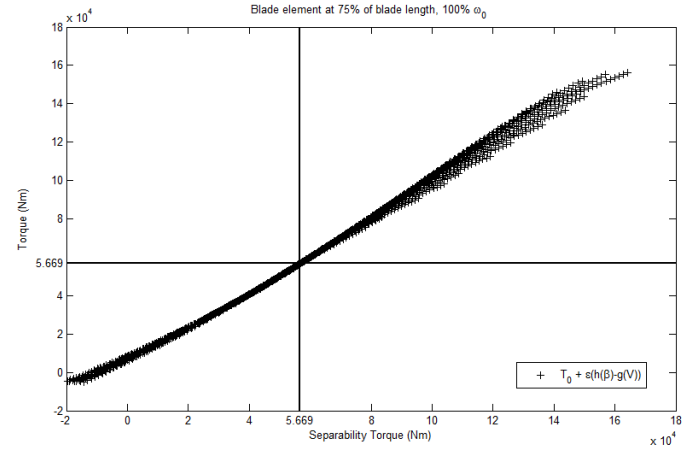
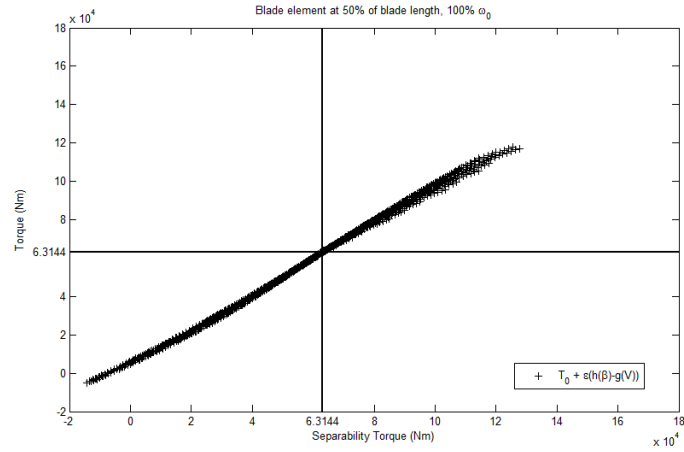


Figure H-4. Separability for a blade element situated at 50% from the root of the blade for 100% ω_0 rotor speed

Figure H-5. Separability for a blade element situated at 75% from the root of the blade for 100% ω_0 rotor speed

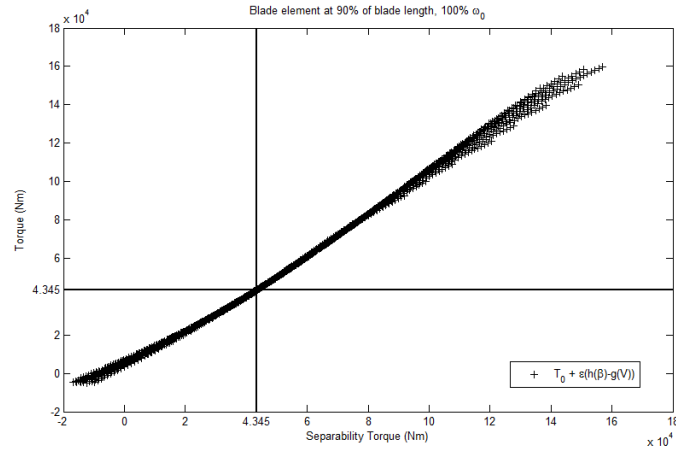


Figure H-6. Separability for a blade element situated at 90% from the root of the blade for 100% ω_0 rotor speed.

- Rotor speed 110% ω_0

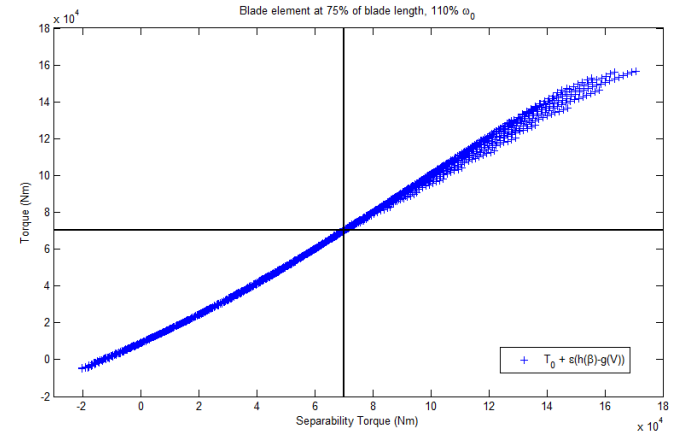
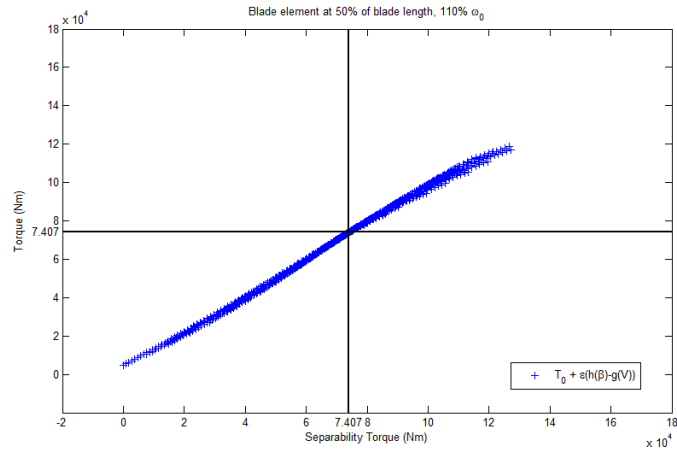


Figure H-7. Separability for a blade element situated at 50% from the root of the blade for 110% ω_0 rotor speed

Figure H-8. Separability for a blade element situated at 75% from the root of the blade for 110% ω_0 rotor speed

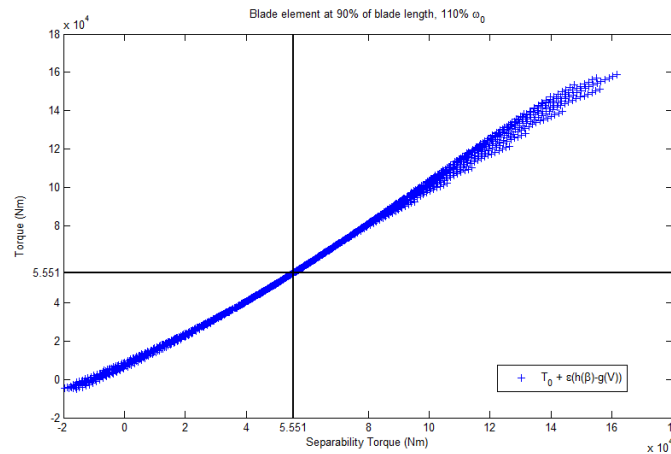


Figure H-9. Separability for a blade element situated at 90% from the root of the blade for 110% ω_0 rotor speed

Appendix K

Commentary on Reference [42]

This appendix concerns the publication Jamieson, P., Leithead, W.E., Gala Santos, M.L., *'The Aerodynamic Basis of a Torque Separability Property'*. Proceedings of EWEA 2011, Brussels, 2011. The paper has been included in the accompanying USB stick.

As understanding of the Separability property has advanced since the above paper was published, it is considered appropriate to address some points previously made that no longer holds. In [42],

- 1) The inference of the functional form on (12) and (14) from (11) is incorrect for the following reasons,
 - a) Basing the derivation on global properties, the $\tau(\cdot)$ function needs to be accounted for. The $\tau(\cdot)$ function although weakly non-linear, cannot be ignored as in the paper.
 - b) Basing the derivation on local properties would require higher order partial derivatives to be correct on the locus of equilibrium points. However, only first order partial derivatives are guaranteed by the local Additivity property.
- 2) Figure 7 and Figure 9 extend curves beyond the domain of Separability. In this way, they are misleading.

Hence, Separability does not imply the functional form in (14), see (4.21) and (4.23) in Chapter 4 of this thesis.

On this basis, it can be established that the majority of the discrepancies seen later in the paper stem from these previous observations.

Appendix L

Matlab Scripts and Instructions

The procedure below has been followed to study the Separability property for the aerodynamic torque of the 3 rotors as described in Appendix A. It is assumed that the C_q table of the rotors are available. The Matlab scripts are functional rather than optimised or elegant.

The instructions are written as direct commands to the user.

J.1 Instructions for Matlab Scripts

- 1) Run **Matlab Function 1**.
- 2) Run **Matlab Function 2**. For this first run of **Matlab Function 2** it is not a problem if the range requested is not known yet. Set a big range that stays within the size of the variable 'torqueoriginal' created by **Matlab Function 1**.
- 3) Find inside the variable 'originalre' the lines that hold the wind speed range between rated wind speed and cut-off wind speed. Note the numbers.
- 4) Run **Matlab Function 2** again.
- 5) Plot the variable 'transformationreal'.

```
figure 1, plot(transformationreal(4:end,1), transformationreal(4:end,2), '+')
```

The first time the variable is plotted it will be noticeable that the resulting curve changes its slope's sign. Identify which points have changed sign and remove them from the plot. As a reference, it is normally the first 4 points.

- 6) Use the evaluation tool available for Matlab plots and evaluate the first column of the variable 'selection' within the plot created in point 4), use the shape preserving interpolant fit. Save the result in the variable 'transformationreal2'.
- 7) Run **Matlab Function 3**.

8) Run **Matlab Function 4**.

9) Run **Matlab Function 5**.

10) Create the following plot:

```
figure2, plot(tlnr(2:end,1), tlnr(2:end, 2:end))
```

```
hold all
```

```
plot(make3(2:end,1), make3(2:end,2:end), '+' )
```

11) Check that the range of values selected by 'tlnr' satisfy the analysis requirements i.e. broader or more stringent range depending on scope. Adjust manually the 'tlnr' variable if required i.e. by adding extra NaNs or by recovering information that has been sieved. Save the modified 'tlnr' variable as 'tlnrREDUCEDcorrect'. Only the pitch columns that have torque values that go above and below T_{rated} should be selected.

12) Create the following plot:

```
figure 3, plot(tlnrREDUCEDcorrect(2:end,1), tlnrREDUCEDcorrect(2:end, 8:24))
```

```
hold all
```

```
plot(make3(2:end,1), make3(2:end,2:end), '+' )
```

13) Check that the variable 'new3' does not have a false first row value (0,0), eliminate as required.

14) Create the following plots:

```
figure 4, plot(new3(:,1), new3(:,2), '+' ) % this is function  $g'(V)$ 
```

```
figure 5, plot(new33(:,1), new33(:,2), '+' ) % this is function  $g(V)$ 
```

15) Use the evaluation tool available for Matlab plots and fit $g'(V)$ with a shape preserving interpolant.

16) Eliminate possible undesired zeros in variable 'xround' created by **Matlab Function 5**. The variable 'xround' has the real equilibrium points (these values are based on β^*).

17) Evaluate 'xround' on the $g'(V)$ plot. Save the $[x, fx]$ generated as variable 'equilibriumincrements', the first column will have pitch values and the second column torque values.

18) The variable 'equilibriumincrements' needs to have the rated torque subtracted to really give the increments. Run **Matlab Function 6**. This function will generate the real equilibrium increments and the function $h(\beta)$.

19) Create the following plot:

```
figure 6, plot hpalternativa(:,1), hpalternativa(:,2), '+')
```

20) From the plots of functions $g(V)$ and $h(\beta)$ extract their equations by doing a quadratic fit with the Matlab fitting tool and introduce these functions within script **Matlab Function 7**.

21) Run **Matlab Function 7** with the entries related to the $\tau(\cdot)$ function an errors muted.

22) Create the following plot:

```
figure 7, plot (e5f(:,1), e5f(:,2), '+' ) %this plot shows Separability in  $\varepsilon(\cdot)$ 
```

23) Define the $\tau(\cdot)$ function as previously explained in Chapter 3

24) Introduce the $\tau(\cdot)$ function in **Matlab Function 7** and run it with the $\tau(\cdot)$ function and error entries un-muted. To see the outcome of Separability with the $\tau(\cdot)$ function plot the following,

```
figure8, plot(tauf(:,1), e5f(:,2), '+' ) %this plot shows Separability in  $\tau(\cdot)$ 
```

25) Run **Matlab Function 8** to generate the error contour plots.

J.2 Matlab Scripts

MATLAB FUNCTION 1

```
%this function simply transforms the tip speed ratios into velocities and  
%cq into torque values in the cq table generated by Bladed  
function [t,torqueoriginal,cqv,vin,top,torqueoriginalin,v]=original  
load cq  
cq=cq;% the column that holds the tip speed ratios (lambdas) goes in  
%crescent order of lambda which means that starts with high velocities then
```

```

%goes down
R=input('Introduce the radius of the machine \n');
w=input('Introduce rated rotational velocity (rad/sec) \n');
[row,col]=size(cq);
c=col-1;
tip=cq(2:end,1);
vin=(w*R)./tip;
zero=0;
v=vertcat(zero,vin);
cqvh=horzcat(v,cq(:,2:end));
t=repmat(vin,1,c);
torqueoriginalin=cqv(2:end,2:end).*t.*t.*(0.5.*1.225.*3.141593.*R.^3);
top=vertcat(cqv(1,2:end),torqueoriginalin);
torqueoriginal=horzcat(v,top);
disp('Remember to save torqueoriginal as torqueoriginal');
end

```

MATLAB FUNCTION 2

```

%creates the variables transformation real (contains the exact wind velocity
value for the equilibrium
%point in each column, and states that the correspondent pitch should be the
same pitch of that particular run),
%originalre (which is just torqueoriginal reorganised with the velocities in
increasing order) and selection (contains
%just the lines that we can work with; the one between rated wind speed and
cut-off (!! not exactly, is the ones that are
%between the velocity values of the equilibrium in transformationreal)) that
are need for the program torquelimofunct
function
[transformationreal,originalre,selection,x1,x2,y1,y2,m,l,cccc,x,y]=pretorqu
uelimofunct
disp('Check in originalre which is the pitch run that first have the first
torque value under-rated, that is going to be the lower limit of valid pitches
for the equilibrium, torqueoriginal');
start=input('Introduce the row number of the start value of the range of
interest from originalre \n');
fin=input('Introduce the row number of the end value of the range of interest
from originalre \n');
Trated=input('Introduce the rated torque \n');

```

```

load torqueoriginal
[rr,cc]=size(torqueoriginal);
k=0;
originalre=NaN(size(torqueoriginal));
for i=2:1:rr
    originalre(i,:)=torqueoriginal(rr-k,:);
    k=k+1;
end
originalre(1,:)=torqueoriginal(1,:);

x1=NaN(1,1);
x2=NaN(1,1);
y1=NaN(1,1);
y2=NaN(1,1);
m=NaN(1,1);
ccccc=NaN(1,1);
x=NaN(1,1);
y=NaN(1,1);
for j=2:1:cc
    for i=start:1:fin
        if originalre(i,j)<originalre(i+1,j) && originalre(i,j)<Trated &&
originalre(i+1,j)>Trated %this finds in the torque table the value
immediately under and immediately over the Trated value. This is for the
case that the exact rated torque value is not in the table (the most likely
situation)
            x1(j)=originalre(i,1);
            x2(j)=originalre(i+1,1);
            y1(j)=originalre(i,j);
            y2(j)=originalre(i+1,j);
            m(j)=(y2(j)-y1(j))/(x2(j)-x1(j));
            ccccc(j)=y1(j)-m(j).*x1(j);
            x(j-1)=(Trated-cccc(j))./m(j);%exact equilibrium wind velocity
            y(j-1)=originalre(1,j);
        end
        if originalre(i,j)==Trated
            x(j-1)=originalre(i,1);
            y(j-1)=originalre(1,j);
        end
    end
end
end
transformationreal=horzcat(x(:),y(:));

```

```

[r,c]=size(transformationreal);
transformationreal1=NaN(1,1);
k=1;
for i=1:1:r
    if isnan(transformationreal(i,1)) || transformationreal(i,1)==0;
        k=k;
    else
        transformationreal1(k,1)=transformationreal(i,1);
        transformationreal1(k,2)=transformationreal(i,2);
        k=k+1;
    end
end
transformationreal=transformationreal1;
[r,c]=size(originalre);
[rr,cc]=size(transformationreal);
selection1=NaN(1,c);
k=1;
l=min(transformationreal(:,1));
for i=2:1:r
    if originalre(i,1)>=l && originalre(i,1)<=transformationreal(rr,1)
        selection1(k,:)=originalre(i,:);
        k=k+1;
    end
end
for i=2:1:r
    if originalre(i,1)>=l && originalre(i-1,1)<l
        hh=i-1;
    end
end
hh=hh;
selection=vertcat(originalre(hh,:),selection1(:,:));
disp('Now plot transformation real, fit shape preserving interpolant and
evaluate the velocities in the first column of selection to find the
correspondent pitches, save x & f(x) in the variable transformationreal2.
Save TRANSFORMATIONREAL2, SELECTION & ORIGINALRE in the directory');
end

```

MATLAB FUNCTION 3

```
%This function creates torquelimo which contains the range of torque values  
%correspondent to the range of wind speeds that the equilibrium points  
%allow us, with the wind velocities being substituted by their equivalent  
%pitch*.
```

```
function [pb,torquelimo]=torquelimofunct  
  
load transformationreal2  
load selection  
load originalre  
  
pb=horzcat(transformationreal2(:,2),selection(:,2:end));  
torquelimo=vertcat(originalre(1,:),pb(:,:));  
  
disp('Remember to save torquelimo as torquelimo');  
end
```

MATLAB FUNCTION 4

```
%this function clears the table torquelimo from the values that we are not  
%interested in and reorders the velocities to have them in increasing order
```

```
function [tlnr]=clean  
start=input('Introduce the column number of the start value of the range of  
pitch of interest from selection \n'); % the first column that precede all  
the following columns in having values of torque under and over rated  
load torquelimo  
t1=torquelimo;  
tln=t1;  
[r,c]=size(t1);  
for i=2:1:r %this loop converts in NaNs any value under -1e6  
    for j=2:1:c  
        if t1(i,j)>=-5e5  
            tln(i,j)=t1(i,j);  
        else  
            tln(i,j)=NaN;  
        end  
    end  
end  
tlnr=tln;
```

```

ma=max(tlnr(2:end,2:end));% find the max value in each column (that contains
the torque values for a fixed pitch angle)
for j=2:1:c %this loop substitutes with NaNs any value that is in the column
under the max value of that column
    for i=2:1:r-1
        if tlnr(i,j)==ma(1,j-1)
            for g=i:1:r-1
                tlnr(g+1,j)=NaN;
            end
        end
    end
end
[r,c]=size(tlnr);
for i=2:1:r
    for j=2:1:start-1
        tlnr(i,j)=NaN;
    end
end
end
end

```

MATLAB FUNCTION 5

```

%This function generates the variable make3 that hold the points of each
%run that are going to be moved up to form g(pitch*), new33 hold the values
%for the function g(v), and incrementx333 & incremnty333 hold the values
%for h(p)
function
[make,make3,new33,new3,xtround,make2,S,vec,I,vec2,pos,sop]=overlap3
load tlnr
load transformationreal2
value=input('Introduce rated torque in Nm \n');
make=NaN(size(tlnr));
make(1,:)=tlnr(1,:);%puts the pitch values in make
make(2:end,1)=tlnr(2:end,1);%puts the pitch* values in make
S=tlnr(2:end,2:end);

[V,I]=min(abs(S-value));%This piece finds the closest value to rated torque
in each column (for the torque values matrix), locates their position (the
row where is found) in vector I
%This piece is going to get rid from the I vector, the repeated positions

```

```

%as well as the higher index ones since the mean that I have no more useful
%data for making the add up later. This will be collected in vector II
[B,in]=max(I);%B has the max value of I and in indicates in which column is
located
II=NaN(size(I));
i=1;
h=0;
for j=1:1:in%it indicates de maximum value of I, that is, no need to worry
if ones start appearing at the end
    if I(1,j)~=I(1,j+1)
        II(1,i)=I(1,j);
        i=i+1;
    end
end
II=II(~isnan(II));
[blink,blonk]=size(tlnr);
for j=2:1:blonk-1
    if isnan(tlnr(2,j)) && isfinite(tlnr(2,j+1))
        h=j-1;
    end
end
h=h;
%%%%%%%%%
[row,col]=size(S);
[rrr,ccc]=size(II);
vec=NaN(size(S));
[rowI,colI]=size(I);
if II(1,1)==1
    %for j=h+1:1:ccc+h-1
    for j=h+1:1:in
        for i=1:1:row
            if i==I(1,j) && h~=0
                for g=j-1:1:j+1
                    vec(I(1,g),j)=S(I(1,g),j);
                end
            end
            if i==I(1,j) && h==0
                for g=j:1:j+1
                    vec(I(1,g),j)=S(I(1,g),j);
                end
            end
        end
    end
end
end

```

```

        end
    end
elseif II(1,1)~=1
    for j=h:1:ccc+h-1
        for i=1:1:row
            if i==I(1,j)&& h>1
                for g=j-1:1:j+1
                    vec(I(1,g),j)=S(I(1,g),j);
                end
            end
            if i==I(1,j) && h==1
                for g=j:1:j+1
                    vec(I(1,g),j)=S(I(1,g),j);
                end
            end
        end
    end
end
end
vec2=vec;
[rrrr,cccc]=size(vec);

for j=1:1:cccc%this loop completes the vector vec which due to the way it
was constructed could have missing values inside the interval of data of
interest (each column has an interval)
    for i=1:1:rrrr-5
        if
            ((isfinite(vec(i,j)))&&(isnan(vec(i+1,j)))&&(isnan(vec(i+2,j)))&&(isnan(vec
(i+3,j)))&&(isnan(vec(i+4,j)))&&(isfinite(vec(i+5,j))))
                vec(i+1,j)=S(i+1,j);
                vec(i+2,j)=S(i+2,j);
                vec(i+3,j)=S(i+3,j);
                vec(i+4,j)=S(i+4,j);
            end
        end
    end
end
for j=1:1:cccc
    for i=1:1:rrrr-4
        if
            ((isfinite(vec(i,j)))&&(isnan(vec(i+1,j)))&&(isnan(vec(i+2,j)))&&(isnan(vec
(i+3,j)))&&(isfinite(vec(i+4,j))))
                vec(i+1,j)=S(i+1,j);
            end
        end
    end
end

```

```

        vec(i+2,j)=S(i+2,j);
        vec(i+3,j)=S(i+3,j);
    end
end
end
for j=1:1:cccc
    for i=1:1:rrrr-3
        if
((isfinite(vec(i,j)))&&(isnan(vec(i+1,j)))&&(isnan(vec(i+2,j)))&&(isfinite(
vec(i+3,j))))
            vec(i+1,j)=S(i+1,j);
            vec(i+2,j)=S(i+2,j);
        end
    end
end
for j=1:1:cccc%this loop completes the vector vec which due to the way it
was constructed could have missing values inside the interval of data of
interest (each column has an interval)
    for i=1:1:rrrr-2
        if
((isfinite(vec(i,j)))&&(isnan(vec(i+1,j)))&&(isfinite(vec(i+2,j))))
            vec(i+1,j)=S(i+1,j);
        end
    end
end

[r,c]=size(I);
for j=1:1:c
    if I(1,j)>=2&&I(1,j+1)==1
        pos=j;
        sop=I(1,j);
    end
end

[r,c]=size(S);
if sop<r
    if S(sop,pos)<=value && S(sop+1,pos)>=value
        vec(sop+1,pos)=S(sop+1,pos);
    end
end
end
%%%%%%%%%%%%%%%%%%%%%%%%%%%%%%%%%%%%%%%%%%%%%%%%%%%%%%%%%%%%%%%%%%%%%%%%

```

```

% this piece of code aims to create make3 which holds the points that are
going to be moved with their correspondent pitch group and torque (matrix
form)
make(2:end,2:end)=vec(:, :);
make2=make;%This step serves the only purpose to be able to visualise the
vector before and after the changes, not really necessary
[r,c]=size(make2);
for j=2:1:c%this loop finds which is the first column with data, and from
there on, it finds in each column the first value below rated and the first
value above rated and keeps them, converting into NaN the other torque values
    if (isfinite(make2(2,j)) && isnan(make2(2,j+1)))
        for g=j:1:c
            for i=2:1:r-1
                if (make2(i,g)<=value && make2(i+1,g)>=value)
                    for ii=2:1:i-1
                        make2(ii,g)=NaN;
                    end
                    for ii=i+2:1:r
                        make2(ii,g)=NaN;
                    end
                end
            end
        end
    end
end
make3=make2;
[r,c]=size(make2);
for j=2:1:c%in the case there is a missing point to allow continuity, this
loop finds which is the column that should deliver that point. The column
that holds the closest value to equilibrium between the two columns in dispute
is the one that will provide. We are looking for column j to the above rated
value and for column j+1 the below rated value
    for i=2:1:r-1
        if isfinite(make2(i,j)) && isnan(make2(i+1,j))
            if abs(make2(i,j)-value)<abs(make(i,j+1)-value)
                make3(i+1,j)=make(i+1,j);
            else
                make3(i,j+1)=make(i,j+1);
            end
        end
    end
end

```

```

end
for j=2:1:c
    for i=2:1:r-1
        if isfinite(make3(i,j)) && isnan(make3(i+1,j))
            if abs(make3(i,j)-value)<abs(make(i,j+1)-value)
                make3(i+1,j)=make(i+1,j);
            else
                make3(i,j+1)=make(i,j+1);
            end
        end
    end
end
end
for j=2:1:c
    if isfinite(make3(r,j)) && make3(r,j)<value
        for i=2:1:r
            make3(i,j)=NaN;
        end
    end
end
end
%%%%%%%%%%%%%%%%%%%%%%%%%%%%%%%%%%%%%%%%%%%%%%%%%%%%%%%%%%%%%%%%%%%%%%%%
%this block serves to locate the pitch* position of the very equilibrium
point of each pitch run, but I'm really not using it, its just curiosity.
Even more I already know it (2,3,4...) it had sense in the old mode of
section moving, now is just a reaffirmation
[filas,colum]=size(make);
j=0;
i=0;
m=0;
for j=2:1:colum
    for i=2:1:filas-1
        if ((make(i,j)<value)&&(make(i+1,j)>value))
            x1(j)=make(i,1);
            x2(j)=make(i+1,1);
            y1(j)=make(i,j);
            y2(j)=make(i+1,j);
            m(j)=(y2(j)-y1(j))/(x2(j)-x1(j));
            c(j)=y1(j)-m(j).*x1(j);
            x(j)=(value-c(j))./m(j);%exact equilibrium pitch*
        end
    end
end
end

```

```

xt=transpose(x);
xtround=round(xt.*100)./100;
xtround=round(xtround.*10)./10;
xtround=round(xtround);
%%%%%%%%%%%%%%%%%%%%%%%%%%%%%%%%%%%%%%%%%%%%%%%%%%%%%%%%%%%%%%%%%%%%%%%%
% This block does the shifting of the fragments, the final position of all
the data points is in the new3 matrix which will become the function
g(V) (stored under variable new33)
incrementy3=NaN(1,1);
incrementy33=NaN(1,1);
new3(:,1)=make3(:,1);
new3(2:end,2)=make3(2:end,h+2);%this puts in new the values that are in make
in the first column that actually have numbers
[r,c]=size(make3);
z=NaN(1,1);
inc=NaN(1,1);
incrementx33=NaN(1,1);
for j=h+2:1:c
    for i=2:1:r-1
        if isfinite(make3(i,j)) && isnan(make3(i-1,j))
            z(j)=i;%this vector helps me to check that the program is looking
into the right positions
            incrementy3(j,1)=abs(new3(i,2)-
make3(i,j));%ATTENTION!!!!!!!!!!!!!!THIS INCREMENT IS PARTIAL EACH INCREMENT IS
HAVING AN EXTRA PIECE, THE BIT BETWEEN THE ORIGINAL POINT AND THE EQUILIBRIUM.
            incrementy33(j,1)=incrementy3(j,1)-(value-make3(i,j));%this is the value of
the vertical increment from the rated line at the same pitch* as the point
we are considering from make3 (this is excluding the piece that is of excess
in incrementy3)
            for ii=i:1:r
                new3(ii,2)=make3(ii,j)+incrementy3(j,1);
            end
        end
    end
end
for j=h+2
    incrementy3(j,1)=abs(new3(2,2)-make3(2,j));
    incrementy33(j,1)=incrementy3(j,1)+(value-make3(2,j));%here there is a +
sign instead of a - sign because this value is the first one and has not
been moved, so incrementy3 is 0 in consequence I have a problem with the
sign

```

```

end
%This section assembles the increments, necessary for getting h(p)---
>incrementx33 & incrementy33 hold the simple increments and incrementx333 &
incrementy333 the sum of them which allows for easy allocation while plotting
for j=h+2:1:c % c is columns of make3
    for i=3:1:r-1 % r is rows of make3
        if isnan(make3(i,j)) && isfinite(make3(i+1,j))
            inc(j,1)=make3(i+1,1);
        end
    end
end
end
inc(h+2,1)=make3(2,1);%!!!!!!CHECK in make3 for the column h+2 which is the
line that has the first number--> in this case line 2 so make3(2,1)
[r,c]=size(inc);
for j=h+3:1:r
    incrementx33(j,1)=inc(j,1)-inc(j-1,1);
end
incrementx33(h+2,1)=inc(h+2,1);
incrementy333(:,1)=inc(h+2:r,1);
incrementy33(:,1)=incrementy33(h+2:r,1).*(-1);

new3(:,1)=transformationreal2(:,1);%this is new3 but with the pitch*
changed back into wind velocities
new3(:,2)=new3(2:end,2);%just gets rid of some zeros that are not part of
the set of data
disp('Now get the equations of g(v) and h(p) and introduce them into
difference33')
%%%%%%%%%%%%%%%%%%%%%%%%%%%%%%%%%%%%%%%%%%%%%%%%%%%%%%%%%%%%%%%%%%%%%%%%

end

```

MATLAB FUNCTION 6

```

%This function calculates  $e=h(p)-g(v)$ , a gives back to ways to look at the
%data: as a full matrix with each e value related to the pitch and velocity
%value (as in the original torque table) or as a two column vector one
%holding the torque value and the other its respective value of e
function
[g5,h5,e5,e5f,v5,p5,t5,tau,tauf,errorMatrixTau,errorMatrixEps,errorMatrixEp
sP,errorMatrixTauP]=difference33

```

```

load transformationreal2
transformation=transformationreal2;
Trated=input('Introduce T rated \n');
lower=input('give the column number of the lower pitch of validity \n');
upper=input('give the column number of the upper pitch of validity \n');
load tlnr
make=tlnr;%it has pitch* values instead of velocities
velocities=vertcat(0,transformation(:,1));%this are the velocities that
correspond to the pitch* values

make2=horzcat(velocities,make(:,2:end));%holds the velocities with the
correspondent torque and pitch values, in a matrix (the usual matrix)
v=make2(2:end,1);%this vector holds the wind velocities
p=make2(1,2:end);%this vector holds the pitches
t=make2(2:end,2:end);%this vector holds the torque values
v5=v;%the following three lines are not really necessary, are just a result
of different version of the program, for not to overwrite
p5=p;
t5=t;

[rr,cc]=size(t);
g5=NaN(1,1);%the next three lines are initialising vectors
h5=NaN(1,1);
e5=NaN(1,1);
tau=NaN(1,1);
errorMatrixTau=NaN(1,1);
errorMatrixEps=NaN(1,1);
errorMatrixEpsP=NaN(1,1);
errorMatrixTauP=NaN(1,1);

for i=1:1:rr
    for j=1:1:cc
        if isfinite(t(i,j))%if the value at that coordinate is actually a
value

            g5(i,j)=-7114.*v(i,1)^2-
2.0465e+005.*v(i,1)+1.6399e+006;%Substitute by the g(v) function that you
want to use
            h5(i,j)=-14696.*p(1,j)^2-10140.*p(1,j)+1.9571e+005-
1.15e5;%Substitute by the h(p) function that you want to use

```

```

e5(i,j)=h5(i,j)-g5(i,j);

tau(i,j)=-2.2372e-021.*(e5(i,j))^4+1.8647e-
014.*(e5(i,j))^3+7.6695e-009.*(e5(i,j))^2+0.84856.*(e5(i,j))+1.5665e+005;%
substitute by the tau function that you want to use

errorMatrixTau(i,j)=abs(t(i,j)-tau(i,j));
errorMatrixTauP(i,j)=(errorMatrixTau(i,j)./Trated)*100;
errorMatrixEps(i,j)=abs(t(i,j)-e5(i,j));

errorMatrixEpsP(i,j)=(errorMatrixEps(i,j)./Trated)*100;
else
    e5(i,j)=NaN;%if the matrix torque doesn't have a value in a
position then neither e5 will hold a value, so we put a NaN instead
    tau(i,j)=NaN;
    errorMatrixTau(i,j)=NaN;
    errorMatrixTauP(i,j)=NaN;
    errorMatrixEps(i,j)=NaN;
    errorMatrixEpsP(i,j)=NaN;
end
end
end
e5=horzcat(transformation(:,1),e5);%this adds the wind velocities
e5=vertcat(make(1,:),e5);%this adds the pitches
tau=horzcat(transformation(:,1),tau);%this adds the wind velocities
tau=vertcat(make(1,:),tau);%this adds the pitches
errorMatrixTau=horzcat(transformation(:,1),errorMatrixTau);%this adds the
wind velocities
errorMatrixTau=vertcat(make(1,:),errorMatrixTau);%this adds the pitches
errorMatrixEps=horzcat(transformation(:,1),errorMatrixEps);%this adds the
wind velocities
errorMatrixEps=vertcat(make(1,:),errorMatrixEps);%this adds the pitches
errorMatrixEpsP=horzcat(transformation(:,1),errorMatrixEpsP);%this adds the
wind velocities
errorMatrixEpsP=vertcat(make(1,:),errorMatrixEpsP);%this adds the pitches
errorMatrixTauP=horzcat(transformation(:,1),errorMatrixTauP);%this adds the
wind velocities
errorMatrixTauP=vertcat(make(1,:),errorMatrixTauP);%this adds the pitches

```

```

[r,c]=size(e5);
e5f=NaN(1,2);%initialising vector
tauf=NaN(1,2);%initialising vector
k=1;
%d=0;
for j=lower:1:upper
    for i=2:1:r
        if isfinite(e5(i,j))
            e5f(k,2)=make(i,j);%torque values
            e5f(k,1)=e5(i,j);%correspondent e value for those torque values
            tauf(k,2)=make(i,j);%torque values
            tauf(k,1)=tau(i,j);%correspondent e value for those torque
values
            k=k+1;
        end
    end
end
end
end

```

MATLAB FUNCTION 7

%This function will use the outputs of Matlab function 7 to generate the error contour plots for the Separability property

```

load transformationreal
x=errorMatrixTauP(2:end,1);
y=errorMatrixTauP(1,5:24);
[X,Y]=meshgrid(x,y);
errorMatrixTauP(errorMatrixTauP < -10 | errorMatrixTauP > 10) = NaN;
errorMatrixTauPT= errorMatrixTauP';
figure
[C,h] = contour(X,Y, errorMatrixTauPT(5:24,2:end),[1 3 5 6 7
9], 'ShowText', 'on');
hold all
plot(transformationreal(:,1),transformationreal(:,2));

xx=errorMatrixEpsP(2:end,1);
yy=errorMatrixEpsP(1,5:24);
[XX,YY]=meshgrid(xx,yy);
errorMatrixEpsP(errorMatrixEpsP < -10 | errorMatrixEpsP > 10) = NaN;

```

```
errorMatrixEpsPT= errorMatrixEpsP';  
figure  
[Cc,hh] = contour(XX,YY, errorMatrixEpsPT(5:24,2:end),[1 3 5 7  
9], 'ShowText', 'on');  
hold all  
plot(transformationreal(:,1),transformationreal(:,2));
```